THE
PHYSICAL REVIEW

A journal of experimental and theoretical physics established by E. L. Nichols in 1893

Published by the American Institute of Physics
for the
AMERICAN PHYSICAL SOCIETY

Officers

President

H. A. BETHE
Cornell University
Ithaca, New York

Vice-President

R. T. BIRGE
University of California,
Berkeley, California

Secretary

K. K. DARROW
Bell Telephone Laboratories
Office:
Columbia University
New York 27, New York

Treasurer

G. B. PEGRAM
Columbia University
New York 27, New York

Local Secretary
for the Pacific Coast

J. KAPLAN
University of California at Los Angeles
Los Angeles, California

Managing Editor

S. A. GOUDSMIT
Brookhaven National Laboratory
Upton, Long Island
New York

BOARD OF EDITORS

Editor

S. A. GOUDSMIT

Assistant Editor

S. [illegible]

Associate Editors

1928–1937	1938–1947	1948–1957
J. M. ALLEN	W. A. FOWLER	P. G. KIRKPATRICK
[illegible]	KENNETH GREISEN	GREGORY BREIT
[illegible]	CHARLES KITTEL	E. J. [illegible]
[illegible]	R. E. MARSHAK	P. [illegible]
[illegible]	W. K. H. PANOFSKY	R. SMOLUCHOWSKI
[illegible]	V. F. WEISSKOPF	J. C. SLATER

Manuscripts for publication should be submitted to S. A. Goudsmit, Brookhaven National Laboratory, Upton, Long Island, New York. The Institutional are requested to pay a publication charge of $15 per page to publish, if accepted, entitles them to 100 free reprints. Instructions for with galley proofs.

and all correspondence concerning papers in the process of publication should be addressed to the Publication Manager, American Institute of Physics, 57 East 55 Street, New York 22, New York.

Subscription Price

United States and Canada $20.00
Foreign $22.00

Back Numbers[1]

Back numbers are sold when complete year is available:
Prior to 1929: $25.00
Current: $30.00
Single copies: $2.50 each, prior to July, 1929;
$3.00 each, July, 1929–December, 1941;
$3.50 each, January, 1942–December, 1946;
$4.00 each, thereafter.
Foreign postage, 1929–1946: $0.60.

Subscriptions, renewals, and orders for back numbers should be addressed to the American Institute of Physics, 57 East 55 Street, New York 22, New York.

Change of address: in the case of members of the American Physical Society, notice should be sent to the Treasurer; in the case of other subscribers to the American Institute of Physics.

[1] Address: Los Angeles, Physics Department, Cornell University, Ithaca, New York.

The Physical Review is published monthly at Prince and Lemon Streets, Lancaster, Pennsylvania.
Entered as second-class matter [illegible] Post Office at Lancaster, Pennsylvania, under the Act of March 3, 1879.
Acceptance for mailing at special rate of postage [illegible] provided for in paragraph (d-2) section 34.40, P. L. & R. of 1948, authorized January 31, [illegible]

THE
PHYSICAL REVIEW

A journal of experimental and theoretical physics established by E. L. Nichols in 1893

SECOND SERIES, VOL. 94, NO. 4 MAY 15, 1954

Magneto-Hydrodynamic Waves in Liquid Sodium

BO LEHNERT
Royal Institute of Technology, Stockholm, Sweden
(Received August 28, 1953)

Liquid sodium, because of its higher electrical conductivity and lower density, is more suitable than mercury for magneto-hydrodynamic experiments. Torsional waves in liquid sodium have been generated in a cylindrical vessel with the axis parallel to a homogeneous magnetic field, and resonance phenomena have been investigated at constant frequency and variable magnetic field strength. The agreement between theory and experiment is satisfactory. It is shown that even with sodium, damping plays an important role under laboratory conditions. The calculations of this paper are also used to improve the results of earlier investigations with mercury.

1. INTRODUCTION

DURING the last ten years the importance of magneto-hydrodynamic phenomena in cosmic physics has been realized in a great number of applications, such as solar physics, cosmic radiation, and the problem of oscillating stars. The investigations of general physical interest made by a number of authors is given in a survey by Lundquist.[1] By far the largest part of the work on magnetohydrodynamics is of a theoretical nature, and there exist only a few experimental investigations, all carried out with mercury.[2-4]

When the theory is applied to special problems in cosmic physics, an exact solution often leads to great mathematical difficulties. Thus, in addition to being a valuable verification of theory, the experimental work serves the purpose of solving problems associated with complicated geometrical configurations through model experiments in the laboratory.[5]

When treating an electrically conducting liquid in a magnetic field from both a theoretical and an experimental point of view, an analogy between magnetic field lines and elastic strings given by Alfvén[5,6] is often a convenient tool. A motion of the liquid perpendicular to the magnetic field gives rise to induced currents and an induced magnetic field. If the conductivity is infinite, the total magnetic field is "frozen in" and the fieldlines act as elastic strings "glued to" the elements of the liquid. This is true in many cosmic applications where the conductivity is high and the dimensions are large. Virtually undamped magneto-hydrodynamic waves are then propagated along the magnetic fieldlines with a velocity independent of frequency in much the same way as elastic waves along strings. However, under laboratory conditions, e.g., in experiments with mercury, the properties of the waves differ from those of "ideal waves," i.e., waves in a liquid with very large conductivity, both at low and high frequencies. The wavelength at low frequencies becomes much larger than the linear dimensions of the apparatus and the wave velocity depends on frequency. At high frequencies the inertia of the liquid becomes too large, and the waves are changed into strongly damped skin waves in a solid body, which also suffer from dispersion. If the conditions are favorable enough, however, there exists an intermediate "ideal" region of frequencies, where the waves are propagated with approximately constant velocity and moderate damping. The condition for such well developed magneto-hydrodynamic wave phenomena is[1,3]

$$BL\sigma\cdot(\mu/\rho)^{\frac{1}{2}}\gg 1, \qquad (1)$$

where B is the magnetic field strength,[7] L the linear di-

[1] S. Lundquist, Arkiv Fysik **5**, 297 (1952).
[2] J. Hartmann and F. Lazarus, Kgl. Danske Videnskab. Selskab, Mat.-fys. Medd. **15**, No. 6 (1937); J. Hartmann, Kgl. Danske Videnskab. Selskab, Mat.-fys. Medd. **15**, No. 7 (1937).
[3] S. Lundquist, Phys. Rev. **76**, 1805–1809 (1949).
[4] B. Lehnert, Arkiv Fysik **5**, No. 5, 69 (1952); Tellus **4**, No. 1, 63 (1952).
[5] H. Alfvén, *Cosmical Electrodynamics* (Oxford University Press, London, 1950).
[6] H. Alfvén, Arkiv mat. astron. fysik **B29**, No. 2 (1942).
[7] Mks units are used throughout this paper. The unit for magnetic field strength is volt sec/m^2 = 10^4 gauss.

TABLE I. Values of the left-hand side of the inequality (1) at different applications. Large values of this quantity correspond to states of motion greatly influenced by electrodynamic forces.

Application	B (volt sec m^{-2})	L (m)	σ (Ω^{-1} m^{-1})	ρ (kg m^{-3})	$BL\sigma\cdot(\mu/\rho)^{\frac{1}{2}}$
Experiments with mercury	1	0.1	10^6	13 600	1
Experiments with liquid sodium	1	0.1	14×10^6	970	50
Sunspots	0.01	10^8	10^8	10^3	3×10^6
Magnetic variable star	1	10^{10}	10^8?	10^3?	3×10^{11}?
Interstellar space	10^{-12}?	10^{22}	10^3?	10^{-21}?	3×10^{19}?

mensions, σ the electric conductivity, ρ the density, and μ the (absolute) permeability. Some possible values of the left-hand side of the expression (1) are given in Table I. It is shown in the table that cosmic conditions are far from being realized in laboratory experiments. Nevertheless the conditions of the experiments with sodium, described in this paper, are improved to such an extent compared to earlier experiments with mercury that it has been worth while to make an experimental investigation with liquid sodium.

The following sections will give an account of some experimental and theoretical investigations of magnetohydrodynamic waves in liquid sodium in the "ideal" region. Section 2 gives a description of the experimental equipment, and a theory of cylindrical waves is presented in Sec. 3. The results are discussed in Sec. 4, and an application to earlier measurements is given in Sec. 5.

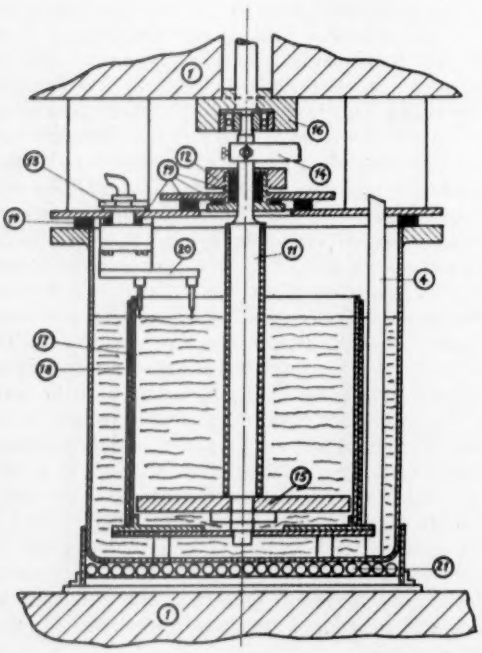

FIG. 1. Outline of the vessel where the waves are generated. 1—Magnet with pole shoes. 4—Pipe for sodium. 11—Axis, isolated with a glass cylinder. 12—Box with packing. 13—Duct bolt. 14—Driving arm. 15—Copper disk. 16—Holder with ball bearing. 17—Cylinder made of brass. 18—Layer of glass tape and silicone resin. 19—Packings of rubber. 20—Probes with holder. 21—Heater.

2. THE EXPERIMENT

(i) The Apparatus

In the experiment, torsional waves are generated in an insulated column of liquid sodium (Fig. 1) placed in a homogeneous, axial magnetic field the strength of which is varied in the range 0.3–1 volt sec/m^2. A copper disk at the bottom of the column is set into oscillations about a vertical axis and generates torsional magnetohydrodynamic waves which are propagated through the liquid along the magnetic field lines to the free surface. There they give rise to an electric potential difference, which is measured by two probes. A frequency of 30 cps has been used.

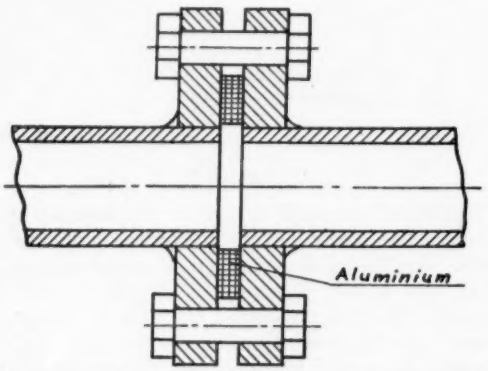

FIG. 2. Joint between two parts of the pipe containing sodium.

To keep the surface of the liquid clean and prevent fire, the interior of the apparatus contains an atmosphere of pure nitrogen. The details are made of nonmagnetic materials, which are not chemically attacked by liquid sodium. Thus the vessels and pipes are made of stainless (nonmagnetic) steel, and the packings in the pipe containing sodium are made of aluminum (Fig. 2). Brass has been chosen with good result for details which are unimportant as regards security and which are not subject to considerable mechanical strain. As shown, e.g., in Fig. 1 all packings not in direct contact with sodium are made of temperature-resistant rubber. A nonconducting surface as that of the inner cylinder in Fig. 1 is obtained by coating a cylinder of brass with glass tape and silicone resin, baked for about 3 hours at 250°C.

Figure 3 is a diagram showing the arrangement of the apparatus. The liquid sodium in the vessel A, which is placed in the magnetic field, is taken from the reservoir B through the pipe C. The levels in the vessels are regulated through the taps J with nitrogen from the

tube *E*. The gas is cleaned in the tube *F* containing pulverized copper at 250°C. The heaters keep the vessels and the middle pipe at about 120°C, controlled by the thermo elements *G*. The parts containing sodium are shielded by sand as shown by the lined regions in Fig. 3. The position of the surface is indicated by signal lamps *H*.

The copper disk at the bottom is set into oscillations through an eccentric shaft, driven by a motor. The vessel in Fig. 1 is strapped between the pole shoes to prevent shaking.

When handling the apparatus, the author wore asbestos clothing as a safety precaution.

(ii) The Method of Measurement

The potential difference at the surface of the liquid is measured by probes placed as shown in Fig. 4. The impedance of the external circuit is very large compared to that of the liquid. Since the diameter of the probes is

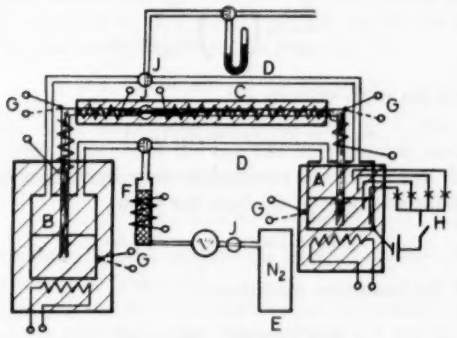

FIG. 3. Sodium system in outline. *A*—Vessel placed in magnetic field. *B*—Reservoir. *C*—Pipe for sodium. *D*—Pipes for nitrogen. *E*—Tube for nitrogen. *F*—Gas-cleaning equipment. *G*—Thermo elements. *H*—Signal lamps. *J*—Taps.

only 0.5 mm, the disturbance caused by the measuring equipment is assumed to be negligible. Above the surface (medium III, which also contains the wires) a homogeneous, axial magnetic field $\mathbf{B}_0$ is assumed since the displacement current can be neglected at low frequencies, and it is shown in Sec. 3 (ii) that the induced currents give no external magnetic field.

The closed paths *ACEDBA*, *ACFDBA*, and *CEDFC* are called C, C_2, and C_1, respectively, where *CFD* has been chosen immediately under the surface and *CED* is an arbitrary path in the liquid. Since the electric field is

$$\mathbf{E}=-\nabla V-\partial\mathbf{A}/\partial t,$$

we have

$$\oint_{C_2}\mathbf{E}\cdot\mathbf{ds}=-\frac{\partial}{\partial t}\oint_{C_2}\mathbf{A}\cdot\mathbf{ds}=-\frac{\partial}{\partial t}\int\int_{C_2}\mathbf{n}\cdot\mathbf{B}_0 dS=0. \quad (2)$$

Further,

$$\mathbf{E}_{III}=-\nabla V_{III},$$

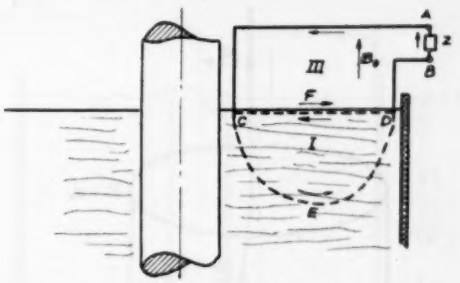

FIG. 4. Calculation of the potential difference between the probes at the surface of a moving liquid in a homogeneous magnetic field $\mathbf{B}_0$. *Z* is the impedance of the external circuit.

which results in a measured potential difference

$$V_{BA}=\int_{CFD}\mathbf{E}\cdot\mathbf{ds}, \quad (3)$$

if the potential drop in the wires is neglected. The same result is deduced for the arbitrary path C, since

$$\oint_{C_1}\mathbf{E}\cdot\mathbf{ds}=\oint_{C}\mathbf{E}\cdot\mathbf{ds}=\int_{CED}\mathbf{E}\cdot\mathbf{ds}+V_{BA}$$

due to Eq. (2), and Eq. (3) is obtained from the first and last member.

The measurements are carried out with the arrangement shown in Fig. 5. The amplitude of the potential difference V_{BA} is measured with the switch J in "direct" position. The amplified signal is measured with a harmonic wave analyzer *H*. The cathode-ray tube *G* and the wave analyzer *H* are adjusted to the right frequency with the oscillator *F*, whereupon the excited frequency in the vessel *A* is adjusted until the pattern on the tube *G* is stationary.

The phase of the potential difference V_{BA} at the surface is measured with the compensating apparatus shown in the lower left-hand corner of Fig. 5, when the switch J is in the upper position. The eccentric shaft *B* affects the strain gauge *C* giving rise to a compensating voltage over the resistance R_2. The phase of the voltage

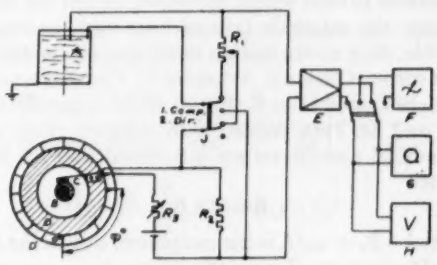

FIG. 5. Diagram of the method of measurement: *A*—Vessel with probes. *B*—Axis with eccentric shaft. *C*—Strain gauge. *D*—Holder. *D'*—Scale. *E*—Amplifier. *F*—Signal generator. *G*—Cathode-ray oscillograph. *H*—Harmonic wave analyzer.

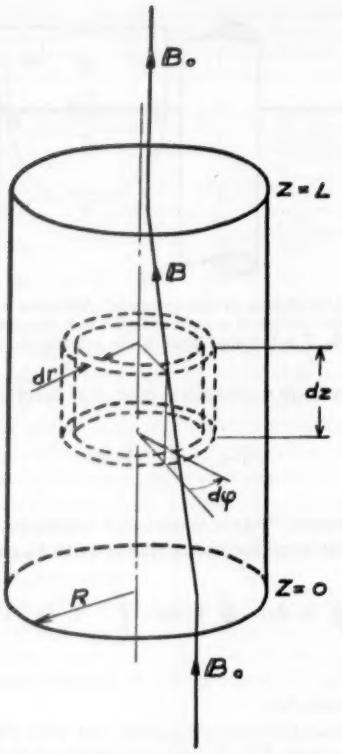

FIG. 6. Twisting of a cylindrical column of liquid with infinite conductivity placed in an axial homogeneous magnetic field $\mathbf{B}_0$.

at the surface is given by the scale D' when the holder D and resistance R_3 are adjusted to give the resulting voltage zero at H. The zero point of the scale D' is determined at maximum magnetic field (1 volt sec/m²) and lowest possible frequency (about 5 cps).

3. THEORY OF THE EXPERIMENT

(i) Cylindrical Waves at Infinite Conductivity

Before an exact treatment is carried out let us consider a simple example in a liquid with density ρ and infinite electrical conductivity. If a magnetic field $\mathbf{B}_0$ is assumed to exist within the liquid, no relative motion between the magnetic lines of force and the liquid is possible, since such a motion would give rise to infinitely large currents (see, e.g., reference 5). Consider a column of height L and radius R (Fig. 6), which is parallel to the field and has been twisted with constant pitch φ_0/L. Cylindrical coordinates are introduced, and the field is written

$$\mathbf{B}=(0,b,B_0),$$

where $b=B_0\cdot r\cdot\varphi_0/L$ is the component due to the twisting. The increase of magnetic energy is

$$U=\int_0^R (b^2/2\mu)\cdot L2\pi r dr=(B_0^2/2\mu)\cdot\tfrac{1}{2}\pi R^2\cdot\varphi_0^2/L. \quad (4)$$

From the theory of elasticity it is known that the corresponding expression for the torque of an elastic rod with a modulus G of torsional rigidity is

$$M=G\cdot\tfrac{1}{2}\pi R^4\cdot\varphi_0/L \quad (5)$$

and the potential energy

$$U=\int_0^{\varphi_0} M\cdot d\varphi=G\cdot\tfrac{1}{2}\pi R^4\cdot\tfrac{1}{2}\varphi_0^2/L. \quad (6)$$

From the results (4) and (6) we define an equivalent modulus

$$G_{eq}=B_0^2/\mu. \quad (7)$$

The dynamic equation of a disk with height dz is given by (5):

$$G_{eq}\cdot\tfrac{1}{2}\pi R^4\cdot\frac{\partial^2\varphi}{\partial z^2}=\frac{\partial}{\partial t}\left[\int_0^R r^2\cdot\frac{\partial\varphi}{\partial t}\rho\cdot 2\pi r\cdot dr\right],$$

which becomes

$$\frac{\partial^2\varphi}{\partial t^2}=\left(\frac{G_{eq}}{\rho}\right)\cdot\frac{\partial^2\varphi}{\partial z^2}, \quad (8)$$

where the wave velocity is

$$V=(G_{eq}/\rho)^{\frac{1}{2}}=B_0/(\mu\rho)^{\frac{1}{2}}. \quad (9)$$

If all quantities are assumed to vary harmonically in time the solutions of (8) have the form

$$\varphi=[Ae^{j\omega z/V}+Be^{-j\omega z/V}]e^{j\omega t}.$$

If the boundary conditions,

$$\varphi(0,t)=\varphi_0 e^{j\omega t} \quad \text{at} \quad z=0$$

and

$$M(L,t)=0 \quad \text{at} \quad z=L,$$

are imposed we get the motion at the free surface $z=L$ of a column of liquid which is in a state of torsional oscillations with a given amplitude at the bottom, $z=0$:

$$\varphi(L,t)=\varphi_0 e^{j\omega t}/\cos(\omega L/V). \quad (10)$$

(ii) Cylindrical Waves with Negligible Viscous Damping

The notations shown in Fig. 7 are used in the calculations of the waves generated in the apparatus described in Sec. 2. The column of sodium (region I), which has the electrical conductivity σ_1 and density ρ, is bounded at the nonconducting surfaces $r=r_0$ and $r=R$. The copper disk at the bottom (region II) has the conductivity σ_2 and thickness δ. Since the viscosity can be omitted[3] the following boundary conditions are imposed:

(1) The radial component i_r of current density vanishes at $r=R$ in regions I and II and at $r=r_0$ in region I.

(2) The axial component, i_z, vanishes at the surface $z=L$.

(3) The result of the following analysis shows that the influence of the sodium layer between the disk and the bottom is equivalent to a slight increase in the thickness δ. Thus the boundary condition at the bottom is approximated to

$$i_z(r, -\delta, t)=0.$$

(4) The solutions in regions I and II are fitted at the boundary $z=0$, where the axial component i_z and the tangential components h_φ and E_z are continuous. h_φ is the induced magnetomotive force ($\mathbf{b}=\mu\mathbf{h}$).

(5) The mechanical influence of the axis is estimated with the results of Sec. 2. At a magnetic field strength $B_0=1$ Vs/m^2 the equivalent modulus of rigidity is

$$G_{Na}=B_0^2/\mu=7.80\times10^5 \text{ newtons/m}^2,$$

whereas an axis made of steel has a modulus of about

$$G_a=7.85\times10^{10} \text{ newtons/m}^2.$$

In this case we have $R=0.068$ m and the radius of the axis $r_a=0.010$ m. At a given twisting, $\partial\varphi/\partial z$, the ratio of the corresponding torques is given by (5):

$$M_{Na}/M_a=(R/r_a)^4\cdot G_{Na}/G_a=0.02.$$

Thus, with the dimensions given in Fig. 7, the mechanical influence of the axis can be neglected, and the velocity of the copper disk is

$$v^{(II)}=v_0\cdot(r/R)\cdot e^{j\omega t}=\Omega_0 r e^{j\omega t}, \tag{11}$$

where Ω_0 is the peak value of the angular velocity of the axis and ω the frequency.

A general treatment of magneto-hydrodynamic waves has been given in earlier works[1,8] and will not be described in detail here. If the liquid and the disk in Fig. 7 are assumed to oscillate around the axis of symmetry and a homogeneous magnetic field $\mathbf{B}_0=\mu\mathbf{H}_0$, parallel with the axis, is generated by external sources, then an induced emf. will arise in a direction perpendicular to the axis. Thus the induced currents will flow in planes through the axis and the induced magnetic field is parallel with the particle velocity. It is shown in the following that the induced magnetic field disappears at the free surface and the bottom of the vessel (see Fig. 7), and the total magnetic field becomes homogeneous all over the region outside the vessel [see Sec. 2 (ii)]. The general solution of a cylindrically symmetric state of torsional oscillations with frequency ω is discussed in the system of cylindrical coordinates given by Fig. 7:

$$\begin{aligned}&\partial/\partial\varphi=0, \quad \partial/\partial t=j\omega,\\ &\mathbf{v}=(0,v,0), \quad \mathbf{h}=(0,h,0), \quad \mathbf{H}_0=(0,0,H_0),\\ &\mathbf{i}=(i_r,0,i_z), \quad \mathbf{E}=(E_r,0,E_z), \quad \mathbf{H}=\mathbf{H}_0+\mathbf{h},\end{aligned} \tag{12}$$

where $\mathbf{v}$ is the velocity of the liquid and $\mathbf{b}=\mu\mathbf{h}$ the induced magnetic field. At low frequencies the displacement current can be neglected, and the fundamental

[8] C. Walén, Arkiv mat. astron. fysik **A30**, No. 15 (1944).

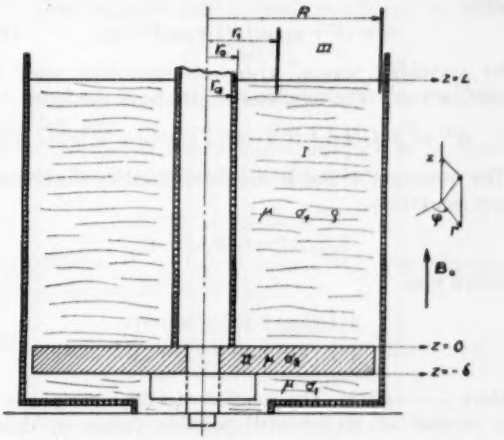

FIG. 7. Notation and starting points for the calculation described in Sec. 3. Inner radius of the outer, nonconducting cylinder and position of outer probe, $R=6.8$ cm. Outer radius of glass cylinder at the axis, $r_0=1.2$ cm. Position of inner probe, $r_1=3.2$ cm. Radius of axis, made of stainless steel, $r_a=1$ cm. Height of the column of liquid sodium, $L=10.5$ cm. Thickness of the copper disk at the bottom, $\delta=1$ cm.

equations at constant permeability μ are

$$\begin{aligned}&\text{curl}\mathbf{h}=\mathbf{i},\\ &\text{curl}\mathbf{E}=-\mu\partial\mathbf{h}/\partial t,\\ &\text{div}\mathbf{h}=0,\\ &\mathbf{i}=\sigma[\mathbf{E}+\mu\cdot(\mathbf{v}\times\mathbf{H})].\end{aligned} \tag{13}$$

In the liquid, which is incompressible, are added the conditions

$$\begin{aligned}&\rho\frac{d\mathbf{v}}{dt}=\mu\cdot(\mathbf{i}\times\mathbf{H})-\text{grad}p,\\ &\text{div}\mathbf{v}=0,\end{aligned} \tag{14}$$

where p is the hydrostatic pressure. In the copper disk the condition expressed in Eq. (11) is added to the system (13). The solution at small amplitudes is:

Solution in Region I

The equations for cylindrical waves are deduced from the expressions (13) and (14):[9]

$$\begin{aligned}&\frac{\partial^2 h}{\partial t^2}=\frac{1}{\mu\sigma_1}\cdot\frac{\partial}{\partial t}\left[\frac{\partial^2 h}{\partial r^2}+\frac{1}{r}\frac{\partial h}{\partial r}-\frac{h}{r^2}+\frac{\partial^2 h}{\partial z^2}\right]+V^2\frac{\partial^2 h}{\partial z^2},\\ &\frac{\partial v}{\partial t}=(\mu H_0/\rho)\cdot\frac{\partial h}{\partial z}, \quad V^2=(\mu/\rho)\cdot H_0^2.\end{aligned} \tag{15}$$

The first equation has the form

$$\frac{\partial^2 h}{\partial r^2}+\frac{1}{r}\frac{\partial h}{\partial r}+\left(k^2-\frac{1}{r^2}\right)h=0, \tag{16}$$

with

$$\gamma^2=(k^2+j\omega\mu\sigma_1)/(1+\mu\sigma_1V^2/j\omega), \tag{17}$$

for travelling waves, where all quantities vary as $\exp(j\omega t+\gamma z)$. The solutions of (16) have the form

$$h^{(\mathrm{I})}=[A'J_1(kr)+B'N_1(kr)][C'e^{\gamma z}+e^{-\gamma z}]e^{j\omega t}. \tag{18}$$

The constants A' and B' are determined by the boundary conditions

$$i_r(r_0,z,t)=i_r(R,z,t)=0,$$

which give

$$\begin{aligned} A'J_1(kr_0)+B'N_1(kr_0)&=0,\\ A'J_1(kR)+B'N_1(kR)&=0, \end{aligned} \tag{19}$$

since $i_r=-\partial h/\partial z$. The solution of (19) corresponds to a number of modes with possible values k_ν determined by

$$J_1(k_\nu r_0)N_1(k_\nu R)-J_1(k_\nu R)N_1(k_\nu r_0)=0. \tag{20}$$

The condition at the surface,

$$i_z(r,L,t)=0,$$

gives the relation

$$C'e^{\gamma L}+e^{-\gamma L}=0, \tag{21}$$

since

$$i_z=\frac{1}{r}\frac{\partial}{\partial r}(rh).$$

If we introduce

$$Z_1(k_\nu r)=J_1(k_\nu r)-\frac{J_1(k_\nu r_0)}{N_1(k_\nu r_0)}N_1(k_\nu r) \tag{22}$$

and B' is eliminated by means of Eq. (19), a particular solution of (16) becomes

$$h^{(\mathrm{I})}=A'Z_1(k_\nu r)e^{-\gamma L}[e^{\gamma(L-z)}-e^{-\gamma(L-z)}]e^{j\omega t}. \tag{23}$$

Finally, from the expressions (13) and (15),

$$E_r=i_r/\sigma_1-\mu H_0v, \quad v=(\mu H_0/j\omega\rho)(\partial h/\partial z). \tag{24}$$

Thus the general solution in region I has the form

$$\begin{aligned} h^{(\mathrm{I})}&=\sum_{\nu=1}^{\infty}A_\nu^{(\mathrm{I})}Z_1(k_\nu r)\sinh[\gamma_\nu(L-z)]e^{j\omega t},\\ i_z^{(\mathrm{I})}&=\sum_{\nu=1}^{\infty}k_\nu A_\nu^{(\mathrm{I})}Z_0(k_\nu r)\sinh[\gamma_\nu(L-z)]e^{j\omega t},\\ E_r^{(\mathrm{I})}&=\sum_{\nu=1}^{\infty}(\gamma_\nu/\sigma_1)(1+\mu\sigma_1V^2/j\omega)A_\nu^{(\mathrm{I})}Z_1(k_\nu r)\\ &\qquad\times\cosh[\gamma_\nu(L-z)]e^{j\omega t},\\ v^{(\mathrm{I})}&=\sum_{\nu=1}^{\infty}-(\mu H_0\gamma_\nu/j\omega\rho)A_\nu^{(\mathrm{I})}Z_1(k_\nu r)\\ &\qquad\times\cosh[\gamma_\nu(L-z)]e^{j\omega t}. \end{aligned} \tag{25}$$

Solution in Region II

From the fundamental equations (13) and the condition (11), the equations for region II are deduced

$$\begin{aligned} -\partial h/\partial z&=\sigma_2E_r+\mu\sigma_2H_0v,\\ -\partial^2h/\partial z^2&=\sigma_2\partial E_r/\partial z, \end{aligned}$$

and

$$\frac{1}{r}\frac{\partial}{\partial r}(rh)=\sigma_2E_z,$$

which is combined with

$$\frac{\partial E_r}{\partial z}=\frac{\partial E_z}{\partial r}-j\omega\mu h,$$

giving

$$\frac{\partial^2h}{\partial r^2}+\frac{1}{r}\frac{\partial h}{\partial r}-\frac{h}{r^2}+\frac{\partial^2h}{\partial z^2}-\mu\sigma_2\frac{\partial h}{\partial t}=0. \tag{26}$$

Equation (26) is also obtained by putting $\rho=\infty$, $V=0$ in the first expression (15).

A separation in the usual manner leads to the particular solution

$$h^{(\mathrm{II})}=[A''J_1(kr)+B''N_1(kr)][C''e^{\kappa z}+e^{-\kappa z}]e^{j\omega t}, \tag{27}$$

where

$$\kappa^2=k^2+j\omega\mu\sigma_2. \tag{28}$$

A small error is committed in neglecting the currents in the region $r<r_0$ at the junction of the disk and the axis. With this approximation the radial boundary conditions become the same as in region I, and the modes are given by (20). With

$$i_z(r,-\delta,t)=0,$$

an analogous treatment gives the general solution in region II:

$$\begin{aligned} h^{(\mathrm{II})}&=\sum_{\nu=1}^{\infty}A_\nu^{(\mathrm{II})}Z_1(k_\nu r)\sinh[\kappa_\nu(z+\delta)]e^{j\omega t},\\ i_z^{(\mathrm{II})}&=\sum_{\nu=1}^{\infty}k_\nu A_\nu^{(\mathrm{II})}Z_0(k_\nu r)\sinh[\kappa_\nu(z+\delta)]e^{j\omega t},\\ E_r^{(\mathrm{II})}&=\sum_{\nu=1}^{\infty}-(\kappa_\nu/\sigma_2)A_\nu^{(\mathrm{II})}Z_1(k_\nu r)\cosh[\kappa_\nu(z+\delta)]e^{j\omega t}\\ &\qquad-\mu H_0\Omega_0re^{j\omega t},\\ v^{(\mathrm{II})}&=\Omega_0re^{j\omega t}. \end{aligned} \tag{29}$$

The velocity distribution v_{II} is now developed into modes

$$\Omega_0r=\sum_{\nu=1}^{\infty}W_\nu Z_1(k_\nu r); \quad r_0\leqq r\leqq R. \tag{30}$$

From the orthogonality relations the coefficients W_ν are

derived in the usual manner:[9]

$$W_\nu = -2\cdot\frac{\Omega_0 R}{k_\nu R Z_0(k_\nu R)} \times\frac{1-(r_0/R)^2[Z_0(k_\nu r_0)/Z_0(k_\nu R)]}{1-(r_0/R)^2[Z_0(k_\nu r_0)/Z_0(k_\nu R)]^2}. \quad (31)$$

Fitting of the Solutions at the Boundary $Z=0$

The field quantities i_z, E_r, and h of the νth partial wave given by (25) and (29) are fitted at the boundary $z=0$:

$$A_\nu^{(\mathrm{I})}\sinh(\gamma_\nu L)=A_\nu^{(\mathrm{II})}\sinh(\kappa_\nu\delta),$$
$$(\gamma_\nu/\sigma_1)(1+\mu\sigma_1 V^2/j\omega)A_\nu^{(\mathrm{I})}\cosh(\gamma_\nu L) = -(\kappa_\nu/\sigma_2)A_\nu^{(\mathrm{II})}\cosh(\kappa_\nu\delta)-\mu H_0 W_\nu. \quad (32)$$

If

$$\lambda_\nu^2 = k_\nu^2 + j\omega\mu\sigma_1 \quad (33)$$

is introduced and Eq. (32) is solved for $A_\nu^{(\mathrm{I})}$, the velocity in the liquid is given by (25):

$$v^{(\mathrm{I})}=\sum_{\nu=1}^{\infty} W_\nu Z_1(k_\nu r)\frac{\cosh[\gamma_\nu(L-z)]}{\cosh(\gamma_\nu L)}F_\nu e^{j\omega t}, \quad (34)$$

where

$$\frac{1}{F_\nu}=\left(1+\frac{j\omega}{\mu\sigma_1 V^2}\right)\left(1+\frac{\sigma_1}{\sigma_2}\frac{\gamma_\nu\kappa_\nu}{\lambda_\nu^2}\frac{\tanh(\gamma_\nu L)}{\tanh(\kappa_\nu\delta)}\right). \quad (35)$$

The result is illustrated by some special cases.

1. If the conductivities σ_1 and σ_2 tend to infinity, we have

$$\gamma_\nu = j\omega/V \quad \text{and} \quad F_\nu = 1.$$

Thus

$$v^{(\mathrm{I})}=\Omega_0 r\frac{\cos[(L-z)/V]}{\cos[\omega L/V]}e^{j\omega t},$$

which is the expression for an ideal column of liquid discussed in Sec. 2 (see also the discussion of convergence at the end of this paragraph).

2. With finite conductivities and vanishing thickness of the disk, $v^{(\mathrm{I})}$ tends to zero.

3. If the magnetic field B_0 tends to infinity, we have

$$v^{(\mathrm{I})}=\Omega_0 r e^{j\omega t},$$

and the liquid behaves like a solid attached to the disk at the bottom.

4. If the disk at the bottom is assumed to be ideal ($\sigma_2=\infty$), the factors F_ν tend to the value

$$F_\nu = 1/(1+j\omega/\mu\sigma_1 V^2).$$

In particular, if $r_0=0$ and $\omega/\mu\sigma_1 V^2 \ll 1$, the formula given by Lundquist[3] is obtained:

$$v^{(\mathrm{I})}=\Omega_0 R\sum_{\nu=1}^{\infty}\frac{2J_1(k_\nu r)}{k_\nu r J_2(k_\nu R)}\frac{\cosh[\gamma_\nu(L-z)]}{\cosh(\gamma_\nu L)}e^{j\omega t}. \quad (36)$$

Indicated Potential Difference at the Surface

The potential difference between the probes at the points $r=r_1$ and $r=R$ is

$$V_{r_1 R}=\int_{r_1}^{R} E_r^{(\mathrm{I})}dr,$$

as shown in Sec. 2 (ii), Eq. (3). Since

$$E_r^{(\mathrm{I})} = -(1+j\omega/\mu\sigma_1 V^2)B_0 v^{(\mathrm{I})}$$

and

$$\int_{r_1}^{R} Z_1(k_\nu r)dr = -(1/k_\nu)[Z_0(k_\nu r)]_{r_1}^{R},$$

the voltage at the surface is found by integrating (34):

$$V_{r_1 R}=(1+j\omega/\mu\sigma_1 V^2)B_0\sum_{\nu=1}^{\infty}(W_\nu/k_\nu) \times[Z_0(k_\nu R)-Z_0(k_\nu r_1)]F_\nu e^{j\omega t}/\cosh(\gamma_\nu L). \quad (37)$$

The asymptotic value for $B_0\to\infty$ is

$$V_{r_1 R}(B_0\to\infty)\to-\Omega_0 B_0\tfrac{1}{2}(R^2-r_1^2),$$

from which a normalized voltage $U=V_{r_1 R}/V_{r_1 R}(B_0\to\infty)$ is defined:

$$U=\underbrace{(1+j\omega/\mu\sigma_1 V^2)}_{(a)}\cdot\underbrace{\frac{4}{1-(r_1/R)^2}}_{(b)}\cdot\sum_{\nu=1}^{\infty}\underbrace{\frac{1-Z_0(k_\nu r_1)/Z_0(k_\nu R)}{(k_\nu R)^2}}_{(c)}\cdot\underbrace{\frac{1-(r_0/R)^2[Z_0(k_\nu r_0)/Z_0(k_\nu R)]}{1-(r_0/R)^2[Z_0(k_\nu r_0)/Z_0(k_\nu R)]^2}}_{(d)}\cdot\underbrace{F_\nu e^{j\omega t}/\cosh(\gamma_\nu L)}_{(e)}, \quad (38)$$

where F_ν are given by (35) and the expression (31) for W_ν has been used. The factor (a) is due to the finite conductivity of the liquid forming a part of the measuring circuit, (b) and (c) are due to the position of the inner probe and the special radial velocity distribution which has been chosen, and (d) corresponds to the finite radius of the axis; (e) is the "axial" factor, where F_ν represents the efficiency of the generating mechanism and $1/\cosh(\gamma_\nu L)$ is the factor of main interest which can give rise to resonance phenomena. This factor reduces to $1/\cos(\omega L/V)$ in an ideal liquid.

Discussion of the Convergence

With the asymptotic formulas for $J_\nu(k_\nu r)$, $N_\nu(k_\nu r)$ and the roots k_ν (see the tables by Jahnke-Emde[9]), it is easily shown that the remainders, v_n and U_n,

[9] E. Jahnke and F. Emde, *Tables of Functions* (Dover Publications, New York, 1945).

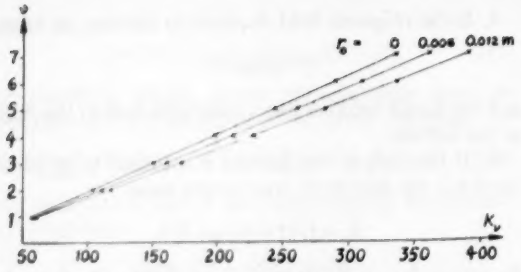

FIG. 8. Values of k_ν as given by (20) for three values of outer radius r_0 of the axis. $r_0=0$ corresponds to the equations $J_1(k_\nu R)=0$.

after n terms of the series (34) and (38) tend to the limits

$$v_n \to \text{const} \sum_{\nu=n}^{\infty} (1/\nu)\sin(\nu\theta) \times[(r_0/R)^{\frac{1}{2}}+(-1)^\nu]F_\nu \exp[-(a+jb)\nu z/L],$$

$$U_n \to \text{const}(1+j\omega/\mu\sigma_1 V^2) \sum_{\nu=n}^{\infty} (1/\nu)^2 \cos(\nu\theta_1) \times[(r_0/R)^{\frac{1}{2}}+(-1)^\nu]F_\nu \exp[-(a+jb)\nu],$$

where $a(\geqslant 0)$ and b are functions of σ_1, V, ω and $\lim a=\lim b=0$ when $\sigma_1\to\infty$ and $\theta=\pi(r-r_0)/(R-r_0)$, $\theta_1=\pi(r_1-r_0)/(R-r_0)$. The remainders are uniformly convergent, even in the limiting case $\sigma_1=\infty$ (see, e.g., Titchmarsh[10] and Hardy[11]).

4. RESULTS OF THE CALCULATIONS AND MEASUREMENTS IN LIQUID SODIUM

The linear dimensions of the apparatus are given in Fig. 7. A magnetic field strength in the range $B_0=0.3-1.0$ volt sec/m^2 and a frequency $\omega=188.5$ sec^{-1} (30 cps) corresponds to a region containing the first resonance of the ideal column of liquid. The temperature is kept at 120°C, corresponding to $\sigma_1=94.0\times10^6$ Ω^{-1} m^{-1} for liquid sodium and $\sigma_2=40.6\times10^6$ Ω^{-1} m^{-1} for copper, and the density of sodium is $\rho=970$ kg/m^3. The axis has been oscillating with a peak angular velocity $\Omega_0=3.84$ sec^{-1}, corresponding to a voltage of the order 10^{-2} volt between the axis and periphery at the bottom when $B_0=1$ volt sec/m^2.

The values k_ν from (20) are shown in Fig. 8. It is seen that they are only slightly modified in the range of values r_0 of the axis given by the figure.

Figures 9(a) and 9(b) show the depth of penetration $1/\alpha_\nu$ and phase velocity ω/β_ν for the five first modes, when the magnetic field is varied. $\gamma_\nu=\alpha_\nu+j\beta_\nu$ is given by (17).

The "axial" factors,

$$S_\nu=F_\nu/\cosh(\gamma_\nu L) \qquad (39)$$

[see Eq. (38)], are shown in Figs. 10(a) and 10(b), where the dotted lines mark the result when the influence of finite conductivity and thickness of the copper disk is neglected ($F_\nu=1$).[12] Thus the influence of the disk is rather small in the actual case. Further, the damping of the waves prevents a formation of resonance maxima of higher order at increasing values of $1/B_0$. The phase difference between bottom and surface [Fig. 10(b)] increases nearly linearly even for the first mode, contrary to the jump of 180° at the resonance when the conductivity is infinite.

The resulting normalized voltage at the surface according to (38) is shown in Figs. 11(a) and 11(b) as well as the corresponding experimental results. The modification of the curves for the first mode ($\nu=1$) depends mainly on the influence of the second mode. The series converges rapidly and the fifth and higher modes become negligible. Thus the sharp resonance of the column with infinite conductivity is reduced by losses in the liquid and the copper disk and through "dispersion" of the composing modes to a barely detectable maximum, displaced in the direction of stronger values of the magnetic field.

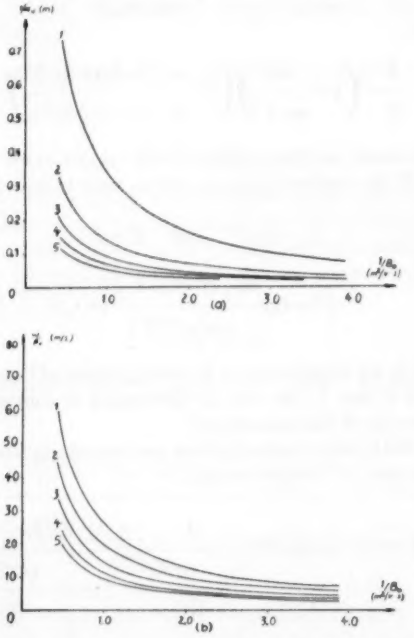

FIG. 9. (a) Depth of penetration, $1/\alpha_\nu$, of cylindrical waves in a column of liquid sodium at 120°C with the dimensions $r_0=0$, $R=6.8$ cm at a frequency $\omega=188.5$ sec^{-1} (30 cps). The five first modes are given. In the experiment $r_0=1.2$ cm and the corresponding curves of Figs. 9 (a), (b) and 10 (a), (b) are modified with less than 10 percent even for the fifth mode. (b) Phase velocity ω/β_ν of the waves.

[10] E. C. Titchmarsh, *The Theory of Functions* (Oxford University Press, London, 1939), p. 42.

[11] G. H. Hardy, *A Course of Pure Mathematics* (Cambridge University Press, Cambridge, 1952), p. 473.

[12] The calculations have been performed with the help of tables and a chart atlas by A. E. Kennelly, *Tables of Complex Hyperbolic and Circular Functions* and *Chart Atlas of Complex Hyperbolic and Circular Functions* (Harvard University Press, Cambridge, 1914).

Even if the phase is measured more precisely than the amplitude, the discrepancy between theory and experiment as regards the amplitude is hardly within the limits of error. The deviation has the same direction as in earlier investigations being greater in the measurement of amplitude than in that of the phase [see Figs. 11 (a), (b) and 12 (a), (b)]. The elasticity of the upper part of the axis in Fig. 1 may introduce an error. Other possible sources of error are mechanical disturbances by the inner probe ($r=r_1$) and impurities of the liquid, the disk at the bottom and the boundary layer between disk and liquid; all these effects increase the apparent damping. An impurity of the free surface may have some mechanical influence but it is not so important as in mercury (Sec. 5). In Sec. 3 it has been pointed out that the currents at the junction of axis and disk and in the layer of sodium below the axis have been neglected. This reduces the effectiveness of the generating mechanism and appears as an increase in the damping when the amplitude at the bottom is kept constant. Finally, the velocity distribution at the bottom has been assumed to have a finite value at $r=R$, which is an approximation when the viscosity is taken into account.

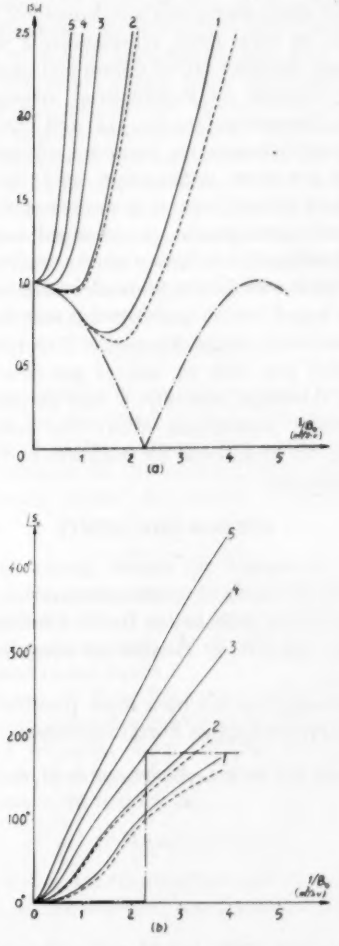

FIG. 10. (a) Amplitude $|S_\nu|$ of the "axial factors" (35), (39) of a column with $r_0=0$, $R=6.8$ cm, $\omega=188.5$ sec^{-1}. —·— column with infinite conductivity; - - - - result when the influence of the disk at the bottom is neglected ($F_\nu=1$); —— resulting theoretical curve; (b) Phase $\angle S_\nu$ of the "axial factors."

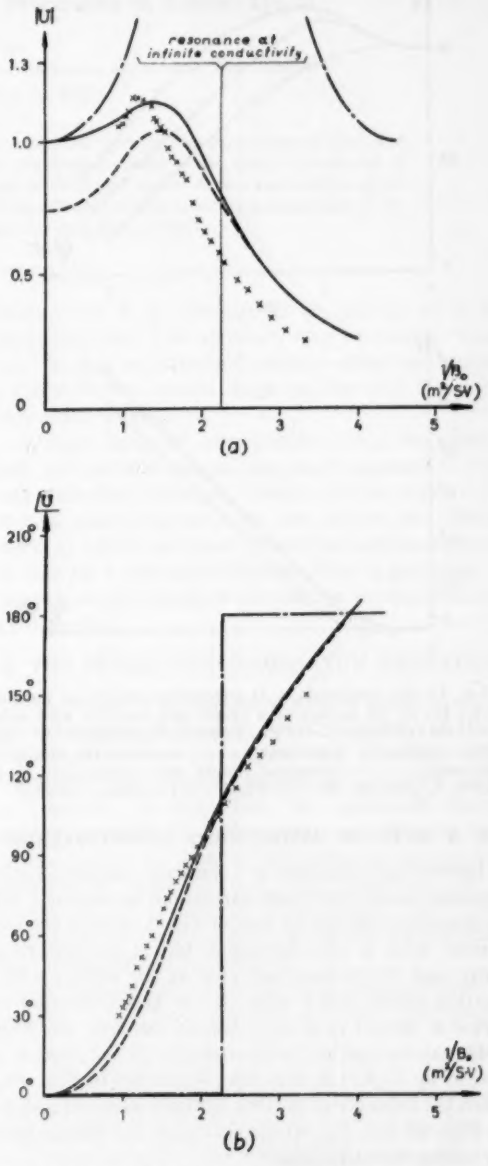

FIG. 11. (a) Amplitude $|U|$ of normalized indicated potential difference at the surface as given by Eq. (38). Linear dimensions according to Fig. 7 and frequency $\omega=188.5$ sec^{-1}. —·— column with infinite conductivity; - - - - first mode ($\nu=1$); —— resulting theoretical curve; ××× measurements. (b) Phase $\angle U$ of the normalized potential difference.

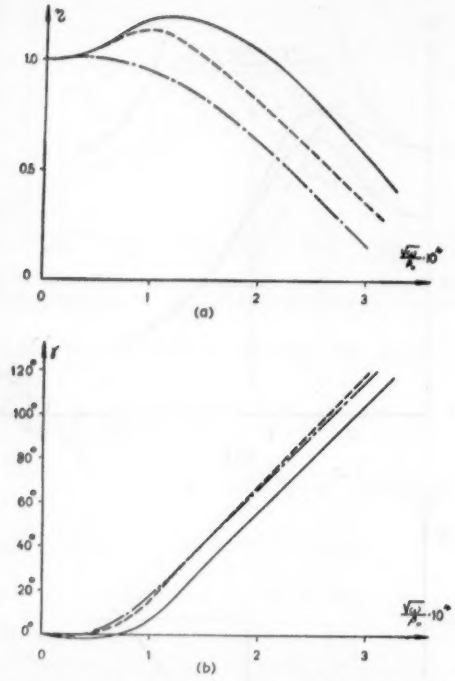

FIG. 12. (a) Amplitude, η, at normalized velocity at the point $r=4.1$ cm at the surface of a vessel with mercury with radius $R=15$ cm and height $L=15$ cm as given by Lundquist.[3] —— theoretical results by Lundquist; —·— experimental results by Lundquist; – – – theoretical results after application of the factors F_r given by (35). (b) Phase γ of normalized velocity.

5. A NOTE ON LUNDQUIST'S INVESTIGATIONS

Earlier investigations of cylindrical magneto-hydrodynamic waves have been carried out in mercury[3] with an apparatus similar to that of Fig. 1. The waves were excited with a disk furnished with 1-cm high radial strips and the motion indicated at the surface with a floating mirror and a scale. If the liquid between the strips is treated as a solid disk of mercury, the result (34) may be applied to the velocity $v^{(1)}$. $Z_1(k,r)$ is replaced by $J_1(k,r)$ in this case, where $r_0=0$. The result when the influence of the disk has been included is shown in Figs. 12 (a), (b), which also show the results given by earlier investigations.[13]

[13] Dr. Lundquist has kindly placed his numerical calculations at the author's disposal for the application of the factors F_r given by (35).

After the application of Eq. (34), however, there still remains a discrepancy for the amplitude [Fig. 12(a)]. It has been pointed out by Lundquist that a source of error may be the tenacious surface layer of mercury. Another possible source is a slipping of the liquid round the strips at the bottom, i.e., the mercury between the strips cannot be considered as a solid. Finally, the inertia of the mirror and impurities of the mercury may introduce some error.

6. CONCLUSION

The investigations of magneto-hydrodynamic waves in sodium and mercury show a satisfactory agreement between theory and experiment. The conditions for model experiments in the laboratory scale, however, cannot give a very good picture of cosmic phenomena, even with such a medium as liquid sodium. A velocity profile with sharp edges, which is demanded, e.g., in an experiment on whirl rings, representing a mechanism for sunspots, becomes rather diffuse and damped after travelling through an experimental arrangement of laboratory dimensions [see Eq. (17) and Figs. 9(a) and 9(b)]. In experiments on resonance phenomena the conditions are more unfavorable since the reflected waves, which virtually travel several times through the experimental arrangement, are damped too strongly to have considerable influence on the resulting amplitude. A liquid with better properties than sodium can hardly be found, but an improvement may be obtained with an increase in linear dimensions. Experiments have been carried out with an ionized gas in a magnetic field.[14] At this stage, however, it may be premature to draw definite conclusions about the possibility of improving the conditions for magneto-hydrodynamic waves in the gas.

ACKNOWLEDGMENTS

I want to express my sincere thanks to Professor Hannes Alfvén for many valuable remarks on this work. I am also greatly indebted to Dr. N. Herlofson, Dr. S. Lundquist, and Mr. E. Åström for many stimulating discussions.

The investigation has been made possible by grants from Naturvetenskapliga Forskningsrådet.

[14] H. Bostick and M. A. Levine, Phys. Rev. **87**, 671 (1952).

Superfluidity and Dissipative Processes in Liquid He II

J. G. DASH
Los Alamos Scientific Laboratory, University of California, Los Alamos, New Mexico
(Received September 28, 1953)

A phenomenological theory of superfluidity of He II is constructed upon the two-fluid models of Tisza and Landau. The postulate that phonons partially represent the thermal energy of the liquid is employed to explain the dependence of critical velocities upon the size of the liquid region. A new assumption, of the production of phonons by the motion of large clusters of superfluid particles, provides a description of the transition between superflow and dissipation at flow velocities exceeding critical.

I. INTRODUCTION

THEORIES of the superfluidity of liquid helium are concerned with the origin and behavior of a "critical velocity" v_c belonging to the superfluid portion of the liquid. Below the critical velocity, dissipation effects associated with the flow of the superfluid are vanishingly small. Experimental investigations of the variation of v_c with temperature and with the dimensions of the liquid region show apparently involved relationships, and the flow character at supercritical velocities exhibits equally involved dependences.

There have been two fundamentally different theoretical attacks on this problem. In the treatments of London[1] and Bijl, de Boer, and Michels,[2] superfluidity is considered to be the macroscopic manifestation of a finite zero-point velocity of the superfluid particles, which, contained in a liquid region of dimension d, have the constant product

$$(v_c d)\sim h/m\simeq 10^{-4}, \tag{1}$$

where m is the mass of the helium atom. Retaining the concept of the superfluid as the population of a minimum energy state, Landau[3] has given the critical velocity criterion as the velocity below which rotons and phonons cannot be excited in the liquid by superflow

$$v_c\simeq(2\Delta/\mu)^{\frac{1}{2}}\leq c, \tag{2}$$

where Δ is the energy gap separating the ground state from the first nonzero roton state, μ is the effective mass of the roton, and c is the velocity of ordinary (first) sound in the liquid.

In contrast to these "quantum" theories of superfluidity, Gorter and Mellink[4] have suggested a velocity-dependent frictional force between the particles of normal fluid and superfluid, giving for the force per unit volume of mutual friction,

$$f=A\rho_s\rho_n(v_s-v_n)^3, \tag{3}$$

where ρ_s and ρ_n are the densities, and v_s and v_n are the velocities of the superfluid and normal fluid, respectively, and A is independent of (v_s-v_n) to a first approximation. This approach may be termed "classical," in that no threshold velocity exists below which f vanishes, but instead drops rapidly with (v_s-v_n) to very small values.

A large body of experimental data, discussed in part in later sections of this paper, appears to agree well with the "quantum" theories in the region $v_s\leq v_c$, and in some respects with the Gorter and Mellink model at higher velocities. There has been no suggestion to date for a transition between these approaches; the present paper represents an attempt to establish such a connection.

II. THE PRODUCTION OF QUANTUM EXCITATIONS

The present considerations will be based upon the general aspects of Tisza's[5] two-fluid theory of He II. The characters of the normal and superfluid liquid "fractions" are assumed similar to Landau's model: ρ_n contains, or comprises, the quantized thermal excitations of He II, while ρ_s acts as a "background" which contains no thermal excitations. ρ_s may undergo superflow at velocities less than necessary for the production of elementary excitations: the critical velocity is established by the production of the excitations of the minimum energy ϵ.

The extremely large critical velocities obtained by Landau[3] from the postulate of roton and phonon

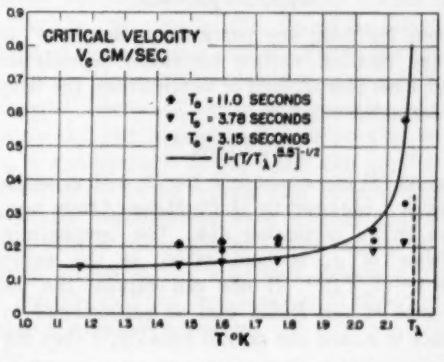

FIG. 1. The variation of critical velocity with temperature: Comparison of theory with measurements on an oscillating disk.

[1] F. London, Phys. Rev. **54**, 947 (1938); Revs. Modern Phys. **17**, 310 (1945).
[2] Bijl, de Boer, and Michels, Physica **8**, 655 (1941).
[3] L. Landau, J. Phys. (U.S.S.R.) **5**, 71 (1941); **6**, 91 (1947).
[4] C. J. Gorter and J. H. Mellink, Physica **15**, 285 (1949).
[5] L. Tisza, Phys. Rev. **72**, 838 (1947).

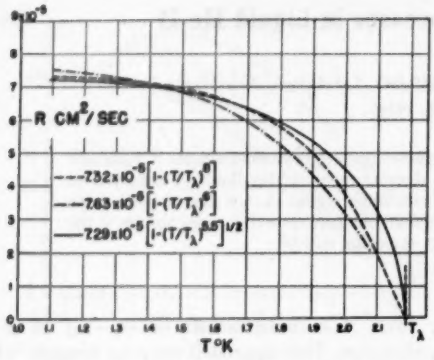

FIG. 2. The variation of film flow rate with temperature.

creation by individual atoms lead us to suggest a large effective mass of the interacting "particle." We will therefore attempt to treat superfluidity on the basis of this consideration, and two assumptions will be added to the two-fluid theory of Tisza and Landau.

(a) The magnitude of the critical velocity is established by the production of excitations due to a relative velocity between the ρ_s and a solid wall in contact with the liquid.

(b) "Clusters" of atoms may cooperate in the production of quantum excitations. The size of the clusters is $V \simeq \sigma^3$, where σ is a "cooperative distance," within which the superfluid moves essentially as a unit.

The unknown mechanism in (a) states that it is v_s, rather than $v_s - v_n$, that is the criterion for superfluidity. It does not replace the interaction between ρ_s and ρ_n that must exist in order to establish and maintain temperature equilibrium. Assumption (b) states that the effective mass of the interacting unit is $\rho_s \sigma^3$, contrary to Landau, who specified it as the mass of the roton (7–8 atomic masses).

On the basis of the above assumptions, the production of elementary excitations of characteristic energy ϵ is energetically possible when

$$V\rho_s v_s^2 > V\rho_s v_c^2 = 2\epsilon. \tag{4}$$

Without ascribing any particular values to V and ϵ, we may establish certain functional dependences. If V and ϵ are independent of temperature, the temperature dependence of v_c is

$$v_c(T) \propto \rho_s^{-\frac{1}{2}}. \tag{5}$$

Equation (5) is compared, in Fig. 1, with experimental values of v_c obtained by Hollis-Hallett,[6] from measurements on an oscillating disk. The temperature dependence of ρ_s is here taken as the empirical[7] $\rho_s/\rho = 1-(T/T_\lambda)^{5.5}$. If one can express the volume flow rate of the Rollin film as proportional to the product of ρ_s and the critical velocity,[8,1] then Eq. (5) yields for the Rollin film rate-temperature dependence, assuming that V, ϵ, and the film thickness are all independent of temperature,

$$R(T) \propto \rho_s^{\frac{1}{2}}. \tag{6}$$

Mendelssohn and White[9] have given the functions $1-(T/T_\lambda)^6$ and $1-(T/T_\lambda)^8$ as the functional bounds of flow rates over a large variety of solid surfaces; these functions are shown in Fig. 2, together with the scaled Eq. (6).

Dissipation effects associated with the production of excitations may have the functional dependence, from Eq. (4),

$$E_f = 0, \quad v_s < v_c,$$
$$E_f \propto \rho_s(v_s^2 - v_c^2), \quad v_s > v_c, \tag{7}$$

where E_f is the energy dissipated per unit liquid volume.

A careful study of dissipation effects in the supercritical velocity region was carried out by Hollis-Hallett. The "excess decrement" $(\delta-\Delta)$ of a disk oscillating in liquid He II was compared with the theory of Gorter and Mellink, and found to be in poor agreement with the theory. Here, δ is the logarithmic decrement of oscillation at all amplitudes, and Δ is the value for small amplitudes, where the damping had the characteristics of laminar, viscous motion. Δ therefore appeared to be associated with the relative motion of the normal fluid; the excess $(\delta-\Delta)$ included all dissipative terms beyond this.

It is interesting to compare this excess dissipation with the present theory, for we may expect that the production of quantum excitations will give a large contribution to $(\delta-\Delta)$.

In an oscillating system, the energy lost per cycle is proportional to the logarithmic decrement of amplitude, when the decrement is small. The excess decrement

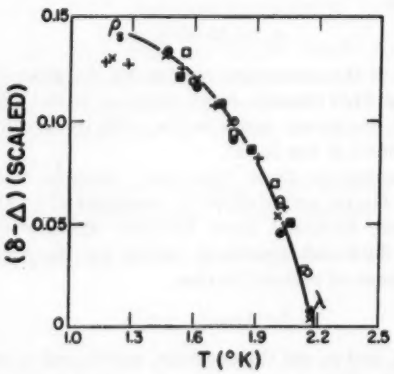

FIG. 3. The variation of dissipation with temperature (after Hollis-Hallett). The solid curve is the calculated $\rho_s(T)$. Experimental points are scaled measurements on systems having various oscillation periods.

[6] A. C. Hollis-Hallett, Proc. Roy. Soc. (London) **A210**, 404 (1951).
[7] E. Andronikashvilli, J. Phys. (U.S.S.R.) **10**, 201 (1946).
[8] J. G. Daunt and K. Mendelssohn, Nature **150**, 604 (1942).
[9] K. Mendelssohn and G. K. White, Proc. Phys. Soc. (London) **A63**, 1328 (1950).

$(\delta-\Delta)$ can then be directly compared with the excitation energy dissipated per unit volume given by Eq. (7). From a frame of reference rotating with the disk, $v_s=v(\text{disk})\propto\phi$, the angular amplitude of oscillations, and Eq. (6) becomes ($\phi_c=\phi_m$),

$$(\delta-\Delta)\sim E_f=0, \quad \phi<\phi_m,$$
$$(\delta-\Delta)\sim E_f\propto\rho_s(\phi^2-\phi_m^2), \quad \phi>\phi_m, \tag{8}$$

for constant period of oscillation. The experimental variation of $(\delta-\Delta)$ with temperature, for constant angular amplitude much greater than ϕ_m was closely as $\rho_s(T)$, in accord with Eq. (8). The force of mutual friction of Gorter and Mellink, however, varies as $\rho_s\rho_n$, in disagreement with the observations. A figure of Hollis-Hallett is given in Fig. 3.

The predicted variation of $(\delta-\Delta)$ with amplitude is compared with experimental curves for two different temperatures, in Fig. 4. For purposes of comparison, Eq. (8) was fitted to one experimental curve at one point, the scale factor for the second curve modified by the ratio of ρ_s for the two temperatures. The ϕ_m values were supplied from the data. There is fair agreement between (8) and the data at moderate amplitudes only; speculations on the reasons for the divergence are discussed later. The shape of the calculated curves in Fig. 4 are similar to the behavior suggested by Atkins[10] and by Hung, Hunt, and Winkel[11] as best representing their independent results from capillary flow.

III. SOME SPECULATIONS ON MAGNITUDES

If we assume the validity of Landau's roton-phonon model, some crude calculations can be carried out for the cases of the film and of bulk fluid.

Considering the film as a thin plate of liquid of thickness d and length L, the number of randomly directed phonons of long wavelength ($\lambda\gg d$) is proportional to the angle $\sim\lambda/L$, which may be considered negligible in the case of the film. Then, the minimum energy phonon in the film has a wavelength $\lambda\sim10^{-6}$ cm and an energy $\epsilon=hc/\lambda=1.5\times10^{-16}$ erg. Taking for the critical velocity 50 cm/sec, we obtain $\sigma=10^{-6}$ cm $\sim d$(film).

A large liquid region may support phonons of considerably smaller energy: assuming the $\lambda_{(\max)}=1$ cm, and the value of σ obtained above, $v_c(\text{bulk})\simeq0.05$ cm/sec, approximately one-half to one-quarter of the velocities observed by Hollis-Hallett.

If the excitation energy is indeed the energy of the weakest phonon $hc/\lambda_{(\max)}$, then the critical velocity varies as d^{-1}, intsead of d^{-1}, as given by the previous quantum theories. Superfluidity should therefore be characterized by the constant product v_cd^1; observed velocities in channels of dimensions ranging between 10^{-6} and 1 cm are shown in Fig. 5. The correspondence of these experimental magnitudes with the present theory is reasonably close over this very large range of d. One might expect this relation to hold for the variation of film flow rates with height, for if the film thickness $d\propto h^{-1/n}$, then the rate of flow from one container of constant periphery into another should be established by the minimum thickness of the film connecting the two vessels; this should be given by the height of the container rim relative to the source liquid, and the observed rate should vary as $v_cd\propto h^{-1/n}$. Experimental determinations of the variation of film thickness with height have yielded coefficients between[12] $n=2$ in a measurement of the static film and[13] $n=7$ in a measurement of the moving film. Observations of film flow rate measurements over a range of heights from less than a centimeter to approximately 10 cm have been carried out by numerous observers. Their results indicate that the flow rate height dependence, if it exists at all, cannot be large.

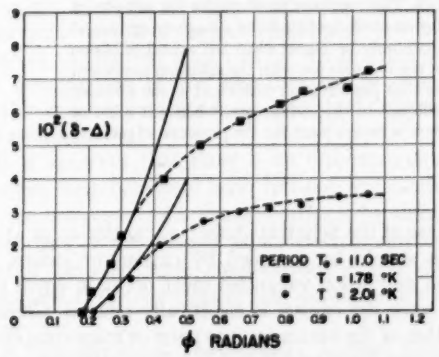

FIG. 4. The variation of dissipation with velocity: comparison of theory with measurements on an oscillating disk. ——— calculated from present theory. – – – smooth curves drawn through experimental results.

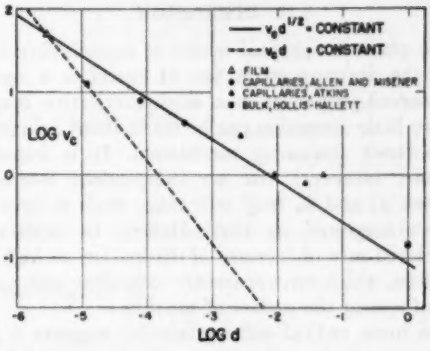

FIG. 5. The variation of critical velocity with channel size.

[10] K. R. Atkins, Proc. Roy. Soc. (London) **A203**, 240 (1950).
[11] Hung, Hunt, and Winkel, Physica **18**, 629 (1952).
[12] R. Bowers, Phil. Mag. (to be published). I am indebted to Professor E. A. Long for this information in advance of publication.
[13] K. R. Atkins, Proc. Roy. Soc. (London) **A203**, 119 (1950).

IV. DISCUSSION

The phenomenological model of superfluidity based upon the assumptions in Sec. II describes a number of observed properties in a semiquantitative manner.

Very little discussion can be made about assumption (a) without discussing mechanism. It is important to note, however, that an independent interaction between ρ_s and ρ_n may still exist. Such a force was in fact suggested by Hollis-Hallett, to explain the diminished rate of increase of dissipation at high disk velocities, which was apparently coincident with a dragging of ρ_s near the surface of the disk.

The more radical assumption (b) suggests a large "momentum cluster" of superfluid, in which the individual atomic momenta are highly ordered, and which acts as a coherent unit. These are not clusters in the usual sense, for the cooperating superfluid is not separated out in configuration space; rather, the densities ρ_s and ρ_n are uniform throughout the liquid region.

It should be noted that the assumption may be replaced by its phenomenological equivalent; that the superfluid congregates in tightly bound clusters whose numerical populations vary as $\rho_s(T)$. There is no distinction between the two variants of (b) at absolute zero.

A number of predictions may be put to experimental test. In addition to the film height-flow rate dependence already mentioned, a systematic study of critical velocities in large volumes of good geometry would provide a more critical test of the theory. It would be well to avoid the acceleration effects attendant with the oscillating disk type of measurement. The temperature dependence of these critical velocities cannot be considered firmly established as yet, and may yield an additional test.

The correlation between the calculated and observed Rollin film curves is only partially obtained. One may obtain an empirical fit to these data by assigning a temperature dependence to σ, which may also depend upon the material of the solid wall; such an analysis must await a more detailed theory.

It is a pleasure to acknowledge the assistance derived from many critical discussions with Dr. Louis Goldstein.

PHYSICAL REVIEW VOLUME 94, NUMBER 4 MAY 15, 1954

Self-Diffusion and Ionic Conductivity in Sodium Bromide*

H. W. SCHAMP, JR.,† AND E. KATZ
Physics Department, University of Michigan, Ann Arbor, Michigan

(Received February 15, 1954)

The self-diffusion coefficient D_{Br} of radioactive bromide ions in sodium bromide (melting point 755°C) has been measured in the temperature range 360–688°C, and the ionic conductivity of sodium bromide in the range 340–600°C. At high temperatures, above 450°C, the results of the diffusion measurements are quantitative and are expressible as $D_{Br}=50e^{-2.02/kT}$ cm²/sec. A comparison of diffusion and conductivity measurements yields the following results. The activation energy for migration of a Na-ion vacancy is 0.80±0.03 ev. The activation energy for the formation of a separated Na-ion vacancy and a Br-ion vacancy is 1.68 ev. The activation energy for the migration of a Br-ion vacancy is 1.18 ev. The transport numbers for the salt can be expressed as $n_{Br}=11.5e^{-0.36/kT}$. At lower temperatures the diffusion coefficient contains a large experimental uncertainty. It is shown, however, that the measured values can only be higher than the actual diffusion coefficients. Comparison of the measured diffusion coefficient of the bromide ion with the diffusion coefficient of the sodium ion calculated from the ionic conductivity shows that the diffusion coefficient of the bromide ion is not more than 2–3 percent as large as the diffusion coefficient of the sodium ion, whence it must be concluded that in the whole temperature range investigated there is no evidence for the presence of pairs of vacancies.

INTRODUCTION

IT has been quite well established by theoretical arguments and by experimental evidence that the major type of defect occurring in crystals of the alkali halides is the Schottky defect,[1] illustrated in Fig. 1. In the case of the Schottky defect, vacancies occur at sites which should be occupied by cations or anions. The cation and anion vacancies must occur in equal numbers since the crystal is electrically neutral. Clumping together of the vacancies into pairs or more complicated aggregates is not prohibited, but the occurrence of interstitial ions of either sign is considered to be improbable. To the existence and mobility of these defects in the crystals are attributable the processes of diffusion and electrical conduction and the more complicated phenomena which depend upon these elementary processes.

* This paper contains the essential portions of the doctoral thesis of H. W. Schamp (1951) and was briefly reported [see Phys. Rev. **85**, 729 (1952), 02].

† Present address: Molecular Physics Laboratory, Department of Chemistry, University of Maryland, College Park, Maryland.

[1] W. Schottky and C. Wagner, Z. physik. Chem. **B11**, 163 (1930); W. Schottky, Z. physik. Chem. **B29**, 335 (1935).

The electrical conductivity of alkali halides has been studied by a number of investigators.[2] Above a temperature several hundred degrees below the melting point the conductivity is characteristic of the compound and is expressible as

$$\sigma=\frac{C}{T}e^{-(U+E/2)kT},$$

and at lower temperatures as

$$\sigma=\frac{C'}{T}e^{-U/kT}.$$

Strictly, the conductivity is the sum of several exponentials, one for each carrier. In practice the contribution of one carrier nearly always exceeds greatly that of all others so that one exponential is an adequate approximation. In the alkali halides this carrier is the alkali ion vacancy. A correction resulting from neglecting the exponential for the halide ion vacancy is discussed in the appendix. The value C' in the foregoing expression varies from specimen to specimen. U is the activation energy for the migration of a positive-ion vacancy, and E is the activation energy for the formation of a separated positive and negative vacancy. The best explanation of the occurrence of two regions of conductivity appears to be that at high temperatures the vacancies occurring through the maintenance of thermodynamic equilibrium are predominant in number—thus the activation energies for formation of vacancies and for migration of vacancies occur in the exponential; at lower temperatures the number of vacancies is independent of the temperature, and determined predominantly by the amount of impurity ions present, and thus only the activation energy for the migration of vacancies occurs in the exponential.

Tubandt[3] first performed experiments to measure the transport numbers of ionic conductors. The following behavior is typical of the alkali halides. At low temperatures all the current is carried by the positive ion, but the contribution of the negative ion becomes measurable at a temperature several hundred degrees below the melting point.

It is apparent that there is an intimate connection between the processes of ionic diffusion and conduction, for the movement of a charged particle by diffusion is equivalent to the passage of an electric current. The relation between ionic conductivity σ and diffusion coefficient D for one type of ion, developed by Nernst

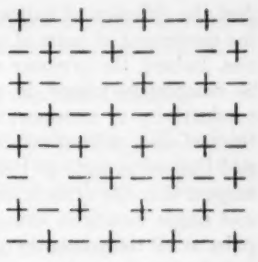

FIG. 1. Schottky defects.

and by Einstein[4] is

$$\sigma/D=Ne^2/kT.$$

In this expression N is the number of ion pairs per cm^3, and the other symbols have their customary meanings. Underlying the derivation of this relation is the assumption that the type of ion considered diffuses and conducts by only one mechanism.

Using the measured electrical conductivities of the alkali halides, the transport numbers, and the Nernst-Einstein relation, one can calculate the diffusion coefficients of both types of ions. One reaches the conclusion that the halide ion diffuses very slowly, and indeed at room temperature changes position by only one or two lattice spaces in a day. Until comparatively recently (1950) no direct measurement of the self-diffusion coefficients of any of the component ions of the alkali halides had been published, but indirect evidence indicated that actual diffusion rates may sometimes be considerably in excess of those calculated from conductivity data. Such indirect evidence was derived, for example, from the study of the formation and the coagulation of F centers in alkali halide crystals. This problem was considered quite extensively by Seitz.[5] He first concluded that during irradiation by x-rays or other high-energy particles the diffusion coefficient of the halide ion in the alkali halides is considerably in excess of the value predicted from transport measurements and conductivity measurements by means of a simple application of the Nernst-Einstein relation. This conclusion was supported by the observed high rate of coagulation of F centers. Later the concept of dislocations was introduced and invalidated the necessity of accepting the conclusion on the first ground, which was not too stringent anyway, because the absorption of x-rays may cause local temperature flashes with all sorts of effects on the number and mobility of vacancies. However, the second ground seems still to be valid.

It is clear that an excess diffusion rate of this sort may be explained if one assumes that transport of material can take place, involving electrically neutral units. Such units contribute to the diffusion without contributing to the conductivity. Seitz specifically suggested

[2] G. Tammann and G. Veszi, Z. anorg. u. allgem. Chem. **150**, 355 (1926); Phipps, Lansing, and Cooke, J. Am. Chem. Soc. **48**, 112 (1926); W. Lehfeldt, Z. Physik. **85**, 717 (1933) and F. Kerkhoff, Z. Physik **130**, 449 (1951).

[3] C. Tubandt in *Handbuch der Experimentalphysik* (Akademische verlagsgesellschaft m. b. h., Leipzig, 1932), Vol. XII, p. 396. See also C. Wagner and P. Hantelman, J. Chem. Phys. **18**, 72 (1950).

[4] W. Nernst, Z. physik. Chem. **2**, 613 (1888); A. Einstein, Ann. Physik **17**, 549 (1905).

[5] F. Seitz, Revs. Modern Phys. **18**, 349 (1946) and Phys. Rev. **80**, 239 (1950).

that the diffusion of halide ion vacancies can occur by the movement of pairs of positive and negative vacancies. Indeed, the presence of these neutral pairs would be completely missed in any simple measurement of conductivity or transport numbers. The possible existence of such pairs of vacancies was mentioned by Mott and Gurney as early as 1940,[6] and their estimate would suggest that the dissociation equilibrium between pairs and single vacancies strongly favors the undissociated pairs at all temperatures up to the melting point. Also Seitz[5] pointed out that pairs should be stable for not too high temperatures and their mobility much greater than that of individual halide vacancies. Dienes[7] calculated the activation energy for the motion of pairs through the crystal and found it low enough (0.375 ev) so that, if present, they should make an important contribution to the diffusion.

Considerably more information is obtained if both the diffusion coefficient and the conductivity of an ion are measured for the same crystal, for then it can be determined directly whether or not the Nernst-Einstein relation holds. If it should not hold, then the excess diffusion must be due to the transport of material by a mechanism involving electrically neutral units, and it will even turn out to be possible to differentiate between various mechanisms of this kind.

An experiment to test this relation for alkali halide crystals was performed by Mapother, Crooks, and Maurer (MCM).[8] They measured the electrical conductivity of sodium bromide and of sodium chloride and the diffusion coefficient of radioactive sodium ions in these two salts. Their experiments proved that the Nernst-Einstein relation is essentially satisfied at high temperatures. The diffusion coefficient directly measured is slightly less than that calculated from the total conductivity of the salt, but this difference is explained quantitatively by taking into account the contribution of the anion to the conductivity at these temperatures. Hence, in the high-temperature range there is no reason to assume that pairs exist.

At lower temperatures the results of their measurements were more difficult to interpret. The errors in the experiment were higher in that region, and the experimental points do not lie on a smooth curve; there is an indication that some of this scattering may be due to a variation in properties from one crystal specimen to another. Even so, it can be concluded that the diffusion coefficient of the sodium ion measured directly is at least twice the diffusion coefficient calculated from the conductivity. If one assumes that this failure of the Nernst-Einstein relation is due to pairs of vacancies, then one must conclude that approximately half the sodium diffusion in this region is due to pairs. This possibility was studied by the above investigators, and they concluded that the occurrence of pairs is unlikely also in this region. They proposed another mechanism involving a different type of an effectively neutral unit: a pair formed by a positive divalent impurity and an alkali ion vacancy. They pointed out that the diffusion coefficient of the sodium ion would also appear too large if there were such pairs of positive divalent impurities and alkali ion vacancies present in the crystal. Etzel and Maurer[9] provided further evidence that there are divalent impurities present.

More recently potassium chloride has been investigated along similar lines. Witt[10] measured the electrical conductivity of potassium chloride, doped with various concentrations of strontium chloride, and the diffusion coefficient of radioactive potassium ions in these salts. His results indicate that the diffusion coefficient of the potassium ion, measured directly, is about 2.4 times higher than that calculated from the conductivity. He remarks that it is unlikely that this discrepancy is due to pairs of vacancies, nor to pairs consisting of a Sr^{++} ion and a K^{+} vacancy, since the factor 2.4 was independent of both the Sr concentration and the temperature. Witt's paper does not give sufficient details regarding corrections that are necessary in working up the data of this type of experiment to convince the reader that the factor 2.4 is not largely due to a systematic error in the working up of the data. This doubt is supported by results of Aschner,[11] who performed similar measurements on KCl and found complete agreement with the Nernst-Einstein relation.

The present paper is based on a new approach for attacking experimentally the question of the nature of deviations from the Nernst-Einstein relation: *If a neutral entity consisting of an alkali ion vacancy and something else is held responsible for part of the diffusion of the alkali ion, it must also contribute an equal amount to the diffusion of that which constitutes the other half of this neutral unit.*

For example, in order to find out whether pairs of divalent impurities and alkali vacancies cause an excess diffusion of the alkali ion, one should directly measure the diffusion coefficient of the divelant impurities in these salts. The diffusion coefficient of the divalent impurities should be at least as great as the excess diffusion coefficient found for the alkali ion, if this type of neutral entity is responsible for the excess diffusion of the latter. Measurements of this sort have not been reported so far.

Likewise the most direct method of determining whether pairs of vacancies exist in the lower-temperature region would seem to be to measure the diffusion coefficient of the halide ion itself. If the high diffusion coefficient of the sodium ion in the lower-temperature region in the experiments of MCM were due to pairs, then the

[6] N. F. Mott and R. W. Gurney, *Electronic Processes in Ionic Crystals* (Oxford University Press, London, 1940), p. 42.
[7] G. J. Dienes, J. Chem. Phys. **16**, 620 (1948).
[8] Mapother, Crooks, and Maurer, J. Chem. Phys. **18**, 1231 (1950). This paper will be referred to as MCM.
[9] H. W. Etzel and R. J. Maurer, J. Chem. Phys. **18**, 1003 (1950).
[10] H. Witt, Z. Physik **134**, 117 (1953).
[11] J. F. Aschner, Phys. Rev. **94**, 771 (1954).

diffusion coefficient of the halide ion in an alkali halide should be measurable and should, in fact, approximately equal the diffusion coefficient of the alkali ion calculated from the electrical conductivity. If such a high diffusion coefficient is not found in this region, then the occurrence of pairs of vacancies in this region must also be extremely unlikely.

The primary pupose of the present paper is to study the question whether pairs of vacancies are responsible for the excess diffusion of the alkali ion, by measuring directly whether such a high diffusion coefficient of the halide ion does exist in the low-temperature range. For practical reasons sodium bromide was chosen and use was made of radioactive Br^{82} as a tracer. This choice enabled us to relate our results to those of Mapother, Crooks, and Maurer for the sodium ion in the same material.

A secondary purpose of the experiments is the determination of the transport numbers in the high-temperature region, by comparing the measured halide ion diffusion coefficient with the diffusion coefficient calculated from conductivity; a procedure of this sort was first suggested by von Hevesy.[12] To apply the method with certainty one must know the mechanism of the conduction and diffusion; this mechanism is explained by the work of MCM. Since the contribution of the halide ion is a much smaller fraction of the whole than is the contribution of the alkali ion, the measurement of the halide ion diffusion coefficient permits a better evaluation of the transport numbers than does the measurement of the alkali ion diffusion coefficient.

EXPERIMENTAL PROCEDURE

a. The Crystals

The crystals used in the experiment were grown from Baker and Adamson reagent quality sodium bromide by the Kyropoulos[13] method. They were cleft into cubical specimens approximately one centimeter on an edge, the dimensions being measured with a micrometer caliper. Unless a crystal was accidentally broken, it was used for measurements at several temperatures either in the high-temperature range or in the low-temperature range but rarely in both. Since it is not certain to what extent the thermal history influences the diffusion of the crystal, a crystal was given a standard annealing treatment before each measurement of conductivity and of diffusion. The treatment chosen was very similar to that used by MCM in order to make our results comparable to theirs, and consisted of four hours of annealing at 705°C (about 50° below the melting point) and cooling to room temperature at the rate of 0.55°C/min, with the crystals contained in a platinum crucible with a mica cover. In order to prevent the moisture in the air from attacking the crystal it was at all times kept at about 30°C above room temperature when exposed to air, by means of properly located heating elements.

b. Measurement of the Self-Diffusion

The radioactive sodium bromide used (Br^{82}, half-life 35.5 hours) was prepared with due precautions from pile-irradiated potassium bromide, by heating it with hydrobromic acid:

$$HBr+K^*Br^*\rightarrow K^*Br+HBr^*\uparrow,$$

and leading the vapors into ice cold sodium hydroxide, thus leaving all radioactive potassium behind:

$$HBr^*+NaOH\rightarrow NaBr^*+H_2O.$$

The asterisk indicates the radioactive atoms. This was followed by gentle drying. The radioactive salt was then evaporated from an electrically heated platinum trough in a vacuum of 10^{-5} mm onto a masked circular area on one face of each of several crystals. The diameter of the masked area was slightly smaller than the crystal. A glass plate received the same treatment along with the crystals and served to determine the thickness of the amount deposited, which ranged in the various experiments between 0.80 and 6.05 microns. The use of this thickness in interpreting the results is explained in the appendix.

Two crystals were then placed into the heating chamber (see Fig. 2) for diffusion to take place. The chamber was made of Vycor and in order to avoid corrosion at the high temperatures used (360°–688°) the only materials heated besides the sodium bromide were Vycor and platinum. The chamber was evacuated and filled with 25

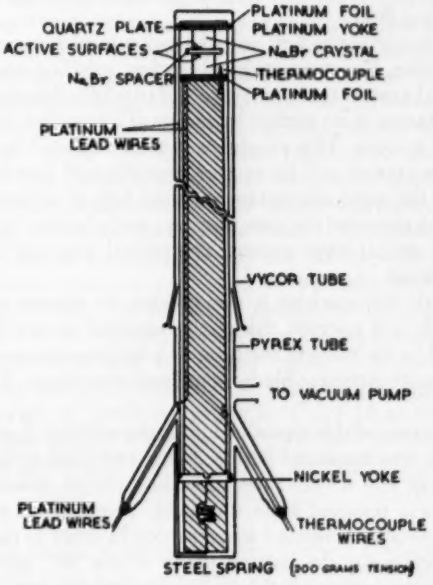

FIG. 2. The heating chamber.

[12] G. von Hevesy and W. Seith, Z. Physik **56**, 790 (1929).
[13] S. Kyropoulos, Z. anorg. u. allgem. Chem. **154**, 308 (1926).

mm of helium in order to reduce the evaporation from the crystal.

A platinum-platinum rhodium thermocouple calibrated against one, recently certified by the National Bureau of Standards, was held within the chamber approximately four mm from the crystals. The chamber was inserted in a hole in a massive copper block in a temperature-controlled electric furnace. The temperature measurement was considered to be accurate to within 1°C. The crystals were heated for a length of time dependent upon the temperature. This time varied from three hours to more than nine days. The crystals did not reach the equilibrium temperature in a negligible time. In order to apply a correction for the lag (see appendix) the temperature was measured frequently during the first hour.

After the heating operation the crystal was cooled rapidly to room temperature. It was then mounted in a special grinding machine.

This machine held the crystal with a constant pressure of about 2500 grams/cm^2 and constant orientation against a movable piece of plate glass, previously ground with No. 220 emery. The crystal was held in a vise with V-shaped jaw profiles of 90° angle, and one jaw could move freely in the (110) direction while the other one was being tightened in the $(1\bar{1}0)$ direction. Thus cleft crystals of not exactly cubic shape were held securely with a minimum of strain. An electric heater was built into the vise head in order to prevent water vapor damage. The ground glass plate was held in a carriage which travelled on machined ways, and was passed along the underside of the crystal once to remove one layer. One drop of absolute ethyl alcohol on both ends of the contact path on the plate was found to be a good grinding fluid.

The crystal was first oriented properly with respect to the plate. This was achieved by first grinding another crystal against the same plate and carefully defining the orientation of its surface by means of a sensitive optical lever system. This crystal was then replaced by the active crystal and its surface was adjusted into accurately the same orientation with the help of adjustment screws provided for this purpose, and checked by the same optical lever system. The crystal was now ready for slicing.

With this machine it was possible to remove layers of salt 2–3 microns thick; the material removed adhered to the plate in the form of a rectangular smear of salt quite reproducible in shape and size (about 1 by 7 cm).

Because of this reproducibility, the activity A_n of the smear was measured with a 2-inch end-window Geiger counter and a conventional scaling circuit before the salt was removed from the plate. The time at which each slice was counted was recorded in order to make a correction for the natural decay of the Br* activity. After the activity had been determined the salt smear was washed from the plate with warm water, all the solution being caught in a small beaker. The plate was then returned to the machine for the next slice. Frequent checks were made to insure that all the activity had been removed from the plate by the washing; no trouble of this sort was ever encountered. The number of slices obtained from one crystal in this way depended on the average diffusion depth which in turn is determined by the time and the temperature of the diffusion. For the lowest temperatures only four slices oculd be used. For the largest diffusion constant measured thirty-seven slices were removed, and several times this number could have been analyzed. After all slices were removed the alignment of the crystal was checked again. Except for one measurement, noted in the results, this was always satisfactory to within the sensitivity of the adjustment.

The solution from each layer was titrated potentiometrically[14] using 0.002 normal silver nitrate; the determination was accurate to within 2 percent. This was the main source of error at the higher temperatures. Since the area of the crystal and the amount of salt in each layer were known, the thickness Δ_n and the concentration of radioactivity $C_n = A_n/\Delta_n$ of each of the layers could be determined.

The approximate solution of the diffusion problem described here is

$$C(x,t) = \frac{dC_0}{(\pi Dt)^{\frac{1}{2}}} \exp\left(-\frac{x^2}{4Dt}\right), \tag{1}$$

in which C is the concentration of radioactivity; d the thickness of the original radioactive layer; C_0 the concentration of radioactivity in the original layer; D the diffusion coefficient; x the distance from the outside of the radioactive layer to the center of the sliced layer; and t the time during which diffusion occurred. This approximate solution was sufficiently accurate to use in the experiments for all but the smallest diffusion coefficients. The manner in which the exact solution differs from the approximate solution, and the corrections which must be applied to the experimentally determined diffusion coefficient, will be discussed in the appendix. Thus the graph of $\log C$ *versus* x^2 should be a straight line with slope $(-\log e)/4Dt$.

Figure 3 shows several typical graphs of the experimental data for individual runs; such graphs were obtained so long as the average diffusion distance was larger than 6–8 microns. The type of graph obtained when the diffusion distance was very short is shown in Fig. 6. Some of the reasons for the shape shown in Fig. 6 will be given later.

c. Measurement of the Conductivity

The measurement of the electrical conductivity was performed using the same chambers which had been used in the diffusion measurement (see Fig. 2). Elec-

[14] E. Zintl and K. Betz, Z. anal. Chem. 74, 330 (1928).

trodes were applied to the crystals by using Hanovia Liquid Bright Platinum, IBM lead, or Aquadag. No essential difference was observed with either type in the results. Aquadag can be very easily applied to deliquescent crystals such as sodium bromide if the crystal is kept warm. Platinum foils were pressed against these electrodes. The foils were welded to platinum leads. The measuring device was a Wheatstone bridge with a Dumont 304-H oscilloscope used as a detector. A dc pulse of approximately 0.1-second duration was applied to the bridge. In most cases separate crystals were used for measurements in the structure-sensitive region from those used in the structure-insensitive region. In each region measurements were taken from low temperatures to high temperatures, with a closing reading at the low temperature again. This closing reading always checked with the first reading to within the error of measurement (5 percent). Spurious effects which might have been due to diffusion or electrolytic decomposition were thus eliminated. Before the conductivity measurements crystals were given the same annealing as described in part a.

EXPERIMENTAL RESULTS AND CONCLUSIONS

The conductivity measurements will be considered first. All conductivity results were translated into corresponding diffusion coefficients by means of the Nernst-Einstein relation. The density of sodium bromide used

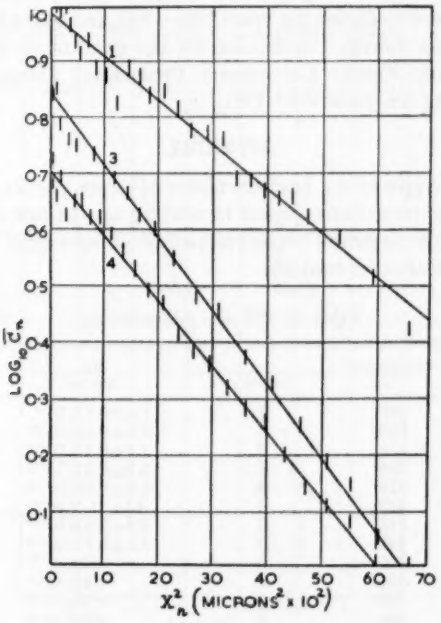

FIG. 3. Individual diffusion measurements. High temperatures. The logarithm of the concentration of tracer ions is plotted *versus* the square of the diffusion depth. The numbers refer to crystals; Crystal 1, 688°C, diffusion time 0.99×10^4 sec; Crystal 3, 624°C, 4.39×10^4 sec; Crystal 4, 586°C, 1.44×10^5 sec. The slope of the line yields Dt.

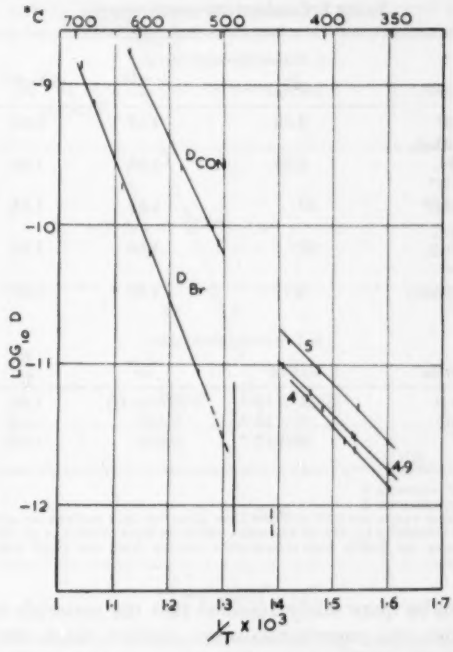

FIG. 4. High-temperature diffusion measurements, D_{Br}, and diffusion coefficient calculated from electrical conductivity, D_{con}. The numbers refer to crystals; Crystal 5 had platinum electrodes, Crystals 4, 9 Aquadag or IBM lead, and Crystal 4 platinum.

was 3.203 grams/cc; the fundamental constants were obtained from Dumond and Cohen.[15]

The diffusion coefficient calculated from conductivity can be represented quite well by the equation $D_{con}=D_0e^{-(U+\frac{1}{2}E)/kT}$ in the upper-temperature range, and by $D_{con}=D_0'e^{-U/kT}$ in the lower-temperature range, Fig. 4. The line marked D_{con} represents the data in the high-temperature range, while the lines in the lower-temperature range show the differences among different crystals in that range. The line marked D_{Br} will be discussed later. The values of the activation energies determined by these measurements and the values reported by other investigators are tabulated in Table I. E is interpreted here as the activation energy for the formation of a separated positive and negative vacancy, and U is approximately the activation energy for the migration of a Na-ion vacancy, neglecting the contribution to conductivity from the Br-ion vacancy. A correction taking this contribution into account is explained in the appendix. It yields the values for $U_{Na}+\frac{1}{2}E$ as listed in the last column. The constants given for Lehfeldt, who fitted his data by $C\exp(-B/kT)$, are recalculated to fit $(C'/T)\exp(-B'/kT)$, matching both equations at 580°C.

The results of the present measurement are seen to be in quite good agreement with the results of MCM,[8] and

[15] J. W. M. Dumond and E. R. Cohen, Phys. Rev. **82**, 555 (1951).

TABLE I. Conductivity measurements.

a. High-temperature region.

Worker	D_0 cm²/sec	$U+\frac{1}{2}E$ ev	$U_{Na}+\frac{1}{2}E$ ev
Present	4.36	1.66	1.64
Mapother, Crooks, Maurer[a]	5.98	1.68	1.66
Lehfeldt[b]	67.	1.85	1.83
Phipps, Lansing, Cooke[b]	57.	1.86	1.84
Tammann, Veszi[b]	0.77	1.40	1.38

b. Low-temperature region.

Worker	D_0' cm²/sec	U_{Na} ev	E ev
Present	$(6\pm4)\times10^{-6}$	$0.80\pm.03$	1.68
MCM[a]	10×10^{-6}	0.840	1.64[c]
PLC[b]	10×10^{-6}	0.850	1.98[c]

[a] See reference 8.
[b] See reference 2.
[c] These values are 0.04 ev lower than given by their authors on account of the correction for the Br transport which we have applied to all data in obtaining the fourth high-temperature column from the third (see appendix).

it can be quite safely assumed that the materials used in the two experiments were similar. Since similar methods of preparation of the specimens were used, this is not surprising. It is noticed that there is considerable variation in the results from one investigator to another in the structure insensitive region. The reason for this is not clear.

The individual results of the diffusion measurements are presented in Table II. The measurements at the five highest temperatures are represented by the equation

$$D_{Br}=50e^{-2.02/kT},$$

as shown in Fig. 4. Since the work of MCM shows that the negative and positive ions diffuse separately in this temperature region, one can interpret the value of the exponent as

$$U_{Br}+\tfrac{1}{2}E=2.02 \text{ ev}.$$

Using the value of E determined from the conductivity measurements one has the result

$$U_{Br}=1.18 \text{ ev}.$$

This compares with

$$U_{Na}=0.80 \text{ ev}.$$

Since the value of D_{Br} arises only from the movement of halogen vacancies, and D_{con} arises from the movement of both halogen and alkali vacancies, the quantity $D_{Br}/D_{con}=n_{Br}$ represents the transport number for the bromide ion; thus

$$n_{Br}=11.5e^{-0.36/kT}.$$

The transport numbers for sodium bromide have not been measured by another method, but comparison of these values with those obtained for other alkali halides shows them to be of the right order of magnitude.[3]

The measurements of the diffusion coefficient in the low-temperature region, Figs. 5, 6, are subject to much greater errors than those in the high-temperature region. The important thing about the measurements, however, is that they can only represent the highest value that the diffusion coefficient can have. Fortunately, all the important sources of error in this region are such that the measured value of the diffusion coefficient is higher than the actual value, as will be explained in the appendix. The points in Fig. 5 are represented with downward arrows to indicate this fact.

Figure 5 shows that the measured coefficient is not more than 2–3 percent as large as the diffusion coefficient of the sodium ion calculated from the conductivity. According to the reasoning given in the introduction it is evident then that the large diffusion coefficient of the sodium ion measured by MCM can certainly not be due to the diffusion of pairs of vacancies. We conclude that the existence of pairs of vacancies in sodium bromide in the whole region above 340°C must be extremely improbable.

ACKNOWLEDGMENTS

The cooperation of the staff of the University of Michigan has been greatly appreciated. The junior author (H. W. S.) is grateful to the Regents of the University of Michigan for the grant of a University Fellowship during the years 1947–1949, and to the U. S. Atomic Energy Commission for the grant of an U. S. Atomic Energy Commission Predoctoral Fellowship during the years 1949–1951.

APPENDIX

We give here a brief discussion of errors, checks, and of the corrections applied in working up the raw data, in order to permit better comparison of our results with those of other workers.

TABLE II. Diffusion measurements.

Temperature (°C)	Crystal	D_{Br} (cm²/sec)
688	1	$1.4\pm0.1\times10^{-9}$
668[a]	2	$7.4\pm0.4\times10^{-10}$
624	3	$1.9\pm0.1\times10^{-10}$
586	4	$6.5\pm0.3\times10^{-11}$
524	4	$8.8\pm0.6\times10^{-12}$
485[b]	1	$42\pm35\times10^{-13}$
447	5	$9.0\pm0.9\times10^{-12}$
447	3	$7.0\pm0.7\times10^{-13}$
420	3	$<2\times10^{-13}$
401	6	$<4\times10^{-13}$
389	7	$<6\times10^{-14}$
389	8	$<9\times10^{-14}$
360	2	$<15\times10^{-14}$
360	9	$<8\times10^{-14}$

[a] Crystal tilted 0.003 radian after slicing.
[b] For some unaccounted reason the points of the $\log C_n$ *versus* x^2 plot deviated strongly from a straight line for this run.

a. Errors in the Measurement of Conductivity

The temperature was measured with an accuracy of $\pm 1°C$. The dimensions of the crystals in the conductivity measurements were known with an error of 2.5 percent for the quantity area/length. The bridge was always balanced within 3 percent. Thus the conductivity measurements should be in error by something less than 5 percent. The conductivity of the apparatus with a quartz block in place of the crystal was negligible at all temperatures used, after the platinum leads were insulated by quartz tubes. In balancing the bridge charge was passed through the crystal forward and reverse. The amount of charge in each direction could have been as high as 2×10^{-4} coulomb$\approx10^{15}$ electron charges. While this quantity seems high, the reproducibility of the results at one temperature after several measurements at other temperatures indicates that no significant error was introduced by electrolysis or possible penetration of electrode material into the crystal.

b. Errors in the Measurement of D

These errors fall into two classes, since the product Dt and the time t are the measured quantities from which D is calculated. The main error in t arises as follows.

While the cooling at the end of the diffusion period was sufficiently rapid to cause no uncertainty in the diffusion time t, the heating of the crystal to the temperature T_0, at which diffusion was supposed to take place, was not instantaneous. Thus the slope of a graph as in Fig. 3 would yield, instead of $D(T_0)t$, the quantity $D(T_0)t_{eff}=\int D(T(t))dt$. By measuring the temperature as a function of the time and using a first approximation for $D(T)$ it was found that t_{eff} was in our case 10 minutes less than the actual furnace time t. The correction was only significant for the highest temperatures with diffusion times of only a few hours.

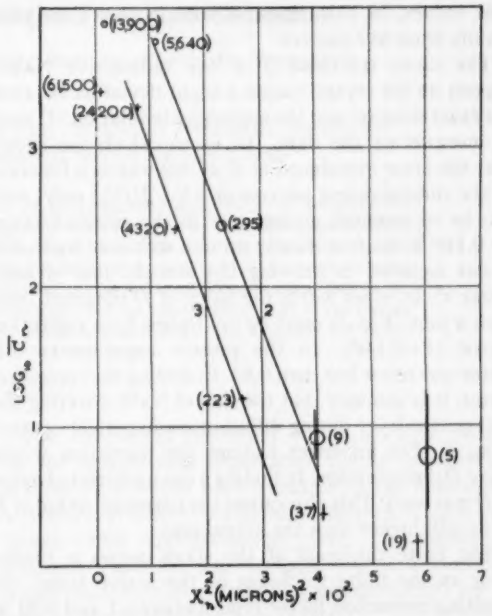

FIG. 6. Individual diffusion measurements, low temperatures. The numbers refer to crystals; Crystal 2, 360°C, diffusion time 7.704×10^5 sec; Crystal 3, 420°C, 3.870×10^5 sec. The numbers in parentheses by each point represent the activity actually measured in the layer in counts per minute above background (115 counts per minute).

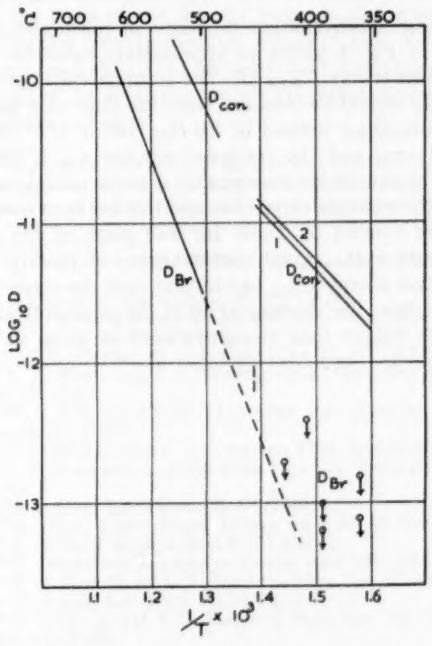

FIG. 5. Low-temperature diffusion measurements and comparison with diffusion coefficient D_{con} calculated from electrical conductivity. Curve 1 represents the results of Mapother, Crooks, and Maurer,[8] and Curve 2 the present work.

The errors in the determination of Dt fall again into two classes: those which affect all diffusion coefficients by the same percentage and those which affect relatively more the small values of D.

In the first class errors can arise from two sources. In the preparation of NaBr* it was assumed that all K^* was left behind. Analysis showed the absence of K^* complete enough to exclude any detectable error from this source. Errors in the titration and in the measurement of the cross section of the crystal combine to cause an error (through x_n) in the diffusion coefficient of about 5 percent, for all values of D.

Errors of the second class will turn out to be negligible for the high diffusion coefficients, but although much larger for the lower diffusion coefficients (say $<10^{-12}$ cm^2/sec) these errors are of such a nature that the measured values of D, even after corrections are applied, are certainly higher than the actual values. In other words, the measured values are upper limits, not prob-

able values, in this range. Errors in this class arise mainly from five sources.

The finite thickness d of the radioactive NaBr* deposit on the crystal causes a slight deviation between the exact solution and the approximate solution (1) used in interpreting the data. An exact calculation shows that the error introduced in D in this way is a function of the dimensionless parameter $\delta = d/2(Dt)^{\frac{1}{2}}$ only, and can be represented numerically in the relevant range by $0.14\delta^2$ if the first slice(s) up to a diffusion depth $d/2$ is not included in drawing the straight line of log$C$ *versus* x^2. In other words the value of D obtained from such a plot (Fig. 3) must be multiplied by a correction factor $(1-0.14\delta^2)$. In the present experiments this factor was never less than 0.84. In finding the correction factor, it is assumed that the slab of NaBr covering the radioactive layer during diffusion made perfect contact (Fig. 2). For imperfect contact the correction would bring D down further. In finding δ the uncorrected value of D was used. This also causes the corrected value of D to be still higher than the actual one.

The finite thickness of the slices causes a similar error as the finite thickness of the active layer, the resulting correction factor lying between 1 and 0.92 in the experiments, and leaving D still higher than the actual value.

The rough nature of the ground surface of the crystal requires another correction factor <1 for D. For the higher diffusion coefficients this correction is negligible, for the lower ones it is less than 15 percent, but since it is difficult to estimate the average groove depth with sufficient accuracy this correction was not applied, leaving the uncorrected D at a value which was certainly too high.

A slight misalignment of the crystal in the grinding machine, within the sensitivity of the optical lever system also would lead to an error in D with the same properties as that due to the roughness of the surface.

The transfer of material from one layer to the next in the grinding process was checked by blank measurements on undiffused crystals and was found to cause a negligible error in practically all cases. Also this error leads to D values which are too large. However, these same blanks showed that a small amount of activity was present on the side and back faces of the crystals. For small diffusion coefficients this caused a tail of the log C *versus* x^2 plot as seen in Fig. 6, which was properly ignored in drawing the straight line. It is recalled that the first point was to be ignored in connection with the correction for finite d discussed above. The remaining points show that we are here near the limit of D values that can be measured with this equipment. This limit is estimated to lie at present at about 6.10^{-14} cm²/sec.

Errors arising from the counting of the activity of the slices were relatively unimportant. Statistical errors were kept below 3 percent by accumulating enough counts. Uneven activity (thickness) of the salt smear was also unimportant. By means of an analysis of auxiliary experiments it was found that a smear, which would be most unfavorably inhomogeneous to a far greater degree than encountered in actual practice, would produce an error less than 5 percent. Thus the error due to this source in the actual measurements was neglected.

Summarizing: for the large diffusion coefficients (high temperatures) the principal error is of the first class and the determination of D is accurate to about 5 percent. For the small diffusion coefficients, below say 10^{-12} cm²/sec errors may be as large as 80 percent, but they are of such a nature that the measured and corrected D values are certainly higher than the actual values, and constitute upper limits.

c. Determination of the Activation Energies

In first approximation the slope of the upper D_{con} graph in Fig. 4 yields an approximate value for the activation energy $U_{Na}+\frac{1}{2}E$. The accurate value for this quantity should be obtained from the slope of a graph of $\log(n_{Na}D_{con})$ instead of $\log D_{con}$ *versus* $1/T$. Since $n_{Na}=1-n_{Br}$ and the transport number n_{Br} is determined by the present experiments it seems warranted to apply the resulting correction, and this has been done in the last column of Table Ia. The slope of the low temperature D_{con} graph yields again not exactly the activation energy U_{Na}, but in that case the correction is negligible. The determination of the other activation energies follows then straightforward as given in the text.

The Magnetic Susceptibility of the Transition Elements

C. J. KRIESSMAN, *Eckert-Mauchly Division, Remington Rand, Inc., Philadelphia, Pennsylvania*

AND

HERBERT B. CALLEN,* *Department of Physics, University of Pennsylvania, Philadelphia, Pennsylvania*

(Received October 30, 1953; revised manuscript received February 1, 1954)

The available data on the temperature dependence of the paramagnetic susceptibility of the transition elements are reviewed. A theoretical treatment according to the band theory of solids is developed explicitly by means of a simple approximation to the Fermi function. Each term in the resulting theoretical formula may be directly and graphically interpreted in terms of the geometry of the density-of-states curve, allowing a simple and intuitive analysis of the susceptibility variation at any temperature. The empirical data on the temperature coefficient of susceptibility, on the absolute magnitude of the susceptibility, and on the specific heats of the transition elements are analyzed to suggest probable alterations in the available theoretical density-of-states curves.

1. INTRODUCTION

ONLY in recent years have enough reliable data been accumulated to encourage an attempt at a general understanding of the temperature dependence of the magnetic susceptibility of the transition elements. These data,[1–16] together with the absolute magnitudes of the susceptibility and of the electronic specific heat, provide some of the most direct information on the electronic density-of-states curves of these materials.

The purpose of this paper is two-fold: first, to critically assemble the data on the temperature variation of the magnetic susceptibility, and to show that certain striking regularities in these data can be understood on the basis of the general features of the available theoretical density-of-states curves;[17] and second, to invert the logic and to suggest certain alterations in the details of the density-of-states curves on the basis of the experimental data.

The theoretical treatment which we shall develop for the temperature dependence of the susceptibility is based on a simple approximation to the Fermi function which avoids the intractable integrals of the precise theory. This approximation yields closed-form expressions valid for any temperature, and permits a simple and intuitive graphical interpretation on the basis of the density-of-states curve.

The theory supplements an earlier theory of Stoner[18] which proceeded by a series expansion valid for low temperatures. On the basis of that theory Stoner recognized the general aspects of the relationship between the density-of-states curve and the temperature dependence of the susceptibility. The geometrical nature of our analysis allows a particularly perspicuous and convenient semiquantitative discussion of recent extensive experimental data and of the various theoretical density-of-states curves.

2. EXPERIMENTAL OBSERVATIONS

The most striking feature of the accumulated data on the temperature dependence of the susceptibility of the transition elements is that each of the elements in a particular column of the periodic table exhibits the

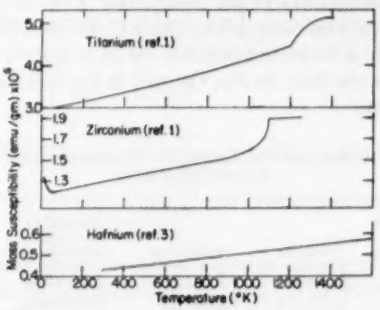

FIG. 1. Experimental susceptibilities of Ti, Zr, and Hf. The high-temperature changes in the susceptibilities of Ti and Zr are associated with crystal structure transitions.

* The contribution of one of the authors (H. B. C.) to this work was supported in part by the U. S. Office of Naval Research at the University of Pennsylvania, and was stimulated and initiated in the course of consultantship to the Eckert-Mauchly Division of Remington Rand, Inc.

[1] C. F. Squire and A. R. Kaufmann, J. Chem. Phys. **9**, 673 (1941).
[2] Li Klemm, Z. Electrochem. **45**, 354 (1939).
[3] C. J. Kriessman and T. R. McGuire, Phys. Rev. **90**, 374 (1953).
[4] C. J. Kriessman, Revs. Modern Phys. **25**, 122 (1953).
[5] F. E. Hoare and J. C. Walling, Proc. Phys. Soc. (London) **B64**, 337 (1951).
[6] W. J. deHaas and P. M. Van Alphen, Proc. Acad. Sci. Amsterdam **36**, 263 (1933).
[7] T. R. McGuire and C. J. Kriessman, Phys. Rev. **85**, 452 (1952).
[8] L. F. Bates and A. Baqui, Proc. Phys. Soc. (London) **B48**, 781 (1936).
[9] H. Söchtig, Ann. Physik **38**, 97 (1940).
[10] M. Isobe, Science Repts. Tôhoku Univ. **A3**, 78 (1951).
[11] A. Serres, J. phys. radium **9**, 377 (1938).
[12] N. Perakis and L. Capatos, Compt. rend. **196**, 611 (1933).
[13] A. N. Guthrie and L. T. Bourland, Phys. Rev. **37**, 303 (1931).
[14] K. Honda, Ann. Phys. **32**, 1027 (1910).
[15] F. E. Hoare and J. C. Mathews, Proc. Roy. Soc. (London) **A212**, 137 (1952).
[16] For a compilation of electronic specific heat data see M. Horowitz and J. G. Daunt, Phys. Rev. **91**, 1099 (1953).
[17] H. M. Krutter, Phys. Rev. **48**, 664 (1935); J. C. Slater, Phys. Rev. **49**, 537 (1936).
[18] E. C. Stoner, Proc. Roy. Soc. (London) **A154**, 656 (1936).

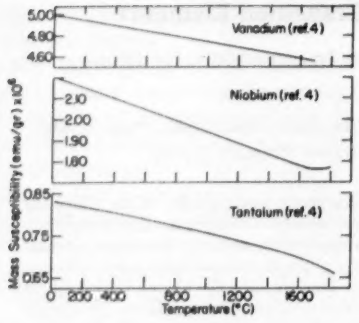

FIG. 2. Experimental susceptibilities of V, Nb, and Ta.

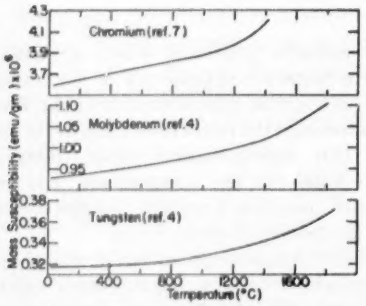

FIG. 3. Experimental susceptibilities of Cr, Mo, and W.

same general type of temperature dependence; thus the susceptibility of each of the elements (Ti, Zr, Hf) in column IV increases with increasing temperature, whereas the susceptibility of each of the elements (V, Nb, Ta) in column V decreases with increasing temperature. Furthermore, the sign of the temperature coefficient of the susceptibility is observed to alternate from column to column of the periodic table. The empirical results are shown in a series of graphs, (Figs. 1–6), references to which are given in Table I. Since many of the room temperature values of the absolute magnitude of the susceptibility which are quoted in handbooks are antiquated, a list of the best values has been compiled in Table II. It should be noted that only a room temperature value is known for Re, and that the data on Ru, Os, and Ir are still somewhat uncertain.

TABLE I. References and figures for the experimental magnetic susceptibility data.

Periodic table column	Elements	References	Dominant temperature dependence	Figure
IV	Ti;Zr;Hf	1,2;1,2;3	increasing	1
V	V;Nb;Ta	4,2;4,6;4,5	decreasing	2
VI	Cr;Mo;W	7,8,9;4,6;4,6	increasing	3
VII	Mn;Re	11,3,10;12	decreasing	4
VIII	Ru;Os	13;13,14	increasing	5
IX	Rh;Ir	5,15,13;13,14	increasing	6;5
X	Pd;Pt	5,13,15;13,15	decreasing	6

As remarked above, one of the most interesting features of the experimental data is that the temperature coefficient of the susceptibility alternates in sign with the columns in the periodic table from column IV to column VIII. This change in temperature coefficient correlates also with an alternation in the magnitudes of both the room temperature susceptibility and the electronic specific heat[16] as shown in Table III. These facts will be discussed in the following section in relation to the band theory. The burden on a theory has become more difficult with the recent discovery of maxima in the susceptibilities of Mn (Fig. 4) and Pd (Fig. 6) and minima in the susceptibilities of Zr (Fig. 1) and Nb (Fig. 2). However, it must be noted that although the maxima have been substantiated, it is possible that the low-temperature minimum in Zr is due to impurities, as indicated by Squire and Kaufmann,[1] and that the apparent high-temperature minimum in Nb may be merely a leveling off. Another interesting result is that the susceptibility of Pd appears to increase again at the lowest temperatures.

3. INTERPRETATION ACCORDING TO THE BAND THEORY

We recall very briefly the mechanism of the Pauli paramagnetism. In the absence of a magnetic field the electronic spins in a paramagnetic material are equally divided between the two possible spin states ("up" and "down"). An applied magnetic field in the up direction lowers the energies of the electrons with spin up relative to those with spin down. The lowest energy state of the system is then achieved by a spontaneous transition of some electrons from the down to the up state. The net

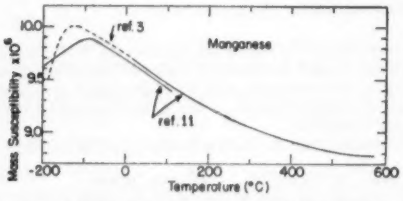

FIG. 4. Experimental susceptibility of Mn. The original dotted data are higher than shown, but have been shifted downward to join continuously with the solid curve.

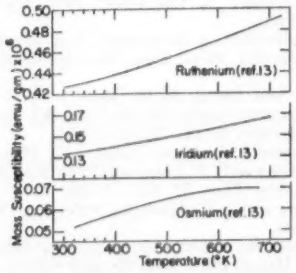

FIG. 5. Experimental susceptibilities of Ru and Os (column VIII of the periodic table) and of Ir (column IX).

uncompensated magnetic moment so induced per unit field is the magnetic susceptibility of the material.

The total number of electrons with spin up is simply $\int n_+(\epsilon)f(\epsilon,\zeta,T)d\epsilon$, where $n_+(\epsilon)$ is the density-in-energy of the electronic spin-up states; $f(\epsilon,\zeta,T)$ is the Fermi distribution function (the *a priori* probability of occupation of a state of energy ϵ); and ζ and T are the Fermi energy and absolute temperature, respectively. The applied magnetic field merely lowers the energy of every spin-up eigenstate by the amount μH, so that

$$n_+(\epsilon)=n(\epsilon+\mu H), \tag{1}$$

where $n(\epsilon)$ is the density-in-energy of the states of a single spin in the absence of a magnetic field. Similarly,

$$n_-(\epsilon)=n(\epsilon-\mu H). \tag{2}$$

The Fermi energy ζ is determined by the requirement that the sum of the numbers of electrons of each spin is the constant total number N:

$$N=\int[n(\epsilon+\mu H)+n(\epsilon-\mu H)]f(\epsilon,\zeta,T)d\epsilon. \tag{3}$$

The susceptibility is given in terms of the difference between the number of spins up and the number of spins down:

$$\chi=\operatorname{Lim}_{H\to 0}\frac{\mu}{H}\int[n(\epsilon+\mu H)-n(\epsilon-\mu H)]f(\epsilon,\zeta,T)d\epsilon. \tag{4}$$

This equation is easily cast into a more convenient form by first explicitly performing the indicated limiting process,

$$\chi=2\mu^2\int n'(\epsilon)f(\epsilon,\zeta,T)d\epsilon, \tag{5}$$

and by then performing a partial integration,

$$\chi=-2\mu^2\int n(\epsilon)f'(\epsilon,\zeta,T)d\epsilon, \tag{6}$$

Equations (3) and (6) are the fundamental equations determining the susceptibility. In principle it would merely be necessary to know $n(\epsilon)$ from the band structure of the material; one would solve for ζ from Eq. (3), insert this into Eq. (6), and then perform the integration to obtain χ explicitly as a function of T.

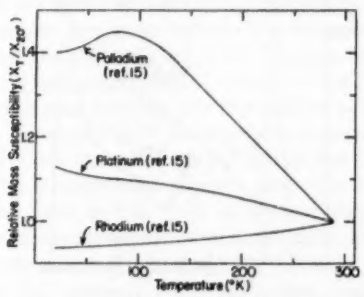

FIG. 6. Experimental susceptibilities of Rh (column IX) and of Pd and Pt (column X). The general trends of the susceptibility dependence continue in the high-temperature region which is not shown in the graph.

TABLE II. Compilation of best magnetic susceptibility values (emu/g) for the transition elements.

Element	$\chi\times10^6$	References
Ti	3.2	1,2
Zr	1.3	1,2
Hf	0.42	3
V	5.0	4
Nb	2.24	4,6
Ta	0.84	4,5
Cr	3.3	8,7
Mo	0.94	4,6
W	0.30	4,6
Mn	9.7	11
Re	0.37	12
Ru	0.43	13
Os	0.05	13
Rh	0.99	5
Ir	0.18	14,16
Pd	5.23	5
Pt	0.97	5

TABLE III. Comparison of the temperature coefficient of the susceptibility, the electronic specific heat, and the magnetic susceptibility of certain transition elements.

	Ti	V	Cr	Mn	(Ru)
Sign of $d\chi/dT$	+	−	+	−	+
Electronic specific heat, $\gamma\times10^4$	8.0	15	3.8	42	3.04
Susceptibility, $\chi\times10^6$	3.2	5.0	3.3	9.7	0.43

However, for any realistic $n(\epsilon)$ functions, this simple procedure is mathematically awkward due to the difficulty of the integrations involving $f(\epsilon,\zeta,T)$. Now although the susceptibility does depend on the Fermi distribution function (which is the same for all the metals), the main differences in the susceptibility from one metal to another will depend on the differences in their $n(\epsilon)$ curves. Since the susceptibility does not depend critically on the fine details of the universal function $f(\epsilon,\zeta,T)$, we replace it by an analytically simple function which still retains the essential character of $f(\epsilon,\zeta,T)$ and which makes the mathematical calculations relatively easy and convenient. Such a function is shown in Fig. 7 and is given algebraically by

$$f^*(\epsilon,\zeta,T)=\begin{cases}1, & \epsilon<\zeta-2.77kT\\ \frac{1}{2}\left(1-\dfrac{\epsilon-\zeta}{2.77kT}\right), & \zeta-2.77kT<\epsilon<\zeta+2.77kT\\ 0, & \epsilon>\zeta+2.77kT.\end{cases} \tag{7}$$

We now proceed to substitute this simple linearized function into our basic Eqs. (6) and (3) in order to obtain a new pair of simplified basic equations. Substituting first into Eq. (6) gives

$$\chi=-2\mu^2\int_{\zeta-2.77kT}^{\zeta+2.77kT}n(\epsilon)\left(-\frac{1}{5.5kT}\right)d\epsilon, \tag{8}$$

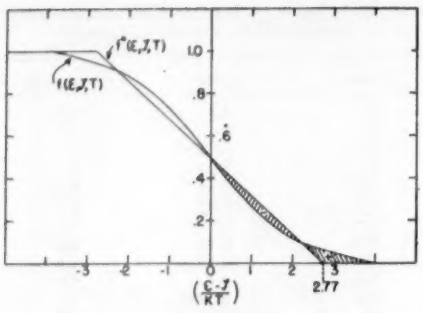

FIG. 7. The "linear" approximation to $f(\epsilon,\zeta,T)$. The slope of the straight line is so chosen that the shaded area vanishes algebraically.

or

$$\chi = 2\mu^2\langle n(\zeta)\rangle_{5.5kT}. \tag{9}$$

That is, the magnetic susceptibility is proportional to the average value of $n(\epsilon)$ in an energy interval of width $5.5kT$, centered at $\epsilon=\zeta$.

The simplification of Eq. (3) proceeds in a similar fashion, but the result is not quite so immediate. For the vanishingly small values of magnetic field in which we are interested Eq. (3) becomes

$$N = 2\int_{-\infty}^{\infty} n(\epsilon) f(\epsilon,\zeta,T)\,d\epsilon. \tag{10}$$

Eliminating N by means of the above equation rewritten for $T=0$, and replacing f by the linearized function f^*, we obtain

$$\int_{-\infty}^{\infty} n(\epsilon)[f^*(\epsilon,\zeta,T) - f(\epsilon,\zeta_0,0)]\,d\epsilon = 0. \tag{11}$$

Now the first fact which may be noted is that ζ is bounded in an interval of width $5.5kT$, centered at ζ_0:

$$\zeta_0 - 2.77kT < \zeta < \zeta_0 + 2.77kT. \tag{12}$$

For if we were to assume $\zeta > \zeta_0 + 2.77kT$, the term in square brackets in the integrand of Eq. (11) would be everywhere nonnegative, and the integral consequently could not vanish. Similarly, if we were to assume $\zeta < \zeta_0 - 2.77kT$, the term in square brackets would be everywhere nonpositive and again the integral could not vanish. It is now convenient to introduce an integrated density-of-states curve defined by

$$N(\epsilon,\zeta_0) = \int_{\zeta_0}^{\epsilon} n(\epsilon')\,d\epsilon'. \tag{13}$$

Thus $N(\epsilon,\zeta_0)$ has the physical significance of the total number of states (of a single spin) between the energies ζ_0 and ϵ. In the counting of states, however, all states of energy higher than ζ_0 give a positive contribution, whereas all states of energy less than ζ_0 give a negative contribution. An $N(\epsilon,\zeta_0)$ curve obtained from the $n(\epsilon)$ curve computed by Slater and Krutter[17] for copper is shown in Fig. 8.

Given a particular $n(\epsilon)$ curve, construction of the $N(\epsilon,\zeta_0)$ curves for various values of ζ_0 is facilitated by the evident relation,

$$N(\epsilon,\zeta_0') = N(\epsilon,\zeta_0) - N(\zeta_0',\zeta_0). \tag{14}$$

Thus we need only compute one integrated density-of-states curve; all others can be obtained therefrom by the simple subtraction of an appropriate constant. Equation (11), which determines ζ, may now be put into a convenient form by a partial integration,

$$\int_{-\infty}^{\infty} N(\epsilon,\zeta_0)\frac{d}{d\epsilon}[f^*(\epsilon,\zeta,T) - f(\epsilon,\zeta_0,0)]\,d\epsilon = 0; \tag{15}$$

and inserting the algebraic form for the parenthetical function yields

$$\langle N(\zeta,\zeta_0)\rangle_{5.5kT} = 0. \tag{16}$$

That is, the Fermi energy is determined by the vanishing of the average value of the integrated density-of-states curve in an interval $5.5kT$ centered at $\epsilon=\zeta$.

Equations (9) and (16) are our new basic pair of equations, replacing (6) and (3). The procedure for computing the susceptibility at any given temperature now resolves into the following sequence of graphical constructions, which are illustrated in Fig. 9. We assume that we are given the density-of-states curve $n(\epsilon)$ and the zero-temperature Fermi energy ζ_0 (or the equivalent quantity N, the total number of electrons). We then construct the integrated density-of-states curve $N(\epsilon,\zeta_0)$. To find the value of ζ at the chosen temperature T we move the interval $5.5kT$ along the energy axis until it intercepts an algebraically vanishing area under the $N(\epsilon,\zeta_0)$ curve. The center of the interval is then $\zeta(T)$. The average value of the $n(\epsilon)$ curve in that interval, when multiplied by the constant $2\mu^2$, is the value of the susceptibility $\chi(T)$.

Although the above constructions permit a simple

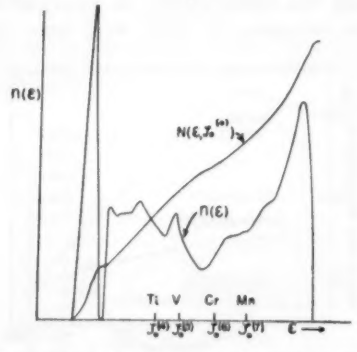

FIG. 8. The density-of-states curve for copper, as computed by Slater and Krutter. The integrated density-of-states curve $N(\epsilon,\zeta_0^{(0)})$ is also shown. The relative positions of other energies $\zeta_0^{(n)}$ for some of the transition elements are indicated (n is the total number of s and d electrons).

calculation of $\chi(T)$ itself, it is in the temperature coefficient $d\chi/dT$ that we are primarily concerned. We shall now see that this quantity may also be directly related to certain geometrical constructions based on the $n(\epsilon)$ curve.

The temperature dependence of χ clearly arises from two distinct sources. These are

1. the variation with temperature of the *width* of the Fermi distribution and consequently of the interval of averaging in Eq. (9). This width is simply $5.5kT$;

2. the variation with temperature of the Fermi energy $\zeta(T)$, which determines the *center* of the interval of averaging in Eq. (9). The dependence of ζ on the temperature is determined by Eq. (16).

The two separate mechanisms of temperature variation are clearly exhibited in the explicit equation for the derivative. Differentiating Eq. (9) (or 8), we find

$$\frac{d\chi}{dT}=\frac{2\mu^2}{T}[\bar{n}(\zeta\pm 2.77kT)-\langle n(\zeta)\rangle_{5.5kT}]$$

$$+2\mu^2\left[\frac{n(\zeta+2.77kT)-n(\zeta-2.77kT)}{5.5kT}\right]\frac{d\zeta}{dT}, \quad (17)$$

where $\bar{n}(\zeta\pm 2.77kT)$ denotes the average of the two values of $n(\epsilon)$ at the ends of the interval:

$$\bar{n}(\zeta\pm 2.77kT)=\tfrac{1}{2}[n(2.77kT)+n(\zeta+2.77kT)]. \quad (18)$$

The two terms of Eq. (17) correspond, respectively, to the two sources of temperature variation mentioned above. The quantity $d\zeta/dT$ may be related to the density-of-states curve by differentiating Eq. (16), yielding

$$\frac{d\zeta}{dT}=-2.77k\frac{N(\zeta+2.77kT,\zeta_0)+N(\zeta-2.77kT,\zeta_0)}{N(\zeta+2.77kT,\zeta-2.77kT)}. \quad (19)$$

Each of the terms of Eqs. (17) and (19) may be given a direct geometrical interpretation in terms of the $n(\epsilon)$ curve, and this geometrical interpretation is very useful in the analysis of susceptibility data. To interpret the first term of Eq. (17), which represents the contribution of the width of the Fermi distribution, we consider a straight line drawn between the values of $n(\epsilon)$ at the ends of the interval $\zeta\pm 2.77kT$. The bracket in the first term is then proportional (with the factor $5.5kT$) to the algebraic area between this line and the actual $n(\epsilon)$ curve, as shown in Fig. 9. To interpret the second term in Eq. (17), we note that the bracket is just the slope of the above mentioned straight line. The quantity $d\zeta/dT$, as given in Eq. (19), is in turn proportional (with the factor $5.5k$) to the fractional difference in the areas to the left and to the right of ζ_0 under the $n(\epsilon)$ curve in the interval $\zeta\pm 2.77kT$. This geometrical interpretation of $d\zeta/dT$ is illustrated in Fig. 9.

We shall now consider each of the two mechanisms of temperature variation in more detail. The first contribution to $d\chi/dT$, arising from the width of the Fermi distribution, is $2\mu^2/5.5kT^2$ times the area between the $n(\epsilon)$ curve and the straight line joining the extremities of the interval. It is clear that this contribution depends essentially on the curvature of $n(\epsilon)$ in the interval $\zeta\pm 2.77kT$. If $n(\epsilon)$ were linear, the curve would be coincident with the straight line, and the area between them would vanish; analytically, the average value of $n(\epsilon)$ appearing in Eq. (17) would just be $n(\zeta)$, independent of the width of the interval. However, if $n(\epsilon)$ were to have positive curvature the curve would be below the line, and the area would be positive, connoting a positive contribution to $d\chi/dT$. In terms of Eq. (9) the average value of $n(\epsilon)$ would be larger than $n(\zeta)$ and would increase with increasing interval width $5.5kT$; as a result the susceptibility would tend to increase with temperature. Similarly, an $n(\epsilon)$ curve with negative curvature leads to a negative temperature coefficient of susceptibility. This connection with the curvature is clearly evident in the first term of Eq. (17), the form of which suggests the finite difference approximation to the second derivative of $n(\epsilon)$.

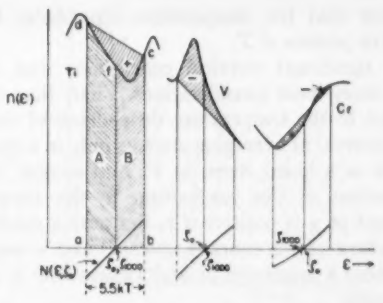

FIG. 9. Geometrical interpretation of the two contributions to the temperature coefficient of the susceptibility. Portions of the Slater-Krutter density-of-states curve have been applied to Ti, V, and Cr. The contributions of the interval width to the temperature coefficient of the susceptibility is (for Ti).

$$(d\chi/dT)_{\text{width}}=2\mu^2/5.5kT^2 \quad (\text{Area } d/c).$$

The contribution of the Fermi energy shift is

$$(d\chi/dT)_{\text{shift}}=2\mu^2(\text{slope of line } dc)(d\zeta/dT),$$

where

$$d\zeta/dT=5.5k[(\text{Area A}-\text{Area B})/(\text{Area A}+\text{Area B})].$$

For low temperatures we may expand $n(\epsilon)$ in a power series about $\epsilon=\zeta$:

$$n(\epsilon)=n(\zeta)+(\epsilon-\zeta)n'(\zeta)+(1/2!)(\epsilon-\zeta)^2n''(\zeta)+\cdots, \quad (20)$$

whence

$$\langle n(\zeta)\rangle_{5.5kT}=n(\zeta)+\frac{(2.77)^2}{2(2!)}n''(\zeta)(kT)^2+\frac{(2.77)^4}{4(4!)}n^{(iv)}(\zeta)(kT)^4+\cdots. \quad (21)$$

Again we note that the leading temperature-dependent term is determined by the curvature of $n(\epsilon)$, and we

also note that the temperature dependence involves only even powers of T.

Two significant physical conclusions thus may be drawn from these considerations. First, that the contribution to the temperature dependence of the width of the interval of averaging appears only in a quadratic, and not in a linear, term in T. And second, that the contribution of this mechanism to the temperature coefficient of χ is positive if ζ_0 lies near a minimum of $n(\epsilon)$ (where $n(\epsilon)$ is concave upward) and is negative if ζ_0 lies near a maximum of $n(\epsilon)$ (where $n(\epsilon)$ is concave downward).

We now consider the second contribution to the temperature dependence of the susceptibility, namely, the variation of the Fermi energy with temperature. If an increase in temperature shifts ζ in the direction of increasing $n(\zeta)$ this mechanism tends to make a positive contribution to the temperature coefficient of χ, whereas if an increase of T shifts ζ in the direction of decreasing $n(\zeta)$ the contribution tends to be negative. Thus the second term of Eq. (17) is roughly of the form $(dn/d\epsilon)_\zeta d\zeta/dT$, the actual slope $(dn/d\epsilon)_\zeta$ being replaced, however, by the slope of the straight line joining the values $n(\zeta\pm 2.77kT)$. The value of $d\zeta/dT$ is found graphically as described above and as indicated in Fig. 9.

It is again of some interest to check the behavior at low temperatures. Expanding $N(\epsilon,\zeta_0)$ in a power series about $\epsilon=\zeta_0$, we obtain

$$N(\epsilon,\zeta_0)=(\epsilon-\zeta_0)n(\zeta_0)+\frac{1}{2!}(\epsilon-\zeta_0)^2n'(\zeta_0)+\frac{1}{3!}(\epsilon-\zeta_0)^3n''(\zeta_0)+\cdots, \quad (22)$$

whence

$$\langle N(\zeta,\zeta_0)\rangle=(\zeta-\zeta_0)n(\zeta_0)+\frac{1}{2!}[(\zeta-\zeta_0)^2+\tfrac{1}{3}(2.77kT)^2]n'(\zeta_0)+\cdots. \quad (23)$$

By ignoring all terms higher than the second in T, the equation obtained by equating $\langle N(\zeta,\zeta_0)\rangle$ to zero may be solved for ζ, giving

$$\zeta-\zeta_0=-\frac{1}{6}\frac{n'(\zeta_0)}{n(\zeta)}(2.77kT)^2. \quad (24)$$

Thus

$$n(\zeta)=n\left(\zeta_0-\frac{1}{6}\frac{n'(\zeta_0)}{n(\zeta_0)}(2.77kT)^2\right)=n(\zeta_0)-\frac{1}{6}\frac{[n'(\zeta_0)]^2}{n(\zeta_0)}(2.77kT)^2+\cdots. \quad (25)$$

Inserting this value in Eq. (21) we find that to the second order in T,

$$\chi=2\mu^2n(\zeta_0)+(2.77)^2\mu^2\left[\tfrac{1}{2}n''(\zeta_0)-\frac{(n'(\zeta_0))^2}{3n(\zeta_0)}\right](kT)^2. \quad (26)$$

The term involving the square of the first derivative of $n(\epsilon)$ is the contribution of the variation of ζ with temperature. Again we find that the temperature dependence appears only in a quadratic, rather than in a linear, term in T. The sign of this leading temperature-dependent term is always negative, so that at low temperatures the shift of ζ with temperature always makes a negative contribution to the temperature coefficient of the susceptibility.

Equation (26) may be compared with a result of Stoner,[18] who by a direct series expansion of the true Fermi function, found

$$\chi=2\mu^2n(\zeta_0)+\frac{\pi^2}{2}\mu^2\left[\tfrac{1}{3}n''(\zeta_0)-\frac{[n'(\zeta_0)]^2}{3n(\zeta_0)}\right](kT)^2+\cdots. \quad (27)$$

On the basis of this low-temperature equation, Stoner[18] has demonstrated the possibility of obtaining a positive temperature coefficient of susceptibility near a minimum of $n(\epsilon)$, and has applied this result to a discussion of the then-available data.

Despite the fact that at very low temperatures the contribution to $d\chi/dT$ of the shift of ζ is always negative, at reasonable temperatures this contribution may be either positive or negative. The graphical solution indicates that ζ has a tendency to move away from the largest peak of the $n(\epsilon)$ curve in the interval $\zeta\pm 2.77kT$, and this "repulsion" may easily result in an increase in $n(\zeta)$ with T. A condition under which this mechanism will contribute a positive temperature coefficient is thus that ζ_0 be on the shallow side of an asymmetric minimum of $n(\epsilon)$.

4. THEORETICAL DENSITY-OF-STATES CURVES[19]

Preparatory to a discussion of the correlation of the theoretical results and the empirical data, we briefly review the several density-of-states curves which have been computed for the transition elements. Precise calculations, although possible in principle, are prohibitively difficult in practice. As a consequence semiquantitative inferences must be drawn from the synthesis of the results of various approximate calculations.

The theoretical density-of-states curve to which we shall make primary reference is that computed by Slater and Krutter[17] for copper, and generally optimistically applied to the various iron-group transition metals. The Slater-Krutter calculation is based on an approximate Wigner-Seitz solution of the Fock equations, using an ion-core potential obtained from the Hartree functions for the free copper ion. As these Hartree functions, in turn, were computed neglecting exchange they are very probably larger than the true inner-core functions. Consequently the width of the d band as computed by Krutter is undoubtedly too wide. The computed width is 5.4 ev, whereas a more probable

[19] G. V. Raynor, "The band structure of metals," Repts. Progr. Phys. 15, 173 (1952).

value on the basis of soft x-ray data, electronic specific heats, and other calculations is of the order of 4 ev.

The general method of the Slater-Krutter calculations on copper have been applied to α Fe by Manning[20] and to γ Fe by Greene and Manning.[21] Comparison of these curves with the copper curve substantiates to some extent the assumption of similarity in form of the d band among the various transition metals, although significant differences in detail are quite apparent. In all three curves the distribution is peaked at each end of the band, and has a third peak just below the center of the band. Although the relative heights of the peaks differ in the various calculations we shall see that it is merely the existence and position of the peaks, rather than their precise height, which is significant in our considerations.

Another calculation with relevance to the Fe-group transition metals is the tight-binding calculation of Ni by Fletcher and Wohlfarth.[22] The tight-binding approximation certainly underestimates the effect of overlap, and in this case predicts a band width of only 2.7 ev.

For our discussions of the density-of-states curves of the elements in the sixth row of the periodic table (Hf, Ta, W, Re, Os, Ir, Pt) we shall refer principally to the calculation of tungsten by Manning and Chodorow,[23] shown in Fig. 10. This calculation employed a rather elaborate Wigner-Seitz cellular approach, using fourteen atomic functions for the representation of the wave functions of the valence electrons. The results for the partially filled d band may be expected to be reasonably accurate, and the extrapolation of the results to Ta at least should be quite trustworthy. Extrapolation to other members of the sixth row, which have other crystal structures, would be questionable.

No theoretical density-of-states curves are available for a discussion of the transition elements of the fifth row of the periodic table (Zr, Nb, Mo, Ru, Rh, Pd).

5. THEORETICAL CORRELATION OF EXPERIMENTAL DATA

Having reviewed both the experimental data and the theory of the dependence of the susceptibility on the density-of-states curves, we now consider the correlation of the observed data with the $n(\epsilon)$ curves described in the preceding section. In particular we shall first attempt to account for the observed alteration in the sign of $d\chi/dT$ from column to column of the periodic table. The empirical susceptibility data will then be analyzed to suggest certain probable alterations in the details of the theoretical density-of-states curves.

We first consider the sequence of the iron-group transition metals, for which we adopt the Slater-Krutter curve as the nominal basis for our discussion. We proceed by assessing the separate contributions to $d\chi/dT$ from the interval width and from the ζ shift mechanisms using the graphical constructions illustrated in Fig. 9. We arbitrarily choose an interval width of 1000°C to obtain the general trend of the temperature coefficient of the susceptibility. If both mechanisms give contributions of the same algebraic sign, the sign of $d\chi/dT$ is known immediately. However, if the two separate contributions are of opposite sign we must inquire more carefully into the ratio of their magnitudes. We shall examine in turn the elements Ti, V, Cr, and Mn. In Fig. 9 we see that for Ti the motion of ζ over the temperature interval to 1000°C is very small because the areas under $N(\epsilon,\zeta_0)$ are almost equal. However, it is evident from the relative heights of the two maxima that ζ will shift slightly to the right, the direction of decreasing $n(\epsilon)$ and decreasing χ. The contribution due to the interval width, however, is positive and large. The ratio of the interval width contribution to the ζ shift contribution is of the order of 80, showing conclusively that the susceptibility of Ti should increase with temperature over 1000°C. This is in agreement with the experimental data in Fig. 1.

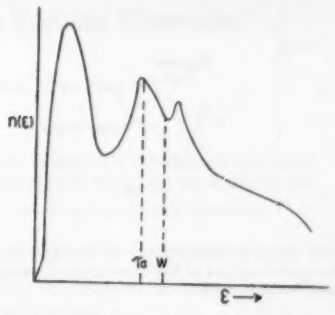

FIG. 10. The density-of-states curve for tungsten, as calculated by Manning and Chodorow. The zero-temperature Fermi energy of W and Ta are indicated.

The same constructions for V are also shown in Fig. 9 It is evident that both the interval width and ζ shift mechanisms give negative contributions to $d\chi/dT$ in this case and that as a result the susceptibility of V should decrease with temperature. Again this is consistent with the experimental data shown in Fig. 2.

Cr is considered next. From Fig. 9 we find that $(d\chi/dT)_{\text{width}}$ is positive while $(d\chi/dT)_{\zeta\text{ shift}}$ is negative. The calculated value of the ratio of these contributions is 1.06 indicating that the χ of Cr should actually increase with temperature in accord with the experimental data in Fig. 3. However, the low value of the ratio is somewhat unconvincing. Also, as Friedberg, Estermann, and Goldman[24] have pointed out, and as is evident from Table II, Cr has a much lower electronic specific heat than its neighbors in the periodic table. Since the electronic specific heat is directly proportional to $n(\epsilon)$ we would expect the Fermi energy of Cr to occur at a very

[20] M. F. Manning, Phys. Rev. **63**, 190 (1943).
[21] J. B. Greene and M. F. Manning, Phys. Rev. **63**, 203 (1943).
[22] G. C. Fletcher and E. P. Wohlfarth, Phil. Mag. **42**, 106 (1951).
[23] M. F. Manning and M. Chodorow, Phys. Rev. **56**, 787 (1939).
[24] Friedberg, Estermann, and Goldman, Phys. Rev. **85**, 375 (1952).

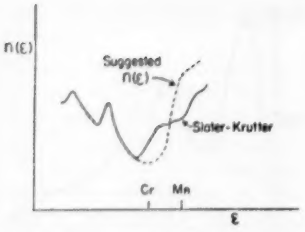

FIG. 11. The Slater-Krutter density-of-states curve qualitatively altered from considerations of the experimental susceptibility and electronic specific heat data.

low minimum in $n(\epsilon)$. This would be most logically accomplished if the minimum in $n(\epsilon)$, which in Fig. 8 occurs between V and Cr, were widened considerably. Then not only would the ζ_0 of Cr occur at a lower value of $n(\epsilon)$, but the density-of-states in the neighborhood of Mn would be increased significantly. This is physically desirable also because the magnitudes of the susceptibility and electronic specific heat of Mn are much larger than those of Cr. This suggests that the actual $n(\epsilon)$ curve is of the form shown in Fig. 11. From this curve it is at once clear that the susceptibility of Cr must increase with temperature since there will now be a larger positive interval width contribution.

The suggested $n(\epsilon)$ curve also serves to clarify the case of Mn, in which the experimental susceptibility decreases with temperature in the intermediate temperature range. The ζ_0 of Mn falls on one side of a large maximum in the $n(\epsilon)$ curve of Slater and Krutter, a position which ordinarily would lead to a negative $d\chi/dT$. However, as can be seen in Fig. 8, the fortuitous positioning of ζ_0 near what is probably only a computational secondary minimum in $n(\epsilon)$ predicts a positive $d\chi/dT$, even though ζ moves toward lower $n(\epsilon)$. Our suggested $n(\epsilon)$ curve eliminates this presumably computational minimum and gives the temperature dependence suggested by the broader features of the Slater-Krutter $n(\epsilon)$ and required by experiment.

Thus we have the important result from our simplified treatment that the band theory applied to a slightly amended approximate calculation of the $3d$ band is capable of explaining the observed alternation in sign of $d\chi/dT$ of the transition elements. This alternation arises from the sequence of maxima and minima which have appeared in roughly similar form in the various various approximate calculations of the density-in-energy curves of the iron-group $3d$ band. Corroborating evidence for the validity of maxima and minima in the density-of-states of the transition elements is found in the electronic specific heat. At low temperatures the electronic portion of the specific heat may be represented by a term linear in temperature, $C_e=\gamma T$, where γ is directly proportional to $n(\zeta)$. Goldman[25] has pointed out that the values of $n(\zeta)$ derived from the electronic specific heats of the transition elements alternate in a manner quite like the maxima and minima in the Slater-Krutter curve. Recently Horowitz and Daunt[16] have also proposed an $n(\epsilon)$ curve, somewhat similar to that of Fig. 11, based on a synthesis of the electronic specific heat data of the transition elements. It seems reasonable therefore, to state that a structure of maxima and minima in the $3d$ band is capable of explaining the susceptibilities of the Fe-group elements, and that this structure is in harmony both with theoretical calculations and with other experimental data.

The temperature dependence of the susceptibility of tungsten, in the sixth row of the periodic table, may be discussed on the basis of the density-of-states curve computed by Manning and Chodorow and shown in Fig. 10. The Fermi energy falls at a minimum as shown, and $d\chi/dT$ is consequently positive, in agreement with the experimental susceptibility shown in Fig. 3. On the basis of the same theoretical density-of-states curve the zero-temperature Fermi energy of tantalum falls at a maximum of $n(\epsilon)$, as indicated in Fig. 10. A negative coefficient of susceptibility is thereby predicted, again in agreement with the experimental observations.

Maxima and minima in the curves of susceptibility *vs* temperature present no special problem to our treatment, although in some cases it may be necessary to resort to fine structure in the $n(\epsilon)$ curves. Minima at low temperatures are easily explained. It has been pointed out that at low temperatures the movement of ζ always results in a decreasing χ; therefore, if the interval width contribution is the smaller at low temperatures (i.e., if the curvature $n''(\zeta_0)$ is small) the χ will necessarily decrease. As T increases the interval width contribution, if positive, can easily cause the sign of $d\chi/dT$ to change, thereby producing the low temperature minima. A maximum at low temperatures is somewhat more difficult to explain because of the tendency of the susceptibility to decrease at low temperatures; but if ζ_0 were to occur at a small depression in $n(\epsilon)$, the susceptibility could increase initially at low temperatures and a maximum could easily result. However, it must be pointed out that in the case of manganese a strong exchange coupling may be responsible for the maximum at low temperatures. Maxima and minima at high temperatures are easily accounted for in terms of the competition of the two mechanisms.

On the basis of the above simplified treatment, it thus appears that the band theory is able to give a natural explanation not only of the increasing χ of certain transition elements, but also of the remarkable alternation in sign of $d\chi/dT$.

[25] J. Goldman (private communication).

Some Optical Properties of MgO in the Vacuum Ultraviolet

PETER D. JOHNSON
General Electric Research Laboratory, Schenectady, New York
(Received February 5, 1954)

The optical absorption and the excitation spectrum for luminescence of synthetic periclase crystals have been determined in the vacuum ultraviolet. From these measurements it is deduced that the width of the forbidden energy band of MgO is approximately 7.4 ev.

INTEREST in the width of the forbidden energy band in crystalline MgO has arisen recently as a result of temperature dependence of conductivity,[1] photoconductivity,[2] and soft x-ray[3] measurements on synthetic periclase crystals. The absorption measurements of several workers[4–7] show that the forbidden band is at least 6 ev wide; however, no measurements at wavelengths shorter than 2000A have been reported. In the present work absorption of synthetic MgO in the vacuum ultraviolet is measured on crystals from three different sources. Since it is not practicable to determine the absorption of bulk crystals of convenient dimensions where the absorption coefficient is above 200 cm^{-1}, the excitation spectrum for fluorescence was measured in order to obtain additional information on the forbidden energy band.

All optical measurements were made with a previously described vacuum ultraviolet monochromator.[8] The sample holder for excitation measurements permitted the observation of fluorescence at right angles to the direction of excitation, and provided for elimination of scattered incident radiation by glass filters.

Synthetic MgO crystals from the Norton Company and from the General Electric Company were selected for clarity and lack of color and were cleaved to thicknesses of 0.27 to 0.75 mm. These crystals were nonluminescent under uv excitation. The average analysis of the Norton Company crystals as supplied by the manufacturer was: Al_2O_3, 0.07 percent; Fe_2O_3, 0.04 percent; TiO_2, 0.015 percent; and SiO_2, 0.005 percent. Analysis of two individual crystals used in this work showed iron concentrations of 0.08 and 0.004 percent. The G.E. crystals were made by a similar industrial process and contain iron and silicon as principle impurities. Some absorption and all the fluorescence measurements were performed on a few crystals containing only a few parts per million of Ca, Fe, Na, and Ni as principal impurities made on a laboratory scale by H. F. John at the University of Missouri. These crystals have a blue-ultraviolet fluorescence under ultraviolet excitation.

Typical absorption spectra uncorrected for surface reflection are shown in Fig. 1 for the Norton and Missouri crystals. The absorption of the G.E. crystals is almost identical to that of the Missouri samples. In all cases the value of the absorption coefficient is greater than 400 cm^{-1} at 1600A. This figure represents a lower limit since the amount of transmitted radiation was below the limit of detection. The absorption coefficients at 1850, 2100, and 2800A agree in all the Norton samples measured. The ratios of the intensities of the last two bands are the same as those found by Molnar and Hartman[5] in MgO crystals colored by x-rays and by Weber[7] in MgO with oxygen excess. The 1850A band has not been reported previously.

It is probably significant that the strong absorption at wavelengths shorter than 1700A is independent of the origin and impurity content of the sample. The impurity concentrations of many of the crystals seem insufficient to cause absorption of the order of 150 cm^{-1}. In addition, no transmission is observed between 1675A and the limit of the monochromator at 950A.

It was found possible to obtain further information regarding the nature of this absorption edge by measuring the dependence of fluorescent intensity of the Missouri MgO crystals on wavelength of excitation. The result of this measurement is shown in Fig. 2. At

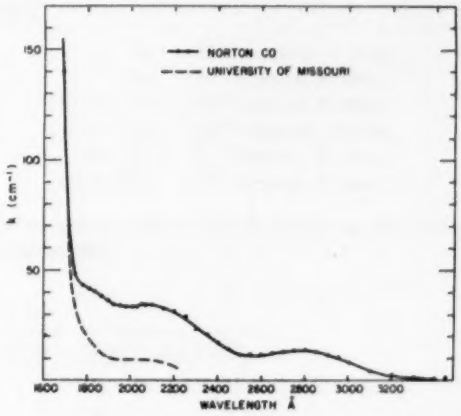

FIG. 1. Optical absorption of typical MgO crystals from two different sources.

[1] A. Lempicki, Proc. Phys. Soc. (London) **B66**, 281 (1953).
[2] H. R. Day, Phys. Rev. **91**, 822 (1953).
[3] J. R. Townsend, Phys. Rev. **92**, 556 (1953).
[4] R. T. Brice and J. Strong, Phys. Rev. **47**, 255 (1935); J. Opt. Soc. Am. **25**, 205 (1935).
[5] J. P. Molnar and C. D. Hartman, Phys. Rev. **79**, 1015 (1950).
[6] W. W. Tyler and R. L. Sproull, Phys. Rev. **83**, 548 (1951).
[7] H. Weber, Z. Physik **130**, 392 (1951).
[8] P. D. Johnson, J. Opt. Soc. Am. **42**, 278 (1952).

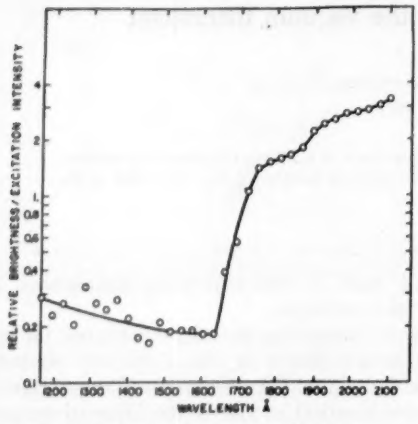

FIG. 2. Excitation spectrum for fluorescence.

short wavelengths of excitation the fluorescent efficiency is substantially uniform. In this region, at wavelengths below 1635A, the incident radiation is strongly absorbed so that only a small volume of crystal near the surface, with a correspondingly small number of luminescent centers, participates in fluorescence. At 1635A an abrupt change in the distance of penetration of the incident radiation results in more activators participating in luminescence and perhaps more efficient direct excitation. A substantial portion of the excitation energy at $\lambda < 1635$A must either be lost in radiationless processes or stored as excited species of long lifetime. The buildup of fluorescence and phosphorescent decay indicate that excited species of long lifetime are created.

It was found that at all wavelengths of excitation there is an initial sudden rise of fluorescence at the beginning of irradiation followed in some cases by a further gradual increase of intensity with a time constant of the order of 10 minutes. The excitation spectrum of Fig. 2 is for the initial rise. An interesting feature of the slow buildup resides in the fact that it exists most strongly in the short wavelength part of the excitation spectrum. At 1635A, for instance, the slow buildup component after 5 minutes of excitation was 70 percent of the initial rise; at 1695A it was only 10 percent. The magnitude and time constant of phosphorescence were comparable to those of the slow buildup. These observations confirm the formation of excited species of long lifetime near the surface by short wavelength excitation which can diffuse into the crystal losing their energy at luminescent centers.

Both optical absorption and luminescence excitation measurements indicate a strong discontinuity in absorption in the neighborhood of 1635 to 1690A which can be attributed to the MgO lattice itself rather than to an impurity. It is not clear whether the process accompanying absorption at these wavelengths is the creation of excitons or excitation of valence electrons to the conduction band. The buildup and decay of luminescence suggest the generation of mobile excited species by wavelengths shorter than 1690A. It is concluded from these results that the first fundamental absorption band in cubic MgO occurs at approximately 7.4 ev.

The author is indebted to Mr. L. B. Bronk for chemical analyses and to Dr. Gordon Finlay of the Norton Company and to the late Professor A. S. Eisenstein of the University of Missouri for the MgO crystals.

Cation Distributions in Mixed Ferrites

J. SAMUEL SMART
United States Naval Ordnance Laboratory, White Oak, Maryland
(Received January 22, 1954)

In materials with the spinel structure, such as the ferrites, the cations are located on two different types of crystallographic sites. Expressions are derived for the equilibrium distribution of cations in mixed ferrites, which contain three different types of cations.

It is suggested that the cation distributions in such ferrites may be determined from the experimental values of magnetic moment and g factor. The method is applied to the nickel ferrite-aluminate series; the results agree reasonably well with x-ray diffraction data.

IN materials which have the chemical formula $MO \cdot N_2O_3$ and the spinel structure, two types of crystallographic sites are available to the cations. For each unit $MO \cdot N_2O_3$ there is one tetrahedrally coordinated, or A, site and two octahedrally coordinated, or B, sites. If the A sites contain only the divalent ions M^{++}, the crystal structure is said to be normal; if the A sites contain only trivalent ions N^{3+}, the structure is said to be inverted. Intermediate arrangements are, of course, possible.

The basic magnetic properties of the ferrites are very sensitive functions of the distribution of the metallic ions among the available A and B sites. For single ferrites, the distributions can be estimated by using a set of rules proposed by Verwey, Haayman, and Romeijn.[1] The gist of these rules is that the Fe^{3+} ion will occupy the A sites except when the divalent ion is Zn^{++} or Cd^{++}. Thus zinc and cadmium ferrites should be normal, and all other ferrites should be inverted. The Verwey rules obviously hold only in some approximation, since at any finite temperature at least some small fraction of the ions will be in "wrong" sites. However, the approximation is apparently a good one for all of the simple ferrites, excepting those of magnesium and copper.

In magnesium and copper ferrites, the magnetic properties have been observed to depend on the previous heat treatment. Néel[2] has suggested that in these cases the energy required to interchange the divalent and trivalent ions among the A and B sites is relatively small, so that the ionic distributions vary appreciably with temperature. Pauthenet[3] has measured the saturation magnetization of quenched magnesium and copper ferrites; the measured moments reflect the "frozen-in" distribution which was the equilibrium distribution for the quenching temperature. His results are in excellent agreement with a theoretical formula obtained by Néel[2] for the equilibrium distribution as a function of temperature.

Little detailed work has been done on the ionic distribution in mixed ferrites; Sage and Guillaud[4] have noted, however, that the Verwey rules do not seem to hold as generally as they do for the single ferrites. In this paper, we discuss some of the features of the ionic distribution problem for mixed ferrites.

EQUILIBRIUM DISTRIBUTIONS

Let the basic ferrite have the formula $MO \cdot N_2O_3$, where M and N are divalent and trivalent ions, respectively. (Strictly speaking, the material is not a ferrite unless N = Fe, but we use the term loosely here to include any material with the spinel structure.) We shall consider two special cases of mixed ferrites which have been the subject of considerable experimental study.

Case A—Two Kinds of Divalent Ions

We wish to determine the distributions of ions on the A and B sites for a ferrite with the formula $M_{(1-d)}P_dO \cdot N_2O_3$. Here P is a divalent ion and d varies from 0 to 1. The distribution can be described by two parameters, x and y. Suppose that for ν molecules of the material we have

$x\nu$	M^{++} ions on A sites,
$y\nu$	P^{++} ions on A sites,
$(1-x-y)\nu$	N^{3+} ions on A sites,
$(1-d-x)\nu$	M^{++} ions on B sites,
$(d-y)\nu$	P^{++} ions on B sites,
$(1+x+y)\nu$	N^{3+} ions on B sites.

The number of ways in which such a distribution can be achieved are

$$w = \frac{[(1-d)\nu]!(d\nu)!(2\nu)!}{(x\nu)!(y\nu)![(1-x-y)\nu]![(1-d-x)\nu]![(d-y)\nu]![(1+x+y)\nu]!}. \quad (1)$$

[1] Verwey, Haayman, and Romeijn, J. Chem. Phys. **15**, 181 (1947).
[2] L. Néel, Compt. rend. **230**, 375 (1950).
[3] R. Pauthenet, thesis, Grenoble, 1951.
[4] M. Sage and C. Guillaud, Comptes rend. **230**, 1751 (1950).

The entropy per molecule corresponding to such a situation can be expressed with the aid of Stirling's approximation as

$$s=(k/\nu)\ln w=k[(1-d)\ln(1-d)+d\ln d+2\ln 2 -x\ln x-y\ln y-(1-x-y)\ln(1-x-y) -(1-d-x)\ln(1-d-x)-(d-y)\ln(d-y) -(1+x+y)\ln(1+x+y)]. \quad (2)$$

In order that x and y represent equilibrium distributions, they must have values which minimize the free energy,

$$f=u-Ts, \quad (3)$$

where u is the internal energy per molecule. By requiring that the first derivatives of f with respect to x and y vanish, we find

$$x(1+x+y)=(1-x-y)(1-d-x)\exp(-u_x/kT), \quad (4a)$$

$$y(1+x+y)=(1-x-y)(d-y)\exp(-u_y/kT), \quad (4b)$$

where $u_x=\partial u/\partial x$ and $u_y=\partial u/\partial y$. The exact form of u_x and u_y is not known in general; for the important case P=Zn and N=Fe, u_x is believed to be positive and u_y to be negative. As a first approximation we shall assume that u_x and u_y are constant. This is equivalent to assuming that the net work required to interchange various ions between the A and B sites is independent of x and y (though not the same for different types of interchanges). A dependence of u_x and u_y on x and y might lead to ordered arrangements at finite temperatures. Such an ordering has been observed by Braun[6] for lithium-iron spinel. Also, the well-known low-temperature transition in magnetite[1,6,7] is believed to be a result of the ordering of the divalent and trivalent atoms on the B sites. These effects, however, seem to be exceptions rather than the rule, so that the assumption of u_x and u_y as being constant is probably justified as a first approximation.

From Eqs. (4) we can obtain two simultaneous nonlinear equations in the distribution parameters x and y. They are

$$[1-A_x]x^2+[1-A_x]xy+(1+(2-d)A_x)x +(1-d)A_xy-(1-d)A_x=0, \quad (5a)$$

$$[1-(A_x/A_y)]xy-dx+(1-d)(A_x/A_y)y=0, \quad (5b)$$

with $A_x=\exp(-u_x/kT)$.

Case B—Two Kinds of Trivalent Ions

Consider a spinel with the composition

$$MO\cdot N_{(2-t)}Q_tO_3,$$

where Q is a trivalent ion and t varies from 0 to 2. Let there be

$x\nu$	M^{++} ions on A sites,
$z\nu$	Q^{3+} ions on A sites,
$(1-x-z)\nu$	N^{3+} ions on A sites,
$(1-x)\nu$	M^{++} ions on B sites,
$(t-z)\nu$	Q^3 ions on B sites,
$(1-t+x+z)\nu$	N^{3+} ions on B sites.

By the same procedure as in Case A, we find that the equilibrium distribution is given by

$$x(1-t+x+z)=(1-x)(1-x-z)\exp(-u_x/kT), \quad (6a)$$

$$z(1-t+x+z)=(t-z)(1-x-z)\exp(-u_y/kT), \quad (6b)$$

or by

$$[1-A_x]x^2+[1-A_x]xz+[1-t+2A_x]x +A_xz-A_x=0, \quad (7a)$$

$$[1-(A_z/A_x)]xy+t(A_z/A_x)-z=0. \quad (7b)$$

Numerical solutions of Eqs. (5) for various values of A_x and A_y and of Eqs. (7) for various values of A_x and A_z have been computed by Miss Elise Fisher of the Applied Mathematics Division of the U. S. Naval Ordnance Laboratory. Tables of these solutions may be obtained upon request from Miss Fisher.

A SUGGESTED METHOD OF DETERMINING CATION DISTRIBUTIONS

The cation distributions in both single and mixed ferrites may be determined experimentally (in principle, at least) by either x-ray or neutron diffraction.[8–10] However, the x-ray and neutron diffraction methods become tedious and inaccurate if different types of ions have nearly equal scattering cross sections; this is especially true for mixed ferrites. We wish to suggest an alternate method of determining the ionic distributions of mixed ferrites (with three kinds of metallic ions) which should be reasonably accurate whenever the different kinds of ions have sufficiently different magnetic moments and g factors.

The Néel theory gives for the average net magnetic moment per molecule of a ferrite the relation

$$\mu=\mu_b-\mu_a, \quad (8)$$

where μ_b is the average net monent on two B sites and μ_a the average net moment on an A site. Tsuya[11] and Wangsness[12] have recently derived an expression for the effective g value of a ferrite:

$$g=\mu/(S_b-S_a), \quad (9)$$

where S_b and S_a are the net average spins per molecule on B and A sites. Here μ is given in Bohr magnetons and

[6] P. B. Braun, Nature **170**, 1123 (1952).
[7] L. R. Bickford, Revs. Modern Phys. **25**, 75 (1953).
[7] S. Abrahams and B. Calhoun, Acta. Cryst. **6**, 105 (1953).
[8] F. Bertaut, Compt. rend. **230**, 213 (1950).
[9] G. E. Bacon and F. F. Roberts, Acta. Cryst. **6**, 57 (1953).
[10] Corliss, Hastings, and Brockman, Phys. Rev. **90**, 1013 (1953).
[11] N. Tsuya, Progr. Theoret. Phys. **7**, 263 (1952).
[12] R. K. Wangsness, Phys. Rev. **91**, 1085 (1953).

the S's in units of $\hbar$. If we evaluate Eqs. (8) and (9) for absolute zero then μ_b, μ_a, S_b, and S_a all depend on the distribution parameters x and y, or x and z, in a simple linear fashion. Thus if experimental measurements on μ and g can be accurately extrapolated to 0°K, we have two simultaneous linear equations which can easily be solved for the distribution parameters.[13]

For example, in Case B, as mentioned, the equations would be

$$2(\mu_N-\mu_M)x+2(\mu_M-\mu_Q)z=\mu-\mu_M+t(\mu_N-\mu_Q), \quad (10a)$$

$$2(S_N-S_M)x+2(S_N-S_Q)z = \mu/g-S_M+t(S_N-S_Q). \quad (10b)$$

For a comparison with experiment, we shall consider the series $NiO\cdot Fe_{(2-t)}Al_tO_3$. Measurements of both μ and g have been made on this complete series at the U. S. Naval Ordnance Laboratory.

Before beginning the comparison, we note that there is an additional complication in that the Ni^{++} ion does not have the same magnetic properties on the A sites as on the B sites. Van Vleck[14] has pointed out that the effect of crystalline electric fields in compounds of the transition elements is, first, to break up the spin-orbit coupling and, second, to at least partially lift the remaining orbital degeneracy. The extent to which the orbital degeneracy is raised depends on the ion and on the symmetry of the crystalline field but for Ni^{++} with $L=3$, the sevenfold degenerate orbital level is usually split into two adjacent triplets and a singlet. When the Ni^{++} ion has an octahedral coordination of surrounding negative ions, i.e., is on the B site, the singlet level lies lowest and is widely separated from the triplet levels. Penney and Schlapp[15] have shown that in this case the magnetic moment and g factor have essentially the spin-only values with a relatively small correction which depends on the ratio of the spin orbit coupling parameter to the singlet-triplet separation. This case has been studied experimentally many different times with the results that $g_{Ni}(oct)\cong 2.2$–2.3. (For Ni^{++}, $S=1$ and μ and g are numerically equal if μ is given in Bohr magnetons.)

For Ni^{++} with tetrahedral coordination, the multiplet is inverted with one of the triplet levels lying lowest; the problem here is complicated because the intratriplet separations are ordinarily not large compared to kT. In a cursory survey of the literature we were unable to find any detailed studies of this case; however Abragam and Pryce[16] and Bleaney and Ingram[17] have both made theoretical and experimental studies of a case which should be similar—that of Co^{++} in a distorted octahedral coordination. Here they find that the g values are highly anisotropic and vary from about 3 to about 6. For our purposes, we shall assume that for polycrystalline samples of the Ni ferrite aluminates, such as have been studied experimentally, the relation

$$\mu_{Ni}(tet)=g_{Ni}(tet)S_{Ni} \quad (11)$$

holds. Here $\mu_{Ni}(tet)$ is an average magnetic moment as determined from magnetization measurements and $g_{Ni}(tet)$ is an average g value determined from magnetic resonance measurements. We shall expect that $g_{Ni}(tet)$ may be relatively large, of the order of 3 or greater.

In order to obtain a value of $g_{Ni}(tet)$ which is appropriate for the nickel ferrite-aluminate series, we have made use of the results of x-ray diffraction and susceptibility measurements which were carried out on $Ni\cdot Al_2O_4$ ($t=2$) at the U. S. Naval Ordnance Laboratory. Pickart and Greenwald[18] have found from x-ray measurements that $x=0.15\pm0.03$ and $z=0.85\pm0.03$ for $Ni\cdot Al_2O_4$.† Grannis[19] has measured the magnetic susceptibility from room temperature to 1500°C. The effective magnetic moment per molecule can be determined from the slope of the $1/\chi-T$ curve; then, using the measured values of x and z and assuming a specific value for $g_{Ni}(oct)$, say 2.3, one can calculate $g_{Ni}(tet)$. Actually, the $1/\chi-T$ curve for $Ni\cdot Al_2O_4$ is not a straight line, probably due to ferrimagnetic interactions and to variation of x and z with temperature. Thus we cannot get a precise value of the effective magnetic moment, but taking all the sources of error into account, it is still clear from the data that $g_{Ni}(tet)$ is about 4.0. This value will be used in our calculations for all t; it should be noted that the values of x and z calculated for the nickel ferrite-aluminates are not very sensitive to the exact value of $g_{Ni}(tet)$ chosen, since a relatively small amount of nickel goes to the A sites in these compounds. Detailed accounts of the x-ray and susceptibility measurements will be published separately.

The Fe^{3+} ions are in S states; consequently, we expect them to show little deviation from spin-only behavior and to have essentially the same μ and g values in the A sites as in the B sites. We assume $\mu_{Fe}=5.0$ and $g_{Fe}=2.0$. The Al^{3+} ions of course have no magnetic moment.

With a slight generalization to take care of the two g values for Ni^{++}, we find that the form of Eqs. (10) appropriate to the nickel ferrite-aluminate series is

$$3.7x+10z=\mu+5t-2.30, \quad (12a)$$

$$3x+5z=\mu/g+5t/2-1.00. \quad (12b)$$

[13] A method essentially the same as this has been proposed independently by E. W. Gorter, Nature **173**, 123 (1954). We are indebted to Dr. Gorter for communicating his results to us prior to publication.

[14] J. H. Van Vleck, Phys. Rev. **41**, 208 (1932).

[15] W. G. Penney and R. Schlapp, Phys. Rev. **42**, 666 (1932).

[16] A. Abragam and M. H. L. Pryce, Proc. Roy. Soc. (London) **206**, 173 (1951).

[17] B. Bleaney and D. J. E. Ingram, Nature **164**, 116 (1949); Proc. Roy. Soc. (London) **208**, 143 (1951).

[18] S. J. Pickart and Selma Greenwald (private communication).

† *Note added in proof.*—F. C. Romeijn, Philips Research Repts. 8, 321 (1953) gives $x=0.24$ for $NiAl_2O_4$. We have considered only the value obtained by Greenwald and Pickart since their measurements were made on the samples whose properties are listed in Table I.

[19] F. H. Grannis and T. R. McGuire (private communication).

TABLE I. Ionic distribution parameters for $NiO \cdot Fe_{(2-t)}Al_tO_3$.

t	μ	g	μ/g	x	z
0.00	2.12	2.35	0.90	−0.01	−0.02
0.25	1.14	2.7	0.42	0.00	0.01
0.50	0.58	5.3	0.11	−0.03	0.09
0.63	0.15	−3.8	−0.04	0.03	0.09
0.75	−0.22	1.6	−0.14	0.10	0.08
0.85	−0.39	1.6	−0.24	0.09	0.12
1.00	−0.58	1.5	−0.39	0.04	0.20
1.25	−0.44	1.5	−0.29	0.07	0.33
1.50	−0.11	1.55	−0.07	0.12	0.47
1.75	−0.07	1.6	−0.04	0.13	0.59

Table I shows the experimental μ and g values (extrapolated to 0°K) and the values of x and z calculated therefrom with the aid of Eqs. (12). The data were taken on samples which had been cooled from 1400°C at the rate of 1°C min. The g values were measured at a frequency of 9240 Mc/sec. It should be noted that the experimental measurements do not give the sign of either μ or g; these must be deduced indirectly. It is believed that the above choices are correct for reasons which will be discussed in the experimental papers on the nickel ferrite-aluminate series.[20]

In Fig. 1, x and z are plotted as functions of t; the indicated errors were estimated very crudely and are probably too small if anything. The solid line shows theoretical values of x and z calculated from Eqs. (7) for $A_x=0.02$, $A_z=0.08$. A detailed agreement between the experimental and theoretical values would be expected only if u_x and u_z were independent of t as well as x and z. However, it is of interest to note that for both cases (x *vs* t and z *vs* t) the experimental and theoretical curves show the same shapes.

There is some question as to whether the data for $t=1.50$ and 1.75 should be used for calculating x and z since it seems likely that in this region $\mu(0)$ may not be the difference in magnetization of a saturated B lattice and a saturated A lattice. For example, the triangular arrangements studied by Yafet and Kittel[21] may occur. However, for the particular case of nickel ferrite-aluminates, μ and μ/g for large t are both small compared to the other terms on the right-hand side of Eqs. (12); thus a relatively large percentage error in μ will not change x and z very much. It is seen that x and z for $t=1.50$ and 1.75 agree well with the trend of the values for smaller t.

In regard to agreement with experiment, the values of x and z calculated from Eqs. (12) are certainly of the right order of magnitude for all values of t. In addition, there is good agreement with the results of Pickart and Greenwald[18] for the two cases where they have made measurements ($t=1.0$ and 1.75). We believe that the over-all results indicate that the suggested method may be used to give resaonably accurate values of the distribution parameters in mixed ferrites.

It should be mentioned in conclusion that resonance measurements on the nickel ferrite-aluminate series were made at 20 800 Mc/sec as well as 9240 Mc/sec and that the g values did show a slight frequency dependence. This discrepancy was not enough to cause any significant error in the calculation of x and z. However, preliminary measurements on the series $NiO \cdot Fe_{(2-t)}Ga_tO_3$ indicate that there is a large frequency dependence of g values here; the values taken at 20 800 Mc/sec seem to give better agreement with experiment than do the 9240-Mc/sec values. A detailed report of this apparent frequency dependence and its interpretation will be made in a future publication of the U. S. Naval Ordnance Laboratory Solid State Division.

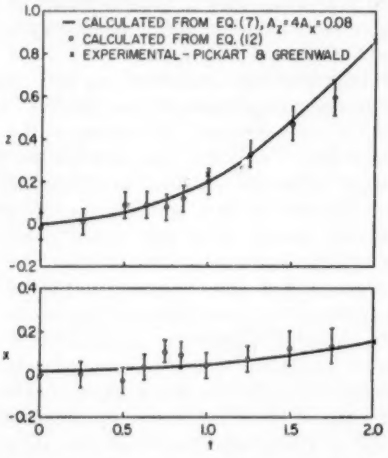

FIG. 1. The circled points are values of x and z calculated from Eqs. (12) with the data from Table I. The solid lines are theoretical curves calculated from Eqs. (7) for $A_z=0.02$, $A_x=0.08$. The × points are the experimental values observed by Pickart and Greenwald.

ACKNOWLEDGMENTS

I am indebted to T. R. McGuire, R. K. Wangsness, and P. R. Weiss for discussions of this problem; to S. J. Pickart, Selma Greenwald, and F. H. Grannis for making the x-ray and susceptibility measurements, and to Elise Fisher for making the aforementioned calculations.

[20] L. R. Maxwell and S. J. Pickert, Phys. Rev. **92**, 1120 (1953); T. R. McGuire, Phys. Rev. **93**, 682 (1954).
[21] Y. Yafet and C. Kittel, Phys. Rev. **87**, 290 (1952).

Elastic Spectrum of Zinc from the Temperature Scattering of X-Rays*

R. E. JOYNSON
Massachusetts Institute of Technology, Cambridge, Massachusetts
(Received February 15, 1954)

The temperature diffuse scattering of x-rays from a single crystal of zinc has been measured at room temperature using a Geiger counter spectrometer and crystal monochromated Cu $K\alpha$ radiation. The theory of Born, together with Begbie's theory of lattice dynamics for a hexagonal crystal, was used in the interpretation. A method was developed to separate the contributions to intensity from the acoustical and optical bands. Frequency curves for the six modes of vibration propagating parallel to the b_3 axis, and for the six modes propagating parallel to the b_2 axis were obtained. Measurements were in agreement with theory for long wavelength acoustical modes, but for shorter wavelengths the first neighbor theory was not in agreement with the measurements. Approximate values for seven of the eight nearest neighbor force constants were obtained, and these values could be used for the calculation of an approximate frequency distribution curve.

I. INTRODUCTION

THE frequencies of elastic waves propagating in the principal directions of cubic crystals have been obtained by Olmer,[1] Cole and Warren,[2] Curien,[3] and Cole[4] for aluminum, β brass, α iron, and silver chloride. Although zinc is monatomic, there are two atoms in the unit cell of the hexagonal lattice, and the elastic spectrum like that of AgCl consists of two bands, the usual acoustical band and an optical band. Unlike the restrahlen frequencies of ionic AgCl, the corresponding long wavelength optical frequencies of zinc cannot be measured, and other means must be used for separating the contributions to the measured intensity from the two bands.

The intensity per atom of the first-order temperature diffuse scattering is expressed at a position P in reciprocal space defined by

$$\mathbf{S}/\lambda = h\mathbf{b}_1 + k\mathbf{b}_2 + l\mathbf{b}_3 + \mathbf{q},$$

where $|\mathbf{S}| = 2\sin\theta$, λ is the x-ray wavelength, hkl are the Miller indices of the nearest crystalline reflection, $b_1 b_2 b_3$ are the reciprocal lattice vectors, and the intensity is due to elastic waves with wave vector $\pm\mathbf{q}$, where $|\mathbf{q}| = 1/\Lambda$ with Λ the wavelength of the elastic wave. Following Born,[5] the intensity is given by

$$I_{eu} = k(\theta) m^{-1} w^{+} D(q)^{-1} w, \qquad (1)$$

with

$$k(\theta) = \tfrac{1}{2} f^2 e^{-2M} |K\mathbf{S}|^2 kT.$$

fe^{-M} is the atomic scattering factor with a Debye temperature correction; the values used were those measured experimentally by Brindley.[6] $K = 2\pi/\lambda$, and m is the mass of the atom. The quantum energy correction was found to be small, and the energy of a vibrational mode was taken to be kT. The symbol w represents a six-component column vector with

$$w_{k\alpha} = s_\alpha \exp[iK\mathbf{S}\cdot\mathbf{r}_k], \quad s_\alpha = S_\alpha/|\mathbf{S}|,$$

where the three directions X_α ($\alpha = 1, 2, 3$) refer to a right-handed rectangular coordinate system in reciprocal space with X_2 in the negative direction of b_2 and X_3 in the positive direction of b_3. w^+ is the transposed conjugate of w and $\mathbf{r}_k$ is the equilibrium vector position of the kth atom ($k = 1, 2$) in the unit cell. $D(q)^{-1}$ is the inverse of the Fourier transform of the dynamical matrix for a hexagonal lattice as given by Begbie[7] in terms of nearest neighbor force constants. Although the first neighbor theory is not found to be in agreement with experiment for regions removed from crystalline reflections, the theory serves as a guide in obtaining approximate frequencies for many of the vibrational modes of a hexagonal lattice.

The intensity may also be expressed in terms of the frequencies of the normal modes by using the expansion of the inverse matrix in terms of the eigenvalues ω_i and eigenvectors u_i of the dynamical matrix:

$$D(q)^{-1} = \sum_{i=1}^{6} \frac{1}{\omega_i^2} u_i u_i^{+}.$$

Both the frequencies and the vectors are determined by

$$[D(q) - \omega^2 I]u = 0,$$

with the u_i subjected to the normalization conditions:

$$\textstyle\sum_i u_i u_i^{+} = I, \quad u_i^{+} u_{i'} = \delta_{ii'}.$$

For the principal directions considered in this investigation, the intensity expression reduces to

$$I_{eu} = \frac{2k(\theta)}{m} \sum_j^3 \left(\frac{v}{\omega_{ae}^2} + \frac{1-v}{\omega_{op}^2} \right)_j \cos^2(\mathbf{S},\mathbf{e}_j), \qquad (2)$$

with $v_j \cos^2(\mathbf{S},\mathbf{e}_j) = \tfrac{1}{2} w^{+} u_{i,ae} u_{i,ae}^{+} w$, where $(\mathbf{S},\mathbf{e}_j)$ is the

* Assisted at different times by the Armco Foundation Fellowship and the National Science Foundation.

[1] P. Olmer, Acta Cryst. **1**, 57 (1948); Bull. soc. franç. minéral. **71**, 144 (1948).
[2] H. Cole and B. E. Warren, J. Appl. Phys. **23**, 335 (1952).
[3] H. Curien, Acta Cryst. **5**, 393 (1952).
[4] H. Cole, J. Appl. Phys. **24**, 472 (1953).
[5] M. Born, Repts. Progr. Phys. **9**, 356 (1942–3).
[6] G. W. Brindley, Phil. Mag. **21**, 790 (1936).
[7] G. H. Begbie, Proc. Roy. Soc. (London) **A188**, 189 (1947).

TABLE I. Relations between elastic constants and force constants for hexagonal lattices.

$$c_{11}=c_{22}=\frac{2}{\sqrt{3}c}\left(-\frac{2\mu^2}{\lambda}+3\alpha+3\beta+\lambda-\mu\right)$$

$$c_{33}=\frac{2c}{\sqrt{3}a^2}\frac{3}{2}\nu$$

$$c_{44}=c_{55}=\frac{2c}{\sqrt{3}a^2}\frac{3}{2}\lambda$$

$$c_{13}=\frac{2}{\sqrt{3}c}\left(\frac{2\mu^2}{\lambda}-3\alpha+9\beta-\lambda-3\mu\right)$$

$$c_{23}=c_{31}=\frac{2}{\sqrt{3}a}\left(2\sqrt{3}\sigma-\frac{3}{2}\frac{c}{a}\lambda\right)$$

$$c_{66}=\frac{1}{2}(c_{11}-c_{12})=\frac{2}{\sqrt{3}c}\left(-\frac{2\mu^2}{\lambda}+3\alpha-3\beta+\lambda+\mu\right)$$

$$\frac{3}{2}\left(\frac{c}{a}\right)^2\lambda=3\gamma+\nu$$

angle between the diffraction vector **S** and the direction of oscillation of a mode. The subscripts *ac* and *op* refer, respectively, to the acoustical and optical frequencies, and the summation is over the three states of polarization of the elastic waves, for example, one longitudinal and two transverse.

In the vicinity of a crystalline reflection with structure factor $F^2=nf^2$ ($n=0, 1, 3, 4$ for zinc), the value of v approaches $n/4$. Thus near a "forbidden" reflection the diffuse intensity is due to the scattering of x-rays by only the optical frequencies. Near reflections of nonzero structure factor, the contribution to the intensity is largely from acoustical modes because for very long wavelengths the acoustical frequencies approach zero and the optical frequencies remain high, so that the optical terms in Eq. (2) may be neglected. By going to the long wavelength limit, Eq. (2) can be written in terms of the acoustical velocities and hence in terms of the elastic constants of the material. Equation (1) can also be expressed in terms of the elastic constants in the long wavelength limit by substitution for the appropriate combinations of force constants as given by the corrected[8,9] elastic-force constant relations of Begbie[7] which are given in Table I.

II. EXPERIMENTAL PROCEDURE

All measurements were made at room temperature with a spectrometer equipped with a crystal goniometer similar to that described by Cowley.[10] By using two crystals cut to 0001 and $10\bar{1}0$ faces, it was possible to reach any position in reciprocal space attainable with Cu$K\alpha$ radiation, while keeping the absorption correction angular independent. X-rays from a full wave rectified copper target tube operated at 35 kv and 16 ma were monochromated by a bent LiF crystal and focused on the face of the zinc sample. A Ni-Al balanced filter was used to eliminate the half-wavelength reflected by the monochromator. The scattered radiation was measured by a Geiger counter for 4-minute counting intervals. The volume averaged over in reciprocal space was that defined by beam divergences of about 2°. Correction was made for air scattering, and the counts converted to absolute intensity units by comparison with the scattering at high angles from a block of paraffin. The Compton modified scattering was subtracted, and the remainder treated as temperature diffuse scattering.

Zinc single crystals of purity 99.999 percent Zn were grown from the melt in Pyrex tubes lined with Aquadag. After preparation of the crystal faces by cleaving and etching, sharp Laue spots were obtained over the regions used for measurement.

III. RESULTS

An example of the measured temperature diffuse scattering for zinc is given by the isodiffusion curves of Fig. 1 for the *hk*0 layer of reciprocal space. The quantity plotted is the difference in counts between the Ni and Al filters with no additional correction. Since the Compton modified scattering varies slowly, the shape of the contours is due to temperature diffuse scattering. The traces of the Brillouin zones in this plane are indicated by the dotted lines. The innermost contour around each reflection represents the same intensity. The contours may be compared with the theoretical curves for hexagonal lattices presented by Begbie[7] using the elastic constants of beryl but without correction for structure factor variation, and with those

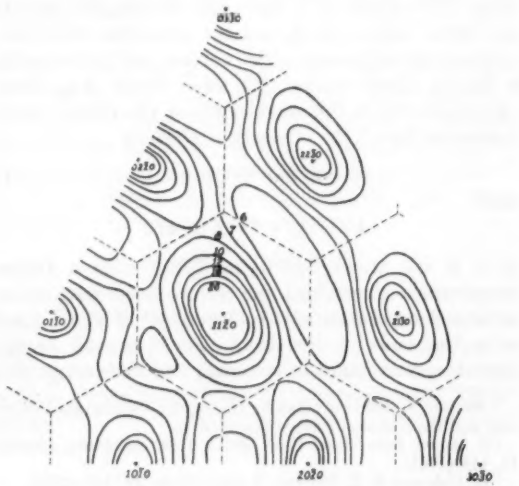

FIG. 1. Isodiffusion curves for the *hk*0 layer of reciprocal space for zinc. The contours in each zone are at values 20, 16, 12, 10, 8, 7, 6 which are proportional to the difference in the Ni and Al filter counts with no additional correction.

[8] From private correspondence with Dr. Begbie, a factor $4\pi^2$ must be inserted on the right-hand side of (2.26) in reference 9. After making this correction, the right-hand side of (4.17) in reference 7, must be divided by an additional factor of 2, that is, divided by a total factor of $8\pi^2$.

[9] G. H. Begbie and M. Born, Proc. Roy. Soc. (London) **A188**, 179 (1947).

[10] J. M. Cowley, J. Appl. Phys. **21**, 24 (1950).

of Pope[11] based on an ideal c/a ratio and central forces.

The second-order temperature diffuse scattering, treated as a correction to the total scattering, was obtained by considering the third term in the expansion of $\exp[M_{jj'}]$ occurring in the Born theory.[5] An approximate expression for the contribution from a region common to the first Brillouin zone about a reciprocal lattice point and a zone erected about the tip of the diffraction vector is

$$I_2 = f^2 e^{-2M} |\mathbf{KS}|^4 (kT)^2 \frac{v_a}{8m^2} \int\int\int \left(\frac{P_+}{\omega_{\alpha,ac}^2 \omega_{\beta,ac}^2} + \frac{2P_-}{\omega_{\alpha,ac}^2 \omega_{\beta,op}^2} + \frac{P_+}{\omega_{\alpha,op}^2 \omega_{\beta,op}^2} \right) dq_1 dq_2 dq_3,$$

where v_a is the volume of the unit cell and

$$P_\pm = 2 \pm \cos[\mathbf{K} \cdot (\mathbf{r}_2 - \mathbf{r}_1)].$$

The integration is over the volume shared by the overlapping zones referred to by the subscripts α and β. The exact phases of the vibrating atoms in a unit cell have been neglected, but account has been taken of whether the atoms are in or out of phase. By considering solutions of the dynamical matrix, it was found that the acoustical frequency distribution could be approximated by the spherically symmetric distribution

$$\omega = 2.04 \times 10^{13} (\tfrac{1}{2}\pi c) q \text{ rad/sec},$$

where q is the length of the wave vector. A constant mean optical frequency was taken to be 2.1×10^{13} rad/sec. The Brillouin zones were replaced by cylinders of the same height and volume as the true hexagonal zone, and the integrals were calculated by machine methods. The second-order scattering did not exceed about 8 percent of the first-order scattering.

The directions of propagation of elastic waves studied were $q_1 = q_2 = 0$ and $q_1 = q_3 = 0$ for which the submatrices

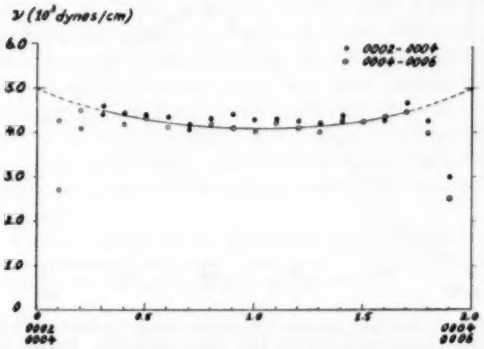

FIG. 2. Values of the force constant ν for zinc, obtained by applying Eq. (3) to measurements along the 0002–0006 line.

[11] N. K. Pope, Acta Cryst. 2, 325 (1949).

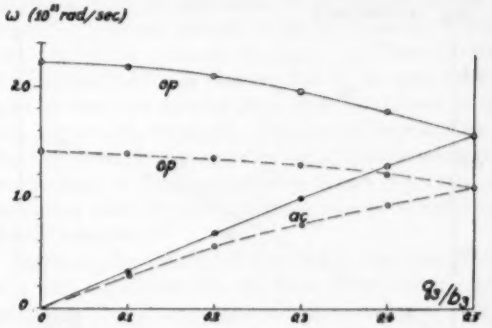

FIG. 3. Frequency curves for acoustical and optical modes for waves in the b_3 direction of zinc. Full line, longitudinal waves. Dashed line, transverse waves.

$D(_k{}^q{}_{k'})$ of the dynamical matrix remain diagonal. By appropriate choice of positions in reciprocal space, the effects of the longitudinal and transverse modes can be separated. For example, along a radial line in reciprocal space in the b_3 direction ($q_1 = q_2 = 0$) the intensity is given by one force constant:

$$I_{eu} = k(\theta) \frac{1}{\nu} \left[\frac{1 + (-1)^l \cos(\pi c q_3)}{3 \sin^2(\pi c q_3)} \right], \tag{3}$$

and in terms of the longitudinal b_3 frequencies:

$$I_{eu} = \frac{k(\theta)}{m} \left[\frac{1 + (-1)^l}{\omega_{ac}^2} + \frac{1 - (-1)^l}{\omega_{op}^2} \right]. \tag{4}$$

It is seen from the last relation that the contribution is entirely from the acoustical mode in zones with l even and from the optical mode in zones with l odd.

Figure 2 shows the values of ν obtained by applying Eq. (3) to the intensity measured along the line from 0002 to 0006. The low points on either end of the figure are due to approaching too close to a strong crystalline reflection. From the relations of Table I and the elastic constant c_{33}, $\nu = 5.0 \times 10^5$ dynes/cm. The x-ray value of ν is a little low but it is not possible to say whether this is experimental error or approximations in the theory such as considering only nearest neighbors.

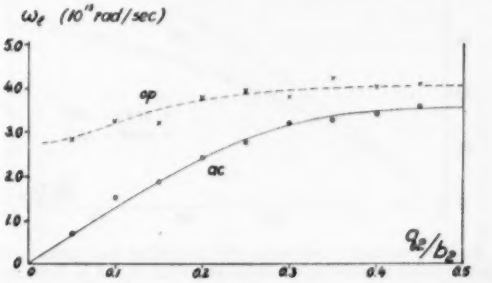

FIG. 4. Frequency curves for acoustical and optical modes for longitudinal waves in the b_2 direction of zinc.

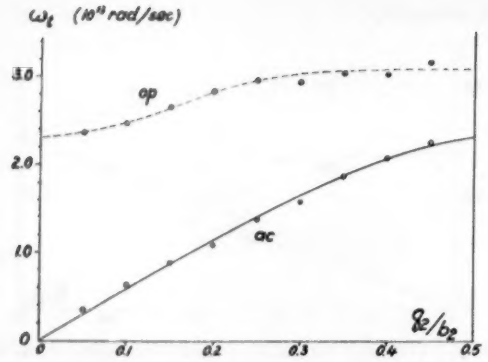

FIG. 5. Frequency curves for the acoustical and optical modes for the $t_1(b_2)$ transverse waves propagating in the b_2 direction of zinc. The vibration direction of $t_1(b_2)$ is in the basal plane.

Figure 3 shows the acoustical and optical frequencies as a function of $q_3=1/\Lambda$ for waves propagating in the b_3 direction. The curves for longitudinal waves were obtained by applying Eq. (4) to the measured intensity along the 0002–0006 line and the curves for the transverse waves were obtained from measurements along the $11\bar{2}0$–$11\bar{2}2$ line.

Figures 4, 5, and 6 give the frequencies of the longitudinal and two transverse wave propagating in the b_2 direction. The oscillation direction of the $t_1(b_2)$ wave is parallel to the basal plane, that of the $t_2(b_2)$ is parallel to the b_3 direction. The curves were obtained by applying Eq. (2) to the measured intensity along the $10\bar{1}0$–$30\bar{3}0$; $11\bar{2}0$–$20\bar{2}0$; and the 0004–$10\bar{1}4$, 0005–$10\bar{1}5$ lines in reciprocal space. The weighting factors v_i for the $l(b_2)$ and the $t_1(b_2)$ waves are functions of the force constants, but for long wavelength the frequency curves are relatively insensitive to the constants.

For some of the force constants there is considerable variation in the values obtained from measurements in different regions. Figure 7 illustrates the worst discrepancy. The full line represents the measured intensity

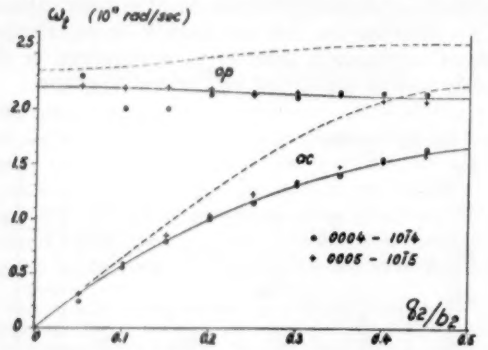

FIG. 6. Frequency curves for the acoustical and optical modes for the $t_2(b_2)$ transverse waves propagating in the b_2 direction of zinc. The vibration direction of $t_2(b_2)$ is normal to the basal plane. The dashed curves represent the frequencies to be expected from the force constants determined at long wavelength.

along the 0005–$10\bar{1}5$ line. It is plotted as $I\sin^2(\frac{1}{2}x)/k(\theta)$, where $x=\pi a\sqrt{3}q_2$, to obtain a finite intercept on the right-hand side. The dashed curve represents the intensity to be expected, using force constants ν and γ computed from the elastic constants. The dotted curve shows the variation in the value of γ which is obtained by using the measured intensities represented by the full line and the value of ν from Fig. 2.

IV. CONCLUSIONS

Frequency curves have been obtained for the six modes of vibration for waves propagating in the b_2 and b_3 directions. Because of the nondiagonalization of the submatrices $D(_kq_{k'})$ it was not attempted to obtain frequency curves for other directions of propagation. Near a crystalline reflection of nonzero structure factor where the contribution is primarily from acoustical modes, the measured intensity of first-order temperature diffuse scattering is in fair agreement with the values

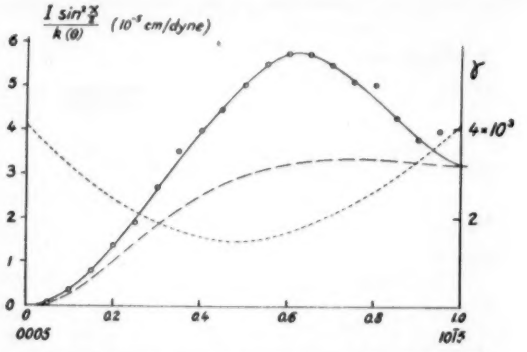

FIG. 7. Full line, measured intensity along the 0005–$10\bar{1}5$ line of zinc plotted as $I\sin^2(\frac{1}{2}x)/k(\theta)$, where $x=\pi a\sqrt{3}q_2$. Dashed line, intensity to be expected from ν and γ computed from the elastic constants. Dotted line, variation in γ obtained from the full line and the value of ν from Fig. 2.

predicted by the elastic constants using the relations of Table I. Away from crystalline reflections the first neighbor theory and measurement are not in as good agreement.

By assuming the validity of the nearest neighbor approximation, or regarding the first neighbor constants as functions of the constants for several neighbors, approximate values for six of the eight nearest neighbor force constants can be obtained from the x-ray intensities. The values listed in Table II show the variation observed in the constants obtained from near the center of the Brillouin zone or from the zone boundary. These values were obtained by applying Eq. (1) to measurements in different regions of reciprocal space:

ν from the line 0002–0006,
λ from the line $11\bar{2}0$–$11\bar{2}2$,
α, β, μ from the combination $10\bar{1}0$–$30\bar{3}0$ and $11\bar{2}0$–$20\bar{2}0$,
γ from the lines 0004–$10\bar{1}4$ and 0005–$10\bar{1}5$ combined with the previous determination of ν.

TABLE II. Values of nearest neighbor force constants for zinc (dynes/cm).

		Zone center	Zone boundary
ν	from acoust.	5.0×10^{3}	4.3×10^{3}
	from opt.	4.1×10^{3}	4.3×10^{3}
λ	from acoust.	3.4×10^{3}	2.1×10^{3}
	from opt.	1.7×10^{3}	2.1×10^{3}
α		17.0×10^{3}	13.0×10^{3}
β		6.5×10^{3}	5.5×10^{3}
γ		4.2×10^{3}	1.7×10^{3}
μ		$\sim-1.0\times10^{3}$	

A value for the force constant σ was not obtained from the x-ray measurements but, as seen from the relations of Table I, the elastic constants c_{44} and c_{23} suffice to give the value $\sigma=6.0\times10^{3}$ dynes/cm. The remaining force constant δ could not conveniently be obtained from the x-ray measurements, and since it does not appear in the relations of Table I it cannot be obtained from the elastic constants.

The elastic constants for zinc obtained from Tyndall's[12] elastic moduli are listed in Table III. Using the relations of Table I, there is fairly good agreement between the elastic constants of Table III and the force constant values of Table II which are obtained from acoustical waves near the zone centers. The accuracy of the x-ray force constants is lower than that of the elastic constants, but since it is impossible to obtain eight force constants from five elastic constants the x-ray values represent the best that can be obtained.

The velocities of the acoustical modes exhibit dispersion as may be seen from the frequency curves. If dispersion were not present, a plot of frequency *vs* wave vector would be a line of constant slope. The velocities of acoustical waves in zinc are less at the zone boundaries by amounts ranging from 20 to 50 percent of the long wavelength velocities. The discrepancy in Figs. 6 and 7 between the measured curves and those computed on the basis of the first neighbor theory is perhaps an indication that the first neighbor theory is not completely adequate.

Assuming the validity of the nearest neighbor theory as a first approximation, we have the necessary data for computing a frequency distribution curve except for the constant δ. Since the final distribution curve may be relatively insensitive to the value of δ, it should be possible to estimate a sufficiently accurate value from the known values of the other seven force constants.

TABLE III. Elastic constants for zinc (dynes/cm^2).

$c_{11}=17.16\times10^{11}$
$c_{12}=2.61\times10^{11}$
$c_{13}=4.95\times10^{11}$
$c_{33}=6.11\times10^{11}$
$c_{44}=4.10\times10^{11}$
$c_{66}=\frac{1}{2}(c_{11}-c_{12})=7.27\times10^{11}$

The author is indebted to Professor B. E. Warren for his continued and helpful counsel and to Professors G. G. Harvey and N. H. Frank for their advice and suggestions. He also wishes to thank Dr. D. C. Jillson of the New Jersey Zinc Company for making available the high-purity zinc.

[12] E. P. T. Tyndall, Phys. Rev. **47**, 398 (1935).

Pressure Effects in Phosphorescence*

L. REIFFEL
Armour Research Foundation of Illinois Institute of Technology, Technology Center, Chicago, Illinois
(Received January 25, 1954)

The influence of hydrostatic stress on the phosphorescence decay of thallium activated sodium iodide is shown to be very marked. Pressures as low as 100 kilograms per square centimeter produce readily observable effects. Interpretation in terms of pressure-increased effective trap depth is given.

THERE have been reported in the literature only a very few experiments in which hydrostatic stress has been applied to crystalline phosphor systems. The most recent work is apparently that of Reinsch and Drickamer,[1] who report the probable existence of a slight shift in the emission spectrum of cadmium tungstate at 10 000 kg/cm².

We have undertaken a study of the effects of hydrostatic pressure on the fluorescent and phosphorescent emission occasioned by gamma-ray bombardment of the activated alkali halides. Because of the very marked dependence of the phosphorescence decay rate on trap depth, it may be reasoned that measurements in the time domain would be considerably more sensitive than measurements in the frequency domain. That this appears to be the case can be seen from the data on thallium-activated sodium iodide[2] presented in Fig. 1 and in Table I. The phosphorescence decay curves are normalized at 0.1 minute after removal of the excitation so that their shapes may be readily compared. The intensities at the time of normalization relative to those during excitation are listed in Table I.

These data were obtained using Co^{60} gamma rays at a constant excitation density of 4.3 roentgens per minute and an excitation time of 10 minutes. Preliminary tests established that pressure induced effects in the mineral oil used as the pressure transmitting medium did not occur. Similarly, no shift in the optical transmission characteristics of the pressure bomb windows was detectable. Precautions were taken to assure isothermal conditions throughout the experiments.

It is interesting to note that pressures as low as 100 kg/cm² will produce readily observable changes in NaI(Tl) decay curves.

These results are tentatively interpreted in terms of a stress-proportional increase in trap depth with the assumption of negligible changes in the associated rate constant. Such an approach is supported by an argument based on a typical configurational coordinate diagram to which is added a linearly increasing potential ascribable to the applied stress. Under pressure, therefore, the effective trap depth should be increased by a term proportional to the product of the stress and the displacement from equilibrium required for thermal escape from the trap.

In the case of NaI(Tl), the data, when fitted either by a power law or by an exponential in the 5-minute to 10-minute interval, indicate a change in trap depth of 4.6 percent for an applied stress of 2400 kg/cm². This type of computation requires the assumption of a unique trap depth, a condition which is not well fulfilled for NaI(Tl). This fact makes precise interpretation in terms of any simple picture rather difficult. Additional data are now being obtained for phosphors of apparently simpler behavior which should permit detailed computations on the pressure dependence of effective trap depth and allied parameters.

TABLE I. Relative phosphorescent intensity.

Pressure (kg/cm²)	Intensity Ratio ×10²
Atmospheric	8.25
700	6.70
1750	5.55
2400	4.25

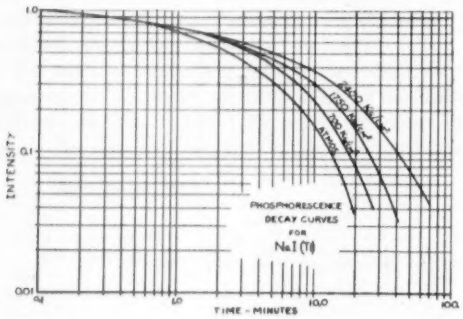

FIG. 1. Phosphorescence decay curves for NaI(Tl).

* This work has been supported in part by the Office of Scientific Research, Air Research and Development Command, U. S. Air Force, Baltimore, Maryland.

[1] A. J. Reinsch and H. G. Drickamer, J. Appl. Phys. 23, 152 (1952).

[2] Crystals were obtained from Harshaw Chemical Company as scintillation grade material.

Effect of Neutron Bombardment on a Zinc Sulfide Phosphor†*

ALAN W. SMITH AND JOHN TURKEVICH
Chemistry Department, Princeton University, Princeton New Jersey
(Received January 14, 1954)

An investigation has been made of the effect of neutron irradiation on the following properties of a copper-activated zinc sulfide phosphor: luminescence efficiency under ultraviolet and x-ray excitation, infrared quenching of luminescence, temperature dependence of luminescence efficiency, thermoluminescence, rise time of luminescence, decay of luminescence, and dependence of the rise time of luminescence on the previous history of the sample. In addition, the analogous changes in the dielectric constant of the phosphor on illumination were measured for samples damaged to varying degree by neutrons. It was shown that neutron damage can be removed by annealing at high temperature.

MANY studies have shown that nuclear radiation changes a number of different properties of solids.[1–13] However, the study of the effects of nuclear radiation on luminescent materials has been exclusively confined, since its discovery by Marsden,[14] and Rutherford[15] to the study of the interaction of alpha-particles with zinc sulfide.[16–32] It was found that alpha-particles decrease the luminescence efficiency of the phosphor not only for alpha-particle excitation but also for ultraviolet excitation. There was also an increase in the rate of phosphorescence decay and an increase in the quenching effect of ultraviolet light. On the other hand, there was a decrease in photoconductivity and the optical exaltation of the dielectric constant change. At the same time the emission spectrum shifted to the longer wavelength. Many investigators have compared the effects of alpha-particle bombardment with those produced by grinding and photolysis.

The present investigation differs from the previous work in using neutrons for producing phosphor damage and in studying a wide variety of property changes on one type of material: a copper-activated zinc sulfide. It is hoped that such a study will not only contribute to our knowledge of the mechanism of luminescence but throw light on the intriguing problem of the interaction of neutrons with solids.

EXPERIMENTAL TECHNIQUE

The phosphor used in these studies was hexagonal ZnSCu(0.006)NaCl(5)1250°C 7 minutes obtained from H. W. Leverenz of the RCA Laboratories. The neutron bombardment was carried out in the nuclear reactor of the Brookhaven National Laboratory. Exposures from 20 minutes to 32 hours were made to fast neutrons inside the pile at the ambient pile temperature (below 200°C). The neutron flux was approximately 10^{12} average n.v. In addition to suffering structural damage, the samples became radioactive in proportion to their exposure in pile. Before making measurements of the structural changes in the phosphor, the radioactivity was allowed to die out. There was, however, some residual radioactivity left as is shown by the fact that a 1-gram sample of the phosphor exposed for 16 hours to the pile neutrons had, after several months, an activity from Zn^{65} of 20 mr/hour. The luminescent properties were measured by placing the samples in small porcelain cups which were held in the cavity of a copper block. The latter was kept in a Dewar flask and could be cooled to liquid nitrogen temperature or heated to 400°C. In the thermoluminescent experiments a linear heating rate of 0.1°C/sec was used. For excitation in the near ultraviolet, a General Electric Sunlamp (RS) with a 5113 Corning

† Preliminary account published in the J. Chem. Phys. **21**, 367 (1953).

* This investigation was carried out with the financial support of the U. S. Atomic Energy Commission.

[1] G. J. Dienes, Ann. Rev. Nuclear Sci. **2**, 187 (1953).
[2] J. C. Slater, J. Appl. Phys. **22**, 237–56 (1951).
[3] W. E. Johnson, and K. Lark-Horowitz, Phys. Rev. **76**, 442 (1949).
[4] W. H. Brattain, and G. L. Pearson, Phys. Rev. **80**, 846–50 (1950).
[5] K. Lark-Horowitz, *Reading Conference on Semi-Conducting Materials* (Buttersworths Publishing Company, London, 1951).
[6] M. M. James and K. Lark-Horowitz, Z. physik. Chem. **198**, 107 (1951).
[7] D. S. Billington and S. Siegel, U. S. Atomic Energy Commission Report AECD-2810, nd, Decl. Mar. 22, 1950 (unpublished).
[8] Casler, Pringsheim, and Yuster, J. Chem. Phys. **18**, 887–91 (1950).
[9] R. Casler and P. Pringsheim, J. Chem. Phys. **18**, 1564 (1950).
[10] P. Pringsheim and P. Yuster, Phys. Rev. **78**, 293 (1950).
[11] Delbecq, Pringsheim, and Yuster, J. Chem. Phys. **19**, 574 (1951).
[12] S. C. Lind and D. C. Bardwell, J. Franklin Inst. **196**, 521 (1923).
[13] C. A. Hutchison, Jr., Phys. Rev. **75**, 1769–70 (1949).
[14] E. Marsden, Proc. Roy. Soc. (London) **A83**, 548 (1910).
[15] E. Rutherford, Proc. Roy. Soc. (London) **A83**, 561 (1910).
[16] G. Berndt, *Radioaktive Leuchtfarben* (Braunschweig, 1920), p. 78.
[17] B. Karlik, Sitzber. Akad. Wiss. Wien, Math.-Naturw. Kl. **139**, 509 (1930).
[18] P. Wolf and N. Riehl, Ann. Physik **11**, 103 (1931).
[19] P. Wolf and N. Riehl, Ann. Physik **17**, 581 (1933).
[20] F. Goos, Ann. Physik **34**, 87 (1939).
[21] E. Streck, Ann. Physik **34**, 96 (1939).
[22] E. Streck, Ann. Physik **35**, 58 (1939).
[23] F. Goos, Ann. Physik **37**, 76 (1940).
[24] A. Becker and I. Schaper, Ann. Physik **42**, 297, 487 (1943).
[25] F. Wecker, Ann. Physik **42**, 561 (1943).
[26] F. Wecker, Ann. Physik **43**, 607 (1943).
[27] A. Becker and F. Wecker, Ann. Physik **43**, 598 (1943).
[28] Becker, Schaper, and Wecker, Reichsber. Physik **11**, 169 (1945).
[29] F. Frey, Ann. Physik **2**, 147 (1948).
[30] A. Becker, Z. Physik **125**, 475 (1949).
[31] I. Broser and H. Kallmann, Z. Naturforsch. **5a**, 381 (1950).
[32] I. Broser and R. Warminsky, Z. Naturforsch. **6a**, 85–102 (1951).

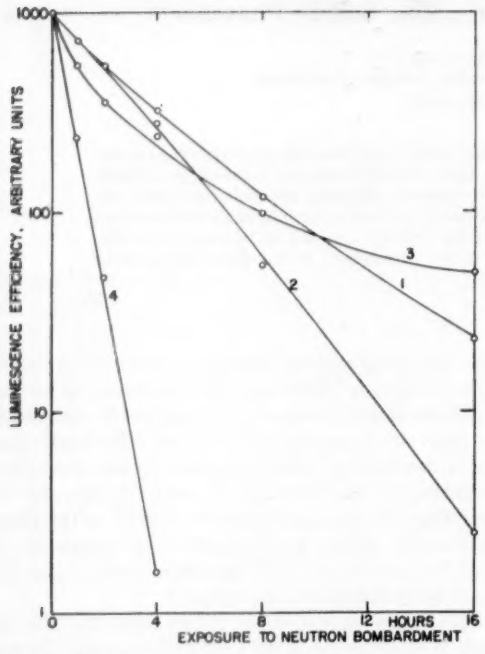

FIG. 1. Effect of exposure to neutrons on luminescence efficiency *1*, ultraviolet excitation (high intensity); *2*, ultraviolet excitation (low intensity); *3*, x-ray excitation; *4*, ultraviolet excitation with infrared quenching.

filter and a 35D Wratten filter were used. For excitation with CuK_α radiation (1.56A) a Phillips copper target x-ray tube was used with a nickel filter. The infrared source was a General Electric heat lamp (250 R40/10) used with a Corning 2540 infrared transmitting filter. The light output of the phosphor was measured by an RCA 1 P-22 photomultiplier tube fitted with a 3384 Corning yellow filter. The photocurrent was amplified by a dc amplifier and recorded on a Brown potentiometer recorder.

The dielectric properties were measured by placing the phosphor in a half-silvered flat-bottomed Pyrex cup which served as one of the condenser plates. The other plate of the condenser was a metal disk held 0.6 mm from the first plate. The condenser was placed in a Dewar flask having at its bottom a flat Pyrex plate. The exciting light was directed through the half-silvered condenser plate onto the phosphor. The dielectric properties were measured at 1 Mc/sec with a tuned tube circuit similar to that used by Garlick and Gibson.[33] The measurements in the 10–200 kc/sec range were carried out with an oscillator and a simple bridge. The balance was detected by a triode amplifier, a cathode follower and a Brown potentiometer recorder.

[33] G. F. J. Garlick and A. F. Gibson, Proc. Roy. Soc. (London) **A18**, 485 (1947).

EXPERIMENTAL RESULTS

A. Luminescence as a Function of Neutron Exposure

Neutron irradiation decreases markedly the efficiency (the ratio luminescence to excitation intensity) of the ZnS phosphor. In general the efficiency drops exponentially with neutron exposure (Fig. 1). The effect, however, depends markedly on how the efficiency is measured. Thus the drop is much greater for low ultraviolet exictation (curve 2) than for high-intensity ultraviolet excitation (curve 1). It is particularly marked if the excitation is accompanied by simultaneous irradiation with infrared from a General Electric heat lamp (curve 4). On the other hand, the neturon damage is least marked for x-ray excitation (curve 3).

B. Luminescence as a Function of Exciting Intensity

The luminescence of the unbombarded sample at room temperature was found to be proportional to the exciting light in intensity over the whole range of intensities that could be measured. This is characteristic of a well-activated and well-crystallized phosphor. If one measures the luminescence efficiency of the bombarded sample at 150°C then the luminescence shows a strong deviation from linearity.

As the neutron exposure increases, the luminescence for a given light intensity decreases, as was shown in the preceding section and in Fig. 1. At the same time the linear dependence of the luminosity on excitation intensity for samples of greater neutron damage,

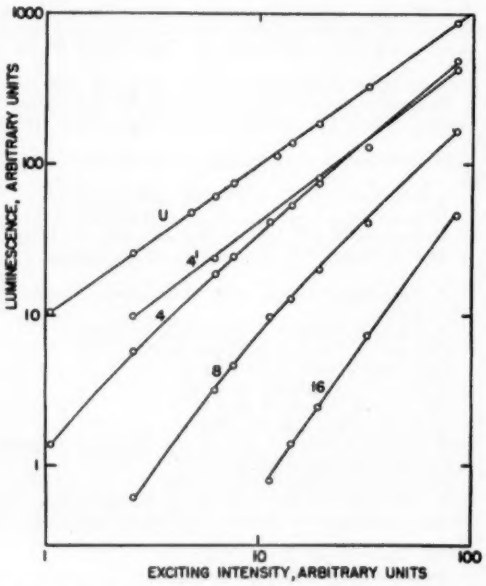

FIG. 2. Luminescence as a function of ultraviolet exciting intensity for the undamaged sample and 4, 8, and 16 hours in the reactor. 4′, 4-hour sample measured at −60°C (others at 22°C).

changes to that of higher power of intensity. The character of the luminescence-excitation intensity curve depends not only on the damage produced in the phosphor by the neutrons, but also on the temperature at which the luminosity measurements are made (curves 4 and 4′, Fig. 2). If the samples are measured at lower temperature, the luminescence for a given intensity is higher but the slope of the luminescence-excitation curve is lower. Under x-ray excitation the luminescence of the unbombarded sample is linear with x-ray intensity and this linear relationship is preserved for the unbombarded sample if the luminosity measurements are carried out at 150°C. Neutron bombardment decreases the luminescence for a given x-ray excitation intensity but does not change the linear relationship between luminescence and intensity.

The quenching of the luminescence by added illumination of the phosphor by infrared during the ultraviolet excitation is well known. Curve 1 in Fig. 3 shows the linear luminescence-excitation intensity relationship for an unbombarded sample as a function of the ultraviolet excitation. Curves 2 and 3 show the quenching of luminescence by the simultaneous irradiation with infrared and ultraviolet of the unbombarded sample. If the infrared intensity is kept proportional to the ultraviolet intensity, the relationship between luminescence and exciting light intensities remains linear (curve 2). If, on the other hand, the infrared is kept constant in intensity while the ultraviolet intensity is varied, the relationship is not linear but shows a 1.4 power dependence on the exciting intensity (curve 3). The bombarded samples show the same effect. Thus for a zinc sulfide phosphor bombarded in the pile for one hour, the luminescence depends on the 1.2 power of the exciting ultraviolet intensity whether infrared radiation is absent (curve 4) or the infrared intensity is kept proportional to the ultraviolet intensity (curve 3). However, when the infrared intensity is kept constant, the dependence is on the 2.6 power of the intensity of the ultraviolet excitation.

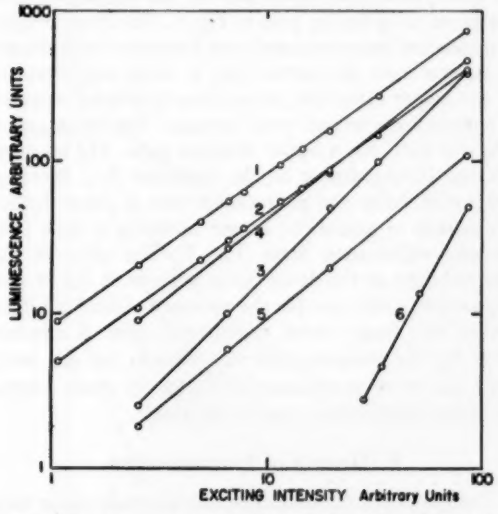

FIG. 3. Luminescence as a function of ultraviolet exciting intensity with infrared quenching: *1*, undamaged sample without infrared; *2*, undamaged sample with infrared intensity proportional to ultraviolet; *3*, undamaged sample with infrared intensity constant; *4*, sample exposed in reactor 1 hour with no infrared; *5*, 1-hour sample, infrared intensity proportional to ultraviolet; *6*, 1-hour sample with infrared intensity constant.

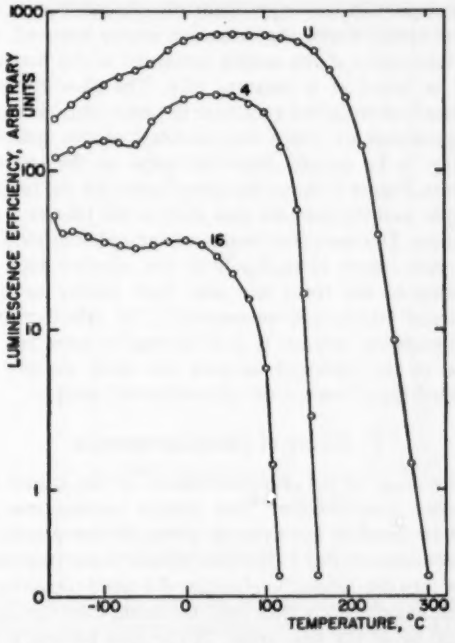

FIG. 4. Luminescence efficiency under ultraviolet excitation as a function of temperature. Undamaged sample and samples exposed in reactor for 4 and 16 hours.

C. Luminescence as a Function of Temperature

A study was made of the steady state luminescence on the zinc sulfide phosphor under constant ultraviolet excitation from liquid air temperature to 350°C. The results are presented in Fig. 4. The curve *U* describes the behavior of the undamaged sample and shows that the luminescence increases from the temperature of liquid air to zero degrees, that it remains constant from 0°C to 140°C, and that from 150 to 300°C the luminescence drops four orders of magnitude. The curve for the 4-hour sample is similar in shape to that of the unbombarded sample except that there is an inflection point at −70°C and the drop in luminosity takes place more rapidly and at a lower temperature. The curve for the 16-hour neutron exposure sample shows a steady decrease in luminosity with increasing temperature and a precipitous drop in luminosity at room temperature.

D. Thermoluminescence

The thermoluminescence experiment can be used to determine the presence of phosphorescence-active elec-

tron traps.[34] In this experiment the phosphor is excited at low temperature, the excitation source removed, and the luminosity of the sample measured as the temperature is raised at a constant rate. The glow curve so obtained often shows a number of peaks which occur at temperatures at which the electrons obtain sufficient energy to be excited from the traps to the emission centers. Figure 5 shows the glow curves for the original sample, and the samples that were in the pile for 4 and 16 hours. It is seen that neutron bombardment modifies the glow curve changing both the number and the position of the traps and also their ability to store electrons which will subsequently be effective in a light-emission process. It is of interest to note that the traps in the damaged samples are more sharply delineated than those in the unbombarded sample.

E. Decay of Phosphorescence

The decay of the phosphorescence of zinc sulfide is a complex phenomenon. Two simple mechanisms are used to account for extreme cases. If the process of light emission is due to the slow release of electrons from traps into the conduction band and a rapid transition to the emission centers with light emission, then the decay should be of the first order. If the slow process is the recombination of the electrons in the conduction band and holes in the filled band, the process should be second order. Neither of these simple laws are obeyed by the zinc sulfide samples studied. Complications are undoubtedly due to the fact that in this phosphor, traps have different depth, and that re-trapping, self-stimulation, self-absorption, and nonradiative transitions occur. The decay curve of an unbombarded sample for two types of excitation and for two temperatures is presented on a log-log plot in Fig. 6. The drop in light emission had been measured over 4 orders of magnitude. It is seen from the curves that at room temperature, at the longer times the curves have a limiting slope of 2, suggesting a second order process. The decay curve taken at 80°C has a higher limiting slope. The effect of neutron bombardment on the phosphor is to increase the rate of decay and at the same time to cause the decay curves to assume at longer intervals a more pronounced exponential form (Fig. 7). The effect of the infrared light on the decay curve is shown in Fig. 8. For the unbombarded sample the presence of infrared light makes the decay curve exponential after 5 minutes while for the phosphor that had been in the pile for 1 hour the curve is exponential during its whole course, involving hundredfold drop in intensity.

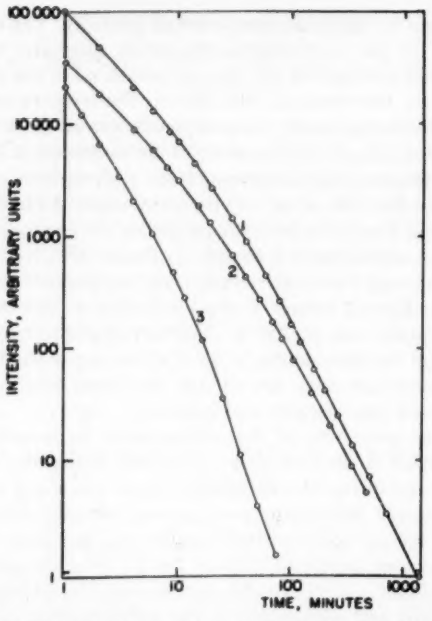

FIG. 6. Decay of undamaged sample: *1*, at 22°C excited by high-intensity light (carbon arc); *2*, at 22°C excited by lower-intensity light (Pointolite); *3*, at 80°C excited by high intensity.

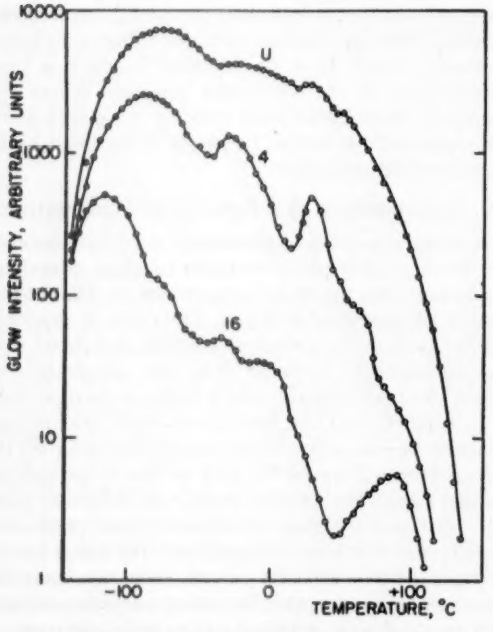

FIG. 5. Thermoluminescence (glow curves) of undamaged and samples damaged for 4 and 16 hours.

F. Growth of Luminescence

The growth of luminescence to the steady value may take measurable time because traps have to be filled before constant emission of the phosphor sets in. The shape of the growth curve is a complicated function of the exciting intensity, the number and depth of traps, the relative cross section of the traps and the character

[34] J. T. Randall and M. H. F. Wilkins, Proc. Roy. Soc. (London) A184, 365 (1945).

of the traps (radiative or nonradiative).[35] However, the area above the growth curve [bounded by the growth curve, the steady-state value of the luminescence intensity projected to the ordinate axis, and the ordinate axis (Fig. 9)] represents the amount of light that has been lost by trapping exicted electrons into traps of *considerable* depth. Light lost by instantaneous nonradiative processes or from nonradiative traps of shallow depth does not affect the rise time of the growth curve but only the steady-state value of the emission. The character of the growth curve was determined as a function of the neutron damage of the phosphor. The undamaged sample under constant ultraviolet illumination (of intensity corresponding to the most intense light used in experiments presented in Fig. 3) gave a rapid rise time of about 3 minutes. On the other hand, the sample bombarded for 16 hours in the pile had a rise time of 50 minutes (curve 9). It should be pointed out that the steady-state value of the luminescence of the latter sample was one-twentieth of that of the undamaged material. In the presentation of the data, the curves are normalized by multiplication of the values by appropriate constant to make equal the steady-stateva lues of the luminescence of all the sample. The undamaged sample under constant x-ray illumination (of intensity necessary to produce the same luminescence intensity as the ultraviolet of the previous section) gave a rise time of less than 1 minute. However, the rise time for the 16-hour sample was again long and slightly greater than that observed for the ultraviolet excitation (curve 2, Fig. 9). There was a slight difference

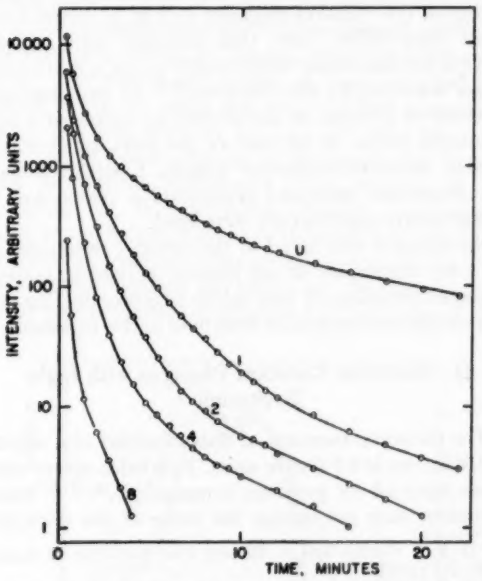

FIG. 7. Decay curves for undamaged sample and samples damaged for 1, 2, 4, and 8 hours.

[35] J. T. Randall and M. H. F. Wilkins, Proc. Roy. Soc. (London) A184, 365 (1945).

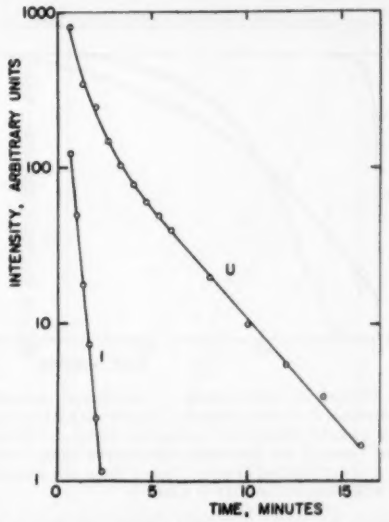

FIG. 8. Decay during infrared exposure of undamaged sample and sample damaged 1 hour.

in the behavior in the first few minutes of the curves obtained by different methods of excitation: electrons excited by x-ray photons seem to get to the emission center more efficiently than those produced by the ultraviolet photons.

The fact that the rise time was considerably longer for the damaged sample suggested that neutron bombardment produced traps of a large cross section for excited electrons and that electrons, once captured in the killer trap, leave it after a given time by a nonradiative transition. The lifetime of the electrons in these killer traps was obtained in the following way: a 4-hour damaged sample was allowed to remain in the dark for several weeks in order to stabilize the material. A growth curve for luminescence was established (curve *L*, Fig. 10). The rise time was about 80 minutes. The excitation source was shuttered off for 2 minutes, and then the shutter was opened for further excitation, and the growth of luminescence curve measured again. Under these conditions the growth curve was very steep, the rise time being 2 minutes (curve 2, Fig. 10). In a similar way, a whole set of growth curves was obtained by removing the exciting source for an increasing number of minutes after the steady-state luminescence had been reached. Figure 10 presents the experimental results obtained. The number on the curves gives the time the phospor was in the dark after the steady-state luminescence had been reached. It is seen that the longer the phosphor was in the dark between excitations, the longer it took it to reach the steady-state luminescence on subsequent exictation. This may be interpreted to mean that before steady-state luminescence is reached, certain traps must be filled; electrons leave these traps slowly in the dark. If one uses the area above the growth curve as a measure of the vacancies in these

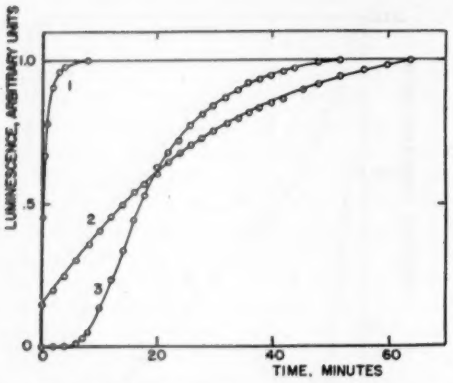

FIG. 9. Growth of luminescence: *1*, undamaged sample, ultraviolet excitation; *2*, 16-hour damaged sample with x-ray excitation; *3*, 16-hour sample, ultraviolet excitation. Intensity of excitation for curves 1 and 3 are the same, the curves being normalized, while the x-ray excitation in curve 2 gave about the same emission intensity at saturation as that in curve 3.

killer traps, one can determine the half-life of electrons in the killer traps at room temperature to be 1000-minutes. At 98°C the half-life is 5 minutes. The depth of the traps as determined by the temperature coefficient is thus about 16 kcal or 0.7 ev. During the process of electrons leaving these killer traps, no radiation is emitted either in the ultraviolet, visible or the near infrared up to 3 microns. It was also determined that the number of killer traps increased with neutron bombardment. In fact, if one plots the time necessary to reach 80 percent of the steady-state value (the 80 percent being chosen for convenience) against the logarithm of the exposure in the pile, one gets a linear relationship (Fig. 11). This is interpreted to mean either that the damage, as expressed in the production of deep killer traps, has a saturation value, or that there is a healing process which takes place simultaneously with the damage but depends on a higher power than 1, of the trap concentration.

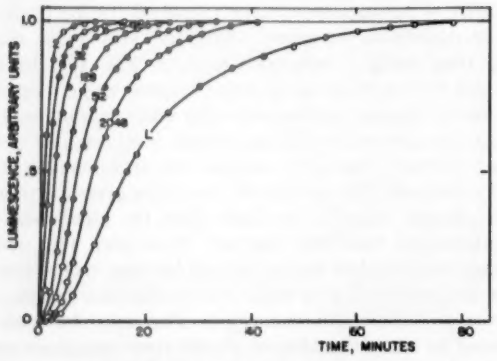

FIG. 10. Growth of luminescence of 4-hour damaged sample: 1, after several weeks in dark; 2, 32, 128, 512, 2048, after decay from saturation for 2–2048 minutes.

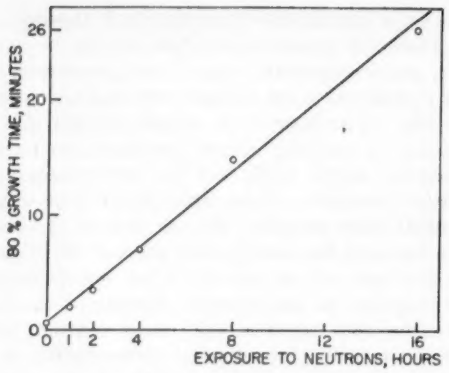

FIG. 11. Emission spectra of undamaged and 16-hour damaged sample.

G. Emission Spectrum

The emission spectrum under x-ray excitation was measured for the unbombarded and the 16-hour neutron-bombarded sample. A medium Hilger quartz spectroscope was used with Eastman Kodak IL plates. In order to obtain comparable photographic density, the exciting intensity used for the unbombarded sample was one-fifteenth of that used for the 16-hour phosphor. Ten-hour exposures were taken in both cases. Wavelength calibration was obtained by a mercury arc and a photoelectric densitometer was used to measure the photographic density. The spectral curves so obtained were not corrected for the spectral sensitivity of the plates. Neutron bombardment produces only a slight change in the emission spectrum as Fig. 12 shows. Our result thus differs from that obtained with alpha-particle bombardment where a shift of the spectrum to longer wavelengths was observed.[19,20] No emission was detected in 10-hours in the ultraviolet region for x-ray excitation either in the case of the undamaged or the 16-hour neutron-bombarded sample. Eastman Kodak 103 ultraviolet sensitized photographic plates and a Hilger quartz spectrograph were used.

No emission was found in the infrared region either on x-ray excitation or on heating a light-saturated, damaged phosphor. A lead sulfide photoconducting cell and an electronic amplifier were used in this experiment.

H. Dielectric Constant Changes with Light Excitation

The dielectric constant of unbombarded zinc sulfide at 100 kc/sec is 8.0 Debye units. This value agrees with those reported by previous investigators.[22, 36–40] Bombardment does *not* change the value of the dielectric

[36] G. F. J. Garlick and A. Gibson, Proc Roy. Soc. (London) **A188**, 485 (1947).
[37] G. F. J. Garlick, *Luminescence Materials* (Oxford University Press, London, 1949).
[38] J. H. Gisolf, Physica **6**, 918 (1939).
[39] F. Goos, Ann. Physik. **34**, 77 (1939).
[40] L. Wesch, Ann. Physik. **40**, 249 (1941).

constant of zinc sulfide. On the other hand, the dielectric constant and the dielectric loss increase markedly with light excitation attaining the values of 14. Debye units for both the unbombarded sample and the 4-hour neutron-irradiated sample. The dielectric constant change on illumination was frequency-independent in the 10–200 kc/sec range but was absent at the 1 Mc/sec where only a large increase in dielectric loss was observed. A similar frequency effect was observed by Garlick. The dependence of the dielectric constant change at 100 kc/sec on excitation light intensity is similar to that reported by Garlick and is the same for both the bombarded and the 4-hour neutron-irradiated sample (Fig. 13). This is in sharp contrast to the marked effect that neutron bombardment has on the relationship between luminescence and excitation intensity of the phosphor. The data in Fig. 13 has been presented in terms of a logarithmic relationship as suggested by Garlick.[36] Another way of interpreting the effect of light intensity on the change in the dielectric constant change is to consider that at high intensities one attains saturation of the dielectric constant change.

The effect of temperature on the dielectric constant change under constant illumination has not been studied but is a subject for future investigation.

I. Temperature Effect on the Dielectric Constant Change Analogous to Thermoluminescence

The unbombarded sample was excited in the condenser at liquid air temperature, the excitation removed, the luminescence allowed to decay for 5 minutes, and the condenser heated at a slow reproducible rate from liquid air temperature to 150°C. The dielectric constant was measured during the heating process at 100 kilocycles. The results are similar to those reported by Garlick[36] (Fig. 14 where the time abscissa is a measure of the temperature) in that the dielectric constant change passes through a maximum just below room temperature reminiscent of the behavior of luminescence in the thermoluminescence experiment. However, our results differ from those ofGarlick in that the dielectric constant change decays to zero for the unbombarded sample at liquid air temperature. A similar type of curve was obtained for the change of the dielectric constant of a previously-excited phosphor with temperature in the case of the 4-hour neutron-irradiated sample. There are minor differences in the behavior of the bombarded sample in that the peak for the dielectric constant change shifted to lower temperatures and the dielectric constant change did not decay to zero in 5 minutes at liquid air temperatures. Thus the results on the dielectric constant change with temperature of a damaged excited phosphor differ markedly from the analogous experiments on the light output of a damaged excited phosphor.

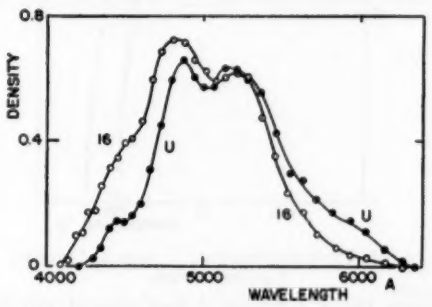

FIG. 12. Emission spectra of unbombarded and 16-hour sample.

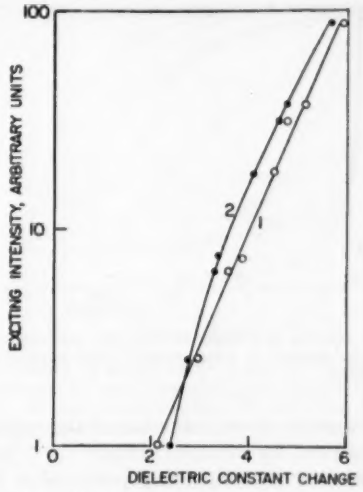

FIG. 13. Dielectric constant change as a function of exciting intensity: 1, unbombarded sample; 2, 4-hour sample.

J. Growth and Decay of the Dielectric Constant Change

The growth of the dielectric constant change at 100 kilocycles on illumination of 4-hour neutron-irradiated sample is rapid and similar in its course to that obtained with the undamaged sample, (Fig. 15). This is in sharp

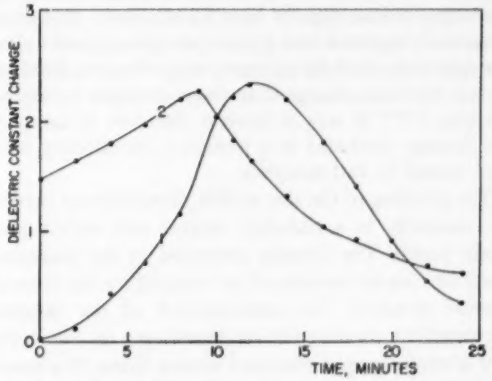

FIG. 14. Dielectric constant change during thermoluminescence: *1*, unbombarded sample; *2*, 4-hour sample.

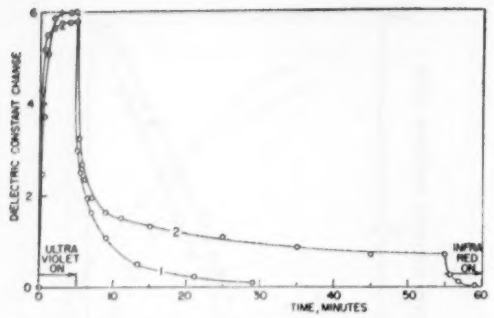

FIG. 15. Growth and decay of dielectric constant change: *1*, unbombarded sample; *2*, 4-hour sample (with infrared turned on at 55 minutes).

contradistinction to the behavior of the luminescence growth curve of the damaged sample.

The dielectric constant change produced on illuminating a phosphor decays, on removal of the excitation, in much the same way as the luminescence decreases with time. The surprising result is that the decay of the dielectric constant change produced by lumination is *much slower* for the neutron damaged sample than for the unbombarded phosphor. This behavior is in sharp contrast to the results reported above, i.e., that the luminescence of the damaged sample decayed much faster than that of the unbombarded sample. The same result type was obtained at liquid air temperature where the dielectric constant change of the unbombarded sample decayed to zero in 5 minutes while that of the 4-hour neutron-irradiated sample dropped only to 50 percent in that time and then remained constant.

On illumination of the photoexcited phosphor with infrared, the dielectric constant change of the bombarded sample drops immediately to zero.

Grinding

It has been suggested that the damage produced by grinding may be similar to that produced by nuclear particle irradiation[20,27,29] in that both processes may be producing similar type of lattice distortions. However, it has been reported that ground phosphors show different sensitivity to infrared quenching[17,20] and a different crystal structure change than those damaged by alpha-particles.[25,26,29] It was of interest therefore to compare the damage produced in a phosphor by grinding with that caused by fast neutrons.

The grinding of the zinc sulfide phosphor was carried out manually in a porcelain mortar and with a porcelain pestle. The damage produced in the phosphor could be closely reporduced by controlling the time of manual grinding. The luminescence of the samples decreased on grinding but its dependence on the intensity of exciting light remained almost linear. No measurements were made on the effect of grinding on the temperature dependence of luminescence. The effect on the thermoluminescence curve is shown in Fig. 16. Grinding produces a new peak at 100°C and at the same time decreases the height of the peaks at other temperatures. The new traps associated with the 100°C peak affect the decay characteristics of the ground phosphor causing a decrease in the slope of the decay curve so that the ground samples become brighter than the unground samples at 23°C after 1000 minutes and at 80°C after 2 minutes. The behavior of the decay curve at 80°C shows vividly the decreased contribution of the deeper traps produced by grinding and associated with the 100°C peak in the glow curve.

The luminescence growth curve for a sample ground 30 minutes is similar to that of the original sample and has a much shorter rise time than the 2-hour neutron-irradiated sample which had the same steady-state efficiency as the ground sample.

Thus the effects of grinding are definitely different from those produced by neutron irradiation.

Annealing

It has been reported that the effects of nuclear bombardment can be removed by appropriate heat treatment.[1,41,42] The behavior of the growth of luminescence curve was used as a measure of the annealing effect of the heat treatment. Figure 17 shows the normalized growth curves for samples bombarded for the times indicated on the curves (solid lines). It also shows the growth curves for the 32-hour neutron irradiated

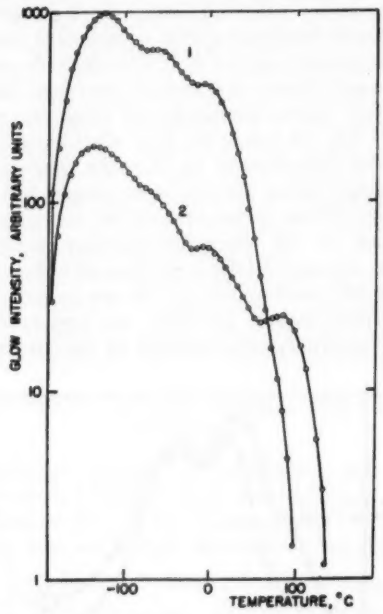

FIG. 16. Thermoluminescence: *1*, unground sample; *2*, ground sample.

[41] Parkins, Dienes, and Brown, J. Appl. Phys. **22**, 1017 (1951).
[42] R. Berman, Proc. Roy. Soc. (London) **A208**, 90 (1951).

sample during the course of the heat treatment to anneal the damage (dashed lines). Curves *A*, *B*, and *C* are the growth curves for samples annealed at 300°C for 1 hour, 1½ hours, and 5 hours, respectively. Curve *D* is the behavior of sample *C* after heat treatment at 500°C for an hour and curve *E* is that of sample *C* heated at 700°C for 1 hour. It is seen that the last curve approximates closely that of the unbombarded sample. The luminescence efficiency of sample *E* was not as great as that of the unbombarded sample due to the darkening of the surface of the phosphor by the impurities in the nitrogen atmosphere used in the heat treatment procedure. It is gratifying to note that a zinc sulfide phosphor that had been irradiated in the pile for 32 hours and had completely lost most of its original luminescence regained completely its luminescence efficiency by heating in nitrogen a few minutes at 900°C. The thermoluminescence curve of sample *E* had the same shape as that of the unbombarded sample. It should be noted that the annealing process is not a mere reversal of the effects of the neutron damage: the annealed samples show a faster growth of luminescence in the first few minutes than samples with less bombardement and no annealing. Thus the growth curve of the 8-hour neutron-irradiated sample crosses that of the samples *B* and *C*.

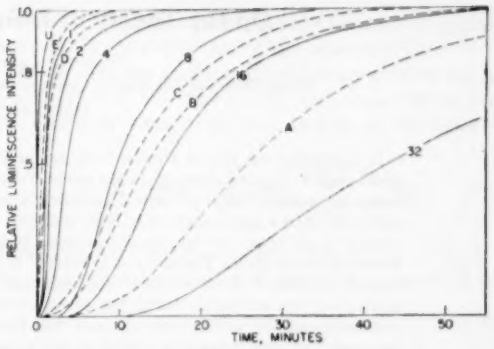

FIG. 17. Growth of luminescence of neutron bombarded and annealed samples: *U*, unbombarded sample; 1, 2, 4, 8, 16, 32-hour samples; *A*, 32-hour sample annealed 30 minutes at 300°C; *B*, sample *A* plus one hour at 300°C; *C*, sample *B* plus 3.5 hours at 300°C; *D*, sample *C* plus one hour at 500°C; *E*, sample *D* plus one hour at 700°C.

DISCUSSION OF RESULTS

A preliminary explanation of the results can be formulated in terms of the Klasens[43] Schoen model. Filled zinc and sulfur electron bands are separated from an empty conduction band by a "forbidden" energy region. In this region there are, however, discrete levels due to the copper-activated emission centers lying close to the filled bands and normal traps lying close to the empty conduction band. Near ultraviolet light (4100A) excites electrons from emission centers while x-rays excite them from the filled band into the conduction band. Electrons in the conduction band either return to the emission band directly with emission of light (fluorescence) or fall into normal traps. Electrons in these traps either may be excited after some delay back into the conduction band and thence to the emission center (phosphorescence) or they may drop into a hole in the filled band with no light emission (radiationless transfer). Holes in the filled band are created by excitation of electrons from the filled band to holes in the emission centers.

The effect of neutron bombardment is visualized in the following way. An occasional fast neutron transfers a small but significant amount of its kinetic energy to a zinc or sulfur atom. The latter can transfer the excess energy very efficiently to its neighbors producing a highly concentrated center of displaced atoms. These lattice defects of varying complexity constitute the killer traps. The cross section of the killer traps for electron capture during the excitation process is high and these traps must be filled before steady state emission can take place. The killer traps lie rather far below the conduction band since electrons on leaving them emit no light. Electrons can remain trapped in these killer traps for several weeks at room temperature, and are lost from these killer traps to the filled band at a rate determined by the number of holes in the filled band.

The change in the dielectric constant caused by light excitation is associated with the passage of electrons from one place in the solid to another and is caused, in the frequency range measure, by both radiative and nonradiative processes.

[43] H. A. Klasens and M. E. Wise, Nature **158**, 306 (1946).

On the Theory of X-Ray Small-Angle Scattering*

YIN-YUAN LI AND R. SMOLUCHOWSKI
Metals Research Laboratory, Carnegie Institute of Technology, Pittsburgh, Pennsylvania
(Received January 21, 1954)

It is pointed out that a Fourier inversion of the intensity distribution of x-ray scattering, taking the small-angle scattering alone, gives the electron density function of the continuum approximation. The procedure of including only the central scattering is practicable, when none of the peaks of the lattice diffraction occurs at such a small angle that their scattered intensity overlaps the central scattering. A general discussion of the choice of the sign of the phase factor in the Fourier transformation and of its experimental consequences is given. The analysis is applied to scattering in a supersaturated Al-Ag alloy and to a discussion of some of the approximate formulas used in fitting experimental data. When the electron density function of the scattering center has an odd symmetry with respect to one of the coordinate variables, conclusions can be drawn about the scattered intensity distribution without actually knowing the density function. The most interesting case of an odd symmetry is the edge dislocation. An experiment is suggested to reveal the pileup of dislocations as well as the aggregation of vacancies along the slip plane of a metal crystal deformed by a pure shear stress.

I. INTRODUCTION

IN most experiments using small-angle scattering techniques[1] the scattering center is so small that the interpretation is based on diffraction theory (wave theory) rather than on the refraction-reflection theory (ray theory) of von Nardroff.[2] Let us thus first recall the general theory of x-ray diffraction in which the intensity is given by

$$I(\mathbf{k})=|A(\mathbf{k})|^2$$

$$=I_e\int_V\rho(\mathbf{r})\exp(i\mathbf{k}\cdot\mathbf{r})d\mathbf{r}\int_V\rho(\mathbf{r}')\exp(-i\mathbf{k}\cdot\mathbf{r}')d\mathbf{r}', \quad (1)$$

where $\mathbf{k}=(2\pi/\lambda)(\mathbf{s}-\mathbf{s}_0)$, $\mathbf{s}_0$=the unit vector in the direction of the incident beam, $\mathbf{s}$=the unit vector in the direction of the scattered beam, $k=|\mathbf{k}|=(4\pi/\lambda)\times\sin(\epsilon/2)$, ϵ=the angle between $\mathbf{s}_0$ and $\mathbf{s}$, λ=the wavelength of the x-ray, $A(\mathbf{k})$=the amplitude of the scattered radiation, I_e=the intensity scattered by a single electron, $\rho(\mathbf{r})$=the number of electrons per unit volume at the point $\mathbf{r}$, and $\int_V\cdots d\mathbf{r}$=an integration taken over the whole space with the understanding that $\rho(\mathbf{r})$ is made equal to zero outside the irradiated volume. The vector $\mathbf{k}$ is used as a variable designating the radiation in the direction $\mathbf{s}$ scattered from the incident beam in the direction $\mathbf{s}_0$. We shall omit the factor I_e in Eq. (1); i.e., regard I_e as the unit of intensity in terms of which $I(\mathbf{k})$ is expressed. One may either assume $\rho(\mathbf{r})$, calculate the diffraction pattern from Eq. (1) and compare it with the observed pattern, or one may obtain the electron distribution from the observed scattered intensity by making the Fourier inversion,

$$\rho(\mathbf{r})=\frac{1}{(2\pi)^3}\int_{V_k}[I(\mathbf{k})]^{\frac{1}{2}}\exp\{-i[\mathbf{k}\cdot\mathbf{r}-\alpha(\mathbf{k})]\}d\mathbf{k}, \quad (2)$$

where the integration is taken over the whole $\mathbf{k}$ space, and $\alpha(\mathbf{k})$ is the phase angle in the equation

$$A(\mathbf{k})=[I(\mathbf{k})]^{\frac{1}{2}}\exp[i\alpha(\mathbf{k})]. \quad (3)$$

Since the experiment can furnish no information about $\alpha(\mathbf{k})$, the Fourier analysis of Eq. (2) can be realized only when the knowledge of $\alpha(\mathbf{k})$ can be derived by some other means. Nevertheless we can always evaluate the Patterson probability function,

$$P(\mathbf{r})=\int_V\rho(\mathbf{r}')\rho(\mathbf{r}'+\mathbf{r})d\mathbf{r}'$$

$$=\frac{1}{(2\pi)^3}\int_{V_k}I(\mathbf{k})\exp(i\mathbf{k}\cdot\mathbf{r})d\mathbf{k}, \quad (4)$$

in which the phase factor is not involved. Equation (4) is obtained from (2) by making use of the following relations:

$$\int_V\exp[i(\mathbf{k}+\mathbf{k}')\cdot\mathbf{r}]d\mathbf{r}=(2\pi)^3\delta(\mathbf{k}+\mathbf{k}'),$$

$$\int_{V_k}f(\mathbf{k})\delta(\mathbf{k}+\mathbf{k}')d\mathbf{k}=f(-\mathbf{k}'),$$

$$I(\mathbf{k})=I(-\mathbf{k}),$$

and

$$\exp\{i[\alpha(\mathbf{k})+\alpha(-\mathbf{k})]\}=1.$$

Since in problems using small-angle techniques, such as the determination of particle sizes, we wish to study the inhomogeneous distribution of electrons over a space of 10 to 1000 wavelengths of the radiation, it is not necessary to consider the discrete and orderly arrangement of the atoms. Therefore, the various electron distribution functions used to calculate the scattered intensity distribution are those in which the variation of electron density from one atom to a neighboring one is smoothed out. For instance, a spherical scatterer containing several to a few thousand atoms is simply

* This work was supported by a U. S. Atomic Energy Commission contract.
[1] See, e.g., A. Guinier, *Radiocrystallographie* (Dunod, Paris, 1945).
[2] R. von Nardroff, Phys. Rev. **28**, 240 (1926); for a comprehensive treatment, see H. C. van de Hulst, Recherches Astronomiques de l'Observatoire d'Utrecht, No. 11 (1946).

represented by $\rho(r)=\text{const}$ for $r<R$ and $\rho(r)=0$ otherwise. We propose to call this customary approximation the continuum model. Naturally, it leads to no Bragg diffraction maxima. It follows that we may exclude all the intensity peaks of lattice diffraction from the integration over $\mathbf{k}$ space, and the resulting contribution in the integration comes only from the scattering of the direct beam within a small region around $\mathbf{k}=0$. The electron density function thus obtained has a different meaning from that evaluated by the same equation but including all the diffraction peaks. The latter yields the complete information on the structure of the irradiated part of the specimen obtainable with the x-ray diffraction method while the former gives only the information as can be demanded within the continuum model. The procedure of including only the central scattering in the Fourier inversion is practicable when none of the Bragg peaks, which appear in the x-ray diffraction pattern obtained from the same solid before the introduction of small-angle scattering centers, occurs at such a small angle that its scattered intensity overlaps that of the central scattering. The present treatment applies to the small-angle scattering of thermal neutrons as well. In that case, we interpret $\rho(\mathbf{r})$ as pertaining to the density of atoms and I_e as the intensity of neutrons scattered by a single atom.

II. THE FOURIER INVERSION

In certain special cases it is possible to determine the phase factor necessary for the Fourier inversion of Eq. (2). In this connection, it is convenient to interpret $\rho(\mathbf{r})$ as a relative quantity; the number of electrons per unit volume at $\mathbf{r}$ minus that in the surrounding medium, or minus that of the undisturbed lattice. Consequently, ρ will be negative where there is an electron deficiency, compared with the surroundings, and we can discuss the case of an even and an odd symmetry in the density function $\rho(\mathbf{r})$. The latter finds no place in the ordinary theory of lattice diffraction, but it is useful in an analysis of small-angle scattering based on the continuum model.

We shall assume that the scattering centers (or particles) are identical in their size, shape, and orientations, and that they are not close enough together to cause coherent diffraction between them. Under these conditions the observed intensity is equal to M times the intensity scattered by one of the particles, where M is the number of particles irradiated. Accordingly, we may treat the problem as one of a single scattering center except that the density function $\rho(\mathbf{r})$ obtained by Eq. (2) will be $\sqrt{M}$ times that of a single particle. When the interference between the neighboring particles must be considered, the assembly of particles as a whole is regarded as one scattering center. In such cases as, for instance in the scattering by closely packed particles, a radial distribution function may be used to approximate the density function of the assembly.[3,4]

When $\rho(\mathbf{r})$ has a center of either an even or an odd symmetry, i.e., $\rho(-\mathbf{r})=\pm\rho(\mathbf{r})$, the phase factor $p(\mathbf{k})$, i.e., $\exp[i\alpha(\mathbf{k})]$ can be derived as follows. We have

$$[I(\mathbf{k})]^{\frac{1}{2}}p(\mathbf{k})=\int_V \rho(\mathbf{r})\left\{\begin{matrix}\cos(\mathbf{k}\cdot\mathbf{r})\\ i\sin(\mathbf{k}\cdot\mathbf{r})\end{matrix}\right\}d\mathbf{r}, \tag{5}$$

where $\cos(\mathbf{k}\cdot\mathbf{r})$ applies for even symmetry; $i\sin(\mathbf{k}\cdot\mathbf{r})$ for odd symmetry. From this equation we see that (a):

$$p(\mathbf{k})=\pm 1, \tag{6a}$$

if $\rho(-\mathbf{r})=\rho(\mathbf{r})$, and (b):

$$p(\mathbf{k})=\pm i, \tag{6b}$$

if $\rho(-\mathbf{r})=-\rho(\mathbf{r})$. For both cases the phase factor is not determined wherever $I=0$ and has ambiguous signs elsewhere. Since for most cases of interest the right side of Eq. (5) is a continuous function of $\mathbf{k}$, we expect no sudden change of $p(\mathbf{k})$ from $+1$ (or $+i$) to -1 (or $-i$), except at places where $I(\mathbf{k})=0$. In other words, the $\mathbf{k}$ space is divided into regions each enclosed by a boundary along which the scattered intensity vanishes, and $p(\mathbf{k})$ remains constant in each of these regions but may suddenly change its sign when a boundary is crossed from one region to another. A similar situation exists in the Fourier analysis of lattice diffraction, in which the phase factor may have opposite signs for different Bragg peaks. Substituting Eq. (6a,b) into Eq. (2), we have for (a):

$$\begin{aligned}\rho(\mathbf{r})&=\frac{1}{4\pi^3}\int_{V_\mathbf{k}^+}[I(k)]^{\frac{1}{2}}p(k)\cos(\mathbf{k}\cdot\mathbf{r})d\mathbf{k}\\ &=\frac{\pm 1}{4\pi^3}\left\{\int_{V_\mathbf{k}(\mathrm{I})}\pm\int_{V_\mathbf{k}(\mathrm{II})}\pm\cdots\right.\\ &\qquad\left.\pm\int_{V_\mathbf{k}(j)}\pm\cdots\right\}[I(\mathbf{k})]^{\frac{1}{2}}\cos(\mathbf{k}\cdot\mathbf{r})d\mathbf{k},\end{aligned} \tag{7a}$$

and for (b):

$$\begin{aligned}\rho(r)&=\frac{\pm 1}{4\pi^3}\left\{\int_{V_\mathbf{k}(\mathrm{I})}\pm\cdots\right.\\ &\qquad\left.\pm\int_{V_\mathbf{k}(j)}\pm\cdots\right\}[I(\mathbf{k})]^{\frac{1}{2}}\sin(\mathbf{k}\cdot\mathbf{r})d\mathbf{k},\end{aligned} \tag{7b}$$

where $V_\mathbf{k}^+$ is the full $\mathbf{k}$ space actually dealt with in experiments, i.e., that half of $V_\mathbf{k}$ where the component of $\mathbf{k}$ in the direction of $\mathbf{s}_0$ is negative or zero. $V_\mathbf{k}(\mathrm{I})$, $V_\mathbf{k}(\mathrm{II})$, $\cdots$ etc., are subdivisions of $V_\mathbf{k}^+$ divided by zero-intensity boundaries. We are now confronted with the problem of how to choose the correct sign before

[3] N. S. Gingrich and B. E. Warren, Phys. Rev. **48**, 248 (1934).
[4] K. L. Yudowitch, J. Appl. Phys. **20**, 174 (1949).

each of the integration symbols in Eq. (7a) and (7b). The simplest case is when the **k** space is not subdivided. We have, then, an important special case of (a)

$$\rho(\mathbf{r})=\frac{\pm 1}{4\pi^3}\int_{V_{\mathbf{k}}'}[I(\mathbf{k})]^{\frac{1}{2}}\cos(\mathbf{k}\cdot\mathbf{r})d\mathbf{k}. \tag{8}$$

The $\pm$ signs at the start of the right side of Eqs. (7a,b) and (8) indicate that the same scattering results from $\rho(\mathbf{r})$ or $-\rho(\mathbf{r})$, and thus the intensity *vs* **k** curve does not distinguish between the two.

The guiding principle in choosing the + or − signs in the bracket of Eqs. (7a) and (7b) is that opposite signs should be taken for two neighboring regions, since $A(\mathbf{k})$ {or $[I(k)]^{\frac{1}{2}}p(\mathbf{k})$} ought to change sign when passing through zero.† The rule fails if the zero intensity coincides with a maximum or a minimum of $A(\mathbf{k})$. This is, however, very unlikely since, in general, $A(\mathbf{k})$ oscillates about zero and decreases in its magnitude as k increases. One does not expect, in general, two regions $V_{\mathbf{k}}(i)$ and $V_{\mathbf{k}}(j)$ which are neighbors of $V_{\mathbf{k}}(\mathrm{I})$ to have a common boundary except at isolated points. There is then a close relationship between the presence or absence of such isolated points in the **k** space for scattering by centers of odd or even symmetry and the position and form of zero intensity lines in a monochromatic scattering pattern.

A comparison between theory and observed scattering pattern is complicated by the fact that the theory deals with an incident beam from a pinhold while the experiment usually uses a beam defined by slits of finite height or a beam focused to an area of finite dimensions. As a result, the observed intensity is a superposition of the scattering of beams from a group of overlapping pinholes and the lines of zero intensity are smeared out, even if the radiation is strictly monochromatic. Instead, only the lines of intensity minima may be found on the photographic film. Guinier and Fournet,[5] and others have worked out formulas for slit-pinhole correction which may be used in certain cases. The observation of the details of the small-angle scattering pattern demands refined techniques in both the instrumentation and the preparation of specimens. Hubbel[6] first succeeded in observing the first secondary maximum of the scattering pattern of packed spherical particles. The experiments by Yudowitch[7] and by Danielson *et al.*[8] on latex particles have recorded a large number of concentric rings of maximum intensity. Between two successive maxima, an intensity minimum is found where we might expect lines of zero intensity if an extremely narrow beam were used. [If one uses the approximation of a radial distribution function $\rho(r)$ for the assembly of packed spherical particles, then $\rho(r)$ has a spherical symmetry, and thus it has a center of even symmetry.]

III. APPLICATIONS OF THE METHOD

In order to illustrate the applicability of our method and its limitation, we shall discuss the following two problems:

(A) Guinier[9] has studied the formation of local composition inhomogeniety in quenched Al alloys containing Ag up to 5.8 atomic percent. He found that the small-angle scattering pattern consists of a single ring of maximum intensity around the direct beam spot and is independent of the crystal orientation with respect to the incident beam. The radius of intensity maximum is of the order of several degrees and decreases with the increase of the duration and temperature of aging. An extrapolation of the intensity *vs* angle curve taken with a Geiger counter gives a zero scattering in the forward direction. The scattered intensity of the Bragg reflections shows that when the (000) reciprocal lattice point is surrounded by a shell of scattering power, each of the other reciprocal lattice points is also surrounded by a similar scattering distribution. This periodic distribution of scattering power indicates that the atoms in the quenched alloy remain on the lattice sites of the parent matrix. The Fourier method used by Walker and Guinier[10,11] in explaining their experiment was originally formulated for x-ray studies of the short-range order of binary alloys from which the probability of finding Ag atoms in the nth shell surrounding a central Ag atom is obtained. Because of the periodicity in scattering power, the integration only extends over one unit cell of reciprocal space, which may be that surrounding the (000) reciprocal lattice point. The necessary integration is finally reduced to an integration over the small-angle scattering. From a Patterson-like probability function $P_{\mathrm{Ag-Ag}}$, Walker and Guinier assert that the inhomogeniety center in the supersaturated alloy consists of an inner Ag-rich core and an outer Ag-poor shell. Our Fourier method [Eq. (8)] applied to the same data yields that the scattering center has an electron-surplus core of radius 10A (where $\rho>0$) and an immediate outer electron-deficit shell about 20A thick (where $\rho<0$), or vice versa that the inner core is deficient in electrons ($\rho<0$) and the outer shell has an electron surplus ($\rho>0$). (Beyond 30A from the center there are slight oscillations about $\rho=0$ but they are not significant, since these variations are within the experimental error and the data has been used without slit-pinhole corrections.) The uncertainty in the sign of ρ is caused by the ambiguity of signs in Eq. (8), while

† *Note added in proof.*—Professor Pepinsky kindly pointed out that a similar rule has been used [Bogers-Waston, Davidson, and Perutz, Proc. Roy. Soc. (London) **A191**, 83 (1947)] in the x-ray study of horse methaemoglobia and was referred to as the "nodal point" method.

[5] A. Guinier and G. Fournet, J. phys. radium **8**, 345 (1947).

[6] H. H. Hubbel, thesis, Princeton University, 1947 (unpublished).

[7] K. L. Yudowitch, J. Appl. Phys. **22**, 214 (1951).

[8] Danielson, Shenfil, and DuMond, J. Appl. Phys. **23**, 860 (1952).

[9] A. Guinier, Z. Metallkunde **43**, 217 (1952).

[10] C. B. Walker and A. Guinier, Compt. rend. **234**, 2379 (1952).

[11] C. B. Walker and A. Guinier, Acta Metallurgica **1**, 568 (1953).

no such ambiguity of signs appears in the Patterson analysis of Eq. (4). The continuous curve of P_{Ag-Ag} of reference 11 is the same as that of $P(r)/P(0)$ derived from our Eq. (4).

Since our density function ρ has an undetermined sign, its physical interpretation has to be obtained from other facts. The most important information here is the large absolute value of ρ in the central core. Even if this core were pure Al, then ρ could be only slightly negative since the average concentration of Ag is low. It follows that the central core must be Ag-rich. This kind of argument fails if the concentration in the clusters is small or if the abundance of the two kinds of atoms is comparable. A similar argument can be applied to the observation by Walker *et al.*[12] of a weak scattering by the same alloy at high temperatures. There ρ has the shape of an error function corresponding to local aggregates of several A in radius. These aggregates must be Ag-rich since Al is too abundant. It should be kept in mind too that a small absolute value of ρ could result from a local change of lattice constant. In the present case this is excluded not only by the large value of ρ but also by high-angle scattering which indicates a periodic distribution of the scattering power in the reciprocal lattice.

(B) The formula

$$I(k,\varphi)=A\exp[-k^2B^2(\varphi)] \tag{9}$$

has been frequently used by experimentalists to find the dimensions of the scattering center by fitting the measured intensity to a straight line of $\ln I$ *vs* k^2. φ is the polar angle in the plane normal to the incident beam, and B is the radius of gyration of the electron density of the particle. The way in which Guinier derives (9) may be put as follows: By expanding the factor $\exp[i\mathbf{k}\cdot(\mathbf{r}_1-\mathbf{r}_2)]$ into the Taylor series, we have

$$\begin{aligned}I(\mathbf{k})&=\int_V\int_V\rho(\mathbf{r}_1)\rho(\mathbf{r}_2)\exp[i\mathbf{k}\cdot(\mathbf{r}_1-\mathbf{r}_2)]d\mathbf{r}_1d\mathbf{r}_2\\&=N^2\Big\{1+\frac{(ik)^2}{2!N^2}\int_V\int_V[(\mathbf{r}_1-\mathbf{r}_2)_k]^2\rho(\mathbf{r}_1)\rho(\mathbf{r}_2)d\mathbf{r}_1d\mathbf{r}_2\\&\quad+\cdots+\frac{(ik)^{2n}}{(2n)!N^2}\int_V\int_V[(\mathbf{r}_1-\mathbf{r}_2)_k]^{2n}\\&\quad\times\rho(\mathbf{r}_1)\rho(\mathbf{r}_2)d\mathbf{r}_1d\mathbf{r}_2+\cdots\Big\}\\&\simeq N^2\exp[-k^2B^2(\varphi)],\end{aligned} \tag{10}$$

where

$$N=\int_V\rho(\mathbf{r})d\mathbf{r}, \tag{11}$$

$$B^2(\varphi)=\frac{1}{N}\int_V[(\mathbf{r})_k]^2\rho(\mathbf{r})d\mathbf{r}, \tag{12}$$

and $(\mathbf{r})_k$ is the component of $\mathbf{r}$ in the direction of $\mathbf{k}$. (The centroid of the electron distribution is chosen as the origin of the coordinates.) The expansion of Eq. (10) is not permissible if $N=0$. This means that Guinier's formula cannot be directly applied to the scattering centers in which the surplus of electrons in one place is balanced by the deficiency in some other place. For $N=0$ the intensity of zero-angle scattering ($\mathbf{k}=0$) vanishes [see Eq. (1)], while the error function Eq. (9) gives only one maximum of intensity, in the forward direction. However, the Guinier formula may be applied to certain cases, including the $N=0$ case, by regarding the scattering center as composed of two or more particles, some with $\rho>0$ and the others $\rho<0$. The diffraction amplitude of the ith component particle is $N_i\exp(-k^2B_i^2/2)$ when $\rho_i(\mathbf{r})=\rho_i(-\mathbf{r})$, and so the intensity of small-angle scattering is given by $[\sum_i N_i\exp(-k^2B_i^2/2)]^2$ (see reference 11).

The last step of Eq. (10) is rather arbitrary, since a great many closed forms may be found to approximate the rigorous solution to the same effect, i.e., accurate to the k^2 term. It is interesting to see which density function $\rho(\mathbf{r})$ makes Eq. (10) a rigorous instead of an approximate solution. Let us consider the simple case where B is independent of φ. Substituting

$$I(k)=A\exp(-k^2B^2) \tag{13}$$

into Eq. (8), we obtain the corresponding density function,

$$\rho(r)=\frac{\pm\sqrt{A}}{(2\pi)^{\frac{1}{2}}B^3}\exp\left(-\frac{r^2}{2B^2}\right), \tag{14}$$

which is a spherical Gaussian distribution. On the other hand, by substituting Eq. (14) into Eq. (10) the coefficient of k^{2n} becomes equal to $(-1)^nB^{2n}/n!$, and so $N^2\exp(-k^2B^2)$ is the exact sum of the series instead of an approximation. Equation (14) indicates that there is no sharp boundary between the particle and the surrounding medium, but rather that they gradually merge into each other. For a spherical particle with the radius R and a uniform electron density Eq. (13) becomes

$$I(k)=A\exp(-k^2R^2/5), \tag{15}$$

since according to Eq. (14) $B=R/\sqrt{5}$ for the present case. On the other hand, the exact solution gives

$$I(k)=A[\Psi(kR)]^2, \tag{16}$$

where

$$\Psi(x)=3(\sin x-x\cos x)/x^3. \tag{17}$$

In order to illustrate the approximate nature of the error function formula, Eqs. (15) and (16) are plotted in Fig. 1 and their corresponding density functions in Fig. 2. We notice that the difference between the two intensity curves, where it is strong, is much less than that between the two density distributions. This indicates that much refined experimental techniques are

[12] Walker, Blin, and Guinier, Compt. rend. **235**, 254 (1952).

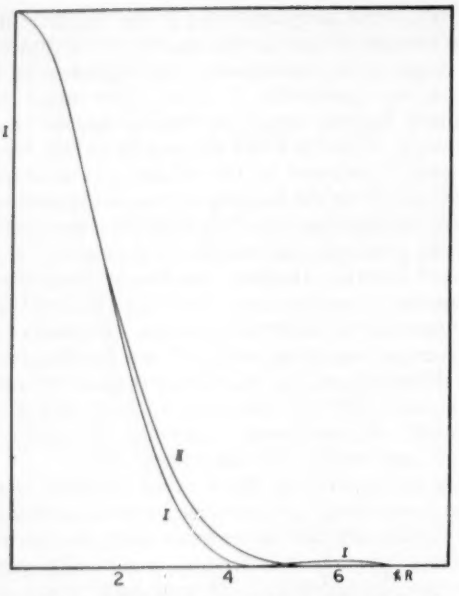

FIG. 1. Intensity I *versus* k. Curve I: $I=[\Psi(kR)]^2$. Curve II: $I=\exp(-k^2B^2)$, $B=R/\sqrt{5}$.

required to distinguish widely different electron distributions corresponding to the same radius of gyration and the same geometrical symmetry.

Another formula sometimes used to fit intensity readings is

$$I(k)=A(1+k^2B^2)^{-1}, \tag{18}$$

which also approximates the rigorous solution to the k^2 term. Using (8) we find the corresponding density function,

$$\rho(r)=\frac{\pm\sqrt{A}}{4\pi B^2}\frac{1}{r}\exp\left(-\frac{r}{B}\right). \tag{19}$$

This density function $\rho(r)\to\infty$ as $r\to 0$ and does not

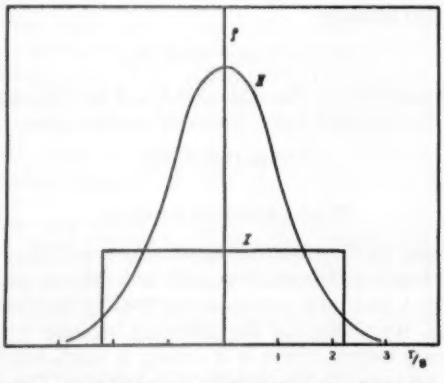

FIG. 2. Density function ρ *versus* r. Curve I: A rigid sphere, $\rho=3N/4\pi R^3$, 0, $r<R$, $r>R$; Curve II: $\rho=\exp(-r^2/2B^2)$.

offer a good physical representation of a particle containing a few atoms. The reason for using the function (18) for comparison with experiments is rather to approximate a certain particle-size distribution[13] which we do not intend to discuss in this article.

IV. THE ODD SYMMETRY AND THE EDGE DISLOCATION

When the scattering center has an odd symmetry with respect to one of the coordinates; say z, Eq. (1) may be written as

$$I(\mathbf{k})=\left|\int\int\int\rho(x,y,z)\sin(k_zz)\times\exp[i(k_xx+k_yy)]dxdydz\right|^2. \tag{20}$$

We draw the following conclusions: (i) A rather trivial result from Eq. (20) is that $I(k_x, k_y, -k_z)=I(k_x, k_y, k_z)$. If the incident beam is the x direction, the scattered intensity appears symmetric with respect to the xy plane. (ii) When $\rho(\mathbf{r})$ is an odd function of one or more of its variables, $I(\mathbf{k}=0)=0$; i.e., the forward scattering is zero, and thus an extrapolation of the intensity distribution curve would give a minimum at zero scattering angle and a maximum scattering would occur elsewhere. This holds not only for $\rho(\mathbf{r})$ with an odd symmetry, but also holds in general for any function $\rho(\mathbf{r})$ which makes $\int_V\rho(\mathbf{r})d\mathbf{r}=0$. If $\rho(x, y, -z)=-\rho(x, y, z)$, $I=0$ wherever $k_z=0$. If the incident beam makes an angle θ with the z axis, the scattered intensity vanishes on the conical surface generated by rotating the forward beam around the z axis. Of special interest is the case where the incident beam is perpendicular to the z axis, since then the scattered intensity in the xy plane vanishes. (Physically this means that the two waves that meet symmetrically on the xy plane, one from the upper half of the scattering center where $\rho>0$ and the other from the lower half where $\rho<0$, are completely out of phase and cancel each other in intensity.) Strong scattering should be found in the plane defined by the z axis and the incident beam perpendicular to it. Furthermore, only very weak scattering can be expected, when the incident beam is parallel to the z axis, since with this geometry $k_z\ll 1$ for small-angle scattering.

The most interesting example of a scattering center with an odd symmetry in the electron density function is an edge dislocation,[14] where the lattice is either in compression above the slip plane and below this plane it is correspondingly in tension, or vice versa. Even

[13] A number of articles have discussed the problem of size distribution; see, e.g., C. G. Shull and L. C. Roess, J. Appl. Phys. 18, 275 (1947).

[14] For an introductory treatment see A. H. Cottrell, *Dislocations and Plastic Flow in Crystals* (Oxford University Press, London, 1953).

if we did not have full information on $\rho(\mathbf{r})$ for an edge dislocation, we may expect that the distribution of the scattered intensity, if not smeared, should show the features stated above in (ii) and (iii). Dexter[15] has calculated explicitly the intensity scattered using the density function derived from the strain field of an edge dislocation,

$$\rho(\mathbf{r})=\kappa z/(x^2+z^2),$$

where κ is a constant of the crystal. The coordinates are chosen with the x axis in the direction of the Burgers vector and the z axis normal to the slip plane. Dexter's conclusions are similar to (ii) and (iii).

An experimental verification of the anisotropic scattering outlined in (ii) and (iii) might be possible with a single crystal deformed in such a manner that the majority of the dislocations are ordered with their Burgers vector parallel. One way of doing this is to deform a single crystal in pure shear along a single slip direction following the technique of Parker and his co-workers.[16] Naturally, other imperfections such as vacancies, interstitial atoms, etc., may also be produced during the slip process. One may speculate that after migration the vacancies will cluster into disk-shaped voids lying along the slip planes in which they were created. If flat specimens are cut from the sheared crystal with the surface normal to the slip direction (x direction) and the monochromatic radiation is normal to the flat surface, the scattering by the vacancy clusters will spread much farther in the direction normal to the slip plane (z direction) than in the y direction because of the large difference of the radii of gyration along these two directions (i.e., normal and parallel to the slip plane). Therefore, one may hope to observe a minimum of intensity along a straight line parallel to the y direction where the contribution to scattering from the dislocation vanishes. Near the central spot this minimum intensity should be smeared out by the strong scattering of voids.

We wish to thank Drs. D. L. Dexter, J. S. Koehler, and C. B. Walker for discussion and comments.

[15] D. L. Dexter, Phys. Rev. **90**, 1007 (1953). We are indebted to Dr. Dexter for having the privilege of seeing his work before its publication.

[16] See the article by E. R. Parker and J. Washburn in *Modern Technique in Physical Metallurgy* (American Society for Metals, Cleveland, 1953).

PHYSICAL REVIEW VOLUME 94, NUMBER 4 MAY 15, 1954

Electrical Properties of Single Crystals and Thin Films of PbSe and PbTe†

S. J. Silverman and H. Levinstein
Department of Physics, Syracuse University, Syracuse, New York

(Received January 7, 1954)

A comparison was made of the electrical properties of single crystals and subsequently formed thin films of PbTe and PbSe. Hall constants and resistivities were measured as a function of temperature from 300° to 77°K. Films were formed and measured without exposure to air. Regardless of whether the original crystal was n or p type, all films were n type, having carrier concentrations within the same order of magnitude for most cases. This observation was attributed to a limited amount of dissociation during evaporation, resulting in an inhomogeneous distribution of Te (or Se) agglomerates throughout the film. Room temperature mobilities in annealed films were about 1/5 that of the bulk values. In general carrier mobilities in films were markedly affected by substrate temperature during film formation, subsequent annealing, and limited oxygenation.

INTRODUCTION

PREVIOUS investigations of the electrical properties of PbSe and PbTe have been confined either to the single crystal and the polycrystalline specimens only, or to thin films sufficiently oxidized to obscure the characteristics of the original material.

Bauer,[1] investigating the temperature variation of electrical properties for single-crystal PbSe, found room temperature values of Hall constant to be between $+0.3$ and -30 cm³/coulomb with corresponding mobilities $\mu_n=1400$ cm²/volt sec and $\mu_p=640$ cm²/volt sec. He detected little difference in electrical properties between specimens grown in vacuum and those melted with a protective coating of borax in air. Putley,[2] who later conducted similar measurements on PbSe, also studied properties of both single-crystal and polycrystalline specimens of PbTe. The range of room temperature Hall constants for the single crystal was from $+1.0$ to -300 cm³/coulomb with corresponding mobilities $\mu_n=2100$ cm²/volt sec and $\mu_p=860$ cm²/volt sec. Room temperature mobilities for polycrystalline specimens were about 1/5 the single crystal values.

Previous studies on thin films seem to give less consistent results, presumably because of the lack of uniformity in conditions during film formation and meas-

† This work was supported in part by the Wright Air Development Center.

[1] K. Bauer, Ann. Physik **38**, 84 (1940).

[2] E. H. Putley, Telecommunications Research Establishment Journal, Gt. Malvern, Worcs., January, 1952 (unpublished).

urement. Lothrop,[3] in studying films of PbSe, was limited to room temperature measurements. Of the three films considered, two were n type with a concentration of 10^{20} cm^{-3} and a mobility of about 4 cm^2/volt sec. The p-type film, with a concentration of 10^{17} cm^{-3} and a mobility of about 50 cm^2/volt sec, was ascribed to the presence of excess Se. Likewise Levy,[4] in making Hall measurements on PbTe, found room temperature mobilities for n-type films to be about 2 cm^2/volt sec and 20 cm^2/volt sec for p type. He presumed the p-type films to be due to the presence of excess Te, although it was conceded that films might have been activated by slight traces of oxygen. Chasmar and Putley[5] measured conductivity of oxidized PbTe films, finding the mobilities about 1000 times smaller than in polycrystalline specimens.

It is the purpose of this investigation to compare the electrical characteristics of PbTe and PbSe single crystals with those of thin films formed by evaporating these crystals under controlled experimental conditions. Such a program requires, first, the successful growth of single crystals, and, second, the development of a technique for thin film formation and subsequent electrical measurement without any exposure to air. The essential electrical measurements involve the Hall constant and the resistivity from which the mobility as well as the number and kind of carriers may be determined. These quantities may be studied as a function of temperature.

The Hall constant may be determined by the simplified formula

$$R=\frac{V_H t}{I_x B_z}\times 10^8,$$

where the transverse Hall voltage V_H is in volts, the longitudinal current I_x is in amperes, the thickness t is in cm, the magnetic flux density B_z is in gauss, and the Hall constant R is in cm^3/coulomb.

If one type of carrier is predominant within the impurity temperature range under investigation, then the conductivity may be expressed as

$$\sigma=ne\mu,$$

where n is the concentration of electrons (or holes) in cm^{-3}, e is the charge in coulombs, and μ is the mobility in cm^2/volt sec. It can be shown that

$$\mu=R\sigma.$$

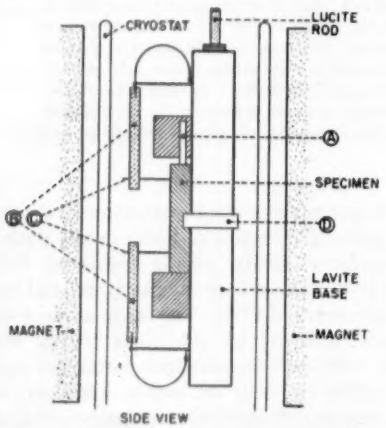

FIG. 1. Sketch of single-crystal specimen holder.

EXPERIMENTAL PROCEDURE

A. Bulk Material

Single crystals were grown in a manner similar to that described by Lawson.[6] The sample was prepared by combining lead and tellurium (or selenium) in stoichiometric proportions. All chemicals were supplied by Johnson Matthey and Company, Ltd., London, England. A quartz capsule, having a 60° apex angle to facilitate spontaneous nucleation, was filled with the desired material. It was then evacuated to less than 10^{-6} mm Hg by a conventional vacuum system. This consisted of a liquid oxygen trap, a three-stage oil diffusion pump, and a mechanical forepump. After preliminary flushing treatments, the material was fused in a reducing atmosphere of purified hydrogen by a portable electric furnace. The melting point temperature (917°C for PbTe, 1065°C for PbSe) was maintained for several hours to insure a completed reaction. Upon cooling to room temperature, the capsule was re-evacuated, sealed, removed from the system, and sent through the modified Stockbarger furnace.[7]

Although visual inspection was sufficient to establish the single crystal nature of the specimen, confirmation was provided by a series of Laue back reflection x-ray photographs.

The sample was next prepared for electrical measurements by either cleaving the specimen or sawing and polishing it to the appropriate dimensions for electrical measurements.[8] The usual specimen size was 9.5×2.3 ×1.7 mm.

The conventional dc circuit employed a Leeds and Northrup type K potentiometer for measuring the transverse Hall voltage, the voltage along the length of the sample associated with the resistivity, and the voltage across a standard resistor in series with the sample to determine the current.

In order to conduct these measurements as a function of temperature from 300°K to 100°K, a suitable specimen holder and a cryostat were constructed. The bulk specimen holder, as shown in Fig. 1 was made of Lavite, machined to accommodate brass current electrodes (A)

[3] E. W. Lothrop, Ph.D. dissertation, Northwestern University, Evanston, Illinois, 1949 (unpublished).
[4] J. L. Levy, Phys. Rev. **92**, 215 (1953).
[5] R. P. Chasmar and E. H. Putley, *Semi-Conducting Materials* (Butterworth Scientific Publications Ltd., London, 1951), pp. 208–217.
[6] W. D. Lawson, J. Appl. Phys. **22**, 1444 (1951).
[7] D. C. Stockbarger, Rev. Sci. Instr. **1**, 133 (1936).
[8] Isenberg, Russell, and Greene, Rev. Sci. Instr. **19**, 685 (1948).

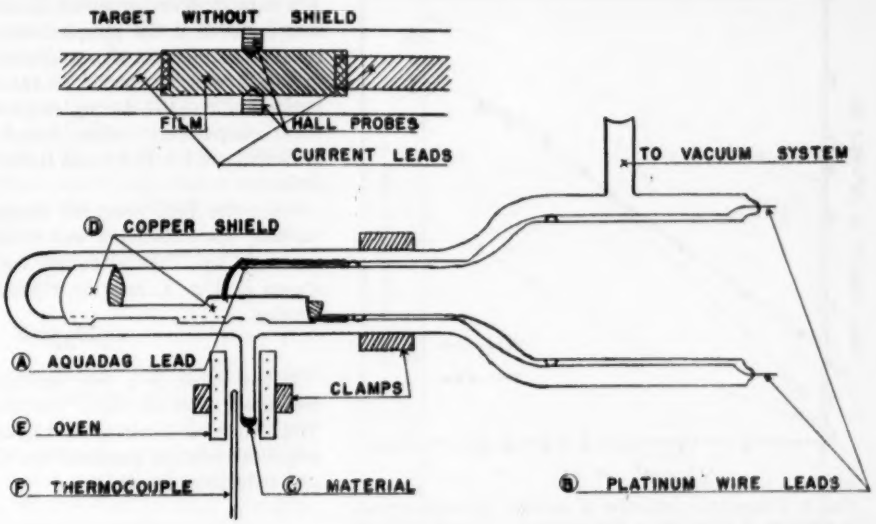

FIG. 2. Sketch of special Dewar cell for electrical measurements on this films.

and conductivity probes (*B*), having molybdenum bases. Extensions from the molybdenum base to the 20-mil tungsten probes (*C*) were of Lucite to reduce the vertical thermal gradient along the specimen because of its relatively low heat conductivity. Copper constantan thermocouples were spot-welded to each point probe, the distance between each being about 5 mm. Molybdenum spring probes (*D*) provided adequate tension under pressure of screws to obtain Hall voltages for the temperature range studied. The assembly was suspended in the cryostat by a $\frac{1}{4}$-in. o.d. Lucite rod.

The cryostat was designed to accommodate the specimen holder and also to fit in the 1.25-in. air gap of the permanent magnet. A controllable flow of oil-pumped nitrogen previously cooled by copper coils immersed in liquid oxygen produced a quasiequilibrium temperature for any particular reading with a maximum fluctuation of ± 1°K.

The flux density of the magnet was 3900 ± 40 gauss.

B. Thin Films

Depending on the nature of the original material, the film from which it is formed may be influenced by the rate of evaporation, the kind and temperature of the substrate, and the vacuum conditions during evaporation. It was, therefore, essential to control as many variables as possible to ascertain the effect of each on the electrical characteristics of the thin film.

A special Dewar cell, schematically represented in Fig. 2 was designed to permit evaporation and subsequent electrical measurements without the film ever being exposed to air. Four painted Pt leads (*A*) protected by a coating of Aquadag to reduce chemical reaction with the film, were extended from Pt wire leads (*B*) to a flattened target area. Two transverse electrodes acted as Hall probes and two longitudinal electrodes furnished the current, as indicated by the sketch in the upper left-hand corner of the figure.

A molecular beam from a small amount of pulverized single crystal (*C*) was collimated by a copper shield (*D*) immediately over the target area. A film was formed, having a rectangular pattern approximately 2×6 mm which insured an undistorted electric field along the length of the specimen. The beam was produced by a temperature-controlled oven (*E*) surrounding the $\frac{1}{8}$-in. o.d. glass side arm perpendicular to the target. The source-to-target distance was $1\frac{7}{8}$ in. During evaporation the oven temperature, as indicated by a chromel-alumel thermocouple (*F*), fluctuated no more than ± 1 percent of the equilibrium value (550°C).

Before each evaporation the substrate was usually outgassed for twelve hours at 450°C. The material in the side arm was outgassed for a half-hour at 550°C while a nickel shield covered the aperture, preventing material from evaporating onto the target. No evaporation was initiated until the pressure in the system was less than 2×10^{-7} mm Hg. When satisfactory vacuum and oven conditions existed, the shield was removed by a magnet and the evaporation was timed. The nickel shield was replaced over the aperture when the film resistance was low enough for Hall measurements. The side arm was then sealed and removed; later the special Dewar cell was sealed and removed at optimum vacuum conditions. Electrical measurements could then be made, employing techniques similar to those in the case of bulk material. Resistivity measurements, however, were made with a Leeds and Northrup Wheatstone bridge, type 4760. At no time during the entire investigation were films exposed to air.

Since determination of the Hall constant required a knowledge of the film thickness, independent measurements of the deposition rate for PbSe and PbTe were

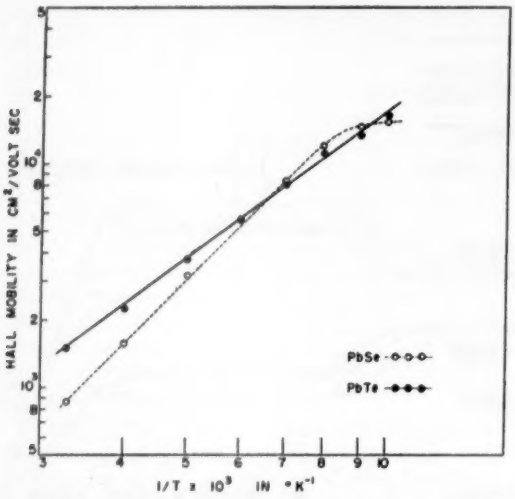

FIG. 3. Temperature variation of mobility in single crystals. The specimen of PbSe had a Hall constant +7.1 cm³/coulomb; PbTe had a Hall constant of −18 cm³/coulomb.

conducted. A second tube similar in geometry to the first had replaceable microscope slide segments instead of the permanent target area. Thicknesses were measured for a series of thin films evaporated at successively longer time intervals under uniformly controlled oven and vacuum conditions. The film thickness was measured by a multiple-beam interferometer technique as described by Tolansky.[9] Both the telluride and the selenide were evaporated at 550°C. The resultant deposition rates under the existing experimental conditions were 1900A/hr for PbTe and 1200A/hr for PbSe.

RESULTS AND DISCUSSION

A. Single Crystals

The range of Hall constant values for PbTe was +3.0 to −18 cm³/coulomb and +2.6 to −8.5 cm³/coulomb for PbSe. The majority of samples exhibited a temperature-invariant Hall constant, indicating that for these relatively impure specimens most of the impurity centers were ionized throughout the temperature range considered.

The resistivities, in general, indicated the semimetallic nature of these two compounds, decreasing from 300°K to 100°K by approximately a factor of 10.

TABLE I. A summary of room temperature electrical measurements on specimens in the vicinity of a nonrectifying $n-p$ barrier in PbTe.

Sample	ρ in Ω cm $\times 10^{-3}$	R in cm³/coulomb	μ in cm²/volt sec	Remarks
A-70-1	4.35	+ 3.7	850	Below barrier
A-70-2	9.79	−11.2	1150	Above barrier

[9] S. Tolansky, *Multiple Beam Interferometry* (Clarendon Press, Oxford, 1948).

The rate of decrease varied somewhat from sample to sample, even if the samples compared possessed Hall constants similar in sign and order of magnitude. This variation was attributed to the degree of lattice imperfection created during single-crystal growth. The room temperature values varied between 0.003- and 0.13-ohm cm for PbTe and 0.002- to 0.013-ohm cm for PbSe.

Since the Hall constant remained temperature invariant, the resistivity was inversely proportional to the mobility. Typical curves for PbTe and PbSe, as shown in Fig. 3, may be represented by the general relation

$$\mu=\mu_0 T^{-\alpha}.$$

If the value of α were averaged for all specimens measured, then $\langle\alpha\rangle\sim 5/2$. The range for α was 2 to 3. Thus there is reasonable agreement with a similar empirical relation proposed for the sulfides, selenides, and tellurides of lead.[2,10]

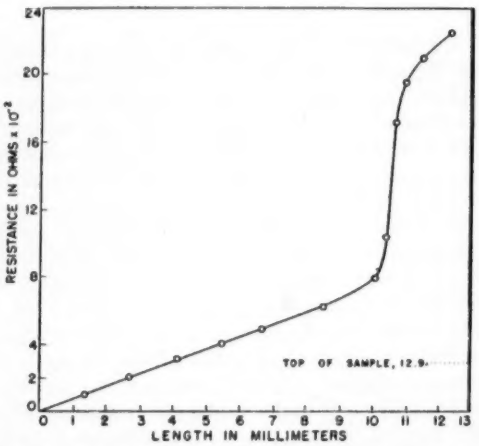

FIG. 4. The variation of resistance along the vertical axis of crystal growth for specimen *A*-70, PbTe, showing a nonrectifying $n-p$ junction toward the top of the melt.

The representative room temperature mobilities for the specimens studied to date fall within the range presented by other workers. In the case of PbTe, $\mu_n=1500$ cm²/volt sec and $\mu_p=750$ cm²/volt sec; for PbSe, $\mu_n=1200$ cm²/volt sec and $\mu_p=850$ cm²/volt sec.

During the course of making melts it was noticed that PbTe exhibited a considerable degree of segregation of Pb from the main body of the melt. In these cases the Pb excess region would be concentrated in the upper extremities of the melt, leaving the major portion of the melt p type. A nonrectifying $p-n$ junction could be detected by measuring the voltage along the vertical axis as a function of increasing length, as shown in Fig. 4. The $p-n$ junction for this typical specimen occurred about 2–3 mm below the melt and appeared

[10] E. H. Putley, Proc. Phys. Soc. (London) **B65**, 388 (1952).

to be about 1 mm thick. Hall measurements were made on specimens in the n region and the p region. If at room temperature one assumes that each excess atom furnishes two electrons (or two holes), then the approximate value for the concentration is 0.001 percent excess Pb in the upper portion, and 0.006 percent excess Te for the lower. From Table I it is seen that the mobilities in the lower p-type region agree with values reported in the literature;[2] those in the n region appear below normal, indicating a deviation from the single-crystal lattice. Similar junctions have been observed for PbSe by Goldberg and Mitchell.[11]

B. Thin Films

Regardless of whether or not the original single crystal is n type or p type, all thin films of PbSe and PbTe in the present investigation exhibited n-type Hall constants of about the same order of magnitude when formed on substrates having temperatures between 25°C and 250°C, as shown in Table II. The Hall

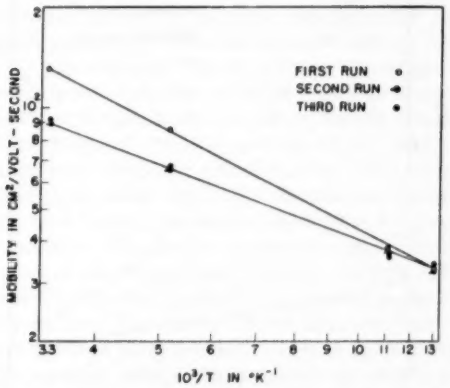

FIG. 5. The effect of cooling a freshly formed film of PbTe. After the first run, the mobility is reduced, most markedly near room temperature. Succeeding runs (Nos. 2 and 3) remain reproducible.

constant varied only slightly within the temperature range between 300°K and 77°K.

As a possible explanation, it is proposed that there is a limited degree of dissociation at 550°C in which the number of atoms released is greater than the stoichiometric excess in the crystal as determined from bulk Hall measurements. A greater amount of free Te (or Se), having a relatively higher vapor pressure than that of free Pb, deposits on the film. In this process of film formation the usual types of imperfections such as Pb and Te (or Se) ion vacancies are present. The bulk residue, on the other hand, should contain proportionately more Pb on continued evaporation. Measurements by Simpson[12] on the residue support this

[11] A. E. Goldberg and G. R. Mitchell, J. Chem. Phys. **22**, 220 (1954).
[12] O. Simpson, Trans. Roy. Soc. (London) **A243**, 547 (1951).

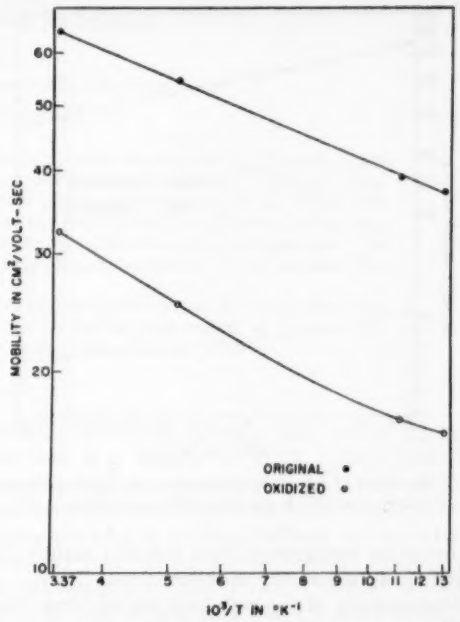

FIG. 6. The effect of oxygenation in reducing the carrier mobility of the film is shown for PbSe, specimen A-31-a.

hypothesis. Since Te (or Se) atoms act as acceptors and Pb atoms as donors, one should expect a p-type film because of the excess Te (or Se). However, it is assumed that the manner in which the impurities are distributed becomes the important factor. It is conceivable that many free Te (or Se) atoms collect randomly in small agglomerates throughout the film. Such a situation is quite plausible if one considers the rather haphazard method of crystal formation in thin films as compared with the more careful growth of single crystals. Whereas isolated Te (or Se) impurities may accept two electrons per atom, the agglomerates cause a reduction in the effective number of electrons captured per atom because of Coulomb repulsion. Consequently an apparent excess of Pb donors within the crystallites give an n-type film. Furthermore, in the case of PbSe, the high vapor pressure of Se may cause

TABLE II. Comparison of room temperature Hall constants for single crystals and thin films.

Material	Specimen	R in cm³/coulomb Single crystal	Thin film
PbTe	A-27-2	−18	−0.51
	A-46-2	−16	−1.5
	A-37-a	+ 2.8	−0.26
	A-42-4	+ 3.2	−1.8
	A-43-3	+ 3.2	−0.51
PbSe	A-31-1	− 5.2	−0.31
	A-38-a	− 2.6	−0.42
	A-32-2	+ 8.5	−0.61
	A-36-1	+ 2.5	−0.57

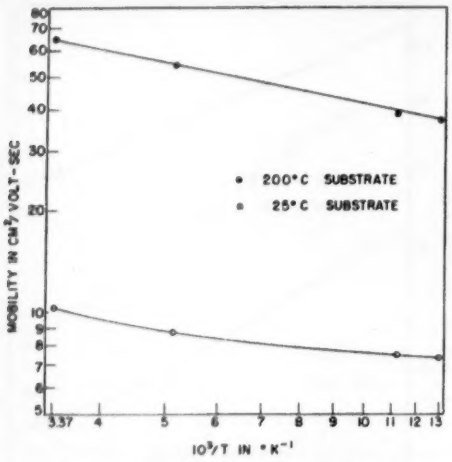

FIG. 7. The effect of substrate temperature during film formation on carrier mobility is shown for PbSe, specimen *A*-31.

the excess to reevaporate from the film surface, producing the apparent *n*-type observations.

Measurements of the mobilities for all films evaporated on a substrate at elevated temperature, or at room temperature and subsequently annealed, give consistent values for room temperature mobilities about 1/5 that of the bulk. It was found that the following essential factors influenced mobilities in the thin films:

(*1*) *The Differential Coefficient of Thermal Expansion*

All freshly formed or freshly annealed films showed a higher room temperature mobility before being cooled to 77°K as shown in Fig. 5. As the film cooled it contracted more than the glass substrate, causing permanent cracks which resulted in a lowered value for the mobility when the film returned to room temperature. It is reasonable to assume that this phenomenon is the same as that observed by Simpson in his study on PbSe films.[13] After the first cooling cycle, values along the modified curve could be reproduced at will.

(*2*) *Degree of Oxygenation*

Traces of oxygen produced by torching the tube not in the vicinity of the PbTe film reduced the mobility and carrier concentration in all films, as shown by Fig. 6 for PbSe. Heating the film to about 300°C returns the mobility close to the original order of magnitude. This suggests that the oxygen atoms are adsorbed on the surface and at the intergranular boundaries, where they act as electron traps. The effect of oxygenation is more pronounced at low temperatures.

TABLE III. Representative room temperature values of film mobilities for PbTe and PbSe.

Representative mobilities in cm²/volt sec PbTe	PbSe	Remarks
100	40	Original film formed on 200°C substrate
60	10	Original film formed on room temperature substrate
330	100	Original film annealed
60	20	Original film oxygenated
200		Oxygenated film annealed

[13] O. Simpson, Nature **160**, 791 (1947).

(*3*) *Substrate Temperature during Film Formation*

At a lower substrate temperature there was reason to believe that (a) the crystallites were decreased in size[14] and (b) a greater number of imperfections were introduced within the microcrystalline lattice. The over-all effect caused a reduction of the carrier mobility with a decrease in the substrate temperature during film formation, as is shown in Fig. 7 for PbSe.

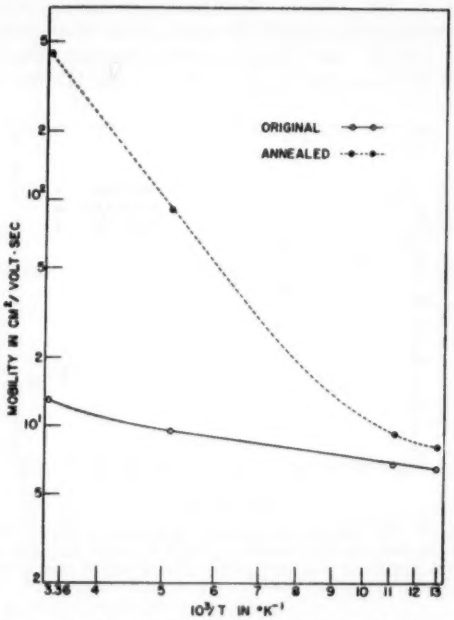

FIG. 8. The effect of annealing on mobility in thin films is shown for PbTe, specimen *A*-27-*h*.

(*4*) *Annealing*

This procedure had the composite effect of decreasing the effect of cracks created during previous cooling, and creating more order within the lattice of the individual crystallites. As a result much higher mobilities were observed. The influence of annealing was most pronounced at room temperatures, as indicated in Fig. 8 for PbTe.

Table III lists the representative room temperature values of film mobilities for PbTe and PbSe.

We wish to thank Dr. Neal F. Beardsley of Wright-Patterson Air Force Base for his interest in this investigation.

[14] G. I. Finch, Proc. Phys. Soc. (London) **41**, 113 (1937).

Avalanche Breakdown in Silicon

K. G. McKay
Bell Telephone Laboratories, Murray Hill, New Jersey
(Received December 23, 1953)

An avalanche theory of breakdown at room temperature is proposed for semiconductors based on the assumption of approximately equal ionization rates for electrons and positive holes. The problem of obtaining ionization rates from data obtained in inhomogeneous fields is solved exactly for two specific field distributions. Ionization rates for silicon thus calculated from experimental data on breakdown voltage and on prebreakdown multiplication for both linear-gradient and step junctions are in good agreement. The temperature coefficient of the ionization rate exhibits a similar internal consistency. It is concluded that internal field emission has not been observed in silicon.

Detailed observations are reported of the pulse-type noise associated with breakdown. It is shown that this noise represents the unstable onset of breakdown and that, for the junctions studied, all of the current flow in the breakdown region can be attributed to the current carried by the noise pulses.

INTRODUCTION

THE Townsend theories of avalanche breakdown in gases have, in general, not been applied to intrinsic electric breakdown in solids. The reason for this is that no comparable regenerative mechanism for the electron avalanche has been postulated for solids. In gases, regeneration was first assumed through ionization by positive ions. This hypothesis was later abandoned in favor of electron emission from the cathode by positive ion bombardment. However, the role played by positive holes in intrinsic breakdown in solids has usually been ignored. Consequently, the principal theories[1] have dealt only with electron multiplication by electron impact or electron production by internal field emission. The former mechanism, represented by the work of von Hippel and Fröhlich, has been reasonably successful when applied to insulators such as the alkali halides. The latter mechanism, proposed by Zener, has been identified with the high-current region of the reverse voltage characteristic of very narrow germanium *n-p* junctions.[2] However, the recently measured charge multiplication at room temperature in the prebreakdown region of germanium and silicon *n-p* junctions[3] shows that avalanche formation can also occur at attainable fields and that electrons and positive holes have approximately equal ionization rates. This makes possible the application of a modified form of simple gas discharge theory to breakdown in *n-p* junctions of germanium and silicon.

The distinction between what is here proposed and what has been observed on narrow germanium junctions[2] should be emphasized. In a narrow junction, it is proposed that the field across the junction eventually attains such a value that internal field emission takes place from the region of the highest field. The observed current is determined by the field strength in that region (and possibly by space charge effects). As the field increases, the current increases but breakdown, in the sense that it is defined for gases, cannot take place solely through this mechanism. In the strict sense, breakdown defines a discontinuity in behavior; it requires some form of positive feedback which, at breakdown, may result in instability. Internal field emission does not result in instability except through secondary effects. In broader junctions with the fields insufficient to produce Zener emission, the field distribution may be such as to permit multiplication by injected carriers, i.e., an injected electron interacts with a valence electron to produce an electron-hole pair and so on. This is a cumulative process and can result in a rigorously defined breakdown. Its existence depends on the fact that *both* holes and electrons can ionize, thus providing what is essentially positive feedback.

A problem associated with the study of breakdown in semiconductors is that the experimental data are obtained from fairly narrow regions across which the fields are not uniform. To compare theory with experiment, it is necessary to transform the observed behavior into what would be observed in an infinite solid with a uniform field. In the following it will be demonstrated how rates of ionization can be derived from observed data for certain specific field distributions.

THEORY

Following Townsend's derivation of his "β" mechanism in gases,[4] we define the rate of ionization α_i as the number of electron-hole pairs produced by an electron per centimeter travelled in the direction of the electric field E. We assume that the rates of ionization for electrons and for holes are equal. The results do not depend critically on this assumption, i.e., if the ionization rates differ by 10 percent the results will be in error by about this amount. As shown in Fig. 1, the barrier has a width W and plane parallel geometry. The field is assumed to be solely a function of the position coordinate x with the E and x vectors coincident. The

[1] These are reviewed by S. Whitehead, *Dielectric Breakdown in Solids* (Oxford University Press, London, 1951).
[2] McAfee, Ryder, Shockley, and Sparks, Phys. Rev. **83**, 650 (1951).
[3] K. G. McKay and K. B. McAfee, Phys. Rev. **91**, 1079 (1953).
[4] L. B. Loeb, *Fundamental Processes of Electrical Discharge in Gases* (John Wiley and Sons, Inc., New York, 1939), p. 372 ff.

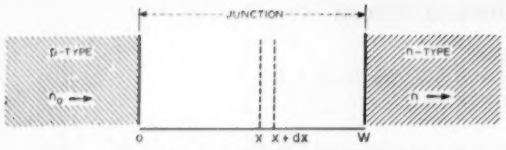

FIG. 1. The geometry assumed for the calculation of avalanche multiplication.

number of electrons injected into the junction at $x=0$ is n_0. These electrons can produce more carriers, both holes and electrons. However, we need only to follow the history of carriers of one sign, the others being automatically taken care of; we choose here to calculate the electron avalanche. Let the number of electrons produced by electrons or holes between 0 and x be n_1 and the number of electrons produced between x and W be n_2. Then the number of electrons produced between x and $x+dx$ is

$$dn_1=(n_0+n_1)\alpha_i dx+n_2\alpha_i dx=n\alpha_i dx,$$

where $n=n_0+n_1+n_2=$ the number of electrons collected at the anode.

Integrating with the boundary conditions $n_1=0$ at $x=0$ and $n=n_1+n_0$ at $x=W$, we obtain

$$1-\frac{1}{M}=\int_0^W \alpha_i dx, \tag{1}$$

where $M=n/n_0=$ the multiplication factor.

When the integral in Eq. (1) attains unity, $M\to\infty$ and breakdown occurs. We should note three assumptions that are implicit in the use of Eq. (1). These are:

(1) $\alpha_i(E)$ is solely a function of E. This neglects the influence of the past history of the ionizing carrier, which assumption seems reasonable if the carrier loses energy primarily through lattice collisions rather than through ionizing collisions. This is probably invalid for very narrow junctions where we should approach the situation found in the cathode fall region in gases.

(2) We neglect the loss of carriers in the junction by recombination. Since the time required for an electron to traverse a typical junction with a field appropriate for appreciable multiplication is of the order of 10^{-10} sec or less, this is negligibly small compared with recombination times of greater than 10^{-6} sec.

(3) We neglect the mutual interaction between conduction electrons (such as postulated by Fröhlich) on the grounds that at any given instant of time, the actual number of electrons in the barrier region is insignificantly small. Although this assumption is not always valid, it is for the experimental data to be considered here.

We shall now consider the direct solution of Eq. (1) for certain specific field distributions.

A. The Step Junction

The step junction considered here is one in which the impurity concentration varies abruptly from p type to n type. If the acceptor concentration on the p side is much greater that the donor concentration on the n side, essentially all of the space charge region will be on the n side. This leads to the Schottky-type barrier[5] as shown in Fig. 2(a). The following relations hold between the field E, the junction voltage V and the width W:

$$E=E_M(1-x/W), \tag{2}$$

$$E_M=2VW^{-1}, \tag{3}$$

$$W=W_1\sqrt{V}=0.5W_1^2E_M, \tag{4}$$

where $E_M=$ the maximum field in the junction, $W_1=$ the width constant for a given step junction

$$W_1=\left[\frac{1.317\times10^7}{N_D-N_A}\right]^{\frac{1}{2}} \text{ for silicon,}$$

$V=V_a$, the applied voltage, plus V_i, the built-in voltage. V_i normally ranges from about 0.5 to 0.7 volt at room temperature in silicon.

Using Eq. (2) to change the variable of integration in Eq. (1) and noting that $W/E_M=W_1^2/2$, we obtain

$$1-1/M=\int_0^{E_M}\frac{W}{E_M}\alpha_i(E)dE=\frac{W_1^2}{2}\int_0^{E_M}\alpha_i(E)dE. \tag{5}$$

Differentiating (5) with respect to E_M leads to

$$\alpha_i(E_M)=\frac{2}{W_1^2}\frac{d(1-1/M)}{dE_M}-\frac{4}{W_1^3}(1-1/M)\frac{dW_1}{dE_M}. \tag{6}$$

The two terms of the right-hand side of Eq. (6) disclose two different ways in which experiments can be

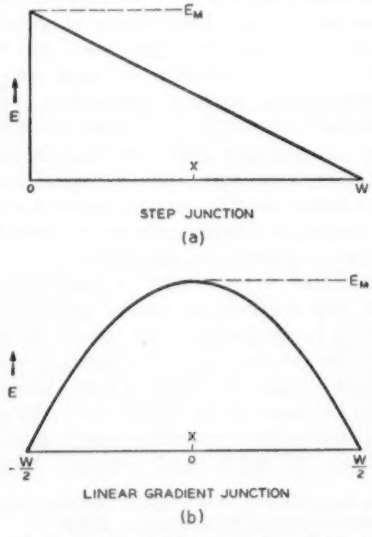

FIG. 2. Idealized field distributions for n-p junctions.

[5] W. Shockley, Bell System Tech. J. **28**, 449 (1949).

performed to determine α_i since the terms can be considered separately in the following manner:

Case I. If we measure M *versus* E_M on a single junction, W_1 is constant and

$$\alpha_i(E_M)=\frac{2}{W_1^2}\frac{d(1-1/M)}{dE_M}. \tag{7}$$

Case II. If we measure E_B, the maximum field in a junction at breakdown for various junction widths W_1, $M=\infty$ and we have

$$\alpha_i(E_B)=-\frac{4}{W_1^3}\frac{dW_1}{dE_B}. \tag{8}$$

Equations (7) and (8) permit a point by point evaluation of $\alpha_i(E)$ from either multiplication data or breakdown data obtained on step junctions.

B. The Linear-Gradient Junction

The second common simple junction is the linear-gradient junction[5] in which the charge density of donors N_D and acceptors N_A is given by

$$N_D-N_A=ax,$$

where the zero of the x coordinate is taken in the center of the junction and a is a constant for a given junction. This leads to the field distribution shown in Fig. 2(b). The following relations hold between E, V, and W:

$$E=E_M[1-(2x/W)^2], \tag{9}$$

$$E_M=1.5V/W, \tag{10}$$

$$W=W_1V^{\frac{1}{3}}=[\tfrac{3}{2}W_1^3E_M]^{\frac{1}{3}}, \tag{11}$$

where E_M=the maximum field in the junction and W_1=the width constant for a given linear-gradient junction.

Using Eq. (9) to change the variable of integration in Eq. (1) and noting that $W/E_M^{\frac{1}{2}}=(W_1^3/1.5)^{\frac{1}{3}}$, we obtain

$$1-1/M=2\int_0^{E_M}\frac{W\alpha_i(E)}{4E_M^{\frac{1}{2}}(E_M-E)^{\frac{1}{2}}}dE$$

$$=\frac{1}{2}\left[\frac{W_1^3}{1.5}\right]^{\frac{1}{3}}\int_0^{E_M}\frac{\alpha_i(E)dE}{(E_M-E)^{\frac{1}{2}}}. \tag{12}$$

By the use of Abel's integral theorem[6] this can be transformed to

$$\alpha_i(E_M)=\frac{1}{\pi}\frac{d}{dE_M}\int_0^{E_M}\frac{(1-1/M)}{(E_M-E)^{\frac{1}{2}}}2\left[\frac{1.5}{W_1^3}\right]^{\frac{1}{3}}dE. \tag{13}$$

As before, two separate types of experimental data can be used to evaluate α_i as follows.

[6] E. C. Titchmarsh, *Theory of Fourier Integrals* (Clarendon Press, Oxford, 1948), p. 331. The use of this transformation was suggested by G. H. Wannier.

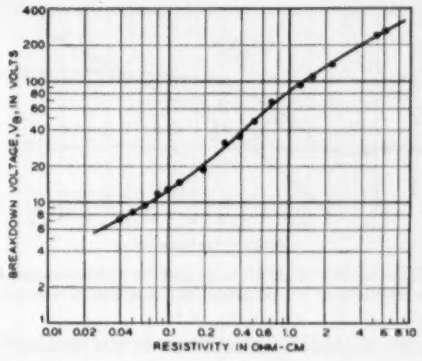

FIG. 3. The breakdown voltage V_B as a function of resistivity ρ of the n-type base of silicon alloy diodes.

Case I. If we measure M *vs* E_M on a single junction, W_1 is constant and

$$\alpha_i(E_M)=\frac{2}{\pi}\left(\frac{1.5}{W_1^3}\right)^{\frac{1}{3}}\frac{d}{dE_M}\int_0^{E_M}\frac{(1-1/M)}{(E_M-E)^{\frac{1}{2}}}dE. \tag{14}$$

Case II. If we measure E_B, the maximum field in a junction at breakdown for various junction widths W_1, $M=\infty$ and Eq. (13) becomes

$$\alpha_i(E_B)=\frac{2}{\pi}(1.5)^{\frac{1}{3}}\frac{d}{dE_B}\int_0^{E_B}\frac{dE}{W_1^{\frac{1}{3}}(E_B-E)^{\frac{1}{2}}}. \tag{15}$$

Again, Eqs. (14) and (15) permit a point by point evaluation of $\alpha_i(E)$ from either multiplication or breakdown data obtained on linear-gradient junctions.

No exact solutions of Eq. (1) have been obtained for field distributions other than those presented above. However, fairly good approximations can be obtained for some commonly encountered distributions, e.g., the extension to a composite junction consisting of part linear-gradient and part step junction is accomplished by assuming that the entire junction has a linear-gradient field distribution with a width constant that varies in an appropriate manner with applied voltage. Some experimental results have been so obtained that are in substantial agreement with those to be discussed later.

EXPERIMENT

A basic assumption of the preceding theory is that both holes and electrons have the same ionization rates for a given field. Photoconduction scanning curves taken with various voltages applied to the junctions indicate that this is a valid assumption for both silicon and germanium within the experimental accuracy limits of about 15 percent as previously published.[3] More accurate measurements over a wide range of field strengths are needed. However, the theory is not highly sensitive to small differences between ionization rates for electrons and holes so it appears reasonable to maintain the assumption of equal rates of ionization.

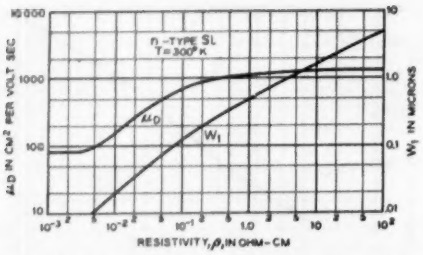

FIG. 4. The mobility of electrons μ_D and the width constant W_1 for step junctions in n-type silicon as a function of resistivity.

One set of data on ionization rates was obtained from the measurement of breakdown voltages in alloyed step junctions. A plot of E_B as a function of W_1 is required to determine α_i from Eq. (8). However, the areas of these particular junctions were too small to make accurate determinations of junction widths from capacity measurements so the data appeared as a plot of breakdown voltage V_B *vs* ρ_n where ρ_n is the resistivity of the n-type silicon. The p-type side of the junction had such a high acceptor concentration that essentially all of the space charge region is assumed to extend through the n-type end. The plot of V_B *vs* ρ_n is shown in Fig. 3.[7] It is now necessary to transform this into a plot of E_B *vs* W_1. Since both the junction width and the resistivity depend on the net donor concentration, we can use the definition of W_1, the width at unit voltage, and that of the resistivity to yield for silicon

$$W_1 = 1.44 \times 10^{-6} (\rho_n \mu_n)^{\frac{1}{2}}, \tag{16}$$

where μ_n is the mobility of electrons in the n-type material. The only data available on mobility as a function of resistivity consisted of Hall mobility measurements.[8] These mobility values were uniformly reduced by 25 percent to provide coincidence with the known electron drift mobility for high-purity silicon. The result is shown in Fig. 4. Combining this with Eq. (16) we obtain the relation between W_1 and ρ_n also shown in Fig. 4. The value E_B, the maximum field in the junction at breakdown, was obtained from Eqs. (3) and (4) as

$$E_B = 2(V_B + V_i)^{\frac{1}{2}}/W_1, \tag{17}$$

where V_i, the built-in voltage, was taken as 0.7 volt. The resultant plot of E_B as a function of W_1 is shown in Fig. 5. It should be noted that this is analogous to the relation between breakdown field and plate to cathode separation obtained in a gas at constant pressure. Differentiation of the E_B/W_1 curve yields dW_1/dE_B which, inserted in Eq. (8), gives the ionization rate α_i as a function of E_B. The values of α_i so obtained are shown as triangles in Fig. 6. This method of determining E_B presupposes that the onset voltage and the sustaining voltage for breakdown are equal. Within the experimental error this is a valid assumption for these junctions.

The use of breakdown voltage for these particular step junctions to obtain values of α_i, is open to some objection. A junction is never perfectly uniform so breakdown will always occur at a somewhat lower voltage than the averaged junction properties would predict. This will tend to yield values of α_i that are too large. A more serious objection is that no check could be made of the actual junction field distribution. It was assumed to be a step junction, but actually, resistivity changes have been noted in the n-type body as a result of junction forming. This probably means that the excess donor concentration is not uniform and that the maximum junction field is probably less than calculated. Consequently the remainder of the data to be presented here on ionization rates has been obtained from studies of the multiplication of injected carriers in the prebreakdown region. In all these cases the junctions were in grown single crystals. Careful measurements were made of junction capacity as a function of bias to ascertain the field distribution. The multiplication measurements were then made by injecting carriers by alpha-particle bombardment and determining the resultant charge transferred across the barrier as a function of bias. This technique has been described previously.[3]

A typical multiplication curve is shown in Fig. 7 for a linear-gradient junction. The voltage scale has been normalized by dividing by V_B, the breakdown voltage, as determined by the current-voltage characteristic of the unit. In this particular case $V_B = 11.18$ volts at room temperature. In general it is not possible to distinguish between linear-gradient and step junctions solely through inspection of the multiplication curve. However, the field distribution can be deter-

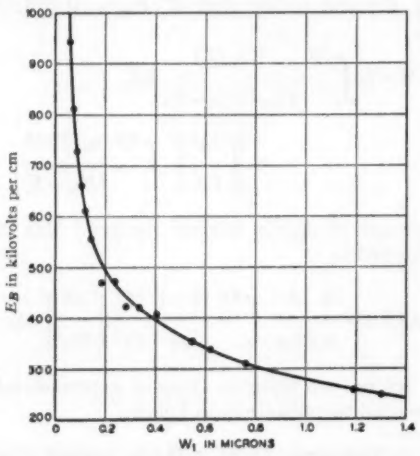

FIG. 5. The maximum field in silicon step junctions at breakdown as a function of the width constant W_1.

[7] The data shown in Fig. 3 were kindly supplied by D. K. Wilson who presented them at the Institute of Radio Engineers Transistor Research Conference, The Pennsylvania State College, July 6–8, 1953 (unpublished).

[8] These data were kindly supplied by F. Morin.

mined from the capacity data and then either Eq. (7) or (14) is used to obtain values for the ionization rate. Experimentally determined multiplication curves have been analyzed in conjunction with capacity data for a number of junctions and the resulting values of the ionization rate are shown in Fig. 6. A few remarks about the properties of the different junctions studied are in order.

The junctions represented by open circles and pluses were linear gradient junctions, i.e., the capacity varied as the cube root of the applied voltage within an accuracy of 2 percent from one volt to the breakdown voltage. The junctions represented by crosses, solid circles, and solid squares were approximately step junctions. In plotting $\log(V_A+V_i)$ *vs* $\log C$, a relation $V=KC^{-n}$ would be obtained where, for various junctions, $2.0<n<2.2$ instead of $n=2.0$ for a true step junction. In obtaining values of α_i, a step junction field was assumed for each value of the applied voltage together with the actual width measured at this voltage. The results so obtained did not differ significantly from those obtained by assuming an ideal step junction characterized by a single width constant W_1.

By calculating the results for each junction with several different approximations, it was shown that for fields of less than 500 kilovolts/cm, the values for α_i are quite consistent; the principal source of error lies in the determination of the appropriate value of the field. For example, the points shown in Fig. 6 for any given junction do not usually follow the averaged curve for α_i. It is believed that this is a consequence of the fact that the exact field distribution of any junction cannot be known in detail merely from capacity measurements. Thus there is some uncertainty as to what value of field should be associated with a given value of α_i and, for this reason, it is not possible at this stage to determine any significant fine structure in the field dependence of α_i.

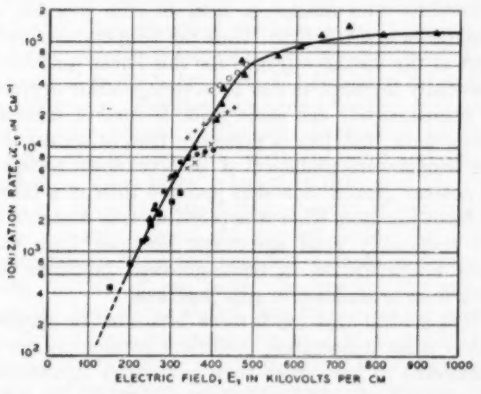

FIG. 6. The ionization rate α_i as a function of field in silicon. △ obtained from step-junction breakdown data. ○+ obtained from linear-gradient multiplication data. ×■● obtained from step-junction multiplication data.

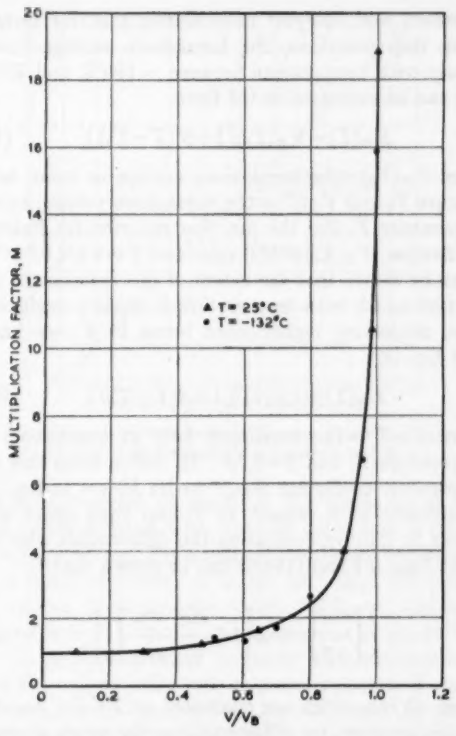

FIG. 7. Multiplication curves for a linear-gradient junction with the voltage scale normalized to the breakdown voltage for different temperatures.

Temperature Coefficient of α_i

One significant parameter in any theory of breakdown is the temperature coefficient. In this section it will be shown that breakdown and prebreakdown multiplication measurements yield consistent and reasonable values for the temperature coefficient of α_i. Neither the data nor the analysis are as extensive or as accurate as that presented in the previous section. However, its qualitative importance warrants its inclusion at this time.

The first significant observation is that the multiplication curve of a junction has the same temperature coefficient as the breakdown voltage. This is illustrated in Fig. 7, where multiplication curves are plotted against V/V_B for a silicon junction at 25°C and −132°C. At the lower temperature, the breakdown voltage had decreased from 11.18 volts to 10.03 volts and the multiplication curve had shifted quite appreciably from the room temperature curve. However, with the normalized voltage as abscissa, the two multiplication curves are indistinguishable. Thus the temperature coefficient of α_i can be determined either from breakdown data or multiplication data provided the appropriate relations are established.

Pearson and Sawyer[9] have shown that for certain silicon step junctions, the breakdown voltage varies linearly with temperature between −196°C and 25°C. This can be expressed in the form

$$V_B(T)=V_B(T_0)[1+\beta'(T-T_0)], \tag{18}$$

where $V_B(T_0)$ = the breakdown voltage at room temperature T_0 and $V_B(T)$ = the breakdown voltage at the temperature T. For the junction reported by Pearson and Sawyer, $V_B(T_0)=32.0$ volts and $\beta'=8.8\times10^{-4}$/°C. It can be shown that the extent of the variation of the junction width with temperature is usually negligible. Thus, neglecting higher-order terms in β', we have, from Eq. (4),

$$E_B(T)=E_B(T_0)[1+\beta(T-T_0)], \tag{19}$$

where $E_B(T)$ = the maximum field at breakdown at temperature T, and $\beta=0.5\beta'$. To derive from this the temperature coefficient of α_i,[10] we let $M\to\infty$ in Eq. (5), differentiate with respect to T and then again with respect to E_B. By evaluating the differentials with the aid of Eqs. (8) and (19), it can be shown that

$$\frac{1}{\alpha_i}\left[\frac{\partial\alpha_i}{\partial T}\right]=-\beta\left\{1+\frac{E_B}{\alpha_i}\left[\frac{\partial\alpha_i}{\partial E_B}\right]_T\right\}, \tag{20}$$

where all quantities are evaluated at $T=T_0$. $\partial\alpha_i/\partial E_B$ can be obtained by differentiating the curve given in Fig. 6 so that if β is known, we can determine $\partial\alpha_i/\partial T$ or *vice versa*. It should be noted that as derived, Eq. (20) is applicable only to step junctions and is subject to the assumptions underlying Eq. (1).

The first measurements to be considered are of the breakdown voltage as a function of temperature for three-step junctions. These are shown in Table I and plotted in Fig. 8. $E_B(T_0)$ has been obtained from Figs. 4 and 5. $(1/\alpha_i)(\partial\alpha_i/\partial T)$ has been calculated from Eq. (20).

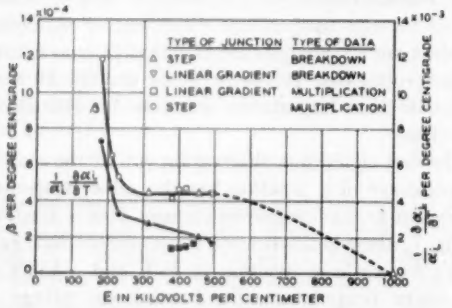

FIG. 8. The temperature coefficient β (open points) of the breakdown field and $(1/\alpha_i)(\partial\alpha_i/\partial T)$ (solid points) as a function of field.

A second approach is that of the measurement of multiplication curves at temperatures other than room temperature. From these α_i and hence $\partial\alpha_i/\partial T$ can be determined directly. Measurements were so made on two linear-gradient junctions at −130°C and α_i determined from Eq. (15). It was assumed that $\Delta\alpha_i/\Delta T=\partial\alpha_i/\partial T$ in calculating the latter. There is some question about the validity of this assumption for such a large temperature differential and the results, plotted on Fig. 8, should be accepted cautiously, particularly those for low field strengths. From these results, values of β could be calculated from Eq. (20) and these are also shown. It is interesting to observe that fairly close agreement is obtained with the values determined from step-junction breakdown voltage.

Finally, a set of measurements of breakdown voltage *versus* temperature for a linear-gradient junction was available.[11] This junction followed a relation of the form given by Eq. (18) from 150°K to 450°K with $V_B(T_0)=11.24$ volts and $\beta'=6.7\times10^{-4}$/°C. Since the field and voltage bear a different relation in a linear-gradient junction from that in a step junction, we must use Eq. (11) to obtain the coefficient for the temperature variation of the breakdown field. Here $\beta=\frac{2}{3}\beta'=4.4\times10^{-4}$/°C. The maximum field in this junction at breakdown is 490 kv/cm. Thus the temperature coefficient of the breakdown field for this linear junction is essentially the same as that for a step junction operated at approximately the same field. If further measurements show that this is generally true, it means that the temperature coefficient β' of breakdown *voltage* is 50 percent greater in a step junction than in a linear-gradient junction. That it is probably true is shown by the reasonably good agreement obtained from data from multiplication in linear-gradient junctions and data from breakdown in step junctions.

TABLE I. The temperature variation of breakdown voltage of step junctions.

$V_B(T_0)$ volts	$E_B(T_0)$ kv/cm	β' (°C)$^{-1}$	β (°C)$^{-1}$	$\frac{1}{\alpha_i}\frac{\partial\alpha_i}{\partial T}$ (°C)$^{-1}$	Ref.
7.5	1000	0	0	0	a, b
32.0	455	8.8×10^{-4}	4.4×10^{-4}	-21×10^{-4}	c
125	315	8.9×10^{-4}	4.45×10^{-4}	-28×10^{-4}	a

[a] See reference 7.
[b] This value of β' has been determined after correcting for the temperature dependence of V_i, the built-in voltage.
[c] See reference 9.

It is evident that much more data must be acquired before these temperature coefficient parameters can be considered to have more than qualitative significance. The behavior for fields greater than 5×10^5 volts/cm is certainly doubtful. It is probable that in this region,

[9] G. L. Pearson and B. Sawyer, Proc. Inst. Radio Engrs. 40, 1348 (1952).
[10] I am indebted to P. A. Wolff who derived the relation between the temperature coefficient of α_i and that of E_B for a step function as given in Eq. (20). This equation neglects one term involving the field dependence of β. This term can be shown to be completely negligible over the range that is considered here.
[11] These data were kindly supplied by G. L. Pearson.

the basic assumption that α_i is solely a function of E is violated. Consequently Eq. (20) is not applicable here. The large rise in temperature coefficient for very low fields should be further substantiated. Nevertheless, the general consistency of the present meager data is quite encouraging.

BREAKDOWN INSTABILITY

One feature of breakdown in silicon that has been noted by many observers is the frequent occurrence of a peculiar form of noise just at the onset of breakdown.[9] The noise sometimes appears "clipped" and has a rather uniform spectrum. This distinguishes it from the kinds of noise normally encountered in semiconductors which have a spectrum that varies approximately as the inverse of the frequency. The noise amplitude decreases as the breakdown current is increased although sometimes it goes through several maxima

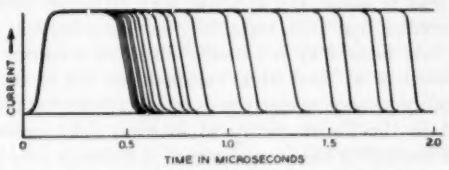

FIG. 9. "Noise" pulses of junction current at onset of breakdown in silicon traced from C.R.T. photograph.

and minima until, at larger currents, it disappears entirely. The amplitude also decreases as the temperature decreases. These are known facts; to these must be added some detailed observations as follows.

Figure 9 is a sketch of a cathode-ray tube representation of some of the "noise" pulses, observed on a silicon n-p junction just at the onset of breakdown. The traces represent noise pulses, each of which has triggered off the sweep so they all started at the same point. The junction was not irradiated or bombarded during these measurements. The amplifier input impedance was set at 100 ohms. This is orders of magnitude smaller than the junction impedance at this bias so the pulses really represent *current* pulses through the junction. The following facts are to be noted. (1) All pulses are in the same direction. (2) All pulses have a leading edge and trailing edge whose widths are determined by the amplifier characteristic, i.e., both the onset and decay of the pulse takes place in less than 0.02 μsec. (3) The pulses are of various lengths but of constant amplitude. In the example shown, the current during the pulse corresponds to 50 μa and does not increase or decrease during the life of the pulse. By varying the sweep triggering bias it was shown that there were no pulses that did not have this current value of 50 μa. (4) Measurements on two other silicon junctions from the same crystal but of different cross-sectional areas yielded the same results with essentially the same pulse current within 10 percent. This was also true of tests on several silicon step junctions.

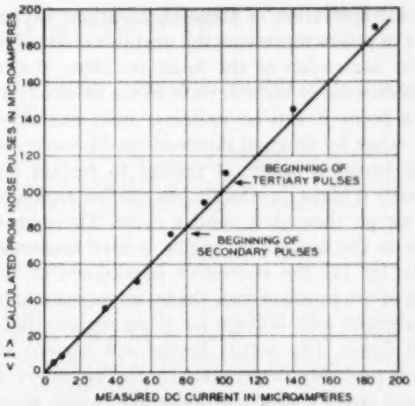

FIG. 10. Averaged current carried by noise pulses as a function of total dc current in the breakdown region.

It is instructive to examine the variation of the pulse characteristics with applied voltage in a representative junction. For a voltage just below breakdown and a junction current of about 10^{-7} amp, the pulses first appear. They are very short, <0.1 μsec, and with an amplitude of about 25 μa. An increase of about 0.05 volt in applied voltage produces the characteristic 50 μa flat-topped pulse with an average length of about 0.5 μsec. No two pulses coincide although the pulse lengths and the distance between pulses both vary in a random manner. As the applied voltage is further increased, the pulse amplitudes increase slightly. However, the principal effect is a lengthening of the pulses and a reduction of the time between pulses. Eventually the pulses are "on" most of the time, giving the appearance of short pulses in the opposite direction. By the time the pulses are on 90 percent of the time, the pulse amplitude has risen to 80 μa. At this stage, a new set of pulses appears, of amplitude about 50 μa, and resembling the initial appearance of the first set. As the voltage is increased further, these go through the same evolution as did the first set. Further sets of pulses appear at still higher voltages and evolve similarly.

Since the amplifiers do not pass dc, it is possible to estimate from the oscilloscope, the average dc current flowing through the crystal solely as a result of the pulses. By suitable bookkeeping, it is possible to carry this up to the point where the first set of pulses is on all the time. Beyond this one cannot go with reasonable accuracy since the steady current, corresponding to the first pulse set, will increase somewhat with voltage in an unknown way. Figure 10 shows a comparison between the average current carried by the current pulses and the actual total dc current through the crystal as measured on a dc ammeter. The agreement between the two currents is well within the experimental accuracy and shows that essentially all of the current in the breakdown region is carried by the pulse currents and by no other mechanism.

The interpretation of these observations is that the first set of pulses represents the unstable onset of breakdown in one region of the junction. Here, the breakdown is essentially bistable; it is either on or off. At this delicate point it can be switched from one condition to the other by thermal fluctuations. However, as the voltage becomes larger, it prefers to remain on and eventually it stays on steadily. As another region breaks down we go through a similar cycle. The increase of current in the breakdown region is then accounted for entirely by (a) the successive breakdown of various regions of the junction and, (b) by an increase in breakdown current with voltage for those regions that have broken down. The actual breakdown current in any region is probably determined by the boundary conditions and space charge considerations which should be rather difficult to compute at the present stage.

Other observations tend to confirm this picture. As the temperature of the silicon is lowered, the pulses reduce in amplitude but increase in length as does also the time between pulses. Thus a reduction in thermal agitation tends to reduce the fluctuation rate of the discharge. This separates the different regions more clearly so that the first set of pulses completes its life cycle before the second set starts, etc. This accounts for the observation of the peculiar cyclic behavior of the noise as a function of breakdown current. Even more striking is the fact that in some step junctions, several slope discontinuities in the current-voltage characteristic have been observed in the breakdown region. Wilson has pointed out that separate groups of noise pulses have been observed at the onset of each slope discontinuity in a single characteristic.

CONCLUSIONS

Data from both the breakdown region and the pre-breakdown multiplication region have been used to calculate ionization rates and their temperature coefficients. The results show sufficiently good agreement to establish that, throughout the range studied, breakdown in silicon is a direct result of multiplication by collision. The fact that the results obtained from different field distributions could be analyzed without approximation to yield substantially the same results, appears to vindicate the underlying assumptions. Minor modifications of the assumptions may be required to account for the fact that values of α_i calculated for a given junction often exhibit considerable variation from the averaged values. However, it seems most probable that this is really due to a lack of detailed knowledge of the actual field distributions in these junctions. For fields above 500 kv/cm, the effective ionization rate levels off, and the temperature coefficient of the breakdown field decreases. It is probable that in this region, the ionization rate is a function, not only of the field, but also of the position of the charge carrier in the junction. In that case, the theory presented here does not apply and the plot of α_i *vs* E in that region should be considered as nothing more than a convenient method of displaying the experimental results obtained from breakdown of step junctions.

The above conclusions are substantiated by several other points. The temperature coefficient of the ionization rate has the proper sign to result from the effect of electron-lattice interaction and the magnitude is reasonable. The equations governing avalanche formation lead to instability at breakdown although they do not predict that such instability can be observed. The fact that instability is actually observed confirms the existence of a "feed-back" mechanism rather than a smoothly increasing electron density with field as postulated in the Zener theory of internal field emission. Such instability has been observed in different junctions throughout the entire voltage range studied which indicates that the same breakdown mechanism is operative throughout this range. Moreover, the variation of breakdown field with junction width shows no evidence of a constant breakdown field even for very narrow junctions. This evidence suggests that internal field emission has not been observed at all in silicon.

ACKNOWLEDGMENTS

It is evident that this work has been made possible only through the cooperative effort of a number of individuals. In addition to the specific footnote acknowledgments, I wish to thank D. K. Wilson and G. L. Pearson who have supplied most of the breakdown data, D. J. Rose and P. A. Wolff for many stimulating discussions concerning the theory, E. Buehler through whose efforts most of the junctions were grown, and H. Meier who prepared and mounted the crystals and maintained the equipment in operating order. I wish also to express my appreciation to R. W. Hamming for the numerical analysis of the linear-gradient junction data.

The Hyperfine Structure of the $3P_{3/2}$ State of Na^{23}†

PAUL L. SAGALYN
Research Laboratory of Electronics and Department of Physics, Massachusetts Institute of Technology, Cambridge, Massachusetts
(Received February 9, 1954)

Two of the separations in the hyperfine structure of the $3P_{3/2}$ state of Na^{23} were measured. The results are 61 ± 2 Mc/sec and 36.6 ± 2 Mc/sec. These results were assigned to the $(F=3\leftrightarrow F=2)$ and $(F=2\leftrightarrow F=1)$ separations. A value of $Q=+0.1\pm0.06\times10^{-24}$ cm² was calculated for the nuclear electric quadrupole moment.

I. INTRODUCTION

UP to the present time it has not been possible to measure the nuclear electric quadrupole moments of the alkali metals. In order to use the results of molecular spectroscopy, more accurate molecular wave functions are required than are available at present. Measurements of the hyperfine structure of the $S_{1/2}$ ground state of the sodium atom have been made by the molecular beam method.[1] Jackson and Kuhn[2] made a study of the absorption spectra of a beam of sodium atoms and succeeded in resolving the hyperfine structure of the $3P_{1/2}$ first excited state, but not of the $3P_{3/2}$ state. All S states and also $P_{1/2}$ states give an electric field with zero gradient at the nucleus. Since the interaction energy of the nuclear quadrupole moment with the atomic electrons is proportional to the gradient of the electric field at the nucleus, these measurements yield no information about the quadrupole moment.

We have made a direct measurement of the hyperfine structure of the $3P_{3/2}$ first excited state of sodium by the "double resonance" method.[3,4] From the deviations from the interval rule for hyperfine structure we obtain a value for the quadrupole moment.

II. THE METHOD

The "double-resonance" method, first proposed by Kastler and Brossel,[3] has been discussed in detail by Brossel and Bitter.[5] Atoms are irradiated with their own resonance radiation and raised from the ground state to the first excited state. Since the incident radiation is not isotropic, the populations of the various levels of the excited state will not all be equal. Consider a pair of levels in the excited state whose energy difference is $E=h\nu$, where h is Planck's constant, and ν is a frequency. If an external alternating magnetic field is applied, then, depending on certain selection rules, transitions may occur between the two levels. (The transition probability is a maximum when the frequency of the magnetic field is equal to E/h.) This redistribution of atoms in the excited state may be observed as a change in the spatial intensity distribution of the re-emitted light.

The word "transition" used above should be treated with caution. When the alternating field is applied to an atom, a time-dependent term is added to the Hamiltonian, and the wave functions describing the excited state are no longer eigenfunctions of the Hamiltonian. A complete wave-mechanical theory which takes into account both the spontaneous electric dipole (optical) transitions and the induced magnetic dipole transitions is not yet available. The notion that the alternating field merely causes the atoms to slip back and forth between the unperturbed states appears to work and will be used here.

The structure of the sodium resonance line is shown in Fig. 1. The nuclear spin of sodium[6] is $I=3/2$. The atomic ground state is $3\,^2S_{1/2}$, that is, a doublet S state

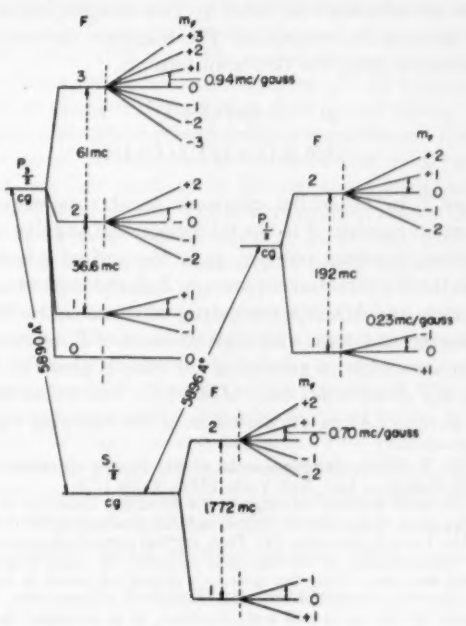

FIG. 1. The sodium resonance lines, not drawn to scale.

† This work was supported in part by the U. S. Signal Corps, the Air Materiel Command, and the U. S. Office of Naval Research.

[1] P. Kusch and H. Taub, Phys. Rev. **75**, 1477 (1949).

[2] D. A. Jackson and H. Kuhn, Proc. Roy. Soc. (London) **167**, 205 (1938).

[3] J. Brossel and A. Kastler, Compt. rend. **229**, 1213 (1949).

[4] I. I. Rabi [Phys. Rev. **87**, 379 (1952)] recently proposed a method of extending molecular beam techniques to excited states. At the time of this writing no results had been published.

[5] J. Brossel and F. Bitter, Phys. Rev. **86**, 308 (1952).

[6] J. E. Mack, Revs. Modern Phys. **22**, 64 (1950).

TABLE I. Hyperfine structure data for the $3P$ levels of sodium.

J state	F values	$E_F-E_{F'}$ calculated Mc/sec	$E_F-E_{F'}$ observed Mc/sec	a calculated Mc/sec
		$Z_i=7.41$		
$P_{1/2}$	2−1	199	192 ±10	99.5
$P_{3/2}$	3−2	59.7	61 ± 2	19.9
	2−1	39.8	36.6± 2	
	1−0	19.9		

with principal quantum number $n=3$ and total electronic angular momentum quantum number $J=1/2$. The two possible values of F, the total angular momentum, are $3/2+1/2=2$, and $3/2-1/2=1$. The hyperfine structure has been measured by molecular beams and is 1772 Mc/sec.[1]

The first excited state of sodium is a doublet consisting of a $3\,^2P_{1/2}$ term and a $3\,^2P_{3/2}$ term. Their separation[7] is 17.18 cm^{-1} or 5.16×10^5 Mc/sec. The $3\,^2P_{1/2}$ state has two hyperfine states corresponding to $F=2$ and $F=1$. The $3\,^2P_{3/2}$ state has four values of F: 3, 2, 1, and 0. The wavelengths of the two resonance lines are 5896A and 5890A, when measured from the center of gravities of the hyperfine structures. The $3\,^2P_{1/2}$ state lies lower and gives the longer wavelength line. The hyperfine separation of the $3\,^2P_{1/2}$ state is $(6.4\pm0.3)\times10^{-3}$ cm^{-1}, or 192 Mc/sec.[2,8-10]

As an experimental guide the hyperfine separation may be calculated from a formula for the magnetic interaction constant derived by Goudsmit.[11] The results are tabulated in Table I. This formula neglects the quadrupole interaction. The magnetic interaction constant is, from the Goudsmit formula,

$$a=\frac{g_I}{1836}\frac{\Delta\nu L(L+1)}{Z_i(L+1/2)J(J+1)}\frac{k}{\lambda}, \tag{1}$$

where L is the orbital electronic angular momentum quantum number, J is the total electronic angular momentum quantum number, g_I is the nuclear g factor, $\Delta\nu$ is the fine structure separation, Z_i is the inner atomic number, and k/λ is a relativistic correction. The shift in energy of a term with a given value of F, measured from the center of gravity of the line, is given by $E_F=a/2[F(F+1)-I(I+1)-J(J+1)]$. The value used for Z_i was 7.41 as calculated from the following equation due to Casimir:[12]

$$\Delta\nu=\frac{dn^*}{dn}Z_i^2\frac{R}{n^{*3}L(L+1)}\alpha^2. \tag{2}$$

n^* is the effective quantum number, n the principle quantum number, and α is the fine structure constant. n^* is determined by E_n, the term value of the doublet center of gravity:

$$E_n=-R/n^{*2}, \tag{3}$$

where R is the Rydberg.

In Table II are tabulated the g factors and splitting factors in (Mc/sec) per gauss for all the levels involved in the sodium resonance line, for a very weak, steady magnetic field, that is, a field which does not decouple I and J.

The values tabulated are calculated from the formulas

$$g_F\approx g_J\frac{F(F+1)+J(J+1)-I(I+1)}{2F(F+1)},$$
$$g_J=1+\frac{J(J+1)+S(S+1)-L(L+1)}{2J(J+1)}, \tag{4}$$

and $-\Delta T_F=g_F M_F(He)/(4\pi mc)$, where M_F represents the projection of F along the magnetic field, H is the magnitude of the steady magnetic field, e is the electronic charge, m the electronic mass, c the velocity of light, and ΔT_F is the shift in the term value of the field free state. Therefore, a positive ΔT_F means that the energy of the level decreases.

The complete Zeeman diagram for $J=3/2$ and $I=3/2$ out to fields large enough to decouple I and J is found in a paper by Davis, Feld, Zabel, and Zacharias.[13] This diagram is reprinted in Fig. 2.

The limit to the accuracy with which the separations can be measured is set by the natural linewidths of the levels. The lifetime τ_n of the P state is known[14] to be 1.48×10^{-8} sec. Then the "half-widths" of the levels are

TABLE II. Zeeman effect data for the states involved in the sodium resonance lines.

J state	F level	g_F	$\lvert T_F/M_F H\rvert$ (Mc/sec) per gauss
$P_{1/2}$	2	1/6	0.234
	1	−1/6	0.234
$P_{3/2}$	3, 2, 1, 0	2/3	0.935
$S_{1/2}$	2	1/2	0.70
	1	−1/2	0.70

[7] H. E. White, *Introduction to Atomic Spectra* (McGraw-Hill Book Company, Inc., New York, 1934), Table 17.5.

[8] An early attempt to measure the hyperfine structure of the $3\,^2P_{3/2}$ state was made by Ellett and Heydenburg (reference 9) and by Larrick (reference 10). Their method consists of measuring the depolarization of the resonance radiation by small magnetic fields, and then fitting the data to a theoretical curve in which the hyperfine structure constant appears as a parameter. The results do not agree well and, moreover, it is necessary in the theory to assume a pure magnetic interaction.

[9] A. Ellett and N. P. Heydenburg, Phys. Rev. **46**, 583 (1934).

[10] L. Larrick, Phys. Rev. **46**, 581 (1934).

[11] S. Goudsmit, Phys. Rev. **43**, 636 (1933).

[12] H. B. G. Casimir, *On the Interaction Between Atomic Nuclei and Electrons* (Teylers Tweede Genootschap, Haarlem, 1936), Eq. (14, 4), p. 54.

[13] Davis, Feld, Zabel, and Zacharias, Phys. Rev. **76**, 1076 (1949).

[14] R. Ladenberg and E. Thiele, Z. Physik **72**, 697 (1931).

given by the expression

$$\Delta\nu_n = 1/(2\pi\tau_n), \quad (5)$$

or 10.7 Mc/sec in the case of sodium. If the transition probability for the radiofrequency is small compared with the optical transition probability, we may expect that the minimum radio-frequency transition width will be approximately 21 Mc/sec.

The amplitude needed for the radio-frequency field can be estimated from the equation for the transition probability by means of perturbation theory:[16]

$$h^2P(FM_F:F'M_F') = \pi^2t^2\mu_0^2g_J^2 \times|(F,M_F|J_xH_x'+J_yH_y'+J_zH_z'|F',M_F')|^2, \quad (6)$$

where t is the time spend by the atom in the oscillating field, μ_0 is the Bohr Magneton, and the expression in parenthesis is the matrix element of the perturbation between levels characterized by quantum numbers F, M_F, and F', M_F', respectively. In this experiment the oscillating field had a component in only one direction. The matrix elements are given in reference 13. If we take 20 as a rough average for the matrix element, t as the lifetime of the state, and $P=0.1$, then $H'=5$ gauss.

III. APPARATUS

A schematic drawing of the experiment is shown in Fig. 3. A standard Cenco sodium arc is placed on the x axis. The collimating lens and polaroid form a beam of plane polarized light which illuminates the front face of the resonance lamp. Two beams of scattered light are taken from the resonance lamp. The horizontal

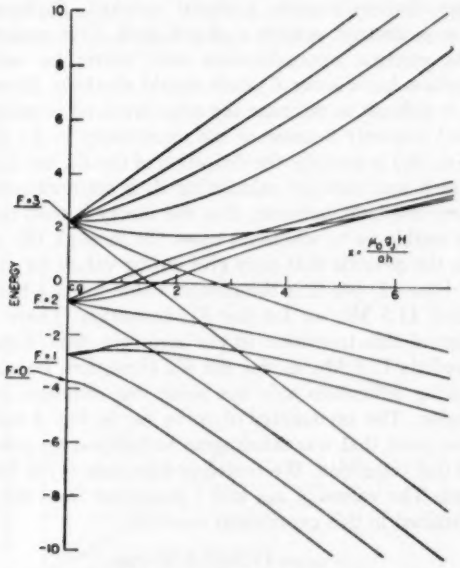

FIG. 2. Theoretical energy level diagram for state with $I=J=3/2$, neglecting the quadrupole interaction.

[16] I. I. Rabi, Phys. Rev. 51, 652 (1937).

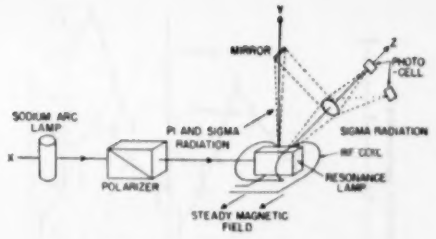

FIG. 3. Schematic drawing of the apparatus.

beam passes directly through the lens on the z axis and hits one photomultiplier. The vertical beam hits a small mirror on the y axis and then passes through the same lens to another photomultiplier. We used 1P21 multipliers because of their high sensitivity in the yellow region. Both phototubes are in the $y-z$ plane. The output currents of the two multipliers are combined in a simple bridge circuit similar to the one shown in Fig. 4 of reference 5. Two galvanometers are used. One is in series with the horizontal beam tube and monitors the full current independent of the beam balance. The body of the resonance lamp is made out of precision square-bore Pyrex tubing made by Fisher Porter Company. The inside surface of this tubing is accurately plane, and when the outside was polished, the walls made very acceptable windows for the re-emitted light. A Pyrex window was sealed on the front of the body and a horn on the back. Sodium is distilled into the lamp under high vacuum. Glow discharges started by the radio-frequency caused considerable trouble in the early cells. Care must be taken to seal off at a pressure well below 10^{-6} mm. The resonance lamp is located inside a water-cooled coil consisting of four turns, each 2 in. in diameter, wound from $\frac{3}{16}$-in copper tubing. The whole assembly is placed inside a simple oven. The resistance of the coil could be measured with the Q meter, and was 0.65 ohms at 36 Mc/sec and approximately 2 ohms at 60 Mc/sec. The power required, theoretically, for $H=5$ gauss was 40 watts at 36 Mc/sec, and 100 watts at 60 Mc/sec. The range of power actually used was 60 to 80 watts.

The output of the rf power amplifier was taken out through a flexible cable and link coupled to the coil in the oven. By tuning the coil and varying the coupling it was possible to match the line impedance. For this purpose a micromatch unit manufactured by the M. C. Jones Company proved valuable. This device reads incident and reflected power separately. With an incident power of 60 watts it was always possible to reduce the reflected power below 1 watt and to monitor the absorbed power to better than ± 2 watts.

IV. DISCUSSION OF RESULTS

Two types of data were taken: (a) curves of signal *vs* radio-frequency in zero (i.e., the earth's) magnetic field, and (b) curves of signal *vs* magnetic field for con-

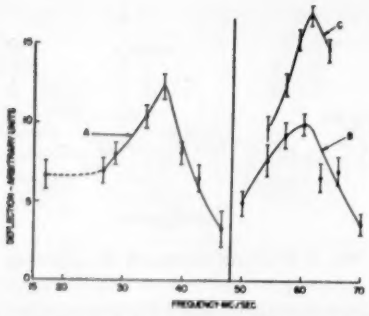

FIG. 4. Experimental resonance curves in zero field. The deflection caused by turning the radio-frequency on and off is plotted *vs* the frequency.

stant radiofrequency. The quantitative data on the hyperfine structure is obtained from the first set of data. These will be discussed first. It has only been possible to give a partial qualitative explanation of the second set of data.

(a) The signal *vs* frequency data is plotted in Fig. 4. Only one point was taken below 26 Mc/sec because of the difficulty in tuning the present equipment. Curve *C* contains the results of a successful attempt to obtain the high-frequency maximum with greater precision.

We take the position of the highest frequency maximum to be $E=61\pm2$ Mc/sec, and the position of the next to be $E'=36.6\pm2$ Mc/sec.

We now identify each of these frequencies with one of the separations in the $P_{3/2}$ state. In support of this we note that the half-width is approximately correct and that the frequencies are close to two of the values previously given by the Goudsmit formula. Also the known separations of the $P_{1/2}$ and $S_{1/2}$ states are much larger than either of these values.

The question now is, to which of the separations in the $P_{3/2}$ state do the experimental values E and E' correspond? Let $E_{FF'}$ denote the separation between levels characterized by F and F'. Then the separations satisfy equations of the form:[15]

$$\begin{aligned} E_{32}&=3a_{3/2}+b,\\ E_{21}&=2a_{3/2}-b,\\ E_{10}&=a_{3/2}-b. \end{aligned} \tag{7}$$

Here $a_{3/2}$ is the magnetic interaction in the $P_{3/2}$ state; it corresponds to setting $J=3/2$ in Eq. (1). The quantity b is the electric quadrupole interaction which is proportional to Q, the nuclear electric quadrupole moment.

There are six possible correlations of Eqs. (7) with the experimental data: (1) $E_{32}=61$, $E_{21}=36.6$; (2) $E_{32}=36.6$, $E_{21}=61$; (3) $E_{21}=61$, $E_{10}=36.6$; (4) $E_{10}=61$, $E_{21}=36.6$; (5) $E_{32}=61$, $E_{10}=36.6$; (6) $E_{10}=61$, $E_{32}=36.6$. If we use Eqs. (7) we obtain 19.5 ± 0.6 Mc/sec for the magnitude of a in cases (1) and (2) and 24.4 ± 2.8 in the other four cases.

Cases (3) through (6) can be eliminated by the following considerations. The theory of atomic structure yields expressions for the magnetic hyperfine structure interactions and the fine structure interaction which are independent of the nuclear electric interaction and can be written in the following way:

$$\langle r^{-3}\rangle_1=\frac{J(J+1)}{L(L+1)}\frac{1}{2\mu_0^2}\frac{1}{g_I/1836}ha_{1/2}, \tag{8a}$$

$$\langle r^{-3}\rangle_2=\frac{J(J+1)}{L(L+1)}\frac{1}{2\mu_0^2}\frac{1}{g_I/1836}ha_{3/2}, \tag{8b}$$

$$\langle r^{-3}\rangle_3=\frac{\Delta\nu}{\mu_0^2(2L+1)Z_i}. \tag{8c}$$

Each of the magnetic interactions is proportional to the average value of r^{-3}. The three values of $\langle r^{-3}\rangle$ are qualitatively the same but are not identical. Equation (1) which was used to calculate the values listed in Table I is based essentially on the assumed equality of these expressions.

If we set (8b) equal to (8c) then we obtain (see Table I) $a_{3/2}=19.9$ Mc/sec. We consider the experimental error in $\Delta\nu$ to be negligible for our purposes. We might also equate (8a) and (8b). This gives $a_{3/2}=19.2\pm0.9$. Here we have taken into account the experimental error in $a_{1/2}$. To each of these numbers should be attached an additional error to take into account the differences in $\langle r^{-3}\rangle$. This problem has been investigated theoretically by Koster.[16] It was shown that in aluminum the three equations agree within 1.5 percent. Aluminum has a $3s^23p$ configuration, that is, one electron outside a closed subshell. Sodium has one p electron outside a closed shell. This makes the one electron approximation even better for sodium. Sodium has a lower Z which should also help. However, it is difficult to estimate the error involved in using Eq. (8c) precisely because of the uncertainty in Z_i. Equation (8c) is actually the definition of the Z_i, but Eq. (2) which was used for calculating Z_i is approximate. We may conclude, however, that the theory is good enough to enable us to eliminate cases (3) through (6) above on the grounds that they give wrong values for $a_{3/2}$.

Case (2) predicts the correct value for $a_{3/2}$ but predicts 41.5 Mc/sec for the E_{10} transition. There is no sign of this transition in the zero-field data. Case (1) predicts 17.1 Mc/sec for the E_{10} transition. Because of tuning difficulties only one point was obtained in this region. The asymmetry of curve (a) in Fig. 4 and the one point that was taken seem to indicate the presence of this transition. We therefore take case (1) to be correct. The values of $a_{3/2}$ and b computed from the data obtained in this experiment are then

$$\begin{aligned} a_{3/2}&=19.5\pm0.6 \text{ Mc/sec},\\ b&=\ 2.4\pm1.4 \text{ Mc/sec}. \end{aligned} \tag{9}$$

[16] G. F. Koster, Phys. Rev. 86, 148 (1952).

The magnetic interaction in E_{32} is just $3a_{3/2}$. If we compute this using the value of $a_{3/2}$ obtained from $\Delta\nu$ and then subtract from our value for E_{32}, we obtain $b=1.3 \pm 2.1$ Mc/sec. Z_i was assumed here to be uncertain to 1 percent. Doing the same but using $a_{1/2}$, gives $b=3.3 \pm 3.4$ Mc/sec. These numbers are not in disagreement with Eq. (9), but because of the actual uncertainty in Z_i and the rather large probable errors here, we take Eqs. (9) as representing our best values for $a_{3/2}$ and b.

It should be emphasized at this point, that, for lack of a theory, we have not taken into account the possibility that, because of the presence of the rf field, the position of the maximum of the curve may not correspond exactly to the energy of the isolated atom. However, as pointed out in the section on signal intensities, the rf transition probability was much smaller than the optical transition probability. Under these circumstances the effect of the rf can probably be neglected.

The quadrupole moment of the nucleus is defined by the expression

$$eQ=\int (3z^2-r^2)\rho_n d\tau, \tag{10}$$

where ρ_n is the nuclear charge density. The averaging is to be done in the state in which $M_I=I$. In reference 13 it is shown that if the electronic wave function is assumed to be separable, the following relationship exists between Q and b:

$$hb=e^2Q\frac{2L}{2L+3}\langle r^{-3}\rangle, \tag{11}$$

where $\langle r^{-3}\rangle$ indicates an average over the electronic state in which $M_J=J$. L is the orbital electronic quantum number. Any part of Eq. (8) may now be used to compute Q with sufficient precision:

$$Q=0.041b \text{ cm}^2\times 10^{-24}, \tag{12}$$

where b is expressed in Mc/sec.

From (9) we obtain

$$Q=(0.1\pm 0.06)\times 10^{-24} \text{ cm}^2. \tag{13}$$

We have not included here any corrections of the type considered by Sternheimer.[17] If case (2) had been taken as the correct interpretation of the data, the value obtained for Q would have been -2.3×10^{-24} cm^2. This would seem unreasonably large in magnitude for a light nucleus.

(b) It is more difficult to account for the data taken by measuring the radio-frequency deflection as a function of the steady magnetic field at various frequencies.

In Fig. 5 are shown most of the possible radio-frequency transitions. These curves were taken from the data used to plot Fig. 1 of reference 13. The transitions left out have very small matrix elements.

Representative samples of the experimental results are shown in Figs. 6 and 7. The experimental curves all appear to be the sum of two curves of the resonance type although the shape of the curves is quite different at different frequencies. The position of the low-field maximum has been plotted as a function of the frequency, shown by dots plotted on the right side of Fig. 8. The crosses are the estimated positions of the high field maximums plotted as a function of frequency. Consider the circles. We can convert any of the theoretical curves of transition frequency *versus* x, Fig. 5, into Mc/sec and gauss by assuming a value for the zero-field separation. For example, if we choose $a=17$ and $1=17$ Mc/sec on the frequency scale, then $H=9.1x$ gauss. The theoretical curves actually neglect the quadrupole interaction. To first order we may assume that the effect of the quadrupole interaction is to change the zero field separation without affecting the shape of the curves. For a frequency of 80.2 Mc/sec, the highest that was used, varying the magnetic field

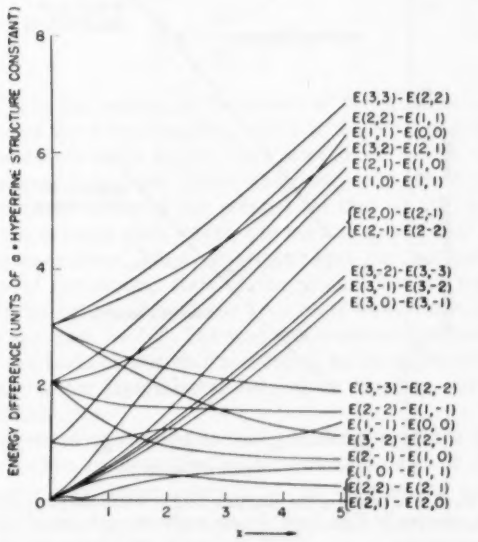

FIG. 5. Theoretical rf transition frequencies in units of *a versus x*.

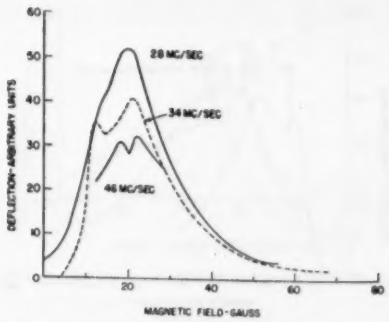

FIG. 6. Experimental resonance curves at constant frequency. The deflection caused by turning the radio-frequency on and off is plotted *vs* the magnetic field, for various frequencies.

[17] R. Sternheimer, Phys. Rev. **80**, 102 (1950).

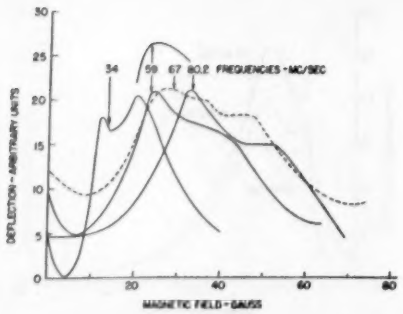

FIG. 7. Experimental resonance curves at constant frequency. The deflection caused by turning the radio-frequency on and off is plotted *vs* the magnetic field, for various frequencies.

moves us horizontally along the 4.7 line in Fig. 5. Two major groups of transitions appear, one centered roughly about $E(11)-E(00)$ and the other centered about $E(3-1)-E(3-2)$. These two transitions have been plotted in Fig. 8 for $a=17$. This value of a was chosen as giving the best agreement at the higher frequencies where the situation is simplest. Accurate correlation with the zero field data cannot be expected because of the overlapping of transitions caused by the large level widths. The most satisfactory feature of this data is that the sharp cutoff of the signal at the high end of the magnetic field scale (Figs. 6, 7) is in agreement with the theoretical curves. At low fields and frequencies the situation becomes very complicated.

A puzzling feature of the curves is the minimum in the signal which always occurs in the region between 0–10 gauss. It is probably significant that this is the region in which the degeneracy is being removed by the steady magnetic field. From Table II we see that a field of 11 gauss will separate two levels by an amount equal to a level width.

V. SIGNAL INTENSITIES

To calculate the effect of the radio-frequency on the scattered light, we start with the radio-frequency off and calculate the populations of the various excited states for a given type of optical excitation in the presence of a weak magnetic field. "Weak" here indicates a field strong enough to remove the degeneracy in the excited state but not strong enough to decouple I and J. The optical transition probabilities have been derived by Van Vleck.[18] Knowing the populations of the excited states we can calculate the relative proportions of π and σ radiation in the re-emitted light. An upper limit to the effect is found by recalculating the π and σ radiation on the assumption that the radiofrequency equalizes the population of certain pairs of levels, subject to the selection rules $\Delta F=0, \pm 1$, $\Delta M_F=0, \pm 1$. The oscillating field was actually always perpendicular to the steady field, which restricted the radio-frequency transitions to $\Delta M_F=\pm 1$. For π optical excitation, the results were:

$(F+1)-F$	Signal (percent)
3−2	4
2−1	2
1−0	1

The deflections caused by turning off the radio-frequency were measured by a galvanometer and bridge circuit arranged in such a way as to measure the sum of the current changes of the two photomultipliers. This deflection, divided by the total current of one of the photomultipliers, represents the percentage signal. The case of π excitation holds down to zero field.[19]

In practice, the signals at 36.6 Mc/sec and 61 Mc/sec were about the same order of magnitude with 60 watts, and equal to approximately 0.1 percent.

In computing the radio-frequency signals three assumptions were made: (1) The intensity of the exciting optical radiation is independent of frequency; (2) there are no depolarizing collisions; (3) the incident light is perfectly polarized. The degree to which the first two of these assumptions are satisfied may vary from run to run. The maximum interval that could be covered in one run was 10 Mc/sec. Different runs were normalized at a common frequency. In the case of curves (a) and (b) in Fig. 4, the closest points taken are too far apart to permit an accurate normalization. The amplitude of the rf field was monitored by measuring the power absorbed by the coil and correcting for the resistance of the coil, as measured on the Q-meter. The transition

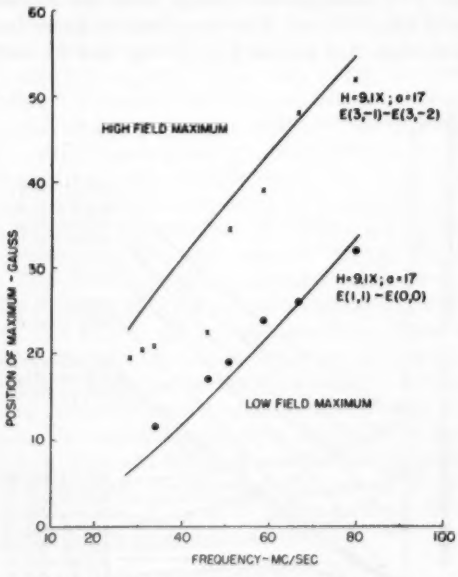

FIG. 8. The values of the magnetic field at which the two principal maxima in Figs. 7 and 8 occur is plotted *vs* the frequency.

[18] J. H. Van Vleck, *Quantum Principles and Line Spectra* (Bulletin of the National Research Council, No. 54, vol. 10, 1926).

[19] W. Heisenberg, Z. Physik 31, 617 (1925).

probability is proportional to $(H')^2$, and, therefore, to the current squared, or to the power divided by the resistance. The resistance of the coil was 0.65 ohm at 37 Mc/sec, and roughly 2 ohms at 61 Mc/sec. Therefore for equal amplitude of the radio-frequency field, the 61-Mc/sec signal would be about three times as large as compared with the previously estimated factor of two. The 17-Mc/sec point appears to be about one-half as high as the 36.6-Mc/sec point as expected. We must conclude, however, that the intensity calculations are too crude to be of much use in identifying the transitions.

The experimental signal strength at 61 Mc/sec corresponds to a transition probability of 1/80. With 60 watts we should have obtained about 1/20, with a coil of the dimensions and resistances used. The degree of polarization of the incident light is very important here. In zero field, rotating the plane of polarization of the incident light by 90° is just equivalent to interchanging the photomultipliers and must therefore change the sign of the signal (as it does). Depolarizing collisions will also reduce the absolute value of the signal. In Fig. 9 is shown one run at 28 Mc/sec of signal *vs* radio-frequency power, demonstrating that the dependence is linear.

To improve the signal-to-noise ratio we must increase the radio-frequency power and the light intensity. The former was limited by a glow in the resonance lamp and arcing in the tuning condensers. It should be possible to design a much better light source, since it was discovered after most of the data was taken that the Cenco sodium arc is badly self-reversed.

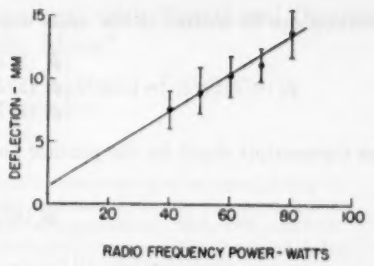

FIG. 9. Radio-frequency deflection *vs* transmitter power.

VI. CORRELATION WITH SHELL MODEL

The quadrupole moment of any one particle system is given by an expression of the form[20]

$$Q=-\frac{2j-1}{2j+2}\langle R^2\rangle_{Av}. \tag{14}$$

$\langle R^2\rangle_{Av}$ is the average of the square of the radial extension of the wave function, and j is the total angular momentum of the system. On a one-particle model, the quadrupole moment should therefore always be negative or zero. Mayer[21] has pointed out that on the basis of the extreme shell model, the nuclear spin of Na^{23} is also anomalous. Mayer suggested that the configuration of the ground state of the sodium nucleus may actually be $(d_{5/2})^3$ with the $j-j$ coupling giving a resultant spin, $I=3/2$. The magnetic moment computed on the basis of this model is found to lie appreciably closer to the experimental value than do either of the Schmidt lines.

We have attempted to find additional evidence for the sodium configuration by computing the sign of the nuclear quadrupole moment on the basis of the configuration proposed by Mayer, assuming a central field approximation. We use the method of Gray and Wills.[22]

In a d state, the orbital angular momentum quantum number is $l=2$. Therefore the ten possible one-particle, strong field wave functions are: $u_2^{\pm}u_1^{\pm}u_0^{\pm}u_{-1}^{\pm}u_{-2}^{\pm}$. The plus as a superscript signifies an orbital wave function with spin up, the minus with spin down. The subscripts give the possible values of m_l. First we find the weak field, one-particle wave functions, $\psi[jm]$ where $j=5/2$, as linear combinations of the strong field functions. Since the operator $J_z=L_z+S_z$ has eigenvalues in both representations, we can write at once $\psi[(5/2)(5/2)]=u_2^{+}$. The other five wave functions of the type $\psi[(5/2)m]$ can be found by application of the operators $J_x\pm iJ_y=(L_x+S_x)\pm i(L_y+S_y)$, where

$$(J_x\pm iJ_y)\psi[jm]=\hbar[(j\mp m)(j\pm m+1)]^{1/2}\psi[jm\pm 1]; \tag{15}$$

with similar equations for L_x+iL_y and S_x+iS_y. The results are

$$\begin{aligned}
&\psi[(5/2)(5/2)]=u_2^{+},\\
&\psi[(5/2)(3/2)]=5^{-1/2}\{2u_1^{+}+u_2^{-}\},\\
&\psi[(5/2)(1/2)]=10^{-1/2}\{6^{1/2}u_0^{+}+2u_1^{-}\}\\
&\psi[(5/2)(-1/2)]=10^{-1/2}\{6^{1/2}u_0^{-}+2u_{-1}^{+}\}\\
&\psi[(5/2)(-3/2)]=5^{-1/2}\{2u_{-1}^{-}+u_{-2}^{+}\}\\
&\psi[(5/2)(-5/2)]=u_{-2}^{-}.
\end{aligned} \tag{16}$$

The wave functions of the type $\psi[(3/2)m]$ could be found by finding a linear combination of u_1^{+} and u_2^{-} which is normal and also orthogonal to $\psi[(5/2)(3/2)]$, but these wave functions will not be needed in the present discussion.

Let $\phi(IM_I)$ represent a strong field wave function for the entire system, where $M_I=m_{j1}+m_{j2}+m_{j3}$. The values of I allowed by the Pauli exclusion principle are 3/2, 5/2, 9/2.[23] Consider the state $\phi[(9/2)\times(9/2)]$, that is, the state with the maximum value of M_I. The only possible set of values of m_j, all of which are different, is $[(5/2)(3/2)(1/2)]$. Then the correct antisymmetric linear combination of the one-particle

[20] J. A. Blatt and V. F. Weisskopf, *Theoretical Nuclear Physics* (John Wiley and Sons, New York, 1952).
[21] M. G. Mayer, Phys. Rev. **78**, 16 (1950).
[22] N. M. Gray and L. A. Wills, Phys. Rev. **38**, 248 (1931).
[23] E. U. Condon and G. H. Shortley, *Theory of Atomic Spectra* (Cambridge University Press, London, 1951), Table 2^{10}, p. 263.

wave functions can be written in the usual way as the determinant:

$$\phi[(9/2)(9/2)]=(3!)^{-1/2}\begin{vmatrix}\psi[(5/2)(5/2)]^{(1)} & \psi[(5/2)(5/2)]^{(2)} & \psi[(5/2)(5/2)]^{(3)}\\ \psi[(5/2)(3/2)]^{(1)} & \psi[(5/2)(3/2)]^{(2)} & \psi[(5/2)(3/2)]^{(3)}\\ \psi[(5/2)(1/2)]^{(1)} & \psi[(5/2)(1/2)]^{(2)} & \psi[(5/2)(1/2)]^{(3)}\end{vmatrix}, \tag{17}$$

where the superscripts stand for the particle number. For simplicity, we abbreviate this as

$$\phi[(9/2)(9/2)]=(3!)^{-1/2}\begin{vmatrix}5/2\\3/2\\1/2\end{vmatrix}, \tag{18}$$

it being understood that this stands for a three-by-three determinant, the numbers given representing the possible values of the m_j. The remaining wave functions of the type $\phi[(9/2)(M_I)]$ can be generated by applying the operator $I_x \pm iI_y$. The result for $\phi[(9/2)(5/2)]$ is

$$\phi[(9/2)(5/2)]=12^{-1/2}\left\{\begin{vmatrix}5/2\\1/2\\-1/2\end{vmatrix}+\begin{vmatrix}5/2\\3/2\\-3/2\end{vmatrix}\right\}. \tag{19}$$

By inspection, we set

$$\phi[(5/2)(5/2)]=12^{-1/2}\left\{\begin{vmatrix}5/2\\1/2\\-1/2\end{vmatrix}-\begin{vmatrix}5/2\\3/2\\-3/2\end{vmatrix}\right\}. \tag{20}$$

We note as proof here that each of the determinants represents a possible strong-field eigenfunction of the system. Therefore each determinant is part of an orthonormal set of wave functions, and therefore $\phi[(9/2)(5/2)]$ is orthogonal to $\phi[(5/2)(5/2)]$. Since there is no other state with $M_I=5/2$, this assignment is unique. We may also generate

$$\phi[(9/2)(3/2)]=(252)^{-1/2}\left\{5^{1/2}\begin{vmatrix}3/2\\1/2\\-1/2\end{vmatrix}+4(2^{1/2})\begin{vmatrix}5/2\\1/2\\-3/2\end{vmatrix}+5^{1/2}\begin{vmatrix}5/2\\3/2\\-5/2\end{vmatrix}\right\}, \tag{21}$$

and

$$\phi[(5/2)(3/2)]=2^{-1/2}\left\{\begin{vmatrix}3/2\\1/2\\-1/2\end{vmatrix}-\begin{vmatrix}5/2\\3/2\\-5/2\end{vmatrix}\right\}. \tag{22}$$

Again, by inspection, we find

$$\phi[(3/2)(3/2)]=2/(63)^{1/2}\left\{-\begin{vmatrix}3/2\\1/2\\-1/2\end{vmatrix}+1/4(10)^{1/2}\begin{vmatrix}5/2\\1/2\\-3/2\end{vmatrix}-\begin{vmatrix}5/2\\3/2\\-5/2\end{vmatrix}\right\}, \tag{23}$$

using the condition that $\phi[(3/2)(3/2)]$ be orthogonal to $\phi[(5/2)(3/2)]$ and $\phi[(9/2)(3/2)]$.

If P_i is the probability of finding the ith proton in the volume element dV at (x,y,z), then

$$P_i(xyz)=\int|\phi|^2dV_1\cdots dV_{i-1}dV_{i+1}\cdots dV_Z, \tag{24}$$

and we may write

$$\rho_n(xyz)=e\sum_{i=1}^{Z}P_i. \tag{25}$$

Using Eq. (10), the quadrupole moment may then be written as

$$Q=\sum_{i=1}^{Z}\int(3z_i^2-r_i^2)|\phi|^2d\tau, \tag{26}$$

where now the integration is taken over all the coordinates of all the particles. If we assume that in sodium the first eight protons go into a closed shell with spherical symmetry, then the summation will extend only over the three $d_{5/2}$ particles. The integration involves only elementary integrals and the result is identically zero. It would thus appear that the $(d_{5/2})^3$ configuration cannot account for the sodium quadrupole moment.

ACKNOWLEDGMENT

The author wishes to acknowledge the valuable guidance of Professor Francis Bitter, Department of Physics, Massachusetts Institute of Technology. He is also indebted to Dr. Jean Brossel and Professor I. I. Rabi for their helpful discussions. The financial assistance of a U. S. Atomic Energy Commission pre-doctoral fellowship is also gratefully acknowledged.

Variations of Hydrogen Rotational Magnetic Moments with Rotational Quantum Number and with Isotopic Mass*

R. G. BARNES,† P. J. BRAY,‡ AND N. F. RAMSEY
Harvard University, Cambridge, Massachusetts

(Received February 15, 1954)

Molecular beam observations have been made of the radio-frequency resonance spectra corresponding to reorientations of the rotational magnetic moment in hydrogen and deuterium molecules. For deuterium in the state $I=J=1$, these observations were made in magnetic fields of approximately 1800, 3500, and 5100 gauss. The direct result of these experiments is that the rotational magnetic moment of the deuterium molecule in the zeroth vibrational and first rotational states is ${}_0{}^D\langle\mu_R\rangle_1=0.442884\pm0.000052$ nuclear magneton, and the dependence of diamagnetic susceptibility on molecular orientation is $(\xi_{\pm1}-\xi_0)=-(3.50\pm0.40)\times10^{-31}$ erg gauss^{-2} molecule^{-1}. Combining these values with the recent theory of Ramsey on zero-point vibration and centrifugal stretching in molecules leads to an improved evaluation of the molecular susceptibility and quadrupole moment of the electron distribution. The experiments also provide a check on the values of the spin-rotational and spin-spin interaction parameters previously obtained from observations of the resonance spectrum corresponding to reorientations of the total nuclear spin.

The observations for hydrogen in the state $I=0$, $J=2$ were made in magnetic fields of approximately 1800 gauss. The direct result of these experiments is that the rotational magnetic moment of the hydrogen molecule in the zeroth vibrational and second rotational states is ${}_0{}^H\langle\mu_R/J\rangle_2=0.882265\pm0.000035$ nuclear magneton. This value in combination with the known value of 0.88291 ± 0.00007 nuclear magneton for the first rotational state provides an independent check on the theory of zero-point vibration and centrifugal stretching in molecules and leads to an improved evaluation of the hydrogen molecular susceptibility.

I. INTRODUCTION

THE radio-frequency spectra of H_2 and D_2 arising from changes in the rotational quantum number m_J have been measured previously by Ramsey.[1] In particular, he investigated the six-line spectra of H_2 and D_2 in the first rotational and zeroth vibrational state and with the nuclear quantum number $I=1$. From these measurements of resonance frequencies, values of the Hamiltonian interaction constants were derived and used as a check on the results obtained by Kellogg, Rabi, Ramsey, and Zacharias[2] from the $I=J=1$ six-line spectra for H_2 and D_2 arising from changes in the nuclear quantum number m_I. In addition, he obtained values for the rotational magnetic moments in the two molecules in the first rotational state and for the diamagnetic interaction parameter $(\xi_{\pm1}-\xi_0)$. An additional measurement of the hydrogen rotational magnetic moment was obtained from a resonance arising from the $J=2$, $I=0$ state.

Recently, Harrick and Ramsey[3] have repeated the measurements for H_2 in the state $I=J=1$, using stronger magnetic fields than previously. The considerable increase in precision over the previous measurements arises from the longer homogeneous field magnet of the Harvard apparatus,[4] use of the Ramsey separated radio-frequency field technique,[5,6] and the employment of more accurate frequency measuring equipment.[7]

The present paper contains the results of similarly improved measurements of the $I=J=1$ rotational spectrum ($\Delta m_I=0$, $\Delta m_J=\pm1$) in D_2 and the $I=0$, $J=2$ resonance in H_2.

II. APPARATUS

The apparatus employed in these experiments is essentially that built and described by Kolsky, Phipps, Ramsey, and Silsbee.[4] Some of the subsequent modifications and improvements made by the authors and Harrick are discussed in references 3 and 7, while others specifically required for the present measurements will be discussed in the following paragraphs.

The size of the $I=J=1$, $\Delta m_I=0$, $\Delta m_J=\pm1$ resonances in D_2 (detected as a decrease in beam intensity at the resonance frequency) is considerably smaller than that of the corresponding H_2 resonances. This is partly explained by the lower population of the $I=J=1$ state for D_2 than for H_2. In fact, the maximum possible number of molecules taking part in any given $\Delta m_I=0$, $\Delta m_J=\pm1$ resonance is[2] 5.4 percent of the total beam in the case of D_2 and 12.5 percent for H_2 when the effects of the velocity distribution among the molecules are taken into account. An additional decrease of resonance size for D_2 arises because of the smallness of its rotational magnetic moment. The force experienced by a molecule in the inhomogeneous fields of the A and B deflecting magnets is of the form $F=\mu\partial H/\partial z$. As a

* This work was partially supported by the joint program of the U. S. Office of Naval Research and the U. S. Atomic Energy Commission.

† Now at the University of Delaware, Newark, Delaware.

‡ Now at Rensselaer Polytechnic Institute, Troy, New York.

[1] N. F. Ramsey, Phys. Rev. **58**, 226 (1940).

[2] Kellogg, Rabi, Ramsey, and Zacharias, Phys. Rev. **56**, 728 (1939); **57**, 677 (1940).

[3] N. J. Harrick and N. F. Ramsey, Phys. Rev. **88**, 228 (1952).

[4] Kolsky, Phipps, Silsbee, and Ramsey, Phys. Rev. **87**, 395 (1952).

[5] N. F. Ramsey, Phys. Rev. **78**, 695 (1950).

[6] N. F. Ramsey and H. B. Silsbee, Phys. Rev. **84**, 506 (1951).

[7] Harrick, Barnes, Bray, and Ramsey, Phys. Rev. **90**, 260 (1953).

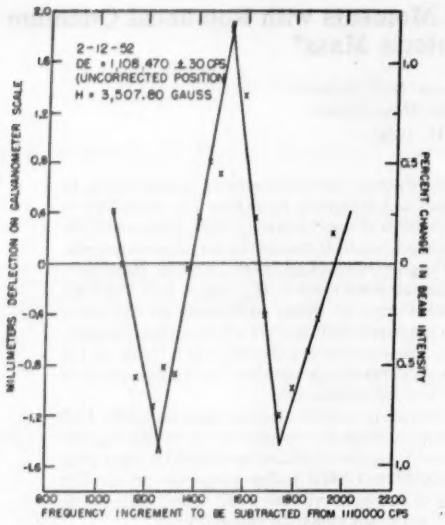
2-12-52
DE = 1,108,470 ±30 CPS
(UNCORRECTED POSITION)
H = 3,507.80 GAUSS
MILLIMETERS DEFLECTION ON GALVANOMETER SCALE
PERCENT CHANGE IN BEAM INTENSITY
FREQUENCY INCREMENT TO BE SUBTRACTED FROM 1110000 CPS

FIG. 1. Typical D_2 rotational resonance, $I=J=1$.

result, when resonance is reached, the reoriented molecules of small moment may not be sufficiently deflected from the nonresonance path to prevent their entering the detector. Harrick experienced this difficulty in obtaining the H_2 rotational spectrum measurements[3] and since the D_2 rotational moment is smaller by a factor of two, the effect is very pronounced in the present case.

Increasing the deflecting magnets' field strength would remedy the problem in principle but is not a good solution in practice. The homogeneous C-magnet field is definitely influenced by the flux stolen from the deflecting magnets. Larger deflecting magnet fields increase the difficulty of achieving a uniform field over the entire length of the C-magnet and increase field regulation problems.

The D_2 rotational resonances when found were approximately 1.5 to 2 mm peak-to-peak on the change in intensity *versus* frequency plot obtained using the Ramsey separated field[5] and 0°–180° phase shifting technique[6] (see Fig. 1). The beam is detected by a Pirani gauge with four heated platinum ribbon elements in a Wheatstone bridge arrangement. The output from the bridge is measured with a Leeds and Northrup HS galvanometer of 12.32-cm/microvolt sensitivity as used. Previous to the preparations for the present measurements, thermal variations, mechanical vibrations, and other disturbances had introduced "noise" and drift into the galvanometer spot location on the scale amounting to 1 to 2 mm and 1 cm/minute, respectively, at times of best behavior. Since it is necessary to take readings to $\pm\frac{1}{4}$ mm in order to determine the shape and center of a resonance measuring 2 mm at its maximum, considerable improvement of the apparatus was required. Rebuilding of the detector circuits with painstaking attention to clean, tight contacts and complete shielding from air currents, magnetic fields, rf fields, and vibration reduced the circuit noise to $\frac{1}{4}$ mm on the galvanometer scale during periods of days and even weeks.

Vacuum system modifications, including the replacement of the previous mechanical pump[4] with a 9 liter/second Kinney VSD 8811 water-jacketed model, made possible a stable main chamber pressure of 3×10^{-7} mm Hg even with the use of a 4- or 5-mm Hg input gas pressure in the source (compared to the 3-mm Hg maximum previously used).

Modifications of the C-magnet current regulator achieved a regulation of five parts in one million in the magnetic field.

III. HAMILTONIAN

The Hamiltonian operator for a homonuclear $^1\Sigma$ diatomic molecule in a magnetic field is given[8] by

$$\begin{aligned}\mathcal{H}/h=&-(1-\sigma_{mJ})a(\mathbf{I})_z-[1-\sigma_J(J)]b(\mathbf{J})_z-c(\mathbf{I}\cdot\mathbf{J})\\&+\{5d/[(2J-1)(2J+3)]\}\times\{3(\mathbf{I}\cdot\mathbf{J})^2+\tfrac{3}{2}(\mathbf{I}\cdot\mathbf{J})\\&-I(I+1)J(J+1)\}-\{5f/[3(2J-1)(2J+3)]\}\\&\times\{3(\mathbf{J})_z^2-J(J+1)\}-g. \quad (1)\end{aligned}$$

The quantity σ_{mJ} denotes the nuclear shielding when the molecule is in the state with $(\mathbf{J})_z=m_J$ and is the same as $\sigma_i(\mathbf{J})$ of reference 8. The remaining symbols appearing in Eq. (1) are defined and discussed in references 1, 2, and 8.

IV. THEORY OF DEUTERIUM ROTATIONAL SPECTRUM

For deuterium molecules in the state $I=J=1$, the following six transition frequencies may be found[8] from Eq. (1) by the use of third-order perturbation theory and the condition that $\Delta m_J=\pm1$, $\Delta m_I=0$:

$$AB/KL-(\sigma_{\pm1}-\sigma_0)a+b'\pm(-c+3d/2)\mp f-C_2', \quad (2)$$

$$BC/GK\quad(\sigma_{\pm1}-\sigma_0)a+b'\mp(\ c+3d/2)\pm f-(C_2-C_2')\pm C_3, \quad (3)$$

$$DE/EF\qquad\qquad b'\quad\mp3d\quad\mp f-C_2'\quad\mp2C_3, \quad (4)$$

where

$$C_2=[(c+3d/2)^2+9d^2/2]/(a-b'),$$
$$C_2'=(c-3d/2)^2/(a-b'),$$
$$C_3=(c+3d/2)^2(c-9d/2)/(a-b')^2,$$
$$b'=(1-\sigma_{11})b.$$

The upper sign in each equation goes with the upper transition (such as AB). σ_{11} is $\sigma_J(J)$ for the case $J=1$ and $m_J=\pm1$.

[5] N. F. Ramsey, Phys. Rev. 85, 60 (1952).

A. Determination of the Deuterium Rotational Magnetic Moment

In order to eliminate the magnetic field value H, the deuteron resonance frequency $\nu_D=(1-\sigma_D)a$ is obtained from the molecules in the $J=0$, $I=2$ state. Then, from Eqs. (2)–(4), one finds the values

$$b'/(1-\sigma_D)a=(1-\sigma_{11})\mu_{RD}/(1-\sigma_D)\mu_D$$

$$=\frac{AB+KL}{2(1-\sigma_D)a}+\frac{C_2'}{(1-\sigma_D)a}+\frac{\sigma_{\pm1}-\sigma_0}{1-\sigma_D} \quad (5)$$

$$=\frac{BC+GK}{2(1-\sigma_D)a}+\frac{C_2-C_2'}{(1-\sigma_D)a}-\frac{\sigma_{\pm1}-\sigma_0}{1-\sigma_D} \quad (6)$$

$$=(DE+EF+2C_2')/2(1-\sigma_D)a. \quad (7)$$

Here the symbol μ_{RD} is equal to the quantity ${}_v{}^x\langle\mu_R/J\rangle_J$ of Ramsey's paper[9] which denotes the expectation value of the rotational moment divided by the rotational quantum number J where, in the present case, $x=D$ (i.e., a deuterium molecule), $v=0$ (the zeroth vibrational state of the molecule), and $J=1$.

It is apparent from Eqs. (5)–(7) that use of the transitions DE and EF will avoid the term $(\sigma_{\pm1}-\sigma_0)/(1-\sigma_D)$ arising from nuclear shielding and not accurately known. Furthermore, if the two average values of $b'(1-\sigma_D)a$ obtained independently from $AB+KL$ transition frequency sums and $BC+GK$ transition frequency sums are again averaged, Eqs. (5) and (6) show that the unwanted term $(\sigma_{\pm1}-\sigma_0)/(1-\sigma_D)$ will be cancelled. This procedure will be used, but in the selection of a final "best value" for $b'/(1-\sigma_D)a$, more reliance will be placed on the values obtained from the DE and EF transition frequencies.

The value of the deuterium rotational moment (in the first rotational state) in nuclear magnetons may be obtained from the relation,

$$(\mu_{RD})_{NM}=(1-\sigma_D)(\mu_D/\mu_H)(\mu_H)_{NM} \times[\mu_{RD}/(1-\sigma_D)\mu_D], \quad (8)$$

where the value of Smaller, Yasaitas, and Anderson[10] for μ_H/μ_D and that of Sommer, Thomas, and Hipple[11] for $(\mu_H)_{NM}$ can be employed. The value of $b'(1-\sigma_D)a$ is used for $\mu_{RD}/(1-\sigma_D)\mu_D$ by neglecting the small unknown correction σ_{11}.

B. Deuterium Molecular Susceptibility

The high-frequency term of the deuterium molecular susceptibility in the zeroth vibrational and first rotational states can be written as [Eq. (14) of reference 9]

$${}_0{}^D\langle\chi\rangle_1{}^{hf}=\frac{e^2L}{12mc^2}R_e^2\,{}_0{}^D\langle(R/R_e)^l\rangle_1/{}_0{}^D\langle(R/R_e)^{l-2}\rangle_1 \times[1-2(\mu_D'/M)\,{}_0{}^D\langle\mu_R/\mu_{NM}\rangle_1]. \quad (9)$$

[9] N. F. Ramsey, Phys. Rev. **87**, 1075 (1952).
[10] Smaller, Yasaitas, and Anderson, Phys. Rev. **81**, 896 (1951).
[11] Sommer, Thomas, and Hipple, Phys. Rev. **82**, 697 (1951).

The quantity ${}_0{}^D\langle(R/R_e)^l\rangle_1/{}_0{}^D\langle(R/R_e)^{l-2}\rangle_1$ can be calculated from Eq. (21) of reference 9 after determination of the exponent l. The determination of l is achieved from the relation

$$\frac{{}_0{}^H\langle(R/R_e)^{l-2}\rangle_1}{{}_0{}^D\langle(R/R_e)^{l-2}\rangle_1}=1+\frac{1-(\mu_H'/\mu_D')\,{}_0{}^H\langle\mu_R/\mu_{NM}\rangle_1/{}_0{}^D\langle\mu_R/\mu_{NM}\rangle_1}{(M/2\mu_D')\,{}_0{}^D\langle\mu_R/\mu_{NM}\rangle_1^{-1}-1}, \quad (10)$$

which is a specific case of Eq. (23), reference 9. All quantities on the right side of Eq. (10) are known or are measured in these experiments. Comparison of the numerical value achieved for the right-hand side of Eq. (10) with the plot of Fig. 2 of reference 9 permits evaluation of l.

R_e is determined from the relation [Eq. (13), reference 9]

$$R_e^2=h/(8\pi^2c\mu_H'{}^HB_0)\cdot{}_0{}^H\langle(R/R_e)^{-2}\rangle_0, \quad (11)$$

where ${}_0{}^H\langle(R/R_e)^{-2}\rangle_0$ is found from Eq. (21) of reference 9.

C. Deuterium Diamagnetic Interaction

For molecules in the first rotational state, the diamagnetic interaction parameter f is related[8] to the diamagnetic susceptibilities $\xi_{\pm1}$ and ξ_0 by

$$f=(\xi_{\pm1}-\xi_0)H^2/2h, \quad (12)$$

where the subscripts ±1 and 0 refer to the value of m_J in the state $J=1$. It is evident that $(\xi_{\pm1}-\xi_0)$ measures the dependence of the diamagnetic susceptibility on molecular orientation. Each pair of the transition frequencies Eqs. (2)–(4) may be used to evaluate f, as follows:

$$2f=(KL-AB)-2c+3d, \quad (13)$$

$$2f=(BC-GK)+2c+3d-2C_3, \quad (14)$$

$$2f=(EF-DE)\qquad -6d-4C_3. \quad (15)$$

The deuterium $I=2$, $J=0$ single resonance frequency ν_D is used to monitor the magnetic field H during operation, since

$$\nu_D=(1-\sigma_D)(\mu_D/\mu_H)(\gamma_H/4\pi)H. \quad (16)$$

The nuclear shielding factor σ_D in Eq. (16) can be neglected here in calculating the magnetic field from ν_D since the uncertainty in $(\xi_{\pm1}-\xi_0)$ is entirely determined by that in f. The third-order correction C_3 is calculated from Eq. (21) below.

D. Quadrupole Moment of the Deuterium Electron Distribution

For the deuterium molecule in the first rotational and zeroth vibrational states the quadrupole moment of

the electron distribution is given by

$$ {}_0{}^{\mathrm{D}}\langle Q_e\rangle_1 = -\frac{20mc^2}{e^2}[(\xi_{\pm 1}-\xi_0)-\tfrac{3}{5}\,{}_0{}^{\mathrm{D}}\langle\xi\rangle_1{}^{\mathrm{hf}}]. \quad (17) $$

Here, ${}_0{}^{\mathrm{D}}\langle\xi\rangle_1{}^{\mathrm{hf}}$ is the high-frequency part of the diamagnetic susceptibility per molecule and is obtained from Eq. (9) by division by L.

E. Evaluation of c and d for Deuterium

From Eqs. (13)–(15) one can deduce the relations

$$ (EF-DE)+(AB-KL) = -2c+9d+4C_3, \quad (18) $$

$$ (EF-DE)+(GK-BC) = 2c+9d+2C_3, \quad (19) $$

$$ (GK-BC)-(AB-KL) = 4c \quad -2C_3, \quad (20) $$

where the small third-order term,

$$ C_3 = (c+3d/2)^2(c-9d/2)/(a-b')^2, \quad (21) $$

can be evaluated using the best values of c and d from nuclear spectrum measurements,[7] the relation

$$ a-b' = \mu_{\mathrm{D}}H[1-(1-\sigma_{11})\alpha]/h, \quad (22) $$

where $\alpha=\mu_{RD}/\mu_{\mathrm{D}}$, and the fact that

$$ \mu_{\mathrm{D}}H/h = \nu_{\mathrm{D}}/(1-\sigma_{\mathrm{D}}). \quad (23) $$

The ratio $(1-\sigma_{11})\alpha/(1-\sigma_{\mathrm{D}})$ is obtained in the present measurements and the deuterium $I=2$, $J=0$ single resonance frequency ν_{D} is measured repeatedly during any operational period in order to monitor the magnetic field H. The nuclear shielding factor σ_{D} may be neglected in computing the small term C_3.

V. THEORY OF HYDROGEN ROTATIONAL SPECTRUM IN THE SECOND ROTATIONAL STATE

For hydrogen molecules in the state $I=0$, $J=2$ the Hamiltonian operator Eq. (1) reduces to the simpler form

$$ \mathcal{H}/h = -[1-\sigma_J(J)]b(\mathbf{J})_z-(5/63)f\{3J_z^2-6\}-g. \quad (24) $$

The matrix elements of this operator are all diagonal, and the energy levels can accordingly be written down directly. The differences between these levels corresponding to the selection rule $\Delta m_J=\pm 1$, $\Delta m_I=0$ are the transition frequencies in the rotational spectrum:

$$ \begin{aligned} \nu_1 &= (1+\sigma_{21}-2\sigma_{22})b-(5/7)f, \\ \nu_2 &= (1-\sigma_{21})b-(5/21)f, \\ \nu_3 &= (1-\sigma_{21})b+(5/21)f, \\ \nu_4 &= (1+\sigma_{21}-2\sigma_{22})b+(5/7)f. \end{aligned} \quad (25) $$

Note that f in Eq. (25) can be related to $(\xi_{\pm 1}-\xi_0)$ of the first rotational state by Eq. (12) if the change in f due to centrifugal distortion is small.

A. Hydrogen Rotational Magnetic Moment

The transitions Eq. (25) average to the value $(1-\sigma_{22})b=b''$. In terms of the rotational magnetic moment,

$$ b = \mu_{RH}H/Jh. \quad (26) $$

The value of the magnetic field is determined from the deuteron resonance frequency ν_{D} in the $J=0$, $I=2$ state of deuterium, Eq. (16). Combining Eqs. (16) and (26) gives for the value of the rotational magnetic moment in nuclear magnetons

$$ (\mu_{RH}/J)_{NM} = (1-\sigma_{\mathrm{D}})(\mu_{\mathrm{D}}/\mu_{\mathrm{H}})(\mu_{\mathrm{H}})_{NM}\{b/\nu_{\mathrm{D}}\}. \quad (27) $$

The quantity actually observed is the ratio (b''/ν_{D}) but the correction σ_{22} for the difference between b and b'' is negligible for the present accuracy. The values of the other quantities are those mentioned in connection with Eq. (8).

B. Hydrogen Molecular Susceptibility

The high-frequency term of the hydrogen molecular susceptibility in the zeroth vibrational and Jth rotational states can be written as [Eq. (14) of reference 9]

$$ {}_0{}^{\mathrm{H}}\langle\chi\rangle_J{}^{\mathrm{hf}} = \frac{e^2L}{12mc^2}R_e^2\,{}_0{}^{\mathrm{H}}\langle(R/R_e)^l\rangle_J/{}_0{}^{\mathrm{H}}\langle(R/R_e)^{l-2}\rangle_{J'} \times\{1-{}_0{}^{\mathrm{H}}\langle\mu_R/J\mu_{NM}\rangle_{J'}\}. \quad (28) $$

In order to evaluate the quantities of the form ${}_0{}^{\mathrm{H}}\langle(R/R_e)^n\rangle_J$ from Eq. (21) of reference 9, the value of l must be determined. This can be done from the hydrogen results by comparing the values of the quantity $(\mu_R/J)_{NM}$ or (b/ν_{D}) in the first and second rotational states. According to reference 9, this gives the ratio

$$ \frac{{}_0{}^{\mathrm{H}}\langle(R/R_e)^{l-2}\rangle_1}{{}_0{}^{\mathrm{H}}\langle(R/R_e)^{l-2}\rangle_2} = 1+\frac{1-{}_0{}^{\mathrm{H}}\langle\mu_R/J\mu_{NM}\rangle_1/{}_0{}^{\mathrm{H}}\langle\mu_R/J\mu_{NM}\rangle_2}{{}_0{}^{\mathrm{H}}\langle\mu_R/J\mu_{NM}\rangle_2^{-1}-1}, \quad (29) $$

whereas this same ratio has the theoretical value[9]

$$ \frac{{}_0{}^{\mathrm{H}}\langle(R/R_e)^{l-2}\rangle_1}{{}_0{}^{\mathrm{H}}\langle(R/R_e)^{l-2}\rangle_2} = \frac{1+8(l-2)(B_e/\omega_e)^2}{1+24(l-2)(B_e/\omega_e)^2}. \quad (30) $$

Direct comparison of the right-hand sides of Eqs. (29) and (30) yields the value of l. The recent spectroscopic results of Herzberg may be used for B_e and ω_e. R_e in Eq. (28) is determined from Eq. (11).

C. Quadrupole Moment of the Hydrogen Electron Distribution

Equation (17) can be carried over directly to the case of hydrogen in the zeroth vibrational and first rotational states. The value of ${}_0{}^{\mathrm{H}}\langle\xi\rangle_1{}^{\mathrm{hf}}$ is obtained from Eq. (28) by division by L.

VI. EXPERIMENTAL RESULTS

Table I contains measurements of the deuterium rotational transition frequencies at three distinct magnetic field strengths (approximately 1800, 3500, and 5100 gauss). Subscripts affixed to each pair of transition frequencies are for ease in distinguishing the values calculated in later sections. The measurements on DE and EF at 5100 gauss were obtained only once due to subsequent continuing detector noise and other problems. All measurements reported here, however, display a clear line shape, low dispersion of points, and complete symmetry of line shape within experimental error. These properties were obtained for such very small resonances by painstaking adjustment of the apparatus

TABLE I. Measurements of deuterium rotational transition frequencies in the first rotational state in strong magnetic fields.

Number of observations of each transition	Transition	Position of resonance (cps)
3	ν_D	1 140 935±20
	KL_I	558 642±30
	AB_I	616 981±30
2	ν_D	1 240 906±20
	KL_{II}	610 339±40
	AB_{II}	668 708±40
	DE_{II}	565 190±30
	EF_{II}	713 956±35
3	ν_D	2 292 652±20
	DE_{III}	1 108 476±30
	EF_{III}	1 258 565±30
2	ν_D	2 270 692±20
	KL_{IV}	1 142 750±30
	AB_{IV}	1 201 584±30
	BC_{IV}	1 121 968±35
	GK_{IV}	1 216 271±40
1	ν_D	3 362 905±20
	DE_V	1 661 760±40
	EF_V	1 811 447±30

and by averaging techniques involving four to eight galvanometer spot deflections for each experimental point. Figure 1 is a typical line trace.

Table II contains measurements of the observed hydrogen rotational transition frequency in the second rotational state and of the deuteron resonance frequency in D_2 in magnetic fields of approximately 1680 and 1865 gauss. The line width listed is measured at the points of zero galvanometer deflection of the 0°–180° phase-shifting resonance pattern. The statements previously made with regard to the line shape and symmetry and low point disperison of the deuterium data apply equally to the hydrogen rotational data. Figure 2 is a typical line trace.

VII. ANALYSIS OF EXPERIMENTAL DEUTERIUM ROTATIONAL SPECTRUM

A. Deuterium Rotational Magnetic Moment

When the data of Table I are used in Eqs. (5)–(7), the values of $b'/(1-\sigma_D)a$ displayed in Table III are ob-

TABLE II. Hydrogen rotational resonance $I=0$, $J=2$, and deuterium nuclear resonance $I=2$, $J=0$.

Transition	Time	Position of resonance (cps)	Line width (cps)
ν_D	10:50 P.M.	1 095 728±20	350
b''	12:00	1 127 522±20	600
ν_D	1:30 A.M.	1 095 716±20	405
b''	2:10	1 127 535±20	560
b''	2:40	1 127 493±20	570
ν_D	3:15	1 095 720±20	400
b''	3:45	1 127 500±20	560
b''	4:15	1 127 495±20	580
ν_D	4:40	1 095 735±20	400
b''	5:10	1 127 542±20	550
(Above data taken with a magnetic field, $H\cong 1680$ gauss)			
ν_D	5:20 P.M.	1 219 842±20	370
b''	6:05	1 255 240±20	500
b''	6:45	1 255 242±20	575
ν_D	7:15	1 219 836±20	425
ν_D	11:40	1 214 335±20	410
b''	12:15 A.M.	1 249 577±20	600
b''	12:45	1 249 565±20	590
ν_D	1:15	1 214 322±20	450
b''	1:45	1 249 552±20	575
b''	2:05	1 249 542±20	580
ν_D	2:30	1 214 335±20	420
(Above data taken with a magnetic field, $H\cong 1865$ gauss)			

tained. The average values obtained from the different transition frequency sums are given in Table IV. Averaging of the first two values in Table IV yields

$$b'/(1-\sigma_D)a=0.516547\pm0.000027, \qquad (31)$$

which is in very satisfactory agreement with the determination from $DE+EF$ transition frequency sums (see Table IV).

The best value from the present measurements is taken to be

$$b'/(1-\sigma_D)a=0.516550\pm0.000016. \qquad (32)$$

The corresponding value obtained from Eq. (8) for μ_{RD}

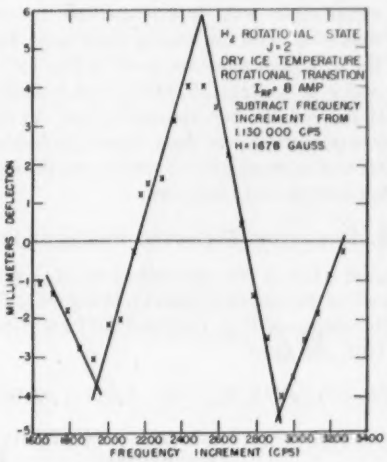

FIG. 2. Typical H_2 rotational resonance, $I=0$, $J=2$.

TABLE III. Values of $b'/(1-\sigma_D)a$ obtained from different transition frequency sums. Subscripts are those appearing in Table I.

Transition frequency sum involved	$b'/(1-\sigma_D)a$
$(AB+KL)_I$	$(0.516544\pm0.000035)+(\sigma_{\pm1}-\sigma_0)/(1-\sigma_D)$
$(AB+KL)_{II}$	$(0.516504\pm0.000041)+(\sigma_{\pm1}-\sigma_0)/(1-\sigma_D)$
$(AB+KL)_{IV}$	$(0.516555\pm0.000018)+(\sigma_{\pm1}-\sigma_0)/(1-\sigma_D)$
$(DE+EF)_{II}$	(0.516543 ± 0.000035)
$(DE+EF)_{III}$	(0.516555 ± 0.000019)
$(DE+EF)_V$	(0.516555 ± 0.000013)
$(BC+GK)_{IV}$	$(0.516558\pm0.000021)-(\sigma_{\pm1}-\sigma_0)/(1-\sigma_D)$

in units of nuclear magnetons is

$$\mu_{RD}=0.442884\pm0.000052 \text{ nuclear magneton.} \quad (33)$$

Here use has been made of the value

$$\sigma_D=(2.64\pm0.04)\times10^{-5} \quad (34)$$

found from the theory of Ramsey[9] and measurements on the H_2 and D_2 nuclear spectra.[7]

The value of μ_{RD} in Eq. (33) can be compared with the value

$$\mu_{RH}=0.88291\pm0.00007 \text{ nuclear magneton} \quad (35)$$

found by Harrick and Ramsey[3] for hydrogen in the first rotational state.

The ratio

$$\mu_{RH}/\mu_{RD}=1.99355\pm0.00022 \quad (36)$$

[obtained from Eq. (32) and Harrick's[3] value for $\mu_{RH}/(1-\sigma_D)\mu_D$] differs from 1.999008 ± 0.000006, which is the ratio M_d/M_p of the deuteron mass to that of the proton. In fact,

$$(M_d/M_p)(\mu_{RD}/\mu_{RH})=1.00274\pm0.00011, \quad (37)$$

which departs from unity by twenty-five times the probable error. Part of this difference may be attributed to the fact that the electrons contribute in part to the moment of inertia of the molecule, in which case the proper comparison ratio is intermediate between the nuclear mass ratio and the atomic mass ratio. However, even if the atomic masses are used in Eq. (37) the resulting value is 1.00247 ± 0.00011, which differs from unity far beyond the experimental error. As discussed in the next paragraph, the departure is probably due to the differences in zero point vibration and in centrifugal stretching for the two molecules.

B. Deuterium Molecular Susceptibility

Equation (10) is the specialization of Eq. (23) of reference 9 to the case of H_2 and D_2 in the state $I=J=1$. When the values of Eqs. (33) and (37) are substituted in Eq. (10), one finds

$$\{{}_0{}^D\langle(R/R_e)^{l-2}\rangle_1/{}_0{}^H\langle(R/R_e)^{l-2}\rangle_1\}-1=(1/1.02108)-1$$
$$=-\left(0.0206\,{}^{+0.0010}_{-0.0020}\right), \quad (38)$$

where the asymmetry in the probable error arises from the uncertainty in the extent to which the electron contributes to the moment of inertia, as discussed in the preceding section. Use of Eq. (9) and Fig. 2 of reference 9 (which is a plot of $\{{}_0{}^D\langle(R/R_e)^n\rangle_1/{}_0{}^H\langle(R/R_e)^n\rangle_1\}-1$ as a function of n) determines the value of l as

$$l=d\ln\xi^{hf}/d\ln R=3.72\,{}^{+0.06}_{-0.12}. \quad (39)$$

This result is in good agreement with the value, $l=3.80\pm0.12$, determined from measurements of the hydrogen rotational magnetic moment in the first and second rotational states [see Eq. (65) below].

From Eq. (39) above and Eq. (21) of reference 9, one finds

$${}_0{}^D\langle(R/R_e)^{l}\rangle_1/{}_0{}^D\langle(R/R_e)^{l-2}\rangle_1=1.0949\,{}^{+0.0012}_{-0.0030}. \quad (40)$$

Values of Herzberg[12,13] and Ramsey[9] are used for the necessary constants appearing in Eq. (21) of reference 9.

One now requires only the further value R_e in order to evaluate the high-frequency term of the deuterium molecular susceptibility in the zeroth vibrational and first rotational state, given by Eq. (9). R_e is found from the value

$${}_0{}^H\langle(R/R_e)^{-2}\rangle_1=0.9747 \quad (41)$$

[determined from Eq. (21) of reference 9] and Eq. (11) (combined with Herzberg's value of ${}^H B_0$) to be

$$R_e=(0.7416\pm0.0001)\times10^{-8} \text{ cm.} \quad (42)$$

Substitution of the values of Eqs. (33), (37), (40), and (42) into Eq. (9) yields

$${}_0{}^D\langle\chi\rangle_1{}^{hf}=(0.0978\pm0.0003)\times10^{-6} \text{ erg gauss}^{-2} \text{ mole}^{-1}. \quad (43)$$

A similar calculation for hydrogen, using the value of Eq. (35) for ${}_0{}^H\langle\mu_R/\mu_{NM}\rangle_1$ gives

$${}_0{}^H\langle\chi\rangle_1{}^{hf}=(0.1036\pm0.0005)\times10^{-6} \text{ erg gauss}^{-2} \text{ mole}^{-1}, \quad (44)$$

with the value $l=3.72$. This value for ${}_0{}^H\langle\chi\rangle_1{}^{hf}$ may be

TABLE IV. Average values of $b'/(1-\sigma_D)a$ obtained from different transition frequency sums.

Transition frequency sum involved	$b'/(1-\sigma_D)a$
$AB+KL$	$(0.516536\pm0.000032)+(\sigma_{\pm1}-\sigma_0)/(1-\sigma_D)$
$BC+GK$	$(0.516558\pm0.000021)-(\sigma_{\pm1}-\sigma_0)/(1-\sigma_D)$
$DE+EF$	0.516551 ± 0.000023

[12] N. F. Ramsey, Phys. Rev. 78, 221 (1950).
[13] G. Herzberg, Can. J. Research A28, 144 (1950).

TABLE V. Data used in the evaluation of c and d and $(\xi_{\pm1}-\xi_0)$. Values of $(\xi_{\pm1}-\xi_0)$ calculated from different sets of c and d values.

Magnetic field H (gauss)	Transition frequency difference	Value thereof (cps)	C_3 (cps)	$(\xi_{\pm1}-\xi_0)$ (from nuclear spectrum) (10^{-31} erg gauss^{-2} molecule^{-1})	$(\xi_{\pm1}-\xi_0)$ (from rotational spectrum) (10^{-31} erg gauss^{-2} molecule^{-1})
1745.63±0.07	$(AB-KL)_{\mathrm{I}}$	58 337±60		−(4.39±1.82)	−(3.15±1.50)
1898.61±0.07	$(EF-DE)_{\mathrm{II}}$	148 765±60	−633	−(2.26±1.10)	−(3.25±1.15)
	$(AB-KL)_{\mathrm{II}}$	58 368±80		−(4.30±1.72)	−(3.25±1.46)
3507.80±0.11	$(EF-DE)_{\mathrm{III}}$	150 089±60	−185	−(3.18±0.32)	−(3.48±0.35)
3474.20±0.11	$(GK-BC)_{\mathrm{IV}}$	94 302±75	−189	−(3.49±0.49)	−(3.51±0.38)
	$(AB-KL)_{\mathrm{IV}}$	58 833±60		−(3.83±0.46)	−(3.52±0.44)
5145.24±0.16	$(EF-DE)_{\mathrm{V}}$	149 687±70	−86	−(3.48±0.16)	−(3.61±0.17)
					−(3.50±0.30)[a]
				−(3.45±0.50)[b]	−(3.50±0.40)[b]

[a] Evaluated from Eq. (46).
[b] Average of 3500 gauss experiments.

compared to the result

$$ {}_0{}^{\mathrm{H}}\langle\chi\rangle_1{}^{\mathrm{h\,f}} = (0.0990\pm0.0010) \times 10^{-6}\ \text{erg gauss}^{-2}\ \text{mole}^{-1} \quad (45) $$

found[3] before the result of Ramsey's work[9] on zero-point vibration and centrifugal stretching effects was available.

C. Deuterium Diamagnetic Interaction

The quantity $(\xi_{\pm1}-\xi_0)$, characterizing the dependence of the diamagnetic susceptibility on molecular orientation, is calculated from Eq. (12) using the values of f obtained from Eqs. (13)–(15) and the data of Table I. A considerable effect on the scattering of the $(\xi_{\pm1}-\xi_0)$ values about the average value can be achieved by choosing slightly different values of the parameters c and d. When the best values of these parameters obtained from measurements on nuclear spectra [Eqs. (57) and (58)] are used, the $(\xi_{\pm1}-\xi_0)$ values calculated from the lines AB/KL at 1800 gauss are significantly greater than the 5100 gauss value from lines DE/EF, and the 1800 gauss value using lines DE/EF is significantly lower than that at 5100 gauss. These various values are tabulated in the first column of $(\xi_{\pm1}-\xi_0)$ values in Table V. On the other hand, when the values of the parameters c and d evaluated from the present measurements [Eqs. (50) and (56)] are used, an almost fivefold reduction in scattering is obtained [second column of $(\xi_{\pm1}-\xi_0)$ values in Table V]. It is also possible to combine Eqs. (13)–(15) to obtain a calculation of $(\xi_{\pm1}-\xi_0)$ directly:

$$ (\xi_{\pm1}-\xi_0)(2H_a{}^2+H_b{}^2)/h = (BC-GK-2C_3) + (KL-AB)+(EF-DE-4C_3). \quad (46) $$

Here, H_a is the magnetic field for the measurements on AB/KL and BC/GK while H_b is the field for measurements on EF/DE. The value of C_3 is very slightly affected by this small difference in field strengths (see Table V). All the values of $(\xi_{\pm1}-\xi_0)$ obtained from the present measurements and Eq. (46) above, are listed in Table V. The results based on nuclear and on rotational spectrum values of c and d are separately listed.

Since only one set of measurements was made at 5100 gauss, the best value of $(\xi_{\pm1}-\xi_0)$ is taken to be the average of the four 3500 gauss values calculated using rotational spectrum results for c and d. The result is that

$$ (\xi_{\pm1}-\xi_0) = -(3.50\pm0.40) \times 10^{-31}\ \text{erg gauss}^{-2}\ \text{molecule}^{-1}, \quad (47) $$

which is not significantly different from that obtained with the nuclear spectrum results for c and d (see Table V).

D. Quadrupole Moment of the Deuterium Electron Distribution

To calculate ${}_0{}^{\mathrm{D}}\langle Q_e\rangle_1$ from Eq. (17) it is first necessary to determine the high-frequency part of the diamagnetic susceptibility per molecule ${}_0{}^{\mathrm{D}}\langle\xi\rangle_1{}^{\mathrm{h\,f}}$ from the value per mole ${}_0{}^{\mathrm{D}}\langle x\rangle_1{}^{\mathrm{h\,f}}$. Using the value of Eq. (43), one finds

$$ {}_0{}^{\mathrm{D}}\langle\xi\rangle_1{}^{\mathrm{h\,f}} = (1.623\pm0.006) \times 10^{-31}\ \text{erg gauss}^{-2}\ \text{molecule}^{-1}. \quad (48) $$

When this is used in Eq. (17) together with the value of $(\xi_{\pm1}-\xi_0)$ from Eq. (47), one obtains

$$ {}_0{}^{\mathrm{D}}\langle Q_e\rangle_1 = (0.318\pm0.030)\times10^{-16}\ \text{cm}^2 \quad (49) $$

for the quadrupole moment of the electron distribution in the deuterium molecule in the first rotational state.

E. Evaluation of c and d for Deuterium

The data displayed in Table I show that measurements which can be used in Eqs. (18)–(21) for evaluation of c and d were obtained during three periods of operation. Table V displays the useful data and the respective field (H) and third-order correction term (C_3) values.

From the data IV and Eq. (20),

$$ c = \tfrac{1}{4}\{(GK-BC)-(AB-KL)+2C_3\} = 8773\pm34\ \text{cps}. \quad (50) $$

If this value of c is used with data II and Eq. (18),

$$ d = (1/9)\{(EF-DE)+(AB-KL)+2c-4C_3\} = 25\,246\pm23\ \text{cps}. \quad (51) $$

A satisfying check of these values can be obtained if use is made of data III. The 30-gauss difference in field existing between measurements III and IV has only a small effect on the transition frequency differences of interest (note the very minor change in C_3 occasioned by this field difference). From the $EF-DE$ measurements III, the $GK-BC$ and $AB-KL$ measurements IV, and Eqs. (18) and (19), one finds

$$2c+9d=244\,765\pm135 \text{ cps}, \quad (52)$$

$$-2c+9d=209\,670\pm120 \text{ cps}. \quad (53)$$

Note that the $EF-DE$ and $AB-KL$ measurements II yield

$$-2c+9d=209\,665\pm140 \text{ cps}, \quad (54)$$

in excellent agreement with Eq. (53). Using the average of Eqs. (53) and (54) with Eq. (52) yields

$$c=8774\pm64 \text{ cps}, \quad (55)$$

$$d=25\,246\pm14 \text{ cps}. \quad (56)$$

The values of Eqs. (50) and (56) offer an interesting comparison with the values

$$c=8788\pm40 \text{ cps}, \quad (57)$$

$$d=25\,237\pm10 \text{ cps}, \quad (58)$$

previously found[7] by the authors and N. J. Harrick from measurements on the deuterium nuclear spectrum.

VIII. ANALYSIS OF EXPERIMENTAL HYDROGEN ROTATIONAL SPECTRUM IN THE SECOND ROTATIONAL STATE

The four transition frequencies which are to be expected in the rotational spectrum of the second rotational state are spaced symmetrically about the reorientation frequency b of the rotational magnetic moment alone [see Eq. (25)] except for the negligibly small shielding correction. The splitting to be expected due to the diamagnetic interaction can be calculated from the known value[3] of $(\xi_{\pm1}-\xi_0)$ for the first rotational state. In a field of 2000 gauss, the splitting away from the frequency b would amount to 79 ± 4 cps. Such a small splitting would not be resolved by the present apparatus, but it was thought that some broadening of the resonance would appear.

The relative population of the second rotational state is only 0.1 percent at 78°K, whereas it increases to 7 percent at 200°K, and to 12 percent at 300°K. Since the width of the resonance pattern also increases with increasing temperature,[6] a temperature close to 200°K was taken as a compromise (195°K, the temperature of a dry ice-acetone mixture). The average over-all height of the resonances was about 4 percent of the total beam.

A. Hydrogen Rotational Magnetic Moment

It is interesting to note whether any indication of the diamagnetic splitting appears. As mentioned above, such splitting might cause a broadening of the resonance. No actual splitting was observed; the widths of the central peak of the resonances at the zero mark (zero deflection when switching phase 180°) are included with the data in Table II.

The theoretically expected line width has been given by Ramsey[5]

$$(\Delta\nu=0.64(3RT/M)^{\frac{1}{2}}/L. \quad (59)$$

L is the path length of the molecules in the homogeneous magnetic field. The application of this equation to the 0–180° phase-shifting pattern supposes that the in-phase and out-of-phase patterns correspond exactly in frequency. Since this may not actually be the case in practice, the equation is used here only to obtain the following expression for ratios of line widths. At the same temperature, one has

$$\Delta\nu(H_2)/\Delta\nu(D_2)=[M(D_2)/M(H_2)]^{\frac{1}{2}}=1.44. \quad (60)$$

By comparison, the ratios of the average measured line widths are (excepting the first value for ν_D in each case, which are probably due to the source oven's not having warmed up to 195° from the 78° temperature used during alignment of the apparatus):

data of 1-24-52

$$\Delta\nu(H_2)/\Delta\nu(D_2)=570/400=1.420, \quad (61)$$

data of 2-4-52

$$\Delta\nu(H_2)/\Delta\nu(D_2)=584/418=1.396.$$

The agreement with the value of Eq. (60) is very good, certainly well within the error incurred in reading the line widths from the plots. Thus there is no evidence for a broadening of the resonance.

Since by Eq. (25) above, the average of the unresolved resonance frequencies is b'', it is assumed that the observed single resonance represents that frequency. Examination of Table II shows that the drift of the magnetic field, indicated by the wandering of either resonance frequency during a run, is less than the experimental error of the resonances themselves. Accordingly, the line positions have not been corrected for drift; instead, the ratio $b''/\nu_D=(1-\sigma_{22})(\mu_{RH}/J)/(1-\sigma_D)\mu_D$ has been evaluated from each ν_D value and the b'' values immediately following and preceding it. In this manner, one obtains six ratios from the measurements of each data. The numerical average of the twelve ratios is almost exactly the mid-point of the two extreme values, and is taken to be the best value:

$$b''/\nu_D=1.029014\pm0.000030. \quad (62)$$

The corresponding value obtained from Eq. (27) for ${}_0^H\langle\mu_R/J\rangle_2$ in units of nuclear magnetons is

$${}_0^H\langle\mu_R/J\rangle_2=0.882265\pm0.000035 \text{ nuclear magneton}. \quad (63)$$

The value of σ_D used here is given by Eq. (34) and the negligibly small difference between b and b'' is omitted.

TABLE VI. Experimental results and derived quantities.

$\sigma_{D\text{-rota}}$	8773±34 cps
$d_{D\text{-rota}}$	25 246±14 cps
$b_D'/(1-\sigma_D)g_D$	0.516550±0.000016
$b_H''/(1-\sigma_D)g_D$	1.029014±0.000030
${}_0^D\langle\mu_R/J\rangle_1$	0.442884±0.000052 nm
${}_0^H\langle\mu_R/J\rangle_1$	0.88291±0.00007 nm[a]
${}_0^H\langle\mu_R/J\rangle_2$	0.882265±0.000035 nm
${}_0^D\langle\mu_R/J\rangle_1\langle M_d/M_p\rangle/{}_0^H\langle\mu_R/J\rangle_1$	1.00274±0.00011
${}_0^H\langle\mu_R/J\rangle_2/{}_0^H\langle\mu_R/J\rangle_1$	0.99927±0.00009
$d\ln\xi^{hf}/d\ln R=l$	$3.72^{+0.06}_{-0.12}$ (from H_2 and D_2); 3.80±0.12 (from H_2 $J=1$ and $J=2$); 3.76±0.10 (average)
${}_0^D\langle\chi\rangle_1^{hf}$	(0.0978±0.0003)×10^{-6} erg gauss^{-2} mole^{-1}
${}_0^H\langle\chi\rangle_1^{hf}$	(0.1036±0.0005)×10^{-6} erg gauss^{-2} mole^{-1}
${}_0^H\langle\chi\rangle_2^{hf}$	(0.1049±0.0008)×10^{-6} erg gauss^{-2} mole^{-1}
${}_0^D\langle\xi\rangle_1^{hf}$	(1.623±0.006)×10^{-31} erg gauss^{-2} molecule^{-1}
${}_0^H\langle\xi\rangle_1^{hf}$	(1.719±0.009×10^{-31} erg gauss^{-2} molecule^{-1}
${}_0^D\langle\xi_{\pm1}-\xi_0\rangle_1$	−(3.50±0.40)×10^{-31} erg gauss^{-2} molecule^{-1}
${}_0^D\langle Q_e\rangle_1$	(0.318±0.030)×10^{-16} cm^2
${}_0^H\langle Q_e\rangle_1$	(0.333±0.019)×10^{-16} cm^2
${}_0^H\langle Q_e\rangle_1^{theor}$	(0.345±0.010)×10^{-16} cm^2

[a] See reference 3.

It is of interest to compare the value of ${}_0^H\langle\mu_R/J\rangle_2$ given above with the value of ${}_0^H\langle\mu_R/J\rangle_1$ given by Eq. (35). Different centrifugal stretching in the two cases accounts for the difference between these values. Direct application of this difference is made in the next section.

B. Hydrogen Molecular Susceptibility

The value of the parameter l characterizing the dependence of the high-frequency matrix elements of the electron angular momentum on inter-nuclear spacing has been calculated [see Eq. (39)] by comparing the rotational magnetic moments of H_2 and D_2 in the first rotational state. A second, and independent, determination of this parameter can be made by comparing the rotational magnetic moments of H_2 in the first and second rotational states. When the values of Eqs. (35) and (63) are substituted in Eq. (29), one obtains

$$ {}_0^H\langle(R/R_e)^{l-2}\rangle_1/{}_0^H\langle(R/R_e)^{l-2}\rangle_2 = 1-(0.005478\pm0.00038). \quad (64)$$

The theoretical value of this expression is given by Eq. (30) and comparison of the right sides of Eqs. (64) and (30) shows that

$$l=3.80\pm0.12. \quad (65)$$

The values of B_e and ω_e are due to Herzberg.[13,14]

Combining the value of Eq. (65) with Eq. (21) of reference 9 yields

$$ {}_0^H\langle(R/R_e)^{l}\rangle_1/{}_0^H\langle(R/R_e)^{l-2}\rangle_1=1.1394\pm0.0080, \quad {}_0^H\langle(R/R_e)^{l}\rangle_2/{}_0^H\langle(R/R_e)^{l-2}\rangle_2=1.1444\pm0.0080. \quad (66)$$

The value of R_e has been determined [Eq. (42)], so that direct substitution of these various values in Eq. (28) (where $J=J'$) yields

$$ {}_0^H\langle\chi\rangle_1^{hf}=(0.0139\pm0.0008)\times10^{-6}\text{ erg gauss}^{-2}\text{ mole}^{-1}, \quad {}_0^H\langle\chi\rangle_2^{hf}=(0.1049\pm0.0008)\times10^{-6}\text{ erg gauss}^{-2}\text{ mole}^{-1}, \quad (67)$$

by using $l=3.80\pm0.12$. The value of ${}_0^H\langle x\rangle_1^{hf}$ should be compared with that obtained via the evaluation of l from the D_2 results [Eq. (44)] and with the earlier value [Eq. (45)].

C. Quadrupole Moment of the Hydrogen Electron Distribution

Equation (17) can be applied directly to the case of H_2 in the zeroth vibrational and first rotational states. The value of $(\xi_{\pm1}-\xi_0)$ has been given by Harrick and Ramsey[3] as $-(3.66\pm0.20)\times10^{-31}$ erg gauss^{-2} molecule^{-1}, and the value of ${}_0^H\langle\xi\rangle_1^{hf}$ is obtained from Eq. (67) by division by L. When these values are substituted in Eq. (17) one finds

$${}_0^H\langle Q_e\rangle_1=(0.333\pm0.019)\times10^{-16}\text{ cm}^2 \quad (68)$$

for the quadrupole moment of the electron distribution in molecular hydrogen. The value computed from the theory of James and Coolidge[15] is ${}_0^H\langle Q_e\rangle_1^{theor}=(0.345\pm0.010)\times10^{-16}$ cm^2.

IX. SUMMARY OF RESULTS

The experimental results and their theoretical implications are summarized in Table VI. In the calculations, the values for the fundamental constants were taken to be those of DuMond and Cohen.[16]

One of the most interesting of the direct results, as

[13] G. Herzberg, *Spectra of Diatomic Molecules* (D. Van Nostrand Company, Inc., New York, 1950).

[15] H. M. James and A. S. Coolidge, Astrophys. J. **87**, 447 (1938).

[16] J. W. M. DuMond and E. R. Cohen, Phys. Rev. **82**, 555 (1951).

shown in the eighth row of Table VI, is that the ratio for H_2 and D_2 of the rotational magnetic moments is not exactly equal to the inverse ratio of the nuclear masses but departs from exact equality by 0.27 percent. Similarly, in row nine of Table VI, the rotational magnetic moment in the second rotational state of hydrogen is not exactly double that in the first but is less than double by 0.07 percent. These discrepancies from the simplest theoretical predictions can successfully be attributed to differences in the zero point vibration and the centrifugal stretching for the molecule. Under such an assumption, $d\ln\xi^{h\,\prime}/d\ln R$ can be calculated independently from each of the above two observed discrepancies. The resulting values agree to within experimental error and average to 3.76 ± 0.10.

With the above value for $d\ln\xi^{h\,\prime}/d\ln R$, the zero point vibration correction can be suitably made in the calculation of the high-frequency term of the diamagnetic susceptibility. The resulting values are given in Table VI along with the best values for the quadrupole moments of the electron distribution that can be inferred from them.

PHYSICAL REVIEW VOLUME 94, NUMBER 4 MAY 15, 1954

Pressure Shift in Helium λ5875*

JOHN R. HOLMES AND LEON PAPE
Department of Physics, University of Southern California, Los Angeles, California
(Received Februrary 8, 1954)

Using a Fabry-Perot interferometer, pressure shift in λ5875($2\,^3P-3\,^3D$) of He^4 was looked for over a pressure range from 5×10^{-2} to 20 mm. A mean shift of 0.0074 cm^{-1} toward lower frequency at the higher pressure was found. As this is within the experimental error, it is concluded that over the above pressure range, pressure shift is not likely to falsify isotope shift measurements in the helium spectrum significantly.

INTRODUCTION

PRESSURE shifts in the helium spectrum have been reported by Hopfield[1] in the vacuum ultraviolet and by Fred, Tompkins, Brody, and Hamermesh[2] in the visible as observed during a study of isotope shift in helium lines. Since they[2] indicated that their observation of pressure shift was only qualitative and could be regarded as accounting partly for certain discrepancies in their isotope-shift data taken with high-pressure and low-pressure sources, it seemed worth while to make a quantitative direct study of the effect.

EXPERIMENTAL

As Fred *et al.* had reported much the largest effect in λ5875($2\,^3P-3\,^3D$), ascribing a pressure shift in this line of 0.0232 cm^{-1} for He^4 and -0.0285 cm^{-1} for He^3 between the low-pressure and the high-pressure source they used, it seemed appropriate to confine our measurements initially to λ5875. The line was excited in an electrodeless discharge coupled to a 10-megacycle oscillator operated at low power to increase sharpness. The discharge was observed side-on in a flattened section of the tube 1 mm thick and was completely immersed in liquid nitrogen. The optical arrangement consisted of a Fabry-Perot interferometer mounted externally in series with a medium Hilger quartz spectrograph. The general method was to photograph the interferometer pattern with a low pressure of He^4 in the discharge tube, shift the photographic plate sideways slightly more than the slit width, take an exposure with a higher pressure of He^4, shift the photographic plate sideways again, and repeat the exposure at the low pressure. Comparison of the first and last exposures provides a check on any drifting of the patterns during the exposures and comparison of the middle pattern with the others should detect a pressure shift.

For the low-pressure exposures a pressure of 5×10^{-2} mm was used and for the high-pressure 20 mm, as this seemed to be about the greatest pressure range over which the discharge operated satisfactorily and gave reasonably sharp lines. As the tubes used by Fred *et al.* were sealed-off tubes initially filled to 0.3 mm and 5 mm, respectively, our pressure range was deemed adequate to detect and measure the effect described.

λ5875 has a resolved fine structure component which is separated from the principal component by about 1.0 cm^{-1}.[3] In order to reduce distortion in the wings of the line fringes an etalon spacer was chosen (1.245 cm) to position the fine structure between the third and fourth succeeding orders. This gives an order separation of 0.4016 cm^{-1}.

The interferometer patterns were densitometered on a Zeiss microdensitometer and the traces corrected for nonuniform intensity distribution across the slit.

* Supported partly by the U. S. Office of Naval Research.
[1] J. J. Hopfield, Astrophys. J. 72, 133 (1930).
[2] Fred, Tomkins, Brody, and Hamermesh, Phys. Rev. 82, 406 (1951).
[3] Brochard, Chabbal, Chantrel, and Jacquinot, J. phys. radium 13, 433 (1952).

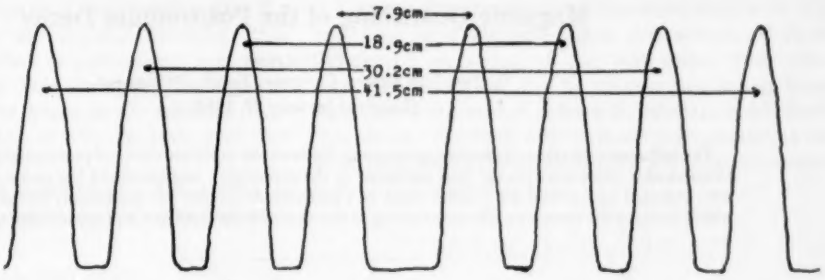

FIG. 1. Low-pressure fringe pattern corrected for intensity distribution and inherent nonlinearity λ5875.

It was found that correcting for the characteristic curve of the photographic plate did not affect the measured values of ring diameters. The traces were then corrected for the nonlinear dispersion of the Fabry-Perot, using a quadratic equation, and ring diameters measured on the corrected trace (Fig. 1). The weak component is omitted since ring diameters were measured only on the strong component peaks.

RESULTS AND CONCLUSIONS

The final measurements appear in Table I. From the scattering of the data and also by analyzing the resolution of the instrument it is felt that a probable error of about 2 percent in the pressure shift is indicated. With this error limit the shifts must be greater than about 0.008 cm^{-1} to be significant. Since the mean of our measurements is 0.0074 cm^{-1}, we conclude that over the range of pressures from 0.05 to 20 mm, pressure shift in λ5875 is negligible to this magnitude.

If these results are compared with those of Fred *et al.*,[2] a distinct disagreement is seen. They give a shift of 0.0232 cm^{-1} toward higher frequency as the pressure increases from a few tenths of a millimeter to about 5 mm. Over the pressure range used in the present work, therefore, a pressure shift of about 0.1 cm^{-1} would be expected, especially since electrical cleanup would have reduced the actual pressure range in their sealed-off tubes. Our result is not only at least an order of magnitude less than this figure but is in the opposite sense; that is, the line, if at all, is shifted to lower frequency as the pressure increases.

TABLE I. Pressure shift in λ5875 determined from corrected traces. Calculated on basis of range between orders, $D=1/2t=0.4016$ cm^{-1}, for $t=1.245$ cm.

	Average distance between orders cm	Average shift per order cm	Shift cm^{-1}
Plate I	5.27	0.088	0.0067
Plate II	5.25	0.088	0.0067
Plate III	5.60	0.113	0.0081
Plate IV	5.30	0.100	0.0076
Plate V	5.31	0.075	0.0057
Plate VI	5.42	0.125	0.0093
		Average shift = 0.0074 cm^{-1}	

Magnetic Quenching of the Positronium Decay

OTTO HALPERN
% American Express Company, Zurich, Switzerland
(Received January 27, 1954)

The influence of static and alternating magnetic fields on the radiative decay of positronium is investigated theoretically. Equations for the time variation of the probability amplitudes of the *ortho-* and *para*-states are presented and solved for various cases of experimental interest. In particular, formulas are derived which describe the resonance effects occurring in the case of a constant and a perpendicular alternating field.

I. INTRODUCTION

IN recent years, experiments by Deutsch[1] and his collaborators have given us a very detailed insight into the structure and decay of positronium. The original experiments have been later on somewhat extended by other authors.[2]

The main achievement of the work of Deutsch was the observation of the theoretically postulated[3] three-quantum decay of the *ortho*-form of positronium, as well as an insight into the modifications of this three-quantum decay which are produced by static or alternating magnetic fields.

It had been shown theoretically[3] that the lifetime of the *ortho*-form of positronium is about 1100 times as large as that of the *para*-form. This is due to the fact that two antiparallel light quanta, the decay product of *para*-positronium, cannot carry a resultant angular momentum of the value $h/2\pi$ with them, which is the original angular momentum of *ortho*-positronium. This leads to a three-quantum decay of *ortho*-positronium with a correspondingly increased life-time as compared with *para*-positronium which decays into two quanta. The observation[1] of the three-quantum decay constituted the first significant experimental advance.

If the positronium is brought into an external magnetic field, the *ortho-* and *para*-states become mixed up. This leads to possible two-quantum decays of *ortho*-states and thereby to a diminution of the observed three-quantum coincidences. Theory and experiment agree in the conclusion that only one of the three *ortho*-states is involved in this change if a homogeneous static magnetic field is applied; only the *ortho*-state with a vanishing component of its angular momentum with respect to the direction of the magnetic field combines with the *para*-state.

A further refinement of the experiment[3] consisted in the use of the by now classical method of applying a small alternating magnetic field perpendicular to the direction of the large constant magnetic field. One can thereby induce transitions between the two *ortho*-states with finite projection of their angular momenta upon the direction of the constant magnetic field and the remaining *ortho-* and *para*-states. Thus an additional quenching of the three-quantum decay can be made observable[3] which is sharply dependent upon the frequency of the alternating magnetic field.

The papers of Deutsch and his collaborators have already given a semiquantitative treatment of these data. Since the basis of this treatment is largely formed by analogies, the meaning of which may not always be unambiguous, it seemed appropriate[4] to present a theoretical discussion of these phenomena which goes back to first principles by studying the time variation of the probability amplitudes of the various states in dependence upon the external magnetic fields. The present paper, the publication of which has been unduly delayed for external reasons, will present such calculations in detail and thereby also cover some limiting cases for which the method of analogies would not seem to be sufficient.

II. THE MATRIX ELEMENTS OF THE PERTURBING MAGNETIC ENERGY

We denote by $\varphi_e(1)$, $\varphi_e(2)$ the eigenfunctions of the electron with its spin parallel and antiparallel to the z axis, with $\varphi_p(1)$, $\varphi_p(2)$ the eigenfunctions of the positron in the corresponding states. If we then neglect very small corrections of relativistic order of magnitude we can write the eigenfunctions of the *para-* and *ortho*-ground states of positronium as follows:

$$\psi_1=\varphi_e(1)\varphi_p(1), \tag{1a}$$

$$\psi_0=[\varphi_e(1)\varphi_p(2)+\varphi_e(2)\varphi_p(1)]/\sqrt{2}, \tag{1b}$$

$$\psi_{-1}=\varphi_e(2)\varphi_p(2), \tag{1c}$$

$$\psi=[\varphi_e(1)\varphi_p(2)-\varphi_e(2)\varphi_p(1)]/\sqrt{2}. \tag{1d}$$

The magnetic perturbation terms of the Hamiltonian in the presence of a constant magnetic field along the z axis and a variable magnetic field along the x axis are given by the expression

$$H_m=\frac{eh}{4\pi mc}[H_z(\sigma_{ez}-\sigma_{pz})+H_x\cos\omega t(\sigma_{ex}-\sigma_{px})]. \tag{2}$$

In (2) the meaning of all symbols is conventional; σ_e and σ_p denote, respectively, the matrices of the spin vector with the eigenvalues ± 1.

[1] M. Deutsch and S. C. Brown, Phys. Rev. **85**, 1047 (1952); there are also references to earlier literature.
[2] J. Wheatley and D. Halliday, Phys. Rev. **88**, 424 (1952).
[3] A. Ore and J. L. Powell, Phys. Rev. **75**, 1696 (1949).
[4] O. Halpern, Phys. Rev. **88**, 164 (1952).

One notices by inspection that the magnetic part H_m of the Hamiltonian has no diagonal elements; this shows that the Zeeman effect of positronium is at least quadratic in the magnetic field-strength. The physical reason for this fact is to be found in the opposite signs of the magnetic moments of the electron and the positron in (2).

The z component of the magnetic field has, as was to be expected, only one nonvanishing (nondiagonal) matrix element

$$M_z=\psi_0 H_m\psi=2ehH_z/4\pi mc. \tag{3}$$

The x component has nonvanishing matrix elements only in reference to states with different total angular momentum:

$$M_x=\psi_1 H_m\psi=\psi_{-1}H_m\psi=\sqrt{2}ehH_x\cos\omega t/4\pi mc. \tag{4}$$

We are now prepared to study the effect of the various magnetic fields on the decay of the two forms of positronium. To make things simpler, we first consider only the case of a static magnetic field.

III. QUENCHING IN A CONSTANT MAGNETIC FIELD

We denote by a_1, a_0, a_{-1}, and a the amplitudes of the four different positronium spin states. The subscripts indicate the magnitude of the projection of j on the z axis in the *ortho*-states; a without subscript stands for the amplitude of the *para*-state ($j=0$). The energy difference between the *ortho*-states and the *para*-state in the absence of external perturbations shall be denoted by $h\omega_0/2\pi$. Since, as shown in (3), there exist no matrix elements of the Hamiltonian between states of unequal m, the amplitudes a_1 and a_{-1} decay as they do in the field-free case.

For the amplitudes a_0 and a we now have the following equations:

$$\frac{da_0}{dt}=-\frac{2\pi i}{h}M_z a e^{i\omega_0 t}-\gamma_1 a_1, \tag{5a}$$

$$\frac{da}{dt}=-\frac{2\pi i}{h}M_z a_0 e^{-i\omega_0 t}-\gamma a. \tag{5b}$$

γ_1 and γ denote, respectively, the amplitude decay constants of the *ortho*- and *para*-states. Since the lifetimes of these states are 1.3×10^{-7} sec and 1.2×10^{-10} sec, respectively, we have for γ_1 and γ the values 3.7×10^{6} sec^{-1} and 4×10^{9} sec^{-1}.

Introducing the expressions,

$$a_0=b_0 e^{-\gamma_1 t}, \tag{6a}$$

$$a=be^{-\gamma t}, \tag{6b}$$

one obtains

$$\frac{db_0}{dt}=-\frac{2\pi i}{h}M_z b e^{i\omega_0 t}e^{-(\gamma-\gamma_1)t}, \tag{7a}$$

$$\frac{db}{dt}=-\frac{2\pi i}{h}M_z b_0 e^{-i\omega_0 t}e^{(\gamma-\gamma_1)t}. \tag{7b}$$

Because the exponents in the exponentials of (7a) and (7b) have opposite signs, this system of linear differential equations of the first order with time-dependent coefficient can be transformed into a linear equation of the second order with constant coefficients. One solves (7a) for b, differentiates with respect to the time, and inserts the expression for db/dt thus obtained into (7b). This leads to

$$\ddot{b}_0+\dot{b}_0(i\omega_0+\gamma')+b_0\frac{4\pi^2}{h^2}M_z^2=0, \tag{8}$$

$$\gamma'=\gamma-\gamma_1\gg\gamma_1. \tag{9}$$

Equation (8) gives for b_0 the expression

$$b_0=C_1e^{\alpha_1 t}+C_2e^{\alpha_2 t}, \tag{10}$$

with

$$\alpha_1=-\frac{i\omega_0+\gamma'}{2}+\frac{1}{2}\left((i\omega_0+\gamma')^2-\frac{16\pi^2}{h^2}M_z^2\right)^{\frac{1}{2}}, \tag{11a}$$

$$\alpha_2=-\frac{i\omega_0+\gamma'}{2}-\frac{1}{2}\left((i\omega_0+\gamma')^2-\frac{16\pi^2}{h^2}M_z^2\right)^{\frac{1}{2}}. \tag{11b}$$

For $\gamma'=0$, (11) reduces to

$$ih\alpha_{1,2}=\frac{h\omega_0}{2}\pm\left(\left(\frac{h\omega_0}{2}\right)^2+M_z^2\right)^{\frac{1}{2}}. \tag{12}$$

The original amplitudes a_0 and a are then given by expressions of the type:

$$a_0=C_1e^{(\alpha_1-\gamma_1)t}+C_2e^{(\alpha_2-\gamma_1)t}, \tag{13a}$$

$$a=D_1e^{(\alpha_1+i\omega_0-\gamma_1)t}+D_2e^{(\alpha_2+i\omega_0-\gamma_1)t}, \tag{13b}$$

$$C_1\sim D_1,\quad C_2\sim D_2. \tag{14}$$

Since $\omega_0\gg\gamma'$, α_1 and α_2 are to a first approximation given by

$$\alpha_1=i\frac{4\pi^2M_z^2}{h^2\omega_0}-\gamma'\frac{4\pi^2M_z^2}{h^2\omega_0^2}, \tag{15a}$$

$$\alpha_2=-(i\omega_0+\gamma')-\alpha_1. \tag{15b}$$

It follows from (13a) and (13b) that one can form linear combinations of the wave functions (1b) and (1d) which decay according to a simple exponential law; if we put for $t=0$,

$$C_2=0,\quad \psi_0=\frac{C_1}{(C_1^2+D^2)^{\frac{1}{2}}},\quad \psi=\frac{D_1}{(C_1^2+D_1^2)^{\frac{1}{2}}} \tag{16a}$$

or

$$C_1=0,\quad \psi_0=\frac{C_2}{(C_2^2+D_2^2)^{\frac{1}{2}}},\quad \psi=\frac{D_2}{(C_2^2+D_2^2)^{\frac{1}{2}}}, \tag{16b}$$

then these aggregates have decay constants $\gamma_1+(\gamma'4\pi^2M_z^2/h^2\omega_0^2)$ and $\gamma-(\gamma'4\pi^2M_z^2/h^2\omega_0^2)$, respectively.

The physical interpretation of this result is clear. In the absence of decay, $\gamma_1=\gamma=0$, the expressions (11), (12) and (16) are the well-known wave functions of a magnetic system which has vanishing diagonal and nonvanishing off-diagonal matrix elements of the magnetic Hamiltonian. The energy-splitting given by (12) is the familiar generalization of the Landé formula.

The discussion for nonvanishing γ_1 and γ can best be carried out remembering the order of magnitude of the various quantities involved. We have $\omega_0\sim10^{12}$ sec^{-1}; γ_1 and γ (or γ') are about $-3.7\ .10^6$ and 4×10^9 sec^{-1} respectively, and $\gamma'4\pi^2M_z^2/h^2\omega_0^2$ becomes for $H_z\sim9000$ gauss about $\gamma'10^{-2}$. One thus sees easily that the imaginary parts of (11) (the energy splitting) are very little affected by the spontaneous decay. The real part of $\alpha_2-\gamma_1$, i.e., essentially the decay constant of the *para*-state, is hardly changed by the presence of a constant magnetic field. The decay of a_0, on the other hand, is strongly influenced by a sizable magnetic field. One sees readily that for values of H_z larger than, say, 2000 gauss the term $\gamma'4\pi^2M_z^2/h^2\omega_0^2$ predominates. This means that the three-quantum decay is progressively replaced by the two-quantum decay of the *para*-state. For $H_z\sim9000$ gauss only a few percent of the three-quantum decays are left; this means experimentally that only $\frac{2}{3}$ of all three-quantum processes originating from the states with the amplitudes a_1 and a_{-1} remain.

It should perhaps be re-emphasized that it is not just the small fraction $4\pi^2M_z^2/h^2\omega_0^2$ of *para*-state present in a_0 that decays rapidly. It is, as shown by (13a) and (13b), the whole linear combination (16a) which decays at the rate $\gamma_1+(\gamma4\pi^2M_z^2/h^2\omega_0^2)$.

IV. THE EFFECT OF AN ADDITIONAL ALTERNATING MAGNETIC FIELD

For the treatment of this problem it is advantageous to change the basic wave functions. It should be noted that the linear combinations (16a) can be made mutually orthogonal and are also orthogonal to the states with the amplitudes a_1 and a_{-1}. If we introduce these expressions in place of (1b) and (1d), we have thereby included the effect of H_z, which as mentioned before does not have matrix elements between states with m different from zero. The equations of variation of constants therefore contain M_x only. We continue to use the notation for the amplitudes of the states $a_1\cdots a$ which will not lead to any misunderstanding.

Keeping in mind the results of Sec. II, one thus arrives at the following equations:

$$\frac{da_1}{dt}=-\frac{2\pi i}{h}\{M_xa_0e^{-i\omega' t}\beta+M_xae^{+i\omega t}\}-\gamma_1a_1, \quad (17a)$$

$$\frac{da_0}{dt}=-\frac{2\pi i}{h}\{M_x\beta e^{i\omega' t}(a_1+a_{-1})\}-\gamma''a_0, \quad (17b)$$

$$\frac{da_{-1}}{dt}=-\frac{2\pi i}{h}\{M_x\beta a_0e^{-i\omega' t}+M_xae^{i\omega t}\}-\gamma_1a_{-1}, \quad (17c)$$

$$\frac{da}{dt}=-\frac{2\pi i}{h}\{M_xe^{-i\omega t}(a_1+a_{-1})\}-\gamma a, \quad (17d)$$

$$\beta=2\pi M_z/h\omega_0, \quad (18a)$$

$$\gamma''=\gamma_1+\gamma'\beta^2, \quad (18b)$$

$$\omega'=\text{imaginary part of }\alpha_1. \quad (18c)$$

A study of this system of equations shows that no simple reduction to a linear equation of higher order with constant coefficients is possible. This has its origin in the factor $\cos\omega t$ in M_x which cannot be eliminated as was done with the exponentials in III. But closer attention to the physical side of the problem allows us to introduce simplifications which lead in the end to another linear equation of the second order with constant coefficients.

One has to keep in mind that we are looking for resonance effects which will occur when $\omega'=\omega$, or in other words when h times the frequency of the alternating field equals the energy difference between the *ortho*-states $a_{\pm1}$ and a_0 created by the constant magnetic field H_z. This energy difference is given by the imaginary part $(h/2\pi)\alpha_1$. General dispersion theory leads to the experimentally confirmed view that the influence of the alternating field will be very small off resonance. This means first of all that all terms containing a in (17) can be dropped; in fact the whole equation (17d) may be neglected. The frequency of the alternating field will always be very small compared with ω_0.

Furthermore, if we write

$$\cos\omega t=\tfrac{1}{2}(e^{i\omega t}+e^{-i\omega t}),$$

than we see that in (17a) and (17c) only the term $e^{i\omega t}$, while in (17b) only the terms $e^{-i\omega t}$, can give rise to a resonance phenomenon. The second term produces only dispersion effects which average out during the time of observation. One thus obtains the following three equations:

$$\frac{da_1}{dt}=-\frac{2\pi i}{2h}M_x'\beta a_0e^{-i(\omega'-\omega)t}-\gamma_1a_1, \quad (19a)$$

$$\frac{da_0}{dt}=-\frac{2\pi i}{2h}M_x'\beta(a_1+a_{-1})e^{i(\omega'-\omega)t}-\gamma''a_0, \quad (19b)$$

$$\frac{da_{-1}}{dt}=-\frac{2\pi i}{2h}M_x'\beta a_0'e^{-i(\omega'-\omega)t}-\gamma_1a_{-1}, \quad (19c)$$

$$M_x=M_x'\cos\omega t. \quad (20)$$

We introduce again in analogy with III the quantities

$$a_1=b_1e^{-\gamma_1t}, \quad (21a)$$

$$a_0=b_0e^{-\gamma''t}, \quad (21b)$$

$$a_{-1}=b_{-1}e^{-\gamma_1t}, \quad (21c)$$

and obtain for the quantities b the equations

$$\frac{db_1}{dt}=-\frac{\pi i}{h}M_x'\beta b_0 e^{-i(\omega'-\omega)t}e^{-(\gamma''-\gamma_1)t}, \tag{22a}$$

$$\frac{db_0}{dt}=-\frac{\pi i}{h}M_x'\beta(b_1+b_{-1})e^{i(\omega'-\omega)t}e^{(\gamma''-\gamma_1)t}, \tag{22b}$$

$$\frac{db_{-1}}{dt}=-\frac{\pi i}{h}M_x'\beta b_0 e^{-i(\omega'-\omega)t}e^{-(\gamma''-\gamma_1)t}. \tag{22c}$$

Solving (22b) for b_1+b_{-1}, and differentiating with respect to the time, we obtain again from (22a) and (22c) the desired equation

$$\ddot{b}_0+\dot{b}_0[i(\omega-\omega')+\gamma_1-\gamma'']+\frac{2\pi^2}{h^2}\beta^2M_x'^2b_0=0. \tag{23}$$

This gives for b_0 the expression

$$b_0\sim e^{-\delta t}, \tag{24}$$

with

$$\delta^2+\delta[i(\omega-\omega')+\gamma_1-\gamma'']+\frac{2\pi^2}{h^2}\beta^2M_x'^2=0. \tag{25}$$

One finally obtains for a_0 a time dependence of the form

$$a_0=Ae^{(\delta_1-\gamma'')t}+Be^{(\delta_2-\gamma'')t}, \tag{26}$$

$$\delta_1=-\frac{i(\omega-\omega')+\gamma_1-\gamma''}{2}+\frac{1}{2}\left([i(\omega-\omega')+\gamma_1-\gamma'']^2-\frac{8\pi^2}{h^2}\beta^2M_x'^2\right)^{\frac{1}{2}}, \tag{27a}$$

$$\delta_2=-\frac{i(\omega-\omega')+\gamma_1-\gamma''}{2}-\frac{1}{2}\left([i(\omega-\omega')+\gamma_1-\gamma'']^2-\frac{8\pi^2}{h^2}\beta^2M_x'^2\right)^{\frac{1}{2}}. \tag{27b}$$

The successive use of (19), (21), and (26) together with the values of δ as given by (27), permits us to determine the decay times of the various states in the presence of both magnetic fields; the parametric dependence on ω gives us the behavior at and near resonance. Two limiting cases are of particular interest and lead to simple results especially at resonance.

(1) H_x small, or, more quantitatively,

$$\gamma''-\gamma_1\ll(3\pi/h)\beta M_x'. \tag{28}$$

We can then expand the square root in (27) and obtain at resonance the following values for δ_1 and δ_2:

$$\delta_1=+\frac{2\pi^2\beta^2M_x'^2}{h^2(\gamma''-\gamma_1)}, \tag{29a}$$

$$\delta_2=\gamma''-\gamma_1-\frac{2\pi^2\beta^2M_x'^2}{h^2(\gamma''-\gamma_1)}. \tag{29b}$$

$\delta_1-\gamma''$ obviously gives essentially the decay time of the state with vanishing m, which is only slightly affected by the alternating field. This can be understood physically by observing that the rate of decay is large compared with the rate of transition to one of the other *ortho*-states.

$\delta_2-\gamma''$, on the other hand, leads by resubstitution easily to that quantity which now represents essentially the decay rate of the two *ortho*-states. We find for it:

$$\delta_2-\gamma''=-\gamma_1-\frac{2\pi^2\beta^2M_x'^2}{h^2(\gamma''-\gamma_1)}.$$

The percentage of the increase of the decay rate is given by

$$\frac{2\pi^2\beta^2M_x'^2}{h^2\gamma_1(\gamma''-\gamma_1)}\sim\frac{e^2H_x^2}{4m^2c^2\gamma\gamma_1}, \tag{30}$$

This value is well observable for moderate H_x since the decay rate of the pure *ortho*-state is in that case no longer overwhelmingly large compared with the rate of transition to the composite state with $m=0$ from which two-quantum decay processes are now possible.

(2) H_x large, or, more quantitatively,

$$\gamma''-\gamma_1\leq\frac{8\pi^2}{h^2}\beta^2M_x'^2. \tag{31}$$

Then for the case of resonance the real parts of δ_1 and δ_2 become equal. Substitution into the relevant equations of the text shows that then *all* three states decay with a decay constant $\frac{1}{2}(\gamma_1+\gamma'')$. This means that the states with $m=\pm1$ decay mostly through two-quantum processes; the state $m=0$ is now partly "dequenched" and decays with a larger percentage of three-quantum processes than in the absence of the alternating field. It should be observed that this effect is independent of the magnitude of H_x as long as the relation (31) holds true.

Absorption Coefficients of Air and Nitrogen for the Extreme Ultraviolet*

J. P. CURTIS
University of Colorado, Boulder, Colorado
(Received January 12, 1954)

A method involving the use of two photomultiplier tubes as detectors has been developed for absorption studies in the extreme ultraviolet. The monochromator was a modified grazing-incidence spectrograph. A capillary discharge tube was employed as a source. Absorption coefficients for dry air and nitrogen were measured in the range 150A–1000A. The total oscillator strength of nitrogen for the transitions appropriate for this range was computed to be 3.2.

INTRODUCTION

DURING an investigation of photometric methods for gas absorption measurements in the spectral region below 1000A some absolute absorption coefficients of air and nitrogen were determined. These gases were studied because of the importance of knowledge of absorption coefficients for the interpretation of solar ultraviolet spectra obtained in rocket instruments. Only one paper[1] presenting air absorption data and two[2,3] concerned with nitrogen absorption were found after a careful survey of the literature. These did not cover the whole of the range included here.

DESCRIPTION OF TECHNIQUE AND APPARATUS

An attempt was made to overcome some of the difficulties common to the kind of photometry used in the vacuum ultraviolet. In order to eliminate the uncertainties of film calibration, photomultiplier tubes (1P28) coated with sodium salycilate were used as detectors.

TABLE I. Measured absolute absorption coefficients (in cm^{-1}) for dry air and for dry nitrogen at various wavelengths in the extreme ultraviolet. K_f and K_n refer to the coefficients determined by using as the path lengths the distances from the slit to the far cell and to the near cell, respectively. K_r is a coefficient computed on the basis of absorption of the gas between the two cells.

λ (angstroms)	K_f N₂	K_f Air	K_n N₂	K_n Air	K_r N₂	K_r Air	K_{Av} N₂	K_{Av} Air
150	81	159					81±40	159±60
202	70	155					70±30	155±50
279	112	162					112±20	162±30
303	125	143					125±30	143±30
374	147	208					147±50	208±50
434	195	225					195±20	225±25
507	268	368	273	402	277	418	273±15	396±30
525		407		390	460	510	460±100	460±100
552	296		298		308		301±15	
554	471	405	254	235	640	585		
580	357	354	346	342	349	339	351±20	345±30
598	313	368					323±40	368±40
608	310	323	341	349	340	340	330±20	335±20
625	416	413	415	387	417	463	413±20	416±20
685	342	359					342±50	359±50
702	353	359					353±40	350±40
760	367	350					367±30	350±30
790	278	298	283	310	382	343	281±15	317±30
835	54	86					54±10	86±10
990	126	142					162±35	142±30

An effort was also made to eliminate the effect of intensity fluctuations found in ultraviolet light sources commonly used. A Lyman-type source was finally employed. This source consisted of a capillary tube through which a 0.5-mf condenser charged to approximately 10 kv was discharged at one-second intervals. A mixture of hydrogen and a small amount of air at a pressure of about 200 microns was allowed to flow through the tube. Many spectral lines of ionized oxygen, nitrogen, and silicon as well as continuous radiation, were obtained from below 150A to the visible. A special mounting for a grazing incidence spectrograph was constructed. The setup is shown in Fig. 1. The arrangement has the advantage of utilizing two detectors simultaneously (which are pointed toward the grating for all positions) and of providing a linear wavelength scale. The source slit was 25 microns wide and the monochromating slit was chosen to include about a two-angstrom band width. The grating used was a one-meter concave replica with 15 000 rulings per inch set at a grazing angle of 10°.

Two detectors were used for the following reasons. First, it was possible to check the linearity of the detectors. This was accomplished by varying the light intensity of the source and observing the constancy of the ratio of the outputs of the detectors. It was found that the detectors were linear for the intensity range used. The second objective of this arrangement was to provide a method of absorption measurement that was independent of fluctuation in the source intensity. The absorption coefficient calculated from the ratio of outputs of the detectors was not a function of the source intensity as long as noise and scattered light were not appreciable.

Absorption coefficients were determined by measuring the outputs of the two detectors as a function of the chamber pressure. The detector outputs were first read after a high vacuum was attained in the chamber. Gas was admitted into the chamber until some absorption could be detected. The detector outputs were recorded after the pressure became constant. This process was repeated with increasing steps in pressure until nearly complete absorption was obtained. The

* The research reported in this paper has been sponsored by the Geophysics Research Directorate of the Air Force Cambridge Research Center, Air Research and Development Command.

[1] E. G. Schneider, J. Opt. Soc. Am. **30**, 128 (1940).
[2] Weissler, Lee, and Mohn, J. Opt. Soc. Am. **42**, 84–90 (1952).
[3] K. C. Clark, Phys. Rev. **87**, 271 (1952).

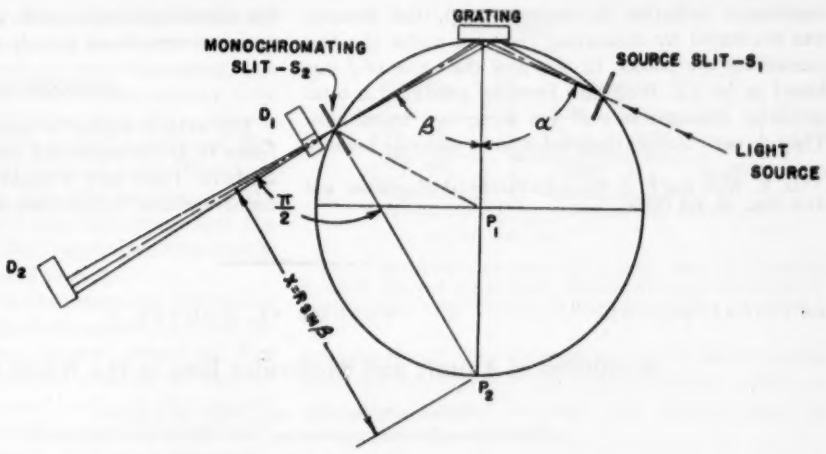

FIG. 1. The monochromator used for measuring the absorption coefficients. The light from a capillary discharge strikes the grating at grazing incidence and is focused along the Rowland circle. The monochromating slit directs the light in a narrow wave band to two coated photomultiplier tubes, D_1 and D_2. (D_1 is above D_2). The two-tube method enables one to eliminate errors arising because of source intensity fluctuations.

chamber was then pumped to high vacuum and the zero reading obtained again. Five readings were taken for each point.

The following method was used to record the light intensity data. The output pulses from the two detectors were individually integrated and used to deflect an oscilloscope. The detector nearest the grating deflected the beam horizontally while the one farthest away deflected the beam vertically. The screen was photographed and the film read later with a measuring eyepiece. All the equipment was operated from a regulated ac supply.

A calibrated Pirani gauge was used for pressure measurements and a liquid nitrogen trap on the gas inlet supply line was used to dry the gases.

Both the output of the two detectors individually and the ratio of the outputs were plotted on semilogarithmic paper for each spectral region used. In all cases a straight line could be fitted to these points in accordance with Beer's Law. This law, in the form

$$I=I_0\exp\left(-\frac{PT_0Kx}{P_0T}\right),$$

was used to calculate the usual linear absorption coefficient K in cm^{-1}. Here K is the reciprocal of the path length (referred to conditions of normal temperature and pressure) required to reduce the intensity to $1/e$ of the original intensity; x is the path length for the detector in question (or the path difference when the ratio of the two detectors is used). Three absorption coefficients were obtained. These were the two values determined from the detectors taken individually and the one value determined from the ratio of the detector outputs.

RESULTS AND DISCUSSION

Table I lists the results of these measurements. In some cases the far detector alone was used. As this detector could "see" only the illuminated part of the grating it had a better signal to scattered light ratio. There was too much scattered light recorded by the near detector in the region below 500A to make the benefits of the two detector method worth while. In only one case did the indicated coefficient from the two detectors fall outside the estimated accuracy. This is in the vicinity of 554A. This was found to be due to a rapid variation in the absorption with wavelength and a slight misalignment of the far detector.

Figure 2 shows the measured points for nitrogen plotted on a frequency scale. The limits of the Hopfield-Rydberg series and the Worley-Jenkins-Rydberg series are indicated. As one expects continuous absorption at the frequencies above these limits, the total oscillator strength f for these transitions was computed from the formula

$$\int K d\bar{\nu}=\frac{\pi Ne^2}{mc^2}f.$$

Here $\bar{\nu}$ is the wave number. Since the measurements represent the average K over a short wavelength band (several lines were usually included together with

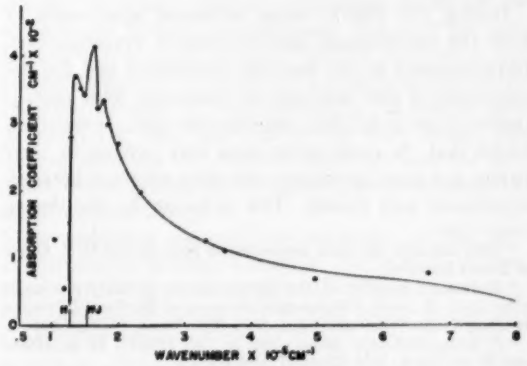

FIG. 2. Absorption coefficient of dry N_2 as a function of wave number. The observed points are connected by a smooth curve for the purpose of estimating the oscillator strength f.

continuous radiation in each setting), the integral was evaluated by measuring the area under the line connecting the points. In this way the value of f was found to be 3.2. Wulf and Deming[4] predicted a total oscillator strength of 3.27 for these two transitions. They do not consider their value to be accurate because the calculations were made on the basis of dispersion measurements down to only 1900A.

[4] O. R. Wulf and L. S. Deming, Terrestrial Magnetism and Atm. Elec. 43, 284 (1938).

ACKNOWLEDGMENTS

The author wishes to express his gratitude to Professor W. B. Pietenpol and Professor W. A. Rense and to Barbara Todd and Donald Erb for their help and encouragement in this research.

PHYSICAL REVIEW VOLUME 94, NUMBER 4 MAY 15, 1954

Mobilities of Atomic and Molecular Ions in the Noble Gases*

MANFRED A. BIONDI AND LORNE M. CHANIN
Westinghouse Research Laboratories, East Pittsburgh, Pennsylvania

(Received February 9, 1954)

A method is described for measuring the mobilities of ions of near-thermal energy. A pulse of ions is generated in a discharge region and passes through a grid into a drift region where a uniform electric field causes the ions to move to a collector electrode. The mobilities are determined from measurements of the transit time of the ions in crossing the drift space. The experimental mobility values for thermal energy ions moving in their parent gases at 300°K and a gas density of 2.69×10^{19} atoms/cc are $\mu_0=10.5$ cm²/volt-sec (He^+), 20.3 (He_2^+), 4.0 (Ne^+), 6.5 (Ne_2^+), 1.60 (A^+), 2.65 (A_2^+), 0.90 (Kr^+), 1.21 (Kr_2^+), 0.58 (Xe^+), and 0.79 (Xe_2^+). These values are in good agreement with available theoretical results. Our measurements join smoothly at higher ion energies with the measurements made by Hornbeck and by Varney except in the case of A_2^+. In addition, our results indicate that earlier measurements at near-thermal energy by Tyndall and collaborators refer to the molecular ions in helium and neon, and to the atomic ions in krypton and xenon.

I. INTRODUCTION

THE mobilities of ions in gases have been the subject of numerous investigations during the last fifty years. The continuing interest in this topic arises from improvements in both the experimental and theoretical situations. Prior to 1930, impurities in the gas samples used led to conflicting results concerning the experimentally determined values of the mobilities.[1] Theoretical calculations of that period followed classical treatments based on ion-atom interactions of electrostatic origins.[2]

During the 1930's, major advances were made in both the experimental and theoretical investigations. Improvements in gas handling techniques and the development of new methods for measuring ionic mobilities[3] resulted in reliable, reproducible data. It was then found that, in cases other than ions moving in their parent gas, good agreement was often obtained between experiment and theory. The inclusion in the theory of charge exchange as part of the ion-atom interaction permitted the accurate calculation of the mobility of a positive ion in its parent gas for the particular case of He^+ in helium.[4] Unfortunately, in this one case in which the new theory could be tested, the measured mobility was roughly twice the theoretical value. As a result it was concluded that the theoretical treatment had overestimated the effect of the charge exchange interaction on the ionic mobility.

The next significant changes in our understanding of ionic mobilities occurred during the post-war period. The recently developed electronic timing and microwave techniques were used in new types of apparatus for studying the behavior of ions in gases. The data obtained from these experiments[5,6] gave a mobility for He^+ in helium which agreed with the theoretical value, but therefore disagreed with the previous measurements. It had been suggested by Meyerott[7] that the earlier measurements applied to the molecular helium ion, He_2^+, moving in helium. The existence of stable diatomic ions of noble gases, e.g. He_2^+, had been experi-

* This research has been supported in part by the U. S. Office of Naval Research.

[1] A detailed account of the history of ion mobility studies is given by L. B. Loeb, *Fundamental Processes of Electrical Discharge in Gases* (John Wiley and Sons, Inc., New York, 1939), Chap. I.

[2] P. Langevin, Ann. chim. phys. 5, 245 (1905); H. R. Hasse and W. R. Cook, Phil. Mag. 12, 554 (1931).

[3] A. M. Tyndall and C. F. Powell, Proc. Roy. Soc. (London) A134, 125 (1931) and A. M. Tyndall, *The Mobility of Positive Ions in Gases* (Cambridge University Press, Cambridge, 1938).

[4] H. S. W. Massey and C. B. O. Mohr, Proc. Roy. Soc. (London) A144, 188 (1934).

[5] M. A. Biondi and S. C. Brown, Phys. Rev. 75, 1700 (1949); 76, 302 (1949); A. V. Phelps and S. C. Brown, Phys. Rev. 86, 102 (1952).

[6] J. A. Hornbeck, Phys. Rev. 83, 374 (1951); 84, 615 (1951).

[7] R. Meyerott, Phys. 70, 671 (1946).

mentally demonstrated[5] in the late 1930's. Hornbeck[6] and Phelps and Brown[6] were able to observe two ions in their experiments. By using a mass spectrometer to identify simultaneously the ions whose mobility they were measuring, Phelps and Brown were able to demonstrate conclusively that the measured mobility of He^+ agreed with the theoretical value. Earlier, Hornbeck had reached this conclusion, basing his ion identification on less direct evidence, and also had found that the mobility of the second ion (He_2^+) agreed with the experimental value of Tyndall and Powell.[3]

The most recent change in the theoretical treatments occurred when Holstein,[9] devised a general method for calculating the mobility of an ion in its parent gas. The theory was used to calculate the mobility of thermal energy He^+, Ne^+, and A^+ ions moving in their parent gases. These values were found to agree quite well with extrapolations of Hornbeck's measurements which applied to ions having greater than thermal energies. The present experiment was devised to extend mobility measurements to the thermal energy range in order to obtain an accurate comparison with theory.

II. PRINCIPLE OF THE EXPERIMENT

The mobility of an ion is defined as the ratio of the drift velocity it acquires to the electric field in which it moves, that is,

$$\mu = v/E, \tag{1}$$

where μ is the mobility, v the drift velocity, and E the applied electric field. Experimental methods for determining ion mobilities are usually based on measurements of the time required for the ion to move a known distance in an applied electric field.

In the present experiment, ions generated in a discharge region (see Fig. 1) are admitted through a grid into a constant field drift region and move through the gas until they strike the collector electrode. The motion of the ions in the drift space induces a current in the external circuit. The decrease in current which occurs when the ions arrive at the collector serves to indicate the transit time of the ions. The mobility may be determined from the relation

$$\mu = d/Et_t, \tag{2}$$

where d is the separation between the grid and collector electrode, and t_t is the transit time of the ions in crossing the drift region.

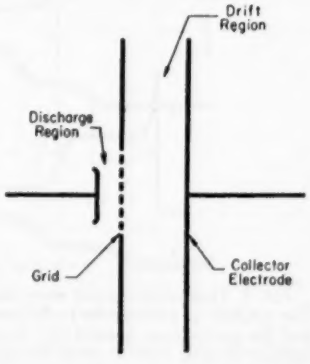

FIG. 1. Schematic arrangement of the electrodes in the mobility tube.

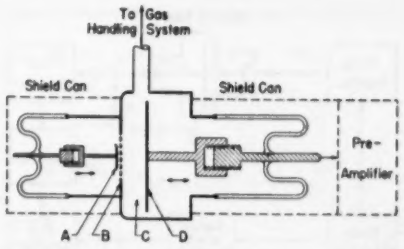

FIG. 2. Simplified drawing of the mobility tube. The discharge electrode (A) and the collector electrode (D) may be moved by means of a fine screw thread and a magnetic armature (not shown).

The generation of ions in a region outside of the drift space permits the use of small enough applied fields in the drift region so that the ions are essentially in thermal equilibrium with the gas. This technique represents an improvement over Hornbeck's method[6] in which the ions were generated by an electron avalanche in the drift space. The latter method of ion generation necessitates a *minimum* drift field which is strong enough to ionize the gas.

III. APPARATUS

The mobility tube is constructed of glass and Kovar. A simplified drawing of the tube is shown in Fig. 2. The discharge region, in which the ions are generated, is at the left. The discharge is created by the application of a short (~0.5-μsec), high-voltage pulse to electrode A. The spacing between this electrode and the grid B can be varied by means of a magnetic armature (not shown) to obtain optimum discharge conditions for various gas fillings and pressures. Some of the ions formed in the discharge move through the grid B into the drift region C. A negative dc voltage is applied to the collector electrode D, which produces the electric field in which the ions move across the drift space. The spacing between the collector electrode and the grid electrode can be changed by means of a second magnetic armature (not shown).

The collector electrode is connected to the drift voltage supply through a resistor. The induced current caused by the motion of ions in the drift space produces a voltage signal across this resistor which is approximately 10^{-4} volt in amplitude. Since a pulse of ~1000 v is used to create the ions in the discharge region, it is clear that excellent shielding is required between the discharge and drift regions. The present tube achieves

[5] D. Tuxon, Z. Physik **103**, 463 (1936); F. L. Arnot and M. B. M'Ewen, Proc. Roy. Soc. (London) **A166**, 543 (1938); **A171**, 106 (1939).

[9] T. Holstein, J. Phys. Chem. **56**, 832 (1952), and Phys. Rev. (to be published).

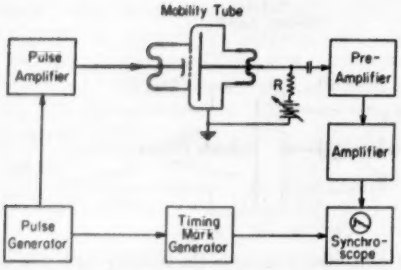

FIG. 3. Simplified block diagram of the electronic equipment used in measuring ionic mobilities.

the required degree of shielding by the use of external shield cans (the dashed lines surrounding the tube in Fig. 2) which screw onto the exterior of the metal mobility tube. The only internal coupling between the discharge and drift regions occurs through the slots in the grid which separates the two regions. The grid consists of a series of slots 0.008 in. wide, spaced 0.024 in. apart. It is found in practice that the leakage pulse from the discharge region results in negligible pickup in the collector circuit.

A simplified block diagram of the electronic equipment is given in Fig. 3. A Hewlett-Packard Model 212A Pulse Generator is used as the master timing generator. A 0.5-μsec pulse from this generator is fed to the pulse amplifier which generates a high-voltage positive pulse. This pulse is fed to the discharge electrode of the mobility tube. The electric field produced by this pulse ionizes the gas and causes the positive ions to move toward the grid. In order to create a sharply defined ion pulse in the drift region, the discharge electrode is made slightly negative ($\sim$10 v) immediately following the pulse. This sets up a retarding field which prevents ions formed in the discharge region from diffusing through the grid after the end of the pulse.

The motion of the ions in the drift space induces a current in the external circuit which is given by the relation

$$i(t)=N(t)ev/d, \tag{3}$$

where $i(t)$ is the instantaneous induced current, $N(t)$ is the number of ions moving in the drift space at the time t, e is the charge of the ions, v is their drift velocity, and d is the plate separation. If ions of more than one type are present, the resultant current is simply the sum of the contributions from each type of ion. This current is amplified by a cathode follower preamplifier which is contained in the collector electrode's shield can. The signal is further amplified by means of two Hewlett-Packard Model 450A Amplifiers and the amplifier of the Tektronix Model 511A Synchroscope. The resulting signal is fed to the y axis of the synchroscope, whose sweep is triggered by the pulse generator. The output of the timing mark generator produces intensified timing marks on the sweep trace. In order to improve the signal-to-noise ratio of the highly amplified signal, suitable filters are used at various points in the amplifiers to reduce the amplifier band width as much as is consistent with accurate reproduction of the mobility current waveform.

The gas samples used in these studies are introduced to the mobility tube by means of an ultrahigh vacuum gas handling system.[10,11] Following bakeout at 420°C for 15 hours, the system attains an ultimate vacuum of $<10^{-8}$ mm Hg and a rate of rise of contamination pressure of $<10^{-9}$ mm Hg/min. The gas samples used in these studies are Airco reagent grade gases. In all cases the source of impurities in the mobility measurements originates in the gas flasks themselves. Except in the case of argon, no further attempt has been made at purification of the Airco samples.

IV. EXPERIMENTAL MEASUREMENTS

According to Eq. (3), the instantaneous current induced in the external circuit depends on the number of ions in the drift space. Suppose that at time $t=0$ we suddenly introduce a sheet of N ions into the drift region immediately adjacent to the grid. If we neglect for the moment the effects of diffusion, all of these N ions will drift toward the collector under the action of the applied field. The current therefore shows an abrupt increase from zero to a constant value at $t=0$. At the time $t=t_t$ (the transit time required for the ions to cross the drift space) the ions all strike the collector electrode. The current will therefore abruptly drop to zero.[12] This idealized situation is illustrated by the solid curve of Fig. 4(a). In the actual experiment, diffusion

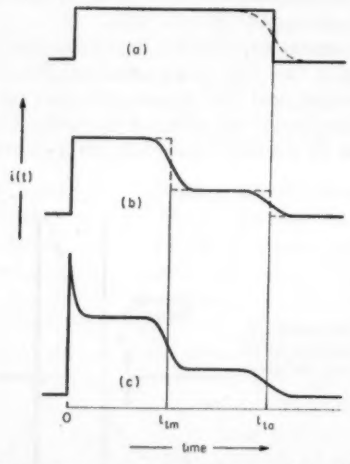

FIG. 4. Theoretical current wave forms for the mobility tube. The symbols t_{tm} and t_{ta} refer to the transit times of the molecular and the atomic ions, respectively. In part (c) the injected pulse contains roughly twice as many ions as in part (b).

[10] D. Alpert, J. Appl. Phys. 24, 860 (1953).
[11] M. A. Biondi, Rev. Sci. Instr. 24, 989 (1953).
[12] We have omitted the effect of electron ejection from the collector by the ions. In our low E/p experiments such effects are negligible, although electron ejection is observed at high E/p.

causes the sharply defined sheet of ions introduced into the drift region at $t=0$ to spread out as the ions drift toward the collector. As a result, the ions do not all strike the collector at $t=t_t$ but arrive at times distributed about t_t. The resultant current is illustrated by the dashed line in Fig. 4(a).

If ions of different mobility or charge are simultaneously present in the injected pulse, the current consists of components whose magnitudes are proportional to the product (Nev) for each ion. For example, in the case of atomic and molecular helium ions in helium, the mobility of He_2^+ is approximately twice that of He^+. If equal numbers of atomic and molecular ions move across the drift region, the resultant current pattern is as shown in Fig. 4(b).

Finally, we must consider the effect of "back" diffusion on the current wave form. The sharply defined ion pulse is injected through the grid into the drift region. As the ion pulse drifts away from the grid electrode toward the collector, the pulse simultaneously broadens as the result of diffusion. Some of the ions which diffuse back toward the grid strike the metallic grid surface and are neutralized. The result is that the number of ions in the drift space diminishes until the ion pulse has moved away from the grid electrode. The effect of this "back" diffusion is illustrated in Fig. 4(c).

An example of the observed current *vs* time wave forms is shown in Fig. 5. The width of the oscilloscope trace results from the noise in the amplified signal. A large amplifier gain is required to permit measurements at sufficiently low ion concentrations to avoid space charge effects. Unless the ion density is small, the applied drift field is distorted and the measurements are subject to unknown error. In addition, the ion pulse itself is broadened by mutual repulsion of the ions, leading to a less sharp indication of the transit time. The observed current wave form closely approximates the theoretically predicted shape[13] when the effects of diffusion and the finite ion pulse width are considered.

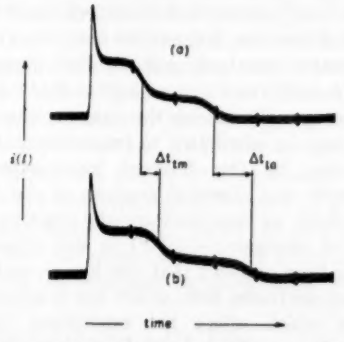

FIG. 5. Photographs of the current *vs* time wave forms for two drift distances; (a) 1.17 cm, (b) 1.54 cm. The helium pressure is 4.35 mm Hg and $E/p=5.2$ v/cm-mm Hg. The dots on the traces are 10-μsec markers.

[13] A detailed analysis of the current wave form has been carried out by I. B. Bernstein, Westinghouse Research Report R-94411-9-N (unpublished). The effect on the wave form of the conversion of atomic ions to molecular ions has not been discussed since such conversion is negligible at the pressures used in the present studies.

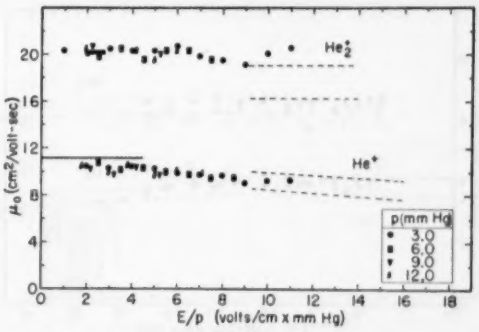

FIG. 6. Mobilities of He^+ and He_2^+ in helium. The present measurements are indicated by the symbols, Hornbeck's data by the dashed lines (mean square deviation shown), and Tyndall and Powell's measurements by the short heavy bar. The theoretical value of Massey and Mohr is shown by the solid line which is extended over the range of E/p such that $El<kT/e$.

The preceding discussion has suggested that the mobilities are determined from the transit time of the ions from the grid to the collector. Since the ions injected through the grid from the discharge region have greater than thermal energy, their motion during the first part of their transit is not characteristic of the equilibrium drift motion. In order to avoid errors due to injection velocities, measurements are actually made of the difference in transit time Δt_t, for two different drift distances. In Fig. 5(a) the grid-collector drift distance is 1.17 cm, while in Fig. 5(b) it is 1.54 cm. The differences in transit time for the molecular and the atomic ions are indicated in the figure. The ionic mobility is then calculated from the relation

$$\mu=\Delta d/E\Delta t_t, \tag{4}$$

where Δd is the difference in the drift distance.

V. RESULTS

The mobilities of atomic and molecular ions have been measured for the noble gases. It is customary to express the mobility in terms of an extrapolated value at atmospheric pressure. In the present paper, we follow Hornbeck's convention[6] and define μ_0 as the ionic mobility at a temperature of 300°K and a gas density of 2.69×10^{19} atoms/cc (equivalent to 760 mm Hg at 0°C). The results of the present measurements are shown in Figs. 6–10. We plot the mobility μ_0 *vs* the ratio of the drift field to the gas pressure E/p, which is a measure of the energy the ions gain from the field.

The results for helium are shown in Fig. 6. Our experimental data are indicated by the various symbols. The experimental values of Hornbeck[6] are indicated by the dashed lines, which show the mean square deviation

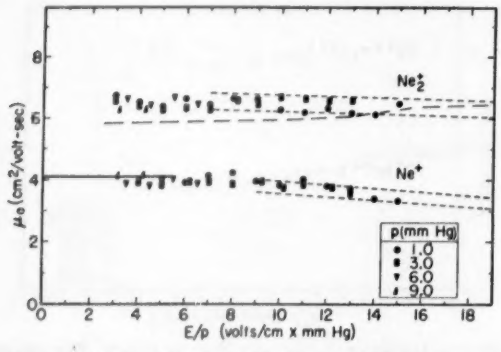

FIG. 7. Mobilities of Ne^+ and Ne_2^+ in neon. The present measurements are indicated by the symbols, Hornbeck's by the short dashed lines, Tyndall's by the long dashed line, and Holstein's theoretical value by the solid line.

in his data. The heavy line at the upper left of the figure represents Tyndall and Powell's measurements.[3] It will be seen that the various measurements agree within experimental error when proper identification is made of the ions under study.

Our measurements for He^+ agree quite well with the theoretical value of Massey and Mohr,[4] indicated by the solid line, which applies to ions which are in thermal equilibrium with the gas. In order to plot the theoretical value over the applicable range of the experimental variable E/p, we have made the assumption that the ions remain essentially in thermal equilibrium with the gas so long as

$$El \ll kT/e, \tag{5}$$

where l is the ionic mean free path, T the gas temperature, and e the ionic charge. Wannier[14] has shown that in the case of constant mean free time between collisions the average energy $\bar{u}$ of the ions is simply

$$\bar{u} = Mv^2 + \tfrac{3}{2}kT, \tag{6}$$

where M is the mass and v the drift velocity of the ions.

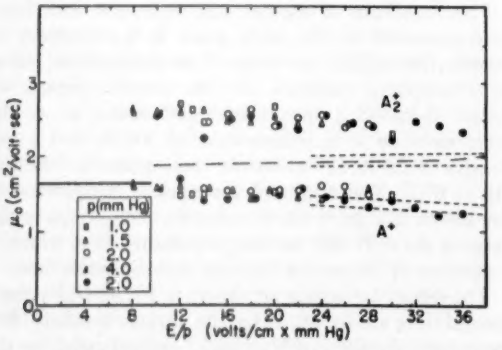

FIG. 8. Mobilities of A^+ and A_2^+ in argon. The solid circles refer to measurements made after running a magnesium clean-up arc for 24 hours. The coding of the various lines is the same as in Fig. 7.

[14] G. Wannier, Phys. Rev. 83, 281 (1951).

In the present case the ionic mean free path, rather than the time between collisions, is nearly constant and hence Wannier's theory is only qualitatively applicable. At $E/p=1.5$, the lowest value for which experimental measurements are obtained, Eq. (6) indicates that the energy acquired from the drift field is less than ten percent of thermal energy. Thus, according to the criteria either of Eq. (5) or (6), we are sufficiently near thermal equilibrium to permit direct comparison between theory and experiment.

The measurements obtained with neon are shown in Fig. 7. Here again our measured values merge smoothly with Hornbeck's data at higher E/p. In addition, as in the case of helium, it is to be noted that the measurements of Tyndall's group apply to the molecular ion rather than to the atomic ion. Our measurements for Ne^+ are in excellent agreement with the results of Holstein's[9] theory.

The results obtained in argon (Fig. 8) disagree in part with previous measurements. Our data for the atomic ion merge smoothly at higher E/p with Hornbeck's results and are in excellent agreement with theory[9] in the thermal range. However, our measurements of the faster ion, which we have indicated as A_2^+, are in disagreement with Hornbeck's and Tyndall's results. (Furthermore, it should be noted that the agreement between Hornbeck and Tyndall disappears at higher E/p, their results diverging[6] at $E/p>40$.)

The discrepancies among the various measurements probably may be attributed to impurities in the argon samples used by the different investigators. Mass spectrometric and chemical analysis of the Airco gas samples which we used indicate the presence of small amounts of nitrogen ($<1:10^4$) in our argon. It has previously been shown[15] that the heavy sputtering of magnesium electrodes from an arc run in argon removes impurities which affect the microwave breakdown potential of argon. Since breakdown measurements are very sensitive to impurities such as nitrogen, we conclude that sputtered magnesium effectively removes these impurities. Consequently, we have used a magnesium electrode arc in our gas handling system. The

TABLE I. Mobilities of thermal energy ions of the noble gases at 300°K and a gas density of 2.69×10^{19} atoms/cc.

	Atomic ion		Molecular ion	
	Exp.	Theory	Exp.	Theory
Helium	10.5	11.1[a]	20.3	22.7[d]
Neon	4.0	4.2[b]	6.5	···
Argon	1.60	1.62[b]	2.65	···
Krypton	0.90	1.0[c]	1.21	···
Xenon	0.58	0.66[c]	0.79	···

[a] H. S. W. Massey and C. B. O. Mohr, Proc. Roy. Soc. (London) **A144**, 188 (1934).
[b] T. Holstein, J. Phys. Chem. **56**, 832 (1952).
[c] I. B. Bernstein (private communication).
[d] S. Geltman, Phys. Rev. **90**, 808 (1953).

[15] Krasik, Alpert, and McCoubrey, Phys. Rev. **76**, 722 (1949).

open symbols of Fig. 8 indicate the data obtained without running the clean-up arc. The solid circles were obtained after the arc had been run for 24 hours, with resultant heavy sputtering of magnesium. The lack of change in the measured mobilities indicates either that the faster ion is indeed A_2^+ or that an impurity is present which is not removed by the magnesium arc. Since nitrogen is the only known impurity present and should be removed by the arc, we feel that our measured mobility is that of A_2^+.

Additional support for this assumption is obtained by considering the mobilities of the various noble gas molecular ions. By substituting the measured thermal mobility values (see Table I) into Langevin's mobility equation[2,16] together with the measured polarizabilities of the various noble gas atoms, it is possible to compute the range of the "hard sphere" repulsion[17] between the systems He_2^+ and He, Ne_2^+ and Ne, etc. The results are summarized in Table II. If one plots the hard sphere repulsion radii calculated from our data against the mass number of the ions, one obtains a smooth curve. The repulsion range obtained from

TABLE II. Range of the hard sphere repulsion between the molecular ion and its parent gas atom.[a]

	Range (A)
Helium	2.7
Neon	3.3
Argon	4.3; [6][b]
Krypton	5.4
Xenon	5.8

[a] See reference 17.
[b] Value obtained from Hornbeck's (see reference 6) and Tyndall's (see reference 3) measurements.

Hornbeck's and Tyndall's data on argon lies 50 percent above this curve. This result supports the assumption that our measurements apply to the molecular argon ion A_2^+, rather than to some impurity ion.

The data obtained for krypton and xenon are shown in Figs. 9 and 10. It is interesting to note that in these gases, where molecular ions are more difficult to form,[18] Tyndall's group[19] actually succeeded in measuring the mobility of the *atomic* ion. Their data are indicated by the long dashes and are in good agreement with our results and the measurements at higher E/p of Varney[20] (short dashed lines). In the case of the molecular ions, Kr_2^+ and Xe_2^+, our results agree with Varney's measurements within the combined experimental errors.

[16] H. R. Hasse, Phil. Mag. **1**, 139 (1926).
[17] S. Geltman, Westinghouse Research Memo 60-94411-9-19 (unpublished). The authors are indebted for permission to use his results in Table II.
[18] J. A. Hornbeck and J. P. Molnar, Phys. Rev. **84**, 621 (1951).
[19] A. M. Tyndall and R. J. Munson, Proc. Roy. Soc. (London) **A177**, 187 (1940).
[20] R. N. Varney, Phys. Rev. **88**, 362 (1952).

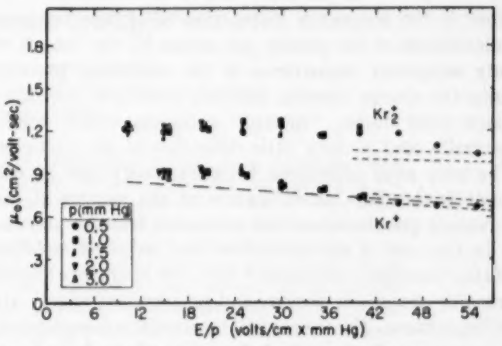

FIG. 9. Mobilities of Kr^+ and Kr_2^+ in krypton. The short dashed lines refer to the measurements of Varney and the long dashed line to those of Tyndall and Munson.

VI. DISCUSSION

The experimentally determined values of the mobilities of thermal energy ions are compared with the theoretical values in Table I. The measured values are believed accurate to ±5 percent. The theory for the ions He^+, Ne^+, and A^+, for which precise calculations have been carried out,[4,9] should involve less than a ten percent uncertainty in the calculated mobilities. The differences between the experimental and the theoretical values (<6 percent) lie well within these limits.

The calculations for Kr^+ and Xe^+ are seriously hampered by the fact that the Hartree-Fock wave functions are not known. Using a Fermi-Thomas core to calculate the wave function of the outermost electron, Bernstein[21] has made an approximate calculation of the Kr^+ and Xe^+ mobilities following the general method of Holstein.[9] The discrepancy between theory and experiment (<13 percent) is smaller than the uncertainties introduced by the imperfect knowledge of the wave functions of krypton and xenon.

The mobilities of the various atomic ions in their parent gases are especially interesting since, at room temperature, the dominant interaction between ion and

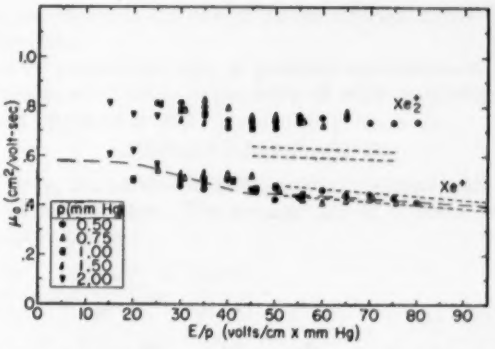

FIG. 10. Mobilities of Xe^+ and Xe_2^+ in xenon. The coding of the lines is the same as in Fig. 9.

[21] I. B. Bernstein (private communication).

atom is the resonance interaction of charge transfer. Polarization of the parent gas atoms by the ions is of only secondary importance in the scattering process, since the charge transfer between atom and ion takes place even during "distant" collisions which would normally lead to very little deflection of the particles. The very good agreement between theory and experiment is therefore an indication of the success of the quantum calculations of the resonance transfer process.

In the case of the molecular ions, only the mobility of He_2^+ has been calculated.[22] Here the resonance charge transfer process is absent, and polarization effects are of importance. The theoretical treatment is complicated, however, by the fact that the calculation of the wave function for the *molecular* ion is not rigorous and that the interaction between the ion and the atom during a collision depends on the orientation of the molecular ion. The uncertainties in the calculations are probably sufficient to account for the discrepancy (11 percent) between theory and experiment.

In Sec. V, it was pointed out that if one treats the molecular ion–gas atom system as a point charge interacting with a polarizable hard sphere, one can estimate the range of the "hard sphere" repulsion between ion and atom from the measured mobility values. The results of such calculations are summarized in Table II. In view of the relative insensitivity of the repulsion range to the value of the mobility, the five percent uncertainty in the measured mobility may lead to a ten percent uncertainty in the calculated range of repulsion. These molecular ion-neutral atom repulsion ranges are all approximately 30 percent larger than the corresponding atom-atom repulsion ranges estimated from viscosity data.

The present experimental techniques provide a simple method for measuring the mobilities of ions at thermal energy. The thermal energy range is especially useful for comparison with theoretical calculations since the treatment of ion distribution functions in nonthermal equilibrium cases is exceedingly difficult[14] and cannot, in general, be carried out for the various collision cross section energy dependences of interest. At the present time, the mobility measurements are being extended to studies of ions in gases other than their parent gases, e.g., Ne^+ in helium, and to the determination of temperature dependences of the various ion mobilities.

The authors wish to thank A. O. McCoubrey and P. R. Malmberg for their very great assistance in the design of various electronic components of the apparatus. We also are indebted to our various associates in the Atomic Physics group for helpful discussions of this work.

[22] S. Geltman, Phys. Rev. 90, 808 (1953).

Annihilation of Positrons in Flight*†

J. B. GERHART, B. C. CARLSON, AND R. SHERR
Palmer Physical Laboratory, Princeton University, Princeton, New Jersey
(Received February 15, 1954)

The weak continuous spectrum of hard γ rays resulting from the stopping of positrons in various materials has been investigated with a NaI(Tl) scintillation spectrometer. Measurements were made chiefly in the γ-ray energy interval from 0.511 Mev to 1.3 Mev, for the continuous β spectra of Ne^{19} and A^{35} (maximum positron energies of 2.2 Mev and 4.4 Mev, respectively). The experimental geometry was chosen to ensure averaging of the annihilation spectrum over all angles. Theoretical spectra were calculated for Lucite, brass, and lead as stopping materials. Comparison with experiment on an absolute basis was made possible by an experimental determination of the spectrometer efficiency as a function of γ-ray energy. The calculations included bremsstrahlung and single-quantum annihilation as well as two-quantum annihilation. In the case of Ne^{19} positrons annihilating in brass, the data are in satisfactory agreement with the calculations. However, the calculated spectra show a conspicuously stronger dependence on the atomic number of the stopping material than do the observed spectra. The experimental spectra from Ne^{19} positrons stopping in Lucite and brass are indistinguishable, while the calculated spectra show a brass to Lucite ratio of 1.3. In addition, the calculated intensities tend to be lower than the observed ones, particularly for A^{35} positrons and for stopping materials of low atomic number.

I. INTRODUCTION

IT has been demonstrated several times that positrons annihilate primarily after they reach the end of their paths of ionization and have only thermal energies. However, there is a small probability that annihilation resulting in two quanta will occur before a positron loses its kinetic energy.[1,2] A large number of experimenters have reported evidence for this annihilation process.[3–19] Their results gave little information, beyond confirming that positrons do annihilate in flight, until the work of Colgate and Gilbert[16] with high-energy positrons and that of Deutsch *et al.*[14,18] with low-energy positrons stopping in anthracene. The present authors were led to the study of hard annihilation radiation by the appearance of a hard γ-ray continuum[20] in the radiation accompanying the β decay of C^{10}, which has subsequently been found in the decays of the positron emitters C^{11}, O^{15}, Ne^{19}, and A^{35}.

II. THEORETICAL CALCULATIONS

Using Dirac's expression[1] for the probability of transition to a negative energy state, Bethe[2] obtained the cross section for two-quantum annihilation of a positron in flight with a free electron at rest:

$$d\Phi=\frac{\pi r_0^2}{\epsilon^2-1}\left[\frac{k}{k'}+\frac{k'}{k}+2\frac{\epsilon+1}{kk'}-\left(\frac{\epsilon+1}{kk'}\right)^2\right]dk. \quad (1)$$

The classical electron radius is $r_0=e^2/mc^2$; the energy of the positron, including rest energy, is ϵmc^2; and the energies of the two quanta are kmc^2 and $k'mc^2$, where $k+k'=\epsilon+1$. The conservation laws require the photon energies to lie between the extreme values

$$k=\tfrac{1}{2}(\epsilon+1)\pm\tfrac{1}{2}(\epsilon^2-1)^{\frac{1}{2}}, \quad (2)$$

corresponding to emission in the forward and backward directions.

The probability that a positron annihilates with emission of a photon in the range dk while traversing a path length dx is then

$$NZd\Phi dx=NZd\Phi(d\epsilon/dx)^{-1}d\epsilon, \quad (3)$$

N being the number of atoms per unit volume with Z electrons per atom. The average rate of collision loss by positrons is

$$-\frac{d\epsilon}{dx}=NZ\frac{2\pi r_0^2}{\beta^2}\left\{\ln\frac{2I^2(\epsilon+1)}{I^2}-\frac{\beta^2}{12}\left[23+\frac{14}{\epsilon+1}+\frac{10}{(\epsilon+1)^2}+\frac{4}{(\epsilon+1)^3}\right]\right\}, \quad (4)$$

* This work was supported in part by the U. S. Atomic Energy Commission and The Higgins Scientific Trust Fund.

† Preliminary reports on this work were presented at the New York meeting of the American Physical Society, January, 1952 [R. Sherr and J. B. Gerhart, Phys. Rev. **86**, 619 (1952)], and at the Washington meeting, April, 1953 [Gerhart, Sherr, and Carlson, Phys. Rev. **91**, 455 (1953)].

[1] P. A. M. Dirac, Proc. Cambridge Phil. Soc. **26**, 361 (1930).
[2] H. A. Bethe, Proc. Roy. Soc. (London) **A150**, 129 (1933).
[3] L. Meitner and H. H. Hupfeld, Z. Physik **75**, 705 (1932).
[4] L. Meitner and H. Kosters, Z. Physik **84**, 137 (1933).
[5] T. Heiting, Z. Physik **87**, 127 (1934).
[6] C. D. Ellis and W. J. Henderson, Proc. Roy. Soc. (London) **A152**, 714 (1935).
[7] J. R. Richardson and F. N. Kurie, Phys. Rev. **50**, 999 (1936).
[8] J. R. Richardson, Phys. Rev. **53**, 124 (1938).
[9] W. Bothe and Ho Zah-wei, Nachr. Akad. Wiss. Göttingen, 59 (1946).
[10] M. Deutsch, Phys. Rev. **72**, 729 (1947).
[11] Huber, Medicus, Preiswerk, and Steffen, Helv. Phys. Acta **20**, 495 (1947).
[12] F. N. D. Kurie and M. Ter-pogossian, Phys. Rev. **74**, 677 (1948).
[13] S. Meric, Rev. fac. sci. univ. Istanbul **15A**, 136 (1950); **15A**, 179 (1950).
[14] J. W. Shearer and M. Deutsch, Phys. Rev. **82**, 336 (1951).
[15] Barkas, Deutsch, Gilbert, and Violet, Phys. Rev. **88**, 1435 (1952).
[16] S. A. Colgate and F. C. Gilbert, Phys. Rev. **89**, 790 (1953).
[17] C. E. Violet, thesis, University of California Radiation Laboratory Report UCRL-2163, 1953 (unpublished).
[18] H. W. Kendall and M. Deutsch, Phys. Rev. **93**, 932 (1954). We are indebted to these authors for allowing us to see a fuller (unpublished) account of this work.
[19] L. H. Gray and G. T. P. Tarrant, Proc. Roy. Soc. (London) **A136**, 662 (1932).
[20] R. Sherr and J. B. Gerhart, Phys. Rev. **91**, 909 (1953).

where $\beta^2=(\epsilon^2-1)\epsilon^{-2}$ is the square of the velocity in units of c, $T=(\epsilon-1)mc^2$ is the kinetic energy, and I is an average ionization potential for an atom of the stopping material. This rate of collision loss is obtained[21] from the Bhabha cross section for positron-electron scattering; it differs by about 5 percent at 100 kev, and by less at higher energies, from the Bethe formula for collision loss by negative electrons.

If every positron started out with the same initial energy ϵ_1, we could obtain the number of annihilation photons in the range dk per positron by integrating (3) over positron energy from ϵ_1 down to the lowest value at which the positron still has sufficient energy to produce a photon in the range dk. This minimum value is found from (2) to be

$$\epsilon_m=k-(k-1)/(2k-1). \tag{5}$$

The resulting spectrum would not be quite correct, since it has been implicitly assumed that each positron passes through the range $d\epsilon$ in the course of slowing down. This is surely not the case for those positrons that annihilate at energies higher than the range in question, but they are a small fraction of the total number of positrons and can be neglected to a fairly good approximation. The errors introduced by disregarding this attenuation by annihilation will be estimated later.

If the positron source is a β emitter, the annihilation spectrum from positrons of a given initial energy can be determined in the manner just described, and the results can then be averaged over the β spectrum of initial energies. For each value of photon energy two numerical integrations are required by this procedure, one over the energy of the stopping positron and the second over initial energies. It is therefore easier to interchange the order of integration and to determine first the fraction of positrons from the β spectrum that pass through a given energy range $d\epsilon$ in the course of slowing down. The probability Q of passing through the interval ϵ to $\epsilon+d\epsilon$ is simply the probability of having an initial energy above this range (attenuation by annihilation again being neglected)

$$Q(\epsilon,\epsilon_0)=\int_{\epsilon}^{\epsilon_0} q(\epsilon,\epsilon_0)d\epsilon, \tag{6}$$

where $q(\epsilon,\epsilon_0)$ is an allowed Fermi spectrum, normalized to unity, with end point ϵ_0. (All the positrons used in the present experiments came from allowed β transitions, and the Coulomb correction to the spectrum was found to be negligible for present purposes in the source with largest atomic number, A^{35}.) The probability (3) that a positron gives rise to an annihilation quantum k, assuming that it reaches the energy interval $d\epsilon$ in the course of slowing down, is now multiplied by the probability Q that it does in fact reach this interval, and the product is integrated from ϵ_0 to ϵ_m, i.e., over the range of annihilation energies compatible with k. Thus the number of photons in the interval dk per positron of the β spectrum is found by a single numerical integration for each value of k, the integration (6) being independent of k:

$$n(k,\epsilon_0,Z)dk=dk\int_{\epsilon_m}^{\epsilon_0} NZ(d\Phi/dk)\times(-d\epsilon/dx)^{-1}Q(\epsilon,\epsilon_0)d\epsilon. \tag{7}$$

Since the average energy loss (4) is proportional to the number NZ of electrons per unit volume, the annihilation spectrum (7) depends on the stopping material only through the logarithm of the ionization potential. This dependence is sufficient to make the hard annihilation spectrum from positrons stopping in lead 15 to 20 percent higher than in brass.

Figures 1 through 4 show $n(k,\epsilon_0,Z)$ for Ne^{19} and A^{35} positrons annihilating in brass and lead. Note that the

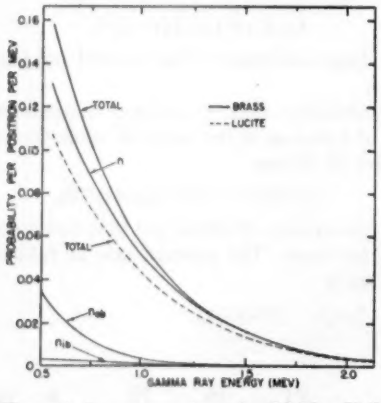

FIG. 1. Theoretical γ-ray spectrum for 2.2-Mev Ne^{19} positrons annihilating in brass and in Lucite.

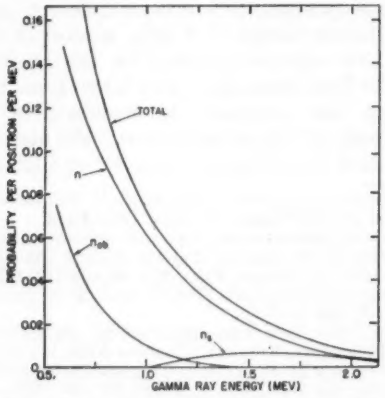

FIG. 2. Theoretical γ-ray spectrum for 2.2-Mev Ne^{19} positrons annihilating in lead. n_{ab} (omitted here) is the same as in Fig. 1.

[21] F. Rohrlich and B. C. Carlson, Phys. Rev. **93**, 38 (1954).

curves shown in the figures are plotted with Mev as the energy unit rather than mc^2; the change in units introduces only a constant numerical factor.

In addition to two-quantum annihilation there are three other sources of hard γ radiation for which corrections to the calculated spectrum (7) must be made: single-quantum annihilation, bremsstrahlung produced in the stopping material, and inner bremsstrahlung produced in the source itself.

Bethe[2] gives the cross section per K electron for single-quantum annihilation:

$$\Phi_s(\epsilon,Z)=\alpha^4Z^5 2\pi r_0^2(\epsilon+1)^{-2}(\epsilon^2-1)^{-1} \times[(\epsilon^2-1)^{\frac{1}{2}}(\epsilon^2+\tfrac{2}{3}\epsilon+\tfrac{4}{3})-(\epsilon+2)\cosh^{-1}\epsilon], \quad (8)$$

where $\alpha=1/137$ and ϵmc^2 is the total positron energy, including rest energy. The energy of the emitted photon

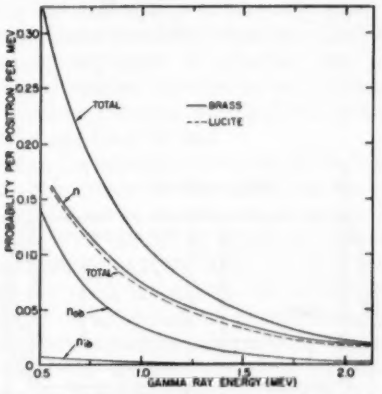

FIG. 3. Theoretical γ-ray spectrum for 4.4-Mev A^{35} positrons annihilating in brass and in Lucite.

is given to a sufficient approximation by $k=\epsilon+1$, without taking into account the binding energy of the K electron or the loss of kinetic energy by the positron in penetrating the Coulomb field. The probability that a positron from the β spectrum will annihilate by this process in the range $d\epsilon$ is

$$N2\Phi_s(\epsilon,Z)(d\epsilon/dx)^{-1}Q(\epsilon,\epsilon_0)d\epsilon, \quad (9)$$

and the resulting photon spectrum $n_s(k,\epsilon_0,Z)dk$ is equal to the probability (9) evaluated at $\epsilon=k-1$, with $d\epsilon$ replaced by dk. The factor 2 in (9) represents the two K electrons per atom; contributions from electrons in higher shells are neglected. Since (9) depends on the stopping material approximately as the fourth power of Z, single-quantum annihilation is negligible in Lucite and brass, although it makes an appreciable contribution in lead.

The cross section for bremsstrahlung, including screening corrections, was obtained in Born approximation by Bethe and Heitler,[22] and their results have been

[22] H. Bethe and W. Heitler, Proc. Roy. Soc. (London) **A146**, 83 (1934). See also W. Heitler, *The Quantum Theory of Radiation* (Oxford University Press, London, 1944). The accuracy of the Born approximation is discussed by J. C. Jaeger, Nature **140**, 108 (1937).

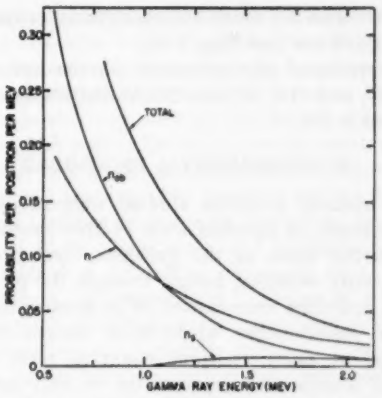

FIG. 4. Theoretical γ-ray spectrum for 4.4-Mev A^{35} positrons annihilating in lead. n_{ib} (omitted here) is the same as in Fig. 3.

plotted for lead in the energy range of a few Mev by Ivanov *et al.*[23] In the present calculations a linear interpolation between the end points of the Bethe-Heitler intensity distribution has been used; the cross section for emission of a photon in the range dk has been taken to be

$$d\Phi_{ob}=k^{-1}dk\alpha Z^2r_0^2 20[1-k/(\epsilon-1)]. \quad (10)$$

This vanishes at the short-wave limit, as does the Born approximation. Although Jaeger[22] has shown that the exact cross section for negative electrons is different from zero at the short-wave limit, the exact cross section for positrons would be expected to vanish there, as in the nonrelativistic theory. The spectrum of radiated photons per positron is found from (10) by numerical integration:

$$n_{0b}(k,\epsilon_0,Z)dk=dk\int_{k+1}^{\epsilon_0}N(d\Phi_{0b}/dk) \times(-d\epsilon/dx)^{-1}Q(\epsilon,\epsilon_0)d\epsilon. \quad (11)$$

It is approximately proportional to the Z of the stopping material.

Finally, the contribution of inner bremsstrahlung has been obtained from the probability $d\Phi_{ib}$, given by Knipp and Uhlenbeck,[24] for emission of a photon in the range dk and an electron of energy $(\epsilon-k)mc^2$ in an allowed β transition. The resulting photon spectrum, which is of course independent of the stopping material, is obtained by an integration over the differential Fermi spectrum

$$n_{ib}(k,\epsilon_0)dk=dk\int_{k+1}^{\epsilon_0}(d\Phi_{ib}/dk)q(\epsilon,\epsilon_0)d\epsilon. \quad (12)$$

[23] Ivanov, Walter, Sinelnikov, Taranov, and Abramovich, J. Phys. (U.S.S.R.) **4**, 319 (1941).

[24] J. K. Knipp and G. E. Uhlenbeck, Physica **3**, 425 (1936). See also F. Bloch, Phys. Rev. **50**, 272 (1936).

The correction for inner bremsstrahlung proves to be a very small one (see Figs. 1–4).

Conversion of the calculated photon spectra (7), (9), (11), and (12) to pulse-height distributions will be discussed in Sec. V.

III. EXPERIMENTAL PROCEDURE

The positron activities studied were produced by bombardment of powders with 18-Mev protons from the internal beam of the Princeton cyclotron.[25] By continuously sweeping helium through the probe, the desired activities were carried off in gaseous form to a suitable gas chamber where their decays could be observed at fairly constant counting rates with a NaI(Tl) scintillation spectrometer. A trap containing ascarite and $CaCl_2$ was placed in the gas line between the probe and the observation chamber to remove possible extraneous activities in the form of CO_2 or water vapor.

The activities studied were primarily Ne^{19} and A^{35} (end-point energies 2.2 and 4.4 Mev, respectively). Ne^{19} was produced through the reaction $F^{19}(p,n)Ne^{19}$ by bombarding PbF_2 powder. $PbCl_2$ powder was bombarded to give A^{35} through the reaction $Cl^{35}(p,n)A^{35}$. In both cases the activities were identified by half-life measurements, by determination of the positron energies in absorption measurements, and by the absence of nuclear γ radiation.

C^{10} and C^{11} (end-point energies 2.1 and 0.97 Mev, respectively) were produced simultaneously by bombarding B^{10} powder. C^{10} resulted from the $B^{10}(p,n)C^{10}$ reaction; C^{11} from the $B^{11}(p,n)C^{11}$ reaction on B^{11} impurity in the target. Both activities were carried off as CO_2, the ascarite-$CaCl_2$ trap being removed from the gas line in this case and the inspection chamber charged with ascarite to absorb the activity. The C^{10} spectrum could be observed directly inasmuch as the C^{11} contributed only a small fraction of the total activity. To observe the 20-minute C^{11} activity, gas was allowed to flow through the gas chamber until sufficient activity had been trapped. The gas flow was then interrupted and the 20-second C^{10} activity allowed to decay through approximately five half-lives before the residual C^{11} activity was observed.

O^{15} (end-point energy 1.7 Mev) was produced by a $F^{19}(p,an)O^{15}$ reaction accompanying the $F^{19}(p,n)Ne^{19}$ reaction. The O^{15} activity was carried off as water vapor and ordinarily was stopped in the ascarite-$CaCl_2$ trap. To observe it the trap was removed and the gas chamber charged with $CaCl_2$. The gas flow was interrupted after the O^{15} activity had been allowed to collect in the $CaCl_2$ and the Ne^{19} activity was allowed to decay before the longer-lived O^{15} was observed.

The gas chambers used to observe the various activities had walls of sufficient thickness to stop all positrons. Hence, the effective source of annihilation radiation was the walls of the gas chamber. The original chamber was a brass cylinder (interior dimensions: 4.4-cm diameter by 5.2-cm, 0.33-cm walls) which was placed about 2 cm above the NaI(Tl) crystal (Fig. 5). This chamber could be filled with ascarite or $CaCl_2$ to study the C^{10}, C^{11}, and O^{15} activities, and was lined with lead foil to study annihilation in lead. A similar chamber of Lucite (interior dimensions: 4.1-cm diameter by 6.4-cm 1.2-cm walls) was used to observe annihilation in Lucite.

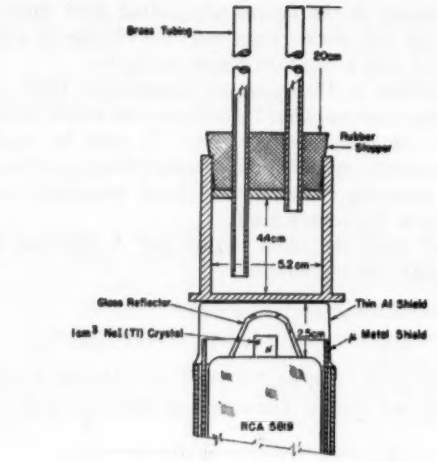

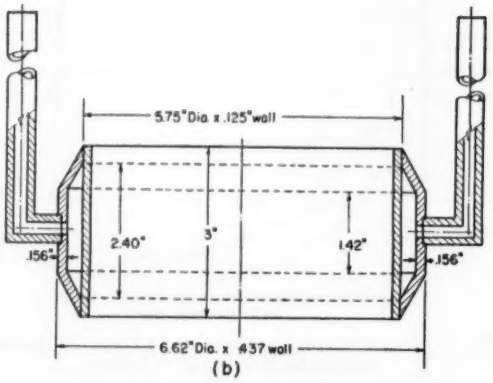

FIG. 5. (a) Cross section of cylindrical brass gas chamber and crystal mounting. (b) Cross section of toroidal brass gas chamber.

The calculations previously outlined assumed that the radiation is emitted isotropically. In the gas chamber just described, positrons enter the walls of the chamber at random and annihilate close to the point of entry to the wall, since the positron range is small. Therefore, we have in effect an extended source for the γ radiation, and the solid angle subtended by the γ-ray detector varies considerably over the chamber. However, if radiation coming from each point of the wall is isotropic, its contribution to the total γ-ray spectrum may vary

[25] Sherr, Muether, and White, Phys. Rev. 75, 282 (1949).

in magnitude but the relative amounts of 0.511-Mev radiation and of hard radiation will be independent of position. Since we use the relative intensities to compare the experimental and theoretical results, the extended source introduces no complications. If each point in the extended source is not isotropic, the resulting spectrum is difficult to interpret. The condition for isotropy will be satisfied if the positrons lose their sense of direction before annihilating. In order to check this point, we repeated the measurements using a brass gas chamber in the form of a hollow toroid with the detector at the center (see Fig. 5). The dimensions were chosen so that the variation of the solid angle of the detector over the toroidal chamber wall was small (less than 10 percent). Hence, no portion of the chamber wall was favored over another as a source of radiation. The chamber was also designed to minimize the possibility of excessive scattering and degradation of the γ rays which reached the crystal. Under these conditions the γ radiation will be isotropic regardless of whether the positrons maintain their original direction or not. It was possible to line a similar chamber with lead foil to study the annihilation spectrum for lead.

With both the cylindrical and the toroidal chambers, less than 5 percent of the radiation reaching the detector originated in the brass pipes leading into the chamber. In Ne^{19} and A^{35} no significant difference was found between the spectra taken with the cylindrical chamber and those taken with the toroidal chamber which could be attributed to geometrical effects. (A small difference caused by unequal γ-ray absorption in the walls of the different chambers was observed.) Consequently, it was assumed that the C^{10}, C^{11}, and O^{15} spectra taken only with the cylindrical brass chamber are free from geometrical effects.

Pulses from the NaI(Tl) crystal, a 1.0-cm cube mounted on an RCA 5819 photomultiplier, were fed to a preamplifier and thence to a Los Alamos model 501 amplifier and recorded on a 10-channel pulse-height analyzer. Both 2- and 5-volt channels were available for inspection of the 0.511-Mev annihilation radiation photopeak and the continuous distribution of hard radiation. A single-channel differential pulse-height discriminator and scalar simultaneously recorded the pulses falling in the 0.511-Mev photopeak and served as a monitor of the effective source strength.

The well-known γ rays of Na^{22}, Sc^{46}, Co^{60}, Zn^{65}, Cs^{134}, Cs^{137}, and Hg^{205} were used to calibrate the pulse-height voltage scale on an absolute basis. Counting rates were kept low enough to prevent pileup and accidental coincidences. Background was less than 5 percent for points at pulse heights corresponding to 1.1 Mev and considerably less for smaller pulse heights.

IV. EXPERIMENTAL RESULTS

In making each run, the 10-channel analyzer was first set to count the 0.511-Mev photopeak pulses in 2-volt channels for approximately 200 seconds. Immediately afterward the hard annihilation radiation was counted with 5-volt channels, the setting of the single channel monitor remaining unchanged, for periods varying from 500 to 2000 seconds. The data obtained in this way were divided by the appropriate channel width and by the simultaneous monitor count. The result is a spectrum independent of both source strength and running time. Separate spectra taken of the same positron source were plotted on an energy calibrated pulse height scale and normalized to the same (arbitrary) 0.511-Mev photopeak area. In this way separate runs were plotted together in a manner eliminating small differences caused by slightly differing monitor settings and amplifier gains. All the data for various sources and stopping materials were normalized finally to the same photopeak area.

The spectra for annihilation in brass were not corrected for absorption of the γ rays in the stopping material. Because of the method of normalization used, the effect of this absorption is to raise the observed hard annihilation spectrum above the true spectrum, but by less than 5 percent. The data for annihilation of positrons in lead and Lucite have been subjected to a correction for the difference in absorption between lead and brass, and between Lucite and brass, respectively. The correction was determined experimentally by inserting a lead absorber of the same thickness as the lead chamber lining between the brass chamber and the detector, and observing the attenuation produced in the annihilation spectrum. A similar procedure was used to determine the correction to the Lucite spectrum.

Figure 6 contains the experimentally observed spectra for the positrons of A^{35} and Ne^{19} annihilating in brass. Both the A^{35} and the Ne^{19} spectra are averages of the two runs made with the toroidal gas chamber which

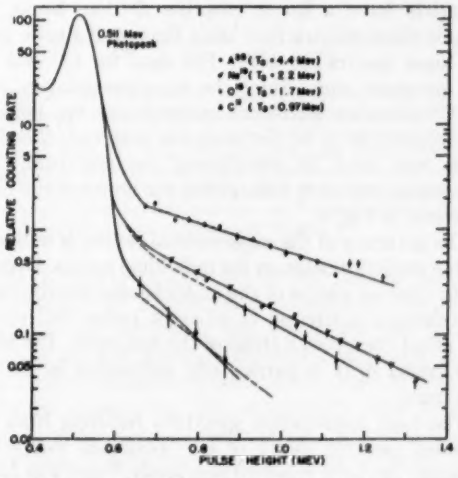

FIG. 6. Observed NaI(Tl) pulse-height distributions for annihilation radiation from positrons stopped in brass. T_0 is the end-point kinetic energy of the positron spectrum. The dashed line passing through the C^{11} points is a calculated spectrum for C^{11}.

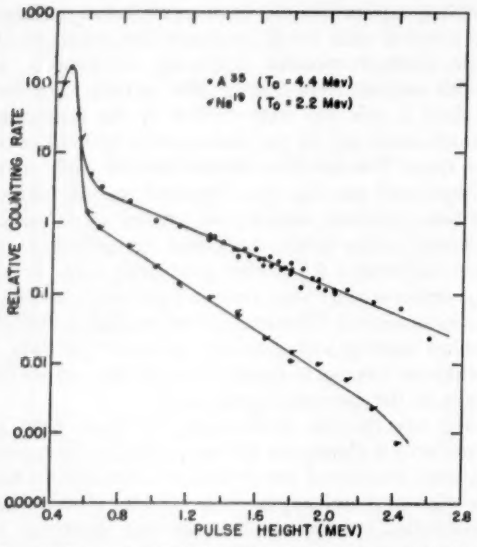

FIG. 7. Observed pulse-height distributions for annihilation of Ne^{19} and A^{35} positrons in brass, showing the absence of high-energy nuclear γ rays. The energy scale shown here is not known to the accuracy of that in Fig. 6. T_0 is the end-point kinetic energy of the positron spectrum.

are freest from instrumental and statistical uncertainties. The A^{35} and Ne^{19} spectra were observed out to higher energies with both 2-volt and 5-volt channels to make certain there were no nuclear γ rays present. None was found, the slopes shown in Fig. 6 persisting out to 2.4 Mev beyond which the counting rates decreased more rapidly until submerged in background counts (see Fig. 7). Also shown in Fig. 6 are the spectra for C^{11} and O^{15} positrons stopping in NaOH and asbestos (Ascarite), and $CaCl_2$, respectively. Although these materials have a lower effective Z than brass, we include these spectra here since brass and Lucite gave the same spectra for Ne^{19}. The data for C^{11} and O^{15} are for single runs. Since the experimental spectrum for C^{11} contains statistical uncertainties too large to distinguish the Z of the stopping material, the Z of brass was used in calculating the spectrum. The theoretical spectrum falls within the limits of the data, as shown in Fig. 6.

The accuracy of the experimental results is indicated by the statistical flags on the individual points. Drifting of the channel widths of the multichannel discriminator introduces a scattering of adjacent points but should not affect the over-all trend of the spectrum. The effect of channel drift is particularly noticeable in the A^{35} spectrum.

The hard annihilation spectrum resulting from the 2.1-Mev positron decay of C^{10} (positrons stopped in ascarite) has been reported previously,[20] and was found to be the same, within experimental error, as the spectrum in brass for the 2.2-Mev positron decay of Ne^{19}.

The data showing the Z dependence of the annihilation spectrum for a single nuclear positron source (Figs. 8 and 9) were taken successively so that the lead and Lucite spectra could be compared with the concurrently observed brass spectra to a better accuracy than had the spectra so compared been observed at different times with different instrumental conditions. The data for annihilation in brass of Figs. 8 and 9 are not the same as shown in Fig. 6.

V. PROCEDURE FOR COMPARISON OF THEORY AND EXPERIMENT

In the present experiments, the annihilation radiation was observed with a NaI(Tl) γ-ray spectrometer; consequently, a calculated γ-ray spectrum, such as that given by Eq. (7), must be converted to a pulse-height distribution before the theoretical calculation can be compared with experiment. Since a large part of the γ-ray spectrum contributes to the counting rate observed at a given pulse height with a NaI(Tl) spectrometer, (7) must be multiplied by a weighting function $f(k,V)$ and integrated over all values of k. In its dependence on pulse height, $f(k,V)dV$ (Fig. 10) gives the probability that a γ ray of energy kmc^2 will produce a pulse in the NaI(Tl) spectrometer of pulse height V (Vmc^2 is the energy of a γ ray whose photopeak maximum falls at V). Relative values of $f(k,V)$ were determined by interpolation between NaI(Tl) spectra for the well-known Au^{198}, Nb^{95}, Zn^{65}, and Na^{22} γ rays as observed with the spectrometer used in this experiment. An experimentally determined[20] photopeak efficiency curve for the spectrometer was used to normalize the spectra to equal source strengths. The functions $f(k,V)$ obtained are accurate to about 5

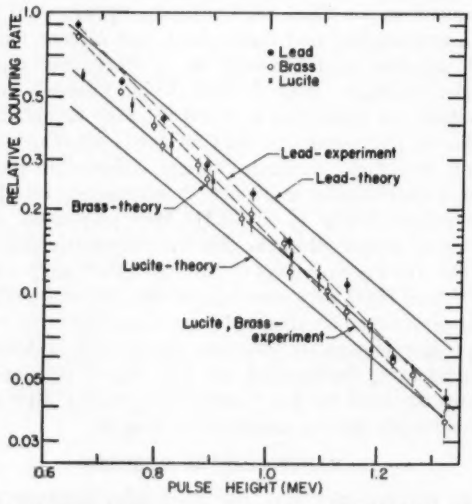

FIG. 8. Comparison of theoretical pulse-height distributions and data for 2.2-Mev Ne^{19} positrons annihilating in lead, brass, and Lucite.

percent. The final calculated spectrum is then given by

$$\mathfrak{N}(V,\epsilon_0,Z)dV = dV\int f(k,V)n(k,\epsilon_0,Z)dk. \quad (13)$$

$\mathfrak{N}(V,\epsilon_0,Z)$ is the number of pulses per unit pulse-height interval per positron in the NaI(Tl) spectrum of the annihilation radiation from nuclear positrons of end point energy ϵ_0 annihilating in material of atomic number Z (see Fig. 10b).

In comparing the calculated distribution (13) with an observed distribution, in which the number of counts per pulse-height interval per second depends on the positron source strength and position, one can avoid a determination of absolute efficiency by using the 0.511-Mev photopeak from annihilation at rest. Since the probability of annihilation in flight is small, there are very nearly two quanta of 0.511 Mev per positron of the β spectrum, and the total spectrum of annihilation quanta per positron is therefore $n(k,\epsilon_0,Z)+2\delta(k-1)$. The second term is a delta function representation of the spectrum of quanta from annihilation at rest. Correspondingly, $\mathfrak{N}(V,\epsilon_0,Z)+2f(1,V)$ is the total pulse-height distribution, whose 0.511-Mev photopeak comes almost entirely from the second term. If this distribution is now multiplied by a constant factor to make the photopeak area of $2f(1,V)$ equal to the photopeak area of the observed distribution, one obtains a direct comparison of the calculated and observed distributions from annihilation in flight. Since all the calibration curves $f(k,V)$ are determined for the same (though arbitrary) source strength, there is no adjustable parameter by which the two parts of the spectrum can be shifted independently.

Tables I and II present the calculated pulse-height distributions to be expected for Ne^{19} and A^{35} positrons, normalized to a prescribed photopeak area in the manner just described. The integration was done for each of the four processes separately, and their individual contributions are included in the tables to show their relative importance. The values at a pulse height of 1.2 Mev are open to some doubt, because the corresponding response curve $f(k,V)$ was obtained by an uncertain extrapolation.

The comparison of theoretical and experimental distributions is shown in Figs. 6, 8, and 9. The theoret-

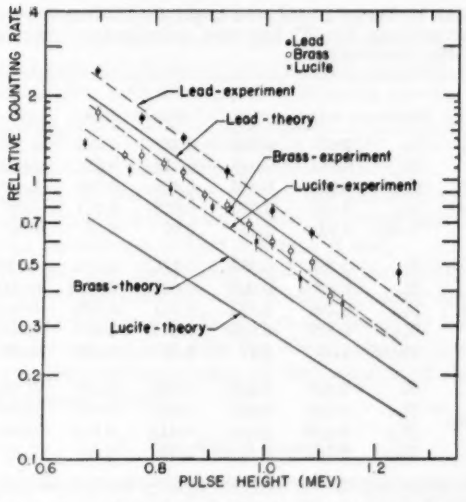

FIG. 9. Comparison of theoretical pulse-height distributions and data for 4.4-Mev A^{35} positrons annihilating in lead, brass, and Lucite.

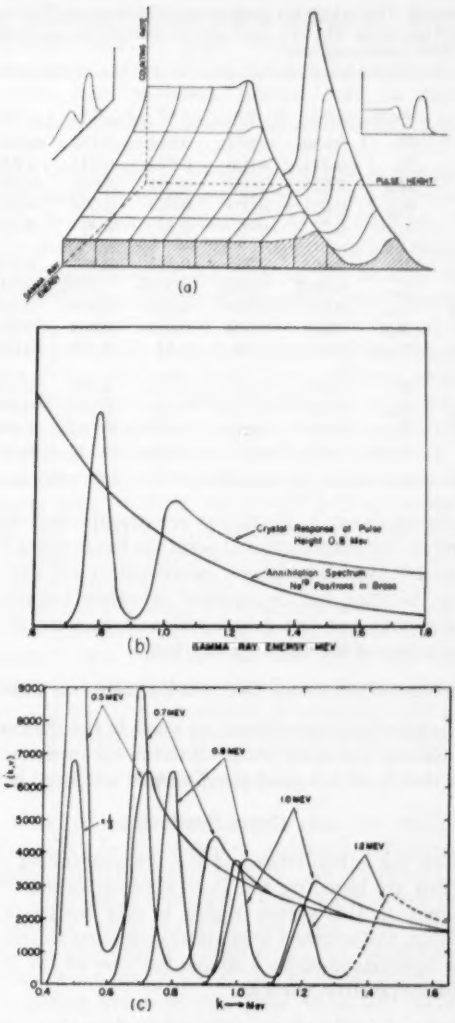

FIG. 10. (a) Three-dimensional plot of the NaI(Tl) crystal response $f(k,V)$ to monoenergetic γ rays as a function of γ-ray energy and pulse height. (b) A typical γ-ray spectrum and a cross section of $f(k,V)$ at a fixed pulse height, which is the weighting function for that pulse height. These two curves are multiplied and integrated over γ-ray energy k to give a single point on one of the pulse-height distributions. (c) Weighting function $f(k,V)$ as a function of k for various pulse heights V.

TABLE I. The calculated pulse-height distributions $\mathfrak{N}(V,\epsilon_0,Z)$ for Ne^{19} positrons. The $\mathfrak{N}$'s have been normalized to a prescribed 0.511-Mev photopeak area.

	V (Mev)	0.7	0.8	0.9	1.0	1.2
Lead	$\mathfrak{N}$	0.556	0.374	0.254	0.178	0.091
	$\mathfrak{N}_s$	0.033	0.033	0.034	0.033	0.030
	$\mathfrak{N}_{ob}$	0.124	0.062	0.032	0.016	0.004
	$\mathfrak{N}_{ib}$	0.007	0.004	0.003	0.002	0.001
	Total	0.72	0.47	0.32	0.23	0.126
Brass	$\mathfrak{N}$	0.465	0.315	0.217	0.151	0.079
	$\mathfrak{N}_s$	0.0004	0.0005	0.0005	0.0004	0.0004
	$\mathfrak{N}_{ob}$	0.038	0.019	0.010	0.005	0.001
	$\mathfrak{N}_{ib}$	0.007	0.004	0.003	0.002	0.001
	Total	0.51	0.34	0.23	0.158	0.081
Lucite	$\mathfrak{N}$	0.367	0.251	0.175	0.123	0.064
	$\mathfrak{N}_{ob}$	0.006	0.003	0.002	0.001	0.0002
	$\mathfrak{N}_{ib}$	0.007	0.004	0.003	0.002	0.001
	Total	0.38	0.26	0.180	0.126	0.065

ical curves shown in the figures are straight lines determined by the four calculated points in the interval from 0.7 to 1.0 Mev. The points calculated at 1.2 Mev lie above the lines, but the upward curvature implied by these points was not taken seriously in view of the uncertainty of the response function.

VI. APPROXIMATIONS AND EXPERIMENTAL ERRORS

The principal approximations made in the theoretical calculations and some uncertainties in the experimental data that have not yet been discussed are listed below.

1. Cross Sections

Both the annihilation and the bremsstrahlung cross sections are based on the Born approximation, whose accuracy in this energy region is very uncertain. In addition, the screened bremsstrahlung cross section has been approximated by a simple function of the initial and final positron energies.

2. Attenuation by Annihilation

The effect of attenuation by annihilation, mentioned in Sec. II, gives rise to two errors that partially compensate one another. Since a positron that annihilates in flight cannot make any further contributions to the γ-ray spectrum, the calculated spectra are too high by an amount varying from less than 8 percent for photons near 0.511 Mev to zero at the extremes of high- and low-frequency quanta. (The total probability of annihilation in flight is found to be 0.08 for A^{35} positrons in lead, and less than this for the other cases of present interest.) On the other hand, it is assumed in the normalization procedure that two quanta of 0.511 Mev are produced for each positron of the β spectrum, and the calculated photopeak area is therefore too high by an amount not exceeding 8 percent. After a normalization factor is applied to equalize the calculated and observed photopeak areas, the calculated hard spectrum will be too low by an amount increasing from zero near the photopeak to probably not more than 5 percent at a pulse height of 1 Mev.

3. Straggling

Further approximations are involved in taking account of the slowing-down of the positrons in the stopping material. Use of the average rate of energy loss in Eq. (3) to replace a path length dx by an energy interval $d\epsilon$ implies the disregard of energy straggling. In the presence of straggling, an expression for the average path length traversed in losing a fixed energy $d\epsilon$ ought to be used, if it were available, rather than the average energy lost in traversing a fixed path length dx.

4. Average Rate of Energy Loss

The mean ionization potential in Eq. (4) was taken to be 13.5 ev times Z. The Z for brass was taken as 29 (copper); for Lucite it was assumed that the stopping power is the sum of the stopping powers of the constituent elements. Since the chemical formula of Lucite is $|CH_2C(CH_3)COOCH_3|_N$, the effective Z is given by $54\ \ln Z = 30\ \ln 6 + 16\ \ln 8 + 8\ \ln 1$, or $Z = 5.0$.

In the calculations several small effects were neglected that influence the Z dependence of $d\epsilon/dx$. These are the density effect, the contribution of radiation loss to the stopping power, and the fact that I is not strictly proportional to Z. The calculations have not been redone with inclusion of these corrections, but their effect has been estimated by computing the corrected stopping power and comparing it with the uncorrected stopping power used in the calculations.

The values of I used in the corrected stopping power were taken from the proton range measurements of Bakker and Segrè[26] for metals and of Thompson[27] for

TABLE II. The calculated pulse-height distributions $\mathfrak{N}(V,\epsilon_0,Z)$ for A^{35} positrons. The $\mathfrak{N}$'s have been normalized to a prescribed 0.511-Mev photopeak area.

	V (Mev)	0.7	0.8	0.9	1.0	1.2
Lead	$\mathfrak{N}$	0.877	0.643	0.487	0.380	0.255
	$\mathfrak{N}_s$	0.054	0.055	0.055	0.054	0.053
	$\mathfrak{N}_{ob}$	0.959	0.614	0.409	0.280	0.145
	$\mathfrak{N}_{ib}$	0.029	0.020	0.015	0.011	0.007
	Total	1.92	1.33	0.97	0.73	0.46
Brass	$\mathfrak{N}$	0.764	0.559	0.426	0.335	0.224
	$\mathfrak{N}_s$	0.0007	0.0007	0.0007	0.0007	0.0007
	$\mathfrak{N}_{ob}$	0.296	0.192	0.127	0.088	0.045
	$\mathfrak{N}_{ib}$	0.029	0.020	0.015	0.011	0.007
	Total	1.09	0.77	0.57	0.44	0.28
Lucite	$\mathfrak{N}$	0.627	0.462	0.351	0.277	0.186
	$\mathfrak{N}_{ob}$	0.049	0.032	0.021	0.014	0.007
	$\mathfrak{N}_{ib}$	0.029	0.020	0.015	0.011	0.007
	Total	0.71	0.51	0.39	0.30	0.20

[26] C. J. Bakker and E. Segrè, Phys. Rev. 81, 489 (1951).
[27] T. J. Thompson, University of California Radiation Laboratory Report No. 1910, 1952 (unpublished).

the constitutents of organic compounds. For lead, $I=758$ ev$=82\times9.25$ ev; for copper, $I=279$ ev$=29\times9.6$ ev; and for brass (two-thirds copper and one-third zinc) we have taken $I=285$ ev. These values are lower than any other measurements of I for lead and copper, but we have used them for consistency because Thompson's results are based on the Bakker-Segrè value for copper. According to Thompson's prescriptions, the value of I for Lucite is 59 ev$=5.0\times11.8$ ev, where account is taken of the fact that the polymerized form of methyl methacrylate has only one double bond per molecular unit.

The correction for density effect was taken from the formulas of Sternheimer.[28] His values for polystyrene should also be a good approximation for Lucite, because Lucite has 10 percent more electrons per unit volume but they are a little more tightly bound and give a weaker polarization per electron. An estimate of the contribution of radiation loss was obtained from the cross section (10) by an integration over photon energy. Radiation loss and density effect produce corrections of opposite sign, with density effect predominating in Lucite and radiation loss in lead and brass.

The new values of average energy loss differ from the values used in the calculations by factors that are fairly constant in brass and Lucite but change significantly over the higher energy range in lead. Averaged over the energy range of importance in the Ne^{19} calculations, the *reciprocal* of the corrected stopping power is equal to the reciprocal value used in the calculations multiplied by 0.99 in Lucite, 0.95 in brass, and 0.90 in lead. The corresponding ratios for A^{35} are 1.00, 0.94, and approximately 0.85. Since the reciprocal stopping power enters directly into every calculated photon spectrum, with the unimportant exception of inner bremsstrahlung, the product of a calculated pulse-height distribution and the appropriate one of the ratios just listed should give a good estimate of the pulse-height distribution that would be obtained from a calculation with the corrected stopping power. The resultant diminution of Z dependence would be in the right direction but not sufficiently marked to produce agreement between theory and experiment. The reduction in magnitude of the calculated counting rates in brass and lead would be in the wrong direction, except for the case of Ne^{19} positrons in lead.

The fact that the Bakker-Segrè ionization potentials are rather low does not alter these conclusions appreciably. If we take $I=29\times10.5$ ev as a probably better value for copper, and raise the other ionization potentials in the same proportion, all the ratios listed above are increased by 0.01.

5. End-Point Energies

The end-point energy of the A^{35} β spectrum was taken to be 4.40 Mev on the basis of two cloud-chamber determinations[29,30] that led to 4.38 ± 0.07 Mev and 4.41 ± 0.09 Mev. A larger value for the end-point energy would narrow the gap between the calculated and observed hard radiation spectra, but an increase sufficient to make a substantial improvement would produce a disagreement in the slopes. It would also violate the pattern of Coulomb energies in the mirror nuclei, since an end-point energy of 4.4 Mev corresponds to a Coulomb radius of $1.45A^{\frac{1}{3}}\times10^{-13}$ cm.

The end point of the Ne^{19} β spectrum was taken in the calculations to be 2.3 Mev on the basis of cloud chamber and particularly of absorption measurements.[25] However, a spectrometer measurement[31] has led to a value of 2.18 ± 0.03 Mev, and a threshold determination of the $F^{19}(p,n)Ne^{19}$ reaction[32] to an end-point value of 2.235 ± 0.005 Mev. In order to check the sensitivity of the calculated hard radiation spectrum to small changes in end-point energy and ionization potential, the calculations for Ne^{19} positrons in brass have been repeated with $I=10.5Z$ and $T_0=2.18$ Mev (instead of $13.5Z$ and 2.3 Mev). The new spectrum is lower than the original one by an amount increasing from 8 percent at a pulse height of 0.7 Mev to 15 percent at 1.2 Mev. The change in I accounts for difference of 4 to 3 percent, and the change in T_0 for the remainder. A spectrum calculated with $I=10.5Z$ and $T_0=2.235$ Mev would therefore be lower than the original one by an estimated 6 to 9 percent. The slope would be essentially the same and the agreement with experiment somewhat worse.

6. Absorption

A principal uncertainty in the data for which no correction has been attempted, as mentioned earlier, is the differential absorption of the γ rays in various parts of the annihilation spectrum by the walls of the brass gas chamber (lower-energy γ rays being more strongly absorbed than harder radiation). An experimental estimate of the magnitude of this effect indicated that the counting rates in the hard radiation NaI(Tl) spectrum should be reduced by less than 5 percent before being compared with the computed spectra. This correction is small because the geometry, from the standpoint of γ absorption, is "bad," so that the absorption of direct radiation is partially compensated by in-scattering.

7. Normalization

A second experimental uncertainty arises in the comparison of the calculations with the data. The method of normalizing the calculations to the data was, in essence, to equate the calculated fraction of radiation from positrons annihilating at rest multiplied by the

[28] R. M. Sternheimer, Phys. Rev. **88**, 851 (1952); **91**, 256 (1953).

[29] White, Creutz, Delsasso, and Wilson, Phys. Rev. **59**, 63 (1941).

[30] D. R. Elliott and L. P. D. King, Phys. Rev. **60**, 489 (1941).

[31] G. Schrank and J. R. Richardson, Phys. Rev. **86**, 248 (1952).

[32] Willard, Bair, Kington, Hahn, Snyder, and Green, Phys. Rev. **85**, 849 (1952). See also C. W. Li, Phys. Rev. **88**, 1038 (1952).

TABLE III. Estimated percentage corrections to calculated and experimental pulse-height distributions. The effects listed refer to those discussed under the same headings in Sec. VI. A positive sign indicates that the correction would raise the theoretical pulse-height distribution relative to the observed distribution.

	Ne^{19}			A^{35}		
	Lead	Brass	Lucite	Lead	Brass	Lucite
Attenuation by annihilation (at $V=0.9$ Mev)	+3%	+2.5%	+2%	+4%	+3.5%	+3%
Average energy loss	−9	−4	0	−14	−5	+1
End-point energy (at $V=0.9$ Mev)	−4	−4	−4	0	0	0
Absorption	+5	+5	+5	+5	+5	+5
Normalization	−4	−4	−4	−8	−8	−8
Total	−9%	−5%	−1%	−13%	−5%	+1%

spectrometer photopeak efficiency for 0.511-Mev γ rays to the corresponding quantity obtained from the data. The former was taken to be the area under the 0.511-Mev photopeak in the response function $2f(1,V)$, which, except for the attenuation effect discussed in subsection 2, is the desired quantity. Correspondingly, for the data, this quantity was taken to be the observed 0.511-Mev photopeak area. This area, however, contains an extraneous contribution from the photopeaks and Compton distributions of the hard radiation on which the 0.511-Mev photopeak is superimposed. Though it was not possible to obtain an accurate value for the necessary correction, it can be estimated that the result of including the correction would be to make the counting rates in the calculated hard radiation spectrum roughly 4 percent lower for Ne^{19} and 8 percent lower for A^{35}. Note that the *relative* heights of the spectra of Figs. 8 and 9 are independent of the normalization procedure.

8. Summary

The estimated corrections discussed in the preceding paragraphs are summarized in Table III, with the exception of the very uncertain errors in the cross sections and the effects of straggling. The estimates listed in the table are in some cases rather crude, but it is felt that they are correct in order of magnitude.

VII. DISCUSSION

The experimental points for annihilation of Ne^{19} positrons in brass are seen (Fig. 8) to be in satisfactory agreement with the calculated spectrum, although they tend to lie above it at the end nearer the photopeak. This tendency is emphasized by a comparison of the areas under the theoretical and experimental curves between 0.7 and 1.0 Mev. The theoretical area is approximately 0.85 as large as the experimental one (defined by a dashed line in Fig. 8), and the corrections estimated in Table III would lower this ratio to 0.80. On the other hand, the calculated curve for lead appears to be distinctly above the experimental points except near the photopeak, but the comparison of areas is more satisfactory in this case, the ratio being 1.05 without corrections and 0.95 with the corrections estimated in Table III.

The ratio of the counting rate in lead to that in brass is much less encouraging than consideration of either stopping material alone. The calculated ratio is approximately 1.4 and the experimental ratio only 1.15. This discrepancy in the dependence on the stopping material is even more marked in the comparison of Lucite and brass; they cannot be distinguished by looking at the experimental points, whereas the calculated curve for Lucite is lower than that for brass by a factor 0.8. Indeed, the calculated counting rates in Lucite are, on the average, only two-thirds as large as the observed rates. Bremsstrahlung and single-quantum annihilation are too small to be relevant to this discrepancy, which is well outside the experimental error. A possible lack of isotropy in the Lucite experiments might decrease the discrepancy slightly, but could hardly account for a major portion of it.

All three experimental pulse-height distributions for Ne^{19} positrons appear to decrease more rapidly with increasing pulse height than the theoretical ones. Lowering the end-point energy of the Fermi spectrum to 2.235 Mev in the calculations would reduce this difference in the slopes only a very little, and corrections for attenuation by annihilation and for possible energy-dependent absorption effects would both tend to increase it.

For A^{35} positrons, the slopes are in better agreement with experiment, but the theoretical curves fall always below the experimental ones. For lead, brass, and Lucite, the ratios of calculated to experimental counting rates are approximately 0.85, 0.65, and 0.5, respectively; the corrections from Table III would lower the first two ratios even further. The theoretical Z dependence is again conspicuously larger than the experimental, and the corrections of Table III, while now in the right direction, remove only a small part of the discrepancy.

It should be noted that the Z dependence of the calculated distributions can be traced directly back to the cross sections and to the rate of energy loss. It is not affected by the normalization procedure nor by the response curves of the γ-ray detector, because these are the same for every stopping material. The excessive Z dependence of the calculated distributions for A^{35} positrons comes chiefly from the contributions of bremsstrahlung, and therefore implies that Eq. (8) represents a serious overestimate of the bremsstrahlung cross section for positrons, perhaps by a factor as large as 2.

From the comparison of Ne^{19} positrons in Lucite and brass, where two-quantum annihilation is the only important source of γ rays, it appears that the $\ln I^2$ term of the stopping power produces a stronger Z

dependence than is observed. This conclusion still holds when the values of I are taken from proton data, instead of being assumed proportional to Z, and when corrections for the density effect are included. The same remarks apply with less force to the comparison of Ne^{19} positrons in lead and brass, since the logarithmic dependence of the stopping power would alone be sufficient to produce a lead-to-brass ratio of 1.17 (1.13 with the corrections of Table III), whereas the experimental ratio of 1.15 could be attributed entirely to the effects of bremsstrahlung and single-quantum annihilation.

If the conclusion is accepted that bremsstrahlung has been considerably overestimated in the calculations, it must also be recognized that a 50 percent reduction in the bremsstrahlung cross section would make the calculated pulse-height distributions for A^{35} positrons in lead and brass smaller than the experimental ones by factors of 0.5 to 0.7. This discrepancy would then be similar for A^{35} positrons in all three stopping materials, but would not be shared by the lower-energy positrons of Ne^{19} and C^{11}.

In summary, the experimental results support the γ-ray energy dependence of the two-quantum annihilation cross section and, in some cases, but not in others, the magnitude of the cross section. The agreement is satisfactory for Ne^{19} positrons stopping in brass or lead and for C^{11} positrons, but not for Ne^{19} positrons in Lucite. The disagreement for the higher-energy A^{35} positrons is large and has no apparent explanation, unless it is due to an inadequacy in the cross section in this energy region.

The authors are very much indebted to Dr. J. A. Wheeler, Dr. C. N. Yang, and Dr. G. C. Wick for their valuable discussions of the experiment, and to Mr. R. V. Krotkov for his assistance in taking the data.

PHYSICAL REVIEW VOLUME 94, NUMBER 4 MAY 15, 1954

A Precise Momentum Measurement of the F Line of Thorium B*†

D. I. MEYER‡ AND F. H. SCHMIDT
Department of Physics, University of Washington, Seattle, Washington

(Received February 15, 1954)

The momentum of the internal conversion electrons of the F line of thorium B has been compared with the momentum of electrons accelerated through a known potential difference. The comparison was made by means of an iron-free high-resolution solenoidal magnetic field beta-ray spectrometer. The value obtained for the F line is 1388.56±0.21 gauss-cm. Other useful calibration lines following the decay of thorium B have also been measured by comparison with the F line.

INTRODUCTION

UNTIL recently the most accurately known beta-ray momentum standard was Siegbahn's[1] measurement of the F internal conversion line in thorium B. The interest in precision beta- and gamma-ray spectroscopy received considerable stimulation by the accurate curved-crystal spectrometer wavelength determinations of nuclear gamma rays and annihilation radiation by DuMond and others.[2,3] The initial objectives of the present work[4] were to improve existing standards, and to endeavor to resolve an apparent inconsistency between the calculated and measured energy of annihilation radiation.[5] DuMond[6] pointed out that the discrepancy had been noted in earlier determinations[3] of the energy of annihilation radiation, and that it could be accounted for by an electron-positron mass difference of ~250 ev.

While the experiment discussed in this paper was in progress, several other careful energy measurements were reported. Lindström[7] determined the momentum of the F, I, and L internal conversion lines of thorium by a direct measurement of the deflecting magnetic field (in terms of the proton magnetic moment) and of the radius of curvature of the electron trajectories. A determination of the momentum of the A, F, and I lines by a different method was made by Craig.[8] In addition, other standard conversion lines and gamma rays have been measured with considerable accuracy.[9,10]

* An abridgement of a thesis presented by D. I. Meyer to the Graduate School of the University of Washington in partial fulfillment of the requirements for the Ph.D. degree.

† Partially supported by the U. S. Atomic Energy Commission.

‡ Present address: Department of Physics, University of Oklahoma, Norman, Oklahoma.

[1] K. Siegbahn, Arkiv. Mat. Astron. Fysik **30A**, No. 20 (1944).

[2] DuMond, Lind, and Watson, Phys. Rev. **73**, 1392 (1948); Lind, Brown, Klein, Muller, and DuMond, Phys. Rev. **75**, 1544 (1949); Lind, Brown, and DuMond, Phys. Rev. **76**, 1839 (1949).

[3] DuMond, Lind, and Watson, Phys. Rev. **75**, 1226 (1948).

[4] Preliminary results reported at the St. Louis meeting of the American Physical Society, November, 1952, by D. I. Meyer and F. H. Schmidt, Phys. Rev. **89**, 908 (1953).

[5] A. Hedgran and D. A. Lind, Phys. Rev. **82**, 126 (1951).

[6] J. W. M. DuMond, Phys. Rev. **81**, 468 (1951).

[7] G. Lindström, Phys. Rev. **83**, 465 (1951); Arkiv Fysik **4**, 1 (1951).

[8] H. Craig, Phys. Rev. **85**, 688 (1952).

[9] Muller, Hoyt, Klein, and DuMond, Phys. Rev. **88**, 775 (1952).

[10] W. L. Brown, Phys. Rev. **83**, 271 (1951); G. Lindström, Phys. Rev. **87**, 678 (1952); K. Siegbahn, Physica **18**, 1043 (1952).

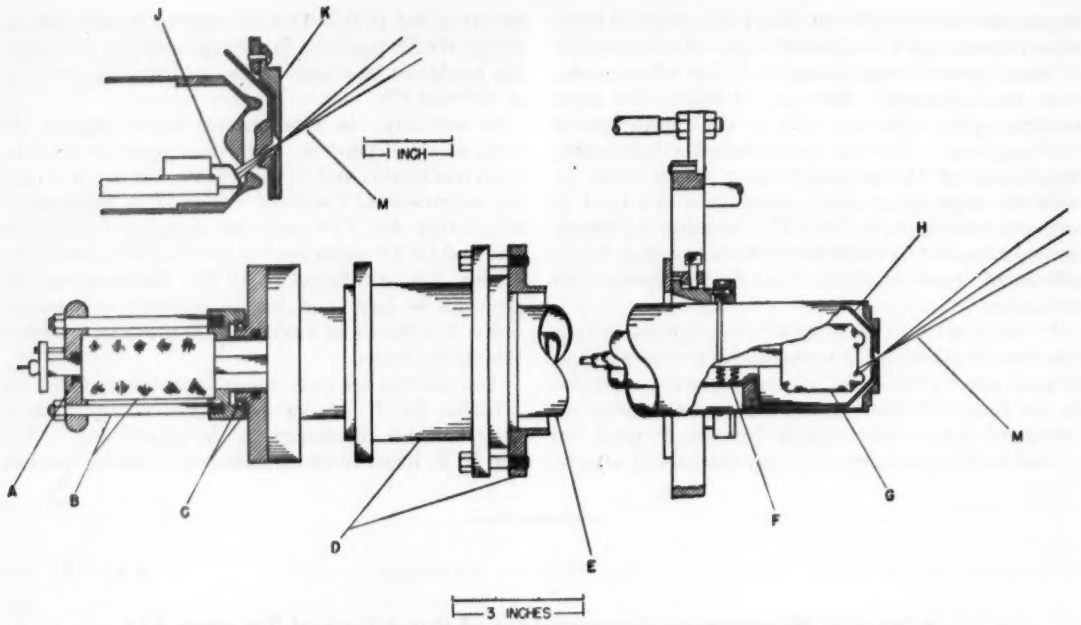

FIG. 1. The electron gun. The unit fits inside the tube (*E*) which is inserted into the spectrometer through a sliding seal and vacuum gate (*D*). The insulated electrode (*G*) is supported by the insulators (*F*) and (*B*). The insulated structure and the grounded shield (*H*) rotate as a unit by means of the vacuum seal and ball bearings (*C*). In addition, the electrode (*G*) and the filament (*J*) can be adjusted to provide a uniform electron beam (*M*) at the correct angle with respect to the spectrometer axis. The details of the accelerating electrodes are shown in the inset. The effective electron source is provided by an 0.014-inch hole in the disk (*K*). The thorium *B* source mounted on the structure in place of the disk (*K*).

The early inconsistency between the crystal spectrometer values for the annihilation radiation and the calculated value assuming equal positron-electron masses has been resolved.[11] Further, a direct comparison of m/e for the positron and for the electron has shown the masses to be equal to within about 100 ev.[12]

In view of these latter developments our method of precision momentum measurement was not pursued beyond a limited objective: viz., to provide an independent determination of one calibration standard, the thorium B *F* line. We have compared the momentum of these internal conversion electrons directly with that of electrons accelerated through an accurately known potential difference. The result constitutes a complementary and independent check of other methods.

I. METHOD

The momentum of electrons focused by an iron-free magnetic spectrometer is proportional to the current through the coils of the spectrometer. Hence, electrons of unknown momentum can be compared with those of known momentum by a simple measurement of the ratio of two currents. Electrons of known momentum were obtained by acceleration in an electron gun through a known potential difference. In principle the method is very simple; however, considerable care is required in order to achieve substantial precision.

A. Spectrometer

A uniform magnetic field solenoidal spectrometer[13] employing a ring focus was used. The delimiting baffles of the spectrometer were set to transmit ~1 percent of isotropically emitted electrons. The theoretical inverse momentum resolution (full width at half-maximum) for the optimum source diameter (0.014 in.) at this setting is 0.10 percent.

Both the vertical and horizontal components of the earth's magnetic field were neutralized. The residual field was less than 0.01 gauss, and constant to about one-fifth of this value. The lowest spectrometer field required for the experiment was ~40 gauss. The effect on the spectrometer calibration of masses of iron deliberately placed nearby was studied. It was concluded that no undetected iron in the vicinity of the instrument could influence the results. In addition, the momentum of accelerated electrons *vs* spectrometer current was studied from 1.9- to 18.6-kv accelerating potential with no indication of nonlinearity.

B. Electron Gun

A diagram of the electron gun is shown in Fig. 1. A set of small insulated electrodes was placed on the

[11] We are indebted to Dr. DuMond for informing us of these results prior to publication (see reference 9).

[12] Page, Stehle, and Gunst, Phys. Rev. 89, 1273 (1953).

[13] F. H. Schmidt, Rev. Sci. Instr. 23, 361 (1952).

baffle structure of the spectrometer. These were used to insure that the current issuing from the "gun" was constant from 34° to 36° elevation angles. The positions of the wolfram filament and of the inner electrode, both of which affected the direction of the electron beam, could be adjusted during operation. The entire internal "gun" structure could be rotated in order to pass electrons through the spectrometer at any desired azimuthal angle. The assembly entered the spectrometer vacuum through an air lock. Its position within the spectrometer was reproducible to within 0.001 inch.

C. Thorium B Sources

Thorium B was deposited on thin ($\sim$50 μg/cm^2) Nylon films over a circular area 0.014 inch in diameter. A jig fixture positioned accurately the film and supporting ring. The Nylon was gently clamped to a Lucite disk which covered the radiothorium container. A 0.014-inch hole in the Lucite allowed the active material to be attracted to the Nylon film by a 600-volts negative potential. With the limited supply of radiothorium available ($\sim$2 mg Ra equivalent) sources prepared in this manner were adequately strong for observation of the F line in the spectrometer, but the other well-known lines were too weak. Accordingly, comparisons of the other lines with the F line were made with larger (0.056-inch) diameter sources. The spectrometer was set at $\sim$2 percent transmission for these measurements.

After each measurement with the electron gun, the disk K (see Fig. 1) was removed and a thorium B source holder substituted in its place. The position of the active deposit was shown to coincide with the original position of the hole in disk K by means of a collimating hole and G-M counter mounted in a jig fixture.

D. Electrical Apparatus and Measurements

A 1- to 20-kv power supply similar to one described by Pepinsky and Jarmotz[14,15] was used to accelerate electrons in the gun. Under operating conditions the maximum voltage variations due to ripple and drift of the balance battery did not exceed one part in 30 000.

Two potential dividers were used to measure the high voltage. One of these, the "standard," was composed of 48–20 000-ohm manganin wire units, and 3–148.15-ohm manganin wire units. The former could be placed in series, and the latter in parallel; the ratio between them is then 18 500. Alternatively, the large units could be placed in parallel, and the small units in series; the ratio between them is then one. Accordingly, a direct comparison can be made between a standard cell and $\sim$18.5 kv. The theory of the method and construction details of a similar resistor have recently been published by Harris.[16] A second potential divider consisting of a 60-megohm nichrome oil-immersed temperature-controlled resistor was compared with the "standard" divider prior to each run. Three unsaturated Weston standard cells constituted the primary voltage standard. These were calibrated by the Bureau of Standards shortly before and immediately after the experiment. Most of the potential drop across the low-voltage section of the high-voltage dividers was balanced out by a standard cell placed in series with a Leeds and Northrup type-K potentiometer. Therefore, only a small residual potential was measured by the potentiometer.

Accelerating voltages were measured to $\pm$0.005 percent. These were corrected for the work function (4.5 v) of the wolfram filament in the electron gun. All other important metals in the system were similar, so that no corrections for contact potentials were required.

For the comparison of the F line with accelerated electrons the current for the spectrometer coils was supplied from a set of large storage batteries. It was constant to $\pm$0.002 percent during a run. Relative values of the coil currents were determined by measuring the potential drop across a precision 100-ampere Leeds and Northrup 0.01-ohm manganin shunt. The currents required for 18.5-kev electrons and the F line were $\sim$4.2 and 12.8 amperes, respectively. A divider consisting of three equal resistances was placed across the 0.01-ohm shunt. The potential appearing across all three was measured on a type-K potentiometer when operating at the lower current value. For the higher current, the potential across each section of the divider was measured. Therefore, very nearly the same place

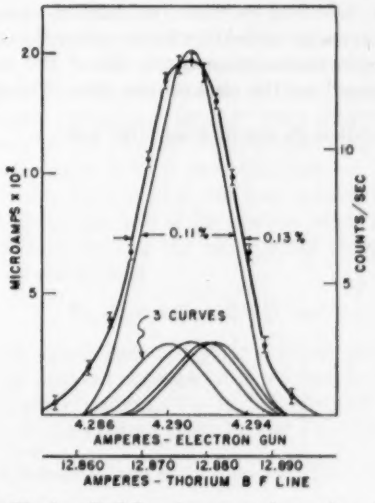

FIG. 2. Thorium B F line shown superimposed on the "line" obtained from the electron gun. The electron line was measured for six azimuthal angles around the ring focus and summed to give the resultant curve. The difference in width between the F line and the electron line is attributed to a natural width of the K-shell energy level in bismuth.

[14] R. Pepinsky and P. Jarmotz, Rev. Sci. Instr. **19**, 247 (1948).
[15] G. Schwartz and E. Byerly, Rev. Sci. Instr. **19**, 279 (1948).
[16] J. N. Harris, Rev. Sci. Instr. **23**, 409 (1952).

TABLE I. Momenta and energies of useful calibration lines in the decay of thorium B.

Th line	Investigator	Electron momentum in gauss-cm	Gamma-ray energy in kev
F	Siegbahn[a]	1384	
F	Craig[b]	1388.5 ±0.3	
F	Lindström[c]	1388.55±0.15[d]	238.63 ±0.04[d]
F	Muller *et al.*[e]		238.595±0.032[f]
F	Present work	1388.56±0.21	238.63 ±0.06
A	Craig[b]	533.66±0.12	
A	Present work[g]	534.11±0.22	
I	Craig[b]	1753.9 ±0.4	
I	Lindström[c]	1754.01±0.20[d]	238.62 ±0.04[d]
I	Present work[g]	1754.0 ±0.7	
L	Lindström[c]	2607.17±0.30[d]	510.85 ±0.08[d]
L	Muller *et al.*[e]		510.90 ±0.09[f]
L	Present work[g]	2606.9 ±1.0	
X	Lindström[h]	9986.7 ±1.5	2614.25 ±0.50
X	Brown[h]	9988 ±2.0	2614.7 ±0.6
X	Present work	9985 ±5.0	

[a] See reference 1.
[b] See reference 8.
[c] See reference 7.
[d] The error listed here is that quoted in the full report in Arkiv Fysik, reference 7.
[e] See reference 9.
[f] Crystal spectrometer measurements.
[g] By comparison with the *F* line at 0.4 percent resolution.
[h] See reference 10.

on the potentiometer slide wire could be used for each of the precision comparison measurements.

II. RESULTS AND DISCUSSION

Data for a typical run on the *F* line and the electron gun are shown in Fig. 2. The focused electron currents from the gun at constant accelerating potential are plotted *vs* spectrometer current for 6 equally spaced azimuthal angles. The variation as a function of angle is due to slight inhomogeneities in the spectrometer magnetic field and to minor mechanical variations.[17] The six curves are added together to obtain the resultant electron-gun transmission curve. The *F* line is shown superimposed on the electron-gun data. The full line width at half-maximum for the accelerated electrons is 0.11 percent, whereas the width for the *F* line is 0.13 percent. The most probable cause for this difference in width is a natural spread of ~0.02 percent, or ~50 ev, in energy of the *F* line. A similar effect was observed by Slätis and Lindström,[18] and attributed by them to the distribution in energy of the *K*-shell electrons.

The average value of six measurements of the momentum of the *F* line are given in Table I, together with other recent work. The agreement among the various investigations, each by a different method, is very good. In converting the energy of the accelerated electrons into momentum, and in calculating the energy of the *F*-line electrons, the least-squares values of the atomic constants given by DuMond and Cohen[19] were used. The *K*-electron binding energy for bismuth was taken from the tables of Cauchois and Hulubei.[20] The internal consistency of the six independent determinations is ±0.01 percent; the probable error quoted in Table I includes the various other uncertainties.

The data for the other thorium lines listed in Table I were obtained with the spectrometer set for ~2 percent transmission corresponding to ~0.4 percent resolution. The focusing current at the peak of each line was compared with that for the *F* line. For these measurements a motor-generator set was used to supply the current, and a type-K potentiometer was employed in the normal manner to determine the coil current. With the possible exception of the *A* line, the agreement between our values and those of others is excellent.

We wish to thank G. L. Keister for the loan of a vacuum evaporator, Lee Meyer for assistance with tedious measurements, and Max Henker for skill in making the numerous small mechanical parts of the electron-gun and standard resistors.

[17] The width of the ring slit is only 0.007 inch.

[18] H. Slätis and G. Lindström, Phys. Rev. **88**, 1429 (1952).
[19] J. W. M. DuMond and E. R. Cohen, Phys. Rev. **82**, 555 (1951).
[20] J. Cauchois and H. Hulubei, *Longueurs d'Onde des Emissions X* (Hermann et Cie, Paris, 1947).

Effect of Atomic Electron Screening on the Shape of Forbidden Beta Spectra

R. H. Good, Jr.
Department of Physics, Pennsylvania State University, State College, Pennsylvania
(Received February 8, 1954)

In Fermi's theory of beta decay the influence of the atomic electrons on the shape of the spectra is often disregarded since the influence is small except at low energies. However, there is some interest in knowing exactly how small it is. This paper gives an approximate calculation of the screening effect, both for allowed and for forbidden spectra. The Thomas-Fermi model for the atomic electrons and WKB approximations for the wave functions of the emitted particles are used. The results for the allowed spectra agree with those of Rose and of Longmire and Brown. The calculations for the forbidden spectra lead to a simple rule for finding the screening effect in any specific case.

I. INTRODUCTION

IN Fermi's original paper on beta decay[1] he neglected the effects of the atomic electrons on the process. This has also been done in many of the subsequent developments of the theory; it is ordinarily assumed that the beta particle is created into the Coulomb field of the daughter nucleus. The justification for this simplifying assumption is that the atomic electrons have only a small influence on the electric field at the nucleus, where the beta particle is created. One expects the atomic electrons to be of importance only when the energy of the emitted beta particle is so small that the wavelength is comparable to the size of the atom. The atomic electrons make the effective electric field smaller than the field of the bare nucleus so that, when they are taken into account, a decreased electron emission and an increased positron emission are predicted by the theory.

The effect of the atomic electron screening was first calculated by Rose[2] and later by Longmire and Brown[3] using methods based on the WKB approximation. Most recently Reitz[4] has published tables of the screening correction, found by solving the equations numerically. All these authors have discussed the allowed beta spectra only. However there is a need for similar information about the forbidden spectra also;[5] the purpose of this paper is to discuss the screening effect with emphasis on the forbidden spectra.

The calculations here are similar to those of Rose and Longmire and Brown,[2,3] and for the allowed spectra the results found here agree essentially with theirs. WKB approximations to the wave functions of the emitted beta-particle are used, and the potential due to the atomic electrons is found from the Thomas-Fermi statistical model.[6,7] A simple procedure is given for finding the effect of the screening on any specific forbidden spectrum. It is found that ordinarily the effect for a forbidden spectrum is of the same order of magnitude as for the allowed spectrum.

II. DERIVATION OF THE SCREENING EFFECT

In the following discussion the notation of Konopinski and Uhlenbeck[8] and of Smith,[9] is used. The Konopinski-Uhlenbeck paper gives formulas for the first- and second-forbidden beta spectra for each of five possible interaction types. Smith's letter gives the cross terms which arise when a linear combination of the five interaction terms is used, assuming no Fierz[10] interference (cross terms have also been calculated by Pursey[11] and by Al-Ghita[12]). Both Konopinski-Uhlenbeck and Smith expressed their results in terms of quanties L, M, N, L^-, M^-, N^- which depend quadratically on wave functions of the electron evaluated at the nuclear radius, and then they substituted the wave functions for an electron in the Coulomb field of the daughter nucleus. The screening will be taken into account here by using the Coulomb field modified by the atomic electron cloud. A consequence of treating the screening this way is that different values of L, M, N, L^-, M^-, N^- are obtained but the formulas expressing the spectrum shapes in terms of these quantities are unchanged. Serber and Snyder[13] have shown that this approach to the problem takes proper account of the binding energies of the atomic electrons.

From this point of view, the beta particle is emitted into the potential field of the neutral parent atom plus the Coulomb field of the single extra charge that it leaves on the nucleus:

$$V_{sc}(Z)=\pm V_{TF}(Z\mp 1)-\alpha r^{-1}. \quad (1)$$

Here the upper signs apply for electron emission, the lower for positron emission, Z is the atomic number of the daughter nucleus, V_{sc} is the screened potential energy of the emitted particle, and $V_{TF}(Z\mp 1)$ is the

[1] E. Fermi, Z. Physik **88**, 161 (1934).
[2] M. E. Rose, Phys. Rev. **49**, 727 (1936).
[3] C. Longmire and H. Brown, Phys. Rev. **75**, 264, 1102 (1949).
[4] J. R. Reitz, Phys. Rev. **77**, 10 (1950).
[5] See, for example, Freedman, Wagner, and Engelkemeir, Phys. Rev. **88**, 1155 (1952).
[6] L. H. Thomas, Proc. Cambridge Phil. Soc. **23**, 542 (1927).
[7] E. Fermi, Z. Physik **48**, 73 (1928).
[8] E. J. Konopinski and G. E. Uhlenbeck, Phys. Rev. **60**, 308 (1941).
[9] A. M. Smith, Phys. Rev. **82**, 955 (1951).
[10] M. Fierz, Z. Physik **104**, 553 (1937).
[11] D. L. Pursey, Phil. Mag. **42**, 1193 (1951).
[12] M. K. Al-Ghita, thesis, University of Michigan (Publication No. 3709, University Microfilms, Ann Arbor, Michigan, 1952).
[13] R. Serber and H. S. Snyder, Phys. Rev. **87**, 152 (1952).

Thomas-Fermi potential energy for an electron in the parent atom of atomic number $(Z\mp1)$. It is assumed that the beta particle has escaped from the atom before any rearrangements in the atomic electrons take place. The connection between this screened potential and the Coulomb field of the daughter nucleus is seen by expanding the Thomas-Fermi potential about the nucleus. Using Fermi's formulation of the statistical potential,[7] Baker's expansion about the nucleus,[14] and converting to relativistic units, one finds easily that

$$V_{TF}(Z\mp1)=-\frac{\alpha(Z\mp1)}{r}\left\{1-1.589\frac{r}{\mu}+O\left[\left(\frac{r}{\mu}\right)^{\frac{3}{2}}\right]\right\}, \quad (2)$$

where

$$\mu=0.885\alpha^{-1}(Z\mp1)^{-\frac{1}{3}} \quad (3)$$

is a characteristic length for the parent atom electron cloud. The screened potential in the neighborhood of the nucleus is then

$$V_{sc}(Z)=\mp\frac{\alpha Z}{r}\pm1.589\frac{\alpha(Z\mp1)}{\mu}\left\{1+O\left[\left(\frac{r}{\mu}\right)^{\frac{3}{2}}\right]\right\}. \quad (4)$$

The first term is the usual Coulomb potential. In what follows, a first approximation to the screening effect will be obtained by taking into account the second term, disregarding the terms of order $(r/\mu)^{\frac{3}{2}}$ compared to 1.

It would be difficult to make exact calculations of the electron wave functions in the potential of Eq. (1); the WKB method developed by Uhlenbeck and Bessey[15] for the Dirac radial wave equation will be used to approximate the functions. This approximation has been reviewed in an earlier paper.[16] The use of this WKB method in this problem requires justification because the values of the wave functions at the nuclear radius are required and this radius is in the neighborhood of the pole of the potential function at the origin. However, it has been shown that for the Coulomb potential $V(r)=\mp\alpha Z/r$ the WKB approximation reproduces the exact results within a few percent both for the function $F(Z,W)$ which gives the shape of allowed spectra and for a representative forbidden spectrum correction factor.[16,17] This indicates that the method will give good results in the problem at hand, where the potential also has a simple pole at the origin and then goes monotonically to zero. For use in the formulas of Konopinski-Uhlenbeck and Smith, radial wave functions f_l, g_l satisfying the Dirac radial wave equations, giving an integrable probability density at the origin, and normalized to one particle in a sphere of unit radius, are required. Referring to Eqs. (12) and (13) of reference 16 and putting $u=rf$, $v=rg$, one finds that the WKB approximations to these functions are, when $r<r_1$,

$$f_l=-\frac{1}{2r}\frac{|l+1|}{l+1}\left(\frac{p\psi(r)}{WR(r)}\right)^{\frac{1}{2}}\times\exp\int_r^{r_1}\left[-\left(1+\frac{\xi\psi'(\xi)}{\psi(\xi)}\right)\frac{l+1}{2\xi^2R(\xi)}-R(\xi)\right]d\xi, \quad (5)$$

$$g_l=\frac{1}{2r}\left(\frac{p\phi(r)}{WR(r)}\right)^{\frac{1}{2}}\times\exp\int_r^{r_1}\left[\left(1+\frac{\xi\phi'(\xi)}{\phi(\xi)}\right)\frac{l+1}{2\xi^2R(\xi)}-R(\xi)\right]d\xi, \quad (6)$$

and are, when $r>r_1$,

$$f_l=-\frac{1}{r}\frac{|l+1|}{l+1}\left(\frac{p\psi(r)}{WQ(r)}\right)^{\frac{1}{2}}\times\cos\left\{\int_{r_1}^{r}\left[Q(\xi)-\left(1+\frac{\xi\psi'(\xi)}{\psi(\xi)}\right)\frac{l+1}{2\xi^2Q(\xi)}\right]\times d\xi-\frac{\pi}{4}\right\}, \quad (7)$$

$$g_l=-\frac{1}{r}\left(\frac{p\phi(r)}{WQ(r)}\right)^{\frac{1}{2}}\times\cos\left\{\int_{r_1}^{r}\left[Q(\xi)+\left(1+\frac{\xi\phi'(\xi)}{\phi(\xi)}\right)\frac{l+1}{2\xi^2Q(\xi)}\right]\times d\xi-\frac{\pi}{4}\right\}, \quad (8)$$

where

$$\phi(r)=W-V(r)+1, \quad (9)$$

$$\psi(r)=W-V(r)-1, \quad (10)$$

$$Q(r)=[\phi\psi-(l+1)^2r^{-2}]^{\frac{1}{2}}, \quad (11)$$

$$R(r)=[(l+1)^2r^{-2}-\phi\psi]^{\frac{1}{2}}, \quad (12)$$

$V(r)$ is an arbitrary potential, and r_1 is the positive root of $[r^2\phi\psi-(l+1)^2]$. Zwann's method[18] was used to connect the approximations across the turning point r_1.

The next step is to evaluate the approximate wave functions, Eqs. (5) to (8), at the nuclear radius ρ and with the potential of Eq. (1). Since ρ is always less than r_1, formulas (5) and (6) apply with r replaced by ρ. The result then depends only on the value of the potential in the region $r<r_1$. It is easily seen that $r_1<\mu$, so one may use the expansion of the potential for small r/μ [Eq. (4)]; as a further approximation the higher-order terms

[14] E. B. Baker, Phys. Rev. 36, 630 (1930).
[15] R. J. Bessey, thesis, University of Michigan, 1942 (unpublished).
[16] R. H. Good, Jr., Phys. Rev. 90, 131 (1953).
[17] R. H. Good, Jr., thesis, University of Michigan (Publication No. 2597, University Microfilms, Ann Arbor, Michigan, 1951).
[18] See, for example, Edwin C. Kemble, *The Fundamental Principles of Quantum Mechanics* (McGraw-Hill Book Company, Inc., New York, 1937), first edition, p. 95.

will be disregarded so that

$$V_{sc}(Z)=\mp\alpha Z r^{-1}+\Delta, \tag{13}$$

where

$$\Delta=\pm 1.589\alpha\mu^{-1}(Z\mp 1) =\pm 1.795\alpha^2(Z\mp 1)^{4/3}. \tag{14}$$

A property of Eqs. (5) and (6) is that W and $V(r)$ always occur in the combination $W-V(r)$ in the integrations. This permits the screened-potential wave functions f_l^{sc}, g_l^{sc} to be expressed in terms of the well-known Coulomb wave functions f_l^{Coul}, g_l^{Coul}. Introducing the notation

$$\bar{K}(Z,W)=K(Z,W-\Delta) \tag{15}$$

for any function $K(Z,W)$, then one sees that

$$f_l^{sc}=(p\bar{W}/\bar{p}W)^{\frac{1}{2}}\bar{f}_l^{\text{Coul}}, \tag{16}$$

$$g_l^{sc}=(p\bar{W}/\bar{p}W)^{\frac{1}{2}}\bar{g}_l^{\text{Coul}}. \tag{17}$$

It is assumed that $W>\Delta+1$. The formula for the allowed spectrum, regardless of the potential used, is [reference 8, Eqs. (1) and (22)]

$$P(W)dW=(G^2/2\pi^3)C_0F(Z,W)pW(W_0-W)^2dW, \tag{18}$$

where

$$F(Z,W)=(g_0^2+f_{-2}^2)p^{-2}(1+s)^{-1}. \tag{19}$$

The result for the screened potential is then easily found to be

$$F^{sc}=(\bar{p}\bar{W}/pW)\bar{F}^{\text{Coul}}. \tag{20}$$

This result is substantially in agreement with the results of Rose[2] and of Longmire and Brown,[3] although they choose a different value for Δ (Reitz's paper[4] shows the connection between their results). The numerical evaluation of this function has been discussed by Fano.[19]

What happens in the forbidden spectra is easily shown by a specific example. For the vector first-forbidden transition the spectrum is [reference 8, Eq. (24)]

$$P(W)dW=dW\frac{G^2}{\pi^3}\frac{q^2W}{p}\Big[|\int\mathbf{r}|^2\Big\{\frac{q^2}{3}\frac{g_0^2+f_{-2}^2}{4\pi} +\frac{f_0^2+g_{-2}^2}{4\pi\rho^2}\Big\}+\text{other terms}\Big]. \tag{21}$$

This is usually written like Eq. (18) except with a correction factor:

$$P(W)dW=(G^2/2\pi^3)F(Z,W)pW(W_0-W)^2dW [|\int\mathbf{r}|^2\{\tfrac{1}{3}K^2L_0+M_0\}+\text{other terms}], \tag{22}$$

where

$$L_0=(g_0^2+f_{-2}^2)(2p^2F)^{-1}, \tag{23}$$

$$M_0=(f_0^2+g_{-2}^2)(2p^2F\rho^2)^{-1}. \tag{24}$$

To find the effect of the screening, one substitutes Eqs. (16) and (17) into Eq. (21) and puts the results in the form of Eq. (22):

$$P(W)dW=(G^2/2\pi^3)F^{sc}(Z,W)pW(W_0-W)^2dW \times[|\int\mathbf{r}|^2\{\tfrac{1}{3}K^2L_0^{sc}+M_0^{sc}\}+\text{other terms}], \tag{25}$$

where

$$L_0^{sc}=\bar{L}_0^{\text{Coul}}, \tag{26}$$

$$M_0^{sc}=\bar{M}_0^{\text{Coul}}. \tag{27}$$

This argument can be applied uniformly to all the terms in the forbidden spectra. One may take the screening into account by using the F^{sc} of Eq. (20) in the basic spectrum formula and by replacing W by $W-\Delta$ in the results of Konopinski-Uhlenbeck and Smith for the quantities L, M, N, L^-, M^-, N^- which arise in the correction factors. Ordinarily these quantities do not depend drastically on the energy, so the screening effect for forbidden spectra is of the same order of magnitude as it is for the allowed spectrum. A very simple interpretation of these results has been given by Huster.[20]

A large part of this work was done while a Horace H. Rackham predoctoral fellow at the University of Michigan. It is a pleasure to thank Professor G. E. Uhlenbeck for proposing the problem and directing the research.

[19] U. Fano, *Tables for the Analysis of Beta Spectra*, Natl. Bur. Standards U. S. Appl. Math. Ser. 13 (U. S. Government Printing Office, Washington, 1952).

[20] E. Huster, Z. Physik 136, 303 (1953).

The Pickup Reactions $B^{10}(n,d)Be^9$ for 14-Mev Neutrons*

F. L. RIBE AND J. D. SEAGRAVE
University of California, Los Alamos Scientific Laboratory, Los Alamos, New Mexico
(Received February 1, 1954)

Measurements have been made of the yields and angular distributions of deuterons resulting from the bombardment of B^{10} by 14-Mev neutrons. The spectrum of charged reaction products was measured by means of a coincidence-telescope spectrometer consisting of two proportional counters and a thin NaI scintillator. The telescope was rotated to obtain measurements at various angles. Deuterons corresponding to the ground state and 2.43-Mev excited state of Be^9 were identified by measurements of both their energy and dE/dx values. The ground-state angular distribution was found to match the expected Butler inverse-stripping curve for $l_p=1$. The Butler analysis for the excited-state deuterons also gave $l_p=1$, corresponding to odd parity and spin 3/2, 5/2, 7/2, or 9/2 for the first excited state of Be^9. In particular, the spin value 1/2, to be expected from the L–S coupling model, is excluded. The cross sections, integrated from zero to 90 degrees (center of mass), are 21 ± 3 and 16 ± 2 millibarns, respectively, for the ground- and excited-state reactions.

INTRODUCTION

THE spins and parities of the energy levels of the Be^9 nucleus have been little investigated. Accurate energy measurements utilizing the $B^{11}(d,\alpha)$ reaction[1] and the $Be^9(p,p')$ reaction[2] showed a narrow (<7 kev) excited level at 2.43 Mev with no further indication of excited states between zero and 5 Mev. A search for α-n and α-γ coincidences from bombardment of B^{11} by deuterons,[3] showed that the 2.43-Mev state decays mainly by neutron emission. In addition to further extensive low-energy inelastic-scattering results[4] on this level, recent inelastic measurements with 32-Mev protons[5] have shown additional levels at 6.8 and 11.6 Mev. The only attempt to determine the spins of excited levels has been that of Mullin and Guth[6] who analyzed the angular distributions and energy variation of the $Be^9(\gamma,n)Be^8$ data and inferred the existence of an $S_{\frac{1}{2}}$ level at about 1.5 Mev with a $D_{\frac{3}{2}}$ level somewhat higher.

Recent work on the disintegration of Li^6 by 14-Mev neutrons[7,8] has shown a striking predominance of the (n,d) pickup reaction, and it was hoped that this process would also be strong in the somewhat analogous case of the $B^{10}(n,d)Be^9$ reaction. Since this is a case of inverse stripping, the well-known theoretical results of Butler[9] on the angular distributions of stripping reactions apply. So long as one considers the same center-of-mass energies for (d,n) and (n,d) reactions, it is clear from the theorem relating inverse nuclear reactions that Butler's stripping curves may be used directly in the case of nucleon pickup. Thus the angular distributions of the deuterons can be used to determine the parities and, within certain limits, the spins of those levels which are excited in the residual Be^9 nucleus.

The object of the present experiment was to measure the differential cross sections of the $B^{10}(n,d)$ reactions to the ground and excited levels of Be^9 and to compare these with Butler's theoretical functions in order to make spin and parity determinations.

APPARATUS

The apparatus for measuring the angular distributions of the charged reaction products from the bombardment of B^{10} by 14-Mev neutrons is shown in Fig. 1. The neutrons bombarded a thin B^{10} radiator, and the charged reaction products emitted into a small solid angle were analyzed by means of a coincidence-telescope spectrometer. The spectrometer was mounted on an indexed stand so that its axis could be rotated in a horizontal plane about a vertical axis lying in the plane of the radiator. The angles made by the reaction products with the incident neutron direction could be read directly from the index of the rotatable stand.

The 14-Mev neutrons were obtained from the $T(d,n)He^4$ reaction by bombarding a thick zirconium-tritium target[10] with the 250-kev monatomic deuteron beam from a Cockcroft-Walton accelerator. The angular position of the boron radiator was 90 degrees with respect to the deuteron beam. At this position the incident neutrons were almost monoenergetic with an energy of 14.10 ± 0.05 Mev. The number of neutrons from the reaction was measured by counting the accompanying alpha particles emitted into a well-defined solid angle.

The radiator was made from 400-mesh amorphous powder containing 98 percent by weight boron enriched to 95.5 percent B^{10}. It was prepared by suspending a small amount of the powder in absolute ethyl alcohol

* Work done under the auspices of the U. S. Atomic Energy Commission.
[1] Van Patter, Sperduto, Huang, Strait, and Buechner, Phys. Rev. **81**, 233 (1951).
[2] Browne, Williamson, Craig, and Donahue, Phys. Rev. **83**, 179 (1951).
[3] G. A. Dissanaike and J. O. Newton, Proc. Phys. Soc. (London) **A65**, 675 (1952).
[4] For a review of the inelastic-scattering results, see F. Ajzenberg and T. Lauritsen, Revs. Modern Phys. **24**, 342 (1952).
[5] R. Britten, Phys. Rev. **88**, 282 (1952).
[6] C. J. Mullin and E. Guth, Phys. Rev. **76**, 682 (1949).
[7] G. M. Frye and L. Rosen, Phys. Rev. **90**, 381 (1953).
[8] F. L. Ribe, Phys. Rev. **87**, 205 (1952).
[9] S. T. Butler, Proc. Roy. Soc. (London) **A208**, 36 (1951).
[10] Graves, Rodrigues, Goldblatt, and Meyer, Rev. Sci. Instr. **20**, 579 (1949).

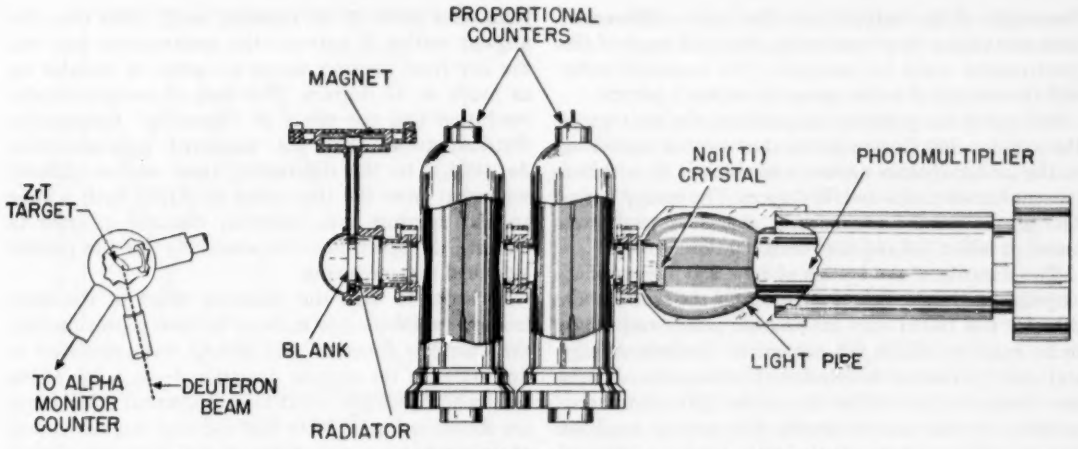

FIG. 1. Apparatus for measuring the $B^{10}(n,d)Be^9$ cross sections, showing $T(d,n)He^4$ neutron source and coincidence-telescope spectrometer.

and allowing the suspension to stand in a vessel, the bottom of which was a detachable platinum disk 0.010 in. thick. When the boron had settled out, the alcohol was drawn off with a pipette and the deposit dried. This deposit was then heated in vacuum to drive off volatile residues, and there resulted a uniform layer which adhered quite well to the platinum backing. The boron radiator thus formed was 2.21 cm in diameter, and its weight was 27.6 mg. The radiator on its platinum backing was attached to one side of a circular collar supported to rotate about a vertical axis as shown in Fig. 1. On the other side of the collar was mounted a platinum blank. At the top of the axle on which the collar was mounted was a small bar magnet which allowed the collar to be rotated inside the spectrometer by means of an external magnet in order to expose either the radiator or the platinum blank to the counters and scintillator of the instrument.

The coincidence-telescope spectrometer consisted essentially of two proportional counters and a thin NaI(Tl) scintillation crystal with light-pipe coupling to a photomultiplier. It operates in the following manner: Neutrons impinge on the boron radiator, and charged reaction products emitted along the spectrometer axis travel through the two counters (which have no foil windows) and strike the NaI crystal of the scintillation detector. The amplified pulses resulting from the ionization in the two proportional counters and from the scintillation of the sodium iodide crystal are fed to a coincidence circuit. An output pulse of the coincidence circuit indicates that a charged particle has traversed the spectrometer. The coincidence output pulse gates open an 18-channel analyzer[11] which records the scintillation pulse in one of its channels. The voltage of this pulse measures the energy of the charged particle traversing the spectrometer. Such a coincidence arrangement is necessary in order to observe the pulse-height spectrum of the reaction products since they occur in the presence of a large (singles) background produced by 14-Mev neutrons and gamma rays striking the scintillator.

The counters were the same as those used by Coon, Bockelman, and Barschall in their *n*-T scattering experiment.[12] They were filled with 71.5 mm Hg of Kr and 3.5 mm Hg of CO_2 and operated in their proportional range at a multiplication of about 10. With this filling the energy loss by a 9-Mev deuteron in traversing each counter was about 64 kev. Therefore the magnitudes of the counter pulses provided a good measure of the quantity dE/dx for the reaction products.

The NaI crystal was in the form of a cylinder 1 in. in diameter and 2.5 mm thick with the edge polished to transparency in alcohol and toluene and the two flat surfaces freshly cleaved in a dry box before insertion of the crystal into the scintillation detector. The crystal was mounted in a glass cup with a plane bottom which fitted into an oil-filled aluminum light pipe leading to the photocathode of a DuMont type K 1177 photomultiplier, as indicated in Fig. 1. With Pu^{239} (5.16-Mev) alpha particles impinging on the whole surface of the crystal in vacuum the resolution (full width at half-maximum) of the scintillation detector was 6.4 percent. The solid angle subtended at the radiator by the last diaphragm aperture before the crystal was 0.0140 steradian.

TESTS OF SPECTROMETER OPERATION

Using a thin polyethylene radiator with the *d-T* neutron source, the strength of which was measured to within 4 percent by means of counted alpha particles, the peaked spectrum of recoil protons was observed and counted. From the known incident flux of neutrons,

[11] C. W. Johnstone, Nucleonics **11**, No. 1, 36 (1953).

[12] Coon, Bockelman, and Barschall, Phys. Rev. **81**, 33 (1951).

the weight of the radiator, and the known differential cross section for $(n$-$p)$ scattering, the solid angle of the spectrometer could be measured. The measured value and the calculated value agreed to within 1 percent.

Still using the polyethylene radiator, the isotropy of the angular distribution for neutron-proton scattering in the center-of-mass system was checked to within 5 percent between zero and 90 degrees. The energy variation of the recoil protons with laboratory angle was found to follow the required $\cos^2\theta$ relation.

The linearity of the system of type 250 preamplifier, amplifier, and pulse-height analyzer for the scintillation detector was tested with an accurate pulser and found to be exact to within 0.5 percent in absolute voltage and about 2 percent in relative channel width. It was also observed that neither the model 250 scintillation amplifier system nor the model 503 counter amplifier system saturated for pulse heights which occurred in the $B^{10}(n,d)$ experiment.

Accidental coincidence counts were observed to be negligible at the counting rates used in the experiment by inserting a 1.3-microsecond delay in the scintillator channel. An additional test was provided by the fact that the recoil-proton counting rate did not change for coincidence-circuit resolving times between 0.35 and 0.80 microsecond. Since scalers were provided on the counter and scintillator channels, the accidentals rate could also be calculated. Neutron fluxes were kept sufficiently low that both the triple-coincidence rate and the double-coincidence rate between the coincidence output and the scintillator singles were negligible.

EFFECT OF THE SPECTROMETER APERTURE

The dimensions defining the angular aperture of the spectrometer were as follows: neutron-source to boron-radiator distance, 13.6 cm; distance from radiator to final scintillator defining aperture, 18.15 cm; radius of radiator, 1.105 cm; and radius of final defining aperture, 1.21 cm. These dimensions were such that the actual scattering angle θ, between an incoming neutron and an outgoing deuteron entering the final defining aperture from some point of the radiator, could differ from the angular setting θ_0 between the spectrometer axis and the line from neutron source to center of radiator by as much as 12 degrees. This lack of perfect angular resolution had the effect of "smearing" the angular distribution so that the measured approximation, $\Delta\sigma/\Delta\Omega(\theta_0)$, to the differential cross section differed somewhat from the true value $d\sigma/d\Omega(\theta)$. Such a large angular aperture was, however, required in order to increase the spectrometer's sensitivity for the present low-yield measurements.

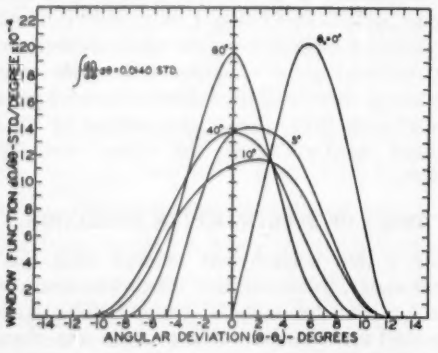

FIG. 2. Window function for counter-telescope spectrometer, showing the effect of finite angular aperture for various angular settings θ_0 of the spectrometer axis.

In order to take the smearing effect of the spectrometer aperture into account to close approximation, the "window function" $d\Omega/d\theta(\theta,\theta_0)$ was calculated to first order in the angular deviation $\theta-\theta_0$. Some of the results of the simple but arduous numerical calculations are shown in Fig. 2. Note that the total angular spread of the window function decreases as θ_0 increases. This is due to the fact that the radiator was kept parallel to the scintillation crystal and hence had a smaller projection perpendicular to the neutron direction as θ_0 increased. The fact that one side of the radiator was closer to the neutron source than the other for $\theta_0>0$ and, hence, had a relatively increased neutron flux was also taken into account in the calculation of the window function.

In terms of the window function $d\Omega/d\theta$, the smeared angular distribution is given by

$$\frac{\Delta\sigma}{\Delta\Omega}(\theta_0)=\frac{1}{\Delta\Omega}\int\frac{d\sigma}{d\Omega}(\theta)\frac{d\Omega}{d\theta}(\theta,\theta_0)d\theta, \qquad (1)$$

where $\Delta\Omega$ is the constant total solid angle of the spectrometer. In order to compare the experimental results with Butler's theoretical angular distributions, the theoretical center-of-mass differential cross sections were transformed to the laboratory system and then smeared numerically according to Eq. (1). The resulting smeared theoretical curves, as well as the experimental data, were then transformed back to the center-of-mass system to present the comparison.

Figure 3 shows, in the laboratory system, the theoretical differential-cross-section curves $d\sigma/d\Omega(\theta)$ and the smeared curves $\Delta\sigma/\Delta\Omega(\theta_0)$ calculated for the ground state reaction $B^{10}(n,d)Be^9$ for 14.1-Mev incident neutrons. The unsmeared curves for the three orbital angular momenta 0, 1, and 2 of the picked-up proton have been arbitrarily normalized to the same maximum value. Although the valleys are filled in somewhat and the peaks diminished, the angular locations of the maxima of the curves are not appreciably affected.

DATA AND EXPERIMENTAL PROCEDURE

Identification of the Deuterons from the Reaction $B^{10}(n,d)Be^9$

The data on the yield and energy of the reaction products were obtained as follows. With the boron radiator facing the spectrometer's active volume, bom-

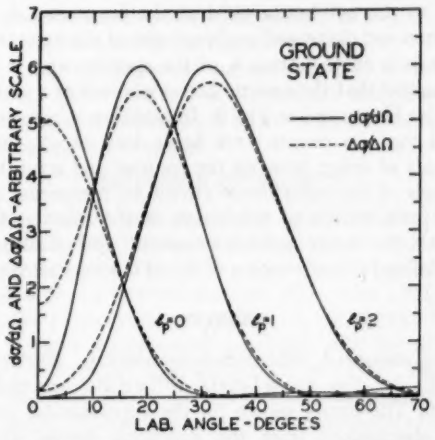

FIG. 3. Theoretical angular distributions for the ground-state $B^{10}(n,d)Be^9$ reaction (solid curves) and the corresponding distributions modified by the effect of finite angular resolution (dashed curves).

bardments were made with an integrated flux of 14.1-Mev neutrons of 1.30×10^9 neutrons/cm^2, and the pulse-height distribution of all charged reaction products which could be recorded for the given proportional-counter biases were recorded on the 18-channel pulse-height analyzer. Using the same integrated flux of neutrons, a bombardment was then made with the platinum blank facing the spectrometer in order to record the background due principally to disintegration of the gas filling of the first counter. This background was then subtracted to give the net pulse-height spectrum of reaction products from the boron radiator. Typical data are shown in Fig. 4 for various angle settings θ_0 of the spectrometer axis. The two peaks due to the (n,d) reaction to the ground and excited states of Be^9 are seen to stand out quite clearly with approximately the resolution to be expected in view of the thickness of the boron radiator—0.56 and 0.75 Mev for the ground- and excited-state deuterons, respectively. The variation of the pulse heights of the groups with θ_0 indicated in Fig. 4 is somewhat arbitrary, since for a given angle setting the scintillator amplifier gain was adjusted to set the deuteron groups comfortably inside the analyzer limits.

In order to determine the energy of the ground-state group of deuterons a thin (4.60 mg/cm^2) radiator of deuterated polyethylene 1.27 cm in diameter was mounted in place of the platinum blank and irradiated at $\theta_0=0$ to determine the pulse-height of the peak due to recoil deuterons of known (12.43-Mev) energy. The boron was then irradiated and the ground-state deuteron pulse-height similarly determined. Comparing the two peaks for five runs, assuming linearity of the NaI crystal, and correcting for radiator half-thickness and energy loss in the counter fillings gave 9.58 ± 0.18 Mev for the forward ground-state deuteron energy. This corresponds to a Q value for the $B^{10}(n,d)Be^9$ ground-state reaction of -4.48 ± 0.18 Mev, in good agreement with the value -4.360 Mev derived from known mass values.[13]

A similar comparison was carried out at $\theta_0=15$ degrees of the pulse heights of the ground-state and excited-state deuteron groups—this time with the platinum blank in order to make background subtractions. Assuming the Q value -4.360 Mev for the ground-state reaction, it was found that the energy of the excited-state group was 7.14 ± 0.12 Mev, corresponding to $Q=-6.85\pm0.12$ Mev and an excited energy of 2.49 Mev, again in good agreement with previously determined values.

It remained to determine the dE/dx values of the deuteron groups in order to identify them positively. This was done by making use of the fact that dE/dx was measured by the proportional counters of the coincidence telescope. A dE/dx comparison was first made between the known recoil deuterons from the deuterated polyethylene radiator and the presumed ground state $B^{10}(n,d)$ deuterons. The numbers of counts in each of the deuteron groups were determined as a function of the common bias of the two proportional-counter

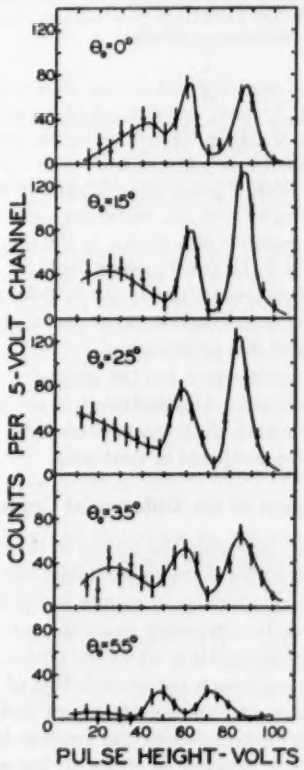

FIG. 4. Scintillator pulse-height distributions for the charged reaction products from the interaction of 14-Mev neutrons with B^{10}, for various spectrometer (laboratory) angles.

[13] Li, Whaling, Fowler, and Lauritsen, Phys. Rev. 83, 512 (1951).

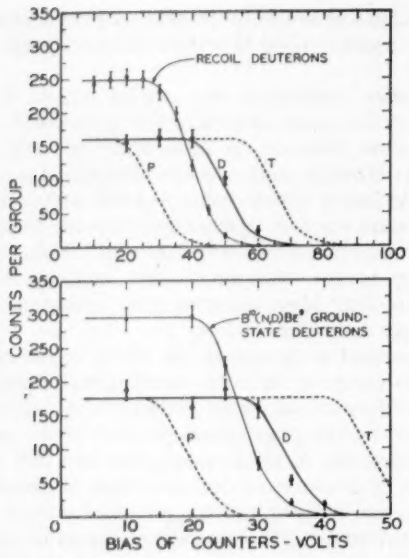

FIG. 5. dE/dx-bias curves used to identify the two principal charged-particle groups as deuterons. The upper curve in each graph corresponds to deuterons of known energy. The lower curves are *calculated* for the particles in question, assuming them to be either protons, deuterons, or tritons.

channels. The resulting bias curves, shown in the upper graph of Fig. 5, show well-defined plateaus. Given the shape of the recoil-deuteron bias curve, one can then calculate the corresponding shape which the bias curve of the lower-energy group should have if it were supposed to be due to protons, deuterons, or tritons. These calculated curves are also shown in the upper graph of Fig. 5, labeled P, D, and T, respectively. It is seen that the experimental points due to the 9.58-Mev group fall closely on the calculated deuteron curve, showing that they are indeed due to deuterons.

A similar comparison for the ground- and excited-state deuteron groups is illustrated in the lower graph of Fig. 5, showing that the excited-state (7.14-Mev) group was also composed of deuterons.

Measurement of the Differential Cross Sections

In order to determine the counts in the ground- and excited-state deuteron groups from data like that shown in Fig. 4, the continuum of counts in the pulse-height spectrum due to competing reactions was subtracted by smoothly interpolating under the peaks. The magnitude of this continuum varied with bias of the proportional counters, and the spectra shown in Fig. 4 represent the condition in which the counter bias was set just below that required to count all the ground-state deuterons.

The magnitude of the platinum-blank background can be inferred from the statistics shown on the points plotted in Fig. 4. Generally this background was about equal to the net boron yield at the lower end of the spectrum and decreased to almost zero at the upper end.

For each angle setting θ_0 of the spectrometer it was ascertained that the counter biases were set at a plateau value as illustrated in Fig. 5. In addition it was determined that no counts were being lost due to undue amounts of delay between the counter and scintillator channels of the coincidence circuit by measuring deuteron-peak counts as a function of the relative delay between the limits ± 0.3 microsecond and observing a well-defined plateau with a width of 0.3 microsecond.

RESULTS

The measured differential-cross-section results are plotted for the ground-state $B^{10}(n,d)Be^9$ reaction in Fig. 6. The errors shown on the experimental points were determined from the statistical spread of the various determinations for each angular setting and include errors due to counting statistics and an allowance for those made in subtracting the continua from the peaks of the pulse-height spectra. The differential-cross-section values have been transformed to the center-of-mass system and correspond to the laboratory angles: 0, 15, 25, 35, 45, 55, and 65 degrees. The (n,d) cross section for the forward hemisphere was obtained by integrating the dashed curve through the experimental points over the solid angle in the center-of-mass system between the angular limits zero and 90 degrees. The resulting integral has the value 21 ± 3 millibarns. The error in this number includes 10 percent due to lack of definiteness in the location of the flat tail, 3 percent due to the effects of smearing by the finite angular aperture, 2 percent in foil-weight determination, 2 percent in solid-angle determination, 4 percent in the flux determination, and 4 percent due to statistics.

The corresponding experimental points for the excited-state differential cross section, also transformed to

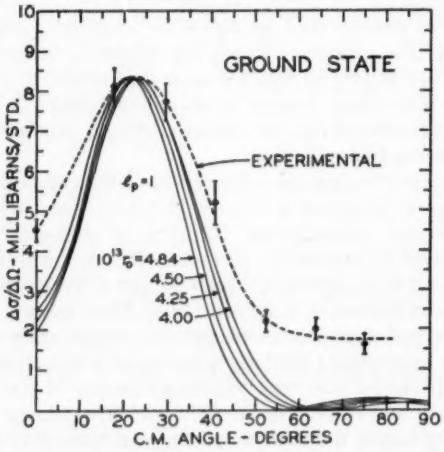

FIG. 6. Experimental and (smeared) theoretical angular distributions for the ground-state $B^{10}(n,d)Be^9$ reaction.

the center-of-mass system, are plotted in Fig. 7. The integrated cross section is 16±2 millibarns.

No group of deuterons corresponding to a state in Be^9 of 1.5-Mev excitation or thereabouts was observed. A differential cross section of as much as 0.4 mb/sterad would have been detected.

DISCUSSION OF RESULTS

When making spin and parity determinations from the angular distributions of (n,d) pickup reactions one is concerned primarily with comparing the observed locations of the forward maxima with those predicted by Butler's theory. As is well known, the angular locations of these maxima vary markedly with the orbital angular momentum l_p of the picked-up proton, leaving little doubt of the proper orbital angular momentum assignment. Following Butler,[9] the conservation of total angular momentum implies

$$\mathbf{l}_p+\mathbf{s}_p+\mathbf{j}=\mathbf{J}, \qquad (2)$$

where $\mathbf{s}_p$ is the proton spin angular momentum, $\mathbf{j}$ is the angular momentum of the final nucleus, and $\mathbf{J}$ is the angular momentum of the initial nucleus.

In the case of the B^{10} ground state the spin is known to be 3 and the parity even. Since Be^9 in its ground state has spin 3/2 and odd parity, the value of l_p for the ground-state pickup reaction must be 1, 3, or 5. The cross section for the lowest value is much favored in magnitude, according to the theory, and one, therefore, expects the experimental angular distribution to be fitted by a theoretical curve corresponding to $l_p=1$. This is indeed seen to be the case in Fig. 6 in which are plotted both the experimental data and theoretical curves from Butler's equation (34) for various values of the parameter r_0, the nuclear radius plus the range of nuclear forces. All four (smeared) theoretical curves correspond to $l_p=1$ and have been normalized to the same maximum value as that of the experimental curve.

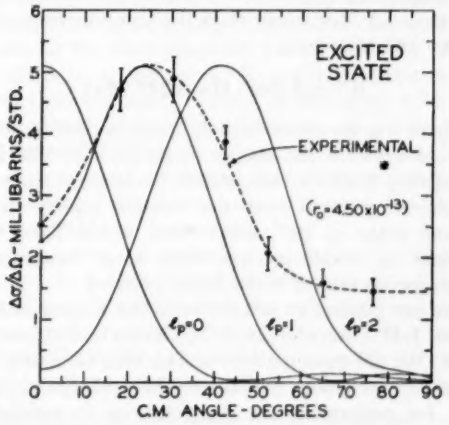

FIG. 7. Comparison of the experimental angular distribution for the excited-state deuteron group with the (smeared) theoretical curves corresponding to various values of the orbital angular momentum of the picked-up proton.

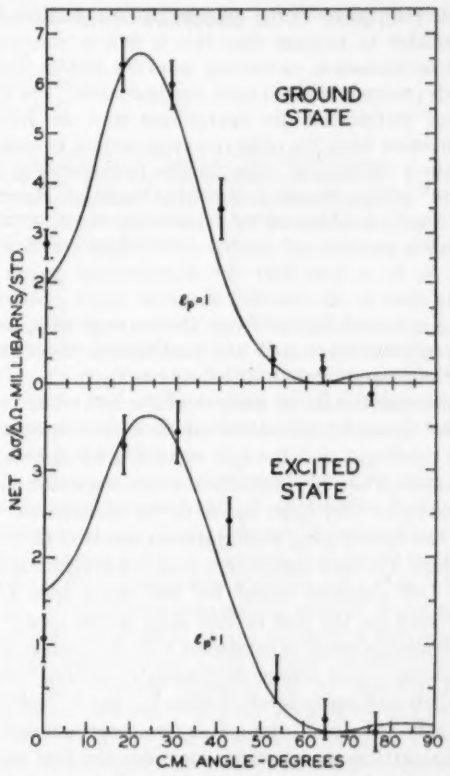

FIG. 8. Comparison with theory of experimental angular distributions after subtraction of isotropic components.

From the total cross section of B^{10} for 14-Mev neutrons[14] one finds $(\sigma/2\pi)^{\frac{1}{2}}=4.84\times10^{-13}$ cm, which one might expect to provide an upper limit for the parameter r_0. It is clear from the curves that the location of the maximum varies little with r_0. Close comparison, however, made it appear that the value 4.50×10^{-13} cm provided the best ground-state fit when an isotropic component equal to the asymptotic-tail value shown was subtracted. This value of r_0 was chosen for calculating the curves corresponding to the 2.43-Mev excited state of Be^9.

In order to study the unknown spin and parity of this excited state, theoretical curves were calculated for the l_p values 0, 1, and 2. A comparison of these curves with the experimental results is given in Fig. 7, where again the theoretical curves have been normalized to the same peak value as that of the experimental results. It is clear that the experimental results correspond to $l_p=1$. Therefore the parity of the 2.43-Mev excited state of Be^9 is odd, and its spin may have any of the values 3/2, 5/2, 7/2, or 9/2.

In both the ground-state and excited-state angular distributions an asymptotic tail of fairly large magnitude occurs, corresponding to an approximately iso-

[14] Coon, Graves, and Barschall, Phys. Rev. 88, 562 (1952).

tropic component of the differential cross section. It is reasonable to suppose that this is due to compound-nucleus formation, as distinct from the pickup process which proceeds without such amalgamation. The theoretical justification for subtracting such an isotopic component from the observed cross section in order to obtain a differential cross section corresponding to a "pure" pickup process is somewhat doubtful. However, the results so obtained by subtracting the asymptotes from the ground- and excited-state results are shown in Fig. 8. It is seen that the experimental points fall quite close to the theoretical curves, again plotted for $l_p=1$ and $r_0=4.50\times10^{-13}$ cm. The isotropic components subtracted amount to 11 and 9 millibarns, respectively, for the ground- and excited-state reactions.

Although the Butler analysis of the first excited state of Be^9 leaves its spin uncertain to within three units, it is significant that the spin value 1/2 for this state is excluded. Thus Be^9 provides the first exception in the sequence of odd light nuclei to the observation that the two lowest-lying levels form an inverted (3/2–1/2) doublet. This spin assignment provides evidence against the L–S coupling model for Be^9, since spin 1/2 is predicted for the first excited level in this case.[15] The experimental result is consistent with the nuclear model involving j-j or strong intermediate coupling[15] which predicts odd-parity levels of spins 7/2 and 5/2 following the spin-3/2 ground state. It is also consistent with the alpha-particle model which identifies the first excited state of Be^9 with one in which the Be^8 core is in its first state of rotational excitation,[16] with odd parity and spin 5/2.

COMPETING REACTIONS

From the pulse-height spectra of Fig. 4 it is clear that the $B^{10}(n,d)Be^9$ reaction was predominant, but one can see that other reactions did enter in the form of a continuous background spectrum beneath the (n,d) peaks. The proportional-counter dE/dx channels were provided with bias settings for both their lower and upper limits of pulse-height acceptance. In order to obtain some idea of the makeup of the continuum, observations at $\theta_0=15°$ were made with various upper- and lower-limit dE/dx settings in order to tell, by their variation with bias, which portions of the continuum were due to tritons, deuterons, and protons. The qualitative conclusions will be discussed in relation to the following possible competing reactions.

$B^{10}(n,\alpha)Li^7$, $Q=2.792$ Mev

All alpha particles produced by this reaction were appreciably degraded in the boron radiator and counter gas. Therefore no attempt was made to observe this reaction, and an upper-limit bias setting prevented any alpha-particle coincidences from registering, due to their large dE/dx values.

$B^{10}(n,t)Be^8$, $Q=0.232$ Mev

Tritons were found between an observed upper energy limit of about 12 Mev down to about 4.7 Mev which was the lowest energy observable, taking account of radiator half-thickness and counter-gas filling. The number of tritons increased with decreasing energy, and the differential cross section in the above energy interval was about 3 mb/sterad. An upper limit could be set on the reaction leading to the ground state of Be^8, giving tritons above 12 Mev. This limit was about 0.3 mb/sterad.

These observations are in agreement with the results of Perkin[17] who observed stars in nuclear plates from the $B^{10}(n,t)Be^8(2\alpha)$ reaction for bombarding neutrons of a continuous energy spectrum extending to 24 Mev. No ground-state reaction was found, and it was observed that the yield of stars increased with excitation of the Be^8 residual nucleus.

$B^{10}(n,dn)Be^8$, $Q=-6.025$ Mev and $B^{10}(n,d)Be^9$, $E_{ex}>2.43$ Mev

No continuum deuterons were observed with energies above about 7 Mev, while below this energy and above the lower limit of the spectrometer of 3.1 Mev, about 4 mb/sterad were observed, again increasing in number toward the lower energies.

The 3.1-Mev lower limit of the spectrometer corresponded to an upper limit on excitation of the Be^9 nucleus of about 7 Mev. However, the resolution for a group from the 6.8-Mev state found in high-energy proton inelastic scattering would have been so poor as to render it impossible to identify. The growth of the continuum toward the lower-energy limit is probably due to this state. It can be stated that no groups of deuterons occurred corresponding to Be^9 excitations of less than 5.5 Mev, other than the group corresponding to the 2.43-Mev level.

$B^{10}(n,p)Be^{10}$, $Q=0.227$ Mev

There was an approximately uniform distribution of protons between the energy limits 2.5 and 12.5 Mev amounting to about 3 mb/sterad. No attempt was made to observe protons from the reaction leading to the ground state of Be^{10}, since these would have been masked by recoil protons from small amounts of hydrogenous matter in the boron radiator.

We are pleased to acknowledge the helpful interest of Dr. J. H. Coon and Dr. E. R. Graves throughout this work. We are most grateful to Dr. Max Goldstein and his computer group, particularly Miss Margaret Johnson, for performing the computations in connection with the Butler curves and the window function of the spectrometer.

[15] D. R. Inglis, Revs. Modern Phys. **25**, 416 (1953).
[16] R. R. Haefner, Revs. Modern Phys. **23**, 228 (1951).
[17] J. L. Perkin, Phys. Rev. **81**, 892 (1951).

Gamma Rays from the Inelastic Scattering of 14-Mev Neutrons in C^{12} and O^{16}†

L. C. THOMPSON AND J. R. RISSER
The Rice Institute, Houston, Texas
(Received January 25, 1954)

A NaI scintillation spectrometer has been used to study the gamma rays produced by the inelastic scattering of 14-Mev neutrons in carbon and oxygen. The scattering material was placed around the neutron source with the gamma-ray detector outside the scatterer. A gamma ray from the 4.43-Mev level in C^{12} was obtained with a cross section of about 0.3 barn. Gamma rays from the known level at 6.13 Mev and levels close to 7 Mev were obtained from O^{16} with a total cross section of about 0.2 barn.

INTRODUCTION

ONE way to obtain information about the energy levels of a nucleus is to ascertain experimentally which of the lines of its gamma-ray spectrum are excited by inelastic scattering of fast neutrons and to determine the excitation cross sections.[1–4] In this experiment the scattering material was placed around the neutron source, and the gamma rays detected in a NaI scintillation spectrometer. Carbon and oxygen were investigated.

EXPERIMENTAL APPARATUS AND PROCEDURE

Monoenergetic 14.1-Mev neutrons were produced in the Rice Institute Cockroft-Walton accelerator using the $H^3(d,n)He^4$ reaction. The target was tritium absorbed in zirconium.

The geometry is shown in Fig. 1. The neutron source was essentially a point source 5 mm in diameter. The carbon scatterer consisted of graphite blocks. Water was used for oxygen. A liquid hydrocarbon (machine oil) was used in addition so that carbon and oxygen could be compared with approximately the same hydrogen content in the scattering material. For water, the end of the target tube was immersed in a beaker of water 5 inches in diameter and 4.5 inches deep. The target was 3 inches from the bottom of the beaker and 1.5 inches from the surface of the water. For machine oil, exactly the same geometry was used as with water. For graphite, a cylinder 4.5 inches in diameter and 4 inches high was used. The end of the target tube was placed at the bottom of a cylindrical hole 1.2 inches in diameter and 2 inches deep drilled in the center of one end of the graphite cylinder. For all three scatterers, the gamma-ray detector was mounted just below and in close proximity to the scatterer.

A NaI crystal 1.5 inches in diameter and 1 inch long mounted on a 6292 photomultiplier tube detected the gamma rays. The pulse sizes from the photomultiplier tube were determined by a single-channel pulse-height analyzer. Crystal and photomultiplier quality were such as to give 10 percent or less full width at half-maximum on the 0.66-Mev gamma ray from Cs^{137} and a peak-to-valley ratio much better than 10 to 1. For energy calibration the Cs and the Po-Be 4.43-Mev gamma rays were used. The window width of the single-channel analyzer was checked in the standard manner with a precision pulse generator.

The neutrons were monitored by a scintillation counter using an anthracene scintillator $\frac{3}{4}$ inch in diameter by 1 inch high, located 18 inches from the target as shown in Fig. 1. The bias was chosen to count proton recoils in the anthracene with more than 9-Mev energy. A calibration relating the number of neutrons counted by the monitor to the number of neutrons at the target was obtained using a special target chamber with a thin window opening into an alpha-particle proportional counter. From the number of alpha-particles counted and the solid angle of the alpha-counter window at the target, the number of neutrons from the source could be determined. In order to correct the monitor for the effect of scattering material placed between it and the target, careful measurements were made of the monitor rates with and without scattering material, using a stable beam.

Measurements consisted in surveying the pulse spectrum from the NaI crystal with scattering material

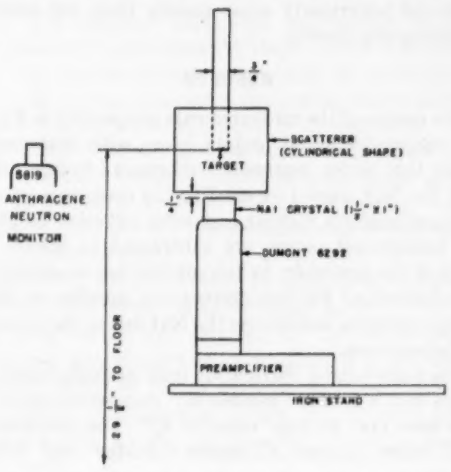

FIG. 1. Diagram of the relative position of the neutron source, scatterer, and NaI crystal.

† Supported by the U. S. Atomic Energy Commission.
[1] Lewis C. Thompson, Phys. Rev. 89, 905 (1953).
[2] Robert B. Day, Phys. Rev. 89, 908 (1953).
[3] Scherrer, Theus, and Faust, Phys. Rev. 89, 1268 (1953).
[4] Scherrer, Theus, and Faust, Phys. Rev. 91, 1476 (1953).

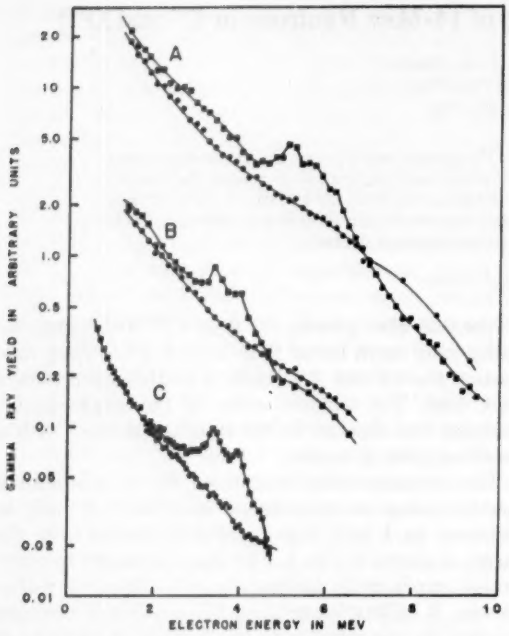

FIG. 2. The squares are the readings with the scatterer in place. The circles are the readings with the scatterer removed. *A* is water. *B* is machine oil. *C* is graphite. Different ordinate scales have been used for each set of curves. The curves of *B* have been plotted as 1/10 and the curves of *C* have been plotted as 1/200 of their intensity relative to *A*.

present and again with scattering material removed. A narrow window (1 volt) was used, and the points were spaced a window width apart in the regions of the peaks. The statistical accuracy was 3 percent up to 8 Mev and 6 percent at higher energies. The number of monitor counts was always at least a factor of 5 greater than the number of gamma-ray counts, so that the statistical uncertainty arose mainly from the number of gamma-ray counts.

RESULTS

The results of the measurements are plotted in Fig. 2. The squares represent points taken with scatterer in place; the circles represent background points taken with the NaI crystal exposed to the neutron source in the same position without scattering material. In Fig. 3 the background curves are subtracted to obtain the effect of the scatterer. In the subtraction no correction was attempted for the decrease in number of high-energy neutrons incident on the NaI due to the presence of the scatterer.

The pulse-height distribution from graphite (curve *C*) shows only a 4.4-Mev gamma ray, corresponding to the 4.43-Mev first excited[5] state in C^{12}. The distribution from water (curve *A*) shows 6.1-Mev and 7-Mev gamma radiation corresponding to the 6.13-Mev excited state and two states at about 7 Mev[6] in O^{16}.

Comparison of curve *A* from water with curve *B* from machine oil rules out the possibility that hydrogenous material increases the background effect in NaI in the 6-Mev region. Comparison of curve *B* with the graphite curve *C* indicates that the presence of two protons per carbon nucleus does not alter the carbon gamma-ray intensity by a detectable amount when intensities are referred to the same number of carbon scattering centers. Within the limits of accuracy of the present experiment, therefore, it is satisfactory to use water for its oxygen content.

The 6.13-Mev gamma ray in oxygen was estimated to have an intensity four times as great as the radiation at 7 Mev. The estimate was made graphically. It was assumed that the gamma radiation could be treated as two single lines, one at 6.1 and one at 7.0 Mev, and that each line would produce a pulse spectrum in the crystal-like curve *B* or curve *C* of Fig. 3 for the 4.4-Mev gamma ray from carbon. Using an intensity ratio of four for the 6.1 to one for the 7-Mev radiation resulted in a curve very similar to the experimental oxygen curve of Fig. 3.

The cross section for exciting the 4.43-Mev level in C^{12} was calculated by a numerical integration over the graphite scatterer, taking into consideration the solid angle subtended by each volume element of the scatterer at the target and at the crystal, the attenuation of neutrons in going from the target to the volume element, the attenuation of the gamma rays in going from the volume element to the crystal, and the probability that a 4.4-Mev gamma-ray incident on the crystal would

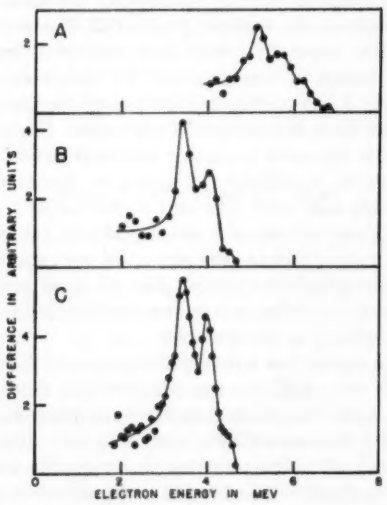

FIG. 3. Difference of the scatterer in place and scatterer removed in the vicinity of the pair peaks for the curves of Fig. 2. *A* is for water. *B* is for machine oil. *C* is for graphite.

[5] F. Ajzenberg and T. Lauritsen, Revs. Modern Phys. **24**, 321 (1952); see p. 355.

[6] See reference 5, p. 376.

result in a pulse in the peak of the pulse distribution. The value obtained by this method was 0.3 barn.

The ratios of the cross sections for exciting the 6.13-Mev level and the 7-Mev levels in O^{16} to the cross section for the 4.43-Mev level in C^{12} were obtained by comparing the areas under the curves A and B in Fig. 3 for water and oil, correcting for the difference in the densities of carbon and oxygen nuclei and for the variation of the probability of gamma-ray absorption by pair formation over the range 4.4 to 7.0 Mev. In this manner the cross section for the 6.13-Mev level in O^{16} was calculated to be 0.2 barn. The cross section for the 7-Mev oxygen gamma rays then becomes 0.05 barn.

The results from carbon are consistent with experiments on the energy distribution of inelastically scattered neutrons from carbon by the photographic plate method, both as regards cross section[7] and the larger probability of exciting the 4.43-Mev level than any other level.[8] The oxygen results are consistent with cloud chamber experiments on oxygen bombarded by 14-Mev neutrons,[9] where recoil O^{16*} nuclei were found with excitation energies principally in the range 6 to 7 Mev.

It can be seen from the character of the curves in Fig. 2, that a difficulty in this method of studying the excitation of gamma rays by inelastic neutron scattering arises from the effect of the neutrons on the NaI crystal itself and the impossibility of separating this effect from the effect of the gamma radiation from the scattering material unless there are clearly resolved peaks which are not observed with NaI alone. A number of geometrical arrangements were tried without finding one free from the objection that the presence of the scatterer changed the neutron background in the NaI crystal. The method, therefore, yields unambiguous results only in the case of scattering nuclei in which the low levels are widely spaced, so that gamma radiation is emitted in the form of a few relatively strong lines of high energy.

Acknowledgment is due Professor T. W. Bonner for many valuable suggestions.

[7] E. R. Graves and L. Rosen, Phys. Rev. **89**, 343 (1953).
[8] B. G. Whitmore, Phys. Rev. **92**, 654 (1953).
[9] J. P. Conner, Phys. Rev. **89**, 712 (1953).

PHYSICAL REVIEW VOLUME 94, NUMBER 4 MAY 15, 1954

Polarization from Isolated Resonances

A. SIMON AND T. A. WELTON
Oak Ridge National Laboratory, Oak Ridge, Tennessee

(Received February 1, 1954)

Polarization from nuclear reactions may be obtained even from a single isolated level of the compound nucleus. Some aspects of this type of polarization are discussed and the implications of the one-level Wigner-Eisenbud formula are considered in this connection. A conjecture of Coester is discussed and compared with the Wigner-Eisenbud result.

I. INTRODUCTION

In a recent paper,[1] the authors have derived a general formula for the state of polarization of the product beam from a nuclear reaction initiated by unpolarized particles. The polarization always results from interference between two different elements of the scattering matrix for the reaction. More explicitly, if the required angular momentum selection rules[2] are satisfied, polarization will arise under one of three conditions:

(a) The reaction goes with appreciable intensity by way of at least *two* compound states, differing in total angular momentum and/or parity. The initial and final orbital angular momenta and channel spins are unrestricted save by the selection rules governing complexity.

(b) The interference is between resonance elastic scattering and potential scattering. This possibility is limited to elastic scattering only, of course.

(c) The reaction goes with appreciable intensity through only *one* compound state. Under this restriction, the compound state must either be assembled or decay by means of at least *two* waves which differ in orbital angular momentum and/or channel spin.

It is further shown in A that the polarization (unlike the intensity) involves coefficients $i(R_1^*R_2-R_1R_2^*)$ [where R_1 and R_2 refer to the interfering matrix elements of $R\equiv S-1$] and therefore vanishes unless R_1 and R_2 differ in phase.

Relatively intense beams of high-energy polarized neutrons have been obtained from the $Li^7(p,n)$ reaction.[3] The polarization was detected by the use of elastic scattering from oxygen as an analyzer. The production reaction seems to be an example of type a and the detection is an example of type b. Reactions of type c seem, however, to offer considerable promise for several

[1] A. Simon and T. A. Welton, Phys. Rev. **90**, 1036 (1953), hereafter referred to as A.
[2] Reference 1, Sec. IV.
[3] H. B. Willard (private communication); Darden, Fields, and Adair, Phys. Rev. **93**, 931 (1954).

obvious reasons (high intensity and ease of interpretation), and it is the purpose of this note to clarify somewhat the conditions under which this third type of reaction can actually be observed.

II. IMPLICATIONS OF THE WIGNER-EISENBUD FORMULA

The Wigner-Eisenbud formula for the S matrix can be written (making the one level assumption),

$$S^{J\pi}{}_{a's'l',\,asl}=\exp[i(\xi_{a'l'}+\xi_{al})]\times\left\{\delta_{aa'}\delta_{ss'}\delta_{ll'}+\frac{ig_{asl}g_{a's'l'}}{E_R-E-\frac{1}{2}i\Gamma}\right\}, \quad (1)$$

where the notation is essentially uniform with that given by Blatt and Biedenharn.[4] The quantity ξ_{al} is the usual potential phase shift, E_R is the "effective" resonance energy (with the energy-dependent shift included), Γ is the total width, and $g_{asl}{}^2$ is the partial width for decay by the indicated subchannel.

Resonant polarization by means of true reaction is of primary interest for this discussion and we will assume henceforth that the reaction is not that of elastic scattering. The R matrix element will then be written (with J and π suppressed):

$$R_{asl,\,a's'l'}=\exp[i(\xi_{a'l'}+\xi_{al})]\frac{ig_{a's'l'}g_{asl}}{E_R-E-\frac{1}{2}i\Gamma}. \quad (2)$$

For convenience, consider the case where two outgoing subchannels interfere, specified by $(\alpha s_1 l_1)$ and $(\alpha s_2 l_2)$. The polarization is then proportional to (suppressing all unnecessary indices, and using a subscript zero to denote the single incident subchannel):

$$\tfrac{1}{2}i(R_1{}^*R_2-R_1R_2{}^*)=\frac{\Gamma_0 g_1 g_2\sin(\xi_1-\xi_2)}{(E-E_R)^2+\frac{1}{4}\Gamma^2}. \quad (3)$$

The fractional, or percentage, polarization is proportional to the above quantity divided by the differential cross section for the reaction. Under our assumption the cross section at fixed angle must be proportional to

$$\left(\frac{d\sigma}{d\Omega}\right)_{a,\,a'}\sim\frac{f[g_1,g_2,\Gamma_0,\cos(\xi_1-\xi_2)]}{(E-E_R)^2+\frac{1}{4}\Gamma^2}, \quad (4)$$

where f is a simple function which may be derived in a straightforward manner.[4] As a result, the percentage polarization (P.P.) becomes proportional to

$$\text{P.P.}\sim(\Gamma_0 g_1 g_2/f)\sin(\xi_1-\xi_2). \quad (5)$$

[4] J. M. Blatt and L. C. Biedenharn, Revs. Modern Phys. **21**, 267 (1952).

None of the quantities in this expression are strongly energy-dependent (except near the threshold of a reaction) and hence the percentage polarization will remain relatively constant over the entire region of the resonance. This is not true of polarization resulting from reactions of type a or b for which the polarization varies widely over the resonance.

Strong resonant polarization will be obtained where g_1 and g_2 are comparable, unless $\xi_1=\xi_2$. This clearly requires that $l_1\neq l_2$ for polarization, since the potential phase depends very weakly (if at all) on channel spin.[5] Further, l_1 and l_2 must differ by at least *two* units (parity conservation), so that if the outgoing particle energy is low it will be difficult to find cases where g_1 and g_2 are comparable. The most favorable cases seem to be those in which the outgoing[6] particle has sufficiently high energy to give similar penetrabilities for s and d waves. It is further clear that this type of neutron polarization cannot result if the residual nucleus has zero spin.

III. COESTER'S CONJECTURE

In a recent paper, Coester[7] has conjectured that the matrix elements for all reactions which go through the same compound nucleus have the same phase. This conjecture is clearly in conflict with the result of the Wigner-Eisenbud calculation,[5] Eq. (1), in all cases where potential scattering plays a role. No polarization would be possible from isolated resonances on Coester's hypothesis. The conflict can in fact be resolved by noting that Coester's tentative proof of his conjecture is apparently invalid by reason of his neglect of the potential scattering. The essential point is that the R matrix, when operating upon an initial state, yields final states which have suffered potential scattering as well as those which have gone through a compound nucleus. As a result, then, ρ_f in Eq. (19) of reference 7 should *not* be independent of ρ_0. Instead, one should deal with the matrix $\omega^{-1}R\omega^{-1}$, where ω is the diagonal matrix defined by Wigner and Eisenbud[8] which contains all the potential phases. The matrix $\omega^{-1}R\omega^{-1}$ operating upon an initial state, yields only final states which have gone through a compound nucleus, and should then have only one nonvanishing eigenvalue. The result is then identical in form with that of Wigner and Eisenbud.

[5] This point has been recognized independently by A. M. Lane (private communication), whose interesting letter stimulated the publication of this note.

[6] If the interfering subchannels are incident rather than outgoing, read "incident" for "outgoing" throughout the discussion.

[7] G. F. Coester, Phys. Rev. **89**, 619 (1953); see also footnote 13 of A.

[8] E. P. Wigner and L. Eisenbud, Phys. Rev. **72**, 35 (1947).

Neutron-Deficient Activities of Holmium

THOMAS H. HANDLEY
Oak Ridge National Laboratory, Oak Ridge, Tennessee
(Received Februrary 4, 1954)

Proton bombardment of pure oxides of Dy, Ho, and Er has served to clear up some uncertainties concerning neutron-deficient activities of Ho. Two previously reported activities, 5.2 day and 65 day, were not found, and reassignment of the 5.0-hour activity to a mass of 162 is made. The gamma-ray spectrum of the 5.0-hour activity shows it to decay by electron capture with gamma energies of 0.19, 0.71, and 0.95 Mev. 41-minute Ho^{161} is shown to decay by electron capture and by β^- emission.

HOLMIUM-164

HOLMIUM-164 has been reported to decay by beta emission with a half-life of 39 minutes;[1-3] it was produced by Dy(p,n), Ho$(n,2n)$, and Ho(γ,n). In the present investigation, a 41-minute activity was produced by Dy(p,n), Ho(p,pn), and Er(p,α), and the assignment of element and mass number were both confirmed. To aid in the assignment, ion exchange methods[4] were used in the separations following bombardment.

The emission of a 0.9-Mev beta particle was determined from measurements of absorption in aluminum. In addition, an x-ray peak of 0.043 Mev was evident in the gamma-ray spectrum as measured with a NaI(Tl) scintillation spectrometer. No other more energetic gamma rays were identified. Decay of the x-ray activity was followed with the scintillation spectrometer, and decay of the 0.9-Mev β^- was followed with an end-window GM tube. No significant difference was found between the two measurements; the average value for the half-life was 41 minutes. It is possible, of course, that the 0.043-Mev peak is not the x-ray but a very weak gamma or secondary radiation from self-bombardment. However, since the energy is that of the x-ray in this region, it is very likely to be due to electron capture.

HOLMIUM-163

A 5.2-day activity has been reported[1] for Ho^{163}, supposedly produced by Dy(p,n), Dy(d,n), and Dy$(d,2n)$, with ion-exchange methods being used for chemical identification. However, as previously reported,[5] this activity was not observed as the daughter of 75-minute Er^{163}. Previously, a limit of <30 minutes or >1 year was placed on the half-life of the daughter of 75-minute Er^{163}. An improvement in ion-exchange techniques[6] has made it possible to place the upper limit on the half-life of the daughter of Er^{163} as <10 minutes. The 5.2-day activity was not observed as a product of the bombardment of Dy_2O_3 with 20.5-, 14.0-, and 8.5-Mev protons, followed by ion-exchange separation for chemical identification. Energy of the incident proton beam was adjusted by use of appropriate aluminum absorbers. To place further limits on the half-life of Ho^{163}, the following experiments were performed.

In separate experiments, Dy_2O_3 was bombarded with 20.5-, 14.0-, and 8.5-Mev protons and, the products were separated by ion exchange. The entire holmium fraction was collected and adjusted to a known volume, and aliquots were taken for counting. These were counted, at the x-ray peak by means of a scintillation spectrometer and on an end-window GM tube, for a sufficient time to allow the 5.0-hour activity of Ho^{162} (see below) to decay. The decay curve did not indicate the presence of any activity with a half-life longer than 5.0 hours. From these decay curves, extrapolations were made to the end of the bombardment to determine the amount of 5.0-hour activity produced. A scavenger carrier was then added to the entire original holmium fraction and recovered by precipitation with oxalate. To determine the maximum amount of activity produced with a half-life $\gg 5.0$ hours, this precipitate was counted in the same manner as the aliquots, after waiting, of course, a sufficient time for the 5.0-hour activity to decay. Since the 5.0-hour and 5.2-day activities would be produced with approximately the same cross sections and from isotopes of approximately the same abundance, it is possible to calculate, with corrections for the time of bombardment, dilution factor, and chemical yields, the maximum half-life of activities longer than 5.0 hours. From these results it can be said that no holmium activity (between masses 158 and 164 inclusive) deficient in neutrons exists with a half-life between 5.0 hours and 20 years.

The 5.2-day activity was not observed as a product of proton bombardment of erbium followed by ion-exchange separation; it would be expected to result from the nuclear reaction $Er^{166}(p,\alpha)Ho^{163}$. In summation, the reported 5.2-day activity definitely does not belong to Ho^{163}; limits placed on the half-life of Ho^{163} indicate that it is not between 10 minutes and 20 years.

[1] G. Wilkinson and H. G. Hicks, Phys. Rev. **79**, 815 (1950).
[2] M. L. Pool and J. D. Kurbatov, Phys. Rev. **63**, 463 (1943).
[3] H. Waffler, Helv. Phys. Acta **23**, 239 (1950).
[4] B. H. Ketelle and G. E. Boyd, Am. Chem. Soc. **69**, 2800 (1947).
[5] Thomas H. Handley and Elmer L. Olson, Phys. Rev. **92**, 1260 (1953).
[6] Thomas H. Handley and Elmer L. Olson, Phys. Rev. **94**, 968 (1954).

HOLMIUM-162

An activity with a half-life of 65 days has been assigned[1] to Ho^{162}. It was reported to have been produced by $Tb(\alpha,n)$, $Dy(p,n)$, and $Dy(d,2n)$ and to decay by β^- emission and K capture. In the present investigation, a 5.0-hour activity is assigned to this mass. It was produced by proton bombardment of Dy_2O_3 and is presumed to be the same activity reported by Wilkinson and Hicks[1] as having a half-life of 4.6 hours and which they assigned to Ho^{161}. Here, again, the limits mentioned in the previous section of this paper apply. Based on the production of the 5.0-hour activity, no holmium activity deficient in neutrons exists with a half-life between 5.0 hours and 20 years, thus eliminating the 65-day activity previously reported.

The 5.0-hour activity was not observed as a product of proton bombardment of erbium, and if it were either 164 or 163 it would be expected to be observed as a product of (p,α) reaction on erbium. It was not produced by proton bombardment (up to 22.5 Mev) of holmium, which again eliminates masses 163 and 164 because it would be observed as the daughter of Er^{163} or by (p,pn) on holmium. It was not observed by milking Er^{161} and could not be isomeric with 2.5-hour Ho^{161}, daughter of 3.5-hour Er^{161}. It was observed as a product of bombarding dysprosium with 8.5-Mev protons; this would eliminate all mass assignments lower than 160. From the relative amounts of the 5.0-hour and 2.5-hour activities, it could not be produced from Dy^{160}, therefore its mass could not be lower than 161. A gamma-ray spectrum, Fig. 1, as measured with a NaI(Tl) scintillation spectrometer, shows it to decay by electron capture, with the x-ray peak at 0.044 Mev and with gammas of 0.19, 0.71, and 0.95 Mev. There is no evidence for 0.51-Mev annihilation radiation; positrons, if present, constitute a small fraction of the total radiation.

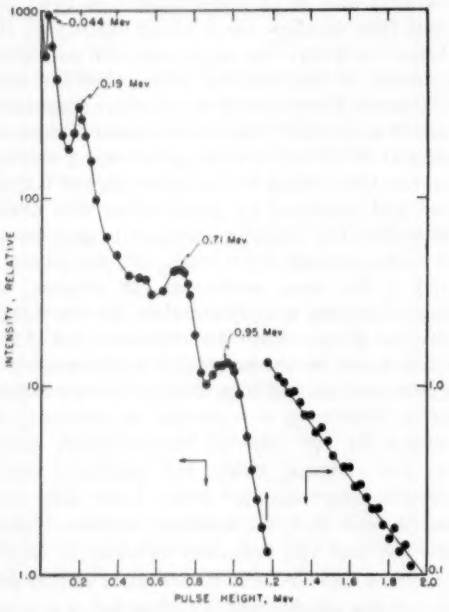

FIG. 1. Gamma-ray spectrum of Ho^{162}.

HOLMIUM-161

Previously, a 4.6-hour activity was assigned to Ho^{161}; however, this activity has not been confirmed, and it is presumed to be the same as the 5.0-hour activity which is assigned to Ho^{162} in the previous section. As reported earlier,[7] a 2.5-hour activity assigned to this mass was obtained from the decay of 3.6-hour Er^{161} which was produced by bombarding erbium with 24-Mev protons and separating by ion exchange. The erbium fraction was milked after an elapse of five hours to permit the Ho^{161} to grow in. A half-life of 2.5 hours was then observed. In the present work, the 2.5-hour activity is also produced by bombarding Dy_2O_3 with 20.5, 14.0, and 8.5-Mev protons. As reported previously, it was found to decay by electron capture, with possible gammas of 0.090 and 0.17-Mev energy.

HOLMIUM-160

An activity with a half-life of 22 minutes has been assigned[1] to Ho^{160}. In the present investigations, proton bombardment of Dy_2O_3 followed by ion-exchange separations gave a half-life of this order with the holmium elution peak. Due to the complexity of radiation from other holmium activities, it was not possible to obtain a gamma-ray spectrum. However, the 22-minute activity was not observed as a result of proton bombardment (up to 22.5 Mev) of either Ho or Er, which would eliminate its assignment to masses higher than 162. It was observed as a result of bombarding Dy_2O_3 with 8.5-Mev protons, which eliminates a mass assignment lower than 160. It was not observed as a daughter of Er^{161}, thus eliminating Ho^{161}. With these restrictions, it is tentatively assigned to a mass of 160.

[7] Thomas H. Handley and Elmer L. Olson, Phys. Rev. 93, 524 (1954).

Comparison of Nuclear and Gamma-Ray Energy Scales*†

K. W. JONES, R. A. DOUGLAS, M. T. MCELLISTREM, AND H. T. RICHARDS
University of Wisconsin, Madison, Wisconsin

(Received February 2, 1954)

Cylindrical and spherical electrostatic analyzers have been used to measure the ratio of the threshold proton energy for the $Li^7(p,n)Be^7$ reaction to the Q of the $Mg^{24}(p,p')Mg^{24*}$ reaction. This ratio was found to be 1.3734 ± 0.0007. The energy of the gamma ray from Mg^{24*} has been compared earlier by Hedgran and Lind to other gamma rays whose energies have been measured absolutely by either the curved crystal spectrometer method (Au^{198}-Caltech) or proton-moment calibrated magnetic field (Co^{60}-Lindstrom *et al.*). The present data fix the $Li(p,n)$ threshold as 1881.4 ± 1.1 kev in terms of the Caltech value for the Au^{198} gamma, or as 1879.7 ± 1.1 kev in terms of the Lindstrom *et al.* value for a Co^{60} gamma ray. The former value is in better agreement with currently used nuclear energy scales.

INTRODUCTION

NUCLEAR reaction energies are usually measured relative to certain easily reproduced calibration values such as the threshold proton energy of the $Li^7(p,n)Be^7$ reaction or one of the sharp $Al^{27}(p,\gamma)$ or $F^{19}(p,\alpha\gamma)$ resonances. Various of these calibration energies have been measured absolutely by electrostatic deflection of the charged incident particle[1] and by a radio-frequency speed gauge.[2] The estimated precision of these absolute measurements was in both cases approximately 0.1 percent. For some calibration purposes[3] alpha particles from naturally radioactive sources are preferred. These alpha energies have been measured absolutely by magnetic deflection and in some cases accuracies of 0.007 percent claimed.[4] Sturm and Johnson[5] have shown that Herb's scale and the old magnetic deflection measurements agree within 0.05 percent. Collins, McKenzie, and Ramm[6] have used a proton-moment calibrated magnetic field to remeasure some of the naturally radioactive alphas and also nuclear reaction Q's. Their energies are somewhat systematically higher than the old magnetic deflection measurements. Recently Famularo and Phillips[7] have measured nuclear reaction energies also in terms of the proton-moment calibrated field and find no systematic disagreement with earlier energy scales.

An attempt was made by Williamson *et al.*[8] to use the first excited state of Li^7 to intercompare the nuclear scale with the gamma-ray scale based upon DuMond's crystal spectrometer. Unfortunately the errors of comparison were at that time too large to display the 0.14 percent systematic error since discovered[9] in the original direct crystal measurement of the gamma ray from Au^{198}.

A more precise intercomparison of the nuclear and gamma scales might be of great help in suggesting the presence or absence of other systematic errors in one or both energy scales.

The recent precise comparison[10,11] of a Na^{24} gamma ray to other gammas whose energies are absolutely determined, makes practical another intercomparison of the nuclear reaction and gamma-ray scales. The gamma rays following the beta decay of Na^{24} correspond to transitions between states of a stable isotope. Therefore the location of these excited states can be readily examined by inelastic scattering of protons from Mg^{24}.

An earlier communication[12] from this laboratory reported measurement of the first excited state of Mg^{24} by inelastic scattering and also by the $Al^{27}(p,\alpha)Mg^{24}$ reaction. No inconsistency between the nuclear and gamma-ray scales was evidenced. The present measurements are an attempt to improve significantly the precision of the intercomparison.

Since the $Li^7(p,n)Be^7$ threshold is perhaps the most convenient and widely used nuclear calibration reaction, we attempt in the present work to determine accurately the ratio R of the proton energy for the $Li^7(p,n)Be^7$ threshold to the energy of the first excited state of Mg^{24}. The latter can then be easily related to the gamma-ray scale by the measurements of Hedgran and Lind.[10,11]

EXPERIMENTAL PROCEDURE

A cylindrical electrostatic analyzer[13] was used to select monoergic (±0.06 percent) incident protons. The energy of the incident protons T_1 is proportional

* Work supported in part by the Wisconsin Alumni Research Foundation and the U. S. Atomic Energy Commission.

† Preliminary report was given at the Washington Physical Society meeting [Phys. Rev. **91**, 482 (1953)].

[1] Herb, Snowdon, and Sala, Phys. Rev. **75**, 246 (1949).

[2] Shoupp, Jennings, and Jones, Phys. Rev. **76**, 502 (1949).

[3] E.g., Strait, Van Patter, Buechner, and Sperduto, Phys. Rev. **81**, 747 (1951).

[4] G. H. Briggs, Proc. Roy. Soc. (London) **157**, 183 (1936).

[5] W. J. Sturm and V. Johnson, Phys. Rev. **83**, 542 (1951).

[6] Collins, McKenzie, and Ramm, Proc. Roy. Soc. (London) **216**, 242 (1953).

[7] Famularo and Phillips, Phys. Rev. **91**, 1195 (1953).

[8] Williamson, Browne, Craig, and Donahue, Phys. Rev. **84**, 731 (1951).

[9] Muller, Hoyt, Klein, and DuMond, Phys. Rev. **88**, 775 (1952).

[10] D. Lind and A. Hedgran, Arkiv Fysik **5**, 29 (1952).

[11] A. Hedgran and D. Lind, Arkiv Fysik **5**, 177 (1952).

[12] Donahue, Jones, McEllistrem, and Richards, Phys. Rev. **89**, 824 (1953).

[13] Warren, Powell, and Herb, Rev. Sci. Instr. **18**, 559 (1947).

to $P_1/(1-\nu_1)$, where P_1 is the cylindrical analyzer potentiometer setting and $\nu_1=T_1/(2M_pc^2)$ is the first-order relativistic correction for the analyzer (see appendix of reference 1).

A spherical electrostatic analyzer[14] with angular opening of less than ½ degree was used to observe inelastically scattered protons at an angle of 134°21′ with respect to the incident beam. The energy of the scattered particles, T_2, is proportional to $P_2/(1-\nu_2)$, where P_2 is the spherical analyzer potentiometer setting and $\nu_2=T_2/(2M_pc^2)$. (The relativistic correction for the spherical analyzer has the same form as the cylindrical, since in each case the mean orbit is a circle.) For the determination of the *ratio R* of the $Li^7(p,n)Be^7$ threshold proton energy to energy of the first excited state of Mg^{24}, it is not necessary to determine the proportionality constants for the two analyzers separately, since it is only the *ratio* of these two proportionality constants which is involved. This last ratio was found by using incident particles (selected by the cylindrical analyzer) to bombard platinum targets and observing with the spherical analyzer the high-energy cutoff of the elastic scattering.

Systematic errors arising from possible nonlinearity of the analyzers were minimized by the use of an incident *diatomic* beam for the intercalibration of the analyzers. If similar *cylindrical* analyzer potentiometer settings are used for the intercalibration (i.e., 0.65240) as for the $Li(p,n)$ threshold energy (~0.6529), then the calibrating protons after scattering from Pt require a *spherical* analyzer potentiometer setting (i.e., 0.4604) not much different (e.g., ~0.4108) from that for the final data on the protons scattered inelastically from Mg^{24}. Intercalibration platinum edges (again with incident diatomic beams) also were taken for the cylindrical analyzer potentiometer settings corresponding to the energy of the resonance in $Al^{25}(E_p=2.41$ Mev). No systematic change in calibration ratio for these different potentiometer settings could be detected.

These platinum intercalibration data were taken immediately before and after each set of data on Mg^{24} inelastic scattering and immediately before and after each $Li^7(p,n)Be^7$ threshold. During the total course of the measurements random changes of this calibration ratio were observed but the platinum data before and after each reaction measurement rarely differed by more than ~0.02 percent so that the correction for drift of analyzer constants is quite small.

Three different Mg targets were used. Two of enriched Mg^{24} were prepared by evaporation of $Mg^{24}O$ from a tantalum boat upon 1000A and 5000A nickel foils.

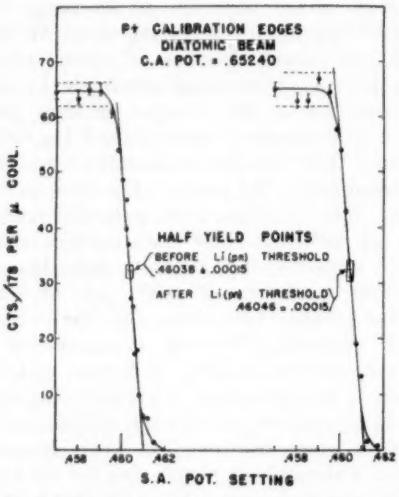

FIG. 2. Typical data for the intercalibration of the cylindrical analyzer (C.A.) and spherical analyzer (S.A.). A diatomic hydrogen ion beam, selected in energy by the C.A., bombarded a thick Pt target, and the energies of the elastically scattered protons at ~135° were measured by the S.A.

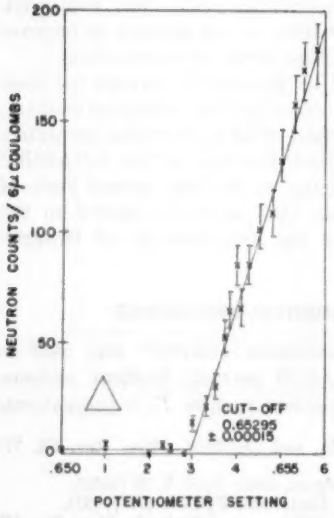

FIG. 1. Typical data on the $Li^7(p,n)Be^7$ threshold.

This method presumably gives metal rather than oxide targets,[15] but observation of the elastically scattered protons did show the presence of some oxygen (and also carbon) throughout the target. Although the concentration of these atoms increased somewhat toward the front surface of the target, no contamination buildup was detected during the course of the experiments. The other target was of ordinary evaporated Mg metal (77 percent Mg^{24}). Thin lithium targets were also evaporated on other 1000A nickel foils and were used for the $Li^7(p,n)Be^7$ threshold determinations. A BF_3 counter in paraffin was used as neutron detector. All targets were kept heated to 200°C to minimize contamination buildup. Two triple collision baffles,

[14] Browne, Craig, and Williamson, Rev. Sci. Instr. **22**, 952 (1951).

[15] Russell, Taylor, and Cooper, Rev. Sci. Instr. **23**, 764 (1952).

one water-cooled and the other liquid air-cooled, separated the diffusion pump from the system.

To get sufficient intensity of the protons scattered inelastically by Mg^{24}, it was advantageous to set the incident proton energy to correspond to the known resonance[16] at $E_p=2.41$ Mev. This resonance is only $\sim$300 ev wide and hence modifies appreciably the line shape as seen by the spherical analyzer. This modification is discussed below in the analysis of the results.

Typical data including a platinum intercalibration edge before and after the run are shown in Figs. 1, 2, and 3.

METHOD OF DATA ANALYSIS

The ratio R of the proton energy for the $Li^7(p,n)Be^7$ threshold to the energy of the first excited state of Mg^{24} can be expressed explicitly in terms of potentiometer settings for the two analyzers. The energy of the first excited state is just the $-Q$ for the $Mg^{24}(p,p')Mg^{24*}$ reaction and hence equals $T_1-T_2-T_3$, where the T's are the energies of incoming, outgoing, and residual nuclei, respectively. T_1 and T_2 are of course immediately expressible in terms of the cylindrical and spherical analyzer potentiometer settings, e.g.,

$$T_1=\frac{P_1}{1-\nu_1}k_c=P_1'k_c \quad \text{and} \quad T_2=\frac{P_2}{1-\nu_2}k_s=P_2'k_s,$$

where the unprimed P's refer to the actual potentiometer settings, and the primed P's are corrected for analyzer first-order relativistic effects; k_c or k_s is the energy proportionality constant for the cylindrical or spherical analyzer. Conservation of momentum permits T_3 to be expressed also in terms of cylindrical and spherical analyzer potentiometer settings since, for inelastic scattering,

$$T_3=\frac{M_1}{M_3}\left[T_1+T_2-2\left(T_1T_2\right)^{\frac{1}{2}}\cos\theta\right]+V,$$

where V is a small relativistic correction[17] which for the present case is only 0.00022 Mev; M_1 and M_3 are the masses of proton and Mg^{24}, respectively. Therefore, when values for the masses[18] and the $\cos\theta$ are substituted,

$$R=\frac{P_{\mathrm{Li}}'k_c}{1.04199P_2'k_s-0.958007P_1'k_c-0.058672(P_2'P_1'k_sk_c)^{\frac{1}{2}}+0.00022\ \mathrm{Mev}}.$$

Intercalibration of the two analyzers via the platinum scattered edges gives the ratio k_s/k_c, which is the only other constant necessary for the calculation of R from the data. (An approximate[19] value of k_c is of course necessary for the calculation of the small relativistic correction V.) If 0.98259 is taken as the relativistically correct ratio of scattered to incident energy when a proton is scattered elastically from platinum at $\theta=134°21'$, and if correction is made for the energy carried by the electron of the incident diatomic hydrogen ion, one can easily show that

$$k_s/k_c=0.491161P_{cd}'/P_{sp}'.$$

The P_{cd}' comes from the cylindrical analyzer potentiometer setting for the incident diatomic beam and P_{sp}' comes from the spherical analyzer potentiometer setting for the half-yield point on the high-energy cutoff for protons scattered from a thick platinum target (see Fig. 2).

P_{Li}, the cylindrical analyzer potentiometer setting corresponding to the $Li^7(p,n)Be^7$ threshold, is chosen as the linear extrapolated cutoff similar to the method of Herb, Snowdon, and Sala.[1]

The choice of the spherical analyzer potentiometer setting (P_2) appropriate to the energy of the protons scattered inelastically from Mg^{24} is more difficult because the resonant character of the scattering cross section invalidates earlier line-shape analysis[20] which showed that the half-yield point is the significant potentiometer setting when the reaction cross section is constant. To find P_2 one can, for this narrow resonance

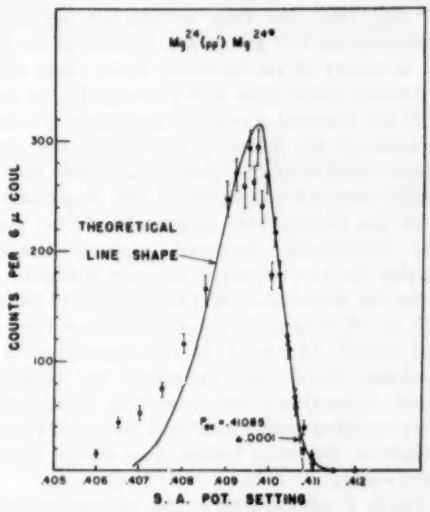

FIG. 3. Typical data on protons scattered inelastically by Mg^{24}. The theoretical line shape is discussed in the text and in Fig. 4.

[16] Mooring, Koester, Goldberg, Saxon, and Kaufmann, Phys. Rev. **84**, 703 (1951).

[17] Craig, Donahue, and Jones, Phys. Rev. **88**, 811 (1952).

[18] Li, Whaling, Fowler, and Lauritsen, Phys. Rev. **83**, 517 (1951); C. W. Li, Phys. Rev. **88**, 1038 (1952).

[19] k_c actually is known to better than 0.1 percent.

[20] R. M. Williamson, Ph.D. thesis, University of Wisconsin, 1951 (unpublished).

(~300 ev), treat the cross section for inelastically scattered protons as a δ function. Because of the finite spread in energy of the incoming beam, there will be some protons which after losing energy in the target arrive at the resonant energy. If one knows the energy distribution of the incoming beam, and the energy acceptance window of the spherical analyzer, then one can easily compute the expected line shape and the point on the curve which corresponds to the energy of the inelastically scattered protons. Graphical integration for the measured analyzer windows, etc., gives the line shape expected (see Fig. 4) and indicates that P_2 is $\sim 0.165 \pm 0.017$ percent less than the extrapolated cutoff. The error in this correction to the extrapolated cutoff was estimated by performing graphical integrations for reasonable deviations of analyzer windows from measured values and for slight deviations of the mean bombarding energy from the resonant energy.

P_1, which is proportional to the resonant energy for the inelastic scattering, is fixed approximately by varying the incident energy until the peak yield in the spherical analyzer is observed. A more sensitive test of the deviation of the mean energy from the resonant energy may be found by comparing the total area under the inelastic proton curve (e.g., Fig. 3) with the total area under a similar thick target curve when the mean incident energy is above the resonant energy by an amount large compared to the width of the resonance and the cylindrical analyzer resolution. If the incident energy is exactly at the resonant energy, the area should be precisely one-half that of the case where the mean incident energy is enough above resonance that all incident protons pass through the resonant energy while traversing the target.

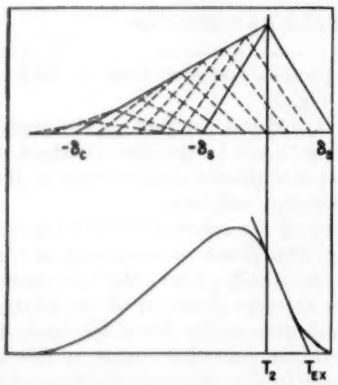

FIG. 4. Graphical integration for the theoretical line shape of the inelastically scattered protons. The incident proton energy T_1 is assumed equal to the energy of the very narrow resonance for inelastic scattering. The spherical analyzer "window" is $T_2 \times \delta_s$. The spread in T_2 arising from the finite energy spread of the incident beam is $\delta_c T_2$ and is equal to $(\Delta_c T_1) \times$(ratio of stopping cross sections of outgoing and incident protons). The cylindrical analyzer resolution is Δ_c.

Nonuniformities in target composition (particularly carbon and oxygen) give the chief systematic uncertainty to this method of finding P_1. The uncertainty in P_1 is estimated to be ~0.015 percent from this cause and from the fluctuations of the areas of different data curves such as shown in Fig. 3.

RESULTS

The mean value of the eight $Li^7(p,n)Be^7$ threshold determinations was $P_{Li}' = P_{Li}/(1-\nu_{Li}) = 0.65354 \pm 0.00012$, where the error is the standard deviation of the eight runs. The nine $Mg^{24}(p,p')Mg^{24}$ edges gave a mean $P_2' = P_2/(1-\nu_2) = 0.41033 \pm 0.00016$, the error including both the standard deviation and the 10 percent uncertainty in the correction to the extrapolated cutoff (see preceding). The calibration ratio k_s/k_e based upon 26 platinum edges was 0.69598 ± 0.00024. The potentiometer setting for excitation of the scattering resonance, $P_1' = P_1/(1-\nu_1)$, was taken as 0.83737 ± 0.00012. This last error estimate has already been discussed in the preceding paragraph.

A possible systematic error is that introduced by uncertainty in the angle of observation θ. This angle was measured to be $134°21 \pm 5'$. The angle measurement was achieved by comparing the energy of the alphas elastically scattered by a carbon target to those elastically scattered by a platinum target. The angle sensitivity of the former scattering process is such that this way of determining the mean angle is preferred to direct geometrical measurement. This method has, however, been earlier checked by direct measurements.[14] For the present experiment $\partial Q/\partial\theta = 0.08$ Mev/radian and hence the uncertainty from this source is only 0.009 percent.

The preceding input values give for the ratio R of the $Li^7(p,n)Be^7$ threshold to the energy of the first excited state of Mg^{24}:

$$R = \frac{E_{\text{thres}}[\text{Li}(p,n)\text{Be}^7]}{E_x(\text{Mg}^{24*})} = 1.3734 \pm 0.0007.$$

$E_x(Mg^{24*})$ from Gamma-Ray Data

The latest result of the Caltech group[9] for the absolute energy of the gamma ray following the beta decay of Au^{198} is

$$E_\gamma(\text{Au}^{198}) = 411.770 \pm 0.036 \text{ kev}.$$

Lind and Hedgran[10] and Hedgran and Lind[11] report the following ratios for momenta of the photoelectrons from various relevant gamma rays:

$$\frac{H\rho(\text{Au}^{198}(U_{LI}))}{H\rho(\text{Co}^{60}(U_K))} = 0.44924 \pm 0.00010,$$

$$\frac{H\rho(\text{Na}^{24},\ 1.37\ \text{Mev})}{H\rho(\text{Co}^{60},\ 1.33\ \text{Mev})} = 1.0229 \pm 0.0002.$$

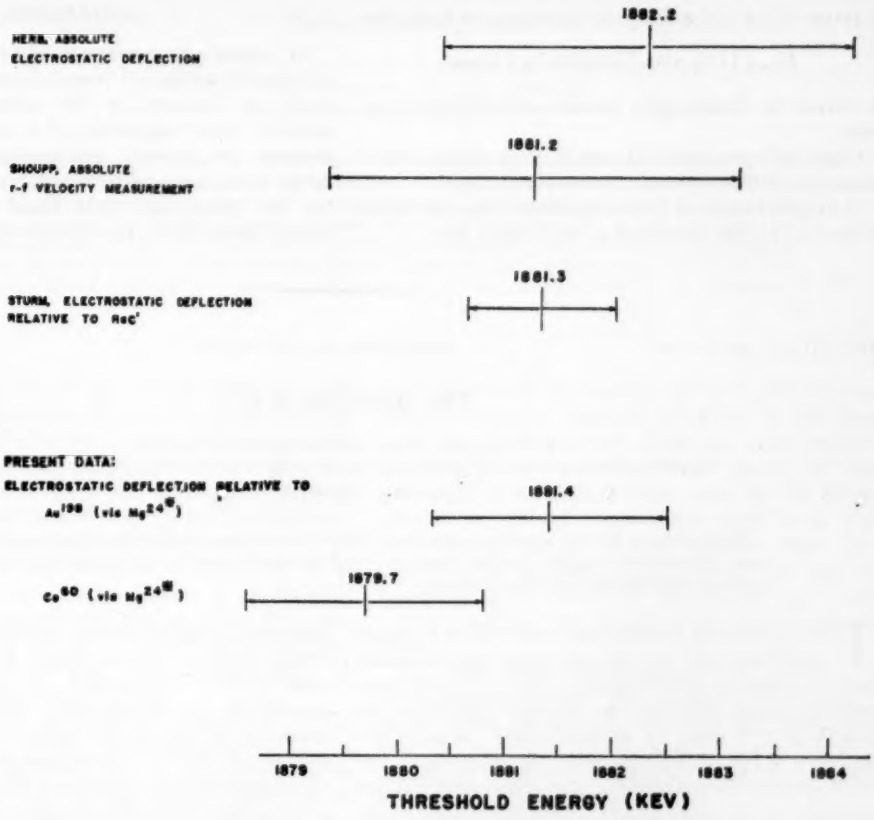

FIG. 5. Comparison of various independent determinations of the $Li^7(p,n)Be^7$ threshold.

When the binding energies of the U_K and U_{LI} electrons are taken as 115.62 kev and 21.76 kev,[21] respectively, the above data yield a value of 1369.91 ±0.40 kev for the Na^{24} gamma-ray energy. When the energy of the recoiling Mg^{24} is included, $(h\nu)^2/(2M_{24}c^2)$, the energy of the first excited state of Mg^{24}, is

$$1369.95\pm0.40 \text{ kev},$$

based on the Caltech crystal spectrometer scale.

A value of comparable precision for the Mg^{24*} state can be found from other gamma-ray data. Recently Lindstrom, Hedgran, and Alburger[22] report 1332.5 ±0.3 kev for the energy of a Co^{60} gamma ray. This value is obtained by comparison with the 1415.8±0.2 kev transition in RaC′ which was measured absolutely (in terms of the proton magnetic moment) by the same authors. If Hedgran and Lind's ratio (=1.0229 ±0.0002) for momenta of the photoelectrons from Na^{24} and Co^{60} is used, then the energy of the Na^{24} gamma ray would be 1368.64±0.45 kev, and when the recoil energy of the Mg^{24} is included, the energy of the Mg^{24} state is 1368.68±0.45 kev. It will be noted that these two independent gamma-ray measurements differ by appreciably more than their assigned probable errors. Hedgran and Lind's $(H\rho)$ ratio for Na^{24} and Co^{60} photoelectrons occurs in the determination of both values, but their $H\rho$ ratio for Au^{198} and Co^{60} photoelectrons occurs only in the former value. So the discrepancy between the two values for the Mg^{24*} could arise from Lind and Hedgran's $H\rho$ ratio[10] of Au^{198} to Co^{60} photoelectrons, or it could indicate a systematic error in one or both of the absolute gamma-ray measurements.

$Li^7(p,n)Be^7$ Threshold

If the abo ve values for the first excited state of Mg^2 are combined with our ratio R of the $Li^7(p,n)Be^7$ threshold to the $-Q[Mg^{24}(p,p')Mg^{24*}]$, then one finds

$$E_{\text{thres}}[Li^7(p,n)Be^7]=1881.4\pm1.1 \text{ kev}$$

[21] V. Cauchois, J. Phys. radium **13**, 113 (1952) but recomputed for latest atomic constants, Jessee W. M. Du Mond, Revs. Modern Phys. **25**, 691 (1953).

[22] Lindstrom, Hedgran, and Alburger, Phys. Rev. **89**, 1303 (1953).

in terms of the Caltech crystal spectrometer scale, but

$$E_{\text{three}}[\text{Li}^7(p,n)\text{Be}^7] = 1879.7 \pm 1.1 \text{ kev}$$

in terms of Lindstrom's proton-moment calibrated scale.

Graphical comparison of various independent determinations of this threshold are shown in Fig. 5.

A weighted mean of these independent measurements of the $\text{Li}^7(p,n)\text{Be}^7$ threshold is 1881.1 ± 0.5 kev.

CONCLUSIONS

No appreciable systematic differences between the gamma-ray scales and current nuclear-reaction energy scales are indicated by the present work. There is, however, some suggestion of a systematic difference between two current gamma-ray scales. Somewhat better consistency with nuclear reaction data is found for the gamma-ray scale based upon the curved-crystal spectrometer measurements.

PHYSICAL REVIEW VOLUME 94, NUMBER 4 MAY 15, 1954

The Half-Life of U^{232}

P. A. SELLERS, C. M. STEVENS, and M. H. STUDIER
Chemistry Division, Special Materials Division, Argonne National Laboratory, Lemont, Illinois

(Received February 5, 1954)

The half-life of U^{232} has been determined to be 73.6 ± 1.0 years by a method involving isotopic dilution, mass spectrometric analysis, and the determination of the specific activity of the diluted sample by conventional weighing and counting techniques.

THE half-life of U^{232} has been reported as 30 years[1] and 70 years.[2] The 30-year value was estimated from the growth of U^{232} alpha activity from its beta-emitting parent Pa^{232} and the 70-year value from the growth of U^{232} from its alpha-emitting parent Pu^{236}. No limits of error have been given for either value, but the 70-year value was based on a later measurement and considered to be more accurate than the 30-year value.

The half-life of U^{232} is sufficiently long that the direct measurement of its decay is difficult. On the other hand, the direct determination of the specific activity is difficult because of the small quantities which are available and is hazardous because of the high specific activity of U^{232}. However, isotopic dilution with a large excess of relatively inactive U^{238} enables one to determine the specific activity of the diluted sample by conventional weighing and counting techniques. A mass spectrometric determination of the ratio U^{238}/U^{232} then permits one to calculate the specific activity of U^{232}.

An aliquot (0.09905 g) of U_3O_8 from a Bureau of Standards sample of natural uranium was accurately weighed and transferred to a preweighed polyethylene bottle containing nitric acid and approximately 100 micrograms of U^{232}. After the oxide was dissolved, the solution was diluted with water to 102.61 g, from which was taken 1.0459 g which in turn was diluted to 101.54 g. From this final solution, about 100-milligram aliquots were weighed, evaporated on platinum plates, and counted in an argon-carbon dioxide counter with a geometry of 50.6 percent and τ of 4×10^{-8} minute. An average of three determinations gave a value of 56 530 disintegrations per minute per 100 mg of solution, with a probable error of 120 disintegrations per minute based on the deviations from the mean, which is a measure of the precision of weighing and counting the samples. This corresponds to a specific activity of the diluted sample of 6.61×10^{10} disintegrations per minute per gram of U^{238}. From the mass spectrometric analysis of the sample [$U^{232}/U^{238} = (1.436 \times 10^{-3}) \pm 1.0$ percent, and $U^{233}/U^{238} = (4.75 \times 10^{-2}) \pm 2.2$ percent, mole ratios] the specific activity of U^{232} was calculated to be 4.65×10^7 disintegrations per minute per microgram. (A mass spectrometric analysis of the original U^{232} sample showed that its U^{238} content was negligible.) This corresponds to a half-life of 73.6 years. The U^{233} was the only isotope other than U^{232} which contributed appreciably (1.5 percent of the total alpha activity) to the activity of the uranium sample, and a correction was applied. A correction was also made for the growth of the daughters of U^{232} by comparing the counting rates of the final samples with that of a sample taken immediately after purification of the U^{232} from its daughters. A consideration of the various errors leads to a probable error of about one year in the half-life.

The authors are grateful to Miss Lillie Mae Porter and Miss Marjorie M. Petheram for their help with the counting.

[1] J. W. Gofman and G. T. Seaborg, *The Transuranium Elements: Research Papers* (McGraw-Hill Book Company, Inc., New York, 1949), Paper No. 19.14, National Nuclear Energy Series, Plutonium Project Record, Vol. 14B, Div. IV, p. 1427.

[2] James, Florin, Hopkins, Jr., and Ghiorso, *The Transuranium Elements: Research Papers* (McGraw-Hill Book Company, Inc., New York, 1949), Paper No. 22.8, National Nuclear Energy Series, Plutonium Project Record, Vol. 14B, Div. IV, p. 1604.

Manganese-57

B. L. COHEN, R. A. CHARPIE, T. H. HANDLEY, AND E. L. OLSON
Oak Ridge National Laboratory, Oak Ridge, Tennessee

(Received Februrary 15, 1954)

A previously unknown isotope, 1.7-minute Mn^{57}, was produced by an (n,p) reaction on isotopically enriched Fe^{57}. It was identified by chemical separations, by measurement of its formation cross section, by investigation of possible impurity effects, and by comparison of its gamma spectrum with that of Co^{57}. It decays principally by 2.6-Mev negatron emission to the 131-kev excited state of Fe^{57}, which in turn decays to either the ground or the 14-kev state of Fe^{57} with approximately equal probability. The gamma-ray spectrum also indicates the presence of a weak 690-kev gamma ray, and possible weak gamma rays of 350 kev and 220 kev. It is shown that a previous assignment of a 7.2-day activity to Mn^{57} is very probably in error.

BY irradiating isotopically enriched iron-57 with high-energy neutrons from the Oak Ridge National Laboratory 86-in. cyclotron, a previously unknown isotope, manganese-57, was produced by the (n,p) reaction. It was found to decay by negatron and gamma emission with a half-life of 1.7 ± 0.1 min. The identification was ascertained by the following tests:

(a) The element was chemically determined to be manganese by a double precipitation of MnO_2 with $KClO_3$ in concentrated nitric acid solution. The ratio of the 1.7-min and the 2.6-hr (Mn^{56}) counting rates in the final precipitate was approximately equal to their ratio in an unprocessed sample.

(b) The fact that the activity is produced by an (n,p) reaction was checked by a measurement of the cross section for its formation. It was found to be about one-half the cross section for the formation of 2.6-hr Mn^{56} by the (n,p) reaction on Fe^{56}. Since the final nucleus in the latter reaction is odd-odd but has a higher threshold, the observed ratio between the two cross sections is approximately that which might be expected if both are (n,p) reactions.[1,2] The fact that the isotope responsible for the 1.7-min activity is Fe^{57} was checked by irradiating natural iron (91.6 percent Fe^{56}) and samples of iron enriched in each of the other isotopes. The 1.7-min activity was found in the Fe^{57} sample only (there were interfering activities in the others) and the upper limit to its intensity in each of the other samples was consistent with the assumption that it was present in an amount proportional to the quantity of Fe^{57}. The possibility that it could be due to $(n,2n)$, (n,α), or (n,γ) reactions is excluded not only by the chemical evidence of item (a), but also by the fact that each of these reactions leads to a stable isotope and therefore would not produce a beta emitter.

(c) Since the Fe^{57} sample was highly purified and spectrochemical analysis revealed no trace element that could give such a half-life, the possibility that the 1.7-minute activity could be due to an impurity seems remote. Even an impurity as large as one percent could not be responsible unless its cross section for cyclotron-produced neutrons[3] was among the largest yet encountered. In a further study of the effects of possible impurities, a survey was made of all known activities of 1.4- to 2.0-min half-lives that can be produced by neutrons. In every case but one these known activities could not account for the observed 1.7-min activity for at least three of the following reasons:

(1) They would be accompanied by other activities of comparable intensity. In the Fe^{57} sample, there were no activities between 30 sec. and 100 days—except near 1.7 min and 2.6 hr—with a production cross section as large as 3 percent of that of the 1.7-min activity.

(2) Their beta and gamma radiations, even with due allowance for incomplete or inaccurate data, do not correspond with those found for this activity.

(3) They would be eliminated in the chemical processing described above.

(4) They are due to elements which are very unlikely to be found as impurities in Fe_2O_3. The single exception was a 1.6-min activity that has been reported from neutron bombardment of nickel and tentatively identified as Co^{62}.[4] The cross section for this was measured and found to be too small, by a factor of at least 10^4, to account for the activity in the Fe^{57} sample.

Since the Fe^{57} was bombarded as Fe_2O_3, consideration must be given to the 2.0-min O^{15} activity that is produced by $O^{16}(n,2n)O^{15}$. This could not be responsible for the 1.7-min activity because it was not found in the natural Fe_2O_3 sample (or in any other oxide with which we have had experience), and, being a positron emitter, would be accompanied by very strong 0.511-Mev annihilation radiation which was not observed. The absence of this activity is explained by the fact that

[1] J. Blatt and V. F. Weiskopf, *Theoretical Nuclear Physics* (John Wiley and Sons, Inc., New York, 1952).
[2] H. Waffler, Helv. Phys. Acta **23**, 239 (1951); B. L. Cohen, Phys. Rev. **81**, 184 (1951); E. B. Paul and R. L. Clarke, Can. J. Phys. **31**, 267 (1953).
[3] All irradiations were carried out in a cadmium-lined facility to reduce thermal neutron-induced activities.
[4] Hollander, Perlman, and Seaborg, Revs. Modern Phys. **25**, 469 (1953).

the oxygen $(n,2n)$ reaction has a very high threshold and, therefore, probably a very small average cross section for these neutrons.

(d) As somewhat of a clinching argument, the gamma-ray spectrum of the 1.7-min activity, described below, was found to contain very intense gammas at 117±4 kev and 134±6 kev, presumably due to decay of excited states of Fe^{57}. These correspond very closely to the 117-kev and 131-kev gammas which accompany[4] the decay of 270-day Co^{57} and are thus known to be due to transitions in Fe^{57}.

The gamma-ray spectrum of 1.7-min Mn^{57} was studied with a NaI(Tl) scintillation spectrometer by displaying the output pulses from the linear amplifier on an oscilloscope screen and photographing them. Several runs were made at different intensities and amplifier settings; in each case the decay was followed by taking photographs at several intervals after the bombardment. The principle feature of these spectra was a very strong line at about 125 kev. This was studied in additional runs, by use of a pulse-height discriminator and counting techniques, and found to consist of two gamma rays of approximately equal intensity with energies of 117±4 kev and 134±6 kev.

The photographs of the oscilloscope screen also showed intensity peaks which decayed with the proper half-life at 690 kev, 350 kev, and 220 kev. The 690-kev peak was also accompanied by a Compton edge at the proper energy and is very probably due to a gamma ray of that energy. By comparing its intensity with that of the 840-kev line from Mn^{56} (which did not decay with the short half-life), the 690-kev gamma ray was judged to accompany only about 2 percent of the 1.7-min decays.

The intensity peaks at 350 kev and 220 kev may be due to gamma rays at those energies although their Compton edges were not observable in the high background. Their intensities were such that they are probably present in only a small fraction of the decays. There was no evidence for 0.511-Mev annihilation radiation; this proves that the 1.7-min activity is not a positron emitter and must therefore decay by β^- emission, as expected. The high energy portion of the gamma-ray spectrum showed no structure which decayed with a short half-life. Judging by the intensity of the Mn^{56} spectrum, it was concluded that there are no gammas in the Mn^{57} decay between 0.9 and 2.0 Mev with a branching ratio as large as 3 percent.

The beta-ray spectrum of the 1.7-min activity was measured by absorption techniques and with an anthracene scintillation spectrometer. In the latter case the powder was sprinkled into a cavity in the crystal; the pulses from the amplifier were exhibited on an oscilloscope screen and photographed as in the gamma-ray case. The film was then measured with a photo-densitometer and compared with a similar photograph of the spectrum of P^{32}. The maximum beta energy of Mn^{57} was thus determined to be 2.6±0.2 Mev. This compares satisfactorily with the value of 2.5±0.4 Mev determined by aluminum absorption methods and it is also in good agreement with the prediction of about 2.5 Mev obtained from Way's charts of beta-decay systematics.[5]

Taking account of the arguments presented earlier, it seems certain that the 1.7-min activity should be assigned to manganese-57. However, a 7.2-day activity produced by cross bombardments of manganese and chromium with alpha particles has previously been identified[6] as manganese-57. To investigate the possibility that this might be isomeric with the 1.7-min activity, two long and intense bombardments were made in an effort to produce the 7.2-day activity by an (n,p) reaction. The activity was not found, and the upper limit to its cross section was determined to be smaller by a factor of 1300 than the cross section for production of the 1.7-min activity. In addition, Nelson and Pool[7] have reported an unsuccessful search for a long-lived Mn^{57} activity from the (α,p) reaction on isotopically enriched chromium-54. Their sensitivity was such that if Mn^{57} decayed with a 7.2-day half-life, the cross section for its formation by the $Cr^{54}(\alpha,p)$ reaction must be less by a factor of 2000 than the cross section for the formation of Mn^{56} by $Cr^{53}(\alpha,p)$. These measurements, plus the fact that isomerism in odd-mass isotopes is unknown in this part of the periodic table,[8] would seem to indicate that the 7.2-day activity is incorrectly assigned. Since it was reportedly produced by low cross-section reactions, (α,p) on chromium and $(\alpha,2p)$ on manganese, there is a strong possibility that Sharma's activity may have been due to impurities.

[5] K. Way (private communication).
[6] H. D. Sharma, University of California Radiation Laboratory UCRL-1265 (unpublished), quoted in reference 4.
[7] M. E. Nelson and M. L. Pool, Phys. Rev. 77, 682 (1950).
[8] M. Goldhaber and R. D. Hill, Revs. Modern Phys. 24, 179 (1952).

The Three-Photon Annihilation of Positrons and Electrons*

S. DeBenedetti and R. T. Siegel†
Carnegie Institute of Technology, Pittsburgh, Pennsylvania
(Received January 22, 1954)

The physical characteristics of the radiations emitted in the annihilation of positrons and electrons in the triplet state have been studied with a triple coincidence method. The energies of the three gamma rays, the angular distribution, and their polarization were found to agree with theory. Triplet annihilation was studied both from positrons stopping in gases where positronium was formed, and from positrons stopping in condensed materials. In the case of metallic absorbers, we verified within the accuracy of the experiment that the number of triplet annihilations is 1/370 of the number of singlet events. Experiments on the number of three-quantum annihilations in different materials are described.

I. INTRODUCTION

IT is well known that a pair of positive and negative electrons can annihilate with the transformation of their rest masses into electromagnetic radiation. In order to satisfy the law of conservation of momentum at least two gamma rays must be emitted, and the main features of the process can be computed as a second-order effect of the interaction of the electrons with the electromagnetic field.

One can expect, however, that higher-order annihilation processes will occur, and in particular that positron-electron pairs should annihilate with the emission of three gamma rays in about 1/137 of the cases. Among the first to carry out a calculation of this effect were Lifshitz,[1] Ivanenko,[2] and Ore and Powell.[3] The result of these last authors (later confirmed by Radcliffe[4] and by Drisko[5]) is that the relative frequency of the three-quantum and two-quantum processes is 1/370 for a random distribution of spin orientations. The effect of spin orientation is simply that singlet pairs annihilate only with the emission of two quanta,[6,7] triplet pairs only with the emission of three.[8]

The purpose of the present work was an experimental investigation of the three-quantum annihilation process, including the probability of its occurrence as well as the physical properties of the emitted gamma rays.[9]

Before our first results were obtained, Rich[10] presented some evidence of the existence of this effect, obtained with a triple coincidence method, and indicating a probability of occurrence of the predicted order of magnitude. Shortly afterwards Deutsch[11] discovered that positronium, the bound positron-electron system, is formed with large probability when positrons are stopped in certain gases. This result was of great help in our work because the formation of positronium, destroying the random distribution in the spin orientations, considerably increases the probability of three-quantum annihilation and thus provides sources from which the characteristics of the radiations emitted can be conveniently studied.

II. INSTRUMENTATION

The three gamma rays emitted in the triplet annihilation process were detected by means of three NaI(Tl) scintillation crystals, each 2.5 cm thick and 4 cm in diameter. The light pulses from the crystals were viewed by RCA 5819 photomultipliers, whose anodes were connected in coincidence, with a resolving time measured to be 1×10^{-7} sec. In addition, the pulses from the last dynode of each tube were amplified by standard linear amplifiers and passed through single channel differential pulse height selectors. The pulse height selector outputs were placed in slow (2×10^{-6} sec) coincidence with the (delayed) output of the fast coincidence circuit. Thus a set of three coincident

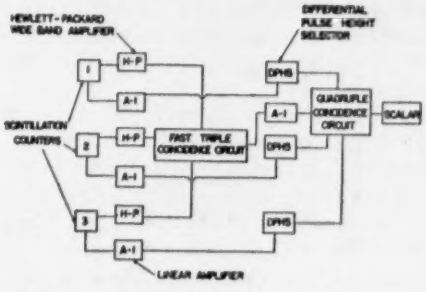

FIG. 1. Block diagram of electronic apparatus.

* Work supported in part by the U. S. Atomic Energy Commission (1951–1952), and in part by the National Science Foundation (1952–1953).
† U. S. Atomic Energy Commission Predoctoral Fellow (1950-1952). Portions of this work were submitted by R. T. Siegel in partial fulfillment of the requirements for the degree of D. Sc. at Carnegie Institute of Technology.
[1] E. M. Lifshitz, Doklady Akad. Nauk. S.S.S.R. **60**, 211 (1948).
[2] D. Ivanenko and A. Sokolov, Doklady Akad. Nauk. S.S.S.R. **61**, 51 (1948).
[3] A. Ore and J. L. Powell, Phys. Rev. **75**, 1696 (1949).
[4] J. M. Radcliffe, Phil. Mag. **42**, 1334 (1951).
[5] R. M. Drisko (private communication).
[6] C. N. Yang, Phys. Rev. **77**, 242 (1950).
[7] L. D. Landau, Doklady Akad. Nauk. S.S.S.R. **60**, 207–209 (1948).
[8] L. Wolfenstein and G. D. Ravenhall, Phys. Rev. **87**, 217 (1952).
[9] For a prelimary communication, see S. DeBenedetti and R. Siegel, Phys. Rev. **85**, 371 (1952).
[10] J. A. Rich, Phys. Rev. **81**, 140 (1951).
[11] M. Deutsch, Phys. Rev. **82**, 455 (1951); M. Deutsch and E. Dulit, Phys. Rev. **84**, 601 (1951); M. Deutsch, Phys. Rev. **83**, 866 (1951).

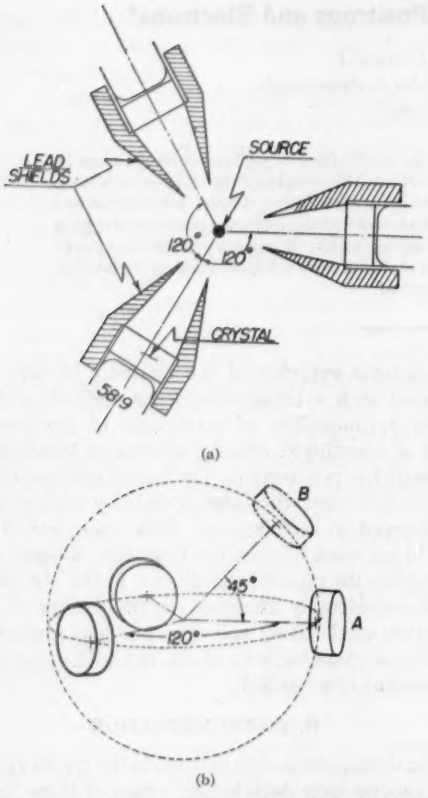

FIG. 2. Arrangement of the counters for detection of three-quantum annihilation (a) Top view, (b) Perspective of the crystals.

gamma rays was accepted only if each yielded a pulse whose amplitude lay in the band accepted by the corresponding differential pulse-height selector. Figure 1 shows a block diagram of the electronic equipment used.

As a source of positrons we used Na^{22}, which is convenient because of its long life. In addition to the positrons and their annihilation radiations, this isotope emits a nuclear gamma ray of 1.3 Mev, which is undesirable since it increases the number of random coincidences. However, when the pulse-height selectors were properly set, this effect was reduced and the random coincidences did not interfere with our measurements.

The three counters (Fig. 2) were placed at a distance of 12.0 cm from the source, and in this position each covered a solid angle of 0.087 sterad. For the measurement of the effect under investigation the counters and the source were coplanar [*A*, Fig. 2(b)] since most pairs annihilate with negligible momentum. For the measurement of the background one of the counters was removed from the plane defined by the source and by the other two, without altering its distance from the source [*B*, Fig. 2(b)].

In order to reduce spurious coincidences due to scattering, each counter was protected by a lead shield as can be seen in Fig. 2.

III. THE PHYSICAL PROPERTIES OF THE THREE QUANTA

(a) The Energy of the Three Quanta

For any given orientation of the counters, the energy of the three quanta of triplet annihilation can be computed in an elementary way from the laws of conservation of energy and momentum. Though the result of such computation needs no experimental confirmation, we have performed the energy measurement to prove beyond any doubt that the coincidences recorded were due to the phenomenon of three-quantum annihilation.

For this purpose a positronium source was used. This consisted of a bell shaped container (1-in. diameter, $\frac{1}{16}$-in. wall thickness) holding SF_6 vapor at 10 atmospheres; the Na^{22} activity (1.4×10^6 dis/sec) was deposited between two thin Zapon foils supported in the center of the container in such a manner that most positrons would stop in the vapor, where the formation of positronium is favored. The pulse-height distributions of the coincident pulses were studied for each counter in succession, with a band width of 90 kev; the background was obtained as previously described by rotating one of the counters away from the coplanar position. The angular arrangements for which data were taken and the computed energies for each configuration are those indicated with an asterisk in Table I. The data are plotted in Fig. 3 after subtraction of background, and after multiplication by a convenient factor in order to equalize the height of the photopeaks. The uppermost curves show the pulse-height distribution of the two-quantum annihilation line, and provide the energy scale for each counter. The other curves, which are the pulse height distributions of the three-quantum annihi-

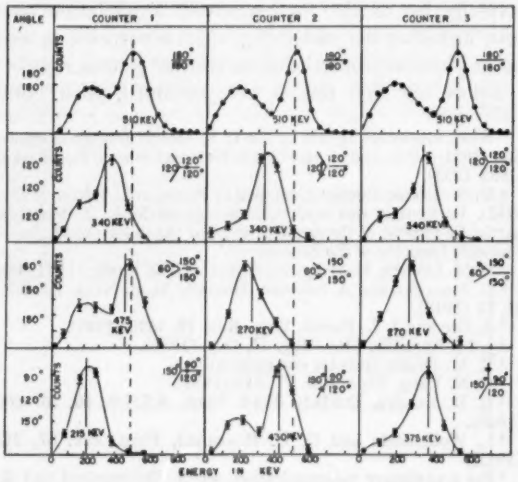

FIG. 3. Pulse-height spectra of three-photon annihilation for different angular arrangements.

TABLE I. Angular distribution data.

A Angles between counters 2–3	3–1	1–2	B Energy in each counter (kev) E_1	E_2	E_3	C Relative intensity (exp.)	D Rel. int. (exp. corrected)	E Rel. int. (theoretical)	F Exp./theory (D/E)	G Exp./stat. theory
*120°	120°	120°	341	341	341	1.00	1.00	1.00	1.00	1.00
100°	120°	140°	263	355	404	1.01±0.04	0.925	0.97	0.95	1.00
100°	100°	160°	435	435	150	1.11±0.05	0.95	0.82	1.16	4.45
*90°	120°	150°	430	215	375	0.86±0.04	0.74	0.89	0.83	0.95
80°	140°	140°	444	289	289	1.09±0.05	0.89	0.97	0.92	1.01
80°	120°	160°	160	404	456	1.05±0.04	0.84	0.75	1.12	1.50
*60°	150°	150°	475	272	272	1.25±0.04	0.82	0.97	0.85	1.04
60°	140°	160°	189	355	478	1.41±0.05	0.96	0.87	1.10	1.43
50°	150°	160°	318	217	487	1.69±0.05	0.91	0.93	0.98	1.25
75°	75°	210°	Forbidden			0±0.05				

lation, show photopeaks near the computed energy (vertical lines) together with evidence for the continuous distribution of Compton electrons. The agreement with expectation is satisfactory in all cases.

In order to prove that our instrument could reliably be used for the study of the rare phenomenon of triplet annihilation in solid media, the energy measurement was repeated with a solid positron absorber as a source. The results, obtained only for the symmetrical configuration, were in agreement with those reported above.

(b) Angular Distribution

In order to measure the angular distribution of the gamma rays, the bands of the pulse-height selectors were opened to accept all the pulses (photo and Compton) due to the appropriate gamma energy; then the number of triple coincidences recorded for any one configuration was compared to that obtained for the symmetrical case. The measured relative intensities are reported in Table I, column *C*.

The data were then corrected for variation in geometrical acceptance and for energy dependence of counter efficiency.

The geometrical acceptances of the different counter arrangements were computed numerically.[12] The errors introduced by correcting the data in this way are no larger than the statistical errors of the measurements themselves.

In order to correct for variation of counter efficiency, it was assumed that the efficiency varies with energy as shown by the curve of Fig. 4. Two points of this curve were experimentally measured. The value 0.38 at 0.51 Mev was obtained from coincidence measurement between the two-quantum annihilation gammas; and the value 0.54 at 0.34 Mev was determined using scattered gamma rays from the annihilation line. The rest of the curve represents an estimate made under the assumption that the efficiency should be unity under 100 kev, and should be proportional to the absorption of the gamma rays at high energy.

Despite our poor knowledge of the efficiency, this correction introduces an error of less than 10 percent in the measurement of angular distribution. This is because all measurements are taken in reference to the symmetrical arrangement, making any error in absolute efficiency at $\frac{2}{3}mc^2$ inconsequential. Furthermore, since the sum of the three energies is constant, the product of the three efficiencies varies much less than any one efficiency, and is in fact constant within 20 percent in all our measurements.

The experimental data corrected for both geometrical and counter efficiency variations are reported in column *D* of Table I. Column *E* shows the theoretical angular distribution, computed by means of a change of variables from the expression for the energy spectrum of the gamma rays given by Ore and Powell.[3] The ratios between the corrected experimental data and the theoretical distribution are shown in column *F* of Table I. The dispersion of these figures is somewhat larger than the purely statistical errors of the measurement, but, considering the errors introduced by the corrections, the disagreements (seldom larger than 10 percent) are within permissible limits.

Column *G* of Table I shows the ratios between the corrected experimental data on angular distribution and a statistical estimate of the distribution, obtained theoretically under the assumption that all matrix elements are independent of energy (and therefore of angle). It can be seen that the experimental data are sufficiently accurate to distinguish between the complete theory and the statistical estimate, favoring the

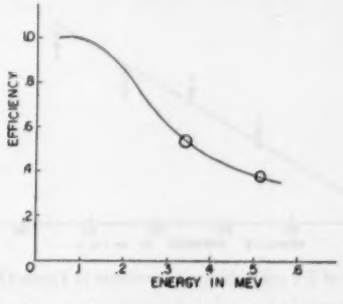

FIG. 4. Assumed efficiency vs energy for a 2.5 cm thick sodium iodide crystal. The two points were measured experimentally.

[12] For details of this computation, see R. Siegel, thesis, U. S. Atomic Energy Commission Report NYO-3302 (unpublished).

first in the cases where the two lead to significantly different conclusions.

Since for each angular arrangement the energies of the gamma rays are fixed, it is clear that a measurement of angular distribution is equivalent to a determination of the energy spectrum of the three-quantum annihilation gamma rays. The results of the angular distribution measurements may therefore be interpreted as verifying the energy spectrum from the complete theory rather than the statistical prediction based on the density of final states.

(c) Polarization

Another interesting characteristic of the three annihilation photons is their polarization. After the polarization effects had been theoretically calculated at our laboratory,[13] we proceeded to an experimental investigation of the polarization of one of the gamma rays relative to the plane of emission of the three,[14] since this is the easiest effect to study from the experimental point of view.

The experimental result was in agreement with the theory, which predicts a polarization ratio 3/1 in favor of rays plane-polarized with the electric vector perpendicular to the plane of the three photons. The experiment itself is described in reference 14.

IV. THE NUMBER OF TRIPLET ANNIHILATION EVENTS IN VARIOUS MATERIALS

(a) The Number of Triplet Annihilations in Aluminum

Since it seems justifiable to assume that, within a metal, the annihilation events occur between electron-positron pairs with randomly distributed spins, one is led to expect that the relative probability of three- and two-quantum annihilation should be 1/370, as computed by Ore and Powell. An attempt to verify this is described in what follows.

A sample of Na^{22} was enclosed in an aluminum capsule. With this as a source, the number of triple coincidences in the symmetrical position (120°, 120°, 120°) was measured and found to be, after background subtraction, $C=0.92\pm0.10$ counts/min.

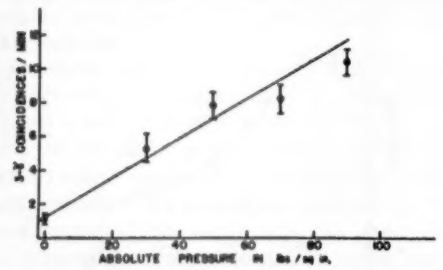

FIG. 5. Rate of 3-γ coincidences *vs* pressure in Freon-12 (CCl_2F_2).

[13] R. Drisko (private communication).

[14] Leipuner, Siegel, DeBenedetti, Phys. Rev. **91**, 198 (1953).

In order to compute the number of coincidences to be expected according to the theory, it is necessary to know the strength of the source, the efficiency of the three counters, and their geometrical acceptance. The geometrical acceptance was calculated as described in reference 12; the efficiency was taken from the curve of Fig. 4; and the strength of the source was obtained by comparison with a source calibrated in Oak Ridge, and also from an annihilation double-coincidence experiment (the same experiment from which the efficiency at 0.51 Mev was computed), the two methods yielding consistent results.

Using the values obtained in these preliminary studies, the expected value of C corresponding to the 1/370 ratio was 1.2 ± 0.16 counts/min. This is not in disagreement with the measured value.

(b) The Number of Triplet Annihilations in Gases

The number of triplet annihilations is considerably enhanced in gases whose chemical properties favor the formation of positronium.[11] In order to verify this effect, we performed the following experiment. The aluminum container described in Sec. III (a) was filled with Freon, and the three-quantum coincidence rate was observed as a function of pressure. The increase in coincidences with pressure (Fig. 5) indicates that ortho-positronium is formed when positrons stop in the gas rather than in the metal walls of the container.

TABLE II. Relative positronium yields in various gases.

Material	Pressure (psia)	Relative electron density	Relative 3-γ counting rate (reduced to equal electron densities)
Freon-12	75	1.0	1.00
SF_6	62	1.0	0.79 ±0.04
He	215	0.099	1.15 ±0.15
H_2	215	0.099	0.96 ±0.25
N_2	212	0.68	0.84 ±0.06
O_2	122	0.46	0.006±0.018

The container was also filled with other gases in order to study relative positronium formation. An estimate of the amount of positronium formed per positron stopped in the gas, was obtained by dividing the triple-coincidence counting rate by the relative electron density of the gases at the pressures used. The results are shown in Table II.

It is noteworthy that all the gases examined (except O_2, which is known to catalyze the conversion of triplet positronium to singlet) give a yield of positronium per stopped positron which is the same within ±25 percent. This average yield has been estimated from the source strength and counter geometry to be about 12 percent, in fair agreement with results of Deutsch and Pond.[15]

Figure 6 shows a graph of 3-γ counting rate (i.e. amount of orthopositronium formed) *vs* density of SF_6

[15] T. A. Pond, Phys. Rev. 85, 489 (1952).

in the gas container. Because of the high density of SF_6 attainable at room temperature, it was possible to follow the 3-γ rate into a density region in which the quenching becomes measurable. The decrease in 3-γ rate in SF_6 between 0.11 and 0.25 gm/cc yields a quenching cross section of $\sigma(SF_6)=9.7\times10^{-22}$ cm^2, with an estimated accuracy of about 15 percent. This result has been confirmed by Wheatley and Halliday.[16]

One concludes from the magnitude of this cross section that the spin-exchange process which probably causes the large quenching effect in oxygen [$\sigma(O_2)=4.0\times10^{-19}$ cm^2][17] is much less effective in the case of SF_6.

(c) Miscellaneous Experiments with Solids and Liquids

An attempt was made to investigate the presence of positronium due to positrons stopped in liquefied nitrogen or Freon. The source of positrons was deposited on the inside bottom of a small Dewar flask and covered with a thin plastic film. A considerable fraction of the positrons emitted traversed the film, as was verified by observing an increase in triplet annihilation when *gaseous* Freon at atmospheric pressure was poured into the Dewar. However, the number of triplet annihilations observed when either *liquid* nitrogen or *liquid* Freon filled the Dewar was of the same order as that expected from an equal number of positrons stopping in a solid metal.

Thus, in the liquid state, even substances like nitrogen or Freon whose chemical properties are known to favor the formation of positronium do not show the presence of triplet positronium in appreciable amounts. This could be due to either of two reasons: (1) either positronium is not formed at all in these liquids because of lack of space between the molecules of a condensed material, or (2) positronium is formed but it is rapidly converted from triplet to singlet in molecular collisions (an effect already evident in the vapors at high pressure).

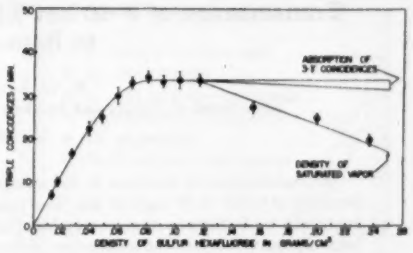

FIG. 6. Rate of 3-γ coincidences vs density in SF_6.

Recent studies on the half-lives of positrons in condensed materials[18] seem to favor the second of these explanations. If this second view is accepted, one can compute from the information on half-lives that the number of triplet annihilations in certain substances should be somewhat larger than in metals (3:1 for Teflon/Al; 1.6:1 for quartz/Al). In order to test this idea experimentally, it was necessary to measure the triplet annihilation rate with far greater accuracy than in the above experiments with liquefied gases.

Thus,[19] two Na^{22} sources of nearly equal intensity were prepared, one of them being deposited on and surrounded by aluminum, the other by Teflon, and the number of triplet annihilations was measured in a series of alternate runs. After reduction to the same source strength the observed ratio Teflon/Al was 1.94 ± 0.21. A similar experiment yielded 1.58 ± 0.28 for the ratio quartz/Al.

These results are in agreement with similar work performed at other laboratories[20] and confirm the presence of positronium in solids, at least in the case of certain insulators.

[16] J. Wheatley and D. Halliday, Phys. Rev. **88**, 424 (1952).
[17] M. Deutsch, Massachusetts Institute of Technology Progress Report of the Laboratory of Nuclear Science and Engineering, August 31, 1951 (unpublished).
[18] R. E. Bell and R. L. Graham, Phys. Rev. **90**, 644 (1953).
[19] The experiment was performed by Mr. L. Leipuner, whom we thank for permission to present his unpublished results.
[20] A. T. Stewart (private communication); T. A. Pond, Phys. Rev. **91**, 455 (1953).

Transmission of 0–40 kev Electrons by Thin Films with Application to Beta-Ray Spectroscopy*

R. O. LANE† AND D. J. ZAFFARANO
Department of Physics and Institute for Atomic Research, Iowa State College, Ames, Iowa

(Received January 25, 1954)

The transmission of electrons in the energy range 0–40 kev by thin plastic and metal films with surface densities of 0.023–1.57 mg/cm² has been measured in detail. The range-energy data resulting is prescribed fairly well by Bethe's average energy-loss theory. One of the films was used as a G-M counter window in a beta-ray spectrometer. The application of the transmission data to the beta-ray spectrum obtained for Pm^{147} gave some over-correction, as judged by the Fermi plot, which was attributable chiefly to the unavoidable difference between the collection geometry of the transmission measurement and that of the G-M counter.

I. INTRODUCTION

THE transmission of electrons by thin films was investigated with two chief purposes in mind: one purpose was the measurement of the ranges of electrons in thin films; the other was the determination of the transmission of electrons by a G-M counter window as a function of incident energy. It was hoped that the latter data could then be used to correct for window absorption when the counter is employed in a beta-ray spectrometer.

II. RANGE-ENERGY MEASUREMENTS

Figure 1 shows the elements of the experimental arrangement used for these measurements. This arrangement is contained in a vacuum system usually operated at a pressure of about 10^{-5} mm Hg, and is somewhat similar to that of Ference and Stephenson.[1] A disk D, shown in Fig. 1, contains some 16 film specimens, each of which can be rotated into a beam of electrons. The electrons are produced by a stabilized filament source and are accelerated across a potential difference, known to within 1 percent, giving a practically monoenergetic beam. After passing through the apertures A, the electrons penetrate the film F, pass on through the grid G, and enter a collecting cup C. For range-energy measurements, RV was set at ground potential, and V_g was set at -90 volts with respect to ground. Under these conditions, secondaries with energies less than 90 ev produced within C would be prevented from escaping from C. Taking into consideration the potentials on F and G, the uniformity of open area in G, and the secondaries[2,3] produced at the carbon-coated surfaces of G and C, calculations show that the ratio of the current collected by C with a film in the beam to that collected without a film in the beam is within 2–3 percent of the actual fractional transmission of the film.

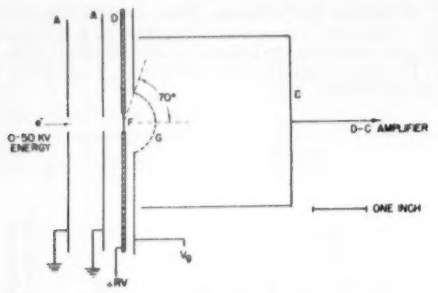

FIG. 1. Drawing of transmission experiment arrangement. Shown are: A, collimating electrodes; D, sample holding disk; F, film; G, guard ring and screen mesh, and C, collector. The Faraday cup defined by G and C was coated with carbon in a sooty flame of illuminating gas to reduce secondary emission.

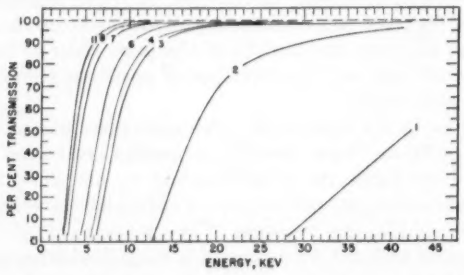

FIG. 2. Transmission curves for various films. See Table I for description of films and values of E_p (intercept on energy axis of extrapolation of descending linear portion of transmission curve). $RV=0$ for all curves shown. For clarity, transmission curves for films 5, 9, and 10 are not shown.

Most of the films studied in this investigation were either formvar or collodion upon which conducting coatings of aluminum had been evaporated. The resistance between points 1 cm apart on each film was of the order of 10^3–10^5 ohms, depending upon the thickness of the aluminum deposit. The transmission of white light by these films was measured with a Densichron, and the transmission was found to be given roughly by the expression, $\exp(-68l)$, where l is the area density of aluminum in mg/cm².

* Contribution No. 305 from the Institute for Atomic Research and Department of Physics, Iowa State College, Ames, Iowa. Work was performed in the Ames Laboratory of the U. S. Atomic Energy Commission.

† Now at the Physics Division, Argonne National Laboratory.

[1] M. Ference and R. J. Stephenson, Rev. Sci. Instr. **9**, 246 (1938).

[2] H. Bruining, Philips Tech. Rev. **3**, 80 (March, 1938).

[3] J. G. Trump and R. J. Van de Graaff, Phys. Rev. **75**, 44 (1939).

The transmission of electrons as a function of incident energy was measured for films of various area densities. Figure 2 shows the resulting transmission curves.[4] Table I lists the material and area densities of the films studied together with the energy-intercept E_p, of the extrapolation of the linear descending portion of the transmission curves. For clarity, the experimental points are not shown on any of the curves in Fig. 2. The repeatability of any given point was within 1 percent of complete transmission. For each curve the transmission was measured on both increasing and decreasing energies to see if any hysteresis effect were present. At each point the film was left in the beam ($\sim 10^{-10}$ ampere spread over a $\frac{1}{4}$-in diameter circle) for periods ranging from 1 minute to 30 minutes to see if the transmission would vary with time because of charging of the film. However, no variation of transmission with time was observed at any of the points. Furthermore, the points repeated to within 1 percent of complete transmission regardless of direction of the variation of energy. The scattering of the points about the curves was very small and was comparable

TABLE I. Properties of conducting films.

Film number	Average area density (mg/cm²)	Material[a]	E_p (kev)
1	1.57	Al	27.3
2	0.39	*F*-Al	12.7
3	0.10	*F*-Al	6.3
4	0.091	*F*-Al	5.5
5	0.082	*C*-Al	5.3
6	0.068	*C*-Al	4.7
7	0.039	*C*-Al	3.2
8	0.032	*C*-Al	2.6
9	0.024	*C*-Al	2.3
10	0.023	*C*-Al	2.3
11	0.024	*C*-Al	2.2

[a] Al indicates aluminum; *F*-Al, aluminum-coated Formvar; and *C*-Al, aluminum-coated collodion.

to that shown for the curve in Fig. 5 and for curves 1 and 2 in Fig. 6.

Curves of transmission *versus* area density were obtained at various energies by making cross-plots (not shown) of the curves of Fig. 2. Extrapolation of the linear portion of the resulting curves to zero transmission gave values of practical range R_p.

Figure 3 is a range-energy plot in which are shown the experimental points for E_p and R_p. Shown also for comparison are the experimental practical ranges of electrons in aluminum as measured by Schonland.[5] The present authors' data agree fairly well with those of Schonland in the region where the two sets of data overlap. The scatter in the range-energy points of this investigation is probably largely caused by the fact that even though the total average area density was determined with fairly good accuracy on a semimicrobalance, the ratio of the area density of plastic to that of the aluminum coating varied considerably from film

[4] Individual curves are shown in larger scale in Ames Laboratory Report ISC-439 by R. O. Lane and D. J. Zaffarano.

[5] B. F. J. Schonland, Proc. Roy. Soc. (London) **A108**, 187 (1925).

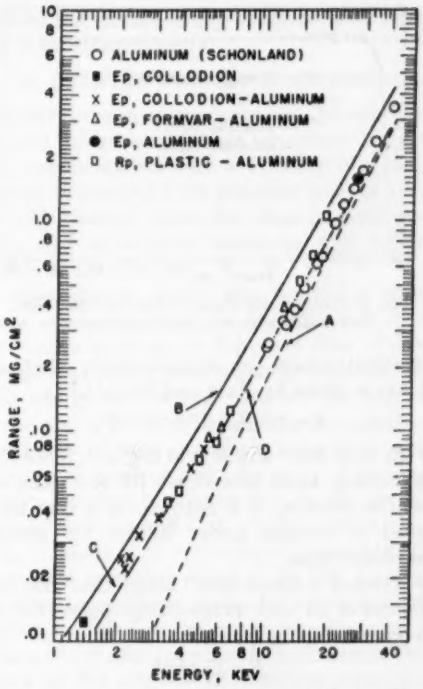

FIG. 3. Range-energy data. Curve *A* is a plot of the empirical relation of Katz and Penfold for practical ranges. Curves *B*, *C*, and *D* are plots of the theoretical mean range as calculated from Eq. (4), for aluminum, collodion, and Formvar, respectively.

to film. Since both scattering and energy loss have appreciable dependence on Z, the atomic number, some scattering in the points is expected as a result of variations in the relative proportions of plastic and aluminum from film to film. Of course, the procedure of weighing the very thin films accurately is difficult in itself. The probable error in the average area densities reported here ranges from 12 percent for the 0.024-mg/cm² films to 1 percent for the 1.57-mg/cm² film. Similarly, the probable error in determining E_p by extrapolation ranges from 10 percent for the 0.024-mg/cm² films to 2 percent for the 1.57-mg/cm² film.

Curve *A* of Fig. 3 is a plot of the empirical relation

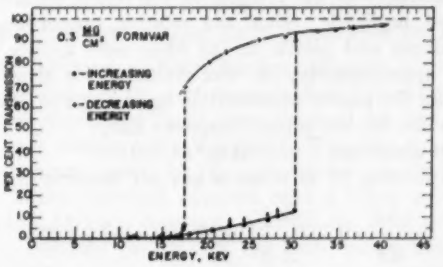

FIG. 4. Typical hysteresis loop obtained for a Formvar film not coated with aluminum. Dotted lines indicate electron energies for which sudden changes in transmission occur. Short arrows on points of lower curve indicate magnitude and direction of transmission drift at these points due to charging effects.

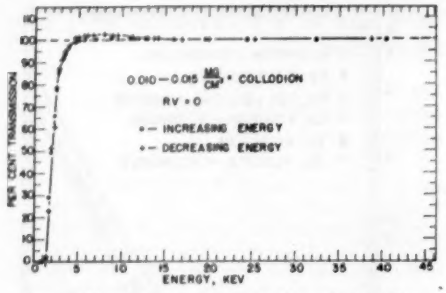

FIG. 5. Transmission curve of thin collodion film, not coated with evaporated aluminum.

for practical ranges of monoenergetic electrons in aluminum as given by Katz and Penfold,[6] i.e.,

$$R=412E_0^{(1.265-0.0954\ \ln E_0)}, \tag{1}$$

where E_0 is in Mev and R is in mg/cm². Since Eq. (1) is based chiefly upon data above 100 kev using aluminum as the absorber, it is not surprising that the fit is not good at energies under 20 kev for aluminum-coated plastic films.

The present authors have found that the energy-coordinates of all their range-energy points fall within 15 percent of those given by

$$E=22.2R^{0.6}, \tag{2}$$

where E is in kev and R is in mg/cm².

For nonrelativistic electrons Bethe[7] gives as the average energy loss per unit of path length,

$$-\frac{dE}{dx}=\frac{4\pi Nq^4}{mv^2}\ln\left[\frac{mv^2}{2\bar{I}}\left(\frac{e}{2}\right)^{\frac{1}{2}}\right](\text{erg}-\text{cm}^{-1}), \tag{3}$$

where N is the number of electrons per cm³ of film material, q is the charge on the electron, $e=2.718\cdots$, and $\bar{I}$ is the average excitation potential of the atoms of the film material. A calculation of the mean range may then be made from

$$R=\int_{\epsilon}^{E_0}(dE/dx)^{-1}dE, \tag{4}$$

with (3) substituted in the integrand. E_0 is the incident energy and ϵ is the energy below which the logarithm in (3) is negative. For all cases considered here the contribution to the integral in the region $0\leqslant E\leqslant\epsilon$ is indeed negligible. Since the relative proportions of aluminum and plastic in the films were known only very approximately, (4) was evaluated for aluminum and for the plastic separately in an attempt to bracket the value for the actual composite film.

For aluminum $\bar{I}$ was taken[8] as 150 ev.

Expressing (3) in terms of kev per (mg/cm²),

$$-\frac{dE}{dx}=0.307\frac{Z}{A}\frac{1}{\beta^2}[\ln(51.1\beta^2)-\ln\bar{I}+8.67]. \tag{5}$$

With the appropriate values of Z, A, and $\bar{I}$ for aluminum substituted in (5), the reciprocal of (5) was calculated for various energies and plotted against energy. The integral (4) was evaluated graphically by measuring the area under the curve with a planimeter for different incident energies. The results are shown as curve B of Fig. 3.

For the plastic windows, effective values of (Z/A) and $\bar{I}$ were used. Assuming the plastic molecule to be represented by the chemical formula, $(Z_1)_{n_1}(Z_2)_{n_2}\cdots$ and neglecting the effect of chemical bonding, the effective values of (Z/A) and $\bar{I}$ were obtained from

$$\left(\frac{Z}{A}\right)_{\text{eff}}=\frac{n_1Z_1+n_2Z_2+\cdots}{n_1A_1+n_2A_2+\cdots}, \tag{6}$$

and

$$\ln\bar{I}_{\text{eff}}=\frac{n_1Z_1\ln\bar{I}_1+n_2Z_2\ln\bar{I}_2+\cdots}{n_1A_1+n_2A_2+\cdots}. \tag{7}$$

The probable formula for collodion was taken as $C_6H_8O_9N_2$, which gave a $(Z/A)_{\text{eff}}$ of 0.52, and an $\bar{I}_{\text{eff}}$ of 66 ev. For Formvar, the probable formula was taken as $C_6H_{12}O_2$ which gave a $(Z/A)_{\text{eff}}$ of 0.55 and an $\bar{I}_{\text{eff}}$ of 49 ev. After substituting these effective values into (5) for collodion and Formvar, graphical integration yielded range-energy curves C and D, respectively, of Fig. 3.

For heavy particles which show relatively little scattering, the mean range can be simply related[9] to the extrapolated range. For electrons, on the other hand, the large amount of scattering and consequent straggling in ranges is so serious that the correct theoretical meaning of the experimental ranges determined by extrapolation is not clear. On the basis of this, an accurate direct comparison of theory with experiment was not attempted here. Rather, it was felt that more theoretical and experimental work was necessary before direct comparisons of theory with experiment

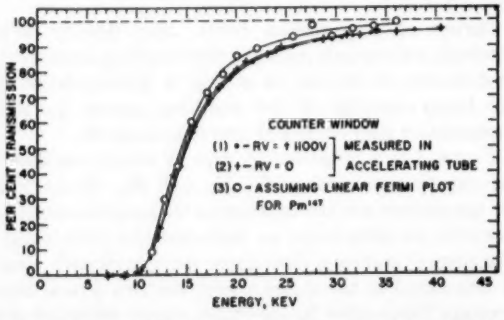
PER CENT TRANSMISSION
ENERGY, KEV
COUNTER WINDOW
(1) • — RV = ↑ HOOV
(2) ↓ — RV = 0
MEASURED IN ACCELERATING TUBE
(3) O — ASSUMING LINEAR FERMI PLOT FOR Pm¹⁴⁷

FIG. 6. Transmission curves for G-M counter window. Window was 0.3 mg/cm² Formvar coated with aluminum. The difference in the ordinates of curve 1 (lowest curve) and curve 2 (middle curve) is proportional to the number of secondary electrons emanating from the side of the film toward the Faraday cup. The open circles represent points computed by assuming that the true Fermi plot for Pm^{147} has an allowed shape to 10 kev.

[6] L. Katz and A. S. Penfold, Revs. Modern Phys. 24, 28 (1952).
[7] H. A. Bethe, *Handbuch der Physik* (Verlag Julius Springer, Berlin, 1933), Bd. 24, p. 519.
[8] B. Rossi, *High-Energy Particles* (Prentice-Hall Company, Inc., New York, 1953), p. 22.
[9] H. A. Bethe and J. Ashkin, as edited by E. Segrè, *Experimental Nuclear Physics* (John Wiley and Sons, Inc., New York, 1953), p. 285.

could be made with confidence. Curves *B*, *C*, and *D* of Fig. 3 were calculated to show what the theory would predict as a first approximation. It should be noted that these three curves have a slight curvature in the same direction as that of a smooth curve drawn through the experimental points, whereas the empirical relation of Katz and Penfold has the opposite curvature.

III. PLASTIC FILMS

Since a hysteresis effect has been reported by Owen and Cook[10] in the transmission of electrons by thin Zapon films, a 0.3-mg/cm² Formvar film which had not been coated with aluminum was examined in the same manner as the aluminum-coated films. Figure 4 shows a typical hysteresis loop obtained when the incident energy was increased from 10 kev to 40 kev and then decreased to 10 kev again. The short arrows on the lower points indicate that the transmission readings increased slightly immediately after the film was inserted in the beam. Dotted lines indicate sudden changes in transmission. Three complete hysteresis loops were obtained. In each case the points on the upper curve repeated very well. However, on successive traversals, the lower curve had both higher and lower slopes than the typical one shown in Fig. 4. On removing this film from the apparatus, a blackened spot was noticed in the general region of the beam-spot on the film. This same series of loops was repeated on this same film 6 months later, with generally the same results as the first time. The high resistivity of $>5\times10^{14}$ ohm-cm for Formvar, together with the blackened area, indicate that at high electron absorption and increasing electron energies the film charges until the potential is high enough to cause an electrical discharge across the surface of the Formvar or into the residual gas in the vacuum system. Upon decreasing the beam energy, the film is practically uncharged until a point is reached where the absorption of charge is greater than can be carried away by secondary electrons and the conductivity of the film. At this point the film begins to charge until the transmission is reduced by the potential barrier to a very few percent.

A thin collodion film which had not been coated with aluminum was also examined for hysteresis. Figure 5 shows the resulting transmission curve for the case of $RV=0$. The rise above 100 percent is presumed to be due to the emission of secondary electrons by the film. Since the resistivity of collodion is $10^{10}-10^{11}$ ohm-cm, a considerable negative steady-state potential difference could exist between the beam spot on the film and the grounded outer edge of the film. This, of course, would partially annul the retarding effect of V_g (-90 volts), allowing secondary electrons to enter the Faraday cup. When RV was set at $+1100$ volts, the transmission was essentially shifted to the right by approximately 0.3 kev and did not show the slight hysteresis effect evident in Fig. 6, again suggesting the role of the secondary electrons is an important one in these measurements.

[10] P. H. Owen and C. S. Cook, Phys. Rev. 86, 961 (1952).

IV. COUNTER-WINDOW TRANSMISSION

Secondary electrons produced on the collector side of the film being measured are important in the transmission measurements with a Faraday cup, but these would not be counted if the film were used as a window in a G-M counter, since the time interval between primary and secondaries would be well within the dead-time of the counter.

An experimental study was made of secondary electrons emanating from the collector side of a 0.3-mg/cm² aluminum-coated Formvar film which was later employed as a counter window. A distinct separation in energy was found between the tail of the primaries and a group of low-energy secondaries. The total intensity of these secondaries amounted to several percent of the incident beam intensity. These secondaries were removed from collection by the application of a retarding voltage RV of $+1100$ volts to the film. V_g (Fig. 1) was held at -90 volts to prevent the escape of secondaries produced within *C*. In Fig. 6 are shown the window transmission curves for two values of RV. The difference between the curves may be taken as an indication of the effect of secondary electrons. Curve 1 was used as the window transmission correction for the film.

The foregoing film was fastened to a frame which could be mounted with an "O-ring" pressure seal in a side-window G-M counter. The use of a conducting side window eliminated any dead space in the counter gas immediately inside the window, since the radial symmetry of the electric field was preserved. Calculations showed that electrons emerging from the window at angles up to 80 degrees would be counted with efficiencies of 99.8 percent or better, and those emerging at angles approaching 90 degrees would still have efficiencies of 90 percent, provided that they traveled at least 2 mm in the gas. In view of these high efficiencies at angles greater than 70 degrees, it is apparent that the counter may demonstrate greater collection efficiency for electrons than that indicated by the transmission measurement with a Faraday cup, as was found in fact, and is discussed in the following section.

V. APPLICATION TO THE BETA SPECTRUM OF Pm^{147}

The spectrum of Pm^{147} has been shown[11] to give a linear Fermi plot for electron energies as low as 10 kev.

Three sources of Pm^{147} were prepared for use in a thin lens beta-ray spectrometer.[12] The two thinnest sources were made by the distillation of $Pm^{147}Cl_3$ from a hot tantalum filament onto a 0.006 mg/cm² collodion backing. Assuming that all the mass in the $PmCl_3$ solution distilled in the same proportion as

[11] Langer, Motz, and Price, Jr., Phys. Rev. 77, 798 (1950); J. P. Mize and D. J. Zaffarano, Phys. Rev. 89, 902 (1953).

[12] Jensen, Laslett, and Pratt, Phys. Rev. 75, 458 (1949); Keller, Koenigsberg, and Paskin, Rev. Sci. Instr. 21, 713 (1950).

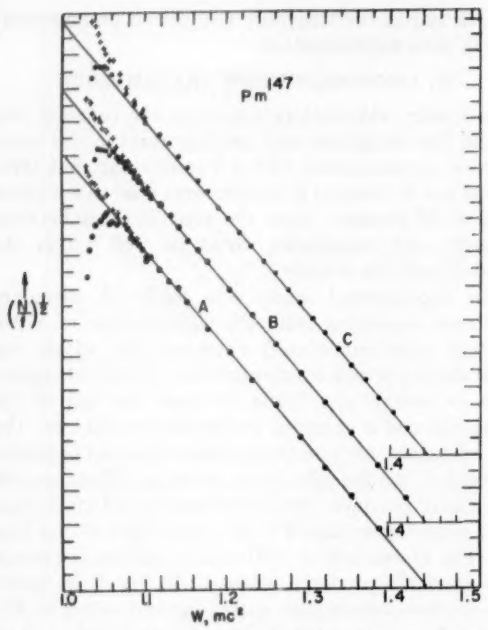

FIG. 7. Fermi plots for Pm^{147}. Plots *A*, *B*, and *C* are displaced vertically with respect to each other, and represent the data obtained from sources having area densities of 0.2, 1, and 30–50 $\mu g/cm^2$, respectively. Dots are uncorrected points. Crosses show application of window transmission curve 1 of Fig. 6.

the active mass, the average source area densities were 0.2 $\mu g/cm^2$ and 1 $\mu g/cm^2$. Autoradiographs showed that these distilled sources were very uniform. A thicker Pm^{147} source of 30–50 $\mu g/cm^2$ area density was made by precipitating $Pm^{147}(OH)_3$. Autoradiographs showed intensity variations as high as 2:1. A hot filament electron source was used to prevent source charging during spectrum measurements.

Figure 7 shows the Fermi plots obtained with the three Pm^{147} sources. The application of the counter window correction, curve 1 of Fig. 6, to the various Fermi plots is shown by the crosses. The end-point energies were 228±1.5 kev, 227±1.5 kev, and 226.5±1.5 kev for plots *A*, *B*, and *C*, respectively, in good agreement with previously reported data. The standard deviation in $(N/f)^{\frac{1}{2}}$ is less than $\frac{1}{4}$ of a small division over the entire plot. The magnitude of the over-correction due to application of the transmission data is clearly evident.

If the allowed Fermi plot for Pm^{147} is believed to be truly straight, one can deduce a window correction curve by calculating backwards from the observed points. When this was done, curve 3 in Fig. 6 was obtained.

A rough multiple-scattering calculation was made to see if it is reasonable to expect a significant number of electrons to be scattered by the counter window into angles between 70 degrees and 90 degrees, the effective solid angle subtended by the counter but not by the Faraday collector. Following the method of Chang, Cook, and Primakoff,[13] and using just the elastic scattering contribution for transmissions greater than 80 percent, the scattering of transmitted electrons into angles between 70 and 90 degrees was calculated for an energy of 20 kev for the two cases of aluminum and Formvar. The calculation indicated that if the counter windows were pure aluminum, curve 1, Fig. 6, should be 11 percent higher at 20 kev, whereas if it were pure Formvar, it should be 3.7 percent higher. The experimental value at 20 kev is about 5 percent too low. Repeating the calculation for an energy of 40 kev showed that curve 1 should be from zero to 1 percent higher, whereas the difference between the experimental curves here is about three percent. Although the calculation is admittedly crude, it appears not unreasonable to ascribe a considerable part of the over-correction to the difference in the geometrical efficiency of the two types of detectors employed, i.e., Faraday cup and G-M tube.

Some of the over-correction might also be due to x-rays produced in the window by some of the incident electrons. These x-rays could produce counts in the G-M tube, but would have little effect upon the Faraday collector current. In view of the relatively small number of incident electrons which produce x-rays in the film, and the low efficiency of the counter for counting x-rays, it would seem that the amount of over-correction due to x-rays would be quite small.

VI. CONCLUSIONS

Range-energy curves for electrons in the energy range 0–40 kev have been obtained for thin plastic films. Because of the large amount of scattering and straggling of electrons during passage through such films, it is difficult to argue for the validity of the application of present theory to such measurements. However, the theoretical mean ranges of electrons in these films do give better predictions of experimental ranges than does the empirical relation of Katz and Penfold in this energy region.

The transmission curve measured for a G-M counter window gave some over-correction when it was applied to the beta spectrum of Pm^{147} as measured with this counter in a lens spectrometer. Considering that the transmission curve was measured by a method completely independent of the counter and spectrometer, it is felt that the window transmission curve was in satisfactory accord with the data obtained from the Fermi plot of Pm^{147}. In view of the agreement with the theoretical allowed spectral shape reported by several laboratories, the use of the Pm^{147} beta spectrum as a standard probably offers the simplest present method of obtaining a transmission curve for a G-M counter window employed in a spectrometer above 10 kev.

The authors wish to express their appreciation to Dr. L. J. Laslett and Dr. A. G. W. Cameron for their interest and helpful suggestions concerning this work.

[13] Chang, Cook, and Primakoff, Phys. Rev. **90**, 554 (1953).

Radiations of 53-Min I^{134} and 86-Sec I^{136}†

MICHAEL MCKEOWN AND SEYMOUR KATCOFF
Brookhaven National Laboratory, Upton, New York

(Received February 5, 1954)

The radiations from 53-min I^{134} and 86-sec I^{136} were examined with a scintillation spectrometer and compared with known radiations. The former was found to emit beta rays of 1.5±0.1 Mev and 2.5±0.2 Mev maximum energy, and γ rays of the following energies: 0.86±0.01 Mev, 1.10±0.03 Mev, and 1.78±0.05 Mev. Coincidence measurements showed that the 2.5-Mev β rays were followed by the 0.86-Mev γ rays and that the first excited level in Xe^{134} is very likely at 0.86 Mev as predicted by the systematics of even-even nuclei. There is some evidence for two additional weak γ rays at 120 kev and 200 kev.

The I^{136} was found to decay by emission of a β-ray branch of 6.3±0.3 Mev maximum energy leading to the ground state of Xe^{136}, a 5.0±0.3 Mev β-ray branch followed by 1.38±0.05 Mev γ rays, and a 3.7±0.2 Mev β-ray branch followed by 2.9±0.2 Mev γ rays. A possible disintegration scheme is proposed. The first excited state at 1.38 Mev corresponds to that expected for the 82-neutron closed-shell nucleus, Xe^{136}.

INTRODUCTION

THE radiations of 53-min I^{134} and 86-sec I^{136} have previously been investigated only by absorption measurements.[1] In neither case was a γ ray reported corresponding to the value predicted for the first excited state by the systematics of excited states of even-even nuclei.[2] Therefore a search was made for these γ rays by means of a scintillation spectrometer. Both were found and, in addition, several other γ rays and β rays were identified. A disintegration scheme is proposed for I^{136}.

INSTRUMENTATION

The radiations were detected and their energies analyzed by means of a scintillation spectrometer. A NaI(Tl) crystal was used for detection of the γ rays, and an anthracene crystal was usually used for the β rays. In a few runs a NaI(Tl) crystal was also used for β rays because our anthracene crystals were not large enough to stop the highest-energy β rays of I^{136}. The crystals were mounted on No. 5819 photomultiplier tubes which were connected through an Atomic Instrument Company 204B amplifier either to an Atomic model 510 single-channel pulse-height analyser or to a Dumont model 303A oscilloscope equipped with a Polaroid Land Camera. The circuitry had provision for sweep blanking (Z-axis blanking), and a variable height pulse generator was available for energy comparisons.

Photographs of pulses due to γ or β rays were taken by connecting either the NaI(Tl) or anthracene detector in the normal self-triggering fashion to the oscilloscope. Gamma-gamma or beta-gamma coincidences could be observed by connecting the appropriate detectors in a coincidence arrangement. One detector would trigger the oscilloscope and the other would be connected to the y axis. In this type of photograph true coincidences would appear as a pulse distribution at the start of the sweep while chance coincidences would fall randomly along the entire sweep. The trigger bias and the Z-axis blanking allowed one to select the energy of the triggering pulses.

Energy determinations from oscilloscope photographs were made by feeding the pulses from a signal generator to the photomultiplier preamplifier, and comparing these pulses with the γ- or β-ray pulses involved. The pulse generator was calibrated with sources emitting radiations of known energies. The maximum energy of a beta spectrum was found by taking a number of photographs of the pulse-height distribution, each time increasing the length of the exposure. The beta end-point could then be determined from these photographs since the maximum pulse height was constant over a wide range of exposure times.

SOURCE PREPARATION

The 86-sec I^{136} sources were prepared by making rapid chemical separations of fission product iodine from 10-mg samples of uranyl nitrate which were irradiated in the Brookhaven pile for about one minute. The method depends on oxidation with $NaNO_2$ to elementary I_2 and extraction into CCl_4, reduction to iodide with $NaHSO_3$ and re-extraction into water. This cycle was repeated four times and the source was mounted as AgI (~20 mg). Measurements were begun about 5 minutes after the irradiations and useful data collected for the following 5 minutes. After this interval the 86-sec I^{136} intensity was too low relative to that of longer-lived isotopes of iodine. The effect of the latter was ascertained by repeating all the measurements of each run, starting at 15 minutes after the irradiation.

The 53-min I^{134} sources were prepared by allowing some fission product Te^{134} (44 min) to decay for an hour and then separating the daughter iodine by the above method. Tellurium activities were isolated from 40-mg samples of uranyl nitrate which were neutron irradiated in the Brookhaven pile for 3–6 minutes. Carrier was

† Work performed under the auspices of the U. S. Atomic Energy Commission.

[1] Hollander, Perlman, and Seaborg, Revs. Modern Phys. **25**, 469 (1953).

[2] G. Scharff-Goldhaber, Phys. Rev. **90**, 587 (1953).

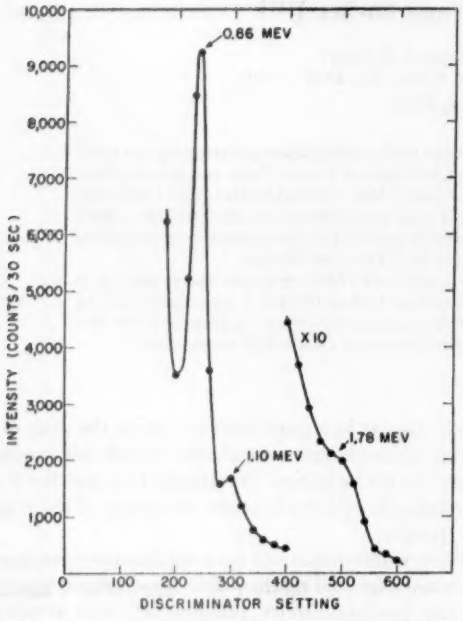

FIG. 1. Gamma-ray spectrum of I^{134} determined with a NaI(Tl) scintillation detector and a single-channel pulse-height analyzer.

added and Te metal precipitated from $3M$ HCl with SO_2 as the reducing agent. The Te was dissolved and reprecipitated twice more before allowing it to stand for growth of the I^{134}. This method of preparing an I^{134} source completely eliminates any interference from 6.7-hr I^{135} which grows from a very short-lived Te parent. The major remaining impurity was 20.8-hr I^{133}; its effect was always determined by repeating the measurements after the 53-min I^{134} had decayed away.

RADIATIONS FROM 53-MIN I^{134}

The γ rays from I^{134} (Fig. 1) were examined with a NaI(Tl) scintillation detector connected to a single-channel pulse-height analyzer. The following three γ rays were definitely established: 0.86 ± 0.01 Mev, 1.10 ± 0.03 Mev, and 1.78 ± 0.05 Mev. The first of these was considerably more intense than the others and they were all observed to decay with a half-life of 52 ± 5 minutes. In addition there was some indication of two more weak γ rays at 120 kev and 200 kev. The energy measurements were made by comparison with the 0.320-Mev γ rays of Cr^{51}, the 0.662-Mev γ rays from a Cs^{137} source, and the 1.51-Mev γ rays of K^{42}.

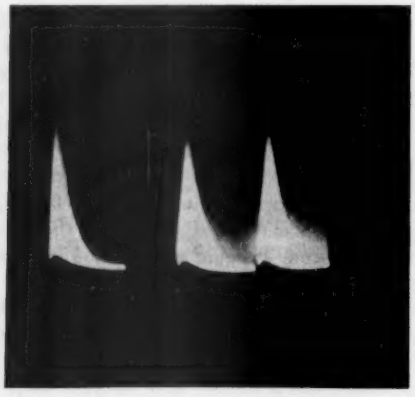

FIG. 2. Left pulse distribution shows 2.81-Mev β rays of Mn^{54}; center and right show 2.5-Mev β rays of I^{134} (10-sec and 20-sec exposures, respectively).

FIG. 3. Upper pulse distributions show 6.3-Mev β rays of I^{136} (2-sec and 8-sec exposures, respectively). Lower spectrum shows the 5.3-Mev β rays of Rb^{88}. The pulse generator pulses are in 4-volt steps from 40 to 80 volts.

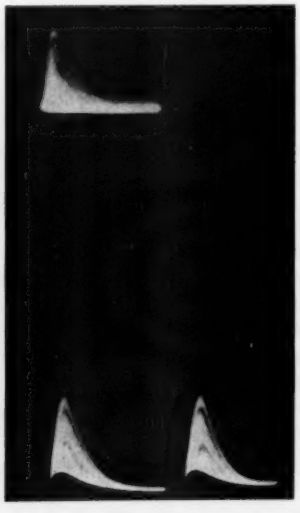

FIG. 4. Upper pulse distribution shows 1.4-Mev γ rays of I^{136} in coincidence with β rays above 3.6 Mev which triggered the oscilloscope. Lower distributions show the 1.51-Mev γ rays of K^{42} used for energy calibration.

The maximum β-ray energy was determined as 2.5 $\pm$0.2 Mev from photographs (Fig. 2) of the pulse-height distribution displayed on the oscilloscope. The same value (2.5 Mev) was also obtained in coincidence measurements when the oscilloscope was triggered by γ rays above 0.40 Mev or above 0.80 Mev. However, when the discriminator was set so that only γ rays above 0.90 Mev or above 1.3 Mev could trigger the oscilloscope, the maximum β-ray energy displayed was 1.5$\pm$0.1 Mev. Thus it appears that there are no ground-state beta transitions, that the 2.5-Mev transitions are to the 0.86-Mev level of Xe^{134} which is the first excited state, and that the 1.5-Mev beta transitions are to a level about 1.9 Mev above the ground state of Xe^{134}. The β-ray energies were calibrated with the 1.39-, 1.48-, 2.81-, and 3.58-Mev β rays of Na^{24}, Si^{31}, Mn^{56}, and K^{42}, respectively.

The above conclusions are also supported by several photographs of γ-ray spectra of I^{134} taken when the oscilloscope was triggered with β rays $>$1.5 Mev: only the 0.86-Mev γ rays were displayed in coincidence. When all β rays $>$0.7 Mev were allowed to trigger the oscilloscope, the 1.10-Mev and probably the 1.78-Mev γ rays were displayed in addition to the 0.86-Mev gammas.

The γ-γ coincidence measurements did not yield conclusive results. When the oscilloscope was triggered with γ rays above 1.1, 1.3, or 1.5 Mev, the 0.86-Mev γ rays were displayed in coincidence. However, it may be that the bremsstrahlung from the 2.5-Mev β rays was triggering the oscilloscope rather than the 1.78-Mev γ rays.

From the above data it appears that the first excited state of the Xe^{134} is almost certainly the 0.86-Mev level. This energy corresponds to the value expected from the systematics of the first excited states of even-even nuclei.[2] Therefore the 0.86-Mev level is very likely a 2+ state[2].

RADIATIONS FROM 86-SEC I^{136}

Scintillation spectrometer photographs of the γ rays of I^{136} showed an intense photoline at 1.38$\pm$0.05 Mev and a Compton electron distribution from γ rays of 2.9$\pm$0.2 Mev. The efficiency of the NaI(Tl) crystal for photoelectron production from 2.9-Mev γ rays is very low. The 1.38-Mev and 2.76-Mev γ rays of Na^{24} were used for calibration. The maximum energy of the I^{136} β rays was measured by taking photographs of the β-ray spectrum (Fig. 3) with an anthracene or NaI(Tl) crystal as detector. A value of 6.3$\pm$0.3 Mev was obtained relative to the 5.0-Mev and 5.3-Mev beta rays of Cl^{38} and Rb^{88}, respectively.

Two more beta transitions were revealed by the γ-β coincidence measurements. When the oscilloscope was triggered with γ rays above 1.5 Mev, the beta rays displayed in coincidence had a maximum energy of 3.7$\pm$0.2 Mev; when all γ rays above 0.1 Mev, 0.6 Mev, or 1.1 Mev were allowed to trigger the oscilloscope the β rays in coincidence were of 5.0$\pm$0.3 Mev maximum energy. These data indicate that the 6.3-Mev beta ray represents a transition to the ground state, that the 5.0-Mev beta ray represents a transition to the first excited state (1.38 Mev), and that the 3.7-Mev beta ray represents a transition to the second excited state (2.9 Mev) of Xe^{136}. These conclusions are supported by photographs (Fig. 4) taken with the oscilloscope triggered by β rays above 3.6 Mev which showed only the 1.38-Mev γ ray in coincidence, and other photographs taken with the oscilloscope triggered by β rays above 5 Mev which showed none of the γ rays in coincidence.

Gamma-gamma coincidence photographs indicated that there is probably a second γ ray of about 1.4 Mev in cascade with the 1.38-Mev γ ray. When the oscilloscope was triggered with γ rays above 0.1 Mev, above 0.8 Mev, or between 0.8 and 1.9 Mev, then the gammas displayed in coincidence had an energy of 1.4 Mev. When γ rays above 1.5 Mev were allowed to trigger the oscilloscope, 1.4-Mev γ rays were also observed in coincidence, but in much lower intensity. These were probably caused by coincidences between bremsstrahlung from the 5.0-Mev β rays and the 1.4-Mev γ rays.

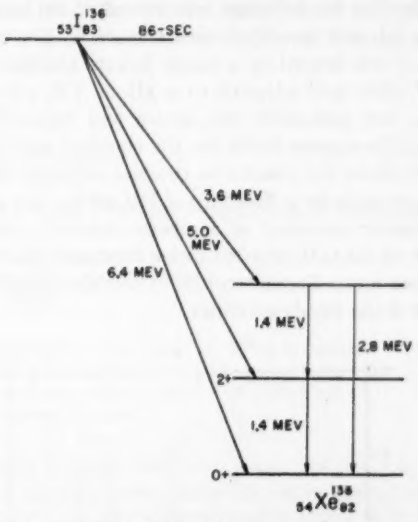

FIG. 5. Probable disintegration scheme for 86-sec I^{136}.

The disintegration scheme suggested in Fig. 5 is consistent with the aforementioned facts. A few of the energy values were adjusted slightly, but they lie well within the experimental error. The first excited level in Xe^{136} at 1.38 Mev corresponds to the value predicted for an 82-neutron nucleus by the systematics of the first excited states of even-even nuclei.[2] Therefore, the 1.38-Mev level is also probably a 2+ state.[2]

ACKNOWLEDGMENT

We wish to express our gratitude to Dr. G. Scharff-Goldhaber for helpful discussions and for suggesting this investigation as a test of the systematics of excited states of even-even nuclei.

Ytterbium-167

THOMAS H. HANDLEY AND ELMER L. OLSON
Oak Ridge National Laboratory, Oak Ridge, Tennessee
(Received January 27, 1954)

Proton bombardment of pure Tm_2O_3, followed by ion-exchange separations, has yielded an activity with an 18.5-minute half-life. Determination of the excitation function and identification of the daughter Tm^{167} assigns the activity to Yb^{167}. A gamma-ray spectrum shows it to decay by electron capture with a 0.118 Mev and possibly other gamma rays.

CAREFULLY purified Tm_2O_3 was bombarded with 24-Mev protons in the ORNL 86-inch cyclotron.[1] Following bombardment, chemical separations were performed by an ion-exchange method similar to that developed by Ketelle and Boyd.[2] It was necessary to modify the method somewhat in order to obtain a separation rapidly enough to detect the 18.5-minute half-life. The ion exchange column was 35 cm long and 1.8-cm i.d. and was filled with Dowex 50, 250 to 500 mesh; it was heated by a steam jacket. The elutriant, 0.25*M* citric acid adjusted to a *p*H of 3.18 with ammonia, was preheated with steam and infrared heat lamps. The storage bottle for the elutriant was placed 20 feet above the column to produce sufficient hydrostatic pressure for a flow rate of 180 ml/hr. The detection system consisted of a pipette counter[2] with the output of the GM tube fed into a log-count rate meter and then into a Brown recorder to provide a continuous record of the eluted activities.

A typical elution curve, Fig. 1, shows that, with suitable techniques, column separations may be performed on relatively short-lived activities. Absorption on the column was completed and elution began 20 minutes from the end of the bombardment, point *A*. The first peak (*B*) is composed of impurities of anions and divalent cations. The ytterbium peak begins to elute at approximately 2.1 hours from end of bombardment. Analysis of the Yb peak by decay curves and gamma spectra reveals three components: 18.5-minute Yb^{167}, 33-day Yb^{169}, and 9.4-day Tm^{167}. The half-lives for Yb^{169} and Tm^{167} are those actually observed. Analysis of the Tm peak shows it to consist of 9.4-day Tm^{167} and 87-day Tm^{168}. In each case, the half-life was established by following the decay for at least five half-lives. The elution peaks, Fig. 1, are not symmetrical because of the decay of the 18.5-minute Yb^{167} and the grow-in of its daughter, 9.4-day Tm^{167}.

The 73-minute activity assigned to Yb^{167} by Michel[3] was not observed as a component of either peak or of

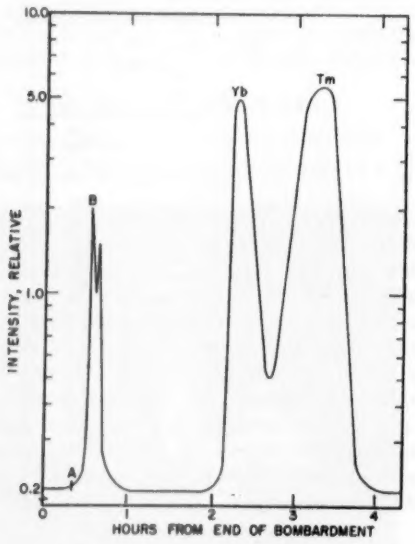

FIG. 1. Elution curve for Yb and Tm.

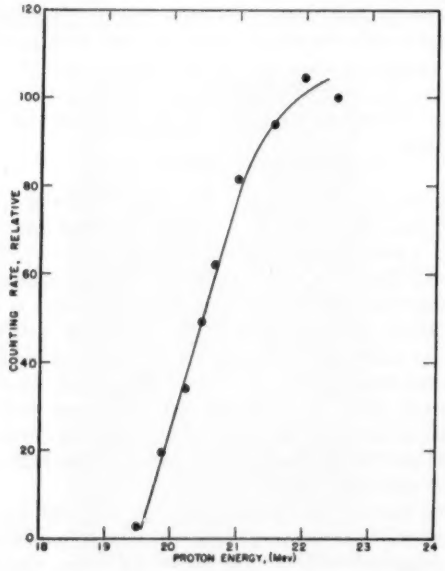

FIG. 2. Excitation function for the reaction $Tm^{169}(p,3n)Yb^{167}$.

[1] R. S. Livingston, Nature **170**, 221 (1952).
[2] B. H. Ketelle and G. E. Boyd, J. Am. Chem. Soc. **69**, 2800 (1947).
[3] L. Michel, University of California Radiation Laboratory Unclassified Report UCRL-2267 (unpublished).

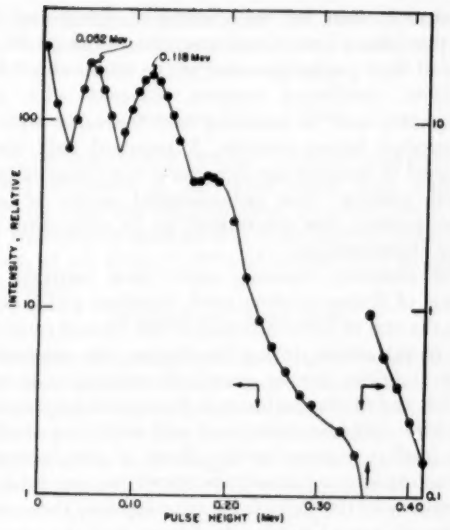

FIG. 3. Gamma-ray spectrum for Yb^{167}.

the gross decay curve obtained before separation. The products were examined specifically for such a half-life by using different counting techniques and by following the decay of various points on the spectrum. If the activity does have a mass of 167, it should have been produced in this bombardment.

For further proof of the mass assignment of the 18.5-minute Yb^{167}, an excitation function, Fig. 2, was determined for production of the activity. This shows a threshold of 19.0±0.5 Mev, which indicates a $(p,3n)$ reaction and, of course, assigns a mass of 167 to the activity.

The gamma-ray spectrum, as measured with a NaI(Tl) scintillation spectrometer, is shown in Fig. 3. A gamma ray of 0.118-Mev energy is apparent, also possible low intensity peaks near 0.18 and 0.33 Mev. The 0.052-Mev peak is the x-ray peak. The 0.51-Mev annihilation peak was not observed; if positrons are present, they constitute a very small fraction of the total radiation.

PHYSICAL REVIEW VOLUME 94, NUMBER 4 MAY 15, 1954

Yields of Fission Products from U^{238} Irradiated with Fission Spectrum Neutrons

R. N. KELLER,* E. P. STEINBERG, AND L. E. GLENDENIN
Chemistry Division, Argonne National Laboratory, Lemont, Illinois
(Received February 8, 1954)

A radiochemical investigation of the fission yields of 15 products in the fission of U^{238} is described. The average energy of the neutrons effective in inducing fission is estimated as 2.8 Mev. The familiar twin-peaked yield-mass distribution is observed with a peak-to-trough ratio of 200 to 1. A comparison of the fission yield-mass curve for U^{238} with those for other fissile nuclei is made.

I. INTRODUCTION

RADIOCHEMICAL determinations of the yields of fission products from the fission of various fissile nuclei have indicated that, in general, asymmetric fission results at low energies[1,2] with the contribution from symmetrical modes ("trough"), and perhaps, also very asymmetric modes ("wings"), increasing as the energy content of the compound nucleus is increased.[3–9] With increasing mass of the fissioning nucleus, the light group distribution shifts toward higher masses, while the heavy group remains relatively constant, with perhaps a slight shift in the direction of smaller masses.[3] A tendency toward wider mass distribution with increasing mass of the fissile nucleus has also been noted.[3,10]

Studies have been made of the fission of Th^{232} [10] and U^{238} [11] with fission spectrum (fast) neutrons to extend the knowledge of the characteristics of fission mentioned above. In the earlier U^{238} investigation[11] samples of of U_3O_8 powder, depleted seventeenfold in U^{235}, and normal uranium metal disks were irradiated in a cadmium can placed inside a hollow uranium cylinder. The U_3O_8 powder became contaminated with Cd^{115} in the process of opening the activated cadmium container making it impossible to determine directly in the depleted uranium the fission yield of Cd^{115} (which essentially establishes the trough yield). An attempt was therefore made to calculate this yield from the

* On leave from the University of Michigan. Present address: Department of Chemistry, University of Colorado, Boulder, Colorado.

[1] *Radiochemical Studies: The Fission Products* (McGraw-Hill Book Company, Inc., New York, 1951), National Nuclear Energy Series, Plutonium Project Record, Vol. 9, Div. IV.

[2] W. E. Grummit and G. Wilkinson, Nature **161**, 520 (1948).

[3] E. P. Steinberg and M. S. Freedman, reference 1, Paper No. 219.

[4] R. H. Goeckerman and I. Perlman, Phys. Rev. **73**, 1127 (1948).

[5] A. S. Newton, Phys. Rev. **75**, 17 (1949).

[6] R. W. Spence in Brookhaven Conference Report BNL-C-9, July, 1949 (unpublished).

[7] Fowler, Jones, and Paehler, Phys. Rev. **88**, 71 (1952).

[8] Turkevich, Niday, and Tompkins, Phys. Rev. **89**, 552 (1953).

[9] H. A. Tewes and R. A. James, Phys. Rev. **88**, 860 (1952).

[10] A. Turkevich and J. B. Niday, Phys. Rev. **84**, 52 (1951).

[11] Engelkemeir, Seiler, Steinberg, and Winsberg, reference 1, Paper No. 218.

observed Cd^{115} yield in the normal uranium. This calculation involved a correction for the Cd^{115} contributed by the U^{235} in normal uranium based on the known fission yield of Cd^{115} in thermal neutron fission of U^{235}. Since the Cd^{115} yield in fast neutron fission of U^{235} was not known, the correction was possibly in error. Moreover, the heavy mass peak was not well defined.

It seemed advisable to reexamine the fast neutron fission of U^{238} radiochemically with particular attention to the yield of Cd^{115} and yields in the region of the heavy mass peak. The accuracy of the fission yield determinations was also improved by the application of somewhat better corrections to the observed beta counting rates for absorption and scattering in the sources.

II. EXPERIMENTAL

A. General Procedure

Samples of U_3O_8 depleted in U^{235} (about 0.02 percent U^{235}) were sealed in cadmium-lined aluminum capsules and irradiated in a hollow uranium rod in the Oak Ridge pile. This arrangement enables irradiation with nearly unmoderated fission spectrum neutrons. The average neutron energy effecting fission in U^{238}, which has a fission threshold of about 1 Mev, is estimated to be approximately 2.8 Mev. Efficient filtering of neutrons of thermal energy was accomplished by the cadmium, minimizing the contribution of U^{235} to the total number of fissions. This contribution was shown to be less than 1.5 percent by comparison with normal uranium samples (0.7 percent U^{235}) irradiated under the same conditions. Several irradiations were carried out varying in duration to suit the half-life ranges of the nuclides under investigation. After irradiation and removal from the pile, the U_3O_8 was dissolved in a minimum quantity of $6N$ HNO_3 and the resulting solution diluted to known volume. This solution was then used for all subsequent aliquots and dilutions.

The fission products were isolated from the active solutions by adding a known amount of isotopic carrier, subjecting it to chemical separations which are specific for the element, and recovering the carrier in a chemically pure and weighable form suitable for counting. Care was exercised that interchange between the carrier and the fission-produced species was effected. If this condition is realized, the chemical yield of the recovered carrier, which need not be quantitative, also can be taken to be equal to the radiochemical yield of the fission product. The aliquot used and the amount of carrier added were adjusted to the chemical yield of the particular procedure and to the approximate fission yield of the isotope so that the recovered carrier in the form of a compound suitable for mounting weighed approximately 20 mg and had a counting rate of approximately 5000 counts per minute. In general, the radiochemical procedures used for the isolation of the fission-produced elements are those given in reference 1, Part VI, with minor modifications. The final precipitate in each case was collected on a 1.75-cm^2 circle of filter paper, mounted at the center of a 2.5-in. $\times$3.25-in. cardboard support, covered with thin Cellophane, and its counting rate measured with an end-window Geiger counter. A standard beta source was used to monitor any changes in the characteristics of the counter. The radiochemical purity of each fission product was determined by its absorption and decay characteristics.

The observed counting rates were corrected for aliquot of fission solution used, chemical yield, decay from the end of the irradiation to the time of counting, lack of saturation during irradiation, the presence of other activities due to genetically related or isotopic species, and resolution losses in the counting apparatus. Empirical self-absorption and self-scattering factors[12] were used to correct for the effects of sample weight, and an exponential absorption correction was made for absorption in the Cellophane covering over the sample, in the air layer between the source and the counter, and in the window of the counting tube. Inasmuch as all samples, including the beta standard, were counted with identical geometry, no correction for counting geometry was required.

B. Individual Determinations

Arsenic (40-hr As^{77})

The radiochemical procedure of Winsberg[13] was modified to include a preliminary reduction of As(V) to As(III) with iodide ion and subsequent oxidation back to As(V) with concentrated HNO_3 to insure interchange between the carrier and the fission-produced species.

According to the genetic relations of the chain of mass 77 the total fission yield of arsenic includes contributions from two Ge^{77} precursors, a 59-second isomer and a 12-hour isomer. In the calculations of the fission yield the assumption was made that the fraction of the total As^{77} that is formed by decay of the 59-second isomer of Ge^{77} is 55 percent and the fraction formed by decay of the 12-hour isomer is 45 percent as has been observed in the fission of U^{233}, U^{235}, and Th^{232}. The aluminum absorption curve for the arsenic activity obtained in this work showed a hard component, apparently due to 26.8-hr As^{76} formed by an (n,γ) process on minute traces of arsenic imputities in the U_3O_8. A correction was made for the contribution of this contaminant to the total observed activity.

Strontium (53-day Sr^{89})

The procedure used for isolating strontium was essentially that of Glendenin.[14]

The determination of Sr^{89} was straightforward since

[12] Engelkemeir, Seiler, Steinberg, and Winsberg, reference 1, Paper No. 4.
[13] Reference 1, Paper No. 228.
[14] Reference 1, Paper No. 236; also E. Hoagland, Paper No. 237.

complete decay of the 9.7-hr Sr^{91} had taken place before the radiochemical separations were made and the activity due to 20-yr Sr^{90} was negligible.

Zirconium (65-day Zr^{95})

The radiochemical procedure of Hume[15] was followed.

Determinations of Zr^{95} were made after allowing sufficient time for the complete decay of 17-hr Zr^{97}, and counting of samples was done before appreciable growth of the 90-hr Nb^{95m} and 35-day Nb^{95} daughters could occur.

Molybdenum (65-hr Mo^{99})

The radiochemical procedure of Ballou[16] was followed, with the exception that molybdenum was finally precipitated as $PbMoO_4$ rather than Ag_2MoO_4.

The 67-hr Mo^{99} decays by beta emission to 5.9-hr Tc^{99m}, which in turn decays by isomeric transition to the ground state, 2×10^5-yr Tc^{99}. Samples of 67-hr Mo^{99} were consequently counted through 15 mg/cm² of aluminum to filter out the low-energy conversion electrons from 5.9-hr Tc^{99m}. Allowance for this additional absorber was then made in the absorption correction.

Ruthenium (42-day Ru^{103} and 1.0-yr Ru^{106})

The radiochemical procedure of Glendenin[17] was used.

The isolated ruthenium contained activities from 40-day Ru^{103}, 1.0-yr Ru^{106}, and 30-sec Rh^{106}. The relative contributions from the two ruthenium isotopes were evaluated by analysis of an absorption curve.

Silver (7.6-day Ag^{111})

Ag^{111} activity was isolated by the procedure of Glendenin.[18] No other long-lived silver activities are produced in fission and no attempt was made to determine the fission yields of shorter-lived isotopes.

Cadmium (2.33-day Cd^{115} and 43-day Cd^{115})

The procedure of Metcalf[19] was used except that the cadmium was mounted for counting as CdS rather than $CdNH_4PO_4\cdot H_2O$.

The cadmium activity obtained was composed of 2.33-day Cd^{115} and 43-day Cd^{115}. The fraction due to the longer-lived isomer, which decays by beta emission to stable In^{115}, was evaluated by an analysis of the decay curves. The 2.33-day Cd^{115} decays to 4.53-hr In^{115} which in turn decays partly to stable In^{115} by isomeric transition and partly by beta emission to stable Sn^{115}. Counting of the samples was delayed until transient equilibrium was reached between 2.33-day Cd^{115} and 4.53-hr In^{115}. The contribution of the 2.33-day Cd^{115} to the total activity was determined from the equations of radioactive growth and decay and the known decay schemes.[20]

Antimony (93-hr Sb^{127})

The procedure used for isolating antimony activity was that of Stanley and Glendenin[21] with final precipitation as pyrogallate after Boldridge and Hume.[22]

The 93-hr Sb^{127} decays to two isomers of Te^{127}, a 90-day upper state and a 9.3-hr ground state with branching of 16 percent and 84 percent, respectively.[23] The 90-day isomer decays by isomeric transition to the 9.3-hr isomer, which in turn decays by beta emission to stable I^{127}. The Sb^{127} was determined after decay of the shorter-lived antimony isotopes by counting the transient equilibrium mixture of 93-hr Sb^{127} and 9.3-hr Te^{127}. The contribution of 93-hr Sb^{127} to the observed activity could then be calculated from the growth and decay relations of parent and daughter. Longer-lived antimony activities were present in negligible intensities.

Tellurium (77-hr Te^{132})

The radiochemical procedure of Glendenin[24] was followed. The method for determining 77-hr Te^{132} activity in the presence of the other tellurium activities from fission involved isolating samples of elementary tellurium of known weight from the fission solution, dissolving these and diluting to known volume, allowing sufficient time for transient equilibrium to be reached between 77-hr Te^{132} and its daughter, 2.4-hr I^{132}, and then analyzing for 2.4-hr I^{132} in aliquots of these solutions.[25] Once the 2.4-hr I^{132} activity in equilibrium with 77-hr Te^{132} is determined, the parent-daughter relations allow calculation of the activity due to 77-hr Te^{132}.

Cesium (33-yr Cs^{137})

The procedure for isolating this activity was essentially that of Glendenin and Nelson.[26]

The 33-yr Cs^{137} decays to stable Ba^{137}, partly by the direct route and partly through 2.6-min Ba^{137m}. The branching ratio for these two paths was taken as 8 percent and 92 percent, respectively, and the conversion in Ba^{137m} was taken as 10 percent.[20]

Barium (12.8-day Ba^{140})

The method for isolating this activity combined the procedures outlined by Glendenin for separating

[15] Reference 1, Paper No. 245.
[16] Reference 1, Paper No. 257.
[17] Reference 1, Paper No. 260.
[18] Reference 1, Paper No. 267.
[19] Reference 1, Paper No. 268.
[20] Hollander, Perlman, and Seaborg, Revs. Modern Phys. 25, 469 (1953).
[21] Reference 1, Paper 271.
[22] Reference 1, Paper 272.
[23] J. Beydon, Compt. rend. 227, 1159 (1948).
[24] Reference 1, Paper 274.
[25] Reference 1, Paper 278.
[26] Reference 1, Paper 283.

strontium and barium activities together[14] and that for separating barium alone.[27]

The 12.8-day Ba^{140} decays by beta emission to 40-hr La^{140} which in turn decays to stable Ce^{140}. For several hours after the removal of 40-hr La^{140} from 12.8-day Ba^{140} the growth of activity due to the former is essentially linear with time. The measurements of the beta activity of the barium samples were made as soon as possible after the last precipitation, and the observed beta activity was corrected to zero time for the 40-hr La^{140} growth by the relation $A_0=A_t/(1+0.015t)$, where A_0 is the original activity and A_t is the activity after t hours.

Cerium (282-day Ce^{144})

The procedure used was essentially that of Boldridge and Hume.[28]

The isolated cerium contained activities from 30-day Ce^{141}, 282-day Ce^{144}, and 17.5-min Pr^{144}. The contribution of Ce^{144} to the total activity was determined by analysis of an absorption curve after the 17.5-min Pr^{144} had reached secular equilibrium.

Europium (15.4-day Eu^{156})

A modification of the procedure by Winsberg[29] was used for separating europium activity. Barium and strontium sulfate precipitations were carried out in the presence of europium carrier prior to the initial EuF_3 precipitation of Winsberg's method and the europium was finally mounted as oxalate. The 15.4-day Eu^{156} was determined in the presence of 1.7-yr Eu^{155} (in low intensity) by analysis of absorption curves after the shorter-lived isotopes had decayed.

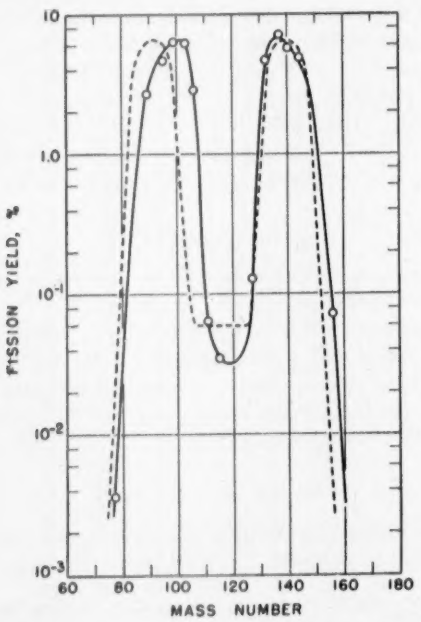

FIG. 1. Yield-mass curve for fast-neutron-induced fission of U^{238} (solid line), compared with that for Th^{232} (dotted line).

[27] Reference 1, Paper 288.
[28] Reference 1, Paper 294.
[29] Reference 1, Paper 303.

III. RESULTS

The fission yield of a nuclear species may be defined as the percentage of fissions which eventually result in the formation of the particular species. Since two fragments are formed per fission, the sum of the fission yields for all mass numbers is 200 percent. If the absolute fission yield for one nuclide has been determined, this can be used as a fission yield reference standard and the yields of other nuclides determined relative to it. Alternatively, an arbitrary value for the fission yield of one nuclide may be selected, the fission yields of other nuclides determined relative to this, and finally the resulting yield-mass curve normalized to 200 percent. The latter method has been employed in the present case. The reference nuclide used was 12.8-day Ba^{140}. The fission yield Y_A of any species A can be determined relative to the arbitrarily chosen value, $Y_{Ba^{140}}$, for 12.8-day Ba^{140} by the relation

$$Y_A=\frac{S_A}{S_{Ba^{140}}}Y_{Ba^{140}},$$

where S_A and $S_{Ba^{140}}$ are the saturation activities of A and Ba^{140} in a given irradiation.

The relative yields of fifteen nuclides obtained by the normalization method indicated above are given with estimates of reliability in Table I, column 3. The data from the earlier work of Engelkemeir *et al.*,[11] normalized to a value of 5.7 percent for Ba^{140}, are given in column 4 for comparison. The fission yields from column 3 are plotted against mass number in Fig. 1 and a smooth yield-mass curve (solid line) has been drawn through

TABLE I. U^{238} fission yields.

Fission product	Mass number	Fission yield (%) Present investigation	Reference 11
40-hr As	77	0.0036±0.001	0.0040
53-day Sr	89	2.7 ±0.3	3.1
65-day Zr	95	4.7 ±0.7	6.8
67-hr Mo	99	6.4 ±0.7	5.5
42-day Ru	103	6.3 ±1.0	6.9
1.0-yr Ru	106	2.9 ±0.3	2.5
7.6-day Ag	111	0.064 ±0.006	0.067
2.33-day Cd	115	0.032 ±0.006	0.053
43-day Cd	115	0.0025±0.0003	0.006
Total chain	115	0.035 ±0.007	0.059
93-hr Sb	127	0.13 ±0.03	0.11
77-hr Te	132	4.7 ±0.7	...
33-yr Cs	137	7.1 ±0.7	...
12.8-day Ba	140	5.7[a]	5.7[a]
282-day Ce	144	4.9 ±0.5	...
15.4-day Eu	156	0.073 ±0.01	0.059

[a] Ba^{140} was used as a fission yield standard for each irradiation.

them symmetrically about mass 118.5 (i.e., assuming binary fission with the emission of two neutrons per fission). The yield summation under this curve is 200 percent, and since the nuclides chosen for analysis are close to the stable ends of the fission chains, the curve should represent total chain yields.[30]

IV. DISCUSSION

The yield-mass curve for the fission of U^{238} with fission spectrum neutrons exhibits the familiar double-maxima and is in essential agreement with that observed previously[11] except for the yield of the trough (i.e., Cd^{115}). As mentioned above (Sec. I), the yield of Cd^{115} in U^{235} fission in the previous work was calculated from data on normal uranium assuming the yield of Cd^{115} in thermal neutron fission of U^{235} (0.011 percent) in the correction for the U^{235} contribution. It is now known that in the fission of U^{235} with fission spectrum neutrons the yield of Cd^{115} rises to a value of about 0.04 percent.[31] If this value is used to correct the old data, a yield of 0.04 percent is calculated for U^{238} fission, in good agreement with the result obtained in the present work using uranium depleted in U^{235}.

A comparison of the yield-mass curves of U^{238} and Th^{232} [10] is given in Fig. 1 to illustrate the effect of increasing the mass of the fissioning nucleus. A shift in mass distribution toward higher mass numbers is seen to take place almost exclusively in the light group. Also, the tendency toward a wider mass distribution is apparent in the heavy group.

The yield of symmetrical fission modes is definitely lower in U^{238} than in Th^{232}. Although the exact shape of the trough in U^{238} is not well defined, the condition of symmetry imposed in drawing a smooth curve through the yield of mass number 115 and its complement, mass number 122, leaves little latitude in the position of the minimum. A trough yield of about one-half that in Th^{232} is indicated. The average energy of the fission spectrum neutrons effective in inducing fission in both U^{238} and Th^{232} is about 2.8 Mev, as deduced from the known neutron energy spectrum[32] and the fission cross sections.[33] Since the neutron binding energies in Th^{232} and U^{239} are 5.1 Mev and 4.9 Mev, respectively,[34] the compound nucleus is slightly more excited in the case of Th^{232} fission and a somewhat higher trough yield might therefore be expected. It has also been suggested by Turkevich[10] that the peak-to-trough ratios in the fission of all heavy nuclei may be a function of the rate of break-up of the compound nucleus. Thus, smaller peak-to-trough ratios would result at excitations where the rate of break-up is faster. It is, of course, difficult to interpret the effect of energy on the peak-to-trough ratios when fission is induced by a spectrum of neutrons. Obviously, more data are needed utilizing various fissile nuclei and monoenergetic neutrons.

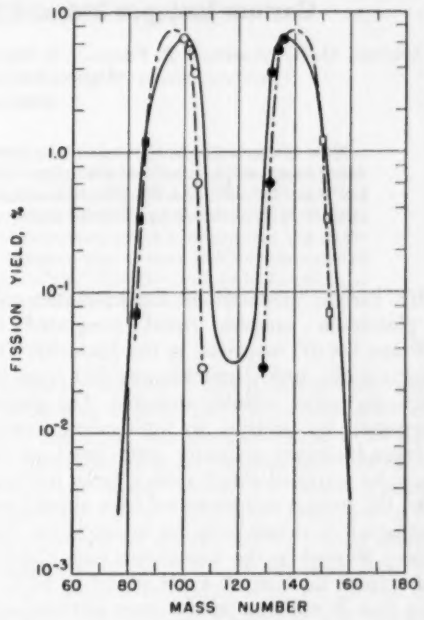

FIG. 2. Yield-mass curves for fast-neutron-induced fission of U^{238} (solid line) and spontaneous fission of U^{238} (dotted line). Solid squares and circles represent data for Kr and Xe isotopes, respectively, from reference 35; open squares and circles represent mirror points.

A comparison of the yield-mass curves for fast neutron-induced fission of U^{238} and spontaneous fission of U^{238} is given in Fig. 2. The data for spontaneous fission are the relative yields of the stable krypton and xenon isotopes produced by spontaneous fission of U^{238} in uranium ores.[35] A dotted curve has been drawn through the data assuming symmetrical reflection about mass 118 (i.e., two neutrons emitted per fission) and normalized to 200 percent yield summation. Narrower peaks and lower yields of symmetrical fission modes in spontaneous fission are apparent.[36] These results are consistent with the trends noted previously regarding the effect of excitation energy on the yield-mass curve.

[30] Glendenin, Coryell, and Edwards, reference 1, Paper No. 52.
[31] R. W. Spence (private communication, September, 1952).
[32] Bonner, Ferrell, and Rinehart, Phys. Rev. **87**, 1032 (1952); D. L. Hill, Phys. Rev. **87**, 1034 (1952); B. E. Watt, Phys. Rev. **87**, 1037 (1952); D. B. Nicodemus and H. H. Staub, Phys. Rev. **89**, 1288 (1953).
[33] Neutron Cross Sections, U. S. Atomic Energy Commission Report AECU-2040 (Technical Information Service, Department of Commerce, Washington, D. C., 1952).
[34] J. R. Huizenga and L. B. Magnusson, Argonne National Laboratory Report ANL-5158, November, 1953 (unpublished).
[35] W. H. Fleming and H. G. Thode, Phys. Rev. **92**, 378 (1953).
[36] More recent mass spectrometric work of G. W. Wetherill [Phys. Rev. **92**, 907 (1953)] on the mass distribution of xenon and krypton from spontaneous fission of uranium and thorium indicates even narrower peaks and lower yields for modes near symmetrical fission.

Curium Isotopes 246 and 247 from Pile-Irradiated Plutonium†

C. M. Stevens, M. H. Studier, P. R. Fields, J. F. Mech, P. A. Sellers, A. M. Friedman, H. Diamond, and J. R. Huizenga
Argonne National Laboratory, Lemont, Illinois

(Received Februrary 15, 1954)

Mass spectrometric analyses show the presence of curium-246 and curium-247 in curium samples produced from neutron-irradiated plutonium. The pile-neutron capture cross sections of Am^{243}, Cm^{244}, Cm^{245}, Cm^{246} are 115±20, 25±10, 200±100, and 15±10 barns, respectively. The alpha-disintegration half-life of Cm^{244} is calculated to be 19.2±0.6 years.

THE curium produced by the irradiation of two plutonium samples (total integrated fluxes 4×10^{21} and 8×10^{21} neutrons) in the Materials Testing Reactor (MTR) was chemically purified from fission products and other actinide elements. The plutonium was removed by utilizing its multivalent character.[1] The transplutonium elements were freed of fission products by standard cation resin column techniques.[2] Finally, the curium was separated from americium and the transcurium elements by an ion-exchange column of Dowex 50 resin in the ammonium form eluted with 0.25*M* citrate solution at a *p*H of 3.3 at 87°C. The column was 20 cm long with a cross-sectional area of 0.1 square cm. The actinide elements elute at different rates and the various fractions were collected and repurified.

The curium samples were analyzed in a 12-in., 60° mass spectrometer with a multiple filament source. The mole percent of the curium isotopes detected in each sample are given in Table I.

Sample I contained 0.24 percent Cm^{246}, whereas sample II contained 1.27 percent Cm^{246} and 0.016 percent Cm^{247}. Both curium samples also contained Cm^{245}, whose decay characteristics were recently identified.[3] The Cm^{247}/Cm^{244} ratio in sample II was constant within experimental error over a three-week interval. Cm^{247} is therefore either beta-stable or has a half-life greater than 2 months.

TABLE I. Mass spectrometric analyses of curium isotopes in mole percent (curium produced from plutonium irradiated in MTR).

Cm isotope	Sample I (Total flux 4×10^{21} neutrons)	Sample II (Total flux 8×10^{21} neutrons)
Cm^{243}	16.8 ±0.3	1.84 ±0.04
Cm^{244}	82.1 ±0.3	95.51 ±0.07
Cm^{245}	$0.93^{+0.10}_{-0.02}$	1.27 ±0.04
Cm^{246}	0.24±0.01	1.36 ±0.04
Cm^{247}	<0.004	0.016±0.002
Cm^{248a}	...	...
Cm^{249}	...	<0.002
Cm^{250}	...	<0.002

[a] The abundance of Cm^{248} metal ions could not be determined due to the interference of the impurity ThO^+ (mass =248).

The mass-spectrometric mole ratio of Cm^{244} to Cm^{242}, in conjunction with an alpha pulse analysis and a known alpha half-life of 162.5 days for Cm^{242}, enables one to calculate the alpha half-life of Cm^{244}. The data from the two curium samples give an alpha half-life of 19.2±0.6 years for Cm^{244}.[4]

Pile-neutron capture cross sections have been calculated for Am^{243}, Cm^{244}, Cm^{245}, and Cm^{246}. A value of 115±20 barns for the pile-neutron capture cross section of Am^{243} was calculated from the relative quantities of Am^{243} and Cm^{244} present at the end of the irradiations. This value is higher than the value of 50 barns reported by Street *et al.*[5] but in agreement with a more recent measurement by Thompson.[6] The pile-neutron capture cross sections of Cm^{244}, Cm^{245}, and Cm^{246} calculated from the mass spectrometric data are 25±10, 200±100, and 15±10 barns, respectively. A previous value of <5 barns[7] for the Cm^{244} pile-neutron capture cross section is in disagreement with the present results. The high ratio of curium-246 to curium-245 indicates that Cm^{245} has a high destruction cross section. The binding energy of the last neutron in Cm^{246} is of the same order of magnitude as that of the last neutron in Pu^{242}. From fission systematics, one predicts that the thermal neutron fission-to-capture ratio[8] of Cm^{245} is greater than one. The large predicted thermal neutron fission cross section is in qualitative agreement with the recent thermal neutron fission measurements on Cm^{245}.[9]

The technical assistance of C. H. Youngquist in the engineering aspects of these experiments is gratefully acknowledged. We also wish to thank W. M. Manning for many stimulating discussions.

† These isotopes of curium have previously been discovered in other work at Argonne National Laboratory, not yet published.

[1] Studier, Fields, Sellers, Friedman, Stevens, Mech, Diamond, Sedlet, and Huizenga, Phys. Rev. **93**, 1433 (1954).

[2] K. Street, Jr., and G. T. Seaborg, J. Am. Chem. Soc. **72**, 2790 (1950).

[3] Hulet, Thompson, and Ghiorso, unpublished results; Cm^{245} was first identified mass-spectrometrically by F. L. Reynolds (unpublished).

[4] Thompson, Hulet, and Ghiorso obtained a value of 19 years by direct decay, Revs. Modern Phys. **25**, 611 (1953).

[5] Street, Ghiorso, and Seaborg, Phys. Rev. **79**, 530 (1950).

[6] S. G. Thompson, private communication, (1953), reported the pile-neutron cross section of Am^{243} to be 100 barns.

[7] Thompson, Ghiorso, and Reynolds, quoted in Chap. 20 of *The Transuranium Elements* (McGraw-Hill Book Company, Inc., New York, 1954), National Nuclear Energy Series, Plutonium Project Record, Vol. 14A, Div. IV.

[8] J. R. Huizenga and R. B. Duffield, Phys. Rev. **88**, 959 (1952).

[9] Bentley, Studier, Fields, Diamond, Pyle, and Fried, Argonne National Laboratory Report ANL-WMM-1138 (unpublished).

Gamma Rays from $N^{15}(p,\alpha\gamma)C^{12}$ and $N^{15}(p,\gamma)O^{16}$†

ALFRED A. KRAUS, JR.*
Kellogg Radiation Laboratory, California Institute of Technology, Pasadena, California
(Received February 1, 1954)

A new resonance in the reaction $N^{15}(p,\alpha\gamma)C^{12}$ giving the 4.43-Mev γ ray from the first excited state of C^{12} has been found at a proton energy of 1.64±0.03 Mev. The angular distribution of the γ rays indicates that the resonant state in the compound nucleus O^{16} at an excitation energy of 13.65 Mev has spin and parity equal to 1^+ or 2^-. The resonance at 1.05-Mev proton energy has been reinvestigated. At this resonance the capture γ rays from the reaction $N^{15}(p,\gamma)O^{16}$ are found to be isotropic, which indicates that this 13.09-Mev level of O^{16} has spin equal to 1. A search was made for capture γ rays at the 0.340-Mev resonance of $N^{15}(p,\alpha)C^{12}$ but there were less than 1 percent of the number at the 1.05-Mev resonance. Therefore, it seems that these two levels do not have identical spin, parity, and isotopic spin values.

THE reaction $N^{15}(p,\alpha\gamma)C^{12}$ has been studied by Schardt, Fowler, and Lauritsen,[1] by Kraus, French, Fowler, and Lauritsen,[2] and by Barnes, Neilson, and James.[3] In the work herein reported the excitation function for this reaction has been extended to a proton energy of nearly 2 Mev. Protons from the 2-Mv electrostatic accelerator of the Kellogg Radiation Laboratory were magnetically analyzed and used to bombard a titanium nitride (TiN) target enriched to 31 percent N^{15}. The detector was a $1\frac{1}{2}$-in. diameter by 2-in. long Na(Tl) crystal which was cemented to a 5819 photomultiplier tube. The tube was surrounded by three magnetic shields. The output was fed through a conventional pulse amplifier, a single channel differential discriminator, and then to decade scalers. The channel was set to select pulses only in the region of the pair and Compton electron peaks of the 4.43-Mev γ rays. The measured excitation curve corrected for a small background is shown in Fig. 1. The resonance at 1.21-Mev bombarding energy is known from the work of Schardt *et al.*[1] A new resonance is observed at 1.64±0.03 Mev with a width of half-maximum of approximately 150 kev. The asymmetrical shape of the resonances shows that the distribution of N^{15} atoms in the target was not uniform, as to be expected from the mode of chemical preparation. The excitation function rises again above 1.9 Mev. Preliminary investigations up to 2.4 Mev indicated a broad resonance somewhat above 2.4-Mev proton energy.

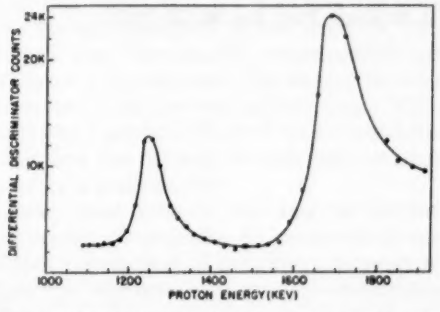

FIG. 1. Excitation function for the reaction $N^{15}(p,\alpha\gamma)C^{12}$.

The angular distribution of the 4.43-Mev γ rays from the 1.64-Mev resonance is shown in Fig. 2. The points have been corrected for background and absorption. The curve shown is given by $1+a\cos^2\theta$ with $a=0.30\pm0.04$. The errors are statistical errors compounded with a 1 percent error of the absorption corrections. If the coefficient of $\cos^2\theta$ is corrected for the finite solid angle of the detector, the corrected value is $a=0.32\pm0.04$.

Since there are no significant $\cos^4\theta$ terms in the angular distribution, it seems likely that the compound nucleus is formed by p-wave protons. N^{15} and the proton are assumed to have spin and parity equal to $\frac{1}{2}^-$ and $\frac{1}{2}^+$, respectively. The excited state of C^{12} is known[2] to be 2^+, its ground state, 0^+. If one specifies the compound state of O^{16} at this point the relevant proton and α-particle waves are then determined.

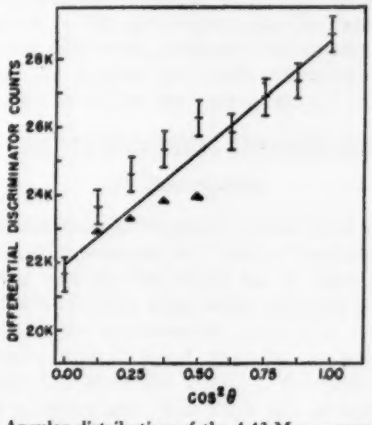

FIG. 2. Angular distribution of the 4.43-Mev γ rays from the 1.64-Mev resonance in $N^{15}(p,\alpha\gamma)C^{12}$. The triangles are the measured points for $\theta>90°$.

† This work was supported by the joint program of the U. S. Office of Naval Research and the U. S. Atomic Energy Commission.

* G. E. Fellow in Physics, 1952–1953 academic year. Now at the Department of Physics, The Rice Institute, Houston, Texas.

[1] Schardt, Fowler, and Lauritsen, Phys. Rev. **86**, 527 (1952).

[2] Kraus, French, Fowler, and Lauritsen, Phys. Rev. **89**, 299 (1953).

[3] Barnes, Neilson, and James, Can. J. Phys. **30**, 717 (1952).

TABLE I. Theoretical angular distributions of the 4.43-Mev γ rays.

Spin of the O^{16} state	Lowest l_p	Lowest l_α	Angular distribution
0^+	1	2	1
0^-	0	Forbidden	None
1^+	1	2	$(7+3\cos^2\theta)+2A(5-3\cos^2\theta)$
1^-	0	1	1
2^+	1	0	$1+\cos^2\theta$
2^-	2	1	$(3+15\cos^2\theta-16\cos^4\theta)$ $+6A(1-3\cos^2\theta+4\cos^4\theta)$
3^+	3	2	$(8-3\cos^2\theta+5\cos^4\theta)$ $+2A(5-12\cos^2\theta+15\cos^4\theta)$
3^-	2	1	$27+78\cos^2\theta-55\cos^4\theta$

Since no information is available about the emission of long-range α particles from this state to the ground state of C^{12}, all possible compound states must be considered. As an additional complication, the proton and N^{15} can come together to form compound systems of channel spin 0 to 1. The channel spin 0 will contribute only if the parity of the O^{16} state is $(-1)^{J+1}$, where J is its spin. Table I gives a summary of the relevant orbital angular momenta and the theoretical angular distributions. The angular distributions were calculated assuming only the lowest possible values of l_p and l_α, the relative angular momenta of the proton and α particle, respectively, in units of $\hbar$. The quantity A is the amount of channel spin 0 compared to unity for channel spin 1. A reasonable fit is obtained by assigning 1^+ as the spin and parity of the O^{16} state and choosing $A\approx 1/14$. However, this fit is not unique. An assignment of 2^- for the 0^{16} state will also fit with $A\approx\frac{2}{3}$ when it is considered that some protons of higher l waves probably contribute to the reaction and the effect of the resonance at a higher energy ($\gtrsim$2.4 Mev) is not known. This resonance could conceivably cause a change of 0.05 in the coefficient of $\cos^2\theta$ at 1.64 Mev. Therefore the spin and parity of the state of O^{16} at 13.65-Mev excitation are either 1^+ or 2^-.

Considerable discussion has been centered on the 1.05-Mev resonance in the reactions[4] $N^{15}(p,\gamma)O^{16}$ and $N^{15}(p,\alpha)C^{12}$. In order to obtain more information about this level, the angular distribution of the γ rays from the reaction $N^{15}(p,\gamma)O^{16}$ was measured. The measured distribution is isotropic to about 7 percent (statistical error). It is assumed that all the γ rays represent direct transitions ($\sim$13 Mev) to the ground state of O^{16} as indicated by their energy as measured with the scintillation counter. Table II gives a list of the theoretical angular distributions of these γ rays. The only isotropic distributions are from spin 1 states and the spin and parity of this state of O^{16} at 13.09-Mev excitation are either 1^- with $A=0$ or 1^+ with $A=\frac{1}{2}$.

TABLE II. Theoretical angular distributions of the capture γ rays.

Spin of the O^{16} state	Lowest proton wave	Angular distribution
0^+	p	Forbidden
0^-	s	Forbidden
1^+	p	$(1+\cos^2\theta)+2A(1-\cos^2\theta)$
1^-	s	1
2^+	p	$1+\cos^2\theta$
2^-	d	$(1-3\cos^2\theta+4\cos^4\theta)$ $+6A(\cos^2\theta-\cos^4\theta)$

A search was made for capture γ rays at the 0.340-Mev resonance of the reaction $N^{15}(p,\alpha)C^{12}$. Less than 1 percent of the number at the 1.05-Mev resonance were found. This result means that quite probably the two states have a different set of spin, parity, and isotopic spin values.

The author would like to thank C. A. Barnes, R. F. Christy, W. A. Fowler, C. C. Lauritsen, and R. J. Mackin, Jr, for many valuable discussions during the course of this work.

[4] D. H. Wilkinson, Phys. Rev. 90, 721 (1953).

Structure and Composition of Air Shower Cores*

HAROLD L. KASNITZ AND KURT SITTE
Department of Physics, Syracuse University, Syracuse, New York
(Received June 24, 1953; revised manuscript received October 14, 1953)

Extensive air showers were observed with an arrangement in which details of their structure and composition could be studied with the help of a large cloud chamber and a 102-counter hodoscope, while extension trays permitted a classification of the showers in three groups according to their initial energy, and a selection favoring events with cores striking near the central cloud chamber-hodoscope set. The electron density distribution is found to be flatter than the Molière structure function, and despite the different shower ages in the three energy groups, to be nearly the same for all the showers recorded. A structure function $\phi(r) \propto r^{-0.76}$ to $r^{-0.85}$ in the immediate neighborhood of the core fits the data best. An attempt to correlate the very dense local cascades started by high-energy electrons or photons with the expected multiple cores representing the high multiplicity of the nuclear interaction initiating the shower failed; the structure of the groups of local cascades observed does not appear to vary with the shower energy. The penetrating component contains N particles interacting in the lead plates of the chamber with a mean free path of approximately 165 g/cm², and consisting of neutrons (41±8 percent) and charged particles. The total abundance of penetrating particles near the core does not differ appreciably from that found by various authors in experiments not as strongly biased in favor of the detection of shower cores. The abundance ratios of N particles to μ mesons, and of penetrating particles to electrons, show only slight variations with the shower age and demonstrate that the nucleonic cascade reaches its maximum somewhat later than the electron cascade.

I. INTRODUCTION

IT has frequently been stressed as a remarkable fact that the theory of cascades initiated by a single particle, when applied to the description of air shower phenomena, is successful although the process of the development of an extensive shower is of a greatly more complicated nature. It has also been recognized that this success is not really fortuitous, but a result of the circumstance that many of the features of electron cascades are essentially determined by the properties of the shower within a few cascade units from the point of observation, and thus independent of the initial development of the cascade as long as the observation is restricted to a region not including the shower axis and its immediate surrounding, the shower core. It is only in this region that the nature of the initiating process strongly affects the shower structure, and that deviations from the classical single-particle cascade theory have been observed. The density distribution, as investigated by various authors (e.g., Williams,[1] Prescott and Campbell,[2] Hazen,[3] Williams and Hazen[4]) is flatter than that calculated by Molière[5] for a cascade initiated by a single particle.

In most cases, however, the analysis has suffered from a surfeit of variables. In particular in counter experiments, showers of all energies—or more correctly, of all particle numbers—were recorded indiscriminately, with detection systems which were rather insensitive to the accurate location of the shower axis. Thus, an analysis averaging over density spectrum, lateral distribution—both presumably depending on the age of the shower—and core location could scarcely be expected to yield an unambiguous picture of the details of the initial distribution.

It seemed therefore worthwhile to perform an experiment with a technique improved in two respects: firstly, by using an arrangement which rejects more strongly events in which the shower core strikes at an appreciable distance from the apparatus and which consequently more stringently registers shower cores; and secondly, by recording—at least within reasonable limits—the total number of shower particles, and therefore classifying the showers as to their average age. A study of the electron density distribution under these controlled conditions, together with a study of penetrating particles in the core region, can be expected to reveal some additional pertinent information on the nature of the process in which extensive showers originate and by which they propagate.

II. THE EXPERIMENTAL ARRANGEMENT

(1) Description

The experimental arrangement consisted of a shower selector set ("masterpulse set") and a "core analyzer." The shower selector was made up of three pairs of counter trays and two large single counters placed at the center of the arrangement. Each tray contained ten counters; those in the A trays had an active area of 1 in.×16 in., while the B and C counters were of 1 in.×12 in. active area. The three sets of trays were situated symmetrically with respect to the core analyzer, as shown in the schematic drawing of Fig. 1(a), with

* Supported in part by the U. S. Atomic Energy Commission. Part of this work is included in the paper submitted by one of us (H.L.K.) as a Ph.D. thesis at Syracuse University.
[1] R. W. Williams, Phys. Rev. **74**, 1689 (1948).
[2] I. D. Campbell and J. R. Prescott, Proc. Phys. Soc. (London) (London) **A65**, 258 (1952).
[3] W. E. Hazen, Phys. Rev. **85**, 455 (1952).
[4] R. W. Williams and W. E. Hazen, Phys. Rev. **90**, 361 (1953).
[5] G. Molière in *Cosmic Radiation*, edited by W. Heisenberg (Springer Verlag, Berlin, 1943, and Dover Publications, New York, 1946).

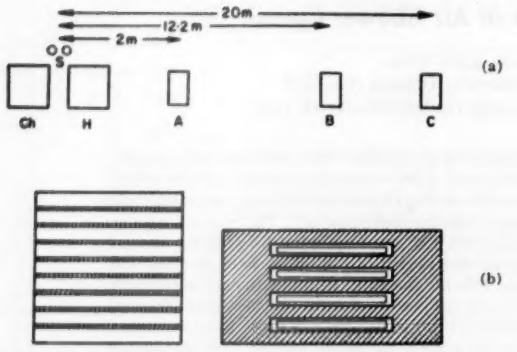

FIG. 1. The experimental arrangement. (a) General layout: Cloud chamber (Ch), hodoscope (H) and three of the six counter trays. (b) The analyzer set: 24-in. square cloud chamber with eight ½-in. lead plates, and hodoscope of four counter trays in lead pile.

the A trays at a distance of 2 m, the B trays at 12.2 m, and the C trays at 20 m from the center. Each of the central counters S had an active area of 2 in.×24 in.

Three different masterpulses were formed, dividing all of the recorded showers into three groups as follows:

(i) At least two counters struck in each of the A trays, less than two counters struck in each of the B trays, and both central counters S triggered ("A showers");

(ii) At least two counters struck in each of the B trays, less than five counters struck in each of the C trays, and both central counters struck ("B showers");

(iii) At least five counters struck in each of the C trays, and both central counters triggered ("C showers").

This triggering system imposed on the events selected at least a rough symmetry with respect to the core analyzer situated at the center, and, because of the anticoincidence arrangement, was strongly biased in favor of showers whose axes struck near the center. It may be noted that the S counters affect the selection only in a very small degree, but they reduce the chance coincidence rate very appreciably.

Diode clippers were used in the masterpulse circuits, and after reduction to uniform height the counter pulses were fed through diode isolating circuits to an integrating circuit. The output of the integrator was amplified by a 12AU7 located at each tray, and fed through a cathode follower to a 6AK5 discriminator. A setting of each tray discriminator allowed the selection of outputs corresponding to two or more, or five or more, counters simultaneously discharged. The appropriate coincidence and anticoincidence circuits, actuated by the outputs of the six tray discriminators and the outputs of the two counters S, formed the masterpulses. As a check on the performance of the triggering system, each tray discriminator and the three masterpulse arrangements separately triggered a thyratron. Whenever a shower was recorded, neon lights were photographed indicating both the type of masterpulse and the trays hit. For instance, for an A shower only the A_1 and A_2 lights should be seen, together with the A masterpulse light.

The analyzer set consisted of a large cloud chamber (24 in.×24 in.×10 in.) fitted with eight ½-in. lead plates, and a hodoscope arrangement of 102 counters arranged in four trays of 20, 24, 28, and 30 counters, respectively. The two upper trays contained counters of 1 in.×12 in. size, the two lower trays 1 in.×16 in. counters. The trays were separated from each other by layers of 2-in. lead, and shielded by 8-in. lead walls from the sides and 2-in. lead on top. Cloud chamber and hodoscope were placed side by side as close as possible to each other. As in an earlier experiment[6] the coordination of the two instruments was simplified by a system of clocks, double registers, and neon indicators.

The analyzer set is schematically shown in Fig. 1(b). It offers the advantage not only of a large area (about 0.25 m²) usable for analysis, but also of observation over a considerable range of penetration. In the hodoscope set the shower development can be followed through a total of 8 in. of lead absorber, and the data in the upper hodoscope tray can be reduced to incident densities with the help of the observations of the transition effect in 2 in. of Pb seen in the chamber. This feature is particularly useful for the study of the penetrating shower component.

A total of about 1300 cloud-chamber photographs and more than 2800 hodoscope records were analyzed. Hodoscope pictures without a corresponding chamber photograph, taken during the recycling period of the cloud chamber or belonging to events where the chamber picture was not considered good enough for full analysis, where still of value for the statistical analysis discussed below.

(2) Discussion of the Triggering Arrangement

It is always useful in an air shower experiment, and necessary for the present one, to analyze the performance of the triggering arrangement. In particular, to substantiate the claims made in Sec. I, the selectivity of the masterpulse system as to shower size and location must be evaluated.

For this calculation the following two customary assumptions have been made:

(i) That the lateral distribution of the shower is represented by the Bethe approximation[7] to the Molière structure function

$$f(r)=\frac{c}{r}(1+4r)\exp(-4r^{2/3}), \tag{2.1}$$

where c is a constant and r the distance from the core measured in shower units. The limitation of the

[6] Froehlich, Harth, and Sitte, Phys. Rev. 81, 504 (1952).
[7] H. A. Bethe, Phys. Rev. 59, 684 (1941).

validity of the Bethe approximation to comparatively small distances r is of no concern since the triggering arrangement efficiently rejects events striking at too large distances from the center.

(ii) That the differential size distribution of the showers can be represented by

$$s(N)dN = KN^{-(\gamma+1)}dN, \tag{2.2}$$

with a constant $\gamma \approx 1.5$ for the entire range of efficient detection. It will be seen that this should certainly hold for the A and B showers which contain on the average less than 10^6 particles, while a correction is needed for C showers.

It will further be assumed that the detection efficiencies of the trays are unity, and that other corrections such as that for the finite resolving time are likewise negligible. These assumptions are of course not quite correct, but will introduce no appreciable error since only relative rates will be considered and not their absolute values.

The calculations follow the well-known pattern (e.g., Ise and Fretter,[8] Singer[9]) and only a few essential points will be repeated here. Denoting by $r_S, r_{A1}, r_{A2} \cdots$ the distances (in shower units) of the central counters, the A_1 tray, the A_2 tray, and so on, from the axis of the shower, by θ the azimuthal angle of the shower axis measured from the line connecting the trays, and by S, AS, BS, CS the areas of the central counters and of the single A, B, and C counters, respectively, one has, for instance, for the rate of A showers:

$$R_A = \int_0^\infty KN^{-(\gamma+1)}dN \int_0^\infty 2\pi r dr \int_0^{\pi/2} \{[p_S(r_S,NS)]^2 \times \sum_{i=2}^{n} p_A(i,r_A,ANS) \sum_{j=2}^{n} p_A(j,r_A,ANS) \times \sum_{k=2}^{n} p_B'(k,r_B,BNS) \sum_{l=2}^{n} p_B'(l,r_B,BNS)\} d\theta, \tag{2.3}$$

where the functions $p(i,r,NS)$ are the exponential expressions for the probability of a shower of N particles hitting in a distance r to trigger exactly i out of n $(=10)$ counters, and the p''s similarly are the probabilities of the shower missing. Thus, for instance,

$$p(i,r_A,ANS) = \{1-\exp[-ANSf(r_{A1})]\}^i \cdot \exp[-(n-i)ANSf(r_{A1})]. \tag{2.4}$$

Similar expressions are obtained for the rates of B and C showers.[10]

The next step in the evaluation is the compution of the triggering probability $I(r,NS)$ due to all showers striking at a distance r from the central counters, as a function of the particle number N:

$$I_A(r,NS) = r \int_0^{\pi/2} \{p_S^2 \sum_i p_{A1} \sum_j p_{A2} \times \sum_k p_{B1}' \sum_l p_{B2}'\} d\theta. \tag{2.5}$$

(The arguments in the expressions of the type (2.4) are omitted.) From it two important functions can be obtained.

(a) By integrating over N, one finds the contribution $P(r)$ to the recorded rates by showers of all sizes as a function of the distance r of their axis from the center of the arrangement

$$P(r) = \int_0^\infty KN^{-(\gamma+1)} I(r,NS)dN. \tag{2.6}$$

The result is shown in Fig. 2. It should be noted that 50 percent of all A showers strike within a radius of less than 2.5 m. The selectivity is less perfect for the B showers with a maximum contribution at about 7 m, and least for C showers (maximum at about 13 m). However, it will be seen later that even for those two types of events an analysis of the core structure can be obtained.

(b) By integrating over r, the contributions $F(N)$ to the recorded rates by showers of various particle numbers striking at all distances r from the central counters are found:

$$F(N) = 2\pi KN^{-(\gamma+1)} \int_0^\infty I(r,NS)dr. \tag{2.7}$$

Figure 3 summarizes the result for the three shower types. It is seen that the selection is remarkably sharp; the A-shower curve, for instance, is centered about

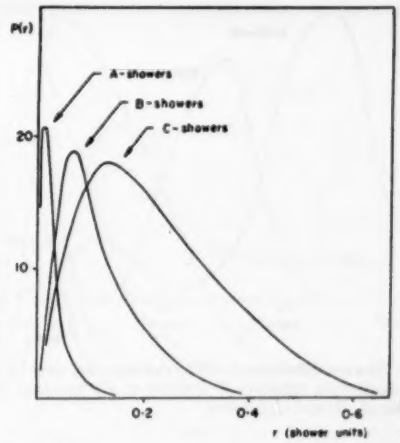

FIG. 2. The contributions $P(r)$ to the recorded rates by showers of all sizes, as a function of the distance r of their axis from the center of the arrangement, for A, B, and C showers.

[8] J. Ise, Jr., and W. B. Fretter, Phys. Rev. **76**, 932 (1949).
[9] S. F. Singer, Phys. Rev. **81**, 579 (1951).
[10] The very slight dependence of the probabilities p and p' on the zenith angle of the shower axis can be neglected in the following considerations.

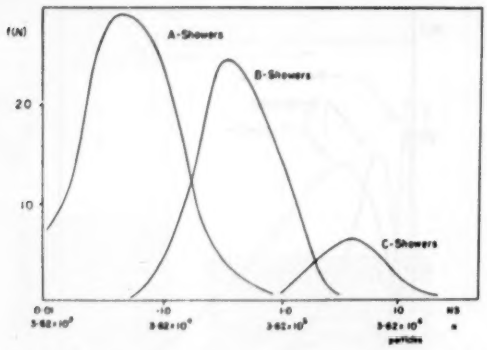

FIG. 3. The contributions $F(N)$ to the recorded rates by showers of various particle numbers N striking at all distances from the center, for A, B, and C showers.

$NS=0.05$ (corresponding to $N=1.81\times10^4$, or an incident energy of 0.91×10^{14} ev for a single-photon initiated cascade). Its width at half-maximum is about 10, from $NS=0.018$ to $NS=0.16$. Similarly, the B masterpulse selects predominantly events between $NS=0.18$ and $NS=1.5$, or from an energy interval centered about $E_0=0.71\times10^{15}$ ev, while the C showers lie mostly between $NS=1.8$ and $NS=10$, with an average $E_0=0.80\times10^{16}$ ev. It is clearly seen that the separation of shower energies is satisfactorily achieved.

III. THE ELECTRON COMPONENT

(1) Density Distribution at the Center

Since the preceding discussion has shown that the requirements of energy classification and of core selection are fairly well met, the density distribution observed in the analyzer set can be expected to exhibit the properties of the structure function near the core as a function of the energy. Using the expressions quoted above for the triggering probabilities, and the Molière-Bethe structure function, one can calculate the frequency of events of a density Δ at the point of observation. Deviations from the theoretical curve can then be used to obtain a corrected structure function which should be compared with that derived from an improved theory. Thus the results could, in principle, yield better values for some of the parameters of shower theory and of the theory of high-energy nuclear collisions. At the present stage, however, a more modest goal should be set: The exact theory of large air showers involves not only the number, the angular distribution, and the energy spectrum of the electron-producing particles ejected in the initial collision, but also a source function representing the continuous replenishment of the electron component from the nuclear cascade. The number of adjustable parameters in the theoretical results is, therefore, so large and the correlation between structure function and basic features of the theory so far from unique, that unambiguous conclusions can scarcely be reached from the data of a single experiment. In other words, uncertainties in fundamental points make it appear premature to attempt a direct comparison between experiment and a more refined theory, although the mathematical methods of shower theory have recently been developed in a rather general form.[11] But even in carrying the analysis of the experimental data only to the point of deriving empirical corrections to the Molière-Bethe theory, one can hope to gain at least semiquantitative evidence on the relative importance of some of these fundamental features.

Both cloud-chamber and hodoscope records were used for the study of the electron density distribution. In the cloud chamber analysis, the particle numbers recorded in the pictures had to be corrected for the transition effect in the brass walls of the chamber. Bethe's multiplication factor $[1+2(1-7.2/Z)t/X_0]$ as quoted by Williams[1] was used (Z is the atomic number, and t/X_0 the thickness in radiation lengths, of the wall material traversed), and the incidence of an equal number of photons and electrons was assumed. As Hazen has pointed out,[8] this last assumption is somewhat uncertain, but the effect is small and the possible errors involved probably negligible. A further correction of the cloud-chamber data was made for electrons not connected with the shower, but crossing the apparatus within the resolving time of the chamber. Their average number was obtained from a careful survey of the data taken with the same chamber and at the same location, but with a different triggering arrangement which demanded the incidence of an unaccompanied penetrating particle.[6]

In the analysis of the hodoscope data, two corrections were needed in order to determine the electron density of the incident air shower from the number of counters struck in the top tray. Firstly, the average number of particles present is always larger than the number of counters discharged. A correction for this effect is easily obtained if random distribution of the shower particles over the tray area can be assumed, so that the Poisson formula can be applied to express the probability that exactly n counters will be hit by a shower of m particles. Secondly, a statistical correction must be made for the transition effect in the 2-in. top lead absorber. For this purpose, the transition effect in the lead plates of the chamber was determined, and the data giving the average number of electrons observed under the fourth of the ½-in. plates as a function of the number of incident electrons were then used to find the true incident density from the number of hodoscope counters struck.

The incident density distribution may be calculated assuming the Molière-Bethe structure function to be valid. Since a shower of density Δ at the center of the arrangement, whose axis strikes at a distance r from

[11] E.g., L. Jánossy and H. Messel, Proc. Roy. Irish Acad. **A54**, 245 (1951); H. Messel, Proc. Phys. Soc. (London) **A64**, 726 (1951); H. S. Green and H. Messel, Phys. Rev. **88**, 331 (1952).

the center, must contain, on the average, a number $N=\Delta/f(r)$ particles, the frequency with which this event will be observed is given by

$$h(\Delta)=2\pi\Delta^{-\gamma}\int_0^\infty \{f(r)^\gamma\}I(r,\Delta S/f(r))dr. \quad (3.1)$$

For the comparison with the experiment, the integral frequency distribution $H(\Delta)$, that is, the frequency of showers of a central density $\geq\Delta$, is preferred:

$$H(\Delta)=\int_\Delta^\infty h(\Delta)d\Delta. \quad (3.2)$$

The evaluation of (3.1) and (3.2) has to be done by numerical integration. $h(\Delta)$ is first constructed by computing for various fixed Δ the contribution from showers incident at various distances, and this procedure yields some interesting auxiliary results. Thus, as it is seen from Fig. 4(a)–4(c), while *A* showers of practically all central densities strike in the immediate neighborhood of the analyzer set, for *B* showers this is true only when the central density exceeds about 50 particles/m², and for *C* showers only for large showers of more than 400 particles/m² at the center. Small *B* showers and an appreciable fraction of the *C* showers will therefore not reveal features characteristic of the core region. On the other hand, the curves of Fig. 4(a)–4(c) show in which density region the observations will refer to true shower cores. It may be noted that, although the number of *events* in which the shower axis strikes at some distance from the analyzer becomes considerable for *C* showers, the fraction of *particles* observed in these events in cloud chamber and hodoscope is not equally large since the "true" cores generally are the denser showers. A statistical analysis of the shower particles, as it is presented below, is therefore more strongly biased in favor of shower cores than those curves may indicate.

The integral density distributions (3.2) for the three types of showers, calculated with the Bethe structure function (2.1) for the three triggering arrangements used, are shown in Fig. 5(a)–5(c) together with the experimental observations in both the cloud chamber (circles) and the hodoscope (crosses). Clearly the theoretical results are a very poor representation of the data. It was therefore decided to improve the agreement by modifying the structure function in (3.1).

Since for small values of r the Bethe function is well approximated by a r^{-1} law, a power law with a changed exponent would appear the logical choice for the corrected structure function. In order to avoid pure guessing, the following procedure was used: It is assumed that the corrected structure function is of the form

$$\phi(r)=Ar^\epsilon f(r), \quad (3.3)$$

where $f(r)$ is again the Bethe function of (2.1), and ϵ a small quantity. It is then evident that using $\phi(r)$ instead of $f(r)$ for the calculation of the rates $h(\Delta)$ and $H(\Delta)$ will have a small effect on the triggering probabilities $I(r,NS)$ and a much more pronounced effect on the terms $(\Delta/f)^{-\gamma}$ as compared with $(\Delta/\phi)^{-\gamma}$

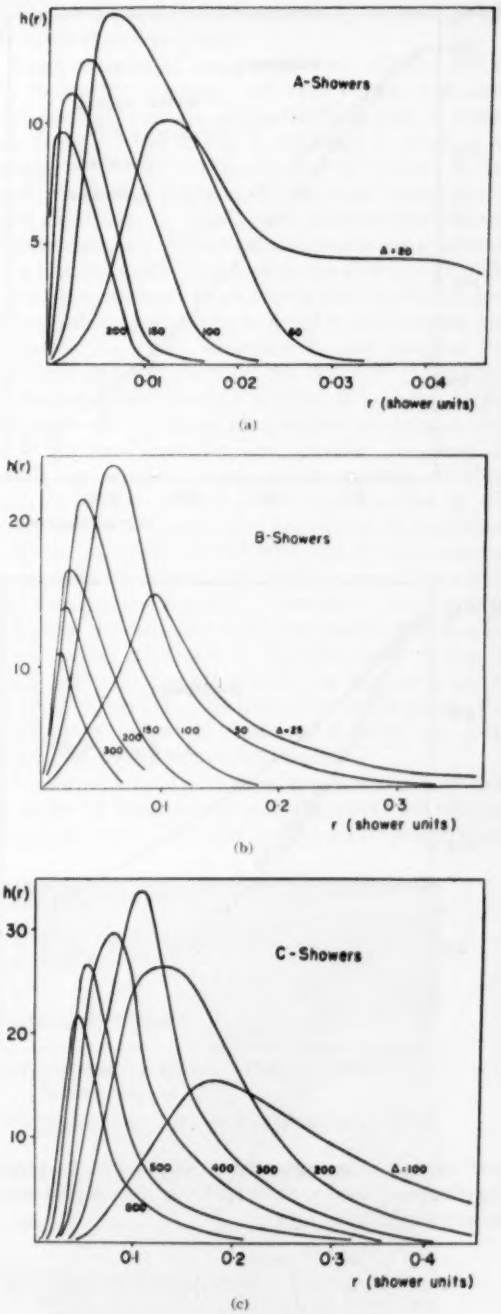

FIG. 4. Differential density distribution $h(\Delta)$ at the center of the arrangement, calculated with the Bethe structure function.

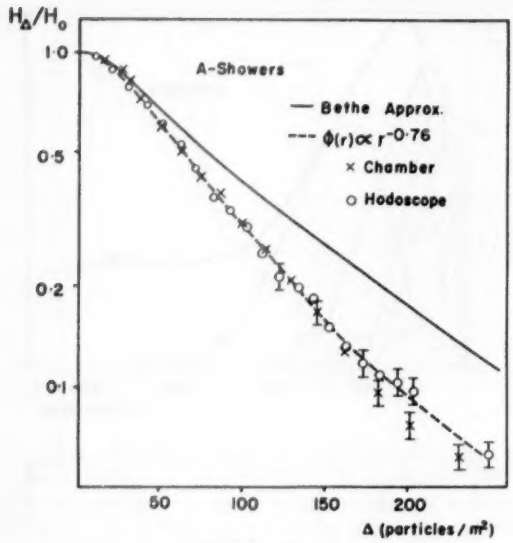

FIG. 5 (a)

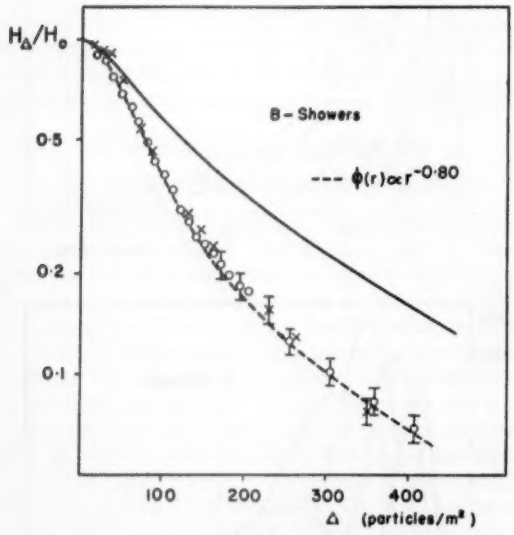

FIG. 5 (b)

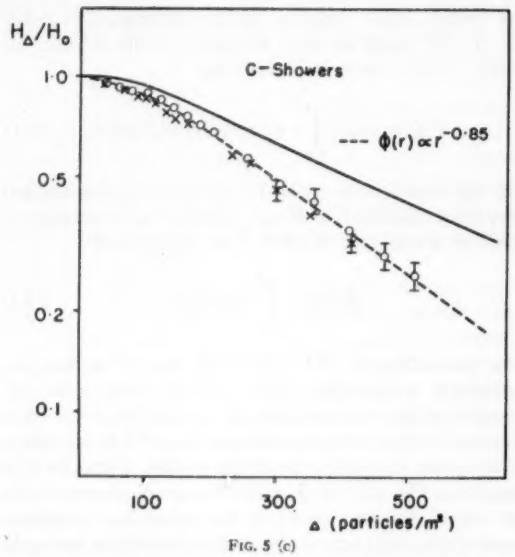

FIG. 5 (c)

FIG. 5. Integral density distribution $H(\Delta)$ at the center of the arrangement, calculated with the Bethe structure function (full line), and calculated according to (3.3) with the best ϵ (dashed line). Circles: cloud-chamber data; crosses: hodoscope data.

$=r^{\epsilon\gamma}(\Delta/f)^{-\gamma}$. Consequently it is possible to neglect the effect on I, and to write for the corrected differential density distribution $h'(\Delta)$:

$$h'(\Delta)=2\pi\Delta^{-\gamma}A\int_0^\infty r^{\epsilon\gamma}\{f(r)\}^\gamma I(r,\Delta/f(r))dr. \quad (3.4)$$

Moreover, in the integral the first factor $r^{\epsilon\gamma}$ is slowly varying with r, in comparison with $\{f(r)\}^\gamma$, so that as a first approximation it can be replaced by the constant $(R_\Delta)^{\epsilon\gamma}$, where R_Δ is the radius from which the maximum contribution derives for a given density Δ. These values can be taken from the graphs of Fig. 4(a)–4(c).

Thus, by comparing the experimentally determined frequency ratio for several densities (in the region where the contribution of true cores is large) with those calculated according to (3.1) or (3.2), an average value for the constant $\epsilon\gamma$ is obtained. With this value the density distribution (3.4) was then recomputed, assuming that the modified structure function would hold exactly up to a core distance of $4m$, and joining it smoothly between 4 and $6m$ to the uncorrected Bethe function.[12] The dashed curves in Fig. 5(a)–5(c) were obtained in that way. They correspond to the following values of ϵ, and structure functions

For A showers: $\epsilon=0.24\pm0.02$; $\phi(r)\propto r^{-(0.76\pm0.02)}$

for B showers: $\epsilon=0.20\pm0.02$; $\phi(r)\propto r^{-(0.80\pm0.02)}$

for C showers: $\epsilon=0.15\pm0.04$; $\phi(r)\propto r^{-(0.85\pm0.02)}$.

C showers showed, however, also another important deviation. Although the effect of the core structure function should be noticeable only for $\Delta\gtrsim400$ particles/m², the agreement between experimental and calculated values was poor even for smaller showers. The reason for this deviation is that even the C showers with small densities at the center of the apparatus still contain a rather large number of particles, since they are striking predominantly at some considerable distance from the center. Figure 3 shows that on the average the particle number in a C shower is of the order 10^8, and for showers of this size the exponent of the number distribution is no longer close to the value $\gamma=1.5$ used in the

[12] A very similar corrected structure function has been used by Campbell and Prescott (reference 2) for the representation of their experimental burst size distribution.

calculation (see Williams,[1] Blatt[13]). In recompting the density distribution, changes in both γ and f were therefore allowed, and the best agreement as shown in Fig. 5(c) was obtained with $\gamma=1.7$ and the value of ϵ given above.

It should be stressed as a remarkable result that, while for all three groups corrections of the structure function were found necessary, these corrections vary only slightly over a wide range of shower sizes: C showers, with an average initial energy of 8×10^{15} ev (for single-photon origin), gave $\epsilon=0.15$; B showers, initiated on the average by photons of 7.1×10^{14} ev, have $\epsilon=0.20$, and A showers with an average initial energy of 9.1×10^{13} ev show $\epsilon=0.24$. Expressed in terms of the "age parameter" s, a variation of the shower energy by a factor 100 corresponding to a change in the value of s according to shower theory from about 1 to 1.3, yields a variation in the exponent of the density distribution near the core by only 0.09.

(2) Multiple Cores

Since in the primary collision the electron-producing particles are ejected with a considerable multiplicity, the existence of multiple shower cores with an angular separation of the order 10^{-4} radian in the observation system has long been suspected. Each of the cores represents a higher concentration of energy than its surroundings, and in traversing the lead absorber of the arrangement should appear as a singularly dense "local cascade." At the observation level, the separation between these multiple cores may be of the order of the dimensions of the core-analyzing set. Consequently, it can be expected that occasionally a multiple-core structure should be found.

Local cascades of energies between 10^9 and 10^{10} ev are frequently observed, and even events with more than one local core are not particullarly rare. A typical case is reproduced in Fig. 6. Although it is not at all certain that these events are directly related to the shower-initiating collision it appeared tempting to make an attempt to correlate the characteristic features of those cascades—in particular their angular separation for a given cascade energy—with the shower energy E_0.

It is then necessary to set a lower limit for the energies of the local cascades to be included in the analysis, and to classify the events according to their energies. For the cloud chamber pictures, the depth of the cascade maximum rather than the number of particles at the maximum was chosen as the criterion for classification, since the local cascades were usually too dense to permit an accurate count of the particle number. Pairs or groups of local cores were included in the survey if none of the cascades had passed the maximum in the fourth shelf, and at least one of them reached the maximum only in the fifth shelf or lower. The events were then grouped according to the depth of the cascade maxima of the two local cores, expressed in the number of lead plates traversed: a "7-plates event" is one in which one local cascade reaches its maximum under the third plate, the other under the fourth plate. The classification indicates, therefore, directly the total energy present in the two local cores.

33 cases with local-core structure were found. Within the limits of these rather poor statistics, the relative frequencies were about the same for all shower types

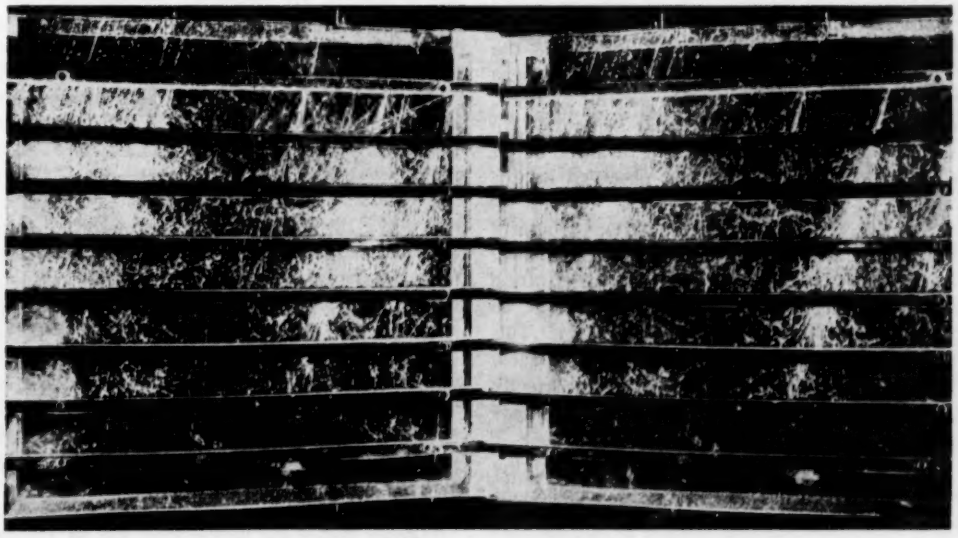

FIG. 6. Cloud-chamber photograph of an event with several "local cores."

[13] J. Blatt, Phys. Rev. 75, 1584 (1949).

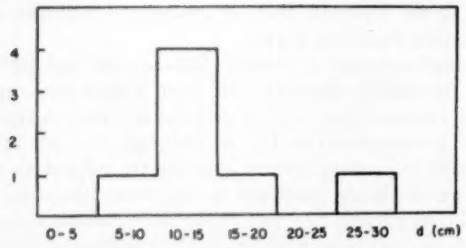

FIG. 7. Histogram of the separations d of B-shower local cores with maxima under less than eight lead plates.

and certainly not markedly higher for C showers as one might expect because of the smaller angular separation of the initial secondaries. Actually, the frequency of the events was in good agreement with the expected rate of high-energy electrons and photons if the flattening of the energy spectrum in the core area is taken in account. All the cascades observed started in the first lead plate or in the upper chamber wall.

Next it had to be determined whether for a given shower type, and for a given energy group of the local cascade, the separation of the two cores is fairly representative of the event. This seems to be so; for instance, the distribution of the distances d between the axes of the two cascades of the "7-plates" and "8-plates" group of B showers is reproduced in Fig. 7 and shows that it is meaningful to ascribe an average distance $\langle d \rangle = 14.9$ cm to the group. Similar results were found for the other groups.

It must be emphasized that the average distance in the chamber thus determined, should not be mistaken for the true average separation between the cascades. The latter could only be construed after due corrections for the finite size of the analyzing set, and this can only be done on the basis of specific assumptions about the theory of nuclear collisions: that is, assumptions otherwise avoided in this paper. On general grounds, however, one will expect the angular separation to decrease with increasing E_0, and such a variation might also be expected for the separation observed in this experiment.

If now the average distances of the various groups of local-core events are compared for the three shower types, one finds a very slight increase of the separation with the total energy of the local cascades, but no significant variation with the shower energy. This result is shown in the histogram of Fig. 8. From these data it appears that the local cores are not directly related to the primary collision and do not demonstrate the multiplicity of the initial interaction. However, it should be stressed again that the assumption underlying this analysis—that even without the corrections necessary to reduce the data obtained to the true angular separations, these experimental data will exhibit a distinct variation with E_0—is somewhat uncertain and difficult to prove. The possibility that the observations reported in this section are essentially determined by instrumental causes can therefore not be excluded.

For the hodoscope pictures, a clear recognition of all multiple electron-core events is not possible; chance configurations resulting in a structure resembling that of a local electron cascade may easily occur with a frequency comparable to that of genuine multiple cores, in particular in the denser showers. Nevertheless a strong energy dependence of the separations might perhaps be found from the comparison of the frequency of such apparent groups with that of single "background" clusters. The result of a survey was again negative: no difference between the three shower groups could be observed.

IV. THE PENETRATING COMPONENT

(1) Mean Free Path and Composition of the Nucleonic Component

Although several measurements of the abundance of penetrating particles in air showers have been reported (e.g., Ise and Fretter,[8] Sitte,[14] Greisen *et al.*,[15] McCusker,[16] and Hodson[17]), their lateral distribution has not yet been carefully investigated. Since in particular the distribution and relative frequency of N particles near the shower core would demonstrate a possible variation with the primary energy of the fractional energy transfer into the electron-producing component, the analysis of the present experiment was extended to include a study of the penetrating component.

All attempts to analyze the penetrating shower component into its two main constituents, N particles and μ mesons, are based on the identification of the nuclear collisions initiated by the first, and on the

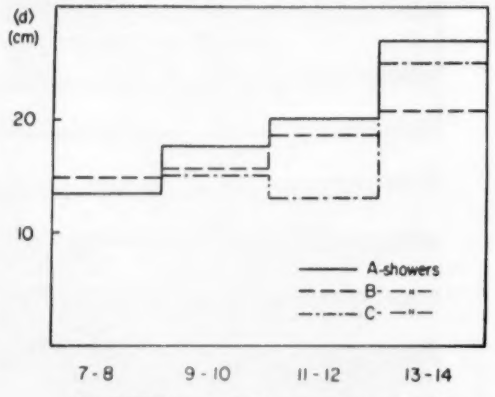

FIG. 8. Histogram of the average separation $\langle d \rangle$ of local cores of various energies.

[14] K. Sitte, Phys. Rev. **78**, 721 (1950); **87**, 351 (1952).
[15] Greisen, Walker, and Walker, Phys. Rev. **80**, 535 (1950).
[16] C. B. A. McCusker, Proc. Phys. Soc. (London) **A63**, 1240 (1950); C. B. A. McCusker and D. D. Millar, Proc. Phys. Soc. (London) **64**, 915 (1951).
[17] A. L. Hodson, Proc. Phys. Soc. (London) **A66**, 65 (1952).

subsequent correction for the cases in which the nucleons failed to interact. Here, obviously, the definition of an identified nuclear collision is rather arbitrary, and the more or less stringent conditions imposed in the various experiments probably account for the sometimes conflicting results of different investigators. Furthermore, in order to apply the corrections for the escaping N particles, their interaction mean free path must be known, and its value is dependent on the choice of a certain type of collision for identification of the N component. Thus, for instance, if local showers of high penetration and multiplicity are required, a "geometrical" mean free path is certainly correct if the measurement is confined to the identification of nucleons of high energy; but contributions from less energetic nucleons which may still in some cases—and hence with a longer mean free path—initiate equally large showers[6] would not be correctly estimated.

Consequently, it was deemed advisable to redetermine independently the mean free path of the interactions chosen in the analysis of the present experiment. Of course it is also preferable to relax the conditions of complexity and penetration of the local interactions so as to include low-energy collisions. The suitable limit is determined by the resolution of the experimental method, and hence not exactly the same for cloud chamber and hodoscope. This point will be discussed later; the determination of the interaction mean free path was based on cloud chamber evidence only. In this case, local interactions were identifiable if either at least one charged penetrating secondary was ejected accompanied by at least one heavy track, or more than one heavily ionizing particle was observed, or a single scattering of more than 10 degrees.

A survey of the distribution among the various lead plates of the origins of nuclear interactions may easily introduce a systematic error, because of the difficulty of identifying a nuclear event against a background of high electron density. If in a part of any one shelf the recognition was deemed uncertain, a corresponding volume in all shelves was excluded from the survey, in order to avoid biasing against the region near the maximum of the electron transition effect. From the location of the observed showers, the total number N_0 of incident N particles can then be calculated even without the knowledge of the mean free path λ [see Eq. (3) in reference 6], and with it the fractions N_x/N_0 of particles which escaped interaction under a layer x g/cm² can be determined. Since $N_x/N_0 = \exp(-x/\lambda)$, the interaction mean free path is directly obtained from a logarithmical plot as in Fig. 9. The data obtained are compatible with the assumption of a geometrical cross section ($\lambda = 165$ g/cm²), and this value was therefore adopted for all subsequent calculations.

A very rough study of the ratio of neutral and charged N particles was also performed. For this purpose, events could be included independent of their location,

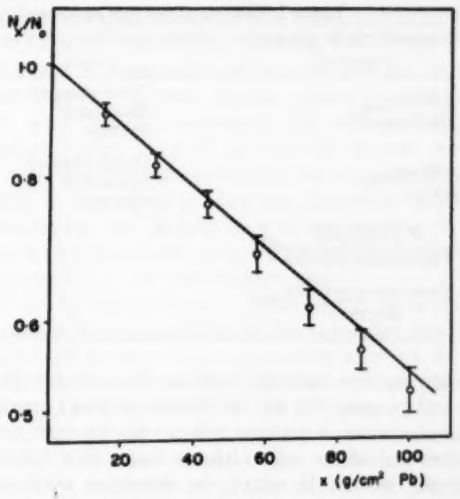

FIG. 9. Ratio N_x/N_0 of N particles which escaped interaction in x g/cm² of Pb, as a function of the thickness x (from cloud-chamber data). The solid line is the distribution calculated with a mean free path of 165 g/cm².

but all those cases were omitted where the nature of the shower primary appeared doubtful because of a possible obliteration of its track by the electron shower. Thus, only 64 events were classified; among them were 26 neutron-produced showers. Accordingly, the neutron component can be estimated as (41 ± 8) percent of all N particles in the shower. In the following, a neutron/proton ratio of 0.8 will be used, in agreement with this analysis and with earlier determinations.[14,15]

(2) Abundance and Abundance Ratio

Both cloud-chamber and hodoscope pictures permit only a classification of the penetrating component into "interacting" and "noninteracting" particles. If, instead, one wishes to group them rather into "N particles" and "μ mesons"—taking the customary view that these two categories comprise at least the bulk of the penetrating shower particles—it should be remembered that the "noninteracting" particles include also all the charged N particles which failed to interact, and that a corresponding number of unobserved neutrons has to be added to the total.

As to corrections for chance coincidences of a soft shower with independently incident penetrating particles, with fast coincidence circuits and with reasonably good cloud chamber technique, only the contribution of single mesons traversing the cloud chamber during its resolving time is of importance. The latter, however, is quite considerable even if mesons travelling at more than 10° from the shower direction are excluded. Fortunately, this good angular resolution is possible as long as the showers are observed near the core. The necessary correction was, therefore, obtained and checked in two ways: by calculating it with the best

TABLE I. Relative abundance and abundance ratio of penetrating particles in air shower cores.

Composition	Events	*A* showers	*B* showers	*C* showers
$\frac{\mu \text{ mesons}}{\text{electrons}}(\%)$	Cloud chamber	0.93±0.17	0.83±0.12	0.80±0.19
	Hodoscope	0.81±0.10	0.86±0.12	0.73±0.09
	Average	0.86±0.08	0.85±0.07	0.74±0.07
$\frac{N \text{ particles}}{\text{electrons}}(\%)$	Cloud chamber	0.68±0.12	0.50±0.09	0.46±0.12
	Hodoscope	0.58±0.10	0.60±0.07	0.41±0.06
	Average	0.63±0.08	0.56±0.06	0.43±0.06
$\frac{N \text{ component}}{\text{Penetrating particles}}(\%)$		0.43±0.05	0.40±0.04	0.37±0.05
$\frac{\text{Penetrating particles}}{\text{electrons}}(\%)$		1.51±0.12	1.41±0.09	1.17±0.09

estimate for the resolving time of the chamber (0.15 sec), and by counting the number of randomly traversing single mesons in pictures taken with the same cloud chamber and at the same altitude, but with a different triggering system in which the initiating event was clearly defined,[6] just as it was done for the electron component. The results of both methods were in fair agreement, and the tables below give the number of μ mesons after correction for the chance traversals.

In the analysis of the hodoscope pictures, events were classified as penetrating if at least one counter was discharged in all four trays, and in such a way that a particle path could reasonably be reconstructed. Thus, a few events with a straggling soft-particle cascade continuing down to the lowest tray were disregarded. On the other hand, it may be noticed that the penetration condition (a total of 8-in. Pb+½-in. Fe) is slightly more stringent than that usually imposed upon the hard component. But in view of the flat range spectrum of the μ-meson component the difference is not of significance.

Events were counted as due to N particles if a penetrating shower was found, i.e., an event containing at least two discharged counters in at least two successive levels, with a separation of at least one space between the counters triggered in each level. Events were registered as due to noninteracting particles if a single counter was discharged in each of the shielded trays, or a small group of neighboring counters in one level together with single counters in the adjacent level or levels (knock-on showers).

A summary of the results of the analysis of the penetrating events as observed both in cloud chamber and hodoscope is given in Table I. The abundance of the components is given in percentage of the electron density, and in each case the cloud chamber and hodoscope data are shown separately as well as their average. In general, they agree fairly well; a possible slight difference in the relative frequency of N particles may be due to the different minimum energies recognized. The errors shown include statistical standard deviations and possible mistakes in the classification of doubtful events; the effect of the uncertainties in the values of the parameters used for correction (mean free path and neutron/porton ratio) was not included. While these uncertainties would affect the results in a systematic way, their possible influence is small compared with the predominant statistical errors and certainly is of no weight in the discussion of the results.

The most essential features of the results shown in Table I are:

(a) The relative abundance of μ mesons near the shower core does not vary significantly with the shower size. Within the limits of the experimental errors, its value is the same as that observed in other shower experiments were the detection system was not as strongly biased in favor of shower cores.

(b) The relative abundance of N particles seems to increase slightly with decreasing shower energy, or with increasing shower age. Similarly, the ratio of the number of all penetrating particles to that of the electrons undergoes a slight change: showers of lower energy contain slightly more penetrating particles than those of higher energy. The difference is mostly due to the N component; the μ-meson fraction remains practically constant.

V. CONCLUSIONS

From the results of the two preceding sections, several conclusions can be drawn.

(i) The electron distribution near the core is considerably flatter than that predicted by the Molière theory. It is also not in agreement with the structure function of an "old" shower initiated by a single particle. This is demonstrated by two facts: the deviation found for C showers is much larger than it could be expected for single-particle initiated cascades in the neighborhood of their maximum development, and furthermore, the differences between the three groups of showers are smaller than those predicted for showers of so widely different energies, under the assumption of a single initiating particle. As it has been pointed out above, it was thought futile, at this stage, to attempt to fit the experimental data by a corrected theoretical distribution based on multiple production of π^0 mesons in the initial collision. However, the general features of the electron distribution near the core, as observed in this

experiment, may be of help in a future more extensive study.

(ii) It is tempting, though still highly speculative, to consider some basic ideas in an attempt to understand the remarkable insensitivity of the structure function with regard to shower size. Three interpretations may be suggested.

The simplest and perhaps most conventional assumption explains this independence as a result of the continuing replenishment of the electronic shower component by the electron-producing secondaries of the nucleon cascade. This replenishment "rejuvenates" the shower and tends to wipe out age differences. But this explanation would require a considerable effect of the "source function" representing the coupling between the nucleon cascade and the electron cascade—an effect which, so far, has been treated as very small.

Secondly, one might try to interpret the similarity in the core structure of all showers, together with the apparent absence of a genuine multiple-core structure representative of the primary interaction, in terms of the energy spectrum of the particles ejected in the first shower-initiating collision. These facts would then suggest a spectrum of the Fermi type[18] rather than of the Heisenberg type.[19] The former predicts a distribution peaked at some medium energy value, and fairly well approximated by the assumption that all secondaries carry the same energy. Since the average multiplicity increases with the primary energy E_0, the average—and representative—secondary energy rises slower than with the first power of E_0. Heisenberg's theory, on the other hand, while it also predicts a slow increase with E_0 of the *average* secondary energy, permits a greater share of high-energy secondaries which would reflect in more typical features of the cores of high-energy showers.

Lastly, one might choose the radical interpretation that, in spite of their difference in particle numbers (and hence presumably in their initial energies), the three groups of showers do not differ appreciably in their average age, but are all observed near the cascade maximum and, accordingly, must have originated at various depths in the atmosphere. Such an interpretation would necessitate major revisions of the customary picture of air showers, but certain observations reported by Piccioni and Cool[20] lead to very similar conclusions.

(iii) The abundance of penetrating particles near the core, summarized in Table I, is not significantly different from that previously reported in other experiments where detection of showers striking nearby was not made a stringent requirement, and where consequently the average distance of the apparatus from the shower axis was larger. Over a considerable region the abundance ratio varies, therefore, only very slowly if at all with the distance from the axis. Since the distribution of the heavier penetrating particles, unlike that of the electrons, is essentially determined not by multiple scattering but by their angular spread at production, and since the core represents the region of highest average energy as well as that of highest particle density, this result suggests that the processes through which, in the nuclear interactions, the energy is distributed among the various shower components do not vary appreciably with energy. This extends the conclusions reached in an earlier experiment.[21]

(iv) The slight difference between the three shower groups in the composition of the cores can easily be understood in terms of the age of the showers. In this connection the decrease of the abundance of penetrating particles, and especially of the N component, with increasing shower energy deserves attention. This decrease demonstrates that the nucleonic cascade reaches its maximum at greater depth than the electronic component, and shows that the frequently reported proportionality between these two components[14–17,20] has only a limited range. This proportionality has usually been interpreted as a proof of the genetic relation between the two cascades, and it can be understood equally well if it is assumed, in the customary way, that the nucleonic cascade produces the electrons or if the nucleons are considered as secondary to the electronic component (Cool and Piccioni[22]).

The discrepancy between the increase in the N component/electron ratio reported here, and the constant values found in the earlier experiments, is probably due to the arbitrariness in the instrumental selection of the N particles. In the present experiment, it was attempted to set the low-energy limit of the recorded nuclear interactions as low as possible, and N particles were registered that might not have been identified in other experiments. A considerable fraction of the nucleons in air showers is in an energy range where the degree of inelasticity of the nuclear interactions depends rather sensitively on the energy. These particles, while continuing the propagation of the nucleonic component, will not contribute much to meson production and hence will not transfer an appreciable amount of energy to the electronic cascade.

The experiment was made possible through the use of the facilities of the Inter-University High Altitude Laboratory at Echo Lake, Colorado, and the authors wish to express their thanks to Professor Byron E. Cohn and Professor Mario Iona, Jr., of the University of Denver for their cooperation. In preparing and running the experiment, Dr. E. M. Harth and Mr. F. E. Froehlich have given valuable assistance. Part of the funds required were obtained under a contract with the U. S. Atomic Energy Commission.

[18] E. Fermi, Progr. Theoret. Phys. (Japan) **5**, 510 (1950); Phys. Rev. **81**, 583 (1951).
[19] W. Heisenberg, *Z. Physik.* **126**, 569 (1949).
[20] O. Piccioni and R. L. Cool, Phys. Rev. **91**, 433 (1953).
[21] K. Sitte, Phys. Rev. **87**, 351 (1952).
[22] R. L. Cool and O. Piccioni, Rochester Meeting on High Energy Physics, December, 1950; Phys. Rev. **82**, 356 (1951).

Development of Air Showers in the Atmosphere*

KURT SITTE AND DON L. STIERWALT, *Department of Physics, Syracuse University, Syracuse, New York*

AND

IRVING L. KOPSKY, *Department of Physics, Smith College, Northampton, Massachusetts*

(Received June 24, 1953; revised manuscript received October 14, 1953)

An experiment was carried out at Mt. Evans, Colorado (altitude 4300 m) to study the development of extensive air showers in the atmosphere. Showers with cores striking near a cloud-chamber-hodoscope arrangement were selected, and the differential energy spectrum of the shower particles determined by observing their transition effect in six ½-in. lead plates with a 68-counter hodoscope. Each shower can be assigned an age classification on the basis of this energy spectrum. The lateral structure function between 2 m and 8 m from the core was obtained from measurements of the particle densities at four extension trays containing 50 counters with a total area of 1.34 m². It was found from the hodoscope data that the lateral structure function of the showers of various ages does not agree well with the predictions of the single-particle cascade theory. The observed structure function for showers at and beyond the cascade maximum is less steep than expected near the axis; this is consistent with multiple production of shower-producing particles in the primary collision. It was also found that the lateral distribution of showers past the cascade maximum varies only slowly with age; this tendency is predicted in a general way by the cascade theory, but only at a much later stage of development than observed and with quite a different slope of the distribution curve. The interpretation of this effect as the result of a "rejuvenation" of the shower by the continuous transfer of energy from the nucleonic cascade to the electron cascade is therefore more likely.

I. INTRODUCTION

EXTENSIVE air showers, the display of the highest particle energies known today, have long been a favorite object of study in cosmic-ray physics. But they are an elusive object, and whenever the goal of fair understanding of their essential features seemed within reach, new observations necessitated basic changes in the picture. Thus, the original theory of single-electron or single-photon cascades as summarized in the classical article by Rossi and Greisen,[1] and later developed by, among others, Bhabha and Chakrabarty,[2] Nordheim and his co-workers,[3] Snyder and Scott,[4] Eyges and Fernbach,[5] and Borsellino,[6] seemed to fit all the important experimental data until the presence of penetrating particles in all air showers was demonstrated, particularly in the work of Broadbent and Jánossy,[7] and of Treat and Greisen.[8] Again in a later phase, when the reinterpretation of air showers as mixed cascades of nucleons, mesons, and electrons seemed well enough understood, and new powerful methods for the treatment of both nucleon and electron cascades had been developed in the work of Jánossy, Messel and their collaborators,[9] the discovery of the various new unstable particles made it very doubtful whether so simple a picture for the production of both penetrating particles and electrons, as descendants of charged and neutral π mesons, is adequate.

In a general way, a number of important deviations from the single-electron picture can be considered as established. For instance, since the incident primaries are almost certainly of nucleonic, not electronic, nature, and since, therefore, the shower originates in a nuclear interaction, we can be assured of the multiple character of the electron-producing act, whether or not all electrons derive from the decay of π_0 mesons. As a result, the electron distribution near the shower core should be less peaked than predicted by cascade theory for a "pure" electron cascade, and this feature has been repeatedly verified.[10–13] But a quantitative comparison of these results with the theory is still of dubious value, not only because of the doubts as to the possible over-simplifications used in the theories, but also because in most cases the numerical evaluation of the theoretical results has not yet been completed, and is a long and tedious task. To get numerical data in a simple manner, the best one can do is to calculate the structure of "average" showers by describing the nuclear interactions in, say, terms of the Fermi theory,[14] and by assuming that all interactions or decays take place

* Supported in part by the U. S. Atomic Energy Commission.

[1] B. Rossi and K. I. Greisen, Revs. Modern Phys. **13**, 240 (1941).

[2] H. J. Bhabha and S. K. Chakrabarty, Proc. Indian Acad. Sci. **A15**, 464 (1942); Phys. Rev. **74**, 1352 (1948).

[3] L. W. Nordheim, Phys. Rev. **59**, 929 (1941); J. A. Richards and L. W. Nordheim, Phys. Rev. **74**, 1106 (1948); J. Roberg and L. W. Nordheim, Phys. Rev. **75**, 444 (1949).

[4] H. S. Snyder and W. T. Scott, Phys. Rev. **76**, 220, 1563 (1949).

[5] L. Eyges and S. Fernbach, Phys. Rev. **82**, 23, 287 (1951); S. Fernbach, Phys. Rev. **82**, 88 (1951).

[6] A. Borsellino, Nuovo cimento **6**, 543 (1949); **7**, 638 and 700 (1950).

[7] D. Broadbent and L. Jánossy, Proc. Roy. Soc. (London) **A190**, 497 (1947); **A191**, 517 (1947); **A192**, 364 (1948).

[8] J. E. Treat and K. Greisen, Phys. Rev. **74**, 414 (1948).

[9] E.g., L. Jánossy and H. Messel, Proc. Roy. Irish Acad. **A54**, 245 (1951); H. Messel, Proc. Phys. Soc. (London) **A64**, 726 (1951); H. S. Green and H. Messel, Phys. Rev. **88**, 331 (1952).

[10] R. W. Williams, Phys. Rev. **74**, 1689 (1948).

[11] W. E. Hazen, Phys. Rev. **85**, 455 (1952).

[12] I. D. Campbell and J. R. Prescott, Proc. Phys. Soc. (London) **A65**, 258 (1952).

[13] H. L. Kasnitz and K. Sitte, Phys. Rev. **90**, 361 (1953).

[14] E. Fermi, Progr. Theoret. Phys. (Japan) **5**, 570 (1950); Phys. Rev. **81**, 683 (1951).

after exactly one mean free path has been traversed. But this method can scarcely be trusted to the extent that agreement or disagreement of its results with experimental data may be taken for a crucial test of the underlying hypothesis of a Fermi-type collision with only π-meson production.

For the present experiment, a goal more modest than an attempt of a detailed correlation between the empirical data and the predictions of any particular theory, was set. It was felt that at least general information concerning the nature and the relative importance of the various processes involved in the development of air showers can be obtained if in a single experiment several shower characteristics—such as age, radial distribution, composition—are recorded. The cloud-chamber-hodoscope arrangement used in previous work offers a convenient method, and the first experiment of a planned comprehensive study applied essentially the same equipment as two of the earlier investigations of the Syracuse group.[13,15] We report here the results of a more or less preliminary run in the summer of 1952 at the Mt. Evans station (4300 meters). Unexpected difficulties in technical performance under the trying conditions at this altitude made continuous and satisfactory operation of the cloud chamber impossible, and so principally hodoscope data were obtained. The experiment will be continued, with slight modifications of the arrangement, at various altitudes.

II. THE EXPERIMENTAL ARRANGEMENT

(a) The Triggering System

It is essential for the purpose of this experiment not only to classify the showers at least roughly according to their age, but also to have information on the primary energy so that eventually the stages of development of a shower of a given initial energy can be compared. During this development the total number of particles will vary widely, and the triggering system must therefore be able to accept showers of very different densities while also providing means to discriminate between them. It should likewise be noted that an air shower detection system must require a multiplicity of coincidences greater than the exponent of the differential energy spectrum if the selection is to be sensitive and subject to control.[16] With these criteria in mind the arrangement shown in Fig. 1 was chosen.

A central tray S of ten counters of 1-in.×16-in. active area was flanked by two larger trays A and B of ten counters of dimensions 2 in.×24 in., placed two meters from the center of the chamber, on opposite sides. Standard integration and discrimination circuits permitted an output pulse from the central tray only when at least two of its counters were struck. A master-pulse was then produced by a threefold coincidence of

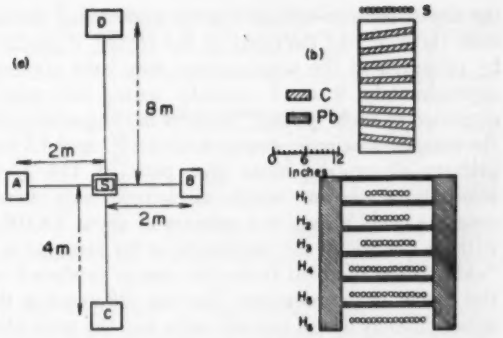

FIG. 1. The experimental arrangement. (a) General layout, top view. (b) Core analyzing system, side view.

this pulse and pulses from at least one counter in both A and B. Additional discriminators were used to record on the hodoscope whether the number of counters struck in the central tray S was two, three, or four; tray S was not fully "hodoscoped."

The triggering system requires, on the average, a higher density at S then at the extension trays A and B, so that showers with cores striking near the center will be favored,[16,17] and actually all others were eliminated by a procedure described in the next section. For the selected showers, however, the average density expected at the distance of the large trays A and B is well above the minimum density required to trigger them so that these extension trays do not impose an appreciable bias against the less dense showers. If, for instance, a shower of a certain primary energy has at its maximum a particle density likely to trigger four S counters, and at a certain earlier stage will on the average strike only two counters at the center, the system will register the event in both cases with about equal probability while allowing us to distinguish between them.

It is useful to remember a few numerical details in considering the age and energy of the showers that will be detected with this apparatus.[18] Since the selection is essentially determined by the central tray S, one verifies easily that showers striking within about two meters from the center are recorded with maximum probability if they contain a total of 12 000 particles in the case that four of the S counters were struck, or 8000 and 5000 particles, respectively, when three or two of the counters in the S tray were discharged. Now consider, for instance, a 12 000-particles shower: if observed at its maximum development (i.e., at a depth of 12 cascade units) its initial energy is about 3×10^{13} ev, and its origin about 2 collision mean free paths below

[15] Froehlich, Harth, and Sitte, Phys. Rev. **87**, 504 (1952).
[16] K. Sitte, Phys. Rev. **87**, 351 (1952).
[17] J. Ise, Jr., and W. B. Fretter, Phys. Rev. **76**, 932 (1949).
[18] For the determination of the total number of shower electrons for a given primary energy, the "Tables of cascade functions" by L. Jánossy and H. Messel, Proc. Roy. Irish Acad. **A54**, 217 (1951), have been used; corrections have been made for the ionization loss and for the extension of the electron spectrum down to the energy necessary to penetrate the counter walls (about one-tenth the critical energy in air).

the top of the atmosphere. On the other hand, showers with three or two electrons at the center, if produced by primaries of the same energy, may have traversed approximately 9 or 7 cascade units; the relative attention of such "young" showers in comparison with the cascade-maximum events is about 2.7 and 5.3 for a primary absorption mean free path of 116 g/cm². Similarly a shower which discharged only two S counters could belong to a primary of about 1×10^{13} ev with its cascade at the maximum, or for instance to an "old" shower of about twice that energy produced near the top of the atmosphere. The age difference is then approximately 4 or 5 cascade units and the rates about comparable since the attenuation factor is counterbalanced by the larger number of less energetic primaries. Considerations of this kind give a useful check on the age assignment described below; they also show that the observation will cover a fairly large age range in the energy range above 10^{13} ev with reasonable efficiency.

(b) The Analyzing System

The central, core-analyzing part of the arrangement consisted of a large cloud chamber (dimensions 24 in. $\times$24 in.$\times$10 in.) fitted with eight 1-in. carbon plates. Below it, six hodoscope counter trays H_1-H_6 were placed, with ½-in. lead plates about 3 in. above each tray and with a total vertical distance of 4½ in. between adjacent trays. This geometry permits the transition-effect shower to spread, and thus reduces the errors made in applying random corrections to a non-random distribution of the core particles over the tray area. The first two trays contained eight counters each, the third ten, and H_4-H_6 fourteen counters, all of dimensions 1 in.$\times$16 in. With the 68 counters of H_1-H_6, the transition effect in lead could therefore be followed to a depth of 3 in., or approximately 13 radiation lengths.

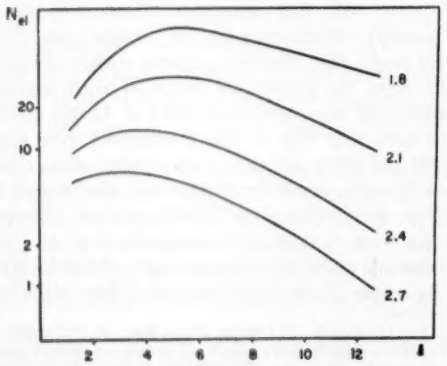

FIG. 2. Transition effect in lead: Number N_{e1} of electrons expected under an absorber of thickness ξ (in radiation lengths). The curves are calculated for a differential energy spectrum of the incident particles $\pi(E)dE=dE/(E+E_c)^\gamma$ for various γ, assuming equal numbers of electrons and photons present.

The radial distribution up to a distance of $8m$ from the core was studied with the help of four further hodoscope trays A, B, C, and D, placed in the arrangement shown schematically in Fig. 1 (a). A and B, at 2 m from the center, are the same trays that serve also for the master coincidence; their ten counters feed their pulses individually through the usual cathode followers mounted in the trays, to the hodoscope circuit, but also through isolating diodes to a common lead and to the integrator-discriminator circuits of the masterpulse system. Tray C, at 4-m distance, contained fourteen counters of size 2 in.$\times$24 in., and the sixteen-counter tray D was placed at 8-m distance. The D-counters were of dimension 2 in.$\times$16 in. Thus, a total of fifty counters covering an area of about 1.34 m² were available for the analysis of the "outside" density distribution. The tray boxes were made of 25-mil aluminum.

It has been pointed out above that the triggering system favors showers incident near the center. As a further improvement of the selection, only those events were used for the analysis in which the density recorded in the outside trays nowhere exceeded that at the center. In this way, showers with cores striking at distances of more than two meters are in general eliminated,[19] and no great error is made by assuming for a statistical analysis that on the average the shower core is situated at the center of the arrangement.

We rejected 450 events for failing to fulfill the above criterion, and about 300 more because of various uncertainties in their analysis. These latter included large-angle showers, showers striking too near the edges of the core selector trays, and what appeared to be local showers due to penetrating particles. The cloud chamber pictures were used only as a check on the direction of the shower and similar generalities. A total of 2618 useful hodoscope records was obtained.

III. RESULTS

(a) The Shower Age

It is known that for showers not too far from the cascade maximum, the differential energy spectrum of the electrons can be represented in a good approximation by a power law with the exponent $(1+s)$, where s is the "age parameter" of the shower;[1] $s>1$ characterizes a shower past the cascade maximum or an "old" shower, while for "young" showers $s<1$. In the experiment reported here, this variation of the electron energy spectrum offers a convenient way to determine the shower age, since the transition effect in lead is appreciably affected by it. However, an exact calculation of the transition effect is difficult since,

[19] A detailed analysis of the performance of the triggering system has been carried out, using the customary methods described also in previous work. (See references 13 and 15.) The inclusion of these lengthy calculations in the present paper was not deemed worth while, but method and results will be more fully presented in a subsequent publication.

because of the much lower critical energy in lead, the slower electrons which no longer contribute much to radiative effects in air, will go on multiplying in the heavy absorber; furthermore, the shape of the energy spectrum of air shower particles below the critical energy in air is not well known. But fortunately this uncertainty is of significance only for the very beginning of the transition curve, and even there only in a slight degree. Numerical calculations were, therefore, made with a differential energy spectrum of the form $dE/(E+E_c)^\gamma$, using for the critical energy E_c in air a value of 86 Mev, and cutting off the spectrum at 20 Mev, the minimum energy required for electrons leaving the lowest cloud chamber plate to reach the first hodoscope tray. For electron energies up to 500 Mev, the results of Wilson's Monte Carlo calculations[20] were used, and for higher energies the tables of Jánossy and Messel.[18] An equal number of incident photons and electrons was assumed.

The results of the computations are shown in Fig. 2 for various exponents γ. To apply them, the sum of the numbers of electrons found under the first, second, and third $\frac{1}{2}$-in. lead plate can be compared with the sum of the numbers observed in the three lower trays. In this way, the effect of fluctuations is reduced, and the statistics for a single event improved. Table I shows the expected ratio of the two sums as a function of γ. The procedure applied to determine the energy spectrum of the individual showers was, therefore, the following: First, to obtain the number of electrons at each tray from the number of counters struck, corrections were calculated under the assumption of random distribution over the tray area; next the sums of these corrected particle numbers were formed for the three upper and the three lower trays, and according to the ratio of these sums the shower was classified into one of four age groups (the data corresponding to the last two columns of Table I were combined since the frequency of the oldest showers was too low).

TABLE I. The ratio R of the sum of the numbers of electrons found under the first, second, and third lead plate, to the sum of the number of electrons under the fourth, fifth, and sixth plate according to the data of Fig. 1, for various exponents γ of the energy spectrum.

γ	1.8	2.1	2.4	2.7	3.0
R	1.2_5	1.7_5	2.2_5	2.7	3.1

It should be remarked that classification of the showers on the basis of the theoretical $(1+s)$ is not completely valid for two reasons. On the one hand, the data were taken near the shower core where the spectrum is flatter than the over-all expression $dE/(E+E_c)^{1+s}$. A more appropriate spectrum could only be calculated if the lateral distribution were already known. Secondly, if s should be representative of the shower incident from the atmosphere, then it must be noted that the electrons and photons impinging on the top lead plate of the transition-effect hodoscope system have traversed an additional amount of over 8 in. of carbon, 1 in. of glass in the 16 reflector mirrors on the 8 carbon plates, and two $\frac{3}{16}$-in. brass chamber walls, or very nearly two additional cascade units: the shower incident on the central hodoscope is somewhat older than that striking the outside hodoscope arrangement. Even so, it is certainly correct to say that increasing values of the exponent γ will correspond to increasingly older showers and further information on this point can be obtained from the frequency of the various age groups. For instance, as has been pointed out above, events with only two particles at tray S should be composed in about equal frequency of old high-energy showers produced near the top of the atmosphere, and showers near their cascade maximum produced a few mean free paths lower by one of the more abundant lower-energy primaries, with a few very young showers initiated even closer to the apparatus: the latter in a frequency of perhaps one-fifth or less of that of the events in which four electrons strike the top tray. The "four-electron-showers," on the other hand, can be expected to consist predominantly of showers near the cascade maximum, and a few events of greater age. A comparison of the frequency distribution of the various spectral groups among the three triggering groups will, therefore, help to establish more closely the relationship between the absolute shower age and the exponent of the transition-effect spectrum.

TABLE II. Frequency of showers in the four age groups characterized by the exponents of their energy spectrum, as a function of the density of the air shower incident at the top tray S.

Number of electrons at tray S	Exponent of the differential energy spectrum $\gamma<1.8$	$1.8\leqslant\gamma<2.1$	$2.1\leqslant\gamma<2.4$	$\gamma\geqslant2.4$	Total
2	134	517	301	207	1159
3	71	289	128	80	568
4 (or more)	133	476	203	79	891
Total	338	1282	632	366	2618

These data are summarized in Table II which shows, for showers of various incident densities characterized by the number of counters struck in tray S, the number of events recorded in each of the spectral groups. The results were considered as a justification of the tentative identification of the groups, according to which events with $\gamma<1.8$ are "young" showers which have not yet reached the cascade maximum, the second group $(1.8\leqslant\gamma<2.1)$ consists of showers near their maximum development, and the two others are old showers in increasing stages of attenuation.

[20] R. R. Wilson, Phys. Rev. 86, 261 (1952).

(b) The Lateral Distribution

Since the fundamental work of Molière,[21] a number of authors have investigated theoretically the lateral structure function of showers at stages other than the cascade maximum for which Molière's original work was done. In particular, Nishimura and Kamata[22] have obtained solutions for the integral lateral structure function, $\pi_1(E_0, o, r, t)$, the number of electrons of all energies in a distance r from the axis at a depth t, which close to the shower core are essentially of the form $\pi_1(r) \propto r^{s-2}$ for $s<2$, and $\pi_1(r) \approx$ constant for $s \geqslant 2$. Their definition of the age parameter s leads to somewhat larger values than that otherwise used, but the difference is slight and in particular the variation of s with depth in the neighborhood of the cascade maximum remains very nearly unchanged. The observations here reported which show the lateral distribution in the region from 2 m to 8 m from the shower axis, and for shower ages from about $s=0.6$ to $s=1.8$, can therefore be related to their expressions.

Ideally, the shower structure should be determined for showers of various sizes in any of the age groups, but for such an analysis to have statistical validity will require a very much larger number of hodoscope records gathered in a correspondingly longer operating time. Long operating times are especially needed to collect information on the rarer very large showers. We have consequently collected into one group all the showers of the same age without regard to their primary energy. In each case the densities observed at trays C and D were normalized to a reference point taken as the average of the densities at the 2-meter trays A and B. The errors arising from counter inefficiency due to failure to produce an ion pair, chance coincidences with unrelated cosmic-ray particles, circuit inefficiencies, wall-generated secondaries which might spread to the neighboring counter (an effect which has been minimized by separating the counters by $\sim\frac{1}{2}$ in.), and counter deadtime, have been estimated by the standard methods. The most important of these errors appears to be deadtime; on the average one of the 50 "outside" counters is insensitive for each masterpulse.

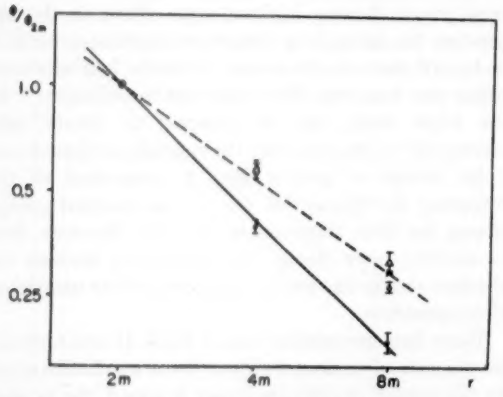

FIG. 3. The lateral distribution. Calculated curves: Bethe approximation (full line) and $\phi(r) \propto r^{-0.85}$ (dashed line). Experimental data for the various age groups: "young" showers ($\gamma<1.8$, full circles), showers near the cascade maximum ($1.8 \leqslant \gamma < 2.1$, empty circles), "old" showers ($2.1 \leqslant \gamma < 2.4$, crosses; and $\gamma \geqslant 2.4$, triangles).

For comparison with the theoretical structure function, the effect of the finite size of the trays must be considered, as it has been shown, for instance, in the work of Broadbent, Kellermann, and Hakeem.[23] This correction was calculated with the help of the Bethe approximation[24] of the structure function $\phi(r)$:

$$\phi(r)=\frac{0.454}{r}(1+4r)\exp(-4r^{\frac{1}{2}}).$$

In Fig. 3 the experimental data for the four age groups are shown together with the calculated Molière-Bethe distribution. The data for the first age group, the young showers of $\gamma<1.8$, are represented by full circles, those for showers near the cascade maximum ($1.8 \leqslant \gamma < 2.1$) by empty circles, and of the two groups of older showers the first, ($2.1 \leqslant \gamma < 2.4$) is marked by crosses, the second with $\gamma \geqslant 2.4$ by triangles. It is seen that the cascade-maximum group deviates quite appreciably from the Molière curve; in fact, the dashed line calculated for a distribution $\phi(r) \propto r^{-0.85}$ corresponding to an age parameter of $s=1.15$ is a much better approximation. For the youngest showers the Molière function appears to be a good representation, while the two groups of old showers differ only very little in their lateral distribution. For these, the change in the differential energy spectrum is certainly more pronounced than that in the lateral structure function.

At a first glance, these results seem to conflict with those of earlier experiments, in particular with those of Williams[10] and of Cocconi *et al.*[25] in which the Molière function was found to be a good approximation for distances above 2 m. However, this discrepancy may not be as serious as at first apparent. While one would hesitate to give too much credit to any attempt at defining the "correct" structure function from the three points of Fig. 3, there are indications that its slope varies rather markedly within the region from 2 m to 8 m, and that beyond about 4 m it quickly approaches that of the Molière curve. A disagreement between these data and the older ones would therefore exist only up to a distance of about 4 m, that is for the closest

[21] G. Molière in *Cosmic Radiation*, edited by W. Heisenberg (Springer, Berlin, 1943, and Dover Publications, New York, 1946).

[22] J. Nishimura and K. Kamata, Progr. Theoret. Phys. (Japan) **5**, 899 (1950); **6**, 262 and 628 (1951).

[23] Broadbent, Kellermann, and Hakeem, Proc. Phys. Soc. (London) **A63**, 864 (1950).

[24] H. A. Bethe, Phys. Rev. **72**, 172 (1947).

[25] Cocconi, Tongiorgi, and Greisen, Phys. Rev. **76**, 1020 (1948).

distances previously reported.[26] On the other hand, the fact that in the neighborhood of the core the variation of the structure function with age is only slow agrees rather well with another recent experiment carried out under widely different conditions.[13]

(c) The Cloud-Chamber Data

As it has been stated above, difficulties in the continuous operation of the cloud chamber at Mt. Evans made it impossible to obtain pictures of good quality for each individual hodoscope record. In general, the cloud chamber data served therefore only as a monitor to exclude events incident at too large an angle, or otherwise unsuitable for hodoscope analysis.

The pictures of better quality were used for a rough analysis of the composition of the shower. Unfortunately, their number was too small to permit a check also on the variation of the multiplicity of nuclear events with the shower age. Even a dependence of the composition of the shower on its age could not be established; the scanty data obtained from the more reliable photographs were for all four age groups consistent with a relative abundance of about 2 percent of penetrating particles, with an about equal frequency of μ mesons and of nucleons.

IV. CONCLUSIONS

From the results discussed above, it can be concluded that the single particle cascade is not a good representation of showers within about 8 m from the core, even in a stage of development not far from the cascade maximum. The age parameter as obtained from the energy spectrum, if applied to calculate the corresponding lateral structure function, does not give the correct curve. This can be stated although an exact determination of the age parameter from the energy spectrum could not be carried out; nevertheless, the relative values of the various exponents γ are significant, and in no plausible way can they be made to fit exactly the observed lateral distribution function.

The fact that for all but the youngest showers the distribution in the neighborhood of the shower axis is considerably flatter than the Molière structure function, is at least qualitatively well understood in terms of the multiplicity of secondary production in the initial shower-producing collision. But the lateral distribution of showers past the cascade maximum was found to be remarkably independent of the shower age. Whether or not this slow variation with s should be quoted as a success of the single-particle cascade theory which demands transition from an integral distribution $\phi(r) \propto r^{s-2}$ to $\phi(r) \approx$ const in the neighborhood of $s=2$, cannot be stated with certainty. But the trend to independence of shower age appears to occur too early for this explanation, and should then rather be interpreted as a demonstrat ionof a "rejuvenescence" of the shower by the continuous injection into the electron cascade from the nucleonic cascade of electron-producing particles. Other possible explanations have been discussed previously.[13]

The experiment will be continued with a number of improvements and extensions. In particular, the lateral distribution will be followed up to a distance of 16 m, and both the transition effect in lead and the composition of the shower near the core will be studied with greater resolution. It is hoped that thus considerably more information will be obtained.

In preparation and running of the experiment, Mr. J. G. Askowith, Mr. F. E. Froehlich, and Mr. J. E. Rizzo have given valuable assistance. The facilities of the Inter-University High Altitude Laboratories were available for the experiment, and thanks are due Professor Byron E. Cohn and Professor Mario Iona, Jr., for their cooperation. Part of the funds required for operation of the experiment were obtained under a contract with the U. S. Atomic Energy Commission.

[26] A study of the distribution inside of 2 m has recently been reported by R. E. Heinemann and W. E. Hazen, Phys. Rev. **90**, 496 (1953).

Analysis of 405-Mev Proton and 222-Mev Negative Pion Stars*

A. D. SPRAGUE, *DePauw University, Greencastle, Indiana*

AND

D. M. HASKIN, R. G. GLASSER, AND MARCEL SCHEIN
Department of Physics, University of Chicago, Chicago, Illinois

(Received February 1, 1954)

An analysis is carried out of star formation in emulsion by 405-Mev protons and 222-Mev negative pions produced in the University of Chicago 450-Mev synchrocyclotron. A comparison of the proton stars with a Monte Carlo calculation is made. The results indicate that the cascade mechanism is important in these stars, but that present evaporation theories cannot completely explain the decay of the residual nucleus. Pion and proton stars of almost the same total excitation have quite different characteristics.

I. INTRODUCTION

THE complicated problem of interactions of high-energy particles with a heavy nucleus cannot be directly attacked. One of the factors which plays a role in this interaction is the total excitation energy of the nucleus. At low energies, this is almost the only important factor, as can be seen from the success of the theory of formation of the compound nucleus and subsequent evaporation of particles.[1] The present experiment was designed to point out to what extent this total excitation plays a role in nuclear interactions at higher energy, by comparing stars produced by negative pions of 222-Mev kinetic energy and protons of 405-Mev kinetic energy, which can give nearly the same total excitation energy to the nucleus.

Bernardini[2] has studied nuclear interactions of protons and neutrons in the region of 400 Mev and compared them with a Monte Carlo computation[3] based on the Goldberger[4] model; he found satisfactory agreement, indicating that the cascade process was probably operating in the nucleus. Recently Morrison, Muirhead, and Rosser[5] have compared the interactions of 140-Mev protons with the experimental data of Lees, Morrison, Muirhead, and Rosser[6] and found satisfactory agreement.

The experimental data for the proton stars in this experiment have been compared with a recent calculation by McManus and Sharp,[7,8] which follows the pattern set by Bernardini *et al.*[3] The agreement was satisfactory with respect to the prompt or cascade particles, but was not completely satisfactory when the evaporation particles were included.

From the comparison of the pion- and proton-induced stars one finds marked differences in both the size of the star produced and in the angular distribution.

The results indicate that the evaporation theory cannot adequately treat the excitation remaining after the cascade at these energies and that the type of fundamental interaction is a very important factor in determining the character of the star.

II. EXPERIMENTAL PROCEDURE AND RESULTS

In order to compare meson- and proton-induced stars of approximately the same total excitation energy, Ilford 600-micron G-5 nuclear emulsions were exposed to the external beams of the University of Chicago synchrocyclotron. The beams used were the 410-Mev external proton beam[9] and the 227-Mev pion[10] beam. The average kinetic energy of the particles in the plates, taking into account straggling and initial spread of the beam, is 405 ± 10 Mev for the protons and 220 ± 8 Mev for the pions. These plates were scanned by the area-scanning technique to detect all stars caused by particles of the beam.

394-proton stars were found in scanning 0.529 cm^3 of emulsion and 500-meson stars were found in 0.531 cm^3 of emulsion. The average prong number was 3.92 for proton stars and 3.10 for meson stars.

The distribution of prong number—number of secondary tracks emerging from the star—is shown in Fig. 1. Since the area-scanning technique has a definite bias in favor of large stars, corrections must be applied to this. A comparison of the track-following and area-scanning techniques in this laboratory shows that for meson-produced stars the efficiency of area scanning for stars with two and more prongs is definitely greater than 90 percent, and could be as high as 100 percent, while the efficiency for one-prong stars is only about 20 percent. The data give no information about zero-prong stars. In order to estimate the relative

* Supported in part by the joint program of the U. S. Office of Naval Research and the U. S. Atomic Energy Commission.

[1] J. M. Blatt and V. F. Weisskopf, *Theoretical Nuclear Physics* (John Wiley and Sons, Inc., New York, 1952), pp. 340–345, 365–379.

[2] Bernardini, Booth, and Lindenbaum, Phys. Rev. **85**, 826 (1952).

[3] Bernardini, Booth, and Lindenbaum, Phys. Rev. **88**, 1017 (1952).

[4] M. L. Goldberger, Phys. Rev. **74**, 1268 (1948).

[5] Morrison, Muirhead, and Rosser, Phil. Mag. **44**, 1326 (1953).

[6] Lees, Morrison, Muirhead, and Rosser, Phil. Mag. **44**, 304 (1953).

[7] H. McManus and W. T. Sharp (private communication).

[8] McManus, Sharp, and Gellman, Phys. Rev. **93**, 924 (1954).

[9] Marshall, Marshall, and Nedzel, Phys. Rev. **91**, 767 (1953).

[10] Anderson, Fermi, Long, Martin, and Nagle, Phys. Rev. **85**, 934 (1952).

number of one-prong stars, it was assumed that, both for meson- and proton-induced stars, approximately the same proportion of the one-prong stars were missed by area scanning. The correction is indicated in Fig. 1. The figures for the average prong number (Table I) should also be corrected by a small amount, but this correction has not been made since the uncertainty in the correction would be large compared to the correction itself.

The projected angle θ in the plane of the emulsion between each prong and the incident direction was measured with an error of one degree with a goniometer. The distribution of this angle is shown in Fig. 2. The much flatter angular distribution for the pion-induced stars is evident in a comparison of the two curves.

III. DISCUSSION

The angular distribution as discussed in the last section can be fitted to a curve of the form $f(\theta)=a+b\times\cos\theta+c\cos^2\theta$ where θ is the observed projected angle. A fit by the method of least squares has been made and

TABLE I. Comparison of pion and proton stars and the calculations for the proton stars. As indicated in the text, the breakdown made here is probably invalid for the pion-induced stars, but is probably meaningful for the proton stars.

	No. of cascade prongs	No. of evaporation prongs
Monte Carlo calculation 400-Mev protons	1.87±0.25	0.4 ±0.1
Experiment 405-Mev protons	1.72±0.07	2.19±0.08
Experiment 222-Mev pions	(0.49±0.03)	(2.60±0.07)

is shown in Fig. 2. For the protons the normalized curve is $f_p(\theta)=0.27+0.18\cos\theta+0.088\cos^2\theta$ and for the pions, $f_\pi(\theta)=0.310+0.055\cos\theta+0.017\cos^2\theta$.

If we assume that all values of the azimuthal angle about the direction of the incident are equally probable, then we can compute from this the angular distribution of the polar angle, that is the space angle between the incident direction and the prong direction. These curves for both proton- and pion-induced stars are shown in Fig. 3.

An attempt has been made to compare the proton data with the recent Monte Carlo calculation of McManus and Sharp. They have computed the number of prompt particles to be expected to leave nuclei of various atomic numbers with 400-Mev protons incident, and have also given their angular distribution. 80 percent of the interactions in emulsion are with AgBr,[3] so an attempt was made to make a comparison between this calculation on AgBr and our data. This can be done in the following way: Any true evaporation particles should be isotropic in the center-of-mass system (which is almost the same as the laboratory

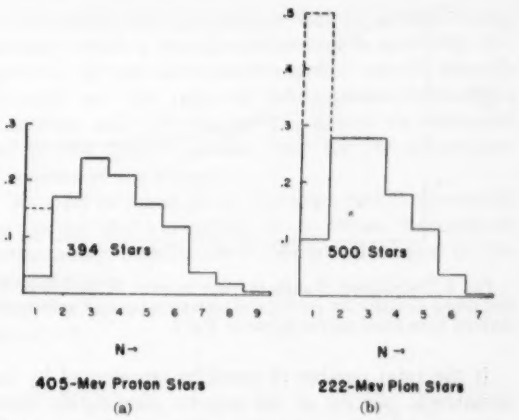

FIG. 1. Experimental prong-number distribution for (a) 394 proton-induced stars; (b) 500 pion-induced stars. The dotted line indicates correction for inefficiency of scanning (see text). The area under each curve is normalized to one.

system since the velocity of the center of mass is less than 0.01 of the velocity of light, while the outgoing tracks are more than 10 times faster). The Monte Carlo curve of McManus and Sharp has no prompt particles at angles larger than 110°, while the distribution in Fig. 2 is very flat beyond 125°. It was, therefore, assumed for the purpose of this analysis that the evaporation particles could be represented by an isotropic distribution of magnitude equal to the height of the empirical distribution in the backward hemisphere, while the prompt particles could be represented by the anisotropic portion of the curve with no particles beyond 125°.

The Monte Carlo calculation is compared with our distribution for the anisotropic component of the angular distribution in Fig. 4. Since McManus and Sharp have stated that the forward drop in their curve is probably a spurious contribution of their model, the only discrepancy between the two curves is the tendency of the calculated curve to drop off faster than the experimental curve, which may not be significant.

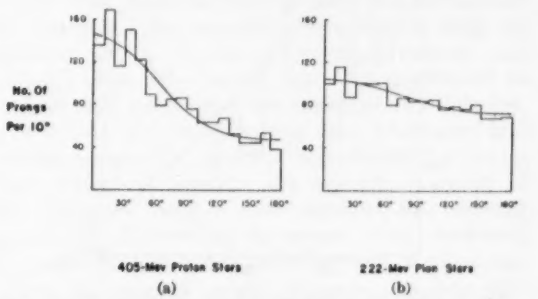

FIG. 2. Distribution of projected angles in plane of emulsion between incident direction and prong direction for (a) proton stars; (b) pion stars. The continuous curves are fitted to the data by least squares.

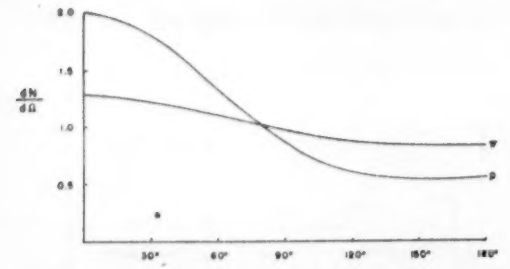

FIG. 3. Distribution of angle in space between incident direction and prong direction for proton and pion stars per unit solid angle, derived from fitted curves shown in Fig. 2.

If the total number of particles represented by the anisotropic portion of the angular distribution curve are assumed to represent cascade particles, then the average number of these per star is 1.72±0.07 while McManus and Sharp give 1.87±0.25. This agreement would not be quite as good if an allowance were made for the zero- and one-prong stars missed in scanning.

To compare the isotropically distributed part of the curve with theory we must use some form of evaporation theory as well. McManus and Sharp predicted an average residual excitation for 400-Mev proton-induced stars of 52±5 Mev, which should, according to calculations by Le Couteur[11] based on evaporation theory, lead to an average of 0.4 charged prongs per event for AgBr. We observe an isotropic distribution corresponding to 2.19±0.08 prongs per event, which Le Couteur's calculations could only agree with if the residual excitation were 120 Mev. Bernardini *et al.*[3] quote the approximate figure of 35 Mev per charged evaporation particle; however, they believe it to be high. Even this figure would result in an excitation of 75 Mev, which is still higher than the calculated value of 52 Mev given by McManus and Sharp.

Since Monte Carlo calculations for the pion-produced stars do not exist, it was impossible to make the same comparison between theory and experiment as that just discussed for proton-induced stars. We might assume that the isotropic part of the prong distribution is due to evaporation and the rest is due to cascade particles, but this assumption is much more tenuous here than for the proton stars since many lightly ionizing particles, probably mesons, are observed in the backward hemisphere. The method gives for the number of anisotropic particles per event, 0.49±0.03, and for the number of isotropic particles, 2.60±0.07. On Le Couteur's theory, if we assume that these 2.6 particles are evaporation particles, a residual excitation energy of 130 Mev would be needed to produce this many prongs, while Bernardini's figure would require a residual excitation of 90 Mev.

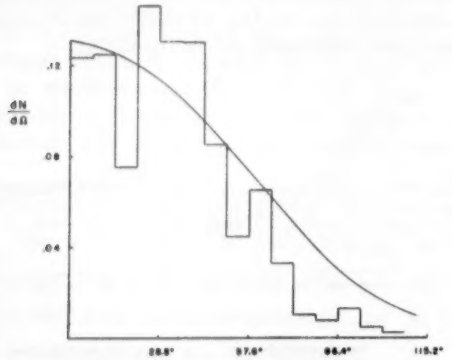

FIG. 4. Comparison between anisotropic portion of our curve (continuous curve) and calculation of McManus and Sharp, corrected to give frequency per unit solid angle (histogram).

A comparison of the proton and the negative pion stars reveals that in both cases there is a marked anisotropy of the angular distribution, which indicates that the process is not one which can be treated by a pure evaporation theory since, as discussed above, the velocity of the center of mass is very small and hence the distribution in the laboratory system would be isotropic. The characteristics of the stars are quite different in spite of the fact that approximately the same total excitation energy is present. As shown in Fig. 3, the anisotropy of the proton distribution is much more pronounced than that of the pion distribution.

In the case of the pion stars, many contained a prompt light prong in the backward hemisphere, which was in most cases a pion of kinetic energy greater than 70 Mev. From the results of the pion-proton scattering[12] we would expect a large number of backscattered mesons in the first collision. The results of Kessler and Lederman[13] on stars in C and Pb show many inelastically scattered pions in the backward hemisphere. Backward particles of high energy make the analysis of the prong distribution from the pion stars considerably more involved. The two important effects of the secondary proton distribution and the scattered pion distribution are mixed together. A reduction in anisotropy can already be expected from the fact that nucleon secondaries in pion stars rarely have energies in excess of 100 Mev.[14] For the proton stars no such effect was observed, which leads to the belief that the analysis as used here can provide an adequate description of the events.

IV. CONCLUSION

The angular distribution and the number of particles predicted by the Monte Carlo computation for 400-Mev proton-induced stars generally agrees with the distribution and number of cascade particles found in this experiment. Allowing that the remaining particles are

[11] K. J. Le Couteur, Proc. Phys. Soc. (London) **A65**, 718 (1952).

[12] Anderson, Fermi, Martin, and Nagle, Phys. Rev. **91**, 155 (1953).

[13] J. O. Kessler and L. M. Lederman (private communication).

[14] A. H. Morrish, Phys. Rev. **90**, 674 (1953).

due to an evaporation process, present evaporation theories do not provide for an adequate number of evaporation particles. A more complete study of the energy distribution and the nature of the outgoing prongs might throw more light on this matter. Morrison *et al.*,[5] have remarked that it seems necessary at their energy to include cascade particles with energy below the Coulomb barrier, but the angular distribution of these particles in the center-of-mass system is not isotropic, so they should yield more anisotropy and cannot resolve the difference found in this experiment.

The results strongly indicate that (1) in high-energy nuclear events a cascade mechanism is operating in a nucleus, (2) the development of the cascade depends strongly on the type of fundamental interactions occurring, and (3) evaporation theory as developed up to now cannot account fully for the subsequent disruption of the nucleus.

We wish to thank H. L. Anderson and L. Kornblith for the use of the cyclotron, K. L. Brown for much of the scanning, and David B. Williams for some of the measurements.

PHYSICAL REVIEW VOLUME 94, NUMBER 4 MAY 15, 1954

Spallation Studies of Bismuth†

W. E. BENNETT*
Institute for Nuclear Studies, University of Chicago, Chicago, Illinois
(Received January 18, 1954)

A study of the relative yields of polonium, bismuth, lead, and thallium isotopes produced in the bombardment of bismuth with high-energy protons has been carried out. It has been shown that the emission of neutrons is favored over the emission of charged particles in the formation of spallation products in this region.

INTRODUCTION

STUDIES have been made of the yields of spallation products produced by the bombardment with charged particles of elements having masses ranging from 55 to 123.[1] The results of these experiments show a consistent behavior in that the yield distribution maxima of the isotopes only a few mass units removed from the target isotope occur in regions one or two mass units removed from the region of maximum stability. At much lower masses than the target, the most probable isotopes appear to be in the region of maximum stability.

Since it is of interest to make similar studies in the heavy-mass region, the following investigation was made of the relative distribution of yields of isotopes produced by the bombardment of bismuth with high-energy protons.

EXPERIMENTAL PROCEDURES

Bismuth metal and bismuth oxychloride targets were bombarded internally in the University of Chicago synchrocyclotron. The bismuth metal targets were approximately 1 $cm^2 \times 1$ mm; the bismuth oxychloride targets were in the form of pills about 1 cm in diameter and 2 mm in thickness. Most bombardments were carried out in such a way that the beam of the synchrocyclotron traversed the 1-cm thickness of the target.

The relative yields of isotopes of polonium, bismuth, lead, and thallium were determined. Following is a description of the chemical separation procedures used:[2]

Polonium separations were carried out by reduction with stannous chloride and precipitation with tellurium carrier as the free metal. The polonium and tellurium were redissolved in concentrated hydrochloric acid solution, and the tellurium was reprecipitated from the hydrochloric acid solution with sulfur dioxide gas after the hydrochloric acid concentration was adjusted to 6*N*. This procedure does not cause the precipitation of polonium. The polonium was extracted from the solution into a mixture of tri-butylphosphate and di-butyl ether. The organic layer was evaporated to dryness and the residue was dissolved in 6*N* hydrochloric acid. The polonium was then re-extracted into the same organic mixture and was retained for successive milkings of bismuth. The bismuth daughters of the polonium isotopes were removed for counting periodically by washing the organic layer containing the polonium with 6*N* hydrochloric acid in which was placed the bismuth carrier. Bismuth was then precipitated as the oxychloride.

† Supported in part by a grant from the U. S. Atomic Energy Commission.
* Now at the State University of Iowa, Iowa City, Iowa.
[1] Cunningham, Hopkins, Lindner, Miller, O'Connor, Perlman, Seaborg, and Thompson, Phys. Rev. **72**, 739, 740 (1947); Miller, Thompson, and Cunningham, Phys. Rev. **74**, 347 (1948); H. H. Hopkins, Phys. Rev. **77**, 717 (1950); M. Lindner and I. Perlman, Phys. Rev. **78**, 499 (1950); Bartell, Helmholtz, Stofuy, and Stewart, Phys. Rev. **80**, 1006 (1950); Batzel, Miller, and Seaborg, Phys. Rev. **84**, 671 (1951).

[2] W. Wayne Meinke, University of California Radiation Laboratory Report AECD-2738 August 30, 1949 (unpublished).

Bismuth separations were carried out as follows: bismuth oxychloride was precipitated from the target solution. This was redissolved in 6*N* hydrochloric acid. Silver chloride scavenging was then carried out. Bismuth oxychloride was reprecipitated. The bismuth oxychloride precipitation and silver chloride scavengings were repeated several times. Then bismuth sulfide was precipitated from 1*N* hydrochloric acid. The sulfide was redissolved in a few drops of concentrated hydrochloric acid, a few milliliters of concentrated sulfuric acid was added, and the solution was heated to fuming. The solution was then diluted to about 3*N* sulfuric acid and lead nitrate carrier was added. After cooling in an ice-bath, the lead sulfate was removed and a second lead sulfate precipitation was carried out.

From this solution, bismuth was precipitated by the addition of ammonium hydroxide. The resultant precipitate was redissolved in 6*N* hydrochloric acid and bismuth oxychloride precipitated by the addition of ammonium hydroxide and dilution. This was redissolved in hydrochloric acid and a final reprecipitation of bismuth oxychloride was made. For further purification either sulfide or oxychloride precipitations were repeated.

Lead separation involved first the precipitation of bismuth oxychloride; then, from the resultant solution, lead chromate was precipitated by the addition of potassium dichromate. Lead chromate was redissolved in hydrochloric acid plus a few drops of Superoxol. This was then evaporated to dryness and fuming nitric acid was added, causing the precipitation of lead nitrate. This was washed with fuming nitric acid. The lead nitrate was dissolved in water and sulfuric acid was added to make the solution about 2*N*. After cooling in an ice-bath, the lead sulfate was removed. The lead sulfate was dissolved in ammonium acetate solution and lead chromate was reprecipitated. The lead chromate was dissolved in hydrochloric acid solution and Superoxol. The lead nitrate precipitation was repeated. The lead nitrate was dissolved in dilute hydrochloric acid. Ten milligrams of bismuth carrier were added and bismuth oxychloride precipitations were carried out. Then lead chromate was precipitated.

Thallium was separated by oxidation with hydrogen peroxide and extraction into either. Thallium was removed from the ether by washing with sodium bisulfite solution. Thallous iodide was precipitated from this solution by the addition of potassium iodide. Thallous iodide was dissolved in hydrochloric acid and hydrogen peroxide. The extraction, removal into sodium bisulfite and precipitation of thallous iodide was repeated.

The samples prepared for counting were mounted on filter paper disks and placed upon cardboard holders. All samples were covered with cellophane, 3 mg/cm² in

TABLE I. Relative yields of isotopes of given masses produced by the spallation of bismuth.

Element	Isotope mass	Yield millibarns	Half-life[a] (literature)	Half-life (observed)	Isotope counted	Half-life[a] (literature)	Half-life (observed)
Pb	209[(b)]	9.8	3.22 hr	4.8 hr[(b)]	Pb^{209}	3.22 hr	4.8 hr[(b)]
Bi	207	20	50 yr[c]	Long	Bi^{209}	50 yr	Long[c]
Po	206	2.0	9 days	9 days	Bi^{206}	6.4 days	6.4 days
Bi	206	16	6.4 days	6.4 days	Bi^{206}	6.4 days	6.4 days
Po	205	0.4	1.5 hr	2.2 hr	Bi^{205}	14.5 days	14 days
Bi	205	3.0	14.5 days	14.5 days	Bi^{205}	14.5 days	14.5 days
Po	204	1.6	3.8 hr	4 hr	Bi^{204}	12 hr[d]	12 hr[d]
Bi	204	15	12 hr	12 hr	Bi^{204}	12 hr[d]	12 hr[d]
Tl	204	1.6	3.5 yr	Long[e]	Tl^{204}	3.5 yr	Long[e]
Po	203	0.39	47 min	50 min	Pb^{203}	52 hr	52 hr
Bi	203	8.2	12 hr	12 hr	Pb^{203}	52 hr	52 hr
Pb	203	6.6	52 hr	52 hr	Pb^{203}	52 hr	51 hr
Po	202	0.78	52 min	52 min	Bi^{202}	95 min	95 min
Bi	202(201?)	18	95 min[f]	96 min	$Bi^{202(201?)}$	95 min[f]	96 min
Tl	202	0.33	12.55 days	12 days	Tl^{202}	12.5 days	12 days
Po+Bi+Pb	201	7[g]	[g]	...	Tl^{201}	72 hr	72 hr
Tl	201	2[h]	72 hr	50 hr[h]	Tl^{201}	72 hr	250 hr[h]
Po+Bi	200	2	35 min[i]	...	Pb^{200}	18 hr	22 hr
Pb	200	5.6	18 hr	22 hr	Pb^{200}	18 hr	22 hr
Po+Bi+Pb	200	11	18 hr[j]	...	Tl^{200}	27 hr	28 hr
Tl	200	1	27 hr	27 hr	Tl^{200}	27 hr	27 hr
Po+Bi+Pb+Tl	199	12	80 min[k]	...	Tl^{199}	7 hr	7 hr
Po+Bi+Pb+Tl	198	22	1.8 hr[l]	...	Tl^{198}	1.8 hr	1.8 hr

[a] Values from "Table of isotopes," Hollander, Perlman, and Seaborg, Revs. Modern Phys. 25, 469 (1953).
[b] Includes probably also 8-hr Pb^{201} and 7-hr Tl^{199}. Calculations of the yield were based solely upon the assumption that it was Pb^{209}.
[c] No observed decay ±3 percent over a period of three months.
[d] Assuming the counting efficiency of Bi^{204} to be much greater than that of Bi^{206}. This is evidenced by the correct observed half-life of the parent Po^{204}.
[e] Decay followed long enough to determine a minimum of 2.5 years for the half-life.
[f] Bi^{201} is reported to have a half-life of 2 hr and might thus contribute to this yield.
[g] Half-life of Po^{201} is 18 min, of Bi^{201} is 62 min, and of Pb^{201} is 8 hr. The yield is calculated on the basis of the production of a 72-hr isotope and thus it represents a minimum for the true sum of the lead, bismuth, and polonium yields.
[h] This represents a maximum since the decay corresponding to a half-life of this magnitude was just detectible.
[i] Very probably most of this yield is due to Bi^{200} alone, the yield of Po^{200} being much lower. The calculation of this yield was based therefore on the formation of 35-min Bi^{200}.
[j] 11-min Po^{200}, 35-min Bi^{200}, and 18-hr Pb^{200}.
[k] Po^{199}(half-life unknown) 25-min Bi^{199}, 80-min Pb^{199}, and 7-hr Tl^{199}.
[l] Po^{198}(half-life unknown) 7-min Bi^{198}, 25-min Pb^{198}, and 1.8-hr Tl^{198}.

thickness. Counting was done with an end-window Geiger tube[3] having a window thickness of 1.9 milligrams per square centimeter.

Yields of polonium isotopes were determined by counting the bismuth daughters, and in the case of Po^{203} by counting the Pb^{203} granddaughter.

Yields of bismuth isotopes were determined directly except for Bi^{203} which produced Pb^{203}, for Bi^{201} which produced Tl^{201} by decaying through Pb^{201} and for Bi^{200} which was counted by its daughter Pb^{200}.

Since the chemical yield of polonium would be difficult to evaluate, the yield of bismuth isotopes relative to the yield of polonium isotopes was determined by separating bismuth from the target solution at intervals and determining the increased activity of Bi^{206} produced by the decay of 9-day Po^{206}.

The yield of Bi^{200} relative to that of Pb^{200} was determined by the separation of lead from the target solution at various intervals. The yield of Bi^{200} determined in this manner, however, would also include the yield of Po^{200} which may be small.

Similarly, the yields of lead isotopes relative to those of thallium were determined by the separation of thallium from the target solution at different times from the end of the bombardment.

RESULTS

Since most of the isotopes in this region decay by K capture, the determination of absolute yields is difficult. For this reason, in this study only the relative yields of isotopes of neighboring elements having the same mass were determined. This could be accomplished by counting the isotope which was the last in a chain of isotopes decaying by K capture. For example, the relative yields of Po^{203}, Bi^{203}, and Pb^{203} could be determined by counting only the Pb^{203} formed.

Table I lists the relative yields of the isotopes studied, showing also the isotopes which were counted in the determination of these yields. Yields are reported in millibarns, not corrected for counting efficiency of the Geiger tube for the radiations emitted.

First, it can be observed that the yields of bismuth isotopes divided by the yields of polonium isotopes increase with a decrease of mass as seen in Table II.

This behavior is in general agreement with that found in previous spallation studies with high-energy deterons in the lower mass region. This indicates that the bismuth isotopes formed are lighter than those of polonium.

[3] Tracerlab Tube Type TGC2.

TABLE II. Ratios of yields of bismuth to polonium isotopes of the same mass.

Bismuth isotope	Bismuth yield	Polonium isotope	Polonium yield	Ratio Bi yield / Po yield
206	16	206	2.0	8
205	3.0	205	0.4	8
204	15	204	1.6	9
203	8.2	203	0.39	21
202?	18	202	0.78	23

Secondly, the relative yields in the mass 203 chain show that Bi^{203} is at the maximum. Similarly, the yield of Pb^{200} is greater than that of Bi^{200} and also appears to be greater than that of Tl^{200}, indicating a maximum at Pb^{200} for this case.

The above results indicate that a line can be drawn through the isotopes having the maximum yield for a given mass, which would pass through Bi^{203} and Pb^{200}. This distribution shows a markedly greater tendency toward the formation of isotopes much more neutron-deficient than those in the stable mass region. The emission of neutrons appears to be very much more probable than the emission of protons or α particles. This result is in agreement with the results of Sugarman and Peters[4] in the study of the photoactivation of bismuth. They found the formation of Pb^{204} to be less probable than the formation of Bi^{204}. Similarly, Pb^{206} was found in much less yield than Bi^{206}.

Experiments were carried out using both 375-Mev and 450-Mev protons. The distribution of yields of polonium isotopes remained the same in both cases. This is in accordance with the findings of Karraker and Templeton[5] from their determination of relative yields of polonium isotopes through alpha counting.

ACKNOWLEDGMENT

The author wishes to express his gratitude to Dr. Nathan Sugarman for his assistance and guidance in this work, and also to the crew of the Institute for Nuclear Studies Synchrocyclotron for their help in the bombardments.

[4] N. Sugarman and R. Peters, Phys. Rev. **81**, 951 (1951).

[5] D. G. Karraker, University of California Radiation Laboratory Report UCRL-1202, April 12, 1951 (unpublished).

High-Energy Photoproton Production by 325-Mev Bremsstrahlung Radiation*

B. T. Feld, R. D. Godbole,† A. Odian, F. Scherb, P. C. Stein, and A. Wattenberg
Physics Department and Laboratory for Nuclear Science, Massachusetts Institute of Technology, Cambridge, Massachusetts

(Received February 8, 1954)

Photoprotons with energies above 120 Mev have been studied at the M.I.T. synchrotron. Angular distributions of protons with 126 Mev, 169 Mev, and 203 Mev were obtained in the angular range from 20° to 160° from both beryllium and carbon targets. These observations showed that the protons in a Be and in a C nucleus behave identically in high energy photoproton production. The energy distribution of photoprotons from carbon at 30° was investigated in particular detail. A break is observed in the energy distribution which appears to be in accordance with Levinger's "quasi-deuteron model." Absolute values for the differential and total cross sections were obtained.

A detailed analysis of existing data is given which raises the possibility that the agreement with the "quasi-deuteron model" may be fortuitous.

I. INTRODUCTION

AMONG the products of the reactions of γ rays with nuclei, protons have been observed and studied by many investigators.[1] For γ rays of energy between the threshold ($\sim$5–8 Mev) and $\sim$50 Mev, most of the photoprotons arise from the absorption of the γ ray in a "dipole resonance" reaction, followed by the evaporation of a proton from an excited compound nucleus.

However, even in the dipole resonance energy range, an appreciable fraction of the proton emission results from a direct interaction between the γ ray and one of the protons in the nucleus.[2,3] These directly emitted photoprotons exhibit two characteristic features (1) they carry away a large fraction of the incident γ-ray energy, and (2) their angular distribution, unlike that of the evaporation protons, is not isotropic, but tends to exhibit the $\sin^2\theta$ distribution characteristic of a photoelectric ejection process.[3,4]

At higher energies, photon absorption usually results in multiple particle emission.[5,6] The energy dependence of the cross section for photon absorption in the energy range $\sim$50–150 Mev is not yet well established but, once the dipole resonance has been passed, the cross section appears to be small and either slowly decreasing or more-or-less flat with increasing energy. In the region of $\sim$140 Mev, which corresponds to the onset of the possibility of π-meson production, the cross section for photon absorption appears to increase. Most absorptions result in "stars," and the increase in cross section is believed to be meson-connected.[7,8] However, in moderately heavy nuclei, a large fraction of the mesons produced may be reabsorbed in the same nucleus, giving rise to the evaporation of a number of neutrons, protons, α particles, and possibly heavier nuclear fragments.[8]

Also, at the higher photon energies, the γ ray frequently ejects a proton of energy comparable to that of the incident photon. The most direct way of studying this process is to observe the high-energy protons emitted from targets bombarded by high-energy x-rays.[9] Such observations are not easy to interpret unambiguously, since the bremsstrahlung spectrum falls off rapidly with increasing energy, so that the resulting proton spectrum represents an integral in which the effects of the lower-energy photons are strongly weighted.

Nevertheless, a considerable amount of information is available as a result of a number of investigations of the high-energy photoprotons from x-rays on various targets. Levinthal and Silverman,[10] using the 322-Mev x-ray beam from the Berkeley Synchrotron, studied the protons of energies between 10 and 70 Mev. They obtained proton energy spectra falling off with energy roughly as E^{-2}. The 10-Mev protons were emitted isotropically; these are probably the tail of the evaporation spectra. The 40-Mev protons, on the other hand, showed a distinct forward peaking. Walker[11] studied the protons of energy $\gtrsim$70 Mev at a number of angles from a carbon target bombarded by a 195-Mev x-ray beam from the Cornell synchrotron. He found a forward peaking in the angular distribution and a rapid decrease with energy $\sim E^{-5}$ in the integral proton spectrum.

Keck,[12] at Cornell, expanded and extended the ob-

* This work was supported in part by the joint program of the U. S. Office of Naval Research and the U. S. Atomic Energy Commission.

† Now at Ramnarain Ruia College, Bombay, India.

[1] For a summary of work up to 1952, see K. Strauch, Ann. Rev. Nuclear Sci. 2, 105 (1953).

[2] O. Hirzel and H. Wäffler, Helv. Phys. Acta 20, 373 (1948).

[3] E. D. Courant, Phys. Rev. 82, 703 (1951).

[4] P. R. Byerly, Jr., and W. E. Stephens, Phys. Rev. 83, 54 (1951).

[5] K. Strauch, Phys. Rev. 81, 973 (1951).

[6] Debs, Eisinger, Fairhall, Halpern, and Richter (private communication).

[7] R. D. Miller, Phys. Rev. 82, 260 (1951).

[8] S. Kikuchi, Phys. Rev. 80, 492 (1950); 83, 1255 (1951); 86, 41 (1952).

[9] In the energy range under discussion, the only available sources of appreciable intensity are bremsstrahlung sources. J. W. Weil and B. D. McDaniel [Phys. Rev. 92, 391 (1953)] have developed a method of making observations with monochromatic photons which, owing to the very small available intensities, is of rather limited applicability.

[10] C. Levinthal and A. Silverman, Phys. Rev. 82, 822 (1951).

[11] D. Walker, Phys. Rev. 81, 634 (1951); 84, 149 (1951).

[12] J. C. Keck, Phys. Rev. 85, 410 (1952).

servations on the high-energy photoprotons from 300-Mev x-rays to proton energies of ~200 Mev and over a wider range of angles and target elements. He found that the cross section for photoproton ejection increased linearly with atomic number; that the angular distributions became more sharply peaked forward with increasing energy; and that the proton energy spectra showed a sharp break in slope at an energy of approximately half of the maximum photon energy (e.g., at 67.5° to the beam, the proton energy distribution changed from E^{-2} to E^{-6} at ~130 Mev).

This last feature gave rise to the suggestion, developed theoretically by Levinger,[13] that the energetic photoprotons result from the direct interaction of photons with deuteron-like sub-units in the nucleus. Subsequent measurements, by Rosengren and Dudley,[14] with the 322-Mev x-rays from the Berkeley synchrotron, by Perry and Keck,[15] who employed a subtraction technique to obtain the effect of monochromatic γ rays, and by Weil and McDaniel,[16] using monochromatic 190-Mev γ rays,[9] as well as by the present authors,[17] have tended to confirm and further elucidate the main features of the photoproduction process suggested by the work of Keck.[12]

However, the "deuteron model," as developed by Levinger,[13] is not nearly as successful in accounting for other features of the high-energy photoproton distributions. In particular, the observed angular distributions appeared to be much more strongly peaked in the forward direction than predicted.

The experiments herein reported were undertaken in an attempt to further clarify the nature of the high-energy photoproton production process. While in many respects they cover the same ground as investigations

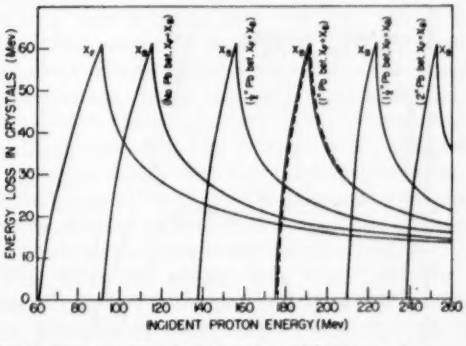

FIG. 1. Proton energy loss in 5.1 g/cm² NaI crystals *versus* the incident proton energy. All curves are for a ¼-in. Pb absorber in front of the crystals. The X_F curve is for the energy loss in the front crystal. The X_B curves are for the back crystal. The dotted curve is for a total absorber of 1¼ in. of Pb placed in front of the first crystal.

[13] J. S. Levinger, Phys. Rev. **84**, 43 (1951).
[14] J. W. Rosengren and J. M. Dudley, Phys. Rev. **89**, 603 (1953).
[15] A. M. Perry and J. C. Keck, Phys. Rev. **86**, 629 (1952).
[16] J. W. Weil and B. D. McDaniel, Phys. Rev. **92**, 391 (1953).
[17] Wattenberg, Feld, and Godbole, Phys. Rev. **90**, 380 (1953).

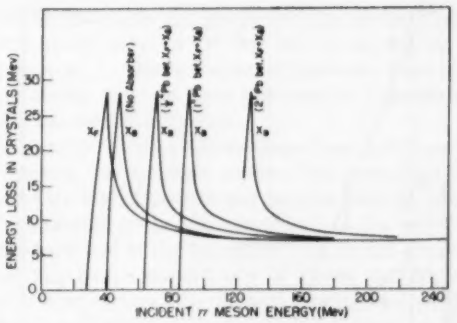

FIG. 2. π meson energy loss in 5.1 g/cm² NaI crystals *versus* the incident π meson energy. All curves are for a ¼-in. Pb absorber in front of the crystals. The X_F curve is for the energy loss in the front crystal. The X_B curves are for the back crystal.

previously reported,[12,14] they have extended these investigations both in energy and in angle, and have attempted to provide a quantitative basis for comparison with theory. In the majority of these investigations a carbon target was employed; however, several other elements were also studied.

II. METHOD OF OBSERVATION

Our method of proton detection is essentially the same as that described by previous investigators.[12,14] However, it differs in a sufficient number of significant details so that a brief description of the main features may be in order.

The protons were detected, and distinguished from other charged particles, by observation of the pulse heights in the two crystals of a scintillation counter telescope. Both crystals usually were about ⅝ in. thick and 4 in. in diameter. NaI:Tl crystals were used to obtain a linear relation between pulse height and energy loss in the crystal. End-window (5819) photomultipliers viewed the crystals at a distance of a few inches in order to increase the uniformity of the light collection from different regions of the crystal. The method of proton energy discrimination may be understood most easily by reference to Fig. 1, which is a plot of the proton ionization energy loss in each of the crystals as a function of the energy of the protons incident on the telescope. The first curve, labeled X_F, shows the proton energy loss in the front crystal while the succeeding curves, X_B, show the proton energy loss in the back crystal for various thicknesses of lead absorber placed between the two crystals. In Fig. 2 are plotted the corresponding ionization energy losses for π mesons. The energy loss data, on which these curves are based, were taken from the compilation of Aron, Hoffman, and Williams.[18]

The detection of protons of a given energy E_0 is accomplished as follows: The approximate thickness of absorber, such that the peak of the energy loss in X_B

[18] Aron, Hoffman, and Williams, Atomic Energy Commission Report AECU-663, UCRL-121, 1949 (unpublished).

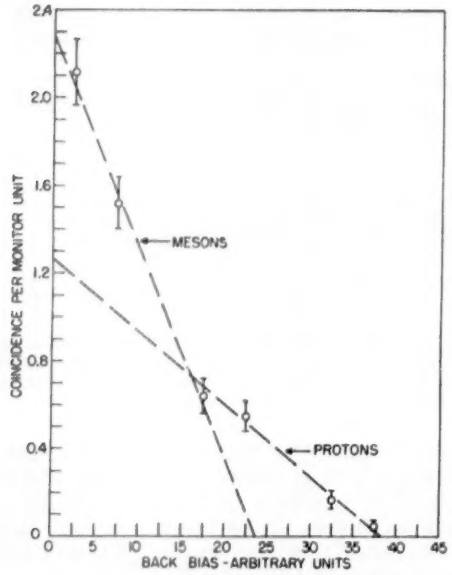

FIG. 3. Coincidence counting rate as a function of the bias on the back crystal. The front bias is set at a value slightly below the value at which protons should be counted. The straight lines are drawn on the assumption that the upper portions of the curves in Figs. 1 and 2 can be approximated by triangles.

(Fig. 1) falls at E_0, is inserted in the telescope. A curve is then taken of the coincidence telescope counting rate as a function of the bias setting (proportional to the minimum pulse height) on the back crystal. While taking this curve, the bias on the front crystal is set rougly somewhat below the value at which protons should be counted, but, if possible, above the value corresponding to the energy loss of a particle at the minimum of its ionization. An example of such an integral "back-bias" curve is shown in Fig. 3. From this curve, the value of the bias setting corresponding to 61 Mev (the peak of the proton energy loss curve) is determined. The back bias is then set to a somewhat lower value such as to make the proton energy resolution as sharp as possible consistent with a reasonable counting rate, i.e., about 45 Mev. In the case of the data to be discussed, the proton energy spread was kept below 15 percent in all cases.

Once this bias setting for the back crystal has been decided, the proper bias setting for the front crystal is determined by taking integral bias curves of the type illustrated in Fig. 4. These curves demonstrate a number of characteristics of our detection technique. It may be noted that above the plateau region, the counting rate falls off with increasing bias over a finite range. In practice, the width of this "fall-off" region is not primarily determined by instrumental factors. Rather, this width is determined by the variation of proton energy loss in the front crystal over the finite range of proton energies accepted by the back crystal. It is seen from Fig. 1 that the width of the "fall-off" region should decrease with increasing absorber thickness, as indeed it does. The width of the break in the front crystal bias curves provides another check on our calibration of the energy resolution of the telescope. In normal operation, the bias of the front crystal is set at a value slightly below that of the "break," so as to count all the protons accepted by the back crystal while, at the same time, minimizing the possibility of counting mesons by setting as far as possible above the bias corresponding to the energy loss in the front crystal of mesons stopping in the back crystal (see Fig. 2).

Another feature of the curves of Fig. 4 is the fact that the bias at which the break occurs decreases with increasing absorber thickness when the absorber is placed between the crystals. This is, again, as expected from consideration of the curves of Fig. 1, and provides an additional check on the calibration of the counter telescope. Actually, this feature represents one of the disadvantages of our detection scheme, since it means that a new calibration curve must be run and a new front crystal bias setting must be determined for each absorber thickness used. (The calibration of the back crystal, however, is independent of the absorber thickness, although the energy resolution, for a given bias setting, changes with absorber thickness.) This difficulty can be overcome by placing the absorber in front of the telescope rather than between the crystals. Curves of energy loss *vs* incident proton energy, corre-

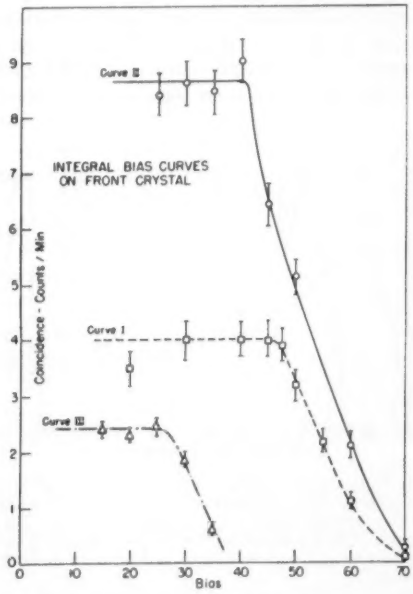

FIG. 4. Coincidence counting rate as a function of the bias on the front crystal. Curve I is for the back bias set close to the maximum for protons with no lead absorbers between crystals. Curve II is for the back bias set at a slightly lower value with no lead between crystals. Curve III is for the back bias set the same as in Curve II, but with a $\frac{1}{2}$-in. Pb absorber between crystals.

sponding to this geometry, are shown as broken curves in Fig. 1. The energy loss in the back crystal is scarcely altered by this modification, and the curve of energy loss in the front crystal is shifted in such a way as to make it essentially independent of absorber thickness.

These predictions have been checked for a number of absorber thicknesses and have been born out by the observations. The reasons that we have normally chosen to operate the telescope with the absorber between the crystals, despite the above mentioned disadvantage, are concerned with the elimination of spurious counts due to neutrons and mesons. Fast neutrons can produce protons in the material in front of the crystals or in the front crystal, and these protons will be counted provided that their energies lie in the range to which the telescope is sensitive. Placing the absorber in front of the telescope enhances the number of such spurious counts, both because of the increased thickness of material available for proton production and because the number of neutrons capable of producing protons of the requisite energy is greater, since the telescope itself is sensitive to lower-energy protons and neutrons, when the absorber precedes the front counter.

The problem of eliminating the background due to π mesons presents greater difficulties. These arise from the fact that a π meson which comes to rest in the back crystal gives rise to a larger pulse height than that which corresponds to its ionization energy loss. If it is positively charged, the decay μ^+ meson has an energy of 4.2 Mev and a very short range; its energy must be added to the energy loss of the π^+ meson. (The μ^+ meson decay, which gives rise to an electron of average energy $\sim$20 Mev, has a sufficiently long lifetime so that it does not add to the pulse height, provided that the detector resolving time is better than $\sim$1 μsec; the π^+ to μ^+ decay time cannot be resolved in a NaI:Tl crystal.) Negative π mesons are captured and give rise to nuclear disintegrations, which can add considerably to the energy losses (from ionization by the π^- meson alone) which are plotted in Fig. 2. Thus, it is possible for a π^- meson, of energy such that it barely penetrates into the back crystal, to trigger the telescope, even though the bias settings are such that it would not be detected if it behaved according to the curves of Fig. 2.

The difficulties arising from this possibility are especially serious in the proton energy range which we have investigated owing to the fact that the cross section for production of π mesons of energy capable of triggering the telescope is a number of orders of magnitude greater than that for the production of the high energy protons here under investigation. Thus, the rapid rise in the counting rates at the low bias settings, as seen in Figs. 3 and 4, can be accounted for by π-meson detection. Furthermore, the probability of counting a π meson is greater when the absorber is placed in front of the telescope than when it is placed between the two crystals, since the energy loss in the front crystal of a π meson which can just penetrate into the back crystal is sufficiently great in the first case to exceed the bias appropriate to the detection of protons. This is the main reason why we have preferred to place the absorber between the crystals.

A number of possibilities have been advanced for minimizing the spurious counts. One technique is to localize the end of the charged particle range by placing a third crystal, set in anticoincidence to the other two, at the back end of the telescope. This device eliminates those negative π mesons one of whose disintegration products penetrates into the anticoincidence crystal.

Another means of decreasing the π-meson background is by use of differential pulse-height analysis on either of the two crystals, or both. The main effect of this modification is to make more stringent the conditions under which a π meson can cause a count. Differential pulse-height analysis is most effective when used on the back crystal, since the additional energy loss due to the capture of negative π mesons is spread over a wide range of energies.

Most of the measurements, discussed in the next section have been made with a simple two-crystal telescope using integral pulse-height discrimination. The more recent measurements employed differential pulse-height analysis in the back crystal. However, a sufficient number of variations—in crystal thickness, position of the absorber, use of an anticoincidence crystal, use of differential pulse-height discrimination—have been tested so as to provide sufficient understanding of the workings of the proton telescope to determine those bias settings which minimize the background counting rates. Thus, we have good reason to believe that our measurements actually represent the fast photoprotons, with only a small fraction of possible neutron or π-meson contamination. Nevertheless, those data for which the counting rates have been especially small (mainly at the highest energies and largest angles) are still subject to a certain amount of uncertainty concerning the extent of the π-meson contamination. Fortunately, the main conclusions which can be drawn from the data are not seriously affected by these uncertainties.

Finally, in evaluating the data, it is necessary to know what fraction of the protons, which enter the telescope, are counted. Protons can be lost by suffering nuclear absorptions or scattering in the absorber, or by (multiple) Coulomb scattering in the absorber. This latter effect can be minimized by using an absorber of light material; we have used aluminum absorbers in some of our later measurements. In addition, the proton loss due to Coulomb scattering is decreased when the absorber is placed between the crystals of the telescope.[19] The

[19] One can avoid losses due to Coulomb scattering by employing a geometry in which as many protons are scattered into the detectors as are scattered out. We have tried to approximate such a geometry by using absorbers that extend beyond the crystals and which are as close as possible to the back crystal.

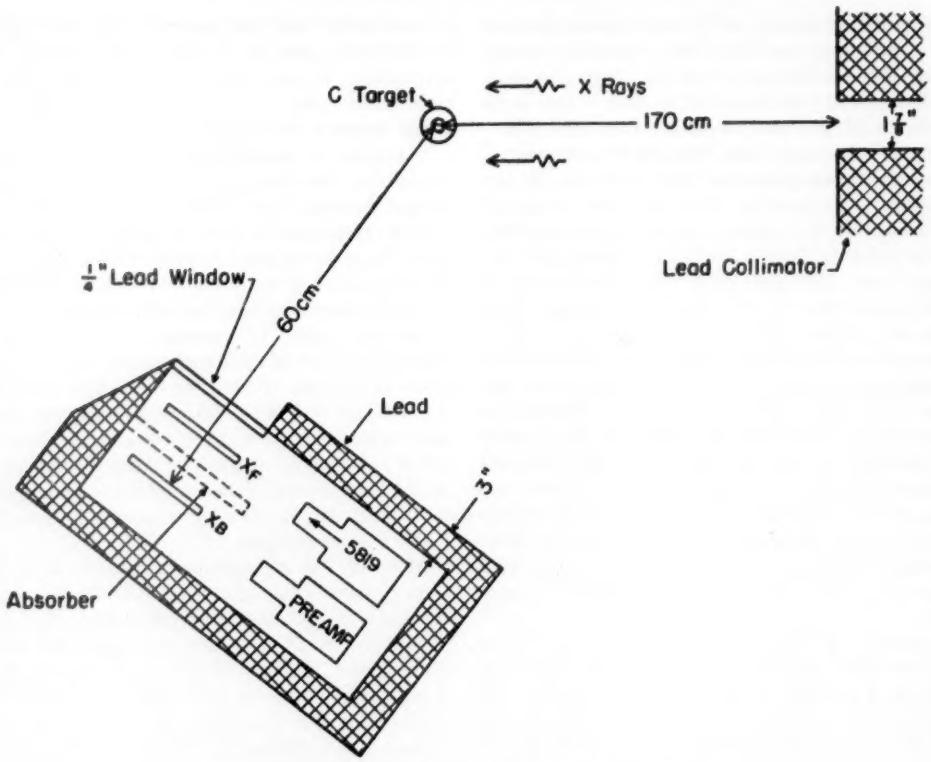

FIG. 5. Schematic drawing of angular distribution apparatus.

data can be corrected for the loss of protons due to nuclear interactions, provided the cross sections are known. We have assumed a nuclear cross section equal to the geometric value (with a radius $R=1.4A^{\frac{1}{3}}\times10^{-13}$ cm) in making this correction.

III. THE MEASUREMENTS

The geometrical arrangement for taking data is depicted in Fig. 5. The targets, which were in the form of cylinders or cylindrical shells, were centered in the x-ray beam with their axes vertical. The target cylinders were of sufficient height to extend over the entire vertical diameter of the (circular) beam and the target diameter was somewhat smaller than that of the beam which was $\sim$3 in. at the position of observation. The proton telescope was placed in a lead house on a turntable which could be rotated to any angle. This angle could be set to $\pm0.5°$ with respect to the beam direction.

This geometry has the advantage of cylindrical symmetry, thus insuring the reliability of angular distribution measurements. Its disadvantages lie in the difficulty of absolute cross-section measurements, since these depend on a determination of the average target thickness (which, together with the corresponding average proton energy loss in the target, was evaluated by graphical integration) as well as on a knowledge of the beam intensity and of its distribution over the area of the beam. However, the cylindrical geometry has been used only for relative cross-section measurements. The determination of the absolute cross section, at a single angle and energy, was achieved by use of a thin, plane target covering the entire area of the beam.

A. Carbon and Beryllium

The major fraction of our measurements were made with a carbon target, which was a cylindrical shell of 2-in. o.d. and $\frac{3}{8}$-in. thickness. The average energy loss of protons in the target, as computed from the range-energy relationships[18] by a graphical integration, were 12, 9.7, and 8.8 Mev for absorbers of 0 in., $\frac{1}{2}$ in., and 1 in., respectively, between the crystals (mean proton energies of 114, 159, and 194 Mev). Measurements at angles of 30° to the beam or greater were made with an angular resolution of $\pm5.4°$; at smaller angles, it was necessary to move the lead house further back, and the corresponding angular resolution was $\pm3.4°$.[20]

Measurements were also made with a Be target[21] of 2 in.-o.d. and $\frac{1}{2}$ in. thickness. These observations showed

[20] These figures include a spread of $\pm0.5°$ introduced by the finite size of the target.

[21] Kindly supplied by Professor A. Kaufmann of the M.I.T. Department of Metallurgy.

that, within the experimental accuracy of ~3 percent, the protons in a Be nucleus and in a C nucleus behave in an identical fashion with respect to high-energy γ rays—i.e., the angular distributions, for a given proton energy, are identical and the ratio of the cross sections of Be and C for the production of high-energy protons is 4:6. Hence, in the following discussions, the data obtained with the Be target have been combined with those obtained with the C target.

1. *Angular Distributions*

Careful measurements of the angular distributions of high-energy photoprotons have been made at three proton energies and at angles ranging from 20° to 160° in the laboratory frame of reference. The results are shown in Figs. 6–8. The limitations in the angular range resulted from the high background of electromagnetic radiation at the small angles, and from the low intensities of high-energy protons at the large angles. The errors plotted on the curves are entirely statistical and do not include provision for a mesonic background. The mesonic background could be important at the largest angles although even there, it is probably less than ~10 percent.

The observations at the various angles were made by taking short "runs" always "bracketed" by observations at 30°. This was done in order to eliminate the effects of drift in the electronic circuits and the consequent variations of the efficiency and energy resolution of the counter telescope.

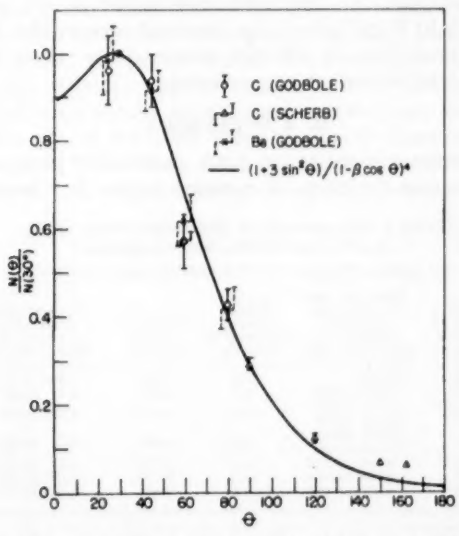

FIG. 6. The angular distribution in the laboratory of 126-Mev photoprotons from beryllium and carbon. The data marked "Scherb" were obtained at a later date than that marked "Godbole." The data are normalized to the value at 30°. The curve is a semiempirical fit to the data with $\beta=v/c$ of the protons.

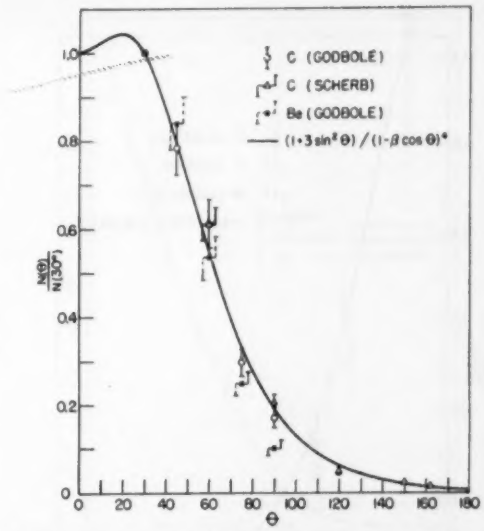

FIG. 7. The angular distribution in the laboratory of 169-Mev photoprotons from beryllium and carbon. The data marked "Scherb" were obtained at a later date than that marked "Godbole." The data are normalized to the value at 30°. The curve is a semiempirical fit to the data with $\beta=v/c$ of the protons.

The curves in Figs. 6–8 represent attempts to fit the data by a formula of the form

$$\frac{d\sigma/d\Omega}{d\sigma/d\Omega(30°)}=\frac{a+b\sin^2\theta}{(1-\beta\cos\theta)^4}, \tag{1}$$

where $\beta=v/c$ of the protons observed. This form, although suggested by the atomic photoeffect,[22] should be regarded in our case only as an empirical formula which provides a very good fit to the data over the range of observation with a relatively small variation with energy of the ratio $a=b/a$. Its possible significance will be discussed in a following section.

2. *Energy Dependence at 30°*

In order to investigate carefully the energy dependence of the cross section for high-energy photoproton production, a separate run was made with the telescope at 30° to the beam. Special care was taken, in this run, to insure stability of the electronics and to evaluate the proton energy resolution of the telescope at each energy. Aluminum absorbers were employed, between the crystals of the telescope, to minimize the effects of multiple Coulomb scattering on the detector efficiency. The results of the run are shown in Table I. Columns 1 and 3 give the mean proton energies and energy spreads accepted by the telescope; these have been determined from curves similar to those shown in Fig. 1, computed for the various aluminum absorber

[22] A. Sommerfeld, *Atombau und Spektrallinien* (Friedrich Vieweg und Sohn, Braunschweig, Germany, 1939), Vol. 2, Chap. 6.

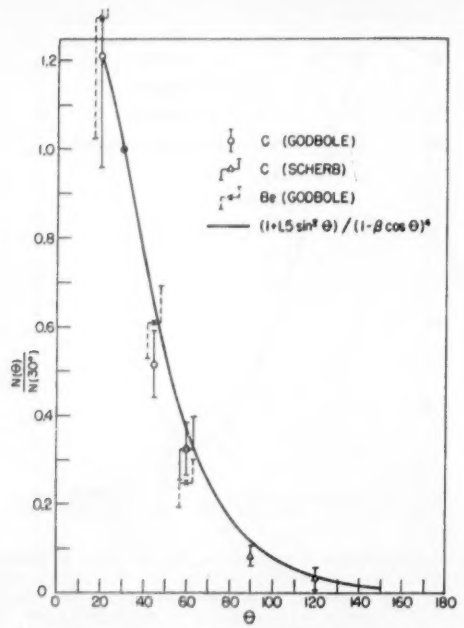

FIG. 8. The angular distribution in the laboratory of 203-Mev photoprotons from beryllium and carbon. The data marked "Scherb" were obtained at a later date than that marked "Godbole." The data are normalized to the value at 30°. The curve is a semiempirical fit to the data with $\beta=v/c$ of the protons.

thicknesses employed. Column 2 gives the observed ratios of the counting rates for the different aluminum absorber thicknesses to the counting rate for no absorber (average energy 126 Mev). Column 4 lists the corrections we have applied for the nuclear scattering and absorption of protons in the Al absorber, computed on the basis of an assumed constant (with energy) mean-free-path of 30 cm. The figures in column 5 represent the corrected ratios of the number of fast protons, per unit proton energy interval, to the number at 126 Mev. The errors given are purely statistical.

The results from column 5 of Table I are shown as a log-log plot in Fig. 9. It is seen that the number of protons falls off as $E^{-2.2}$ at the lower energies and as $E^{-7.6}$ at higher energies, with a relatively sharp break in the spectrum occurring at 193 Mev. The position of the break in the spectrum is, from these data, determined to within a few Mev.

The sharp break in the proton spectrum is in accordance with the "deuteron" model of Levinger.[13] At a laboratory angle of 30° and a maximum photon energy of 325 Mev, a static deuteron model would lead to a proton energy cutoff at 226 Mev. The cutoff becomes a break in the yield curve when account is taken of the motion of the nucleons inside a complex nucleus; however, this modification should not appreciably shift the position of the break. Nevertheless, the observed position of the break can be reconciled with the deuteron model provided it is assumed that our bremsstrahlung spectrum has actually started to fall off appreciably at ~300 Mev and, further, that the average proton has a binding of about ~15 Mev in a carbon nucleus. That this possible agreement may be somewhat fortuitous, will be seen in the subsequent discussion of Sec. IV B.

3. *Absolute Value of the Differential Cross Section*

In order to convert the relative cross-section measurements to absolute values, a measurement was made of the differential cross section for the production of 126-Mev protons at 45° to the beam. A thin plate of carbon, 1 cm thick, was mounted with its plane at 45° to the beam direction, so as to minimize the proton energy spread introduced by ionization energy loss in the target. The plate covered the entire area of the beam, thus allowing us to employ the beam calibration of Ratz.[23]

The value of the differential cross section obtained for the photoproduction by 325-Mev bremsstrahlung radiation per carbon nucleus of 126 Mev protons at 45° in the laboratory system is 0.40×10^{-30} cm²/Mev-steradian-Q.[24] The statistical uncertainty in this measurement is ±6 percent. However, the uncertainty of the calibration of the beam is considerably greater (as much as ~30 percent). Within these uncertainties the above value is in agreement with the value of 0.47×10^{-30} cm²/Mev-sterad-Q obtained by Keck[12] at the same angle and approximately the same energy.

Using the above value and the measured angular distribution, we obtain the values 0.45×10^{-30} cm²/Mev-sterad-Q for the differential cross section at 30°, and 2.22×10^{-30} cm²/Mev Q for the total cross section for the production of 126-Mev protons from carbon by 325-Mev bremsstrahlung radiation.

B. Z Dependence

Previous investigators have observed[12,14] that, at least over the range of energies, angles, and targets

TABLE I. The spectrum of photoprotons from carbon at 30° from 325-Mev bremsstrahlung.

Mean energy of protons (Mev)	Observed ratio of the No. of protons at energy E to that at 126 Mev	Energy spread accepted by telescope	Fraction of protons detected	Corrected ratio of the No. of protons at E to that at 126 Mev
126	1.000	18.0	0.960	1.000
148	0.591 ±0.05	15.8	0.907	0.72 ±0.07
165	0.395 ±0.04 0.415 ±0.04	14.7	0.859	0.55 ±0.04
186	0.252 ±0.03 0.282 ±0.03	13.6	0.808	0.42 ±0.03
203	0.153 ±0.015	12.7	0.770	0.27 ±0.03
212	0.098 ±0.011	12.5	0.739	0.186 ±0.025
243	0.030 ±0.007	11.6	0.654	0.068 ±0.013

[23] H. Ratz, Massachusetts Institute of Technology Master of Science Thesis, 1952 (unpublished).

[24] One Q, or equivalent quantum, corresponds to 325 Mev of photon energy; i.e., the number of Q is the energy in the beam divided by the maximum photon energy. Thus, for a $1/E$ spectrum we have, for the number of quanta of energy E, $dN=QdE/E$.

studied, the cross section for fast photoproton production in a given element is essentially proportional to the number of protons Z in the nucleus. Our own observations on this question are in agreement with those of the others, so we shall confine ourselves to a brief summary of our results.

Mention has been previously made of the comparison between carbon and beryllium. This comparison is interesting mainly in that the identity of protonic behavior is established over a very wide range of angles and energies (see Figs. 6–8). However, the nuclei involved are not very dissimilar.

Another series of observations, made in the rather early stages of this investigation, is summarized in Fig. 10. In this comparison targets of three elements—carbon, aluminum, and iron—were compared at four settings (absorber thickness) of our proton telescope at an angle of 45°. The targets were made to have the same diameters and equal absorption for the high-energy photons [equal values of the number of atoms $\times Z(Z+1)$]. In order to achieve this, it was necessary to construct the Al and Fe targets in the form of thin wafers. Due to the decreasing mass of the higher-Z targets, the corrections for proton energy loss in the targets also decreased with increasing Z; hence the fact that the points for the different targets, at the same telescope setting, are plotted at different proton energies.

The significant feature of Fig. 10 is that all the points, when plotted as yields per proton, lie on the same smooth curve. While the accuracy of this comparison is not especially high, the range of energies covered is rather greater than that of the previous work. At the time this comparison was made, in the early stages of our work, our understanding of the workings of the proton telescope were not complete, so no particular significance should be attached to the exact shape, slope, etc., of the curve drawn in Fig. 10. However, it should be noted that, for instance, had the true dependence of the photoproton production been on the

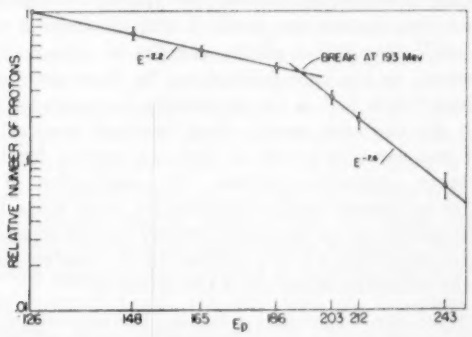

FIG. 9. The energy distribution of photoprotons from carbon at 30°. Both scales are logarithmic. The original data have been corrected for the attenuation in the telescope and the energy spread accepted by the telescope (see Table I). All the data are normalized to the value at 126 Mev.

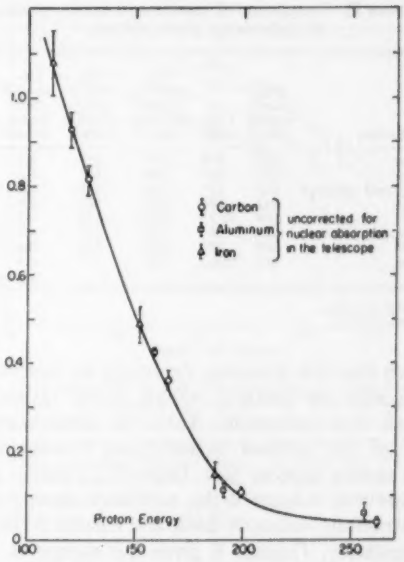

FIG. 10. The relative yields *per proton in the nucleus* of photoprotons from carbon, aluminum, and iron as a function of proton energy at 45°. Both scales are linear. The data are corrected for the energy spread accepted by the telescope but not for the attenuation in the telescope. (These are early data—see text.)

nuclear surface area rather than on Z, the points in Fig. 10 would have separated into three sets, one for each target, with the curve through the carbon set lying ~55 percent above that through the Fe set. Since indeed the cross section for charged photomeson production is more in proportion to the nuclear area than volume, the results shown in Fig. 10 helped to increase our confidence that the proton telescope was detecting mainly nucleons.

It should also be noted that these data are consistent with the linear dependence of the cross section on (NZ/A) which is predicted by the Levinger deuteron model;[13] the difference between a strict Z dependence and such a dependence would be only 7 percent for the case of a comparison of Fe and C targets.

IV. DISCUSSION

A. Comparison with Other Investigators

A detailed comparison with the results of other experiments in this field is difficult. Owing to the very rapid variation of the spectral properties with energy and angle, a slight difference in the conditions of angle or energy can lead to a large difference in the proton spectrum observed. In general, the various observations exhibit the same gross features, namely sharply forward-peaked angular distributions and power-law energy spectra; all the experiments show a break in the slope of the spectrum at some energy more-or-less consistent with the predictions of a deuteron model.

However, any attempt at a more critical comparison

TABLE II. Comparison of experiments on the spectra of high-energy photoprotons.

Observer	Max photon energy (Mev)	Lab. angle	Observed energy of break (Mev)	Predicted energy of break (Mev)	Observed slope below break	Observed slope above break
This paper	325	30°	193	211	2.2	7.6
This paper	325	45°	190	191	2.6	8.3
Rosengren and Dudley[a]	322	45°	140	189	1.7	3.0
This paper	325	60°	185	168	2.9	8.4
Keck[b]	320	67.5°	130	155	1.7	6
Rosengren and Dudley[a]	322	90°	140	122	1.7	4.4
This paper	325	90°	185	123	3.4	9.0
This paper	325	total	190	···	2.9	8.1

[a] See reference 14.
[b] See reference 12.

indicates that the situation, especially as regards comparison with the deuteron model, is still rather more confused than otherwise. Table II summarizes the results of the various investigators concerning the proton energy spectra (see Table II). Column 1 lists the observers, column 2 the maximum energy of the bremsstrahlung radiation used, and column 3 the angle of observation. Column 4 gives the energy at which the break in the proton spectrum was observed. (The observed values of lines 2, 4, 7, and 8—corresponding to the present paper—have been deduced from other observations, rather than measured directly, in a fashion to be described in the next section.) Column 5 lists the energies at which the break is predicted on the basis of a static deuteron model; the energies given are those corresponding to the maximum photon energy (column 2) minus 15 Mev for the nuclear binding. The last two columns list the observed slopes of the straight lines on log-log plots of the proton energy distributions below and above the "breaks" in the spectra, respectively.

It is clear from Table II that there exist serious discrepancies, both in the comparison with the predictions of the static deuteron model and the comparison between the various experiments. These discrepancies probably arise from a number of causes. In the first place, as has been discussed in Sec. II of this paper, the problem of eliminating completely the pi-meson background is quite difficult, especially at the higher proton energies or larger angles where the relative number of mesons incident on the telescope is exceedingly high. A small meson contamination in the highest-energy points can have a large effect, both on the energy of the "break" and on the slope of the curve above the "break." Since the techniques used by the various investigators, although similar in principle, differed in many details, the spurious backgrounds (probably small in all cases) could have been sufficiently different to account for some of the differences in the observed spectra.

However, even assuming ideal proton detection in all the experiments, the discrepancies of Table II could, in actual fact, be more apparent than real. Let us assume for instance that the proton spectrum does not, in fact, break sharply but, rather, has a monotonically increasing slope which changes most rapidly in the region of the "break" predicted by the static deuteron model.[25] The observed "breaks" might then simply result from the fact that a relatively small number of points have been recorded in each of the investigations, together with the desire of the investigators to represent the data in the form of straight lines on a log-log plot. It would also follow that the higher the energy range of the investigations the higher the apparent energy of the "break" and the greater the apparent slopes of the energy spectra, both below and above the "breaks." Since the measurements of this paper covered a range of higher energies than those of the previous investigations, this would help to account for some of the discrepancies observed in Table II.

However, the above considerations, while they may weaken the apparent contradictions between the various experiments, do not remove the most serious discrepancies between the observations and the "deuteron model," as will be seen in the following discussion.

B. Comparison with the Deuteron Model

There are essentially three aspects in which the experimental results have been compared with the model of Levinger,[13] in which it is assumed that the fast photoprotons originate from the photodisintegration of deuteron-like subunits within the nucleus. These are angular distributions, energy distributions, and total cross section. All of these have been touched upon in the preceding. However, these aspects are not unconnected, and it is of some interest to attempt to summarize the results of this comparison.

The angular distributions for 126-, 169-, and 203-Mev protons, plotted in Figs. 6–8, are quite different from those predicted in the paper of Levinger. The differences are manifest in two aspects: the positions of the maxima (if any) and the failure to observe a kinematical "cutoff."

According to Levinger, the angular distributions at the energies of our observations should show pronounced maxima in the region between 30° and 60°. According to our observations, the peaks (if they are there at all) lie well below 30° at all the energies of observation. However, as has been pointed out by Rosengren and Dudley,[14] this fact is not necessarily in contradiction with the deuteron model, since Levinger assumed a $\sin^2\theta$ angular distribution in the c.m. system for the deuteron photodisintegration; the assumption of a flatter or forward peaked distribution could move the peak sufficiently far forward to remove this discrepancy. Such a distribution is not excluded by the existing data on the photodisintegration of the deuteron.[26,27]

[25] Indeed the computations of Levinger (see reference 13), in which account is taken of the motion of the protons within the nucleus, point to just such a behavior.
[26] T. S. Benedict and W. M. Woodward, Phys. Rev. 85, 924 (1952).
[27] W. S. Gilbert and J. W. Rosengren, Phys. Rev. 88, 901 (1952).

The failure to observe a kinematical cutoff in the angular distributions is more difficult to reconcile with a deuteron model. For a static deuteron, the angular distributions plotted in Figs. 6–8 should cut off at ~90°, 60°, and 35°, respectively (account being taken of ~15-Mev binding per nucleon in the carbon nucleus). When consideration is given to the internal motion of nucleons within the nucleus, the kinematical cutoffs should at least manifest themselves by an abrupt change in the nature of the angular distributions above the angles, with the cross sections falling off much more rapidly beyond the cutoff angles. No such effect is observable in Figs. 6–8. Indeed, if anything, the data at 126 Mev indicate that the falloff is even less rapid than anticipated by the empirical relationship of Eq. (1).[28]

It might be argued that the more rapid decrease in the angular distribution for 203-Mev protons [$\alpha=1.5$ as compared to 3 for the lower energies, see Eq. (1)] is a manifestation of this effect. However, this change in the angular distributions is certainly considerably less striking than the effects predicted by the calculations of Levinger. Indeed, in order to reconcile our results with the deuteron model, it would be necessary to assume that the momentum distribution of the nucleons within a carbon nucleus contains a *very* large component of nucleons with relatively higher momenta than predicted by the Fermi distribution.

On the other hand, our energy distribution at 30° (Fig. 9) appears to manifest the expected kinematical cutoff, in a rather striking fashion, at a position more or less in agreement with the prediction of the deuteron model. This might be encouraging for the model, were it not for the fact, as seen in Table II, that this agreement does not carry over to other angles, when our observed angular distributions are taken seriously. This contradiction is made more clear by consideration of the curves in Fig. 11, from which the numbers exhibited in Table II have been extracted. The energy distributions plotted in Fig. 11, at 45°, 60°, 90°, and for the total cross section have been computed from the data at 30° (column 5 of Table I) and the assumption that the angular distributions are given by Eq. (1), with $\alpha=3$ for the four lower-energy points and $\alpha=1.5$ for the three high-energy points. However, points have also been plotted which were computed on the assumption of $\alpha=2$ at 186 Mev and $\alpha=1$ at 243 Mev, and it is clear that these alterations do not have a serious effect on the deduced energy distributions. It would appear difficult to reconcile these results with the deuteron model unless we are prepared to question the reality of the spectral break (as discussed, in the preceding section) and to assume that the dynamical effects of the internal motion of the nucleons within the nucleus

[28] However, a rough estimate of the effects of scattering within the carbon nucleus indicates that the empirical relationship may indeed fit well over the entire energy range (see reference 16).

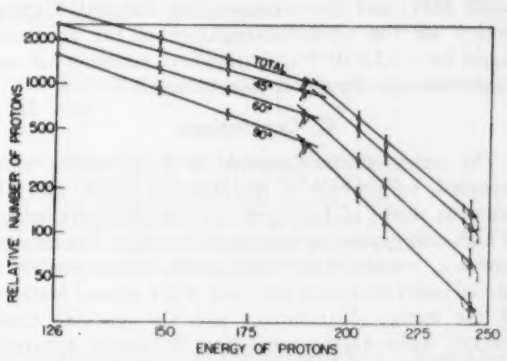

FIG. 11. Calculated energy distributions of photoprotons at various angles. Both scales are logarithmic. The relative number of protons at each angle is arbitrarily normalized to the value at 126 Mev. The values were computed from the data at 30° by means of the semiempirical formulas. The solid line points have a value of $\alpha=3$ from 126 Mev to 186 Mev and 1.5 from 203 Mev to 243 Mev. The dotted line points have a value of $\alpha=2$ at 186 Mev and a value of $\alpha=1$ at 243 Mev.

are considerably greater than indicated by the computations of Levinger.

It is perhaps of some interest, at this point, to remark once more on the empirical relationship, Eq. (1), which shows such surprisingly close agreement with the angular distribution data. Since this formula has been adopted from the atomic photoelectric effect, it is tempting to conclude that its applicability is evidence that we are dealing with a direct nuclear photoeffect. This conclusion is, however, for the time being unwarranted, since there does not exist a theory of the nuclear photoeffect at these energies. Nevertheless, it must be admitted that the authors find the suggestion difficult to avoid.

However, if we were indeed observing a direct nuclear photoeffect, we might also expect that the angular distributions of the emitted protons would depend on the states of initial angular momentum of the protons within the nucleus. It was for this purpose that we undertook a rather careful comparison between the angular distributions from beryllium and carbon, with the result that we were unable to observe any difference. Since, according to the shell model, the ratio of protons in a p state to those in an s state is 1:1 in Be and 2:1 in C, a difference of the type noted above might have been quite marked. These observations, then, would seem to indicate that we are not dealing with a direct photoeffect.

The absolute cross section for the production of 126-Mev protons (Sec. III A.3) is also quite large as compared to what would be expected on the basis of a direct photoeffect. Thus, if we neglect the nuclear recoil, the cross section per 126-Mev photon would be $126\times2.22\times10^{-30}$ cm^2 or 2.8×10^{-28} cm^2.

On the other hand, assuming a deuteron model, 126-Mev protons at 30° would result from photons of

$\sim$200 Mev, and the corresponding differential cross section for the photodisintegration of the deuteron would be $\sim 1.5 \times 10^{-29}$ cm^2/steradian, which is not inconsistent with the direct observations.[26,27]

C. Conclusions

The measurements described in the preceding were intended to provide a quantitative check on the deuteron model of Levinger[13] for the photoproduction of high-energy protons from complex nuclei. The results, however, remain rather ambiguous. They provide a partial confirmation on the basis of the general features of the energy distributions and the absolute cross section, while at the same time indicating apparent contradictions on the basis of the angular distributions. These contradictions may be a result of inadequate theoretical treatment of the momentum distribution of the protons within the carbon nucleus.

However, some of the contradictions indicated in the preceding may result from experimental difficulties, which should certainly be investigated further. In addition, it seems evident that a direct proof of the deuteron hypothesis, in the form of observation of the simultaneous emission of a neutron and a proton together with measurements of their angular correlations, would be highly desirable. More careful measurements of the energy distributions at various angles, to establish definitely the existence and the position of a kinematical cutoff, are also necessary before more precise conclusions can be drawn from the data. These problems are receiving further attention in our laboratory.

Finally, provided that a model for the origin of the high-energy photoprotons can be definitely established, accurate measurements of the type outlined above should provide useful information concerning the momentum distributions of nucleons within complex nuclei.

The authors wish to thank Professor P. Morrisson for his valuable discussions. We are very grateful to Professor W. L. Kraushaar for much of the electronic equipment employed in these measurements. It is also a pleasure to thank the members of the synchrotron staff and especially J. S. Clark for the many hours which were contributed to these experiments.

μ-Meson Decay Spectrum*

J. H. VILAIN† AND ROBERT W. WILLIAMS‡
Physics Department and Laboratory for Nuclear Science, Massachusetts Institute of Technology, Cambridge, Massachusetts

(Received February 15, 1954)

The energy spectrum of positrons from the decay of muons at rest has been measured, using a synchrotron as the meson source and a magnetic-field cloud chamber as the spectrometer. A total of 830 tracks was obtained, and the relation between this sample and the true decay spectrum is discussed in some detail; difficulties which may have led to the discrepancies among previously measured spectra are pointed out. A strict set of selection criteria reduced the sample to 280 tracks; from this it is found that the spectral intensity does not go to zero at the upper energy limit, but retains a large value. In terms of Michel's parameter, $\rho=0.50\pm0.13$.

I. INTRODUCTION

ALTHOUGH the general nature of the energy spectrum of electrons from μ-meson decay has been known for several years,[1] the published results on the spectral shape do not agree among themselves.[2–5] The speculation that this process is related to beta decay, or indeed that all "Fermi interactions" are in some sense the same,[6,7] lends interest to a determination of the spectrum; several recent theoretical papers[8] have assumed that the spectrum goes to zero at the upper energy limit. We describe here an experiment[9] which shows that the spectrum in fact does not go to zero; in Sec. IV we point out some considerations which tend to bring previous results into consonance with this conclusion. The possible physical significance of this finding is also discussed in Sec. IV.

II. APPARATUS AND METHOD

A. Experimental Layout and Procedure

As a source we used π mesons produced by the action of the gamma-ray beam from the M.I.T. 330-Mev electron synchrotron on a block of paraffin. An expansion-type cloud chamber, mounted horizontally in a magnetic field of 9000 gauss, was used to observe both the incoming meson and the positron from the $\pi-\mu-e$ decay that occurred after the meson was brought to rest. The experimental arrangement is shown schematically in Fig. 1(a) (plan) and Fig. 2 (elevation): the paraffin target was placed in the fringing field of the cloud-chamber magnet; those positive mesons which emerged at approximately 90° with momentum in a broad band centered around 60 Mev/c entered through one cloud-chamber wall, crossed the chamber, and stopped in the opposite wall.

By adding considerable lead shielding we were able to obtain clean pictures with full synchrotron intensity and a large target; nevertheless, it was necessary to trigger the cloud chamber by counter control to obtain a satisfactory rate of usable pictures. For this reason, the cloud-chamber wall in which the mesons stopped was actually an anthracene scintillation counter backed by a pair of large Lucite light pipes which led to magnetically shielded photomultipliers. The cloud chamber was triggered whenever a large pulse in the counter was followed within one to five microseconds by another pulse. This event corresponded to the arrival of the meson (which in general stopped in the Lucite) followed by the delayed emission of a decay electron. Figure 1(b) shows a vertical section through the counter, which was

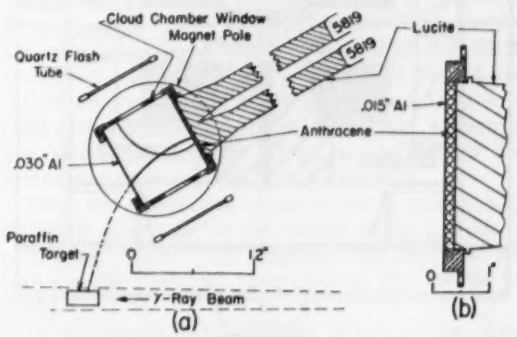

FIG. 1. (a) Plan view of the experimental arrangement, showing schematic trajectories of a meson and its decay electron. Shielding and thermal insulation are not shown. (b) Vertical section through the scintillation counter which comprises one wall of the cloud chamber.

* Supported in part by the joint program of the U. S. Office of Naval Research and the U. S. Atomic Energy Commission.

† Present address: Ecole Nationale Supérieure de Télécommunications, Paris.

‡ Presently on leave at Princeton University, Princeton, New Jersey.

[1] R. W. Thompson, Phys. Rev. **74**, 490 (1948); J. Steinberger, Phys. Rev. **74**, 500 (1948) and Phys. Rev. **75**, 1136 (1949); Leighton, Anderson, and Seriff, Phys. Rev. **75**, 1432 (1949).

[2] A. Lagarrigue and C. Peyrou, J. phys. radium **12**, 848 (1951); A. Lagarrigue, Compt. rend. **234**, 2060 (1952).

[3] Sagane, Gardner, and Hubbard, Phys. Rev. **82**, 557 (1951).

[4] H. W. Hubbard, University of California Radiation Laboratory Report UCRL-1623, 1952 (unpublished).

[5] Bramson, Seifert, and Havens, Phys. Rev. **88**, 304 (1952).

[6] Tiomno, Wheeler, and Rau, Revs. Modern Phys. **21**, 144 (1949).

[7] L. Michel, Nature **163**, 959 (1949); Proc. Phys. Soc. (London) **A63**, 514 (1950); Phys. Rev. **86**, 814 (1952); L. Michel and R. Stora, Compt. rend. **234**, 1257 (1952).

[8] D. C. Peaslee, Phys. Rev. **91**, 1447 (1953); E. J. Konopinsky and H. M. Mahmoud, Phys. Rev. **92**, 1045 (1953); R. Finkelstein and P. Kaus, Phys. Rev. **92**, 1316 (1953).

[9] A brief preliminary report has already been given: J. H. Vilain and R. W. Williams, Phys. Rev. **92**, 1586 (1953).

a $\frac{3}{16}\times 3\times 6$ in. composite crystal. The illuminated volume of the chamber was $3\times 7\frac{1}{2}\times 7\frac{1}{2}$ in. (a square cross section was chosen to facilitate the introduction of the counter). An example of a meson and its decay electron is shown in Fig. 3.

The cloud chamber was thermally isolated and maintained at constant temperature by thermostatted circulating water. The magnet was maintained at nearly constant temperature by hand adjustment of a pressure regulator in the cooling water input. With this precaution we could assume that constant current meant constant field. The current was held constant to ± 0.3 percent (maximum fluctuation) by precise electronic control of the voltage across the magnet combined with half-hourly checks of the magnet current proper.

The value of the field was determined with a flip coil-G.E. fluxmeter-mutual inductance apparatus which was calibrated in fields measured by the proton resonance. The longitudinal field was mapped with the same device (it varied by ± 10 percent) and the radial field was calculated from this map.

We obtained 830 pictures which clearly show a meson and its decay electron, out of a total of 4350 pictures. This proportion, and the absolute counting rates, are in rough agreement with our geometrical estimates.

B. Selection Criteria and Measurements

We wish to examine a sample from the energy spectrum of positrons resulting from the decay of μ mesons at rest.[10] Since the point of origin of the (positive) electron is not visible, great care must be taken to choose the sample in an unbiased way. The lower limit of acceptable kinetic energy[11] was set at 20 Mev (15 percent of the spectrum lies below 20 Mev).

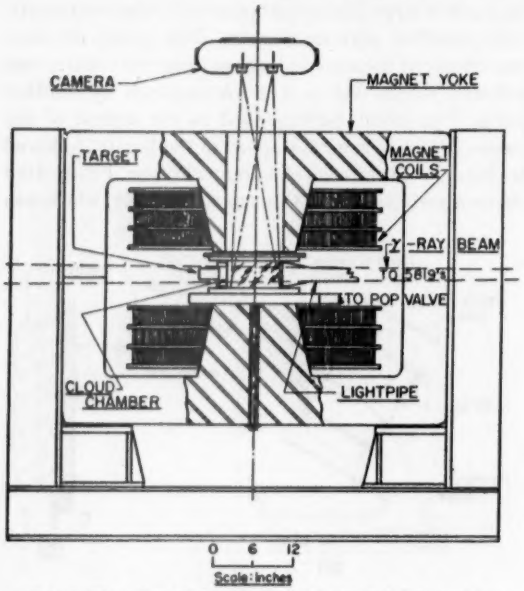

FIG. 2. Elevation of the magnet and cloud chamber with shielding removed.

Each accepted event was required to pass the following tests: (a) the electron trajectory, extended back into the counter, must intersect the meson end point within prescribed limits; (b) the location and initial direction determined by this extended trajectory must be such that the electron would have had a path length in the Lucite plus anthracene of less than 4.2 cm (10-Mev energy loss) regardless of its energy (within the limits 20 Mev to 52.4 Mev); (c) the location and initial direction must be such that the electron would have had a visible track in the cloud chamber of more than 5 cm of arc regardless of its energy (within the limits 20 Mev to 52.4 Mev).

This procedure is intended to insure that each electron which is accepted would have been seen and accepted had it had any other energy within the limits, and therefore is part of an unbiased sample. It is straightforward and safe (with reservations as noted below), and sacrifices a large number of tracks in the interest of great reduction of the principal source of systematic error. The alternative would be to calculate an acceptance-and-resolution function which could not be checked by experiment.

Electrons of lower energy will suffer more scattering in the lucite, so that reconstruction of their point and direction of origin is less certain. For this reason the limits of intersection for test (a) were calculated individually for each track, and were set at $\pm$ two standard deviations in the horizontal plane and $\pm$ three standard deviations vertically. The distribution in space of the meson end point was determined from the meson momentum as measured on the cloud-chamber film, plus calculated straggling and scattering. About 10 percent of the mesons decayed to μ mesons before entering the cloud chamber, but these were readily recognized because they led to intersection points considerably deeper in the Lucite. Happily only seventeen events had to be rejected because of poor intersection. At the same time we verified that the selection was sufficiently severe to exclude accidentally space-coincident electrons, by calculation based on background runs (the probability proved to be small that there would be even one accidental in the entire sample).

A difference in reconstruction accuracy between low- and high-energy trajectories might be expected to have an effect on tests (b) and (c); however, the effects are such as to cancel out to a good approximation.

Of the 830 tracks, 280 were accepted. The tests described above were made on an orthogonal projection

[10] Negative μ mesons present a special problem because they decay from bound "atomic" states. See C. E. Porter and H. Primakoff, Phys. Rev. 83, 849 (1951).

[11] The great advantages gained by a fairly high cut-off energy are not accompanied by much loss in information. Since we cannot determine the shape of the spectrum in detail with only a few hundred tracks, we must try to find a one-parameter description of our data, and it turns out that the description chosen is insensitive to the part of the spectrum below 20 Mev.

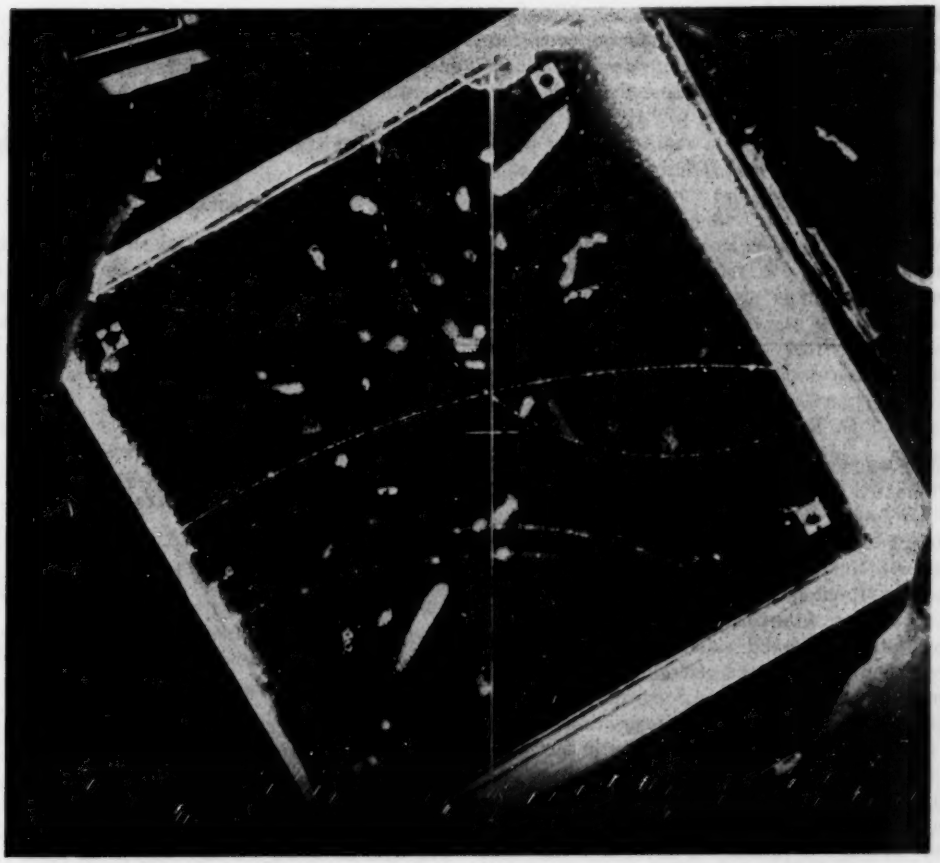

FIG. 3. Example of a meson (heavy track) and its associated decay electron (light track).

of the event.[12] To construct this projection and to supply geometrical information necessary to the determination of the electron energy we projected the two images of an event, through the lenses with which the pictures were taken, onto a translucent screen with one degree of freedom (vertical translation).

The observed momentum of each electron was computed from the curvature of its track image on the film. To achieve the necessary high accuracy, with tracks as short as 5 cm in many cases, it was necessary to measure track coordinates with a microscope fitted with a micrometer stage, and fit these coordinates to a circular arc. (Actually, of course, the coordinates are expanded, and fitted with an ellipse.) Because the track image is a conical projection of a helix (and, to a much lesser extent, because the magnetic field is not homogeneous) it will not actually be an exactly circular arc; the error we make by forcing a fit can be shown to average less than 0.1 percent.

Each track was corrected for the first-order effects of conical projection (average ± 6 percent) and radial component of magnetic field (average ± 0.7 percent). Average values for the second-order corrections, which are systematic, were found and applied to the sample as a whole; the largest terms were $+0.37$ percent and -0.26 percent. Momenta were computed from both right and left views for a few tracks; the agreement was within the expected errors, so the bulk of the measurements were made on one view only.

From the coordinates of five or seven points along the track (corrected for the motion of the gas during expansion) values of the magnetic field were read off, and the effective field computed by the method of Ascoli.[13]

To the energy of the electron as seen in the cloud chamber one must, of course, add the energy lost in the

[12] It might appear that test (c) involves consideration of those tracks that disappear out the top or bottom of the chamber as well as out the sides. One can easily show, however, that the length of arc of such tracks is independent of the momentum of the particle.

[13] G. Ascoli, thesis, Massachusetts Institute of Technology, 1951 (unpublished). We are indebted to Dr. Ascoli for sending us an elaboration of his elegant calculation.

lucite and anthracene. We used the calculation of Halpern and Hall[14] for water as a basis for our "collision loss" correction (which includes Čerenkov radiation). The average collision loss was 6 Mev; the upper limit allowed by our selection criteria was 10 Mev. Energy loss by bremsstrahlung presents a quite different problem: the most probable loss is zero but the average loss is quite appreciable, and fluctuations are large. The average path length in solid material, in our experiment, was 0.069 radiation lengths. Since the bremsstrahlung loss for each electron is not known, one must apply a bremsstrahlung distribution function to the family of theoretical (or empirical) spectra, and compare the resulting "folds" with the data. We have done this, using the calculation of Eyges.[15]

C. Estimate of Errors

We shall assume that the procedures outlined above have eliminated any possible sources of bias, and shall discuss here only errors in energy determination. Our estimates of the standard deviations describing important sources of uncertainty are detailed in Table I under the headings "Random" and "Systematic." Among the former, evaluation of the turbulence error presents some problems for a horizontal cloud chamber. We have measured counter-age tracks of cosmic-ray mesons of large zenith angle; the figure 1.5 percent is then an upper limit, since all of the measured curvature of these tracks is ascribed to turbulence, whereas in fact some of it is true magnetic deflection. The figure for multiple scattering corresponds to our gas filling of 1.3 atmospheres of argon. The combined random error of about 6 percent standard deviation will affect both the value and the uncertainty of the parameter (ρ) which we wish to determine from the data. Both effects could be completely accounted for by folding a Gaussian function into the family of theoretical curves; however, the extensive numerical work did not seem warranted, and we have followed a simpler procedure outlined in Part D.

TABLE I. Standard deviations assigned to the principal sources of error, expressed as *percent of the electron energy*.

Random errors (%)		Systematic errors (%)	
Multiple scattering	3	Energy loss in solid	0.7
Curvature measurement	3	Magnetic field	0.4
Path length in solid	2.5	Magnification	0.3
Geometrical factors	2	Meson mass	0.3
Turbulence	1.5		
Combined error	6	Combined error	0.9

Among the systematic errors the meson mass, which determines the maximum energy W and therefore the energy scale, deserves special mention. Several recent determinations[16] of M_μ, M_π, and the ratio M_π/M_μ are in good agreement with a value of $M_\mu=207.0$, and a standard deviation ± 0.6 does not seem unduly optimistic.

D. Statistical Analysis

Determination of a spectral shape in this type of observation depends on resolution—in which we include the effects of biases—and the number of counts which make up the sample. Since we have in general sacrificed the number of counts available in order to obtain good resolution, we cannot trace the shape of the curve in detail, but must determine one free parameter in a family of theoretical or empirical curves. If the decay scheme is assumed to be[17] $\mu\rightarrow e+\nu+\nu$, the energy spectrum which is calculated from a direct-interaction theory, in analogy with beta-decay theory, is[7]

$$P(E)=\frac{E(E^2-1)^{\frac{1}{2}}}{A+\eta B}\left[3(W-E)+2\rho\left(\frac{4}{3}E-W-\frac{1}{3E}\right)+3\eta\left(\frac{W}{E}-1\right)\right]dE,$$

where E is the electron total energy in units of $M_e c^2$, W its maximum value, $W=\frac{1}{2}[M_\mu c^2+(M_e^2c^2/M_\mu)]=52.9$ Mev, $A+\eta B$ is a normalizing factor depending on W, and ρ and η are functions of the coupling constants introduced in the theory; $0\leqq\rho\leqq 1$; $-1\leqq\eta\leqq 1$). The term involving η is small except for small E, where the common factor is small, so that it is a reasonable approximation to ignore this term, neglect 1 with respect to E, and obtain

$$P(E)dE=4(E^2/W^4)\{3(W-E)+2\rho[(4/3)E-W]\}dE.$$

This has become the standard form for interpreting experiments on μ decay.

This spectrum, folded with the bremsstrahlung loss and renormalized to the interval $0.4\leqq E/W\leqq 1$, is shown for three values of ρ in Fig. 4. On the same graph our results are plotted in histogram form; it is clear by inspection that of the three curves only $\rho=0.5$ will fit the data. To obtain quantitative results for the best value of ρ, and its standard deviation, we have available several standard procedures of sampling theory. The most efficient procedure (in the sense that the standard deviation is smallest) is the method of maximum

[14] O. Halpern and H. Hall, Phys. Rev. **73**, 477 (1948).

[15] L. Eyges, Phys. Rev. **76**, 264 (1949). The actual calculations are clumsy, because we apply the bremsstrahlung fold on the basis of an average path length, while we add the collision loss to each electron energy individually. Eyges' formula takes collision loss into account. We therefore have to add the average collision loss back on to the folded spectrum before comparing it with the data.

[16] Smith, Birnbaum, and Barkas, Phys. Rev. **91**, 765 (1953); G. Ascoli, Phys. Rev. **90**, 1079 (1953); Lederman, Booth, Byfield, and Kessler, Phys. Rev. **83**, 685 (1951) (ratio m_π/m_μ); Val L. Fitch (private communication) (m_μ from meson-atomic spectroscopy).

[17] Bransom, Seifert, and Havens, reference 5, have observed the annihilation of the positron in flight, thus proving that it is indeed an ordinary positron.

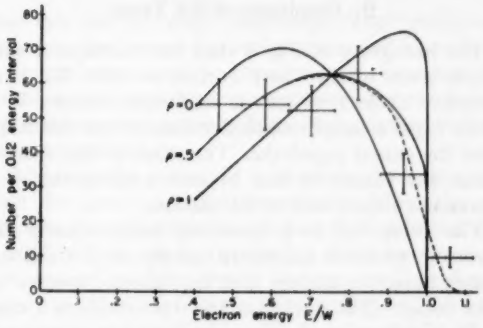

FIG. 4. Calculated spectra for three values of ρ, folded with the radiation-loss distribution function and normalized over the interval $0.4 \leq E/W \leq 1.0$. The dotted line shows the effect of folding in the resolution in energy measurement. The experimental data are lumped into numbers of events per 0.12 energy interval.

likelihood,[18] which maximizes the probability that this particular sample was drawn from the specified population.

Since this method is very tedious, we have first utilized the simpler method of comparing theoretical and experimental moments, to obtain a close approximation to the final answer. The moment method also affords an easy way to correct the results for the effect of the 6 percent random error in energy measurement. The dotted line in Fig. 4 shows the $\rho=0.5$ spectrum after folding in the error; the calculated reduction in ρ is 0.05. Results from the second, third, and fourth moments are $\rho=0.46$, 0.50, and 0.51, respectively. The corresponding[19] value from the maximum likelihood method is $\rho=0.49\pm0.10$.

To see how large an effect the bremsstrahlung correction made, we calculated ρ assuming no radiation loss, and found $\rho=0.31\pm0.07$. Since this represents a large correction, its accuracy was checked by dividing the data in half according to whether the path length in solid material was greater or less than the median. The resulting values of ρ agreed with each other within 0.01, showing that the correction is sound.

The spectrum with which we compare our data has been calculated with neglect of radiative processes. However, an approximate evaluation of the energy lost to "inner bremsstrahlung"[20] shows that it averages about 0.6 percent of the maximum energy of the electron. This will reduce the measured value of ρ in a way which depends somewhat on how the data are analyzed; in our case we find that our measured ρ should be raised by about 0.01 to 0.50.

[18] H. Cramer, *Mathematical Methods of Statistics* (Princeton University Press, Princeton, New Jersey, 1951), p. 498.

[19] Actually the maximum-likelihood calculations were finished before we corrected the meson mass from its old value ($209m_e$). We computed the change in ρ caused by this scale change by use of the moment method.

[20] A. Lenard, Phys. Rev. **90**, 968 (1953).

Finally, the standard deviations in ρ caused by the 6 percent random error and 0.9 percent systematic error in energy measurement are computed to be ±0.04 and ±0.072, respectively. The combined standard error in ρ is, therefore, $(0.10^2+0.04^2+0.072^2)^{\frac{1}{2}}=0.13$.

III. RESULTS

The analysis of the preceding section leads to the value $\rho=0.50\pm0.13$, which means that the energy spectrum of the decay electrons is well represented by

$$P(E)dE=\left(8\frac{E^2}{W^2}-\frac{20}{3}\frac{E^3}{W^3}\right)\frac{dE}{W}.$$

This spectrum is shown in Fig. 5, along with the spectra $\rho=0$ and $\rho=1$ for comparison. Taking the maximum kinetic energy, $W-M_e c^2$, as 52.4 Mev, the average energy is 35 Mev, and the most probable energy is 42 Mev. Geometrically, ρ is just $\frac{3}{8}$ times the intercept of the normalized spectrum at the maximum energy, and we see that this intercept is quite high, nearly as high as the maximum point of the curve.

The principal contribution to the standard deviation in ρ is the statistical fluctuation due to the finite size of the sample; in the limit of large numbers (which our sample fulfills fairly well) this leads to a normal (Gaussian) distribution for the probability that ρ has a value different from 0.50. Since the magnitudes of the systematic errors have been included in a fairly conservative way, we feel that the quoted combined error can safely be regarded as describing a normal distribution; in other words, the chance that ρ will be as high as 0.75, for example, is about 0.03; the chance that it will be zero is less than 10^{-4}.

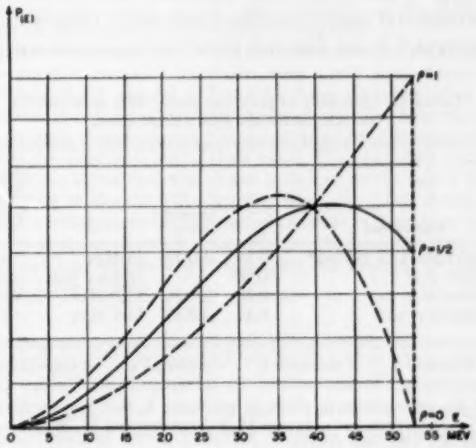

FIG. 5. The spectrum of decay electrons as determined by this experiment is the solid curve, $\rho=\frac{1}{2}$. Dashed curves show $\rho=0$ and $\rho=1$ for comparison.

IV. DISCUSSION

A. Previous Work

The previously published[3–6] experimental results which yield quantitative statements about the meson decay spectrum are summarized in Table II. The column labeled "ρ corrected approximately for m_μ" is an estimate of the result expected if W had been taken as 52.9 Mev. The change in ρ for a change in W depends somewhat on the method of analysis: in our experiment $\delta\rho = -8\delta W/W$; in that of Bramson *et al.* $\delta\rho = -7\delta W/W$. Two points are clear from Table II: (a) the results as published are in definite disagreement, but the corrected results, except for the work of Sagane *et al.*, are in reasonable harmony with our result; (b) the correction can easily be quite large.

We suggest that the effect of error in the absolute energy scale (which includes both the value of the meson mass and the accuracy of the energy calibration) has not been treated adequately in the results shown in Table II, and that this fact is mainly responsible for the apparent discrepancies. Uncertainty in the energy scale (i.e., in W) may be treated as it has been in this paper, by an estimate of δW and its effect on $\delta\rho$; presumably the rather large error quoted by Hubbard[4] includes such an estimate. Alternatively, one may determine W from the data along with ρ, using a sort of internal calibration. This was done by Lagarrigue and Peyrou (the method is explained in reference 2) and presumably by Bramson *et al.*[21] However, determination of *two* parameters from the same set of data results in a larger statistical error for each of them, and this consideration was not included in the quoted errors. The same consideration probably applies to the work of Sagane *et al.*,[3] who derive values for both W and the intercept [which is $(8/3)\rho$] from their data. Inspection of Fig. 4 will show that statistical fluctuations and instrumental resolution effects can easily mask a finite intercept,[22] if one does not know the maximum energy.

TABLE II. Summary of previous work, with approximate corrections for the new meson mass.

Experiment	ρ	Quoted error	W	ρ corrected approximately for m_μ
Lagarrigue and Peyrou[a]	0.19	±0.13	55 Mev	~0.4
Sagane *et al.*[b]	<0.06	···	53.5±2 Mev	<0.1
Hubbard[c]	0.26	±0.26	53.7 Mev	~0.4
Bramson *et al.*[d]	0.41	±0.13	53.6 Mev	~0.5

[a] Reference 2. [b] Reference 3. [c] Reference 4. [d] Reference 5.

[21] No explanation is given in reference 5, but this method is implied in a previous note; see H. J. Bramson and W. W. Havens, Phys. Rev. 83, 861 (1951).

[22] It was reported at the Rochester Conference on High Energy Physics, January, 1954, that the resolution of Sagane's instrument has now been improved to the point where the finite intercept is visible.

B. Goodness-of-Fit Tests

The histogram of Fig. 4 does not correspond very closely even to the "best" curve, $\rho = 0.50$. We have therefore made a χ^2 test to determine whether it is likely to get a sample which deviates at least this much from the parent population. The result is that there is about one chance in four of such a deviation, so it represents a quite normal fluctuation.

The curve for $\rho = \frac{1}{2}$ resembles rather closely the spectrum which is calculated purely on a statistical weight basis,[23] in analogy with the "allowed spectra" of beta decay. (The statistical spectrum contains a term in E^4, and therefore does not correspond exactly to any value of ρ.) Applying the χ^2 test, we find that our data could not distinguish between $\rho = \frac{1}{2}$ and the statistical curve; indeed, it would require at least 50 000 counts even with perfect resolution to distinguish between them. Evidently the agreement between the observed spectral shape and one form of the direct-interaction theory of μ-meson decay does not constitute a strong confirmation for that theory.

C. The Nature of the Interaction

The theory of μ-meson decay assumes, in analogy with beta-decay theory, that the interaction between meson, electron, and neutrino fields is a linear combination of the five invariant combinations of four Fermi-particle operators. The parameter ρ, which appears in the theory as a function of the five coupling constants, has a functional form depending on the ordering of the operators and on the question of distinguishability of the two neutrinos. A particular value of ρ, therefore, does not uniquely select one type of interaction (such as scalar, vector, etc.). Among the (infinitely many) combinations which will yield $\rho = \frac{1}{2}$ is the one for which there is no ambiguity associated with the ordering of the operators, the Wigner-Critchfield combination.[24] This interaction is antisymmetric under exchange of particles, and therefore is effectively independent of the order chosen for the operators. Aside from this symmetry property, however (whose physical significance is unknown), there is no *a priori* reason to suppose that the Wigner-Critchfield combination is correct.

The hypothesis of a universal Fermi interaction, i.e., that μ decay and beta decay are in some sense the same process, can be tested by inquiring whether the combination of coupling constants which explains beta-decay experiments can also lead to the correct value of ρ and the meson lifetime. Michel and Wightman[25] have recently investigated this question, for $\rho = 0.50$, and find that there are several combinations which make

[23] E. Fermi, *Elementary Particles* (Yale University Press, New Haven, 1951), p. 44.

[24] For a complete discussion of these points see reference 7, and also L. Michel, thesis, Sorbonne, 1953 (unpublished).

[25] L. Michel and A. S. Wightman, Phys. Rev. 93, 354 (1954).

the two sets of data compatible. They point out, however, that recent theoretical attempts[8] to motivate a particular connection between the two processes (for example, by symmetry arguments) and therefore eliminate the remaining ambiguities, are in conflict with the experimental results.

The foregoing discussion is based on the assumption that the decay process is $\mu \rightarrow e+\nu+\nu$, where the two neutrinos may be either identical or distinguishable (for $\rho<0.75$ either case is possible). A finite rest mass for the neutral particles would be very hard to detect, since the difference between the observed and expected maximum energies, $\delta=W_0-W_{\text{observed}}$, cannot be measured with much precision unless one has an *a priori* knowledge of ρ; and even a small δ leads to a large value of the mass of the neutrals: $M_{\text{neutrals}}=(2M_\mu\delta/c^2)^{\frac{1}{2}}$. Thus an M_{neutrals} as large as 20 electron masses would go undetected.

V. SUMMARY

A reexamination of the experimental problems relating to a determination of the energy spectrum of positrons from μ^+ decay has shown that the result is critically sensitive to the combination of finite resolution and errors in the energy scale. Our finding is that the spectrum has a large intercept at the upper energy limit; in terms of Michel's parameter, $\rho=0.50\pm0.13$, where the standard deviation includes estimates of the systematic errors.

The often-mentioned striking similarity between μ decay and beta decay is not diminished by this result; however, no satisfactory answer is available to the question of the nature of the relation between the two processes.

ACKNOWLEDGMENTS

We are indebted to J. S. Clark and the entire synchrotron staff for their assistance and cooperation, and to Seymour Weiner for aid in building and operating the equipment. The initial design and construction of the experiment was mainly the work of V. P. Henri; G. de Saussure and D. A. Hill also contributed to its successful operation; many others have contributed both labor and valuable advice.

The completion of this work was made possible by the repeated leaves of absence which the French Service des Télécommunications generously granted to one of us (J.H.V.).

PHYSICAL REVIEW VOLUME 94, NUMBER 4 MAY 15, 1954

Cosmic Radiation Intensity-Time Variations and Their Origin. IV. Increases Associated with Solar Flares*†

JOHN FIROR‡
Institute for Nuclear Studies and Department of Physics, University of Chicago, Chicago, Illinois
(Received November 17, 1953)

The distribution on the earth of the impact points for particles of magnetic rigidities 1 to 10 Bv, which originally approach the earth from the direction of the sun, is derived, using principally the published results of numerical integrations of cosmic-ray orbits and model experiments on the motion of charged particles in a dipole magnetic field. Three impact zones for such particles are discussed. Two of these zones include only a small range of local times, and for the special case of the sun in the plane of the geomagnetic equator, are centered near 4 A.M. and 9 A.M. The third zone has no strong local time dependence. Assuming the source of charged particles to subtend a finite angle at the earth, the relative counting rates for detectors in the three zones are estimated. The counting rate due to particles from the sun is expected to be three to seven times larger in the morning zones than in the background, or nonlocal-time-dependent, zone. The morning impact zones are shown to have a seasonal motion of several hours in local time.

Reports of observations made during four large increases of cosmic-ray intensity at the times of solar flares are compared with the distribution predicted for particles from the sun. The observed increases agree with the predicted distribution and counting rate except at very high latitudes on the earth. A possible reason for this discrepancy is suggested.

Cosmic-ray data from the Climax neutron detectors are analyzed for possible increases associated with small solar flares. An increase of $\approx$1 percent is found for flares occurring when the detector is in a morning impact zone for particles from the sun. No increase of more than $\approx$0.3 percent is found for flares occurring when the detector is not in these zones. The mean daily cycle of cosmic-ray intensity is also shown to depend on the rate of flares occurring on the sun. The intensity curve is peaked during the early morning hours for flare periods relative to periods in which few or no flares occurred, in agreement with the supposition that new particles approach the earth from the direction of the sun at the times of flares.

I. INTRODUCTION

A. Time Variations of Cosmic Rays

IT has long been known that the cosmic-ray intensity varies with time. Some terrestrial phenomena can be related to the cosmic-ray variations and that part of the variations eliminated (as in the case of the barometric pressure), but after carefully correcting for atmospheric effects there remains to date significant varia-

* Assisted by the Office of Scientific Research, Air Research and Development Command, U. S. Air Force.

† Based on a dissertation submitted in partial fulfillment of the requirements for the degree of Doctor of Philosophy in the Department of Physics, University of Chicago.

‡ Present address: Department of Terrestrial Magnetism, Carnegie Institution of Washington, Washington 15, D. C.

tions which are not known to be related to any purely terrestrial phenomena. These residual variations, which may well be due to variations of the primary cosmic rays, can by their periodicities and their statistical associations with astronomical phenomena, give clues to the origin of the cosmic rays, or at least to the solar and other influences on cosmic rays.

In this paper some variations which can be related to visually observed occurrences on the sun will be discussed.

B. Large Solar Flare Effects

On four occasions during the last twelve years the cosmic-ray intensity has been observed[1] to increase sharply for an hour or two following the beginning on the sun of large chromospheric eruptions. In three cases the "solar flare" was actually seen; in all four cases radio fadeouts of the type associated with solar flares were recorded. The cosmic-ray increase began in one case 15 minutes after the beginning of the flare and fadeout. In the other cases the time was perhaps as much as an hour.

A typical solar flare[2–4] is a region in the chromosphere having a projected area of a few hundred millionths of the visible disk of the sun and which emits light in the hydrogen and other lines with a greater intensity than the steady background of the solar disk. Flares usually start suddenly, reach maximum intensity in a few minutes, and disappear within an hour. Many variations from the typical behavior have been observed, for example, "pulsing" flares with repeated maxima of intensity, multiple flares (several separate but simultaneous bright spots), flares lasting several hours, flares reaching maximum intensity an hour or more after their beginning, flares lasting less than five minutes, etc. Observatories usually report the times of beginning, maximum, and end of the flare, the area, the intensity in the center of the H_α line, and the line width of the H_α line. Flares are also given an "importance" rating on a scale of 1,2,3 with sometimes + or − added. This scale is based mainly on area (area between zero and 300 millionths = importance 1, 300 to 750 = importance 2, above 750 = importance 3), but the limits are not rigid and the rating is frequently adjusted if the flare is exceptionally bright or weak for its area. The importance ratings are thus a somewhat subjective measure, but they serve to roughly rank flares as to size and intensity.

The three flares observed at the times of three of the cosmic-ray increases were all larger in area, of higher intensity, and the width of the H_α line was greater than for the average flare. The flare observations for these three events are summarized in Table I.[3,5–11]

The magnitude of the cosmic-ray increase in each of the large events depended on the latitude and longitude of the observing station. None of the increases was observed (with amplitude >2 percent) at Huancayo, near the geomagnetic equator. An ionization chamber at Teloyucan, Mexico (geomagnetic latitude $\lambda = 30°$) did not show the increase for the one event occurring during its operation. These facts indicate that the new particles arriving at the top of the atmosphere were charged and that only a small percentage of them had magnetic rigidities (pc/Ze) of more than the cutoff at $\lambda = 30°$ (≈ 10 Bv).

For one event a local production neutron monitor and a counter telescope at the same location observed the increase. The counter telescope recorded[12] an increase of ≈ 10 percent while the neutron rate[13] was ≈ 550 percent high. These observations indicate[13] that the new particles have for the most part rigidities of less than 5 Bv.

The close time connection between the solar flare and the cosmic-ray increase in each of these events and the large magnitude of the increases leave no doubt that additional particles are arriving from the region of the sun at these times. We will examine here the question of whether a simple picture—positively charged particles of rigidities 1 to 10 Bv leaving the region of the sun and moving toward the earth under the influence *only* of the earth's dipole magnetic field—can account for the observed facts. Also, using the results of such an analysis, the cosmic-ray intensity recorded by a local production neutron monitor will be examined for increases associated with small solar flares.

C. Related Work

Elliot[14] and Biermann[15] have, in two recent review articles, summarized some of the observations of the four large solar flare effects. Previously an article by Ehmert[16] discussed three of the increases in terms of particles coming from the sun. Ehmert shows, using a few orbits of cosmic-ray particles integrated by Störmer,

[1] Forbush, Stinchcomb, and Schein, Phys. Rev. **79**, 501 (1950).
[2] R. G. Giovanelli, Astrophys. J. **91**, 334 (1940).
[3] M. A. Ellison, Monthly Notices Roy. Astron. Soc. **109**, 3 (1949).
[4] R. S. Richardson, Astrophys. J. **114**, 356 (1951).
[5] International Astronomical Union, *Quarterly Bulletin on Solar Activity* (Eidgen. Sternwarte, Zurich, 1942–49), Nos. 57–88.
[6] H. W. Newton, Observatory **64**, 260 (1942).
[7] M. A. Ellison, Nature **158**, 450 (1946).
[8] R. Muller *et al.*, J. Atm. and Terrest. Phys. **1**, 37 (1950).
[9] A. C. B. Lovell and C. J. Banwell, Nature **158**, 517 (1946).
[10] M. A. Ellison and M. Conway, Observatory **70**, 77 (1950).
[11] Central Radio Propagation Laboratory, "Ionospheric Data," (Natl. Bur. Standards, Washington, D. C., 1949–1953), Nos. F-64 to F-108.
[12] H. Elliot, as reported by E. P. George, *Progress in Cosmic Ray Physics* (North Holland Publishing Company, Amsterdam, 1952), p. 422.
[13] N. Adams and H. J. J. Braddick, Z. Naturforsch. **6a**, 592 (1951).
[14] H. Elliot, *Progress in Cosmic Ray Physics* (North Holland Publishing Company, Amsterdam, 1952), Chap. VIII.
[15] L. Biermann, *Kosmische Strahlung* (Springer-Verlag, Berlin, 1953).
[16] A. Ehmert, Z. Naturforsch. **3a**, 264 (1948).

that the distribution of the increase of 28 February 1942, which was observed in America but not in Germany, indicates that positive particles are arriving from the direction of the sun. Ehmert further examines his counter telescope data for obvious increases lasting a few hours and is able to relate some of them to flares. Clay[17] in Holland also finds many increases and is also able to relate some of them to solar flares.

Schlüter[18] has integrated twenty trajectories of cosmic-ray particles using the method originated by Störmer, in which particles are assumed to be initially moving along a line parallel to the sun-earth line. He concludes from an examination of the impact points on the earth of these orbits that for positive particles from the sun there should be a sharp maximum near 0900 local time, and he regards the observation of one of the large increases in Germany in the afternoon as in disagreement with the theory. Using Störmer's *null-bahnen*, i.e., orbits which would pass through the dipole if extended, as representative of all orbits striking the earth, Schlüter discusses the seasonal change in the impact points on the earth for particles from the sun, as well as the existence of forbidden zones near the poles of the earth for solar particles. The observation of the increases at Godhavn, Greenland ($\lambda = 80°$) he also regards as in disagreement with the theory, since this station lies in such a forbidden region.

TABLE I. Observations of three large solar flares.

Date	Observatory	Time of Obs. (UT)	Importance	References
28 Feb. 1942	Arcetri	1100	3	a
	Sherborne	1242–1522	3	a,b
	Greenwich	1415–1505	2	a,c
		Radio fadeout at 1107		c
25 July 1946	Meudon	1504–1830	3+	a
	Sherborne	1513–1527	2	a
	Zurich	1610–1800	3+	a
	Cambridge	1612–1740	3	a
	Sherborne	1615–1810	3+	a,d
	Mt. Wilson	1621–2030	3+	a
		Radio fadeout at 1615		d
		Radio noise burst at 1624		e
19 Nov. 1949	Wendelstein	1029–1119	3	a,f
	Edinburgh	1030–1209	3+	a,g
	Greenwich	1037–1130	3	a
	Ondrejov	1037–1057	2+	a
		Radio fadeout at 1030		f,h
		Solar flare effect in magnetogram		f

[a] See reference 5.
[b] See reference 3.
[c] See reference 6.
[d] See reference 7.
[e] See reference 9.
[f] See reference 8.
[g] See reference 10.
[h] See reference 11.

II. IMPACT POINTS AND TRAJECTORIES

A. Known Orbits

In order to discuss the distribution on the earth of the solar-flare-connected increases the answer to the following question is sought: If particles leave a point source far from the earth and travel in straight lines until influenced by the earth's magnetic field, where will they strike the earth? The magnetic field of the earth can be represented to a good approximation by the field of a dipole near the center of the earth,[19] and the equations of motion for a charged particle moving in a dipole magnetic field are well known,[20] but no general solution to these equations has been found. However, a partial answer to the above question can be found in terms of numerical integrations of particular trajectories and by model experiments.

Trajectories of charged particles in a dipole magnetic field have been integrated by Störmer,[21] Dwight,[22] and Schlüter,[18] and model experiments have been performed by Malmfors[23] and Brunberg.[24] In the case of the orbits integrated by Dwight and some of the orbits integrated by Störmer, the computation was carried out by considering the path of a negatively charged particle projected vertically away from the earth. A positive particle will follow the same path when approaching the earth. This method of integration insures that the final orbits will be of interest in connection with a cosmic-ray detector deep in the atmosphere, since vertically incident particles are the most efficient in producing counts in such a detector.

In the model experiments electrons were projected away from a uniformly magnetized sphere and the direction of motion of the electrons when far from the sphere measured. Most of the orbits so investigated were vertically "incident" at the sphere. In both the integrations and the model experiments the results are in the form of particular trajectories or impact points on the earth, so it is necessary in order to get a more complete picture to interpolate between the known orbits and, to some extent, to extrapolate beyond the known orbits.

For our purposes an orbit is sufficiently well described by four angles and the rigidity of the particle. The four angles are λ, the latitude of incidence on the earth; λ_s, the latitude of the particle when very far from the earth (Dwight's "latitude of the asymptotic velocity vector," or, more simply, source latitude); β_s, longitude

[17] J. Clay, Proc. Koninkl. Ned. Akad. Wetenschap. **52**, 899 (1949).
[18] A. Schlüter, Z. Naturforsch. **6a**, 613 (1951).
[19] S. Chapman and J. Bartels, *Geomagnetism* (Clarendon Press, Oxford, 1940), Chap. XVIII.
[20] C. Störmer, Z. Astrophys. **3**, 31 (1931).
[21] C. Störmer, Astrophysica Norv. **1**, 1 (1934); *Book of the Opening* (Rice Institute, Houston, 1912), Vol. 3.
[22] K. Dwight, Phys. Rev. **78**, 40 (1950).
[23] K. G. Malmfors, Arkiv. Mat. Astron. Fysik. **A32**, No. 8 (1945).
[24] E. Brunberg, J. Geophys. Research **58**, 272 (1953).

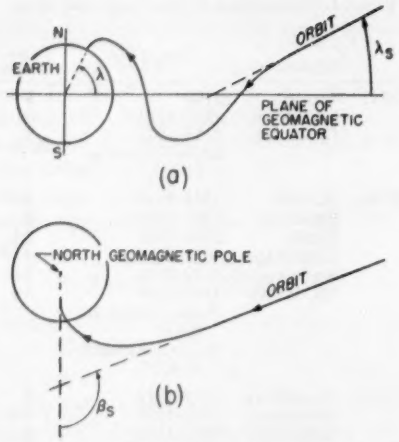

FIG. 1. Angles used to describe cosmic-ray orbits. (a) Orbit in the meridian plane which moves with the particle, showing the latitude of incidence λ and the latitude of the asymptotic velocity vector λ_s. (b) Projection of the orbit on the equatorial plane. Angle β_s is the longitude of impact relative to the source. Orbit shown is one of the 0400 group of paths.

of the source relative to the point of incidence (longitude of the asymptotic velocity vector); and the zenith angle of incidence. The latitudes and longitude, which are shown in Fig. 1, are in geomagnetic coordinates; these may be converted to geographic coordinates by formula or by graphs given by McNish.[25]

As a check on the accuracy of the numerical integrations and as an indication of the reliability of the model experiments, the results of the different workers can be compared where their orbits overlap. For example, in Fig. 2 is plotted, for particles of 6-Bv rigidity, the latitude of impact on the earth as a function of the latitude of the source. Points show integrated orbits[26] by Störmer and Dwight and model experiment orbits by Malmfors. Such comparisons indicate that the agreement is always within a degree or two for the integrated orbits and within five degrees for the measured orbits. However, Dwight's *extrapolations* to lower rigidities (2 and 1 Bv) differ by as much as 8 or 9 degrees in the asymptotic latitude from the model experiments of Malmfors. Therefore, a vertically incident orbit of 2-Bv rigidity was numerically integrated, and it was found that the extrapolations in reference 22 are in error and the model experiment orbits in this rigidity range essentially correct. The angles describing the orbit integrated by the present author are $\lambda = 60°$, $\lambda_s = -20.7°$, $\beta_s = 78.4°$.

New curves have therefore been constructed, similar to Figs. 7 and 8 in reference 22, showing the behavior of the impact points on the earth as a function of rigidity and of the latitude of the source. These curves are shown in Figs. 3 and 4. In constructing these curves all of the available orbits (about 80 in all) which arrive vertically have been employed, as well as some of Störmer's *nullbahnen*. The latter are near vertical incidence for the rigidities considered here.

Figure 3 is simply an extended and corrected version of the similar graph in Dwight's paper. Figure 4, however, is somewhat different from the corresponding graph in reference 22. In that paper is plotted the longitude of the source against the latitude of incidence. Here we plot longitude against latitude of source. In the rigidity range 1 to 10 Bv such curves do not depend strongly on rigidity and form a narrow band, only about an hour wide. This band, essentially the envelope of the 1- to 10-Bv curves, is what is shown in Fig. 4. In this paper we will always be interested in impact "zones" on the earth for particles from the sun, and these zones will be several hours wide. Hence a plot such as Fig. 4, which does not have rigidity as a parameter, is useful in easily constructing impact zones for various situations.

To determine the impact point on the earth for a particle of a certain rigidity leaving a point source far from the earth one notes in Fig. 3 the intersection of the line representing the latitude of the source with the curve of orbits of the desired rigidity. The abscissas of the intersections give the latitudes on the earth of possible impact points. Then using these latitudes and Fig. 7 of Dwight's paper, or using Fig. 4 of this paper, one gets the longitudes, relative to the source, of the impact points.

In Fig. 5 are plotted as smooth curves the impact points in the northern hemisphere for particles leaving a point source far from the earth and in the plane of the geomagnetic equator, and arriving at the earth with vertical or near vertical incidence. Also shown are the impact points of some orbits integrated by Schlüter which arrive with large zenith angles. The line attached

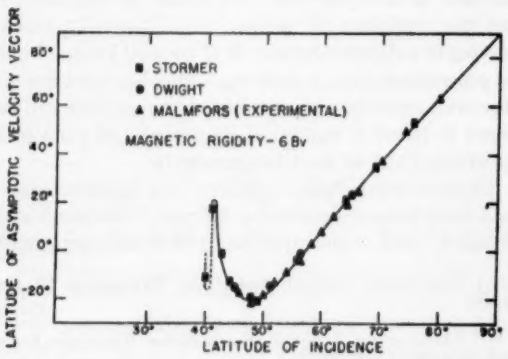

FIG. 2. Example of comparison of the cosmic-ray orbits derived by different workers. The Störmer and the Dwight orbits were obtained from numerical integrations of the equations of motion; the Malmfors orbits are from model experiments.

[25] A. G. McNish, Terrestrial Magnetism and Atm. Elec. 41, 37 (1936).

[26] It is necessary, when making these comparisons, to reduce all of the orbits given by the different workers to a common value of dipole moment for the earth. Störmer and Schlüter used an older value (8.4×10^{25} gauss-cm^3), whereas the others used 8.1×10^{25}.

to each Schlüter orbit in Fig. 5 is a projection on the earth's surface of the velocity vector of the particle at the time of arrival. The length marked "E" in the figure gives the reference length of the velocity vector. Later we wish to identify the source with the sun, so in Fig. 5 the lower longitude scale is marked in units of hours local time, the source being at local noon.

B. Groups of Impact Points

In Fig. 5 one sees the division of the impact points into three groups. The late morning group ($\approx$0900 local time) represents orbits that remain north of the equatorial plane; the early morning ($\approx$0400) orbits pass once through the equatorial plane; the late evening group ($\approx$2000) contains orbits passing twice through this plane, and so on. The three curves in Fig. 5 do not exhaust the possible impact points for vertically incident particles in the 1- to 10-Bv range. Störmer[37] points out that one can find an infinite number of families of impact points on the earth by considering orbits with increasingly more complicated paths near the earth. This can be seen in Fig. 4, where a line representing a particular source latitude, within certain limits, has an infinite number of intersections with the impact curve, since, as Störmer points out, this curve continues to oscillate back and forth through $\lambda_s=0$ for increasing longitude. These groups of impact points, not shown in Fig. 5, have latitude distributions similar to the 2000 group.

For the purpose of constructing Fig. 5 the source was considered to be in the plane of the geomagnetic equator. If the source is at some angle, λ_s, away from the plane of the geomagnetic equator an impact point plot can easily be made using Figs. 3 and 4. As the source is moved south of the equator the two morning groups of impact points in the northern hemisphere move

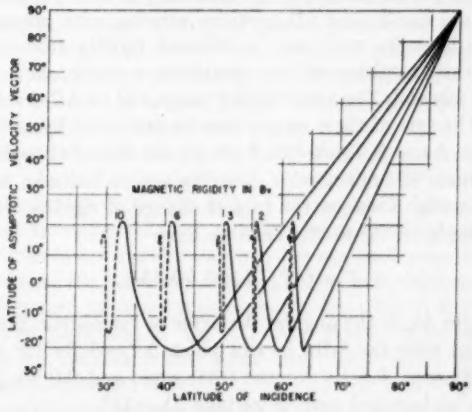

FIG. 3. Geomagnetic latitude of impact on the earth of particles arriving vertically with magnetic rigidities of 1–10 Bv as a function of the geomagnetic latitude of the source.

[37] C. Störmer, Astrophys. Norv. 1, 115 (1934); Terrestrial Magnetism and Atm. Elec. 22, 23 (1917).

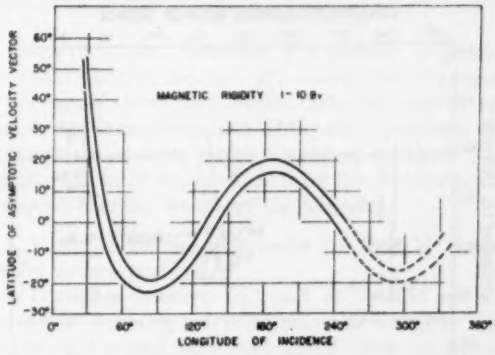

FIG. 4. Geomagnetic longitude of impact on the earth of particles with magnetic rigidities of 1–10 Bv. Curves shown are the envelope of the individual curves for each rigidity.

closer together, and the evening group moves toward earlier evening. The motion is reversed for the source north of the equator. When the source is identified with the sun this motion of the impact points or zones will appear as a seasonal effect.

Instead of considering only particles coming from a point source, it is perhaps more realistic to consider that the source of charged particles (the sun) subtends a finite angle at the earth, perhaps larger than the visible sun. Strong local magnetic fields are known to exist in sunspots, and particles of rigidities below 10 Bv would be appreciably deflected by these fields, even when several sun's radii away from the spot. This assumes that the magnetic fields of spots are not "shielded" by the high conductivity gases of the sun. However, so little is known of the magnetic (and electric) fields in the solar corona that we will just keep in mind that we are considering a finite source and later see if the experimental data place some limits on the size of the source.

The effect of a finite particle source on the impact point diagram can be seen in terms of the change in the impact points as the (point) source moves off the equator, which was discussed above. The rate of change of latitude of impact for a 3-Bv particle as the source latitude changes (see Fig. 3) is 0.3 degree per degree for the 0900 impact point, -0.1 for the 0400 point, and 0.0 for all other points. The rates of longitude change with change of source latitude from Fig. 4 are, respectively (longitude measured in local time), -0.07, $+0.12$, and -0.14 hr/degree. Thus a particle source of finite size would produce impact *zones* instead of the lines of impact points as shown in Fig. 5. These zones are about an hour wide for a source 10° in diameter. The 0900 zone has the least spread, while the 2000 zone, and presumably all of the similar zones, are the widest. Since each of the latter is at a larger longitude than the preceding one, this infinity of impact zones will fill the whole range of local times between the latitudes of 25° to 60° for 1- to 10-Bv particles. We are

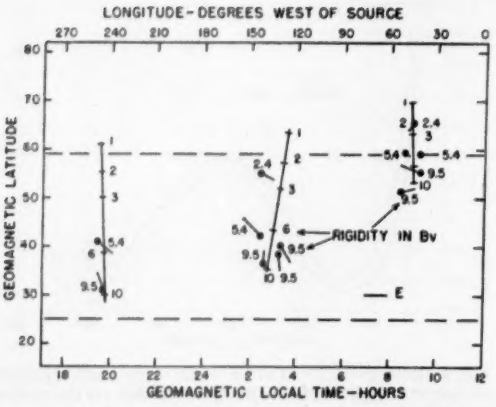
LONGITUDE-DEGREES WEST OF SOURCE
270 240 210 180 150 120 90 60 30 0
GEOMAGNETIC LATITUDE
80 70 60 50 40 30 20
RIGIDITY IN Bv
E
18 20 22 24 2 4 6 8 10 12
GEOMAGNETIC LOCAL TIME-HOURS

FIG. 5. Impact points on the earth for particles approaching in the equatorial plane. The solid lines show the impact points for particles arriving vertically. The circles give the impact points for some orbits which arrive with large zenith angles. The line attached to each of the latter shows the azimuth and zenith angles of arrival. This line is the projection on the earth's surface of the velocity vector, length "E," at the time of arrival. The longitude scale in hours local time assumes the source of particles to be at noon local time. The dashed lines indicate the band of latitudes which is filled with impact points of 1- to 10-Bv particles.

left then with only three distinct zones—the 0900, the 0400, and a background zone covering all local times.

C. Intensity in Impact Zones

The methods used in selecting the initial conditions for the numerically integrated orbits and the agreement with the model experiment orbits insure that the orbits are not "singular," i.e., there are similar orbits infinitely near to the computed orbits. An application of Liouville's theorem shows, then, that the intensity of particles in a small rigidity range striking a small area around the impact point must be the same as the intensity at the source. An infinitesimally small detector with a small angular aperture would receive (if outside the earth's atmosphere) the source intensity if the detector happened to be at an impact point and if the aperture opened along the orbit. The measured counting rate R_m for a real detector in the atmosphere thus depends on the fraction of the aperture which is filled with orbits from the source, as well as the zenith angles of the allowed directions and the rigidity range which can reach the detector.

The counting rate $R_m(P)$ due to particles of rigidity P is given by

$$R_m(P)=\sum\int I_s(P)S(x,P,\theta,\phi)\sin\theta d\theta d\phi, \qquad (1)$$

where $I_s(P)$ is the intensity near the source, x is the atmospheric depth, $S(x,P,\theta,\phi)$ is the yield function[28] appropriate for the detector considered, and θ and ϕ are the zenith and azimuth angles describing the direction of arrival of the particle. The integral is taken over all directions from which particles of rigidity P can arrive at the detector from the source. The sum is taken over all kinds of particles emitted by the source. The total measured counting rate is then given by

$$R_m=\int R_m(P)dP, \qquad (2)$$

where the integral is taken over all rigidities arriving at the detector from the source.

In order to compute the counting rate measured by a particular detector from Eqs. (1) and (2), it is necessary to know all the possible orbits connecting the sun and the detector. Since relatively few orbits are known the calculation cannot be performed, but some general conclusions concerning the relative counting rates in the different zones can be reached.

In Eq. (1) the integration is made over all directions from which particles can arrive at the detector from the sun. Malmfors[23] found in his model experiments that for the 0900 group of impact points practically the whole sky was filled with orbits from a small source. For the 0400 zone and other zones the proportion of the sky which is "allowed" is not known, but cannot be larger than for the 0900 zone. The quantity $R_m(P)$ would therefore remain constant or become smaller as we move from the 0900 zone to the 0400 zone or to the background zone.

From Eq. (2), where the integration is taken over all rigidities arriving at the detector, one expects a difference in the counting rate measured in the different zones, due to the integral being taken over different ranges of rigidity for the different zones. Two factors contribute to this range of rigidities: (1) For particles which arrive vertically the finite size of the source will cause a finite range of rigidities ΔP_f to reach a point on the earth; and (2) particles arriving with nonzero zenith angles may have a different rigidity from the vertical particles and so contribute a range, ΔP_a, to the integral. The total rigidity range will be $\Delta P_f+\Delta P_a$.

The first of these ranges may be estimated by use of Figs. 3 and 5. From Fig. 3 we get the rate of change of latitude of impact with changing source latitude, and from Fig. 5 we get the rate of change of rigidity with latitude on the earth. Then we have

$$P_f=(dP/D\lambda)(d\lambda/d\lambda_s)\Delta\lambda_s,$$

where $\Delta\lambda_s$ is the angular diameter of the source. For a point near the 3-Bv impact point $\Delta P_f=3$ Bv for the 0900 zone, 0.5 Bv for the 0400 zone, and 0.0 Bv for the background zone, if we take $\Delta\lambda_s\approx 15°$.

We may estimate the range of rigidites associated with the range of zenith angles in the following manner. Störmer has shown[27] that the asymptotic latitude of an orbit is determined almost solely by the value of the

[28] S. B. Treiman, Phys. Rev. 86, 917 (1952).

constant of the motion γ, given by

$$\gamma = -\tfrac{1}{2}[r\cos\lambda\cos x + (\cos^2\lambda)/r], \quad (3)$$

where r is the distance of the particle from the dipole in Störmer units, λ is the latitude of the particle, and x is the angle the velocity vector of the particle makes with a vector pointing west. Stated differently, only particles of a small range of γ can hit the earth for rigidities less than 10 Bv. The values of γ appropriate to a source in the plane of the geomagnetic equator are -0.46 for the 0900 zone, -0.86 for the 0400 zone, and -0.93 for the background zone.[27] The range of γ around these values which may hit the earth with x between 0 and π seems to be[27] only ± 0.01 for the last two zones and somewhat larger for the 0900 zone.

Differentiating (3) and rearranging, we have

$$d\gamma/dx - A\cos\lambda\sin x = [(\cos^2\lambda)/A^2 - \cos\lambda\cos x]dA, \quad (4)$$

in which we have set r at the earth equal to A. Using 8.1×10^{25} gauss-cm^3 for the earth's dipole moment, the rigidity of the particle in Bv is given by $P = 60A^2$. So the rate of change of rigidity with angle x is

$$dP/dx \approx (120A^4\sin x)/(A^2\cos x - \cos\lambda). \quad (5)$$

We have neglected $d\gamma/dx$ since it is only about 1/20 as large as the other term on the left in Eq. (4). Then a formula for ΔP_a, the range of rigidities associated with a range of x from $\pi/2$ (particles arriving in the meridian plane) to $\pi/2\pm\alpha$, is conveniently obtained by assuming A = constant in (5) and integrating. This yields

$$\Delta P_a \approx 120A^2 \ln \frac{\cos\lambda}{\cos\lambda \pm A^2\sin\alpha}.$$

For a 3-Bv particle ($A = 0.224$) arriving at $\cos\lambda = 0.645$ the range of rigidities for $\alpha = 30°$ is 0.48 Bv. The value 30° is, of course, arbitrary, but it represents the openings of typical counter telescopes. A similar estimate of the range of rigidities due to the spread in zenith angles be obtained brom an examination of curves of asymptotic latitude as a function of azimuth and zenith angles given by Malmfors.[22]

Thus the total range of rigidities to be integrated over in Eq. (2) is about 3.5 Bv for the 0900 zone, 1.0 Bv for the 0400 zone, and 0.5 Bv for the background zone. Assuming that the rigidity spectrum of the new particles is not rapidly varying, the expected counting rates near the 3-Bv impact point in the 0900, 0400, and background zones are roughly in the ratio 7:2:1. If the allowed directions in Eq. (1) vary greatly from one zone to another these ratios may be higher. This estimate does not depend strongly on the assumption of a particular angular opening for the detector nor on a source 15° in diameter. For example, if a 30° source is assumed, the predicted ratio becomes 7:3:1. Since later it is indicated that the larger source is appropriate, we will use the later ratio.

D. Summary on Orbits

From the above discussion it is possible to predict the distribution on the earth of particles from the region of the sun if those particles are deflected only by the earth's dipole magnetic field. If the sun, while near the geomagnetic equator, emits a pulse of particles with rigidities up to 10 Bv, identical detectors scattered over the earth's surface would see the following:

1. Detectors located at latitudes less than 25° would receive no new particles.[29]
2. Detectors between 25° and 35° would see an increase in counting rate. This increase would be due to the background zone and would have no strong longitude (local time) dependence.
3. Detectors above 35° would see an increase as in 2, but in addition those detectors at local times around 0400 would see an increase about three times as large as in 2.
4. Detectors above 50° would see an increase as in 2, but detectors near 0400 or 0900 would see additional increases, up to seven times as large as in 2.

The highest latitude at which detectors would see increases, either the background type as in 2 or the strongly local time dependent increase as in 3 and 4, would depend on the lowest rigidity particles to which the detector was sensitive.

In summary, we have predicted, using a simple model, the geographical distribution of the increase in cosmic-ray intensity associated with solar flares. This distribution differs from that arrived at in earlier work[18] in several ways; most importantly, the existence of a background zone, or a band of latitudes in which the solar flare effect will have no strong local time dependence, is pointed out. Further, a rough estimate of the relative intensities in the different zones is made, and the effect of a finite source, larger than the visible sun, is considered. Earlier work[16,18] has considered only a source of particles about the size of the earth.

III. THE FOUR LARGE EVENTS

A. General

The flare observations for the four large events are summarized in Table I. In Table II is given a list of the cosmic-ray stations reporting on one or more of the large increases associated with these flares and references to the reports.

The observed increases will be compared with the predicted distribution by simply constructing an impact zone diagram appropriate for the position of the sun at the time of the increase, using Figs. 3 and 4, and marking on the plot the positions of the stations reporting on the increase. It is then possible to compare the size of the increase observed by a station with its position relative to the impact zones.

[29] The exact latitudes mentioned here are of course dependent on our assumption that there are no new particles with $P > 10$ Bv.

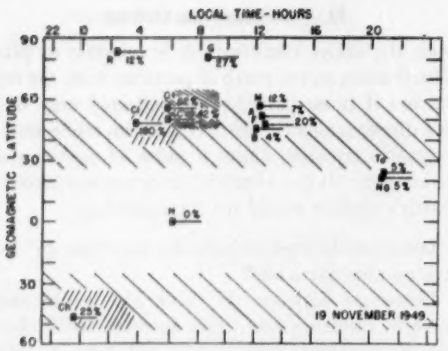

FIG. 6. Impact zones on the earth at the time of one of the large cosmic-ray increases—1100 UT on 19 November 1949. The cross-hatching indicates the positions of the zones with the density of crosshatching giving roughly the relative intensities predicted for the different zones. The cosmic-ray stations are indicated by solid squares; the lines attached to each station shows its motion during the increase. Near each station is an identifying letter (see Table II) and the percentage increase observed.

The increases in the cosmic-ray intensity were quite sharp, remaining at maximum intensity for only a few minutes. Thus the size of the increase reported will depend on the length of the time intervals used for averaging the counting rate and how the intervals were related in time to the peak intensity. So, in comparing data from two observers, it is desirable to use similar time intervals similarly centered. The reports in the literature do not always make this possible.

Observations made in Germany[8] during one of the events with both counter telescopes and ion chambers indicate that the magnitude of the increase does not depend strongly on the directional properties of the detector, so observations of both directional and non-directional detectors will be used here. Only reports of charged particle detectors will be used, since the yield function for neutron detectors differs greatly from that for charged particle detectors,[30] and only one report from a neutron detector is available for these four events.

B. November 19, 1949

The latest and best known large cosmic-ray increase occurred[1,8] on November 19, 1949, following a large flare and a radio fadeout, both of which began very nearly at 1030 UT. Figure 6 shows a rectangular projection of the earth at this time, with the impact zones which are predicted as discussed above indicated by crosshatching. The density of the crosshatching indicates roughly the relative intensities to be expected in the different zones. The lack of symmetry between the zones in the northern and southern hemispheres is an example of the seasonal effect mentioned earlier. The small squares are the positions of the cosmic-ray stations reporting the increase (or its absence), with the line attached to each indicating its motion during the increase. Near each station is marked the percentage increase observed using for the most part short time intervals (5 to 15 minutes). The zones were constructed assuming a source 15° in diameter.

It is seen in Fig. 6. that there is a clear tendency for the stations in the morning impact zones to show the largest increase. In particular we note that the station in Ottawa, in the 0900 zone, recorded an increase about five times as large as that at Manchester, located in the background zone. This is consistent with the ratio seven predicted above. The 0900 and 0400 zones may be compared by using Cheltingham and Christchurch, giving a ratio of about two, consistent with the predicted 7:3. The 20 percent increase at Freiburg seems large compared with the other European observations and is probably due to the fact that this figure is derived from a very short time interval at the peak intensity. Similarly, the 7 percent at Amsterdam is a one hour average and should be made somewhat larger for comparison with other stations. Two German stations,[8] not shown in Fig. 6 for lack of room, gave increases of 15 percent for each of two similar counter telescopes and 17 percent for a shielded ion chamber. The very large increase at Climax can in part be

TABLE II. Observations of large cosmic-ray increases.

Station	Symbol used here	λ (degrees)	Altitude[a] (meters)	References 28 Feb. 1942	7 Mar. 1942	25 Jul. 1946	19 Nov. 1949
Amsterdam	A	54N		b	b	c	d
Bagneres	B	46N	550	...	...	...	e
Bargteheide		54N		...	...	...	f
Cheltingham	C	50N		g	g	g	g
Christchurch	Ch	48S		g	g	...	g
Climax	Cl	48N	3500	...	...	...	g
Darmstadt		50N		...	...	...	f
Freiburg / Friedrichshafen	F	48N		h	h	...	f
Godhavn	G	80N		g	g	g	g
Huancayo	H	1S	3350	g	g	g	g
London	L	54N		i	i	...	...
Manchester	M	57N		...	...	j	k
Nagoya	Na	25N		...	...	...	l
Norfolk	N	49N		m	...	...	...
Ottawa	Ot	56N		...	...	...	n
Resolute	R	83N		...	...	...	n
Teloyucan	T	30N	2285	g	...	...	...
Tokyo	To	25N		o	o	...	p
Weissenau		49N		...	...	...	f
Mt. Wilson		43N	1800	...	...	q	...

[a] Altitude listed only for mountain stations.
[b] Clay, Jongen, and Dijker, Proc. Koninkl. Ned. Akad. Wetenschap. **52**, 923 (1949).
[c] See reference 17.
[d] J. Clay and H. F. Jongen, Phys. Rev. **79**, 908 (1950).
[e] A. Dauvillier, Compt. rend. **229**, 1096 (1949).
[f] See reference 8.
[g] See reference 1.
[h] See reference 16.
[i] A. Duprerier, Proc. Phys. Soc. (London) **57**, 468 (1945).
[j] D. W. N. Dolbear and H. Elliot, Nature **159**, 58 (1947).
[k] See references 12 and 13.
[l] Sakido, Kodama, and Yagi, Rept. Ionos. Research Japan **4**, 207 (1950).
[m] E. B. Berry and V. F. Hess, Terrestrial Magnetism Atm. Elec. **47**, 251 (1942).
[n] D. C. Rose, Can. J. Phys. **29**, 227 (1951).
[o] J. Nishimura, J. Geomag. Geoelec. **2**, 121 (1950); Sekido, Yoshida, and Kamiya, Rept. Ionos. Research Japan **6**, 195 (1952).
[p] Miyazaki, Wada, and Kondo, Rept. Ionos. Research Japan **4**, 176 (1950).
[q] H. V. Neher and W. C. Roesch, Revs. Modern Phys. **20**, 350 (1948).

[30] W. H. Fonger, Phys. Rev. **91**, 351 (1953).

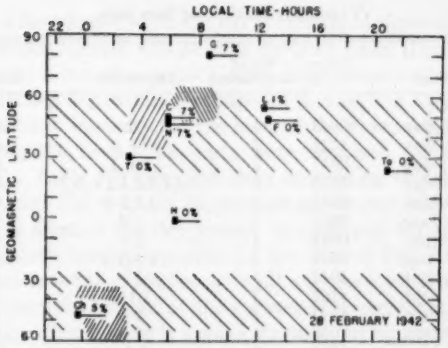

FIG. 7. Impact zones and cosmic-ray stations at 1100 UT on 28 February 1942. Symbols same as in Fig. 6.

attributed to the high altitude of that station. A reasonable altitude correction to sea level lowers the percentage increase to about the same value as at Cheltingham.[1]

The high latitude stations, Resolute and Godhavn, recorded increases although they were not in any impact zone.

C. February 28, 1942

The first large cosmic-ray increase to be noticed was reported by Berry and Hess (see Table II) in 1942. This increase followed a flare and fadeout beginning around 1100 UT on February 28 of that year. Figure 7, similar to Fig. 6, shows the earth at that time, with the positions of the impact zones and stations. In this case the increases marked in the figure are for one hour averages centered on the half hour. It is seen (with Godhavn again the possible exception) that the distribution of the increase is again consistent with positive particles arriving at the earth from the direction of the sun. All of the increases for this event began roughly an hour after the flare began.[31] The ratio of the increases in and out of the morning impact zones is, in this case, seven or greater.

D. March 7, 1942

For the second solar flare-type increase to be observed the flare was not seen, but the characteristic radio fadeout was recorded.[1] Figure 8 shows the impact zones at 0400 UT on March 7, 1942, when the increase occurred, and the increases in the one hour averages. Once again the largest increase was in the morning impact zones.

E. July 25, 1946

The third large increase of the solar flare type was recorded on July 25, 1946 at around 1700 UT. No report has been found from a cosmic-ray station which was in the morning impact zones at this time. The increase was seen by five stations (see Table II), all with roughly the same amplitude of about 15 percent. No increase was seen at Huancayo. These observations again agree with the predicted distribution. For this event the maximum of the cosmic-ray increase was about two hours later than the maximum of the flare.

F. Conclusions on Big Events

From the above discussion and Figs. 6, 7, and 8 it is seen that the middle and low latitude observations of the four large cosmic-ray increases are consistent with positive particles with magnetic rigidities of less than 10 Bv approaching the earth along the sun-earth line and being deflected only by the earth's dipole magnetic field. The relative magnitudes of the increases at different stations is in rough agreement with the estimate based on general properties of the cosmic-ray orbits.

Although the above comparison was made assuming that the source of particles is $\approx 15°$ in diameter, none of the results are changed if one takes a source twice as large.

The observations of the increases at very high latitudes (Resolute and Godhavn) are not consistent with the predictions of the simple model used here, unless there exists a whole family of orbits and impact points, having small values of γ, which have been overlooked by all workers in the field. As this is unlikely, and as the simple model gives good agreement at lower latitudes, it seems reasonable to examine the simplifying assumptions made in setting up the simple model to find one that could produce the high-latitude disagreement.

In particular it is suggested that the deviations of the earth's magnetic field from that of a dipole may produce high latitude impact zones. Particles contributing to the background zone travel large angles around the earth at distances where the nondipole terms in the earth's field amount to a few percent of the dipole field, and a small perturbation in the path of a particle at one point can produce a large change in the orbit by

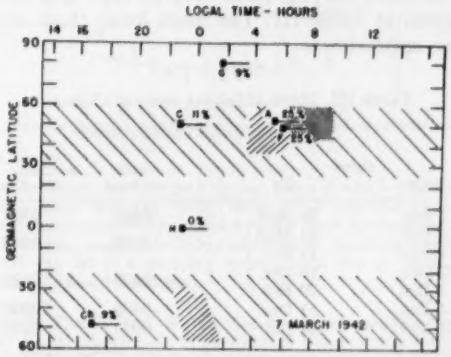

FIG. 8. Impact zones and cosmic-ray stations at 0400 UT on 7 March 1942. Symbols same as in Fig. 6.

[31] In reference 1 and elsewhere the flare is listed as having started *after* the cosmic-ray increase. Apparently the report of an observation by the Arcetri Observatory of a flare in progress at 1100 UT, before the increase, has been overlooked. See Table I.

time the particle has made a circuit of the earth. Thus particles may be deflected to points nearer the poles than is predicted by the simple theory.

This possibility for explaining the high-latitude observations could be checked by a model experiment such as Malmfors', but with a more complicated magnetic field. Also, the equations of motion could be integrated numerically, preferably with a digital computer. It would also be helpful if, during the next large increase, there were a variety of detectors (neutron monitor, shielded ion chamber and so on) at a high-latitude station so that the energy of the new particles arriving there could be extimated.

IV. EFFECTS OF SMALL FLARES

In the preceding sections it has been shown that the simple model adopted here gives a fairly consistent picture of the solar-flare-connected increases of cosmic-ray intensity. If, then, a small increase associated with a small solar flare is sought, the preferred local times of arrival for particles from the sun should be taken into consideration. It was shown in the discussion of impact zones that an increase due to particles from the sun might be seen at any local time in the middle latitudes, but that a higher intensity is expected at certain times.

We will use pressure corrected hourly averages of cosmic ray intensity from the Climax neutron detector, which has been described earlier.[32] Neutron detectors are particularly suited for observing solar flare effects because most of the counts recorded by such a detector are due to particles of low rigidities (less than 13 Bv).[32]

This detector is at a geomagnetic latitude of 48°. For latitudes less than 50° the 0900 impact zone is of little importance, since it stays for the most part farther north. So for Climax the preferred local times for observing solar flare effects are largely determined by the 0400 zone. For a given declination of the sun and Greenwich time the magnetic latitude of the sun can be found from McNish's graphs.[25] Then, from Figs. 3 and 4, the impact zones on the earth can be found. In particular, at Climax, the centers of the zones pass over at times varying from 0300 to 0700. The details are given in Table III. The dates listed there are, of course, approximate.

TABLE III. Times of impact zones at Climax.

Dates From	Dates To	Type of zone	Center of zone to nearest hour (local time)
1 Apr.	10 Sept.	0400	0300
21 Feb.	31 Mar.	0400	0400
11 Sept.	21 Oct.		
22 Oct.	10 Dec.	0400	0500
1 Jan.	20 Feb.		
11 Dec.	31 Dec.	0400	0600
21 Nov.	21 Jan.	0900	0700

[25] Simpson, Fonger, and Treiman, Phys. Rev. **90**, 934 (1953).

TABLE IV. Small solar flare data.

Date	Time[a] (UT)	No. of observations	Importance	Group
1951				
13 May	0943	1	2	*A*
15 May	1127	2	2+,2	*A*
17 May	0947	2	1+,1	*A*
18 May	1020	9	3,2,2,3,3,3,2+,3,2	*A*
20 May	0817	3	2,1,1+	*A*
16 June	0901	2	1,2	*A*
28 July	0841	1	1+	*A*
12 Aug.	0837	3	1+,1,2	*A*
3 Sept.	1012	1	1+	*A*
7 Sept.	1108	2	1,1+	*A*
18 Sept.	1145	1	1+	*A*
22 Dec.	1058	1	1+	*A*
8 May	1505	3	2,2,1	*B*
14 May	1545	1	2	*B*
17 May	1754	2	2,2	*B*
18 May	1956	2	2+,1	*B*
19 May	1949	1	3−	*B*
6 June	1240	1	2	*B*
15 July	2316	1	2	*B*
28 July	1535	3	1,2,2	*B*
3 Sept.	1308	4	3,3,2,2	*B*
14 Sept.	1338	6	2,2,1+,2,2,1	*B*
15 Sept.	1505	4	2+,2,2,1	*B*
23 Sept.	2032	3	1,2,2	*B*
1952				
22 Apr.	1155	1	2	*A*
1 May	1037	2	2,1	*A*
27 Mar.	2300	1	1+	*B*
30 Mar.	0034	1	1+	*B*
4 Apr.	0403	1	2	*B*
11 Apr.	0545	2	2,2	*B*
1 June	1629	1	2	*B*
12 July	1450	1	2	*B*
25 Oct.	1945	2	2,2	*B*
18 Nov.	2045	1	2	*B*
1953				
25 June	1000	1	1+	*A*
20 July	1048	1	2	*A*
1 Jan.	2054	1	2	*B*
15 July	1418	1	1+	*B*
21 July	1424	1	1+	*B*
22 July	1532	1	1+	*B*

[a] Time given is either first observation or beginning of flare. For sources of data see references 5, 11, 33, and 34.

Since the Climax (*D*-1) detector has been in operation (May, 1951) no changes in intensity of more than a few percent in an hour have been observed. Any intensity changes associated with solar flares, therefore, must be separated from other changes of about the same magnitude, such as the 24-hour cycle[30] and the 27-day-recurring[30] changes. The latter offer no particular difficulty, since they occur slowly, but correction for the 24-hour cycle may be necessary.

To look for a small cosmic-ray increase at the time of small solar flares the following analysis has been performed. Flares which were reported[5,11,33] as occurring in 1951 and which were rated as importance 1+ or higher were placed in one of two groups. Group *A* contained those flares the starting time of which put Climax in a morning impact zone, the zones considered

[33] K. O. Kiepenheuer (editor), Sonnen-Zirkular, published quarterly by the Fraunhofer Institute, Freiburg-in-Baden, Germany, 1951–53.

to be four hours wide. Group *B* contained those flares for which Climax was at least an hour away from the edge of a morning impact zone. The cosmic-ray data for each group were superimposed so that the average cosmic-ray intensity for the hour of the flare, the hour before, the hour after, etc., were obtained for each group. Table IV gives the data concerning the flares used, and Fig. 9 shows the average cosmic-ray behavior during flares of the two groups. A correction for mean daily cycle has been applied to the data of Fig. 9, but in this case the correction is small and does not change any essential feature of the curves. It is seen that for Group *A* flares there is a small increase during the hour of the flare with a return to normal in two hours. The Group *B* points are consistent with a much smaller, or no, increase.

In seeking a more detailed relationship between the Group *A* flares and the cosmic-ray increases we ask whether the size of the flare and the magnitude of the cosmic-ray increase are related for the individual events. We take as the size of the cosmic-ray increase the difference between the mean of the hourly counting rates for the two hours during and after the flare, and the hourly average just before the flare. As the size of the flare we take its "average importance," that is, the average of the importance ratings given to the flare by the different observatories which reported the flare. The importance rating is, as mentioned earlier, a somewhat subjective measure of the flare size, but it is the only measure that is always reported. As an indication of how well different observatories agree in their rating of a flare we may inspect the importance ratings in Table IV for those flares seen by two or more observers. The correlation coefficient of flare size and cosmic-ray increase for the events in Group *A* is $+0.6\pm0.2$, indicating that the two sizes, with good probability, are related, the larger flares yielding the larger increases.

A similar analysis can be made for the 1952 and part of 1953 data,[34] although flares of any size were much less frequent in these years than in 1951. This decline in the rate of occurrence of flares is associated with the general decline in the level of solar activity, part of the 11-year "solar cycle." Only four flares could be found that could be placed in Group *A*. The results for 1952–1953 are also shown in Fig. 9, and are similar to the 1951 results, although much less conclusive. Table IV gives the data on the flares.

It has been assumed in this method of examining the cosmic ray data that the impact zones are about four hours wide. No attempt has been made to narrow the zones further, since the number of events in Group *A* would become too small. The question of the time width of the zones, however, has been examined in the following manner. A flare activity index has been published[35] giving values for each day during 1951, 1952, and part of 1953. This index is intended to be proportional to the energy radiated per unit time during the day in H_α light by flares occurring on the visible hemisphere of the sun. During periods when flare observations are made every day, this index is a slowly varying function of time. It will gradually increase in value for several days and then decrease in a like manner. This behavior is a result of the fact that flares usually occur in certain active regions on the sun, and, as such a region comes over the limb, flares in it begin to be observed, slowly increasing the index. These regions vary with time in their flare-producing activity, but this change is also usually slow. Hence, this flare index represents the likelihood of flares occurring in the early morning hours, even if the index for the day is derived from observations made at some other time. If small flares are associated with new cosmic-ray particles approaching the earth from the direction of the sun, the cosmic-ray intensity for days of high flare index should then be peaked in the early morning hours relative to days of low flare index. In Fig. 10 is seen that such is the case. The plotted

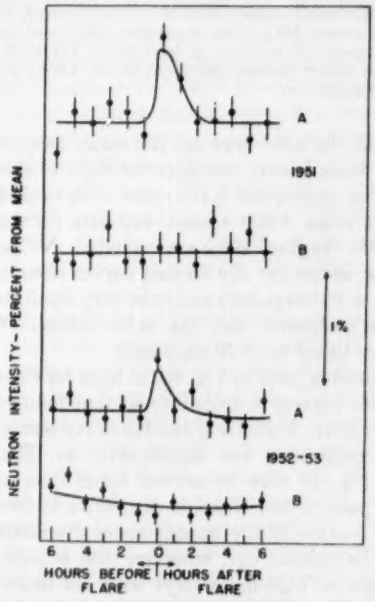

FIG. 9. Cosmic-ray intensity during times of small solar flares. Curves *A* show behavior during flares which occurred when the detector was in a morning impact zone for particles from the sun. Curves *B* show cosmic-ray behavior for flares occurring when the detector was *not* in a morning impact zone. Errors shown are estimated standard deviations.

[34] We thank Dr. Yngve Ohman of the Swedish Solar Station on Capri for communicating to us the results of his flare observations for the summer, 1953, prior to publication.

[35] D. E. Trotter and W. O. Roberts, Flare Activity Index, Report No. HAO-NBS 20, High Altitude Observatory, Boulder, Colorado, 1953 (unpublished). Preliminary values of the flare index are given in Preliminary Chart of Solar Activity, issued weekly by the High Altitude Observatory.

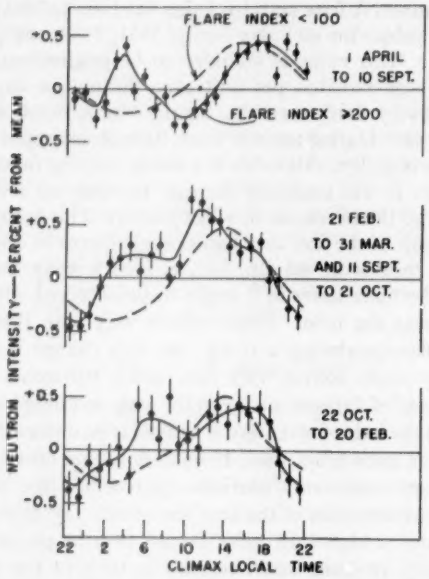

FIG. 10. Mean daily cycle of cosmic-ray intensity for days of many flares (solid curve) and for days of few flares (dashed curve). No points or errors are shown for the dashed curve since the errors are much smaller than for the solid curve. Data used are for the period May, 1951, to August, 1953, and the dashed and solid curves are matched at 1600 hours. The solid line is a smooth line drawn through the mean of the 3-hour and 1-hour running averages.

points and the solid lines are the mean daily behavior of the Climax hourly averages for days of flare index ≥ 200. The dashed line is the mean daily cycle for days with flare index <100. Cosmic-ray data for the period May, 1951–August, 1953 are included. No points or errors are shown for the dashed curves since they are based on ≈ 200 days each and have very small statistical errors as compared with the solid curves. The solid curves are based on ≈ 20 days each.

The morning peak in Fig. 10, at least for the summer and winter curves, is indeed about four hours wide, as assumed above. The spring and fall curve seems to have a wider peak, but not significantly so. The winter peak in Fig. 10 may be several hours later than the summer peak, a fact which is suggestive in view of the seasonal motion of the impact zones discussed above. It must be pointed out, however, that implicit in this comparison of high-index days with low-index days is the assumption that the shape of the mean daily cycle outside of the early morning hours is unaffected by varying states of activity on the sun. Since changes in the daily cycle associated with earth's magnetic field disturbances, which in turn are related to solar activity, have been reported[36–38] this assumption seems doubtful and results dependent upon it must be used with caution. On the other hand, if the small-solar-flare effect discussed here actually exists, then workers seeking associations between cosmic-ray changes and magnetic field disturbances must take care that the effects of the early morning peak in statistical analyses of the daily cycle (shifting the phase of the first harmonic to earlier morning, increasing the amplitude of the second harmonic, etc.) are not attributed to magnetic field changes.

Some limits can now be placed on the angular size of the particle source, using the experimental result that the impact zone at Climax is about four hours wide. Clearly a line source, 60° in longitude and small in latitude would give such a time spread. Similarly, in Fig. 4, one finds that a source 30° in latitude and small in longitude would give such a spread. So our results limit the source to an elongated region of the sky, containing the sun, which has its longest dimension (about 60°) parallel to the plane of the geomagnetic equator and with a width of about 30°.

V. CONCLUSIONS

From the results discussed above it is concluded that the large cosmic-ray increases associated with solar flares are mainly the result of positive particles which approach the earth from the direction of the sun. We further find that small solar flares produce similar cosmic ray effects to the big flares, but considerably smaller in magnitude. The results suggest that perhaps all flares are associated with additional cosmic-ray particles approaching the earth. In both small flare and large flare events the results are consistent with a source of particles located in the direction of the sun and 60° or less in longitude and 30° or less in latitude.

ACKNOWLEDGMENTS

The writer wishes to thank Professor J. A. Simpson, under whose guidance this work was done, for his aid, encouragement, and advice. We also thank Dr. S. B. Treiman and Dr. W. H. Fonger for interesting and helpful discussions concerning this work. For help of many kinds we are indebted to Farnam Jory and Mary Weiss of this laboratory. The data from Climax could not have been obtained without the aid of R. Allen, G. Athay, F. Dolder, and R. Hansen, all of the High Altitude Observatory. We also wish to thank the National Science Foundation for a fellowship.

[36] Y. Sekido and S. Yoshida, Rept. Ionos. Research Japan **4**, 37 (1950).
[37] H. Elliot and D. W. N. Dolbear, J. Atm. and Terrest. Phys. **1**, 205 (1951).
[38] A. Ehmert and A. Sittkus, Z. Naturforsch. **6a**, 618 (1951).

Solar Magnetic Moment and Cosmic-Ray Effects Associated with Solar Flares*

S. B. TREIMAN
Palmer Physical Laboratory, Princeton University, Princeton, New Jersey, and Institute for Nuclear Studies, University of Chicago, Chicago, Illinois†

(Received November 17, 1953)

A close correlation between solar flares and small cosmic-ray intensity increases has recently been established by the Climax, Colorado, neutron monitor data. The correlation, however, is restricted only to those flares which occur when the station lies within a certain interval of local solar time. This has been explained by supposing that the new cosmic-ray particles approach the earth preferentially along the earth-sun line, before deflection in the terrestrial magnetic field takes place. In the present paper, this evidence is used to establish an upper limit to a possible solar magnetic dipole field. Allowance is made for the fact that the dipole field may be seriously perturbed by local fields near the sun; but on the assumption that the dipole field predominates far from the sun (at distances greater than one-fifth the earth-sun distance), the upper limit on the solar dipole moment is 5×10^{33} gauss-cm^3.

ANALYSIS of the neutron-monitor data for Climax, Colorado, has revealed that small cosmic-ray intensity increases are frequently associated with solar flares.[1] Although small in magnitude, these events resemble the large cosmic-ray increases which on rare occasions in the past have been observed to accompany large solar flares.[2] Aside from its inherent interest in demonstrating a solar influence on cosmic radiation, the new evidence has an important bearing on the question of the magnitude of a possible solar dipole field. It is this aspect of the problem which we shall consider here.

The association between small flares and cosmic-ray intensity increases is found to be pronounced only for those flares which occur when the cosmic-ray detector lies within a certain interval ("impact zone") of local solar time.[1] For the Climax detector, the center of the impact zone is at ~4 A.M. and the width of the zone appears to be no larger than ±2 hours. For flares which occur when the detector lies outside of the impact zone, there is no measurable cosmic-ray effect.

This local time, or longitude dependence of the cosmic-ray effect, has been interpreted along the following lines.[1] If the new cosmic-ray particles which give rise to the intensity variation approach the earth from a specified direction (in particular, if they approach along the earth-sun line), they will be deflected in the terrestrial magnetic field and will strike the earth at calculable "impact points," whose locations depend on the magnetic rigidity. For particles which arrive vertically at the latitude of Climax, one such impact point (which involves particles of rigidity 4 Bv) occurs at 4 A.M. local solar time. The impact points spread out into impact zones of finite width when one takes into account the whole range of zenith angles of arrival at the earth. The zones will be further widened if the particles approach the earth over a range of angles with respect to the earth-sun line.

Not only the small cosmic-ray increases associated with solar flares, but also the four large solar-flare events seem to fit this picture.[1] We shall therefore consider it established that the cosmic-ray particles which are produced[3] on or near the sun in connection with solar flares, and which reach the earth, approach essentially along the earth-sun line before they are deflected in the short-scale terrestrial field. The width (±2 hours) of the 4 A.M. impact zone at Climax implies that the particles make an angle of at most 30° with respect to the earth-sun line in the geomagnetic equator.

It is difficult to reconcile this evidence with the large solar dipole moment (6.5×10^{33} gauss-cm^3) implied by the cosmic-ray latitude cutoff observed at the earth.[4,5] For this value of the dipole moment, the earth would not be accessible to 4-Bev particles coming from the vicinity of the sun unless they are produced at very large heliomagnetic latitudes. Even in this case it appears very doubtful that in the vicinity of the earth the orbits are preferentially directed along the earth-sun line.[6]

However, during solar-flare periods one might well expect that local magnetic fields seriously perturb the dipole field near the sun, so that the above arguments lose their force. For example, Forbush *et al.*[7] have suggested the possibility that the interaction of sunspot fields with the general solar dipole field produces a "tunnel" through which particles can escape the vicinity of the sun at low heliomagnetic latitudes. Nevertheless, in the cases considered by them, and perhaps in general, it appears that the simple dipole field becomes predominant at distances greater than about one-fifth the sun-earth distance r_e. At any rate,

* Assisted by the Office of Scientific Research, Air Research and Development Command, U. S. Air Force.
† For work performed, summer, 1953.
[1] John Firor, preceding paper [Phys. Rev. **94**, 1017 (1954)].
[2] Forbush, Stinchcomb, and Schein, Phys. Rev. **79**, 501 (1950).
[3] Although we speak of the new particles as being "produced," we also have in mind the possibility that the cosmic-ray intensity variations may be due to the acceleration ("modulation") of pre-existent cosmic radiation by fields in the vicinity of the sun. Our discussion does not depend on the distinction between production (*de novo*) or modulation.
[4] J. A. Van Allen and S. F. Singer, Nature **170**, 62 (1952).
[5] Neher, Peterson, and Stern, Phys. Rev. **90**, 655 (1953).
[6] In this connection, see C. Stoermer, Astrophys. Norv. **1**, 116 (1935) for plots of typical dipole orbits.
[7] Forbush, Gill, and Vallarta, Revs. Modern Phys. **21**, 44 (1949).

we shall make this assumption; i.e., we suppose that for distances greater than $r_1=r_e/5$, the orbits are those appropriate to a pure magnetic dipole.

One can, however, imagine a special kind of magnetic perturbation which might be appreciable all the way out to the earth, namely, a neutral, ionized beam of particles from the sun, which carries with it a magnetic field. In fact, it has been suggested[8] that an induced electric field associated with the magnetic field is responsible for the acceleration of particles to cosmic-ray energies during solar disturbances. However, the ion beam travels very slowly. Unless the emission of beam particles had begun many hours before the emission of the cosmic-ray particles, the latter would overtake the beam before the distance r_1 is reached.

We also assume that the new cosmic-ray particles which give rise to the intensity variation at the earth are produced somewhere within the sphere of radius r_1, although we need not consider the details of the process or of the trajectories inside the sphere. Finally, we assume that the earth lies in the plane of the heliomagnetic equator.

Consider now a particle, of rigidity 4 Bev, which emerges from the sphere and reaches the earth. We have seen that in the vicinity of the earth the particle travels essentially along the earth-sun line. The entire trajectory between r_1 and r_e can therefore be considered, in good approximation, to lie in the plane of the heliomagnetic equator.

Making use of the well-known Stoermer integral of motion, we can write

$$-R_1\cos x_1+1/R_1=-R_e\cos x_e+1/R_e,$$

where $R=r(cp/eM)^{\frac{1}{2}}$. The solar dipole moment is designated by M, p is momentum of the particle, and x is the angle between the velocity vector and a reference vector which points eastward about the solar dipole axis. Letting $f=r_1/r_e=R_1/R_e$, we find that

$$R_e^2=(-1+1/f)/(f\cos x_1-\cos x_e).$$

The smallest possible value of R_e (hence the largest possible value of M) is now obtained by setting $\cos x_1=1$ and $\cos x_e=-0.5$ (this corresponds to the upper limit of 30° which the experimental observations set for the angle between the earth-sun line and the direction of motion near the earth). For $f=r_1/r_e$ we have adopted, as an upper limit, the value one-fifth. Inserting these numbers, we find

$$R_e^2>5.71,$$

or

$$M<5\times10^{22}\text{ gauss-cm}^3.$$

This upper limit on the solar dipole moment is one order of magnitude smaller than the value implied by the cosmic-ray latitude cutoff at the earth.

It is best, however, to recall again the two most important assumptions which have gone into the present calculation. We have assumed that: (1) the new cosmic-ray particles have been generated at distances from the sun no greater than $r_1=r_e/5$; (2) at distances between r_1 and r_e the solar dipole field is not seriously perturbed by any other large-scale field.

The first assumption is supported by the very fact that the new cosmic-ray particles associated with small solar flares always approach the earth from the same general direction (the earth-sun line) within a fairly small cone; i.e., the "source" region for each event always lies within a fixed cone of small aperture. The most reasonable choice for the source region is of course the sun and its vicinity. The second assumption is more difficult to justify and our result must therefore rest explicitly on its validity. Nevertheless, we note that if the solar dipole moment were apprecialby larger than the upper limit which we have set, it would require very special kinds of perturbation fields in order to give rise to orbits which, in the vicinity of the earth, are preferentially directed along the earth-sun line. As it is, even the "tunnels" postulated by Forbush *et al.*[7] would develop only under unusual circumstances. On the other hand, the cosmic-ray effect which we are considering is a frequently-occurring phenomenon.

The author wishes to express his thanks to Professor J. A. Simpson and to Dr. John Firor for many valuable discussions.

[8] K. O. Kiepenheuer, Phys. Rev. 78, 809 (1950).

Cosmic Radiation Intensity-Time Variations and Their Origin. V. The Daily Variation of Intensity*

J. W. Firor,† W. H. Fonger,‡ and J. A. Simpson
Institute for Nuclear Studies, University of Chicago, Chicago, Illinois
(Received November 30, 1953)

Properties of the 24-hour intensity variations which were established by ion chamber and counter telescope measurements at high primary-particle energies have now been extended to the low-energy portion of the primary spectrum by measurements with high-altitude neutron piles at geomagnetic latitudes 0° and 48°. The observations demonstrate that the peak-to-peak amplitude of the 24-hour variation increases with latitude and, hence, is dependent on primary-particle rigidity. The latitude ratio for the peak-to-peak variation is $\sim 1.4 \pm 0.2$ and the amplitude at 48° is of the order 1 percent. These facts preclude primary neutrons or a general solar dipole field as the origin of this intensity variation.

It is shown that although the amplitude of the variation changes from day to day, the amplitudes of the intensity variations of particles at low and at high energy are related. It is further shown that the amplitude on one day persists for only the next 1 or 2 days and that there is not a strong 27-day recurrence tendency.

The general features of the changes in peak-to-peak amplitudes of the monthly average 24-hour variations appear in both neutron detectors and in the Freiburg ionization chamber. Arguments based on the experimental observations are presented to exclude meteorological factors, the terrestrial magnetic field variations, and simple geoelectric field accelerations as the origin of the variation. Since it is shown that the particles which produce the 24-hour variation are charged and have their highest intensity near or after noon local time, it does not appear probable that they come from the direction of the sun. Although it is doubtful that this variation is of terrestrial origin, no proof has yet been given that the variation is of extra terrestrial origin.

I. INTRODUCTION

THE following experimental facts concerning cosmic-ray intensity variations within 24-hour periods, as measured by detectors deep in the atmosphere, are now well established.

a. Existence.[1–7] On the average the intensity near noon is greater than the intensity near midnight. The amplitude of the variation has an average value of ≈ 0.2 percent for shielded ion chambers, ≈ 0.4 percent for counter telescopes, and ≈ 1.0 percent for local production neutron detectors. The variation is present after the data are carefully corrected for atmospheric effects.

b. Variability with time.[4–9] The amplitude of the daily variation is not constant, and the changes which occur in the amplitude are world-wide in extent, both for the day to day changes and for the long time changes in the average values.

Some facts which are less well established than these two are the following:

c. Association with the geomagnetic field.[4,5,8,9] The amplitude and perhaps the time of maximum of the daily variation are related to the occurrence of geomagnetic field disturbances. The amplitude tends to be larger during times of disturbances than during quiet periods.

d. Energy dependence.[6,7,9] Both the amplitude of the daily variation and the changes which occur in this amplitude are energy dependent, being larger when measured by a low-energy detector (neutron monitor) than when measured with a high-energy detector (charged particle detector). The variation exists at Huancayo, near the magnetic equator, and the changes in the monthly averages of amplitude also appear there. Hence the variation and its changes extend to high energy—greater than 13 Bev if produced by primary protons.

The preceding summary represents mostly observations obtained with ion chambers or counter telescopes deep within the atmosphere, and, therefore, the effects of intermediate- and high-energy particles in the primary-particle spectrum. We have shown that the measurements of intensity variations may be extended to much lower mean primary energies by measuring the local neutron production from the nucleonic component.[10] Intensity variations of primary particles down to ~2-Bv rigidity may be observed at large atmospheric depths, and we have already reported the existence of the 24-hour intensity variation in the neutron component.[6,7] In this paper we shall present a preliminary report on the properties of this variation as a function of primary particle rigidity and show

* Assisted by the Office of Scientific Research, Air Research and Development Command, U. S. Air Force.
† Present address: Department of Terrestrial Magnetism, Carnegie Institution of Washington, Washintgon 15, D. C.
‡ Present address: Sarnoff Research Center, R.C.A. Laboratories Division, Princeton, New Jersey.
[1] F. Lindholm, Gerlands Beitr. Geophys. **20**, 12 (1928).
[2] S. E. Forbush, Terrestrial Magnetism and Atm. Elec. **42**, 1 (1937).
[3] A. R. Hogg, Mem. Commonwealth Obs. **2**, No. 5 (1949).
[4] H. Elliot and D. W. N. Dolbear, J. Atm. and Terrest. Phys. **1**, 205 (1951).
[5] A. Ehmert and A. Sittkus, Z. Naturforsch. **6a**, 618 (1951).
[6] Fonger, Firor, and Simpson, Phys. Rev. **89**, 891 (1953).
[7] W. H. Fonger, Phys. Rev. **91**, 351 (1953). Hereafter we refer to this paper as reference II.
[8] Sekido, Yoshida, and Kamiya, Report Ionos. Res. Japan **6**, 195 (1952).
[9] V. Sarabhai and R. P. Kane, Phys. Rev. **90**, 204 (1953).
[10] Simpson, Fonger, and Treiman, Phys. Rev. **90**, 934 (1953). Hereafter we refer to this paper as reference I.

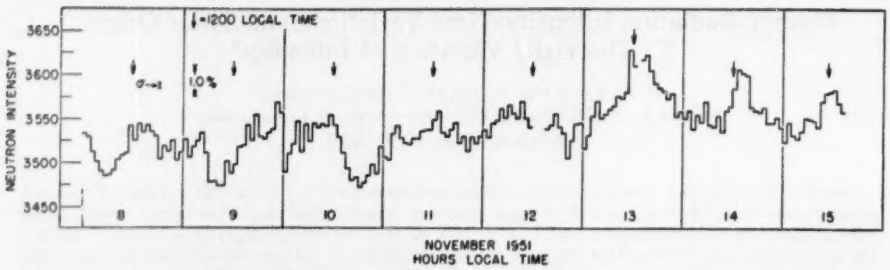

FIG. 1. Hourly values of local neutron production in pile *D*-3 for the period November 8–15, 1951. The standard deviation and the magnitude of a 1 percent change of intensity are shown. The local time is 106°W. meridian time. The arrows indicate 1200 hour.

that these results restrict the possible hypotheses for the origin of this variation.

Two additional properties of neutron intensity measurements are important for studying the 24-hour variation. First, the counting rate is high and second, there is no observed temperature coefficient. This latter property is especially useful in view of the difficulties encountered by charged particle detectors in removing effects of meteorological origin.

The results in this paper are based on data from the neutron pile monitors located at Huancayo, Peru (Station *H*-1, $\lambda \approx -0.5°$ and mean atmospheric depth $\bar{x}=694$ g-cm^{-2}) and Climax, Colorado (Stations *D*-1 and *D*-3, $\lambda=48°$N and $\bar{x}=672$ g-cm^{-2}.) For further details on the instrumentation and the method of measurement the reader is referred to reference I. All data are corrected for barometric pressure variations; even though the pressure coefficients are well established by experiments the peak to peak amplitudes of the corrected curves of intensity variations are insensitive to changes in the pressure coefficient as large as 20 percent.

For observations at mean primary particle rigidities higher than obtained with a neutron pile at $\lambda=0°$ we shall use the data published by Sittkus for a shielded ionization chamber.[11] The instrument and its temperature and pressure coefficients have been described elsewhere.[12]

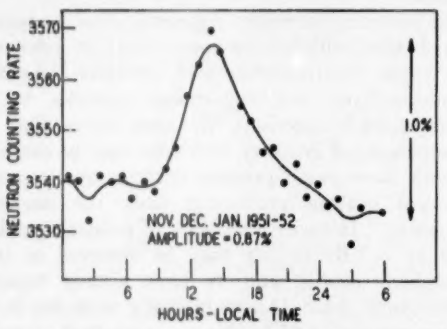

FIG. 2. The average 24-hour variations of neutron intensity for the months November-December, 1951, and January, 1952, for pile *D*-3.

[11] Ionization intensity records published quarterly by A. Sittkus in the "Sonnen-Zirkular" of the Fraunhofer Institute, Freiburg-in-Baden, Germany, 1951–1952.

In the following sections we shall first consider the behavior of the 24-hour variation, averaged over extended intervals of time, and then report on the individual day characteristics.

II. THE AVERAGE 24-HOUR VARIATION

A typical interval of several days is sufficient to indicate the variable character of the 24-hour cosmic-ray intensity variation. For example, the hourly values of the *D*-3 neutron pile counting rate for 7 consecutive days is shown in Fig. 1. Clearly the character of the 24-hour variation is changing day by day and the average 24-hour variation over these days will not represent any of the individual days. In Fig. 2 the average intensity curve for the months November, December, 1951, and January, 1952, displays the outstanding feature of the averaged 24-hour variation; namely, there is an intensity maximum somewhat after local noon.

Although there are difficulties in interpreting the "average" behavior of this variation over extended intervals of time we have examined the changes of the peak-to-peak amplitude of monthly average 24-hour variations to search for changes of amplitude at different times of the terrestrial year. The average peak-to-peak amplitude of the variation for each month between May, 1951, and March, 1953, was prepared for piles *D*-1 and *D*-3, from all the data available on pile *H*-1, and from the Freiburg ionization chamber for the same 2 year period. The results are shown in Fig. 3. We note that (1) there are continuous changes in the monthly averages of the peak-to-peak amplitude, and (2) these changes are observed in all detectors. Hence, we conclude that this month by month change in the average amplitude of the variation is observed over a wide range of primary particle energy. Since seasonal meteorological effects are negligible for the neutron pile *H*-1 (~12°S. geographic latitude), and since the temperature coefficient for a local neutron production detector can at most be only a small fraction of the

[12] A. Sittkus, Z. Naturforsch. 1, 204 (1946).

charged particle coefficient, we do not ascribe this variation of the monthly peak-to-peak amplitude to meteorological factors.

III. BEHAVIOR ON INDIVIDUAL DAYS

To study the amplitude of the intensity variation which occurs on a single day, Fonger[7] adopted a procedure which gives a measure of the amplitude of variations in phase with the *mean* 24-hour cycle. This measure, called D, is the difference in intensity of a period near noon and the average of two periods, one from the preceding night and one from the succeeding night. The time limits chosen for these periods are so adjusted that, for the mean daily cycle the ratio of D to the statistical error in D is a maximum. Figure 4 gives an example of a mean daily cycle for a 3 month period and the times used to compute D values for the individual days in the period.

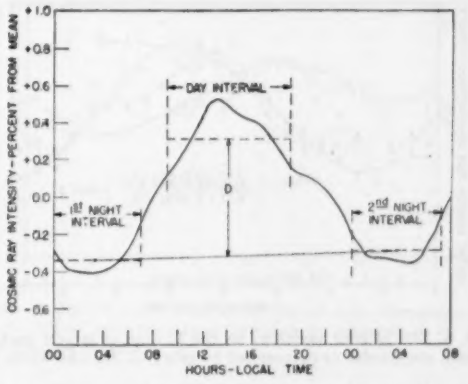

FIG. 4. The mean daily cycle for the period July-October, 1951, using pile D-1. The procedure for computing the difference, D, between the daytime and nightime intensity is shown.

a. The Persistence of the 24-Hour Variation

It is clear from Fig. 1, and similar figures given by Ehmert and Sittkus[6] and Sekido *et al.*,[8] that the amplitude of the 24-hour variation changes from day to day. One question of interest in this connection is: is the amplitude of the variation on one day related to the amplitude the next day, or τ days later? To investigate this question the autocorrelations of the D values for two periods (July–October, 1951, and January–April, 1952) have been obtained and are shown in Fig. 5. Clearly the changes from the mean amplitude which are in phase with the mean cycle persist for only a day or two, and do not have a strong 27-day recurrence tendency as do the daily averages of intensity.[7]

It is obvious from this lack of persistence that two identical detectors separated by many hours in local time will not observe identical 24-hour variations in local time. Thus the 24-hour intensity variation is a continuously changing local time effect.

b. Energy Dependence of the Daily Variation

To investigate the dependence of the daily variation on mean primary-particle energy, we have selected the neutron piles located at $\lambda=0°$ and $\lambda=48°$. These detectors are separated by only 2 hours in local time. The measurements with pile H-1 at 0° are limited at present by the precision of the barometric pressure corrections. Hence, rather than compare single-day amplitudes at $\lambda=48°$ with single-day amplitudes at $\lambda=0°$ we select small groups of days in order to study with greater precision the change in amplitude with geomagnetic latitude. Using an interval of 76 days at $\lambda=48°$, the individual days were listed in descending order of D values. Five groups of days were formed beginning with group a as the 17 days of largest D value, group b as the next largest 10 days, and so forth. Within each group the average intensity for each hour of the 24-hour period was obtained for the D-3 pile. These same days were then used to obtain corresponding average 24-hour curves for the H-1 pile. The curves for groups a through e at both latitudes are shown in Figs. 6, 7, 8, 9, and 10. These results along with the already reported correlation of the daily intensity variation at Climax with the ion chamber at Freiburg, demonstrate that the amplitude variation of the daily variation appears over a wide range of the primary

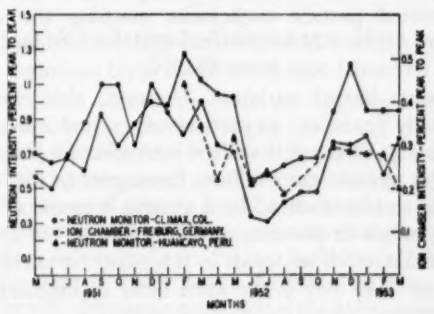
NEUTRON INTENSITY-PERCENT PEAK TO PEAK
ION CHAMBER INTENSITY-PERCENT PEAK TO PEAK
o - NEUTRON MONITOR-CLIMAX, COL.
o - ION CHAMBER-FREIBURG, GERMANY
• - NEUTRON MONITOR-HUANCAYO, PERU
M J J A S O N D J F M A M J J A S O N D J F M
1951
1952
1953
MONTHS

FIG. 3. The average peak to peak amplitude for the 24-hour variation averaged over each month between May, 1951, and March, 1953.

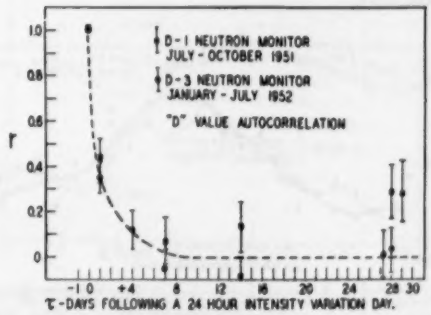

FIG. 5. The persistence of the amplitude of the 24-hour variation is shown for two independent periods; one for pile D-1, the other for pile D-3. There does not appear to be a strong 27-day recurrence tendency.

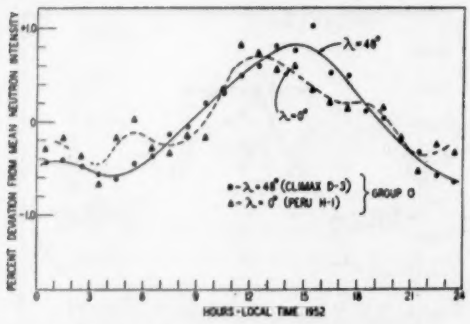

FIG. 6. The 24-hour variation for the 17 days of largest peak-to-peak amplitudes as determined by pile *D*-3. See also Table I.

spectrum. Since only a small number of days were selected for each group, this conclusion may be safely extrapolated to describe the most probable individual-day behavior at these latitudes.

In view of the response of neutron piles to primary radiation at low energy discussed in references I and II, we can state that the primary radiation spectrum with mean energy at least as low as ~5 Bev undergoes this daily variation. The dependence of daily variation amplitude upon latitude and, hence, upon primary particle rigidity can only be estimated at this time. From the data in Figs. 6 and 7 the ratio of peak to peak amplitude variation at 48° and 0° is 1.4 ± 0.2. This shows that the amplitude of the 24-hour variation is dependent upon primary particle energy. We assume primary particles of $z\geq1$ participate in the intensity variation.

IV. ON THE ORIGIN OF THE DAILY VARIATION

Although we are not prepared to describe a theory which will account for the daily variations, we now have sufficient evidence from the combined results of the neutron intensity and charged particle intensity observations to discard some hypotheses which have been proposed to explain the origin. We shall consider some of them here.

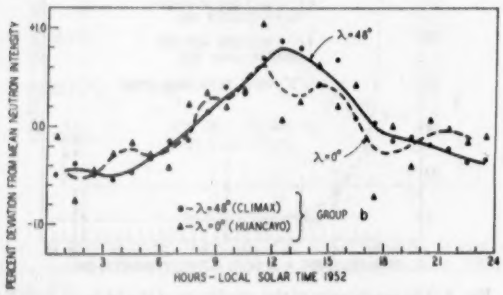

FIG. 7. The 24-hour variation for the 10 days comprising the second largest peak-to-peak amplitudes as determined by pile *D*-3. See also Table I.

a. A 24-Hour Atmospheric Temperature Cycle

The neutron detector with its negligible temperature coefficient displays larger 24-hour intensity variations at $\lambda=0°$ and $\lambda=48°$ than the shielded ion chamber which has a temperature coefficient. As shown in reference I the largest fraction of temperature sensitive links in the nucleonic component occur at high energy, and if sufficient in number would lead to a measureable negative coefficient. Thus the largest effect, if it existed, would occur at $\lambda=0°$. The mean daily atmospheric temperature cycle is known in tropical regions to have a maximum near noon at all altitudes.[13] Thus, if the neutron detector *H*-1 were only influenced by these temperature links in the nucleonic component a series of small noon day intensity *minima* would have been observed. This does not agree with the experimental observations.

Also, the similar behavior of the detectors at 0° and 48° over extended periods of time precludes meteorological factors as the origin of the variation.

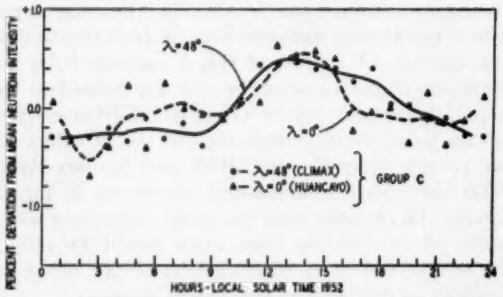

FIG. 8. The 24-hour variation for the 12 days comprising the third largest peak-to-peak amplitudes as determined by pile *D*-3. See also Table I.

b. A General Solar Dipole Magnetic Field

Recent evidence indicates that the general solar dipole moment is probably less than $\sim6\times10^{32}$ gauss-cm^3. If we assume, however, that it is a factor of ten larger there may be an appreciable effect due to the solar cone from Stoermer theory which limits the permitted particle trajectories reaching the earth. There will be a 24-hour variation of the combined solar and terrestrial cone effect which could produce a small 24-hour diurnal variation. However, this effect is strongly dependent on particle energy, and it has been shown by Vallarta[14] that there is no effect for protons of energy greater than 6 Bev. Consequently this effect would not be observed by a neutron detector at $\lambda=0°$ for protons or particles of $Z\geq2$. Clearly the 24-hour variation which we report in this paper for particles of energy ≥13 Bev is the same order of magnitude as

[13] H. Riehl, Bull. Am. Meteorol. Soc. **28**, 311 (1947).

[14] M. S. Vallarta and O. Godart, Revs. Modern Phys. **11**, 180 (1939) and references therein.

for primary particles of much lower energy as shown in IIIb.

c. Primary Neutron Emission from the Sun

If we assume that a stream of particles of cosmic-ray energy approaches the earth from the direction of the sun, then it might also be assumed that high-energy neutrons are part of the cosmic radiation. Since neutrons are not deflected by the geomagnetic field, the most probable impact point on the earth is local noon irrespective of latitude. We shall assume the case where the equatorial plane lies in the plane of the solar system.

It is well established (reference I) that the latitude factor of increase for the nucleonic component is 2.4 between $\lambda=0°$ and $\lambda=48°$ for $x\approx 600$–700 g-cm^{-2}. Consequently a 1 percent noon peak at $\lambda=0°$ due to a plane source of neutrons from the direction of the sun would appear as a 1 percent/2.4=0.42 percent effect at $\lambda=48°$ neglecting the oblique absorption of the primary neutrons at this latitude. However, since the observations are made deep within the atmosphere the intensity observed at high-latitude stations must be corrected for absorption at oblique incidence. This

TABLE I. Neutron pile *D*-3. $\lambda=48°$.

Group	Peak-to-peak amplitude	K_p day average
a	1.4%	33.8
b	1.2%	27.0
c	0.7%	27.8
d	0.5%	23.8
e	0.3%	22.7

further reduces the effect at $\lambda=48°$ ($\sim 39°$ geographic) to $0.42(0.2)\approx 0.08$ percent. Thus the ratio of the amplitudes at Climax to the amplitude at Huancayo would be 8×10^{-2}, whereas the neutron measurements given in part IIb show that this ratio is approximately 1.4. We conclude that primary neutrons in the cosmic radiation do not account for the main features of the daily variation. For a mixed beam of neutrons and protons a peak in the region of the 0400-hour local-time impact zone[15] could be expected at $\lambda=48°$.

d. Modulation by Geomagnetic Field Disturbances

It has been pointed out that the amplitude of the daily variation is enhanced during periods of geomagnetic field disturbances.[4,6,8,9] We may further illustrate this effect by using the 5 groups of days studied in IIb. For the groups of days at $\lambda=48°$ the average values of K_p (a measure of the degree of magnetic disturbance)[16] have been determined with the results shown in Table I. Clearly there is a significant decline of geomagnetic activity with decreasing amplitude of the daily variation.

[15] J. W. Firor, Phys. Rev. **94**, 1017 (1954).
[16] J. A. Simpson, Phys. Rev. **94**, 426 (1954).

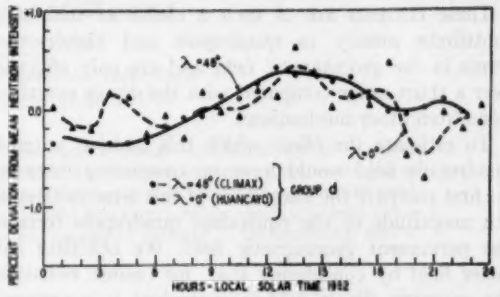

FIG. 9. The 24-hour variation for the 16 days comprising the fourth largest peak-to-peak amplitudes as determined by pile *D*-3. See also Table I.

We cannot conclude, however, that geomagnetic phenomena *produce* the variation. This physical problem may be somewhat analogous to the problem of identifying the origin of the 27-day variation,[16] i.e., the phenomena may be associated by means of a common mechanism located either near the earth or in the vicinity of the sun. In fact, there are some serious difficulties with the assumption that the geomagnetic field produces the daily variation. We may consider this problem first for the periods of undisturbed geomagnetic field variations.

1. The observed variations of the horizonaal magnetic field intensity component are believed to be the combined effect of fields produced by a westward current flow outside the ionosphere (e.g., the Chapman-Ferraro ring current) and circulating currents within the ionosphere. There is no evidence to indicate that the ring current could produce 24-hour oscillations with respect to the axis of the permanent geomagnetic field even though this axis does not coincide with the rotation axis. At present there is increasing and good evidence that the 24-hour variation of the geomagnetic field intensity arises entirely from circulating currents within the terrestrial ionosphere,[17] along with corresponding currents in the surface of the earth.

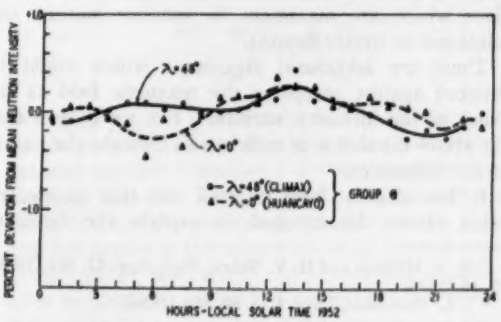

FIG. 10. The 24-hour variation for the 21 days comprising the smallest peak-to-peak amplitudes as determined by pile *D*-3. See also Table I.

[17] S. Chapman and J. Bartles, *Geomagnetism* (Clarendon Press, Oxford, 1940).

These currents are of such a character that they contribute mostly to quadrupole and higher-order terms in the geomagnetic field and are only effective over a short range compared with the dipole contributions from other mechanisms.

To estimate the effect which this 24-hour variable quadrupole field would have on cosmic-ray intensity we first compare the magnitude of this term relative to the magnitude of the equivalent quadrupole term of the permanent geomagnetic field. We calculate this latter field by considering that, for cosmic radiation, the eccentric dipole field is equivalent to a centered dipole with the addition of quadrupole and higher-order terms. We find that this quadrupole term is 5×10^2 to 10^3 larger than the equivalent quadrupole term of the 24-hour variation magnetic field.

Now the cosmic ray intensity longitude effect which is produced by the permanent quadrupole term is considered to be the order of a few percent,[18] but for the following argument we shall assume it may be as large as 20 percent for the nucleonic component since we lack precise measurements of this effect.

Then, the contribution to the cosmic ray intensity variation of the quadrupole term in the geomagnetic field daily variation is certainly less than 0.5×10^{-3} of the total intensity during undisturbed days. It is well established that for disturbed days the amplitude of the 24-hour variation of the horizontal field component increases, but not by more than a factor of 2. Consequently, we can state that the *maximum* 24-hour variation in the cosmic radiation intensity would be <0.2 percent for the neutron component. Clearly, the geomagnetic field variations cannot account for the observed 1–2 percent peak-to-peak amplitude of the daily variation.

Thompson,[19] by a different argument, reaches the same conclusion.

We have shown in IIa that the monthly average of the daily variation amplitude changes with time. These changes are, however, in disagreement with the amplitude variations of the daily magnetic field variations which are maximum in summer months and minimum in winter months.[17]

There are additional arguments which might be invoked against accepting the magnetic field as the cause of the intensity variation, but we believe that the above discussion is sufficient to indicate the nature of the difficulties.

It has already been pointed out that geoelectric fields cannot be invoked to explain the intensity variations occurring in local time due to the high conductivity of the ionosphere.[7]

V. CONCLUSIONS

We have shown that the properties of the 24-hour intensity variations, which were established by ion chamber and counter telescope measurements for the intermediate to high-energy range of the primary spectrum, are also found in the low-energy part of the spectrum. The peak-to-peak amplitude of the 24-hour variation displays a latitude dependence between the geomagnetic cut-offs at 0° and 48° which precludes primary neutrons or a general solar dipole field as the origin of the variation. From the energy dependence and other properties of the neutron observations, we present arguments to exclude meteorological factors, the terrestrial magnetic field variations, and simple geoelectric field accelerations as the origin of the variation. Although doubt is cast on the terrestrial origin of this variation, we have no proof that the variation is of extra terrestrial origin. Since we have shown that the particles which produce the energy dependence of this variation are charged, and since these particles pass through the geomagnetic field arriving at the earth near or somewhat after local noon, then, assuming that the particles carry positive charge, they would approach the earth from the direction of the eastern sky. Consequently, there would be serious difficulties in assuming that these particles have come from the direction of the sun.

The possibility exists that more than one mechanism is producing the observed 24-hour intensity variations. For example, it is possible that one mechanism produces a true 24-hour variation cycle while another mechanism modulates the amplitude of this variation.

At present we do not know whether the charged particles which undergo this variation are protons, heavy nuclei, or a mixture of both. Evidence from the high-altitude observation of heavy nuclei in photographic emulsions indicates that there is probably an effect.[20] Since observations indicating both the presence and absence[21] of the effect have been made, perhaps the effect has the properties of changing amplitude as shown in Fig. 5 for the total radiation.

We wish to thank both the staff at the High Altitude Observatory, Climax, Colorado and A. Giesecke, Jr., and H. Goller at the Instituto Geofisico de Huancayo for their excellent cooperation in maintaining the experimental apparatus.

[18] R. A. Millikan and H. V. Neher, Phys. Rev. **47**, 204 (1935); **50**, 15 (1936).
[19] J. L. Thompson, Phys. Rev. **50**, 869 (1936).
[20] V. Yngve and M. Schein, Phys. Rev. **91**, 432 (1953).
[21] Anderson, Freier, and Naugle, Phys. Rev. **91**, 431 (1953).

Classical Scattering of Mesons

S. P. PANDYA*
Department of Physics, Delhi University, Delhi, India
(Received October 19, 1953)

The theory of "action at a distance" proposed by Wheeler and Feynman for electrodynamics has been extended by various authors to meson fields. It is shown here that the cross sections for the scattering of mesons by nucleons in various cases (charge, dipole, or isotopic spin scattering for scalar or vector mesons) obtained in this theory differ from those obtained in the classical field theory by the absence of those terms which have been interpreted as modification of the nucleon parameter involved in the scattering, due to the reaction of the meson field on the nucleon.

THE theory of "action at a distance" proposed by Wheeler and Feynman for classical electromagnetic fields has been applied to classical scalar and vector meson fields by Kanazawa,[1] Havas,[2] and others to deduce the equations of motion of a point particle with a mesonic charge. Majumdar *et al.*[3] extended the theory to obtain the equations of motion of a point particle with a spin in a scalar or vector meson field. In a recent paper Havas[4] has evaluated the cross sections for scattering of neutral scalar or vector mesons by the mesonic charge of a nucleon on the basis of the equations of motion obtained in the "action at a distance" (a.d.) theory, and compared them with the results obtained in the retarded field theory. For the scalar meson scattering, his result is given by

$$\sigma=\frac{4\pi}{3}\frac{g^4}{\omega_0^4}\frac{k^4}{}\left(M^2+\frac{1}{9}\frac{g^4}{\omega_0^4}k^6\right)^{-1},$$

where the notation is the same as that used in his paper, except that here $k^2=\omega_0^2-\chi^2$. The corresponding field-theoretic result is

$$\sigma=\frac{4\pi}{3}\frac{g^4}{\omega_0^4}k^4\left[\left(M+g^2\chi-\frac{1}{3}\frac{g^2}{\omega_0^2}\chi^3\right)^2+\frac{1}{9}\frac{g^4}{\omega_0^4}k^6\right]^{-1}.$$

Thus the field-theoretic result has some additional terms in the denominator, which are interpreted as the additional mass contributed by the reaction of the field on the nucleon. A similar result holds for the scattering of vector mesons also, though it is not quite clear from the expressions given by Havas. However, they can be rewritten as

$$\sigma=A\cdot\frac{4\pi}{3}g^4\left[M^2+\frac{4}{9}g^4\left(\omega_0^2-\frac{3}{4}\frac{\chi^4}{\omega_0^2}-\frac{1}{6}\frac{\chi^6}{\omega_0^4}\right)\right]^{-1}$$

in the "a.d." theory, and

$$\sigma=A\cdot\frac{4\pi}{3}g^4\left[\left(M+\frac{1}{3}\frac{g^2}{\omega_0^2}\chi^3\right)^2+\frac{4}{9}g^4\left(\omega_0^2-\frac{3}{4}\frac{\chi^4}{\omega_0^2}-\frac{1}{6}\frac{\chi^6}{\omega_0^4}\right)\right]^{-1}$$

for the field-theoretic case, A being a factor depending on the transverse or longitudinal character of incident and scattered mesons. We are only interested in the now obvious fact that in this case also, the a.d. cross section does not contain the terms which correspond to the modification of the nucleon mass by the field reaction.

The author has obtained cross sections for the scattering of neutral scalar and vector mesons by the spin of the nucleon, using the equations of motion derived previously[3] which provide an exactly similar conclusion. It has already been stated in reference 3 that the results given by the a.d. theory do not contain certain terms, which occur in the cross sections given by the field theory, and which were interpreted as an additional moment of inertia perpendicular to the spin axis, contributed by the field reaction. This remark may be amplified here by an example. For scalar mesons scattered by the spin of the nucleon, the field-theoretic cross section is[5]

$$\sigma=\frac{32\pi}{9}f^4\frac{k^4}{\omega_0^2}\left(I^2+\frac{4}{9}f^4\frac{\chi^6}{\omega_0^2}+\frac{4}{9}f^4\frac{k^6}{\omega_0^2}\right)\times\left[\left(I^2+\frac{4}{9}f^4\frac{\chi^6}{\omega_0^2}+\frac{4}{9}f^4\frac{k^6}{\omega_0^2}\right)^2-4\cdot\frac{4}{9}f^4\frac{\chi^6}{\omega_0^2}\right]^{-1},$$

whereas the a.d. theory gives

$$\sigma=\frac{32\pi}{9}f^4\frac{k^4}{\omega_0^2}\left(I^2+\frac{4}{9}f^4\frac{k^6}{\omega_0^2}\right)^{-1}.$$

Here $\frac{2}{3}f^2\chi^3/\omega_0$ has been interpreted as the moment of inertia perpendicular to the spin axis contributed by the field reaction,[6] whereas I is the moment of inertia along the spin axis. Thus we see that in this case again, the field reaction modifying the spin of the nucleon does not appear in the cross sections of the a.d. theory.

The author has carried out similar calculations for cross sections of scattering of neutral vector mesons by the spin of the nucleon and of the scattering of charged scalar and vector mesons by the isotopic spin of the

* Now at the University of Rochester, Rochester, New York.
[1] H. Kanazawa, Progr. Theoret. Phys. 5, 1050 (1950).
[2] P. Havas, Phys. Rev. 87, 309 (1952).
[3] Majumdar, Pandya, and Gupta, Progr. Theoret. Phys. 8, 672 (1952).
[4] C. Mehl and P. Havas, Phys. Rev. 91, 393 (1953).
[5] Harish-Chandra, Proc. Indian Acad. Sci. 21, 435 (1945).
[6] H. J. Bhabha, Proc. Roy. Soc. (London) A178, 314 (1941).

nucleon. In each case it has been found that the result of the a.d. theory differs from that of the retarded field theory by the absence of the terms that correspond to the contribution of the field reaction to the nucleon parameter—be it mass, moment of inertia, or isotopic spin—involved in the scattering. It may be noted that the field reaction terms corresponding to radiation damping (which save the cross section from ultraviolet catastrophe) are the same in both the theories. The details of the calculations show quite clearly that this cancellation of field reaction occurs in virtue of the reactive terms in the equations of motion of the a.d. theory, representing the effect of the future motion of the particle, i.e., terms involving integrals of the type $\int_\tau^\infty \cdots d\tau$, where τ is the proper time of the particle.

I wish to thank Dr. R. C. Majumdar for suggesting the above problem and for helpful discussions. I also wish to thank the Atomic Energy Commission, Government of India, for the award of a research fellowship.

PHYSICAL REVIEW VOLUME 94, NUMBER 4 MAY 15, 1954

Nuclear Interaction of Fast μ Mesons*†

MARTIN ANNIS,‡ HOMER C. WILKINS,§ AND JOHN D. MILLER
Washington University, St. Louis, Missouri

(Received January 28, 1954)

An experimental study has been made of events in which a fast μ meson interacts with a nucleus to produce at least one evaporation neutron. The experimental results of major importance are $\sigma\bar{m} = (9.1\pm1.2)\times10^{-27}$ cm²/Fe-nucleus; $1.03<\bar{m}<7.7\pm2.2$; and $(1.2\pm0.4)\times10^{-27}$ cm²/Fe-nucleus$<\sigma<(8.8\pm1.1)\times10^{-27}$ cm²/Fe-nucleus, where σ is the cross section for such events and $\bar{m}$ is the mean multiplicity of evaporation neutrons emitted. These results are in good agreement with the results of calculations based on present information on the nuclear interaction of γ rays, which lead to the prediction of a σ of about 2.4×10^{-27} cm²/Fe-nucleus and an $\bar{m}$ of about 3.3. The surprisingly large cross section and small mean multiplicity of neutrons are shown to be reasonable by calculating that about 90 percent of all μ-meson nuclear interactions result in the transfer to the nucleus of less than 300 Mev.

INTRODUCTION

IT is now generally known that the μ meson has a weak but nonvanishing interaction with nuclei, both in capture processes and in interactions in flight. Several experiments have been done by other workers in an attempt to determine the cross section for interaction of a fast μ meson with a nucleus. The numbers quoted in the literature[1] differ considerably, due to the fact that the various experimental techniques employed are not equally sensitive to all the processes by which μ mesons interact with nuclei.

Knowledge of the interaction cross section under various conditions makes it possible to draw conclusions as to the nature of the interaction processes involved. Specifically, the fact that the cross section measured in the present experiment is large compared to previous measurements leads, as we show later, to the conclusion that μ mesons of about 11-Bev energy in their interaction with nuclei lose on the average only several hundred Mev.

The data taken by Cocconi and Tongiorgi,[1] in an experiment rather similar to the present one, are, we feel, consistent with the data presented here. The present experiment was designed to detect unambiguously nuclear interactions of μ mesons in which the neutron multiplicity is low; while the Cocconi experiment detected high-multiplicity interactions very efficiently, there was some ambiguity in their assignment of low-multiplicity interactions to mesons.

The present experiment is an outgrowth of the studies at this laboratory[2] of neutron production by fast μ mesons in lead; attention was shifted to iron in order to reduce the neutron yield from γ rays in knock-on showers.

* This article is based on a doctoral dissertation presented to the Graduate Board of Washington University by H. C. Wilkins.

† Assisted by the joint program of the U. S. Office of Naval Research and the U. S. Atomic Energy Commission.

‡ Present address: University of Padua, Padua, Italy.

§ U. S. Atomic Energy Commission Predoctoral Fellow; present address: Alfred University, Alfred, New York.

[1] E. Amaldi and G. Fidecaro, Phys. Rev. **81**, 339 (1951); Castagnoli, Gigli, and Schinto, Nuovo cimento **10**, 893 (1953); Amaldi, Castagnoli, Gigli, and Schinto, Nuovo cimento **9**, 453 (1952); **9**, 969 (1952); Proc. Phys. Soc. (London) **65**, 556 (1952); G. Cocconi and V. C. Tongiorgi, Phys. Rev. **84**, 28 (1951); E. P. George and J. Evans, Proc. Phys. Soc. (London) **A63**, 1248 (1950); E. P. George in *Progress in Cosmic Ray Physics* (North-Holland Publishing Company, Amsterdam, 1952), p. 428.

[2] R. D. Sard, Phys. Rev. **80**, 134 (1950); Sard, Crouch, Jones, Conforto, and Stearns, Nuovo cimento **8**, 326 (1951); M. F. Crouch and R. D. Sard, Phys. Rev. **85**, 120 (1952); H. C. Wilkins, thesis, Washington University, St. Louis, September, 1952 (unpublished). The result of Crouch and Wilkins for the cross-section multiplicity product in 7.6 cm Pb—$(83\pm4)\times10^{-27}$ cm² per nucleus—has been quoted in E. J. Althaus and R. D. Sard, Phys. Rev. **91**, 382 (1953); as pointed out in this paper, it was necessary to assume a large cross section for μ-meson events in which little energy was transferred to the nucleus, in order to explain the large number of cloud chamber pictures containing only a single penetrating particle.

APPARATUS AND DATA

In this experiment nuclear interactions were studied by counting low-energy (less than about 10 Mev) neutrons associated with the passage of μ mesons through a slab of iron. The penetration by the μ meson was indicated by a coincidence of pulses from Geiger counters placed above and below the absorber (Fig. 1). Neutrons were slowed down in the paraffin and were recorded as associated with a penetration if the thermalized neutrons were detected within a 186 μsec time interval starting 7 μsec after the penetration. The equipment was arranged to record those penetrations that were followed by the detection of one or more, two or more, and three or more neutrons within this time interval.

Special features of the experiment included the following:

(1) The number of penetrations was recorded directly.

(2) Penetrations were rejected if in any tray of Geiger counters above the absorber two or more counters were discharged.

(3) In part of the experiment the equipment was arranged so as to discriminate against soft showers initiated by knock-on electrons in the absorber.

The experiment was performed in a limestone cave with a coverage of about 2000-g cm^{-2} (average energy of the μ mesons = 11 Bev). The equipment used was basically the same as that used in the former experiment of Crouch and Sard[3] on the neutron multiplicity associated with the capture of negative μ mesons. A few simple modifications had to be made in order to detect events associated with penetrating particles rather than with particles which reach the end of the range in the absorber; otherwise, no major changes in the geometry or circuitry were made. For a detailed description of the site and the equipment the reader is referred to the report of the previous experiment. Only a very brief description will be given here.

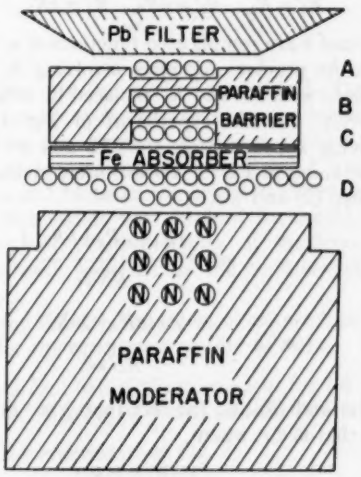

FIG. 1. Schematic of the apparatus—front view. A, B, C, and D refer to the respective trays of Geiger counters. The BF_3 neutron counters are embedded in the paraffin moderator.

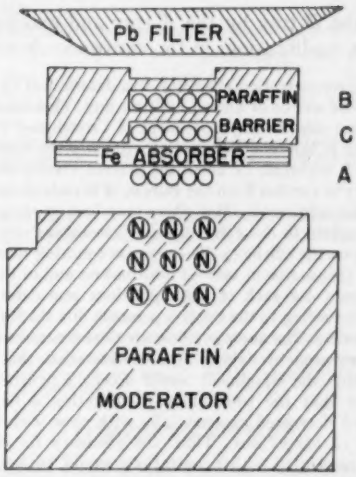

FIG. 2. Schematic of the apparatus for "control" experiment—front view. Note that the D counters have here been replaced by the A counters.

The three trays of Geiger counters A, B, and C, the Pb filter, the paraffin barrier, and the absorber were mounted on horizontal tracks to facilitate changes in the geometry. The bank of D counters was made large enough to cover the solid angle included by the A and C trays above the absorber. The boron trifluoride counters were embedded in a 700-kg block of paraffin, which served to thermalize the neutrons and thus render them detectable by the BF_3 counters.

A penetration was indicated by a fourfold coincidence $ABCD$. If this coincidence was accompanied by the simultaneous discharge of at least one other counter in either the A, B, or C trays, then the event was recorded as a "multiple" and the event was discarded in the analysis. Other events were designated as "singles."

The arrangement of the equipment in Fig. 2 deserves comment. As indicated above, the arrangement shown in Fig. 1 permitted single-multiple discrimination only in the trays of Geiger counters placed above the absorber. The counters in the D tray were simply connected in parallel, thus not making it possible to distinguish between events in which one or more than one charged particle emerged from the absorber. It is evident that if the tray below the absorber could be made to distinguish between single and multiple discharges, then the equipment could be made to discriminate against events in which large showers develop in the absorber. This was accomplished by re-

[3] M. Crouch and R. D. Sard, Phys. Rev. 85, 120 (1952).

placing the D tray by the A tray and making the appropriate modifications in the electronic circuits.

The neutron detection efficiency was determined by the use of a Ra$-\alpha-$Be source of known neutron flux. This source was the same as that used in the experiment of Crouch and Sard and as pointed out in the report of that experiment,[3] the neutron flux of the source is uncertain by about ten percent, corresponding to the uncertainty in the flux from the Bureau of Standards source which was used for calibration. Thus there may be a systematic error of up to 10 percent in our value of the efficiency and any quantities depending on the efficiency. The neutron counting rate was measured with this source in various positions on and in the absorber. The efficiency for each of these positions was determined and weighted according to the relative μ-meson flux through that part of the absorber. The average efficiency thus determined had to be further corrected by taking into consideration the finite time during which the equipment would accept a neutron count. It was found that the probability of detecting a neutron once thermalized decreased exponentially with time with a detection mean life of 162 ± 7 μsec. Thus, the efficiency for detection of neutrons associated with penetrations would be less than that for source neutrons by a factor

$$(1-e^{-T/\tau}),$$

where T is the gate length for counting neutrons and τ is the detection mean life. This factor is 0.68 ± 0.02 for the experiment. The efficiency for the 7.6-cm Fe absorber was 0.0178 and for the 5.1-cm Fe absorber it was 0.0176.

Another source of inefficiency was in the neutron detecting circuits. After a neutron discharged one of the BF_3 counters, the circuit would not accept another neutron pulse for a time d which we call the dead time of the neutron detecting circuit.

Since the energy spectrum for neutrons from nuclear interactions in the absorber is not the same as for the artificial source neutrons, it might be expected that the detection efficiency for artificial source neutrons differs from that for the neutrons from nuclear interactions. If this were true then it would be expected that the top 3 neutron counters would be of different importance in the two cases. By disconnecting the top neutron counters the counting rate for neutrons associated with penetrations decreased by a factor 3.63 ± 0.97. The efficiency for source neutrons decreased by a factor 3.84. Thus, one can think of the detection efficiency as being flat as a function of neutron energy, up to an energy of the order of 10 Mev, then dropping rapidly to zero. *In this experiment, neutrons of energy much greater than 10 Mev cannot be thermalized, and thus are not detected.*

ANALYSIS OF DATA

The quantities that we are interested in evaluating are (1) the cross section (per nucleus) σ for a nuclear interaction in which at least one neutron is released, and (2) the mean number $\bar{m}$ of neutrons released in such interactions. From an experiment of the present type, neither of these quantities can be evaluated separately; rather the product $\sigma\bar{m}$ emerges from an analysis of the data.

Let us define the following quantities:

x = effective thickness of the absorber in g cm^{-2},
N = Avogadro's number,
σ = cross section per nucleus for a nuclear interaction in which at least one neutron is released,
$P(m)$ = probability that in this interaction, m neutrons will be released,
ϵ = efficiency for detection of neutrons associated with penetrations,
R = number of penetrations per unit time,
R_n = number of penetrations recorded per unit time that are accompanied by the detection of n or more neutrons,
R_n' = the value R_n would have if the dead time d of the neutron detecting circuit were zero,
A = atomic weight for the material of the absorber.

In terms of these quantities one can write

$$R_n'=\frac{RNx\sigma}{A}\sum_{m=n}^{\infty}P(m)\left[1-\sum_{i=0}^{n-1}{}^mC_i(1-\epsilon)^{m-i}\epsilon^i\right], \quad (1)$$

where ${}^mC_i=[m(m-1)(m-2)\cdots(m-i+1)]/(i!)$. It can be shown that

$$R_1'+R_2'+R_3'+R_4'+\cdots$$
$$=\frac{RNx\sigma}{A}\sum_{m=1}^{\infty}P(m)m\epsilon=\frac{RNx\sigma}{A}\epsilon\bar{m}, \quad (2)$$

$$R_2'+2R_3'+3R_4'+4R_5'+\cdots$$
$$=\frac{RNx\sigma}{A}\sum_{m=1}^{\infty}P(m)\epsilon^2\frac{m^2-m}{2}=\frac{RNx\sigma}{2}\epsilon^2(\langle m^2\rangle_{Av}-\bar{m}). \quad (3)$$

In the actual experiment there are only three channels, but the error introduced in $\sigma\bar{m}$ by neglecting R_n' for $n\geq4$ is negligible.

In our experiment, the dead time d, during which the neutron circuit could not accept another neutron count, was not negligible, so that the observed R_n rates are too low. A straightforward but laborious calculation shows that the corrected rate R_n' is related to the observed rate R_n by the relations

$$R_1'=R_1, \quad R_2'=aR_2, \quad R_3'=bR_3,$$

where a and b are complicated functions of ϵ, d, T, and τ. Thus the previous formulas involving R_2' and R_3' can be used with R_2' and R_3' replaced by aR_2 and bR_3, respectively. For the experiment of Fig. 1, $d=13.3$ μsec, giving approximately $a=1.18$ and $b=1.66$. For the experiment of Fig. 2, $d=48.9$ μsec, giving $a=1.71$. From Eqs. (2) and (3),

$$\sigma\bar{m}=\frac{(R_1+aR_2+bR_3)A}{RNx\epsilon}, \quad (4)$$

$$\sigma(\langle m^2\rangle_{Av}-\bar{m})=\frac{2A(aR_2+2bR_3)}{RNx\epsilon^2}. \quad (5)$$

From (4) and (5) and the fact that $\langle(m-\bar{m})^2\rangle_{Av}>0$, it follows that $\bar{m}<r$, where

$$r=1+\frac{2(aR_2+2bR_3)}{\epsilon(R_1+aR_2+bR_3)}. \quad (6)$$

Thus, using Eq. (6) an upper bound on $\bar{m}$ can be calculated from the counting rates. Corresponding to

TABLE I. Summary of the data.

Absorber	Arrangement of Fig. 1 7.6 cm Fe	Arrangement of Fig. 1 5.1 cm Fe	Arrangement of Fig. 1 None	Arrangement of Fig. 2 7.6 cm Fe	Arrangement of Fig. 2 None
Penetration rate	39.7/min	42.5/min	40.3/min	35.4/min	36.6/min
Penetrations with N					
raw rate	0.793±0.035/hr	0.724±0.034/hr	0.576±0.036/hr	0.686±0.046/hr	0.446±0.042/hr
corrected rate[a]	0.594±0.035/hr	0.493±0.034/hr	0.328±0.036/hr	0.456±0.046/hr	0.205±0.042/hr
Penetrations with $2N$					
raw rate	0.011±0.004/hr	0.014±0.005/hr	0.002±0.002/hr	0.016±0.007/hr	0.008±0.006/hr
corrected rate[a]	0.011±0.004/hr	0.011±0.005/hr	0.002±0.002/hr	0.016±0.007/hr	0.008±0.006/hr
Penetrations with $3N$					
raw rate	0	0.002±0.002/hr	0	0	0
corrected rate[a]	0	0.002±0.002/hr	0	0	0

[a] The corrections applied to the data were of two types: (1) correction for accidental coincidences and (2) correction for events recorded both in the "single" and the "multiple" channels. The latter kind of event was due to the accidental overlapping of the "single" and the "multiple" long gate pulses used in the recording equipment. These data are not corrected for the finite dead time of the equipment.

this upper bound on $\bar{m}$ there is a lower bound on σ given by Eq. (4).

An upper bound on σ can also be obtained. Another expression for R_1 is $(RNx\eta\sigma)/A$, where η is the efficiency of the system for detecting the nuclear event. η would be equal to ϵ if only one neutron were emitted and would be 1 if an infinite number of neutrons were emitted. Thus, an upper bound on σ is

$$\sigma<(R_1A)/(RNx\epsilon).$$

It can also be shown that if the neutron production is due to a combination of processes, each corresponding to a different σ and a different multiplicity distribution, then the results are additive, i.e.,

$$R_1+aR_2+bR_3=[(RNx\epsilon)/A](\sigma\bar{m})_T,$$

where $(\sigma\bar{m})_T$ is given by

$$(\sigma\bar{m})_T=\sum_{i=1}^{N}\sigma_i\bar{m}_i.$$

The data are summarized in Table I. The neutron coincidence rates R_n are the corrected observed rates reduced by the corresponding rates without absorber. R is the penetration rate given in Table I. The effective thickness is 1.14 times the actual thickness of the absorber. This factor was obtained by taking into consideration all possible angles of incidence on the absorber, each weighted by the $\cos^2\theta$ law of μ-meson intensity.

By using Eq. (4), the values of $\sigma\bar{m}$ are found to be as follows for the experiment of Fig. 1:

$\sigma\bar{m}=(9.2\pm1.6)\times10^{-27}$ cm^2/nucleus for 7.6 cm Fe,
$\sigma\bar{m}=(7.5\pm2.4)\times10^{-27}$ cm^2/nucleus for 5.1 cm Fe,

and for the experiment of Fig. 2,

$\sigma\bar{m}=(9.9\pm2.5)\times10^{-27}$ cm^2/nucleus for 7.6 cm Fe.

(It is seen that the double and triple neutron rates are too small to permit evaluation of $\sigma\langle m^2\rangle_{\text{Av}}$ and higher moments.)

COMPETING EFFECTS

The results given above are the cross-section multiplicity products for all possible processes by which a charged particle penetrating the absorber can release one or more evaporation neutrons in the absorber. To obtain results for the primary interaction of a μ meson with a nucleus, an estimate must be made of the contribution of other processes. Among these competing processes the following might be considered important.

1. Effect of Shower γ Rays

Evaporation neutrons could possibly arise by the following process (see Fig. 3): a μ meson imparts energy to a knock-on electron in the absorber; the knock-on electron then initiates a soft shower, the γ rays of which interact with nuclei of the absorber to produce evaporation neutrons. This event would be accepted by the apparatus shown in Fig. 1. A lengthy calculation

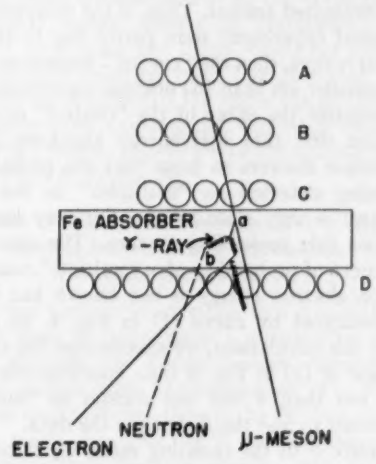

FIG. 3. Effect of shower γ rays in absorber. A μ meson knocks on an electron in the Fe absorber at a. This electron initiates a soft shower, and one of the γ rays in the shower causes a nuclear interaction at b.

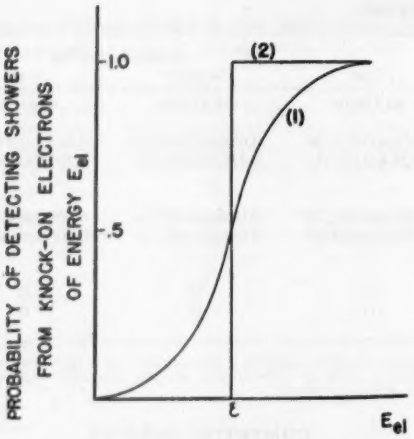

FIG. 4. Curve 1 represents the probability that a knock-on electron of energy E_{el} initiate a shower that is detectable as a "multiple" event. Curve 2 is a simplified version of 1 for the purpose of calculations.

based on Snyder's solution[4] of the approximation "B" shower theory diffusion equations and on the observed neutron yield from the "giant resonance" interaction of 20-Mev γ rays leads to the prediction that shower γ rays could contribute to $\sigma\bar{m}$ as much as 10×10^{-27} cm^2/nucleus for the experiment with 7.6-cm Fe absorber. This is approximately the observed value. Of course, one would not expect approximation "B" to give very good results for γ-ray energies as low as 20 Mev. The "control" experiment, illustrated in Fig. 2 and discussed earlier, was designed to test the effect of shower γ rays in producing neutrons. Since in the "control" experiment events were discarded if more than one charged particle emerged from the absorber, events associated with large showers in the absorber are discriminated against. Thus, if the observed $\sigma\bar{m}$ for the original experiment were partly due to the effect of shower γ rays, then the "control" experiment should yield a smaller $\sigma\bar{m}$ than the original experiment.

To evaluate the effect of the "control" experiment we reason first that high-energy knock-on electrons will produce showers so large that the probability of their being detected as "multiples" in the control experiment is very close to one. For very low-energy knocksons this probability is zero. The exact shape of the curve of probability of a "multiple" count *versus* knock-on electron energy is not known but it might be as indicated by curve (1) in Fig. 4. In order to simplify the calculations, we assume that the curve has the shape of (2) in Fig. 4 (i.e., knock-on electrons of energy less than $\mathcal{E}$ will not register as "multiples") and proceed to find the $\mathcal{E}$ that fits the data.

To relate $\mathcal{E}$ to the counting rates, we calculate the probability, $P(E_{el}>\mathcal{E})$, that a μ meson in passing through the absorber will give to a knock-on electron an energy greater than $\mathcal{E}$:

$$P(E_{el}>\mathcal{E})=\frac{Nx}{A}\int_{E_\mu=0}^{\infty}\int_{E_{el}=\varepsilon}^{E_{el\max}}N(E_\mu)dE_\mu\frac{\partial\sigma}{\partial E_{el}}dE_{el}, \quad (7)$$

where[5]

$$N(E_\mu)dE_\mu=\frac{(4.27)10^6dE_\mu}{(E_\mu+7700)^{2.65}}$$

is the number of μ mesons 2000 g cm^{-2} underground with energy between E_μ and $E_\mu+dE_\mu$,

$$E_{el\max}=\frac{2m_{el}c^2E_\mu^2}{m_\mu^2c^4+2m_{el}c^2E_\mu}$$

is the maximum transferable energy, and

$$\frac{\partial\sigma}{\partial E_{el}}dE_{el}=(25.1)(Z)(10^{-26})\frac{dE_{el}}{E_{el}^2}$$

is the differential cross section per atom for a μ meson to give to a knock-on electron an energy between E_{el} and $E_{el}+dE_{el}$.[6]

In all of these equations, energies are measured in Mev. Figure 5 is a plot of $P(E_{el}>\mathcal{E})$ *vs* $\mathcal{E}$.

To obtain the rate at which tray A of Fig. 2 counts "multiples" produced in the absorber, the experiment illustrated in Fig. 6 was performed. The Pb was used to insure that the particles triggering the array of counters were penetrating particles. Only those "multiples" occurring in tray A were counted and the difference between the multiple rates "with" and "without" the Fe absorber was taken as the rate of

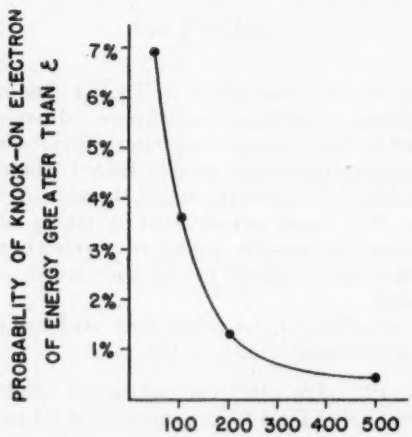

FIG. 5. Plot of the probability that a μ meson knock on an electron of energy greater than $\mathcal{E}$ *vs* $\mathcal{E}$.

[4] H. Snyder, Phys. Rev. **76**, 1563 (1949).

[5] D. C. Peaslee, Nuovo cimento **9**, 61 (1952); Barrett, Bollinger, Cocconi, Eisenberg, and Greisen, Revs. Modern Phys. **24**, 133 (1952).

[6] B. Rossi, *High Energy Particles* (Prentice-Hall, Inc., New York 1952).

detection of multiple events produced in the absorber. To make sure that the μ-meson spectrum did not change, the run "without" absorber was made with the Fe still in the telescope, but now over the B tray [Fig. 6(b)]. The results are given below:

	Absorber above	Absorber below
AB rate	(49.6±0.2)/min	(48.9±0.2)/min
A_mB rate	(2.79±0.05)/min	(1.90±0.04)/min.

Thus, 1.8 percent of the μ mesons produce knock-on electron showers that are detected.

Referring to Fig. 5, we see that this probability corresponds to $\mathcal{E}=170$ Mev. This means that, on the average, showers initiated by knock-on electrons of energy greater than 170 Mev are detected, whereas those of smaller energy are not detected as "multiples."

In the calculation (approximation B) of an equivalent μ-meson cross section for evaporation neutron production through the intermediary of shower γ rays, it was found that showers resulting from knock-on electrons of energy greater than 170 Mev contribute roughly half the total calculated cross section. Since conventional shower theory overestimates the number of 20-Mev photons near the beginning of a shower,[7] the contribution of shower γ rays to $\sigma\bar{m}$ in the "control" experiment must be less than half the contribution in the other experiment with 7.6-cm Fe. If, for example, all of the measured $\sigma\bar{m}$ observed in the experiment of Fig. 1 had been due to shower γ rays as predicted by shower theory, then the expected value for the "control" experiment of Fig. 2 would have been less than

$$0.5(9.2\pm1.6)10^{-27}=(4.6\pm0.8)10^{-27}\ \text{cm}^2/\text{nucleus}.$$

But the observed value is $(9.9\pm2.5)10^{-27}$ cm^2/nucleus; in the same time the standard deviation would have been about 1.7 if the value of $\sigma\bar{m}$ had been 4.6, and the difference between the expected value and the observed value is 5.3×10^{-27}. If one assumes that the true value of this difference is zero (i.e., 0 ± 1.9) the probability of a fluctuation as large as 5.3×10^{-27} is about 0.004. Therefore, the $\sigma\bar{m}$ value for 7.6-cm Fe cannot all be ascribed to the effect of shower γ rays. On the contrary, the experimental results suggest that the effect of shower γ rays is negligible.

2. Effect of Nuclear Cascades Beginning in the Absorber

The neutrons detected in the experiment are those due to the original event plus any that are produced in nuclear cascades developing in the absorber and in the paraffin surrounding the neutron counters. Therefore, in order to give a $\sigma\bar{m}$ value that can be ascribed to the primary nuclear interaction of a μ meson, the effect of nuclear cascades must be considered.

The experiment gives evidence that nuclear cascades have at most a small effect. This evidence consists of the following considerations:

[7] R. R. Wilson, Phys. Rev. 86, 261 (1952).

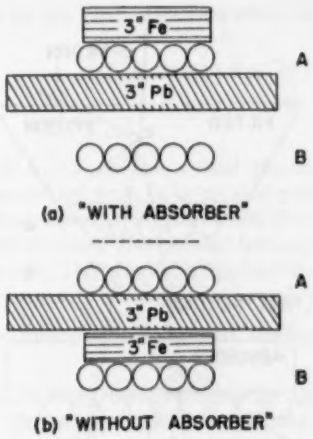

FIG. 6. Schematic of the apparatus used to test the efficiency of the "control" experiment for shower detection.

(a) If a nuclear cascade continued to develop in the paraffin surrounding the neutron counters, the lower counters would be more important for the detection of neutrons from the cascade than for the detection of neutrons from the original event. Thus, by disconnecting the top three neutron counters, the neutrons from the cascade in the paraffin would be favored. The results given earlier indicate that the efficiency for detecting neutrons from the absorber (and cascade, if any) is not significantly different from the efficiency for detection of neutrons from the artificial source. This result suggests that there is very little, if any, effect of nuclear cascade in the paraffin.

(b) It is reasonable to assume that if nucleons from nuclear interactions of μ mesons are energetic enough to cause a large nuclear cascade, then protons and π mesons would often be able to get out of the absorber. Such events would register as "multiples" in the "control" experiment and hence would not contribute to the neutron counting rate. The fact that $\sigma\bar{m}$ for the control experiment did not differ significantly from the corresponding quantity for the other experiment suggests that neither shower γ rays nor nuclear cascades are important in 7.6-cm Fe.

3. Effect of Neutrons, Protons, and π Mesons Arising from Nuclear Interactions Outside the Absorber

For a fast neutron to give rise to a spurious count, it would have to accompany a penetrating charged particle through the Geiger-counter telescope and initiate a nuclear event in the absorber (Fig. 7). Neutrons from nuclear interactions in the Pb filter above the telescope might thus give rise to spurious counts. This process is unlikely because protons that might accompany the neutron out of the Pb filter would trigger another counter in the Geiger-counter telescope and thus the event would not register.

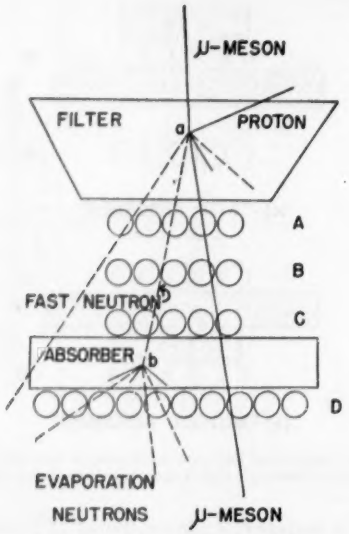

FIG. 7. A possible sequence of events resulting in a "single" accompanied by a spurious neutron count. A μ meson interacts at a, and continues on through trays $ABCD$. One of the secondary fast neutrons interacts at b.

Protons and π mesons originating in the filter can be neglected since in most cases a proton from an interaction in the filter will be accompanied by the original μ meson, thus triggering a multiple count. Protons and π mesons originating in the roof of the cave have a relatively small chance of penetrating the filter.

The most powerful evidence for believing that few high-energy secondary nucleons are produced per μ meson-nucleus interaction is the fact that the "control" experiment gives the same $\sigma\bar{n}$ as does the experiment of Fig. 1. Secondary protons or mesons would register as "multiples" in the "control" experiment, so that if they were produced with any frequency, the "control" experiment would have resulted in a far smaller $\sigma\bar{n}$.

These considerations indicate that neutrons, protons, and π mesons produced outside the absorber have no important effect on the neutron counting rates in the experiment.

SUMMARY OF RESULTS

The experimental data indicate that competing effects are unimportant in the experiment. Therefore, it is justifiable to lump the results of the three experiments—that with 7.6-cm Fe absorber, with 5.1-cm Fe absorber, and the control experiment. The results of major importance are

$$\sigma\bar{n}=(9.1\pm1.2)\times10^{-27}\ \text{cm}^2/\text{Fe-nucleus},$$
$$1.03<\bar{n}<7.7\pm2.2,$$
$$(1.2\pm0.4)\times10^{-27}\ \text{cm}^2/\text{Fe-nucleus}<\sigma<(8.8\pm1.1)\times10^{-27}\ \text{cm}^2/\text{Fe-nucleus}.$$

DISCUSSION OF RESULTS

The work of George and Evans[8] gave 4.4×10^{-30} cm^2/nucleon for the cross section for production of stars of at least one minimum ionizing track in the lower hemisphere and at least 3 "heavy" prongs (presumably protons). (The minimum excitation energy of these stars was of the order of 150 Mev.) The mean number of ionizing prongs for these stars was about 6, so that the mean number of neutrons must have been about 7;[9] so that $\sigma\bar{n}=1.7\times10^{-27}$ cm^2/Fe-nucleus, a value much smaller than the $\sigma\bar{n}$ measured in the present experiment. As we shall show below, this apparent discrepancy can be explained, when the low-energy interactions of μ mesons with the nucleus are taken into account.

In an experiment rather similar to the present one, in that nuclear interactions were detected by observing evaporation neutrons, Cocconi and Tongiorgi[1] evaluated $\sigma\bar{n}$ for Pb and for Al. However, as mentioned previously, the low-multiplicity events could not unambiguously be assigned to μ-meson interactions. From measurements on the nuclear interactions of γ rays, it is possible, as we show below, to calculate a partial $\sigma\bar{n}$ for interactions in which μ mesons transfer less than about 300 Mev to the nucleus. This corresponds, on the average, to a neutron multiplicity of about 6. Hence we shall use the Cocconi and Tongiorgi data to calculate a partial $\sigma\bar{n}$ for events in which more than 300 Mev is transferred to the nucleus. If one ignores the data in their first six channels, one can calculate a $\sigma\bar{n}$ for events in which 7 or more neutrons are emitted. Making a very crude interpolation between the Cocconi results for Pb and Al, one finds that $\sigma\bar{n}$ is between 2×10^{-27} [10] and 4×10^{-27} cm^2/Fe-nucleus and that $\bar{n}\approx11$. The two limits on $\sigma\bar{n}$ correspond to extreme assumptions concerning the effect of the secondary particles capable of producing nuclear interactions.[11]

A photoplate experiment on star production is biased against low-energy interactions. The present experiment requires only that at least one evaporation neutron be released. That such low-energy events occur is evident if one represents the electromagnetic field of the μ meson as a spectrum of "equivalent" γ rays.

In order to analyze this model further, it is assumed that μ mesons interact with nuclei by way of these equivalent photons. The spectrum of photons is given by the Williams-Weizsäcker formula

$$R(E_\gamma)dE_\gamma=\frac{2}{137\pi}\frac{dE_\gamma}{E_\gamma}\ln\left[\frac{2}{3}\frac{E_\mu}{E_\gamma}\right].$$

[8] E. P. George in *Progress in Cosmic Ray Physics* (North-Holland Publishing Company, New York, 1952), p. 428.
[9] K. J. LeCoutenur, Proc. Phys. Soc. (London) **A63**, 259, 498 (1950).
[10] This value of $\sigma\bar{n}$ is about twice as large as the corresponding quantity for the George data.
[11] This effect was probably larger in the Cocconi experiment than in the present one.

In this equation, $R(E_\gamma)dE_\gamma$ is the number of photons with energy between E_γ and $E_\gamma+dE_\gamma$ associated with a μ meson of energy E_μ. It is further assumed that these equivalent photons interact with matter by the same processes as do real γ rays. The processes by which real γ rays are known to interact with nuclei are the following.

(1) Star Production

The process by which high-energy γ rays (E_γ greater than about 100 Mev) produce high-energy stars is thought to be one in which a π meson is first produced in and then absorbed by the (same) nucleus. The cross section for this process is about 2×10^{-28} cm^2/nucleon per effective quantum at low energies.[12] Assuming that this value is applicable for all E_γ, and making use of the Williams-Weizsäcker formula and the μ-meson energy spectrum, one obtains a value of cross section

$$\sigma_{\text{theor}}\approx0.15\times10^{-27}\text{ cm}^2/\text{Fe-nucleus}$$

for events in which more than 300 Mev is transferred to the nucleus. Thus, it is not unreasonable to assume that this process can account for a $\sigma\bar{m}$ of between 2×10^{-27} and 4×10^{-27} cm^2/Fe-nucleus in the present experiment (e.g., take $\sigma=0.2\times10^{-27}$ cm^2/Fe-nucleus and $10<\bar{m}<20$ for events in which 7 or more neutrons are emitted).

(2) "Giant Resonance" Interactions

The interaction cross section of γ rays with Fe has a "giant resonance" in the vicinity of 20-Mev γ-ray energy. This interaction leads to the production of one or possibly two neutrons. Let us assume that the cross section for such low-energy γ rays can be expressed as a δ function:

$$\bar{m}\sigma(E_\gamma)dE_\gamma=\Pi\delta(E-E_{GR})dE_\gamma,$$

in which Π is the integrated cross-section multiplicity product around $E_\gamma=E_{GR}$, and E_{GR} is the energy at the peak.

Then, for a given μ meson, the cross section for an interaction by the giant resonance effect is

$$\sigma=\int_0^\infty \Pi R(E_\gamma)\delta(E_\gamma-E_{GR})dE_\gamma$$
$$=\Pi R(E_{GR}),$$

in which $R(E_\gamma)dE_\gamma$ is the virtual photon spectrum. Such a cross section must be integrated over the energy spectrum of μ mesons, $N(E_\mu)dE_\mu$. Using $\Pi=0.735\times10^{-24}$ cm^2 Mev per nucleus,[13] one obtains $(\sigma\bar{m})_{GR}\approx0.8\times10^{-27}$ cm^2/Fe-nucleus. This would be the contribution of this process to the result of the present experiment.

(3) Low-Energy Interaction of Higher-Energy γ Rays

In recent months more information has been obtained on the energy dependence of the interaction cross section of γ rays of energies up to about 300 Mev. It is found, for example by Terwilliger and Jones,[13] that the cross section for production of evaporation neutrons increases as energy increases (beyond ≈80 Mev) above the giant resonance region. Taking into consideration this rise in cross section with energy up to 300 Mev, the corresponding equivalent photons could contribute about 3.9×10^{-27} cm^2/Fe-nucleus to the $\sigma\bar{m}$ value for the present experiment. These events probably have a neutron multiplicity less than 7, so this number can be combined with our previous results. We will assume a mean multiplicity of 3 for these events.

These three processes thus account for roughly 8×10^{-27} cm^2/nucleus, in reasonably good agreement with our result. Using the numbers in (1), (2), and (3), one finds $\sigma\approx2.4\times10^{-27}$ cm^2/Fe-nucleus for events in which one or more neutrons is emitted, and $\bar{m}\approx3.3$. The "star" producing events, (1), contribute only about 10 percent to the cross section.

ACKNOWLEDGMENTS

The authors wish to express their thanks to Professor H. Primakoff and Professor R. D. Sard for many helpful discussions.

Our thanks also go to the International Shoe Company for permitting us to use the Lemp Cave site, and Mr. J. D. Campbell and his staff for their cooperation and help in making the experiment possible.

[12] Panofsky, Steinberger, and Stellar, Phys. Rev. **86**, 180 (1952); R. D. Miller, Phys. Rev. **82**, 260 (1951).

[13] L. W. Jones and K. M. Terwilliger, Phys. Rev. **91**, 699 (1953).

Decay of τ Mesons of Known Charge*†

R. H. DALITZ‡
Laboratory of Nuclear Studies, Cornell University, Ithaca, New York
(Received February 9, 1954)

The experimental data on the 3π decay of τ mesons is summarized on a convenient two-dimensional plot, both (a) when the π-meson charges are known and (b) when they are not. Some events may be included in plot (a) only if the parent τ meson is assumed positive and arguments supporting this identification for τ mesons decaying in an emulsion are discussed. The dependence of this plot on the τ-meson spin (j) and parity (w) is discussed in general terms and those features depending particularly on w and on its relation with j are emphasized—for example, if the density of events does not vanish at the bottom of the plot, the τ meson must have odd parity and even spin. Simple estimates of the distribution, using only the lowest allowable angular momenta and a "short range" approximation, may be modified by final-state meson-meson attractions, whose effects are discussed qualitatively. The available data are insufficient for any strong conclusion to be drawn but rather suggest even spin and odd parity for the τ meson; the need for careful assessment of geometrical bias in the selection of experimental material is stressed.

1. INTRODUCTION

IN a previous paper,[1] the analysis of τ-meson decay events which give rise to three charged π-meson secondaries has been discussed. In this analysis it was generally assumed that the charges of the outgoing π mesons were not known; at that time the data available consisted of events in which the emitted π mesons generally escaped from the emulsion before coming to rest. However, it was emphasized in this work that the identification of the π meson which has charge opposite to that of the parent τ meson would enable a more complete analysis of the distribution of decay configurations and would give a more sensitive indication of specific τ-meson properties such as spin and parity.

Recently, as a result of the widespread adoption of the "stripped emulsion" technique, a number of τ-meson decay events have been reported[2–5] in which the unlike π meson (charge opposite to the parent τ meson) could be identified. In the block of emulsion, the product π mesons may be followed from layer to layer, the probability that a π meson comes to rest before escaping is correspondingly increased, and the sign of charge of each π meson which stops may be established as positive or negative according as it undergoes π-μ decay or not at the end of its range. In one case[3] the geometry of the event was such that all three π mesons could be identified in this way. Further, there have been reported[6] two τ-decay events which were observed in a cloud chamber with a magnetic field present, and for which the π-meson charges were all established.

In several of the emulsion examples, the π mesons identified have been sufficient to establish the sign of charge of the parent τ meson, since its magnitude is known to be $|e|$, and in each case the τ-meson charge has been positive. There are good reasons to suppose that all τ mesons which decay to three π mesons in an emulsion are of positive charge. The statistics of the sign of charge of the identified secondary π mesons also suggests that the parent τ mesons are at least predominantly positive (to the present seventeen π^+ mesons have been identified, compared with nine π^- mesons). The fact that the three π mesons emitted are coplanar (to better than 1° in the most complete decay examples) and, to a less significant extent, the fact that the vector sum of the π-meson momenta is zero to a good accuracy, indicate that at the moment of decay the τ meson had a very small momentum. Now the lifetime of the τ meson is known to be sufficiently long ($\gtrsim 10^{-9}$ sec) for a τ^- meson to come to rest in the emulsion, to be captured into an atom of the emulsion and, by successive Auger processes, to be captured into a low-lying Bohr orbit of the atom. At the time of decay the τ^- meson would then have a considerable velocity and, because of its large mass, a high momentum (of order $(ZM_\tau c)/137n$, Z being the nuclear charge, M_τ the τ-meson mass and n the principal quantum number of the Bohr orbit). The coplanarity of the 3π decay is particularly sensitive to the τ-meson velocity at the time of decay and even a velocity of order $c/137$ would upset the coplanarity by $\sim 3°$ on the average. The τ^+ meson, on the other hand, would move only with thermal velocities after being slowed down by the emulsion and strict coplanarity of the product mesons would be expected. Although it is not possible to argue

* The essential contents of this paper were reported at the American Physical Society, Chicago Meeting [Phys. Rev. **93**, 914 (1954)].

† Supported in part by the joint program of the U. S. Office of Naval Research and the U. S. Atomic Energy Commission.

‡ On leave of absence from the Department of Mathematical Physics, University of Birmingham, Birmingham, England.

[1] R. H. Dalitz, Phil. Mag. **44**, 1068 (1953).

[2] Lal, Pal, and Peters, Phys. Rev. **92**, 438 (1953). These events are denoted by prefix *B*.

[3] Belliboni, Sechi, and Zorn, Nuovo cimento (to be published). This is event *PAD*3 of Fig. 3.

[4] Bristol group, events prefixed by *BR* (private communication).

[5] H. Yagoda, event *Y*1 (private communication); M. F. Kaplon, event *R*2 (private communication).

[6] R. B. Leighton and S. D. Wanlass, Phys. Rev. **86**, 426 (1952); V. A. J. Van Lint and G. H. Trilling, Phys. Rev. **92**, 1089 (1953).

in this way that particular cases are examples of τ^+ rather than τ^- mesons, statistically the conclusion is again that the majority of τ mesons observed to decay in emulsions are of positive charge.

It is known that there exists some strong interaction involving τ mesons and nucleons, since τ mesons are produced directly in high-energy nuclear interactions. However, this interaction need not necessarily permit the direct absorption of τ mesons by nuclei, since it may well be a τ-meson pair interaction or one connecting the τ meson with some other heavy meson. It is therefore of interest to emphasize that the nuclear absorption of heavy mesons does not require a strong direct interaction between nucleons and heavy mesons, because of the small probability per unit time for the heavy meson decay. Whether a τ meson in an atomic K orbit is absorbed or decays may depend on the competition of a weak nuclear interaction with this slow rate of decay. Even if, for example, it is supposed that the only direct interaction of the τ meson with nucleons is that occurring in virtue of the τ-meson decay scheme, i.e.,

$$\begin{aligned}&\tau^-+P\rightarrow\pi^++\pi^-+\pi^-+P\rightarrow\pi^-+P\\ \text{or}\quad&\\ &\rightarrow\pi^++\pi^-+N,\end{aligned}\qquad(1.1)$$

then a τ^- meson in an atomic K orbit of the heavier elements (Ag, Br) of the emulsion will certainly undergo nuclear capture[7] rather than decay. About 30 percent of the τ^- mesons will be captured into atoms of the lighter elements (C,N,O) of the emulsion and these will reach the K orbit before decay; for these τ mesons, nuclear capture will then be, at the least, strongly competitive with decay, even if (1.1) is the only absorptive mechanism effective. It is also to be expected that about 5 percent of the τ^- mesons will be captured into the hydrogen of the emulsion, but most of these will be transferred from the hydrogen to atoms of higher Z (in a time $\sim10^{-11}$ sec) as a result of the diffusion of the neutral $H-\tau^-$ complex. It is therefore plausible, even in the absence of detailed knowledge of the τ-meson production process, to suppose that the majority of negative τ mesons[8] undergo nuclear capture in an emulsion rather than decay. In the analysis of the data (Sec. 3) it will be assumed that a τ meson observed to decay in an emulsion had positive charge; any corrections due to negative τ-mesons decaying in outer atomic orbits or to τ mesons decaying in flight in the emulsions will clearly be quite small.

The importance of establishing the existence of the alternative decay mode $\tau^\pm\rightarrow\pi^\pm+\pi^0+\pi^0$ has been emphasized recently.[9] Some events which may be interpreted as examples of this mode of decay have now been observed.[10] It is of course very difficult to establish definitely for any particular event that it represents this mode of decay rather than, for example, $\tau^\pm\rightarrow\pi^\pm+2\gamma$. However, the former hypothesis does not involve any essentially new decay modes and is therefore a very reasonable assumption at the present stage. In this decay only the energy of the charged meson is known and the distribution of this energy will give considerable information on the consistency of this hypothesis and on the nature of the parent meson. The relation between this distribution and that for the π^--meson in τ^+-decay will not in general be unique and a comparison between these would be of considerable interest.

The purpose of the present paper, then, is to discuss briefly the analysis of the decay of the τ^+ meson into three π mesons of known charge and to emphasize some uncertainties in the possible interpretation resulting from the possibility of bias in the selection of experimental material and to the inadequacies of any proposed theory.

2. THE ANGULAR CORRELATION IN τ-MESON DECAY‖

The decay of a τ^+ meson, initially at rest, into three π mesons is specified uniquely by the momentum $\mathbf{p}$ of the π^- (unlike) meson and by the momenta $\pm\mathbf{q}/2$ of the π^+ (like) mesons in the center-of-mass system for the two like mesons. As in Fig. 1 the like mesons will be specified, where necessary, by suffices 1, 2, the unlike meson by suffix 3. The magnitudes of $\mathbf{p}$ and $\mathbf{q}$ are related by the conditions of conservation of energy and momentum. The quantity $(\epsilon_1+\epsilon_2)^2-(\mathbf{p}_1+\mathbf{p}_2)^2$ is a Lorentz invariant (units being chosen such that $c=1$; ϵ_i, $\mathbf{p}_i$ are the total energy and momentum of meson i), having the value

$$(M_\tau-\epsilon_3)^2-p^2=M_\tau^2+m_\pi^2-2m_\tau\epsilon_3$$

[7] If the coupling constant between τ-meson and π-meson fields is g, the decay probability per unit time is

$$\sim g^3(M_\tau-3m_\pi)^2c^4h/192\pi^3\sqrt{3}M_\tau.$$

The capture rate from the K orbit of a nucleus of charge Z, resulting from the process $\tau^-+P\rightarrow\pi^-+P$ of (1.1) is

$$\sim G^2(M_\tau{}^3c^4/h^3)(e^2/hc)^2Z^4/8\pi^3,$$

where G, the coupling constant for this process, is expected to be $\lambda g(g_\pi{}^2/hc)(h^3/M)$, g_π being the π-meson nucleon coupling constant, M the nucleon mass, and λ a constant of order 1. This capture rate is equal to the decay rate for $Z\sim3$. Any other capture processes will contribute to increase this capture rate. For higher τ-meson spin values, the matrix element will be energy dependent, but generally speaking, this will increase the ratio of capture rate to decay rate since higher momenta are concerned in the capture process. It should be remarked here that it appears probable theoretically that nuclear absorption will in fact be effected by some strong interaction of the type $\tau^-+P\rightarrow\pi^0+\Lambda_0$.

[8] It should be noted here that there is no doubt concerning the existence of the negative τ meson since the τ meson observed by Van Lint and Trilling (reference 6) in a cloud chamber was of negative charge.

[9] R. H. Dalitz, Proc. Phys. Soc. (London) **A66**, 710 (1953).

[10] Crussard, Kaplon, Klarmann, and Noon, Phys. Rev. **93**, 253 (1954); P. Barrett (private communication).

‖ In this section we shall refer specifically to the decay of τ^+ mesons since it is very probable that the emulsion events exemplify this case. For the description of τ^--meson decay it is only necessary to reverse the sign of all charges, assuming the principle of charge symmetry to be valid.

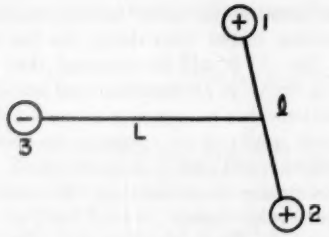

FIG. 1. A τ-meson decay configuration.

in the τ-meson rest system and the value $4m_\pi^2+q^2$ in the c.m. system of the like mesons. Hence,

$$q^2=M_\tau^2-3m_\pi^2-2M_\tau(m_\pi^2+p^2)^{\frac{1}{2}}, \tag{2.1}$$

M_τ, m_π being the masses of the τ meson and π meson, respectively, and $M_\tau=3m_\pi+E$, where E is the kinetic energy released in the decay.

For a τ meson of spin j and parity w, the form of the matrix element describing the 3π-decay from a τ-meson state of magnetic quantum number m may be written generally as

$$T_m(\mathbf{p},\mathbf{q})=\sum_{Ll m_L m_l} C(Llj;m_L m_l) \times Y_L^{m_L}(\theta_p,\phi_p)Y_l^{m_l}(\theta_q,\phi_q)f_{L,l}(p^2,q^2), \tag{2.2}$$

where l is the angular momentum of the like mesons in their rest system and L is the angular momentum of the unlike meson in the τ-meson rest system. Owing to the Bose statistics for the like π^+ mesons, this matrix element must remain unchanged when the coordinates of mesons 1, 2 are interchanged, i.e., when $\mathbf{q}\rightarrow-\mathbf{q}$. This requires l to be even; $l=0, 2, 4\cdots$. The condition for parity conservation is then

$$w=(-1)^2(-1)^L, \tag{2.3}$$

so that L is confined to odd or even values according as the τ-meson parity is even or odd, respectively. The conservation of angular momentum $\mathbf{j}=\mathbf{L}+\mathbf{l}$ is insured by the properties of the Clebsch-Gordan coefficient $C(Llj;m_L m_l)$. The probability of the configuration $\mathbf{p}$, $\mathbf{q}$ is proportional to the average[12]

$$\Sigma=\{\textstyle\sum_m[T_m(\mathbf{p},\mathbf{q})]^*[T_m(\mathbf{p},\mathbf{q})]\}/(2j+1). \tag{2.4}$$

This quantity is rotationally invariant and is therefore a function only of p^2 (since q^2 is given by (2.1)) and of θ, where $\cos\theta=(\mathbf{p}\cdot\mathbf{q})/pq$.

It is important to note the lowest values of L and of l possible for given (j,w) since for small p or q, it is reasonable to expect the behavior of (2.2) to be dominated by the term with the lowest value of L or l, respectively. For odd parity w, the allowed L are even. If j is even and w odd, the lowest values of L, l which may occur (not necessarily associated together) in (2.2) are $L=0$ and $l=0$. If j is odd and w odd, L and l are confined to even values and the equation $\mathbf{j}=\mathbf{l}+\mathbf{L}$ cannot be satisfied if either $L=0$ or $l=0$; the lowest allowed values are $L=2$ and $l=2$. For even parity w, the allowed L are odd. If j is odd and w even, the lowest values are $L=1$ and $l=0$. For even j and even w, the equation $\mathbf{j}=\mathbf{l}+\mathbf{L}$ cannot be satisfied with $l=0$, and the lowest values are $L=1$ and $l=2$. For the τ meson one may hope to distinguish at least between these four possibilities, i.e., between (even j, odd w), (odd j, odd w), (odd j, even w), (even j, even w), from qualitative features of the decay data, as will be discussed later. It is of interest to note that, if the τ meson belongs to the second or fourth class, a competitive 2π decay of the τ meson would be forbidden since this requires $w=(-1)^j$.

The matrix elements used previously[1] for some particular values of (j,w) may be obtained from (2.2) by retaining only those terms corresponding to the lowest possible pairs of angular momenta (L,l) and supposing that the functional form of f_{Ll} is $c_{Ll}p^Lq^l$, where c_{Ll} is a constant. This approximation supposes that the momentum variation of the matrix element is governed essentially by the penetration of the centrifugal barrier, the internal conditions being assumed to vary only slowly with the magnitude of the momentum. In general this approximation may be expected to be a reasonable one when the meson wavelengths are long relative to the "size" of the τ meson; however it is difficult to estimate quantitatively its region of validity and exceptional cases may well be relevant. For very many of the low j values, this approximation leads to a unique expression for the matrix element: for spin values $j\leqslant 5$, there are never more than three combinations of (L,l) possible. Thus, for example, for spin 5 and even parity, the (L,l) pairs relevant are (5,0), (3,2), and (1,4).

At the present stage a nonrelativistic description will be sufficient since the kinetic energy of an emitted π meson cannot exceed $(M_\tau-3m_\pi)(M_\tau+m_\pi)/2M_\tau$ which is close to 50 Mev, and the errors following from this simplification will not affect the general features found. A convenient two-dimensional representation for τ-meson decay events may then be defined in the following way: relative to an equilateral triangle YUV (Fig. 2), a decay event may be specified by the point P such that the perpendiculars (PL,PM,PN) are proportional to the meson kinetic energies (t_1,t_2,t_3) where PN refers specifically to the unlike meson. P depends essentially on the ratios of the squares of the meson momenta, which may be obtained most readily from the angles between the tracks of the outgoing mesons. Since the mesons (1,2) are indistinguishable, the decay event may be represented equally by P or by its reflection in the altitude YDC, so that one need

[12] A general form may be given for this sum, using the techniques of Racah:

$$\Sigma=\sum_{LL'll'K} Y_K^0(\theta)\left[\frac{(2L+1)(2L'+1)(2l+1)(2l'+1)}{(2K+1)}\right]^{\frac{1}{2}} \times(LL'00/LL'K0)(ll'00/ll'K0)W(lLl'L';jK)\text{R.P.}(f_{lL}{}^*f_{l'L'}).$$

consider only that ordering of (t_1,t_2) for which P lies to the right of YDC. In the previous work, it has been shown that momentum conservation requires that P lie within the circle inscribed to the triangle YUV. The Cartesian coordinates (x,y) of P with respect to the axes OX, OY are given by

$$x=(t_1-t_2)\sqrt{3}/E, \quad y=(2t_3-t_1-t_2)/E, \qquad (2.5)$$

when the radius of the inscribed circle is taken to be unity. If numerical factors and relativistic effects are neglected, the density of states is

$$\delta(t_1+t_2+t_3-E)dt_1dt_2dt_3=dxdyE^2/6\sqrt{3},$$

so that variations in the density of events in the semicircle $DABC$ can reflect only the behavior of the probability function. Now PN is proportional to p^2, while PQ is proportional to q^2. The value of $\cos\theta$ associated with P is given by the ratio $x/(GH)$, so that events with constant $\cos\theta$ lie on an ellipse with DC as major axis. Points on the diameter DOC correspond to events with $\theta=\pi/2$, and points on the semicircular boundary correspond to events with $\theta=0$, i.e., to a decay in which the π mesons are collinear. An angular correlation between $\mathbf{p}$ and $\mathbf{q}$ is therefore reflected by a variation of the density of events across the semicircle at any level. If the assumption that only the lowest pairs (L,l) possible contribute singificantly is tenable, such an angular correlation will give very direct indications concerning the spin and parity values possible for the τ meson.

A direct and rather reliable indication concerning the parity of the τ meson may be obtained from a study of the events in the lower part of the semicircle. Here the density of events, averaged along lines parallel to OX, should vary with PN in a way depending on the least L possible, since the unlike meson wavelength is $\gtrsim 0.5\times10^{-13}$ cm for a meson energy $\leqslant 10$ Mev, and the next allowed L is two units larger. The average density of events may be expected therefore to rise roughly with the Lth power of PN. According to (2.3) the τ-meson parity is then $(-1)^{L+1}$ and there are some limitations

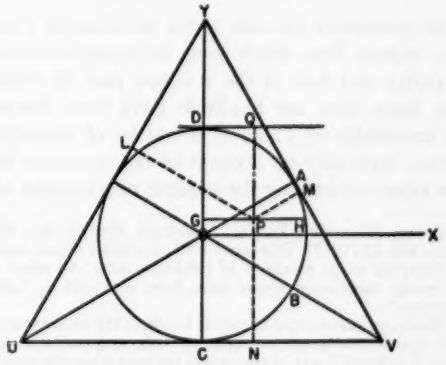

FIG. 2. A triangular diagram for the representation of τ-meson decay events.

on the corresponding j value. The distribution near the upper part of the semicircle may similarly give an indication of the least l—however it will be pointed out shortly that any strong meson-meson attraction which may exist in the $T=2$ two-meson state would distort the distribution in this region. One further specific conclusion may be stated, that, for $w=(-1)^j$, the density of events must vanish on the semicircular boundary. This may be seen from the fact that, for $w=(-1)^j$, all tensors of rank j formed in (2.2) from tensors of rank L and l must contain a factor $\mathbf{p}\times\mathbf{q}$; alternatively it follows from the fact that $C(Llj;00)=0$ for l even and $(j+L)$ odd.

When the charges of the emitted π mesons are not known, it can only be said that the corresponding point is one of three, P itself or its reflections in the altitudes OA and OB. Consequently, in the previous work,[1] the representation of τ-meson events was confined to the area AOB. This diagram, which here corresponds to giving up knowledge of the meson charges, may be obtained from the diagram above by folding DOA and BOC across OA and OB, respectively, and summing the three densities arriving on point P.

For the decay process $\tau^+\to\pi^++2\pi^0$, only the quantity p^2 is observable and the distribution of this (i.e., the energy of the charged meson) is obtained by integrating the two-dimensional plot $DABC$ perpendicular to DOC, i.e., by averaging over $\cos\theta$. In a similar way to that described above a strong indication of the τ-meson parity may be obtained from the behavior of this distribution at the low-energy end.

If there exist strong interactions between the emitted π meson, the assumption that only the lowest angular momenta are significant will certainly be inadequate in some parts of the diagram. However, it has been pointed out by Brueckner and Watson[13] for the process $p+p\to n+p+\pi^+$ and by Stuart and Watson[14] for the process $\pi^-+d\to n+n+\gamma$ that the short-range interactions between the final nucleons may greatly modify the angular and energy distributions of the products although playing no important part in the primary mechanism of the reaction. For these cases it has been found possible to separate the processes into two stages, the primary mechanism and the final-state interaction, which may be discussed consecutively. If this separation is possible in the case of τ-meson decay, the meson-meson final-state interaction may be taken account of most simply by extracting from the matrix element (2.2) a factor $\prod(a_{ij})$, where a_{ij} is the scattering amplitude for the mutual scattering of mesons i, j with the relative momentum appropriate to the configuration considered and the product goes over all meson pairs. The remaining part of the matrix element, describing the primary mechanism, may then be expected to contain mainly terms corresponding to low angular momentum. The relative momentum K_{ij} of mesons

[13] K. Brueckner and K. M. Watson, Phys. Rev. 87, 621 (1952).
[14] K. M. Watson and R. N. Stuart, Phys. Rev. 82, 738 (1951).

i, j may be expressed in terms of the kinetic energy of the third meson k according to an expression similar to (2.1),

$$K_{ij}^2=(M_\tau-3m_\pi)(M_\tau+m_\pi)-2M_\tau l_k. \qquad (2.6)$$

In general the final-state interaction effect may be expected to be large for small relative momentum of two mesons, in which case, according to (2.6), the third meson has energy close to the maximum allowed energy. In the diagram of Fig. 2, meson-meson attraction effects may greatly increase the density of events close to point A or to point C, depending on the isotopic-spin dependence of this interaction. For the decay of the τ meson into three charged mesons, an increase in the density of events near to A is to be expected only if there is a strong attraction in a two-meson state of total isotopic spin $T=2$, whereas an increase in the region of C may result from attraction in states $T=0$ or 2. If the matrix element is antisymmetric in (1,3) in the region near to C, as would be the case if the mesons (1,3) are predominantly in a $T=1$ state, the unmodified density of events would be zero at C and small in this neighborhood. A strong $T=1$ meson-meson interaction would not then give a peak in this region although it would greatly increase the density over that of the unmodified theory: an example of this case is that of the vector τ meson discussed previously for the case of nonidentified charges.

3. THE EXPERIMENTAL DATA

To the present, twenty-nine τ-meson decay events have been reported, as well as three events which may possibly represent $\tau^+\to\pi^++2\pi^0$ decay. Of the former, a complete analysis is possible for the two events observed in cloud chambers in the presence of a magnetic field and for three emulsion events where the charges are definitely established. Six other emulsion events[2,4,5,15] may be included in the analysis if it is assumed that the parent τ meson is of positive charge. The data on these eleven events is given in Fig. 3. Three events (each observed in a single emulsion layer) for which only a π^+ meson is identified have also been included—the assumption of a τ^+ parent still allows two possible positions for the corresponding point. These have been included in order to emphasize the possibility of systematic bias in the data. For example, if we suppose the decaying τ mesons to be positive, then for an event leading to a slow π^- meson to be included in this plot, it is only necessary for the π^- meson to come to rest and be identified. But for an event giving a slow π^+ meson to be included, it is necessary that at least two π mesons come to rest in the emulsion; and since the second of these must be quite fast, the probability of this occurrence is considerably less, from geometrical considerations. It is clear that no definite conclusions[16] can be reached at the present stage owing to uncertainties of this kind and to the small number of events available. The purpose of presenting such a discussion at the present time is rather to draw attention to the necessity for assessing these uncertainties when the data are collected from block emulsions of various dimensions and examined by differing techniques. It should also be remarked that τ-meson data obtained from cloud-chamber events with a magnetic field applied are not subject to these uncertainties and it has been shown by Van Lint and Trilling[6] that these may be sufficiently accurate to allow a clear picture of the event in the τ-meson rest system to be deduced.

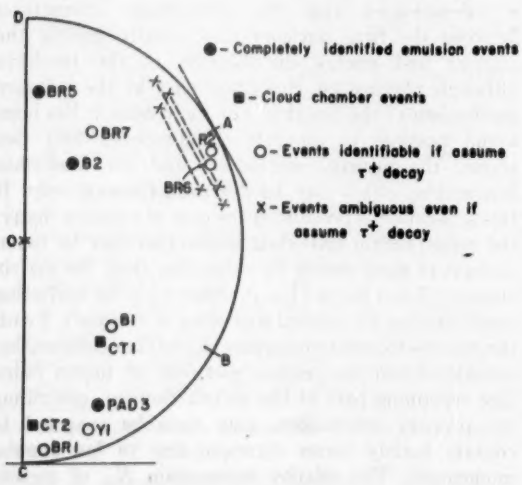

FIG. 3. The data on τ-meson decay events in which the signs of π-meson charges are established.

In Fig. 4, 29 available τ-meson events are plotted, without regard to knowledge of charges. This distribution is not yet inconsistent with a random distribution, nor does it give evidence for a tendency for the events to crowd towards the corner B, a distortion which would be characteristic of a strong meson-meson interaction.

4. CONCLUSION

The qualitative features of the statistics of τ-meson decay events, from which some indications concerning the parity and spin of the τ meson may be obtained when more data are available have been discussed. The knowledge of j and w would be of considerable interest, especially on account of the questions which have arisen concerning the possible relationships of the

[15] Brown, Camerini, Fowler, Muirhead, Powell, and Ritson, Nature 163, 82 (1949). This event $BR1$, the first τ meson reported, was observed in an emulsion of thickness 600μ. All other emulsion events mentioned above have been observed in "stripped emulsions."

[16] However, the number of events in which the unlike π meson is much the slowest is not inconsistent with, and perhaps suggests a least L value of $L=0$. If this is still the case when the number of available events is more adequate, it would imply a negative parity and even spin for the τ meson.

τ meson with the χ meson[17] and with the θ^0 particle.[18] The angular momentum and parity selection rules governing the possibility of competition between 2π and 3π decay of a heavy meson are well known—in particular, 2π decay is forbidden unless $w=(-1)^j$. Other selection rules have also been proposed[19] which would forbid this competition and which originate from the requirements of invariance of the theory with respect to charge symmetry (relevant to the θ^0 decay) and charge conjugation (both relevant in the $\tau^\pm$ decay). These selection rules are however not absolute and the experimental evidence on unstable supernucleonic particles suggests that charge symmetry may not hold for these [in particular there does not appear to be a charged counterpart to the well-known $V_0{}^1(\Lambda^0)$ particle]. Such a failure would have only minor effects in situations where charge symmetry is most accurately tested. However, insofar as the τ meson may be strongly coupled with these supernucleons, it is very much a possibility that the violation of charge symmetry for the τ meson might be sufficient to permit the competition of a 2π decay with the well established 3π-decay mode.

In the present paper, it has been shown that this question of the possibility of a competitive 2π decay for the τ meson could be settled (at least in the negative) from a qualitative study of the τ-meson decay statistics. This could decide to which of four classes the τ meson belongs, the 2π decay being forbidden for two of these classes. At the present stage, the number of τ-decay events giving a slow unlike π meson rather suggests that the least L is $L=0$, which would imply that the τ meson belongs to the class of even j and odd w, a class for which the 2π decay is forbidden. This tentative conclusion is given some support by the existence of the two events *R2* and *BR6* since the condition $w=(-1)^j$ necessary for 2π competition to be possible, requires the τ-meson decay probability to have an over-all factor $\sin^2\theta$ and therefore to be small on the ellipses of constant θ close to the semicircular boundary ($\theta=0$). In conclusion, it should be emphasized that any such conclusion can be only tentative at the present, in view of the small number of events available for analysis and the possibility that there may be some experimental bias favoring observation of events in which a slow π meson is emitted.

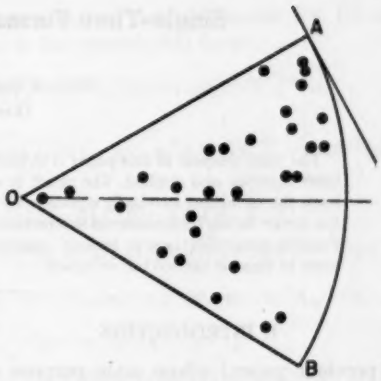

FIG. 4. The data on twenty-nine τ-meson decay events.

It is a pleasure to acknowledge here the assistance of all those groups and individuals who have contributed to this investigation by sending detailed information concerning τ-meson decay events observed by them.

[17] M. G. K. Menon and C. O'Ceallaigh, Proc. Roy. Soc. (London) **A221**, 292, 1954.

[18] Thompson, Buskirk, Etter, Karzmark, and Rediker, Phys. Rev. **90**, 329 (1953); K. H. Barker, Proc. Roy. Soc. (London) **A221**, 328, 1954.

[19] A. Pais and R. Jost, Phys. Rev. **87**, 871 (1952); L. Michel, Proceedings of the International Cosmic Ray Conference, July, 1953 (unpublished).

Single-Time Formalisms from Covariant Equations

ABRAHAM KLEIN*
Harvard University, Cambridge, Massachusetts
(Received February 15, 1954)

The main purpose of this paper is to provide a concise general deduction of a result which has previously been reported and applied. The result is a single-time wave equation for a two-nucleon system obtained from the covariant two-body equation by means of an iteration procedure which employs the solution of the latter for an instantaneous interaction. The single-time wave function contains only positive energies. Possible generalizations to include negative-energy components and higher amplitudes are discussed, but none of these is carried out in detail.

I. INTRODUCTION

IN a previous paper,[1] whose main purpose was the derivation of potentials from pseudoscalar meson theory, the author outlined a method for obtaining a single-time equation from the relativistically covariant two-particle equation (R.E.),[2,3] which could be correlated with the Tamm-Dancoff formalism.[4] More recently Macke[5] has published a complete and elaborate proof of the procedure for carrying out the reduction to equal times, exhibiting also alternative forms of the three-dimensional equation differing from each other in the treatment of self-energy effects. This note has a twofold purpose: to present a simplified derivation of the above results which employs the method already suggested in the appendix of reference 1, and to discuss possible extensions and generalizations of the method.

The alternative treatment of self-interactions emerges immediately from the remark that either of two forms of the R.E. can be used as the starting point of the reduction. These are most readily obtained from the differentio-integral equation given by Schwinger,[2] in symbolic form

$$F_1'F_2'\psi = I\psi, \tag{1}$$

where[6]

$$F_i' = (\gamma p + m + M)_i = (G_i')^{-1} \quad (i=1,2) \tag{2}$$

is the inverse of the outgoing wave Green's function. With all one-particle radiative effects included in the mass operator, M and I can be represented by the totality of irreducible two-particle diagrams.[7] The integral equation form of (1),

$$\psi = G_1'G_2'I\psi, \tag{3}$$

if we think of the expansions of G_i' in terms of free-particle propagation functions and vertices, then contains on the right-hand side the matrix product of two interaction complexes, with that represented by $G_1'G_2'$ containing both reducible and irreducible interactions (in the sense of reference 3). The product complex is therefore also reducible.

The alternative version of the R.E., the one we shall take as fundamental *for our work*, is obtained from Eq. (1) by constructing the integral equation by means of free-particle Green's functions, G_i,

$$\psi = (-G_1M_1 - G_2M_2 - G_1G_2M_1M_2 + G_1G_2I)\psi. \tag{4}$$

In this case, since M_1 and M_2 constitute a totality of irreducible interactions, only the third term on the right-hand side of Eq. (4) contains reducible interactions. The complex consisting of all interactions in Eq. (4) and *all iterations thereof* is identical with the complex analogously defined for Eq. (3). Only when viewed in terms of a completely expanded interaction kernel is (4) preferable to (3).

Given either equation, we turn to the method for obtaining a single-time equation as explained in reference 1. It is necessary first to choose a relative time dependence for the covariant wave function. It is worth emphasizing that a single-time equation will not exist in general for the exact covariant wave function. The possibility of constructing such an equation proceeds from the assumption of approximate separability of the relative time and spatial coordinate dependences, as in the relative time dependence for an instantaneous interaction. The latter is chosen for zeroeth approximation, all higher approximations being obtained by iteration of the R.E. This results in the following prescription for obtaining the single-time equation with kernel correct up to and including order $2n$ in the coupling constant:

Proceed from the equation

$$\psi(\xi,\xi') = \int G_1(\xi - x)G_2(\xi' - x')I_{2n}(x,x';\eta,\eta') \times \psi(\eta,\eta')(d\eta)(d\eta'), \tag{5}$$

where I_{2n} consists *only* of diagrams of order $2n$, but contains all reducible as well as irreducible ones. Since we require an equation for the positive energy part of the three-dimensional wave function,[8] only the relative

* Junior Fellow, Society of Fellows.
[1] A. Klein, Phys. Rev. 90, 1101 (1953).
[2] J. Schwinger, Proc. Natl. Acad. Sci. U. S. 37, 452, 455 (1951).
[3] E. E. Salpeter and H. A. Bethe, Phys. Rev. 84, 1232 (1951).
[4] M. M. Lévy, Phys. Rev. 88, 72 (1952).
[5] W. Macke, Z. Naturforsch. 8a, 599, 615 (1953).
[6] Note the slight change in definition of the mass operator, which here excludes the bare mass.
[7] That is, interactions in which at least one meson is exchanged by the nucleons. To order g^2, I describes only the exchange of a meson.
[8] Possible generalizations are discussed in Sec. III.

time dependence of the positive energy part of $\psi(\eta,\eta')$ is required,[1]

$$\psi(\eta,\eta')\cong\exp[-i(\eta_0+\eta_0')\tfrac{1}{2}W]\{\theta_+(\eta_0-\eta_0')\Lambda_+^{(1)}(\mathbf{q})\times\exp[-i(\eta_0-\eta_0')(E(\mathbf{q})-\tfrac{1}{2}W)]+\theta_+(\eta_0'-\eta_0)\Lambda_+^{(2)}(\mathbf{q}')\exp[-i(\eta_0'-\eta_0)\times(E(\mathbf{q}')-\tfrac{1}{2}W)]\}\phi(\mathbf{n},\mathbf{n}'). \quad (6)$$

Here W is the total energy, $\theta_+(t)=1$, 0 for $t>0$, $t<0$, respectively, $\Lambda_+^{(1)}(\mathbf{q})$ is the positive energy projection operator, and $E(\mathbf{q})$ the energy of particle one, the latter set of quantities to be understood as differential operators with respect to $\mathbf{n}$, and correspondingly for particle two.

Similarly we require only the positive energy parts of $G_1(\xi-x)$, $G_2(\xi'-x')$, for example,

$$G_1(\xi-x)\cong i\theta_+(\xi_0-t)\Lambda_+^{(1)}(\mathbf{p})\beta\times\exp[-i(\xi_0-t)E(\mathbf{p})]\delta_p(\xi-\chi), \quad (7)$$

where the subscript on the δ function will be employed to label the momentum variable of its Fourier transform. Setting $\xi_0=\xi_0'$ and removing the total time dependence from $\psi(\xi,\xi')$, we obtain

$$\phi(\xi,\xi')=\int\Omega_{2n}(\xi,\xi';\mathbf{n},\mathbf{n}')\phi(\mathbf{n},\mathbf{n}')d\mathbf{n}d\mathbf{n}', \quad (8)$$

where

$$\Omega_{2n}(\xi,\xi';\mathbf{n},\mathbf{n}')=(i)^2\int\exp[i(\xi_0-\tfrac{1}{2}(\eta_0+\eta_0'))W]\times\theta_+(\xi_0-t)\Lambda_+^{(1)}(\mathbf{p})\exp[-i(\xi_0-t)E(\mathbf{p})]\delta_p(\xi-\chi)\times\theta_+(\xi_0-t')\Lambda_+^{(2)}(\mathbf{p}')\exp[-i(\xi_0-t')E(\mathbf{p}')]\times\delta_{p'}(\xi'-\chi')I_{2n}(x,x';\eta,\eta')\{\theta_+(\eta_0-\eta_0')\Lambda_+^{(1)}(\mathbf{q})\times\exp[-i(\eta_0-\eta_0')(E(\mathbf{q})-\tfrac{1}{2}W)]+\theta_+(\eta_0'-\eta_0)\Lambda_+^{(2)}(\mathbf{q})\exp[-i(\eta_0'-\eta_0)\times(E(\mathbf{q}')-\tfrac{1}{2}W)]\}(dx)(dx')d\eta_0d\eta_0'. \quad (9)$$

A useful symmetrization of Eq. (9) can be achieved by noting that the expression is independent of ξ_0. We can therefore apply the linear operation $T^{-1}\int d\xi_0$, where T is a large time interval, to both sides, and immediately carry out the integral with respect to ξ_0. The factor T^{-1} remains to be canceled by one of the time integrations to be performed at a later stage. For the ξ_0 integral, we have according to (9) [$m(t,t')$ means the greater of the two times],

$$\int_{m(t,t')}^{\infty}\exp\{-i\xi_0[E(\mathbf{p})+E(\mathbf{p}')-W]\}d\xi_0=\{i[E(\mathbf{p})+E(\mathbf{p}')-W]\}^{-1}\times\exp\{-im(t,t')[E(\mathbf{p})+E(\mathbf{p}')-W]\}. \quad (10)$$

A little consideration then shows that Eq. (9) may be rewritten in the symmetrical form

$$\Omega_{2n}(\xi,\xi';\eta,\eta')=iT^{-1}[E(\mathbf{p})+E(\mathbf{p}')-W]^{-1}\times\int\exp[i(t+t'-\eta_0-\eta_0')\tfrac{1}{2}W]\{\theta_+(t'-t)\Lambda_+^{(1)}(\mathbf{p})\times\exp[-i(t'-t)(E(\mathbf{p})-\tfrac{1}{2}W)]\delta_p(\xi-\chi)+\theta_+(t-t')\Lambda_+^{(2)}(\mathbf{p}')\exp[-i(t-t')(E(\mathbf{p}')-\tfrac{1}{2}W)]\times\delta_{p'}(\xi'-\chi')\}I_{2n}(x,x';\eta,\eta')\{\theta_+(\eta_0-\eta_0')\Lambda_+^{(1)}(\mathbf{q})\times\exp[-i(\eta_0-\eta_0')(E(\mathbf{q})-\tfrac{1}{2}W)]+\theta_+(\eta_0'-\eta_0)\Lambda_+^{(2)}(\mathbf{q}')\exp[-i(\eta_0'-\eta_0)\times(E(\mathbf{q}')-\tfrac{1}{2}W)]\}dtdt'd\eta_0d\eta_0'd\chi d\chi'. \quad (11)$$

The remainder of the calculation amounts to carrying out the time integrals shown explicitly in Eq. (11), as well as the remaining $2n-4$ integrals over time variables of which I_{2n} is also a function. The method of performing these will be indicated in the next section which also contains a description of the results.

II. CALCULATION OF THREE-DIMENSIONAL KERNEL

The most general interaction of order $2n$ is specified by a set of integers n_1, n_2, l_i, and a set of instructions α. Here, $n_1(n_2)$ is the number of interactions undergone by the first (second) particle and l_i the number of interactions in the ith closed loop,

$$n_1+n_2+\sum_{i=1}^{m}l_i=2n. \quad (12)$$

Given n_1, n_2, and l_i, α describes the order of emission and absorption of the mesons. Analytically, we have (for pseudoscalar theory)

$$I_{2n}(n_1,n_2,l_i,\alpha;x_1,x_1';x_{n_1}x_{n_2}')=(-ig^2)^n(-1)^m\int(dx_2)\cdots(dx_{n_1-1})(dx_2')\cdots\times(dx_{n_2-1}')\prod_{i=1}^{m}(d\xi_1^i)\cdots(d\xi_{l_i}^i)[\gamma_\delta G(x_1-x_2)\gamma_\delta\cdots\times\gamma_\delta G(x_{n_1-1}-x_{n_1})\gamma_\delta]^{(1)}[\gamma_\delta G(x_1'-x_2')\gamma_\delta\cdots\times\gamma_\delta G(x_{n_2-1}'-x_{n_2}')\gamma_\delta]^{(2)}\prod_{i=1}^{m}\mathrm{tr}[\gamma_\delta G(\xi_1^i-\xi_2^i)\gamma_\delta\cdots\times\gamma_\delta G(\xi_{l_i}^i-\xi_1^i)]\Delta_1\cdots\Delta_n. \quad (13)$$

In Eq. (13), the space-time points belonging to particles one and two and to the closed loops have been distinctly labeled, and the points x, x', η, η' of Eq. (11) relabeled accordingly. The coordinates of the meson propagation functions, Δ_i, which have been omitted, are determined by the specification α. We insert (13) into (11) and

introduce representations of the functions G and Δ, as exemplified by the following expressions,

$$G(x_1-x_2)=i[\theta_+(t_1-t_2)\Lambda_+(\mathbf{p}_1)-\theta_-(t_1-t_2)\Lambda_-(\mathbf{p}_1)]\beta \times\exp[-iE(\mathbf{p}_1)|t_1-t_2|]\delta_{\mathbf{p}_1}(\chi_1-\chi_2), \quad (14)$$

$$\Delta_1=\tfrac{1}{2}i\omega_1^{-1}\exp[-i\omega_1|t_1-t_{n_1}|]\delta_{\mathbf{k}_1}(\chi_1-\chi_{n_1}), \quad (15)$$

where ω is the meson energy. [Compare Eqs. (6), (7).] The momentum variables are chosen as follows: $\mathbf{p}$, $\mathbf{p}_1$, $\cdots\mathbf{p}_{n_1}$ for the first nucleon; $\mathbf{p}'$, $\mathbf{p}_1'$, $\cdots\mathbf{p}_{n_2}'$ for the second nucleon; $\mathbf{q}_1{}^i$, $\cdots\mathbf{q}_{l_i}{}^i$ for the nucleon momenta of the closed loops; and $\mathbf{k}_1$, $\cdots\mathbf{k}_n$ for the meson momenta.

In order to unlock the absolute value signs involved in the time dependence, the $2n$-dimensional space defined by the time integrals is divided into $2n!$ regions, each one corresponding to a definite permutation of the coordinates. For convenience of discussion, choose a particular permutation and relabel the times t_1, $\cdots t_{2n}$ in order of increasing time. The region of integration is then given by

$$T^{-1}\int_{-\infty}^{\infty}dt_{2n}\cdots\int_{-\infty}^{t_3}dt_2\int_{-\infty}^{t_2}dt_1. \quad (16)$$

Each integration yields an energy denominator, except the last, which cancels T^{-1}. The complete specification of the result therefore requires only the statement of the general form of the energy denominator and the disposition of over-all sign and factors of $(-1)^l$.

Suppose, for example, that t_{n_1}, t_{n_2}, t_1, t_1' become t_α, t_β, t_γ, t_δ in the sequence $t_1\cdots t_\alpha\cdots t_\beta\cdots t_\gamma\cdots t_\delta\cdots t_{2n}$ as a result of the relabeling. The first time integral to be obtained is

$$\int_{-\infty}^{t_2}dt_1\exp[-iE(1,\lambda_1)|t_1-t_{\lambda_1}|-iE(\mu_1,1)|t_{\mu_1}-t_1| -i\omega(1,\nu_1)|t_1-t_{\nu_1}|], \quad (17)$$

where we have also relabeled the nucleon and meson momenta in an obvious way to accord with the relabeling of the times. As a consequence of the time-ordering, we have

$$|t_1-t_{\lambda_1}|=(t_{\lambda_1}-t_2)+(t_2-t_1), \quad (18)$$

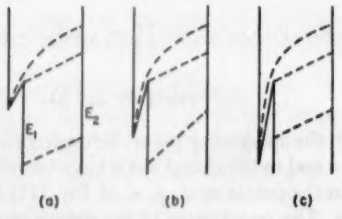

FIG. 1. Diagrams whose sum is again a diagram of the form of Fig. 1(a), but with energy denominators corresponding to reducible pieces.

and similarly for the other time differences. Equation (17) then yields

$$\{i[E(1,\lambda_1)+E(\mu_1,1)+\omega(1,\nu_1)]\}^{-1} \times\exp[-iE(1,\lambda_1)(t_{\lambda_1}-t_2)-iE(\mu_1,1)(t_{\mu_1}-t_2) -i\omega(1,\nu_1)(t_{\nu_1}-t_2)]. \quad (19)$$

If no member of the set t_{λ_1}, t_{μ_1}, t_{ν_1} equals t_2, Eq. (11) will contain three additional exponentials involving t_2, and the second energy denominator will have the form

$$E(1,\lambda_1)+E(2,\lambda_2)+E(\mu_1,1)+E(\mu_2,2) +\omega(1,\nu_1)+\omega(2,\nu_2). \quad (20)$$

Under similar conditions we find for the lth energy denominator,

$$\sum_{i=1}^{l}[E(i,\lambda_i)+E(\mu_i,i)+\omega(i,\nu_i)]. \quad (21)$$

Equation (21) holds as long as λ_i, μ_i, $\nu_i>l$ for all $i<l$ and $t_l<t_\alpha$. Indeed, Eq. (21) holds in all cases for $t_l<t_\alpha$ with the following added conventions. First, it is possible that a meson emitted in the interval t_1-t_l is also absorbed in that interval and therefore no longer occurs in subsequent energy denominators. This is automatically taken care of if we adopt the convention

$$\omega(i,j)=-\omega(j,i). \quad (22)$$

Second, in the formal sum in (21) it is possible for a member of the set $E(i,\lambda_i)$ to equal a member of the set $E(\mu_i,i)$ $(\mu_i,\lambda_i<l)$. When this occurs the two equal terms are to be dropped, since examination shows that this can arise only after such times at which the nucleon in question has made a transition to another momentum state or annihilated with an antiparticle.

We arrive next at the time t_α (formerly t_{n_1}). For the special case considered here, $t_1'>t_1$, $t_{n_2}'>t_{n_1}$, the dependence on these variables can be put in the form

$$\exp[-iE(\mathbf{p})(t_1'-t_1)-iE(\mathbf{p}_{n_2}')(t_{n_2}'-t_{n_1})+iW(t_1'-t_{n_1})] =\exp[-iE(\mathbf{p})(t_\delta-t_\gamma)-iE(\mathbf{p}_{n_2}')(t_\beta-t_\alpha) +iW(t_\gamma-t_\alpha)]. \quad (23)$$

The form of (23) is enough to show that all energy denominators are given by Eq. (21) and the conventions following it, except that for $t_\gamma<t<t_\alpha$, there is an additional term $-W$ in the energy denominators. For other relative orders of t_1, t_1', t_{n_1}, t_{n_2}', the appearance of the total energy is determined by rules which can be derived similarly. These have essentially been given in reference 1 and are summarized below.

Without entering into further detail about the results of the time integrations, we merely record the contribution of a given time-ordering P_α of the graph

$I_{2n}(n_1,n_2,l_i,\alpha)$ to Ω_{2n} of Eq. (11),[9]

$$\int \Omega_{2n}(n_1,n_2,l_i,P_\alpha;\xi,\xi';\mathbf{n},\mathbf{n}')\phi(\mathbf{n},\mathbf{n}')d\mathbf{n}d\mathbf{n}'$$
$$=g^{2n}(-1)^m(-1)^{N(\theta_-)}\int\prod_{i=1}^{n}[(2\omega_i)^{-1}\delta k_i(\ \ )]$$
$$\times(D_0D_1\cdots D_n)^{-1}d\chi_1\cdots d\chi_{n_1}[\Lambda_+(\mathbf{p})\gamma\Lambda_\pm(\mathbf{p}_1)\gamma\cdots$$
$$\times\gamma\Lambda_+(\mathbf{p}_{n_1})]^{(1)}\delta_{\mathbf{p}}(\xi-\chi_1)\prod_1^{n_1-1}\delta_{\mathbf{p}_i}(\chi_i-\chi_{i+1})$$
$$\times d\chi_1'\cdots d\chi_{n_2}'[\Lambda_+(\mathbf{p}')\gamma\Lambda_\pm(\mathbf{p}_1')\gamma\cdots\gamma\Lambda_+(\mathbf{p}_{n_2}')]^{(2)}$$
$$\times\delta_{\mathbf{p}'}(\xi'-\chi_1')\prod_1^{n_2-1}\delta_{\mathbf{p}_i'}(\chi_i'-\chi_{i+1}')\prod_{i=1}^{m}(d\xi_1^i\cdots d\xi_{l_i}^i)$$
$$\times\mathrm{tr}[\gamma\Lambda_\pm(\mathbf{q}_1^i)\gamma\cdots\gamma\Lambda_\pm(\mathbf{q}_{l_i}^i)]$$
$$\times\delta_{\mathbf{q}_1^i}(\xi_1^i-\xi_2^i)\cdots\phi(\chi_{n_1},\chi_{n_2}'). \quad (24)$$

Here $N(\theta_-)$ is the number of negative energy intermediate states, $\gamma=\beta\gamma_5$, $D_0=W-E(\mathbf{p})-E(\mathbf{p}')$, and the remaining energy denominators are determined in the following manner: For each permutation P_α draw a time-ordered diagram as described and illustrated in reference 1; such a diagram will consist of two continuous nucleon lines with segments directed upwards for positive energy intermediate propagation and downwards for negative energy propagation, j closed loops also consisting of directed line segments, and meson lines connecting appropriate vertices. A horizontal line drawn between two successive vertices completely determines the energy denominator associated with an intermediate state according to the formula

$$D=W-\sum E-\sum\omega, \quad (25)$$

where $\sum E$ is the sum of the energies of those nucleon lines which are cut by the horizontal line, and $\sum\omega$ the corresponding sum over meson energies, with the proviso that if both $E(\mathbf{p})$ and $E(\mathbf{p}')$, or both $E(\mathbf{p}_{n_1})$ and $E(\mathbf{p}_{n_2}')$ occur in the summation, their sum is to be replaced by W. The latter part of the rule accounts, for example, for Eq. (21), which obtains so long as neither of the initial particles has undergone an interaction and the final particles have not *both* been created.

Several remarks are required to complete the sketch of the derivation. First, Eq. (24) is conveniently transformed to momentum space by Fourier-analyzing the wave function and the δ functions. This will be assumed to have been done without recording another equation the size of Eq. (24). Second, the relation of Eq. (24) to the final equation sought,

$$[W-E(\mathbf{p}_1)-E(\mathbf{p}_2)]\phi(\mathbf{p}_1,\mathbf{p}_2)$$
$$=\int V_{2n}(\mathbf{p}_1,\mathbf{p}_2;\mathbf{p}_1'\mathbf{p}_2')\phi(\mathbf{p}_1',\mathbf{p}_2')d\mathbf{p}_1'd\mathbf{p}_2', \quad (26)$$

[9] Note that in Eq. (24) $\mathbf{p}_{n_1}$, $\mathbf{p}_{n_2}'$ replace $\mathbf{q}$, $\mathbf{q}'$ of Eq. (11).

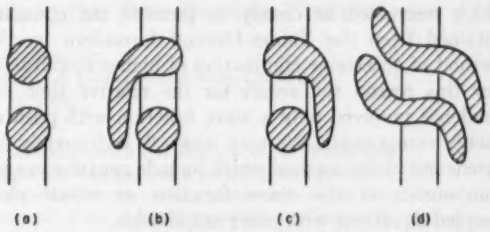

FIG. 2. Topological structure of reducible diagrams.

must be stated. It is necessary to remark in this connection that for an irreducible covariant interaction of order $2n$ all $2n!$ contributions to the three-dimensional kernel to which it gives rise are irreducible in the sense that there is no intermediate state with only two nucleons. Reducible covariant interactions of order $2n$, on the other hand, give rise to both reducible and irreducible interactions. The result for V_{2n} is then defined by induction and is simply that V_{2n} equals V_{2n-2} plus all irreducible time-ordered interactions of order $2n$ determined from I_{2n}. The remaining (reducible) terms of I_{2n} are to be understood to arise from iterations of the equation involving V_{2n-2} in place of V_{2n}.

One essential proviso must be added in defining the complex of reducible three-dimensional kernels,[10] which proviso is illustrated by Figs. 1 and 2. According to the definition given so far, Fig. 1(a) represents a reducible interaction, whereas Figs. 1(b), (c) do not. In the third intermediate state of Fig. 1(a), when it becomes the first intermediate state of one of the reduced pieces, E_1+E_2 should be replaced by W, whereas in Fig. 1(a) the former combination actually occurs. It is easily shown, however, by partial fraction composition, that the sum of the diagrams of Fig. 1 is again of the form of Fig. 1(a), with all energy denominators appropriate to the separate reduced pieces. This is a special case, then, of the requirement that the class of reducible interactions be enlarged to include all those represented by diagrams with the topological structure shown in Fig. 2 and any iterates thereof. Here Fig. 2(a) represents the class previously termed reducible, whereas Fig. 2(b) represents interactions like those of Figs. 1(b), (c).

Finally, one is led to the conclusion that even putting disconnected vacuum interactions aside (which do not occur at all in the covariant equation), there is not a one-to-one relation between the elements of the Tamm-Dancoff kernel and that of Eq. (26), in that structures of the form of Figs. 2(b)–(d) do occur as irreducible ones in the Tamm-Dancoff case. The differences occur first in terms of sixth order in the coupling constant.

III. POSSIBLE GENERALIZATIONS

The original motivation of the work of the previous sections was to obtain a form of single-time equation

[10] This point was overlooked in reference 1 and was first noted by Macke, reference 5, whose discussion we follow.

which resembled as closely as possible the equation obtained from the Tamm-Dancoff formalism by the method of successive elimination of higher amplitudes. For this reason the *ansatz* for the relative time dependence involved only a wave function with positive energy components. We may now ask legitimately for extensions of the method which include negative energy components of the wave function or which yield coupled equations with other amplitudes.

We recall that the relative time dependence was chosen as that of the positive energy components of the solution for an instantaneous interaction whose complete form is [compare Eq. (6)]

$$\begin{aligned}\psi(x_1,x_2)=&\exp[-i\tfrac{1}{2}W(t_1+t_2)]\\&\times\{\theta_+(t_1-t_2)\Lambda_+^{(1)}(\mathbf{p}_1)\exp[-i(E(\mathbf{p}_1)-\tfrac{1}{2}W)(t_1-t_2)]\\&+\theta_+(t_2-t_1)\Lambda_+^{(2)}(\mathbf{p}_2)\exp[-i(E(\mathbf{p}_2)-\tfrac{1}{2}W)(t_1-t_2)]\\&-\theta_-(t_1-t_2)\Lambda_-^{(1)}(\mathbf{p}_1)\exp[-i(E(\mathbf{p}_1)+\tfrac{1}{2}W)(t_2-t_1)]\\&-\theta_-(t_2-t_1)\Lambda_-^{(2)}(\mathbf{p}_2)\\&\quad\times\exp[-i(E(p_2)+\tfrac{1}{2}W)(t_1-t_2)]\}\chi(x_1,x_2),\end{aligned}\tag{27}$$

where $\chi(\mathbf{x}_1,\mathbf{x}_2)$ is the wave function associated with $\phi(\mathbf{x}_1,\mathbf{x}_2)$ in the manner defined by Salpeter,[11] in particular,

$$\chi_{++}=\phi_{++},\quad \chi_{--}=-\phi_{--},\quad \phi_{-+}=\phi_{+-}=0,\tag{28}$$

whereas χ_{+-} and χ_{-+} are nonvanishing. In view of Eq. (28), one obvious generalization of previous results that suggests itself is to use a wave-function that contains both ϕ_{++} and ϕ_{--} as a basis for iteration, since this is consistent with the known adiabatic limit. Without going into detail here, we may remark that one is led along this road to interpret ϕ_{--} as the amplitude for two nucleons plus two pairs, in the following sense. The object of the reduction to equal times in the present case is to obtain coupled equations for ϕ_{++} and ϕ_{--}. Essentially the same method of constructing the three-dimensional kernel as described in the previous sections can be employed, the only difference being the enlargement of the class of reducible diagrams which now include interactions with intermediate states in which there are two nucleons plus two pairs at the same time.

Since the terms in which there is at most one pair at a time certainly predominate over those in which there are two, at least in the nonrelativistic limit, the consistency and usefulness of this method of summing higher order interactions can be viewed with a high degree of skepticism. On the other hand, any attempt to include the mixed energy components by means of Eq. (27) is foiled *a priori* by Eq. (28) which exhibits the lack of a method of expressing $\chi_{\pm,\mp}$ in terms of $\phi_{\pm,\mp}$. The only obvious guess would be to establish an equality between these two sets of components. Though apparently contravening the adiabatic result, this need not be viewed as an insuperable objection.[12] One would hope that this definition would lead to the interpretation of the mixed components as the amplitudes for two nucleons plus a pair in the sense of distinctly enlarging the class of reducible diagrams, as discussed above. That this is not the case can be seen simply by a consideration of the ladder diagram of two rungs, where one might expect to encounter first such reducible diagrams. It is seen, however, that intermediate states which contain an additional pair also contain an additional meson. Further, it can be shown that a small subset of such terms can be converted to reducible form, but a general prescription for all such terms does not appear to be possible.

The equation obtained to order g^2 by including all energy components of the wave function according to the conjectures set forth above[13] is similar in form to an equation proposed by Dyson on the basis of his new Tamm-Dancoff formalism,[14] except that one does not encounter certain objectionable singularities found in the latter. Since the amplitude that enters Dyson's equation is, formally at least, the covariant wave-function for equal times, one may ask whether there is any assumption for the relative time dependence which will reproduce that equation when inserted into the R.E. It can be shown that there is no such dependence, as will be discussed in detail in a later publication. Qualitatively, it can be seen from the work of Sec. II that for high order interactions, the structure of the energy denominators in the presence of nucleon pairs is already largely determined from the form of the interaction (propagation in intermediate states), independent of the relative time dependence of the wave-function, and therefore the occurrence in a systematic way of the singularities characteristic of Dyson's equation is precluded.

Finally, one may ask for a set of coupled equations for matrix elements of Heisenberg operators, which would be the covariant analog of the Tamm-Dancoff equations and which might—under suitable reduction hypotheses—yield a useful set of coupled single-time equations. The former object has been achieved,[15] but the latter object, to the author's knowledge, has not. One would expect that such a set of equations, if it exists, would yield by successive elimination of higher amplitudes the equation constructed in Sec. II. The structure of the latter leads the author to believe, however, that such a set of equations will not be found in any obvious way.

The author has enjoyed conversations on topics related to those of this paper with F. J. Dyson, B. Kursunoglu, S. Schweber, and J. Schwinger.

[11] E. E. Salpeter, Phys. Rev. **87**, 328 (1952).

[12] This assumption was actually made by Lèvy, reference 4, and has recently been used again by R. Arnowitt and S. Gasiorowicz, Unclassified University of California Radiation Laboratory Report UCRL-2402, December, 1953 (unpublished).

[13] For this equation, see reference 4, Eqs. (41), (42).

[14] F. J. Dyson, Phys. Rev. **91**, 1543 (1953).

[15] J. Schwinger, unpublished lectures on field theory, spring semester, 1952, and E. Freese, Göttingen dissertation, March, 1953 (unpublished). See also E. Freese, Z. Naturforsch. **8a**, 776 (1953).

Effect of Negative Energy Components in the Two-Nucleon System

R. ARNOWITT AND S. GASIOROWICZ
Radiation Laboratory, Department of Physics, University of California, Berkeley, California
(Received January 11, 1954)

A feature of the Lévy-Klein solution of the Bethe-Salpeter equation for the deuteron is the elimination of ϕ_{+-}, ϕ_{-+}, and ϕ_{--} in terms of the ϕ_{++} component of the wave function via a perturbation expansion. To investigate the validity of this procedure, the coupled equations for the various components in the first nonadiabatic approximation to the Δ_+ interaction were examined. A set of first-order radial equations with multiplicative potentials (in the region $r>1/m$) was obtained, involving $\phi_{\pm\pm}(r)=\frac{1}{4}(1\pm\beta_1)(1\pm\beta_2)\phi(r)$. A rigorous elimination of ϕ_{+-} and ϕ_{-+} led to equations containing ϕ_{++} and ϕ_{--}. By neglecting velocity-dependent terms, potentials of the type

$$\frac{\mu^2}{2m}\frac{g^2}{4\pi}\tau_1\cdot\tau_2\frac{Y(r)}{P_0+\frac{1}{2}(g^2/4\pi)\tau_1\cdot\tau_2 Y(r)}$$

appear. Expanding the denominator yields the usual Yukawa second-order potential plus a term proportional to $g^4(\tau_1\cdot\tau_2)^2$. Such an expansion, however, is poor even for $r\lesssim 1/\mu$, a pole actually existing near $r\sim 0.7/\mu$ for the charge singlet state. (For $J=1$, the structure of the lowest-order tensor interaction is greatly altered.) Thus, the perturbation expansion appears to radically alter the structure of the equations.

I. INTRODUCTION

THE difficulties in obtaining solutions to the four-dimensional two-nucleon equation[1] have resulted in calculations being confined to approximations involving instantaneous interactions, and their nonadiabatic corrections. This approach, carried out in a number of papers by Lévy[2] and Klein,[3] led to the construction of a series of static potentials appearing in a nonrelativistic Schrödinger-type equation. A feature of the method used (from the point of view of the Bethe-Salpeter formalism) involves an elimination of the negative energy components of the wave function by a perturbation procedure. The nature of the pseudoscalar interaction and the large size of the coupling constant enhance the importance of the negative energy states, a fact brought out in a calculation for the meson-nucleon system.[4] It was therefore felt worthwhile to examine the validity of such an expansion.

For reasons of simplicity, and because comparison with experiment was not an object of this work, the calculations were limited to consideration of the lowest-order interaction corresponding to the exchange of one meson. In particular, the coupled equations between the positive and negative energy components of the wave function for the first nonadiabatic approximation were examined. The "potential energy" parts of these equations are of the form of integral operators. The assumption of a short-range hard core allows one to limit the investigation to the asymptotic region ($r\sim\hbar/\mu c$), where these integral operators may approximately be replaced by multiplicative potentials, correct to order μ/m of the leading term.[5] The velocity-dependent terms were neglected. Beyond this, no further approximations were made. Although the negative energy components were found to be $\mu/2m$ times smaller than the positive energy components, the perturbation expansion of Lévy and Klein completely alters the structure of the potentials and thus appears to be incorrect.

While this conclusion could have been arrived at in a more direct fashion, the development of Secs. III and IV was included because of its more general applicability to equations of the type considered.

II. WAVE EQUATION FOR THE FIRST NONADIABATIC APPROXIMATION

We briefly review the derivation of the first nonadiabatic approximation to the Δ_+ interaction given by Lévy and Klein. The wave equation in momentum space, after the separation of the center-of-mass motion, is[6]

$$[(\tfrac{1}{2}P_0+p_0)-\mathcal{H}_1][(\tfrac{1}{2}P_0-p_0)-\mathcal{H}_2]\psi(p)=\int I(p,p')\psi(p')dp', \quad (2.1)$$

$$\mathcal{H}_1=\alpha_1\cdot\mathbf{p}+\beta_1 m, \quad \mathcal{H}_2=-\alpha_2\cdot\mathbf{p}+\beta_2 m,$$

$$P_0=\text{total energy},$$

where

$$I(p,p')=-\frac{ig^2}{(2\pi)^4}\tau_1\cdot\tau_2\beta_1\gamma_5^{(1)}\beta_2\gamma_5^{(2)}\Delta_+(p-p'). \quad (2.2)$$

To obtain the first nonadiabatic approximation the following ansatz for $\psi(p)$ is inserted on the right-hand

[1] J. Schwinger, Proc. Natl. Acad. Sci. U. S. 37, 452, 455 (1951); E. Salpeter and H. A. Bethe, Phys. Rev. 84, 1232 (1951).
[2] M. M. Lévy, Phys. Rev. 88, 72, 725 (1952), denoted hereafter by L1 and L2, respectively.
[3] A. Klein, Phys. Rev. 90, 1101 (1953).
[4] R. Arnowitt and S. Deser, Phys. Rev. 92, 1061 (1953).
[5] The inclusion of $(\mu/m)^2$ terms would, for consistency, require a treatment of the second nonadiabatic approximation.
[6] The natural system of units $\hbar=c=1$ is being used. Also $\gamma_5=\beta\alpha_4$, $\gamma_0=\beta$ and $\gamma_5=\gamma_1\gamma_2\gamma_3\gamma_0$.

side of Eq. (2.1):

$$\psi(p)=(2\pi)^{-4}[-2\pi i\{(\tfrac{1}{2}P_0+p_0)-3\mathcal{C}_1\}\times\{(\tfrac{1}{2}P_0-p_0)-3\mathcal{C}_2\}]^{-1}(P_0-3\mathcal{C}_1-3\mathcal{C}_2)\chi(\mathbf{p}), \quad (2.3)$$

where[7]

$$\chi_{\pm\pm}(\mathbf{p})=\pm C_{\pm}^{(1)}(\mathbf{p})C_{\pm}^{(2)}(\mathbf{p})\phi(\mathbf{p}),$$

$$\chi_{\pm\mp}(\mathbf{p})=C_{\pm}^{(1)}(\mathbf{p})C_{\mp}^{(2)}(\mathbf{p})\phi(\mathbf{p}).$$

$\phi(p)$ is the equal times wave function defined by

$$\phi(\mathbf{p})=(2\pi)^{-\frac{1}{2}}\int\psi(p)dp_0, \quad (2.4)$$

and $C_{\pm}^{(i)}[\equiv(C_{1,2}^{(i)})]$ are the usual Casimir projection operators. Carrying out the indicated integration over p_0' and integrating both sides with respect to p_0, one obtains the desired three-dimensional equations:

$$(P_0-3\mathcal{C}_1-3\mathcal{C}_2)\phi(\mathbf{p})=(2\pi)^{-3}\int d\mathbf{p}'C_i^{(1)}(\mathbf{p})C_j^{(2)}(\mathbf{p})\lambda\times C_k^{(1)}(\mathbf{p}')C_l^{(2)}(\mathbf{p}')K_{ij}^{kl}(\mathbf{p},\mathbf{p}')\phi(\mathbf{p}'), \quad (2.5)$$

where

$$\lambda=g^2\boldsymbol{\tau}_1\cdot\boldsymbol{\tau}_2(\beta_1\gamma_5^{(1)})(\beta_2\gamma_5^{(2)}),$$

and

$$K_{ij}^{kl}(\mathbf{p},\mathbf{p}+\mathbf{k})=\tfrac{1}{2}(1+\epsilon_k+\epsilon_l-\epsilon_k\epsilon_l)\frac{1-\frac{1}{4}(\epsilon_i-\epsilon_j)(\epsilon_k-\epsilon_l)}{4\omega_{\mathbf{k}}}\times\sum_{\substack{\mu=i,j\\ \nu=k,l}}\epsilon_\mu\epsilon_\nu[\omega_{\mathbf{k}}-\epsilon_\mu\Lambda_\mu(\mathbf{p})-\epsilon_\nu\Lambda_\nu(\mathbf{p}+\mathbf{k})]^{-1}, \quad (2.6)$$

in the notation of Lévy.[8]

It is convenient at this stage to return to coordinate space. Equation (2.5) then becomes

$$(P_0-3\mathcal{C}_1-3\mathcal{C}_2)\phi(\mathbf{r})=\int V(\mathbf{r},\mathbf{r}')\phi(\mathbf{r}')d\mathbf{r}', \quad (2.7)$$

where

$$V(\mathbf{r},\mathbf{r}')=-(2\pi)^{-6}\int d\mathbf{p}d\mathbf{k}e^{i\mathbf{p}\cdot(\mathbf{r}-\mathbf{r}')}C_i^{(1)}(\mathbf{p})C_j^{(2)}(\mathbf{p})\times\lambda C_k^{(1)}(\mathbf{p}-\mathbf{k})C_l^{(2)}(\mathbf{p}-\mathbf{k})K_{ij}^{kl}(\mathbf{p},\mathbf{p}-\mathbf{k})e^{i\mathbf{k}\cdot\mathbf{r}'}. \quad (2.8)$$

The assumption of a short-range repulsive core limits the region of interest to values of $r\sim1/\mu$. Since $V(r,r')$ is a function sharply peaked at $\mathbf{r}\simeq\mathbf{r}'$, $\int V(\mathbf{r},\mathbf{r}')\phi(\mathbf{r}')d\mathbf{r}'$ may be replaced by

$$\int V(\mathbf{r},\mathbf{r}')\phi(\mathbf{r}')d\mathbf{r}'=V(\mathbf{r})\phi(\mathbf{r}),$$

where

$$V(\mathbf{r})=-(2\pi)^{-3}\int d\mathbf{k}e^{i\mathbf{k}\cdot\mathbf{r}}C_i^{(1)}(\mathbf{k})C_j^{(2)}(\mathbf{k})\lambda\times C_k^{(1)}(0)C_l^{(2)}(0)K_{ij}^{kl}(\mathbf{k},0). \quad (2.9)$$

Furthermore, the potential $V(r)$ can formally be expanded in the usual power series in μ/m. To order μ/m of the leading term, the function K becomes[9]

$$\begin{aligned}
&K_{11}^{11}=1/\omega_k^2;\\
&K_{11}^{12}=K_{11}^{21}=K_{12}^{11}=K_{21}^{11}=1/(2\omega_k^2)-1/(4E_k\omega_k),\\
&K_{11}^{22}=-K_{22}^{11}=1/(2\omega_kE_k)-1/(4E_k^2);\\
&K_{12}^{12}=K_{21}^{21}=0,\\
&K_{12}^{21}=K_{21}^{12}=1/(2\omega_k^2)-3/(8\omega_kE_k);\\
&K_{22}^{22}=-1/(4E_k\omega_k)+1/(16E_k^2),\\
&K_{12}^{22}=K_{21}^{22}=-K_{22}^{22}=-K_{22}^{21}=1/(8\omega_kE_k)-3/(32E_k^2),\\
&\omega_k=(\mathbf{k}^2+\mu^2)^{\frac{1}{2}};\quad E_k=(\mathbf{k}^2+m^2)^{\frac{1}{2}}.
\end{aligned} \quad (2.10)$$

By a straightforward but tedious calculation the potential may be recast in the form:

$$\begin{aligned}
V(\mathbf{r})=g^2\boldsymbol{\tau}_1\cdot\boldsymbol{\tau}_2\Big[&V_1(\mathbf{r})-(\beta_1+\beta_2)V_2(\mathbf{r})\\
&-(\boldsymbol{\alpha}_1\cdot\mathbf{p}-\boldsymbol{\alpha}_2\cdot\mathbf{p})\frac{1}{m}V_3(\mathbf{r})\\
&-(\boldsymbol{\gamma}^{(1)}\cdot\mathbf{p}-\boldsymbol{\gamma}^{(2)}\cdot\mathbf{p})\frac{1}{m}V_4(\mathbf{r})\\
&-(\beta_1\boldsymbol{\gamma}^{(2)}\cdot\mathbf{p}-\beta_2\boldsymbol{\gamma}^{(1)}\cdot\mathbf{p})\frac{1}{m}V_5(\mathbf{r})\\
&-(\beta_1\boldsymbol{\alpha}_2\cdot\mathbf{p}-\beta_2\boldsymbol{\alpha}_1\cdot\mathbf{p})\frac{1}{m}V_6(\mathbf{r})-\beta_1\beta_2V_7(\mathbf{r})\Big],
\end{aligned} \quad (2.11)$$

where

$$V_i(\mathbf{r})=(2\pi)^{-3}\int d\mathbf{k}e^{i\mathbf{k}\cdot\mathbf{r}}V_i(\mathbf{k}),$$

$$\begin{aligned}
&V_1(\mathbf{k})=m/(4\omega_k^2E_k)-(E_k+2m)/(16\omega_kE_k^2),\\
&V_2(\mathbf{k})=(5m+3E_k)/(32\omega_kE_k^2)-(E_k-m)/(8\omega_k^2E_k),\\
&V_3(\mathbf{k})=3m/(32\omega_kE_k^2);\\
&V_4(\mathbf{k})=m/(8\omega_k^2E_k)-m/(16\omega_kE_k^2),\\
&V_5(\mathbf{k})=m/(8\omega_k^2E_k)+m/(16\omega_kE_k^2);\\
&V_6(\mathbf{k})=m/(32\omega_kE_k^2),\\
&V_7(\mathbf{k})=1/4\omega_k^2-(m+2E_k)/(16\omega_kE_k^2).
\end{aligned} \quad (2.12)$$

[7] As pointed out by Klein, such a definition of $\chi(\mathbf{p})$ gives results that are equivalent to those obtained from the Tamm-Dancoff method, which allows one to overlook the fact that it is somewhat inconsistent.

[8] See L1, Eq. (42). The factor $\frac{1}{2}(1+\epsilon_k+\epsilon_l-\epsilon_k\epsilon_l)$ has been inserted to take account of an error in sign appearing in that equation.

[9] In the expression for K_{ij}^{kl} in (2.10) the velocity-dependent terms were neglected, since to investigate them consistently would require consideration of terms in the fourth-order potential. It is not totally clear that they will cancel, as they do in the work of Klein.

Equation (2.7) involves the sixteen-component wave function $\phi(r)$. The next section is devoted to a natural rearrangement of the component equations.

III. REDUCTION OF THE 16-COMPONENT EQUATION

The 16-component wave function may conveniently be labeled by two spinor indices, (each running from 1 to 4) $\phi_{a\alpha}(\mathbf{r})$, where the Greek index is chosen to refer to particle 1, and the Latin index to particle 2. In this scheme $\phi(\mathbf{r})$ may be viewed as a 4×4 matrix. The left side of (2.11), when in matrix form gives:

$$\begin{aligned}(P_0-\mathcal{H}_1-\mathcal{H}_2)_{a\alpha,\,b\beta}\phi_{\beta b}&=[P_0\delta_{a\beta}\delta_{ab}-(\mathcal{H}_1)_{a\beta}\delta_{ab}-(\mathcal{H}_2)_{ab}\delta_{a\beta}]\phi_{\beta b}\\&=P_0\phi_{a\alpha}-(\mathcal{H}(\mathbf{p})\phi)_{a\alpha}-(\phi\mathcal{H}^T(-\mathbf{p}))_{a\alpha},\end{aligned}\tag{3.1}$$

where the superscript T denotes "transpose," and the derivatives in the last term act to the left. By defining a new function,

$$\Phi_{a\alpha}(\mathbf{r})=(\phi(\mathbf{r})C^{-1})_{a\alpha},\tag{3.2}$$

where C is the usual unitary charge conjugation matrix,[10] the right-hand side of (3.1) becomes

$$[(P_0\Phi-\mathcal{H}(\mathbf{p})\Phi+\Phi\mathcal{H}(-\mathbf{p}))C]_{a\alpha}.\tag{3.3}$$

The matrix Φ may be expanded in a complete set of 4×4 matrices,[11]

$$\Phi_{a\alpha}(\mathbf{r})=\sum_{\sigma=0}^{4}\sum_{\rho}\lambda_\rho{}^\sigma(\mathbf{r})(\Gamma_\rho{}^\sigma)_{a\alpha},\tag{3.4}$$

where the $\Gamma_\rho{}^\sigma$ are the sixteen Dirac matrices:

$$\Gamma_0{}^0=1;\quad \Gamma_\mu{}^1=(\gamma_1,\cdots\gamma_0);\quad \Gamma_\rho{}^2=(\gamma_2\gamma_3,\cdots;\gamma_0\gamma_1,\cdots);$$

$$\Gamma_\rho{}^3=(\gamma_0\gamma_2\gamma_3,\cdots;\gamma_1\gamma_2\gamma_3);\quad \Gamma_0{}^4=\gamma_5.$$

The ρ index may alternately be specified by the set of numbers (s_1, s_2, s_3, s_0) which can take on values 0 or 1. They are defined by

$$\Gamma_\rho{}^\sigma=\pm(\gamma_1)^{s_1}\cdots(\gamma_0)^{s_0},\tag{3.5}$$

where

$$\sum_{\mu=0}^{3}s_\mu=\sigma.$$

Manipulations similar to the ones leading to (3.3) can be carried out for the right-hand side of our equation. Inserting (3.4) in Eq. (2.7) and cancelling C on both sides one obtains after some rearrangement:

$$\begin{aligned}&P_0\lambda_\rho{}^\sigma\Gamma_\rho{}^\sigma+p_i\lambda_\rho{}^\sigma[1+(-1)^{s_0+s_i}]\gamma_i\beta\Gamma_\rho{}^\sigma\\&\quad-m\lambda_\rho{}^\sigma[1-(-1)^{\sigma-s_0}]\beta\Gamma_\rho{}^\sigma\\&=g^2\tau_1\cdot\tau_2\{\lambda_\rho{}^\sigma[(-1)^{1+\sigma}V_1(\mathbf{r})+(-1)^{1+s_0}V_7(\mathbf{r})]\Gamma_\rho{}^\sigma\\&\quad+m^{-1}p_i[1+(-1)^{s_0+s_i}][(-1)^{s_0}V_5(\mathbf{r})\\&+3(-1)^{1+\sigma}V_3(\mathbf{r})]\lambda_\rho{}^\sigma\gamma_i\beta\Gamma_\rho{}^\sigma+\lambda_\rho{}^\sigma(-1)^\sigma V_2(\mathbf{r})\\&\quad\times[1-(-1)^{\sigma-s_0}]\beta\Gamma_\rho{}^\sigma+m^{-1}p_i[1+(-1)^{\sigma+s_i}]\\&\quad\times[(-1)^\sigma V_4(\mathbf{r})+(-1)^{1+s_0}V_6(\mathbf{r})]\gamma_i\Gamma_\rho{}^\sigma\}.\end{aligned}\tag{3.6}$$

On the right-hand side, the p_i operate both on the potentials and $\lambda_\rho{}^\sigma$. The equations for the $\lambda_\rho{}^\sigma(\mathbf{r})$ may now be obtained by multiplying (3.6) by $\Gamma_{\rho'}{}^{\sigma'}$ and taking the spurs of both sides. Introducing the notation

$$\begin{aligned}&\Lambda=\lambda_0{}^0,\quad \mathbf{a}=(\lambda_1{}^1\cdots\lambda_3{}^1),\quad a_0=\lambda_0{}^1,\\&\mathbf{H}=(\lambda_{23}{}^2,\cdots\lambda_{12}{}^2),\quad \mathbf{E}=(\lambda_{01}{}^2,\cdots\lambda_{03}{}^2),\\&\boldsymbol{\lambda}=(\lambda_{023}{}^3,\cdots\lambda_{012}{}^3),\quad \lambda_0=\lambda_{123}{}^3,\quad \Gamma=\lambda_0{}^4,\end{aligned}\tag{3.7}$$

one obtains the set of eight equations:

$$\left.\begin{aligned}&P_0\Lambda-2\mathbf{p}\cdot\mathbf{E}=g^2\tau_1\cdot\tau_2[-\Lambda(V_1+V_7)\\&\quad+(2/m)\mathbf{p}\cdot\mathbf{E}(V_3+V_5)+(2/m)\mathbf{p}\cdot\mathbf{a}(V_4+V_6)],\\&-P_0\mathbf{a}-2\mathbf{p}\times\boldsymbol{\lambda}+2m\mathbf{E}\\&\quad=g^2\tau_1\cdot\tau_2[-\mathbf{a}(V_1-V_7)-2\mathbf{E}V_2\\&\quad+(2/m)\mathbf{p}\times\boldsymbol{\lambda}(V_5-V_3)+(2/m)\mathbf{p}\Lambda(V_6-V_4)],\\&a_0=0,\\&P_0\mathbf{E}-2\mathbf{p}\Lambda-2m\mathbf{a}\\&\quad=g^2\tau_1\cdot\tau_2[-\mathbf{E}(V_1-V_7)-(2/m)\mathbf{p}\Lambda(V_5-V_3)\\&\qquad-(2/m)\mathbf{p}\times\boldsymbol{\lambda}(V_6-V_4)-2\mathbf{a}V_2],\\&-P_0\boldsymbol{\lambda}+2\mathbf{p}\times\mathbf{a}\\&\quad=g^2\tau_1\cdot\tau_2[-\boldsymbol{\lambda}(V_1+V_7)+(2/m)\mathbf{p}\times\mathbf{a}(V_3+V_5)\\&\qquad+(2/m)\mathbf{p}\times\mathbf{E}(V_4+V_6)],\end{aligned}\right\}\tag{3.8a}$$

$$\left.\begin{aligned}&-P_0\mathbf{H}-2\mathbf{p}\Gamma\\&\quad=g^2\tau_1\cdot\tau_2[\mathbf{H}(V_1+V_7)+(2/m)\mathbf{p}\Gamma(V_3+V_5)\\&\qquad-(2/m)\mathbf{p}\lambda_0(V_4+V_6)],\\&P_0\lambda_0+2m\Gamma\\&\quad=g^2\tau_1\cdot\tau_2[\lambda_0(V_1-V_7)-2\Gamma V_2\\&\qquad-(2/m)\mathbf{p}\cdot\mathbf{H}(V_6-V_4)],\\&P_0\Gamma+2m\lambda_0+2\mathbf{p}\cdot\mathbf{H}\\&\quad=g^2\tau_1\cdot\tau_2[-\Gamma(V_1-V_7)+2\lambda_0V_2\\&\qquad+(2/m)\mathbf{p}\cdot\mathbf{H}(V_5-V_3)].\end{aligned}\right\}\tag{3.8b}$$

As can be seen, the equations split into two uncoupled sets (3.8a and 3.8b) involving Λ, $\mathbf{a}$, $\mathbf{E}$, $\boldsymbol{\lambda}$, and Γ, λ_0, $\mathbf{H}$, respectively. In the nonrelativistic limit, the first set corresponds to the charge singlet state and the second to the charge triplet state. Each set may further be rearranged in terms of positive and negative energy components by making use of the fact that

$$\begin{aligned}4\Lambda_{\pm\pm}\phi=4\phi_{\pm\pm}=\sum\lambda_\rho{}^\sigma\{&[1-(-1)^{\sigma-s_0}]\Gamma_\rho{}^0\\&\pm[1-(-1)^{\sigma-s_0}]\beta\Gamma_\rho{}^\sigma\}C,\end{aligned}\tag{3.10}$$

$$\begin{aligned}4\Lambda_{\pm\mp}\phi=4\phi_{\pm\mp}=\sum\lambda_\rho{}^\sigma\{&[1+(-1)^{\sigma-s_0}]\Gamma_\rho{}^\sigma\\&\pm[1+(-1)^{\sigma-s_0}]\beta\Gamma_\rho{}^\sigma\}C,\end{aligned}\tag{3.11}$$

where[12]

$$\begin{aligned}&4\Lambda_{++}=(1+\beta_1)(1+\beta_2);\\&4\Lambda_{+-}=(1+\beta_1)(1-\beta_2),\quad\text{etc.}\end{aligned}\tag{3.12}$$

[10] $C\gamma_\mu{}^TC^{-1}=-\gamma_\mu$; $C^T=-C$.

[11] See, for example, R. Finkelstein, Phys. Rev. **88**, 555 (1952).

[12] These definitions differ from those of Levy and Klein by terms of order v/c. In their work Casimir operators replace our $\Lambda_{\pm}$.

Equations (3.10) and (3.11) imply that for the triplet state

$$\begin{aligned}&\phi_{++}=\tfrac{1}{2}(1+\beta)\gamma_4 C(a_i+E_i);\\ &\qquad\qquad \phi_{--}=\tfrac{1}{2}(1-\beta)\gamma_4 C(a_i-E_i),\\ &\phi_{+-}=\tfrac{1}{2}(1+\beta)(\Lambda-i\boldsymbol{\sigma}\cdot\boldsymbol{\lambda})C;\\ &\qquad\qquad \phi_{-+}=\tfrac{1}{2}(1-\beta)(\Lambda+i\boldsymbol{\sigma}\cdot\boldsymbol{\lambda})C,\end{aligned}\tag{3.13}$$

and for the singlet state

$$\begin{aligned}&\phi_{++}=\tfrac{1}{2}(1+\beta)\gamma_1\gamma_2\gamma_3 C(\lambda_0-\Gamma);\\ &\qquad\qquad \phi_{--}=\tfrac{1}{2}(1-\beta)\gamma_1\gamma_2\gamma_3 C(\lambda_0+\Gamma),\\ &\phi_{+-}=\tfrac{1}{2}(1+\beta)(-i\boldsymbol{\sigma}\cdot\mathbf{H})C;\\ &\qquad\qquad \phi_{-+}=\tfrac{1}{2}(1-\beta)(-i\boldsymbol{\sigma}\cdot\mathbf{H})C.\end{aligned}\tag{3.14}$$

IV. ANGULAR SEPARATION

The angular momentum integral allows one to separate the angular dependence of the wave function. For a system in a state J, M, one finds

$$\begin{aligned}&\{(J^2-L^2-\tfrac{3}{2})\\ &\quad+\tfrac{1}{2}(-1)^{\sigma+s_0}[(-1)^{s_1}+(-1)^{s_2}+(-1)^{s_3}]\}\lambda_\rho{}^\sigma\Gamma_\rho{}^\sigma\\ &\qquad=L_k\lambda_\rho{}^\sigma\sigma_k\Gamma_\rho{}^\sigma[1-(-1)^{\sigma+s_0+s_k}],\end{aligned}\tag{4.1}$$

$$[M-L_z]\lambda_\rho{}^\sigma\Gamma_\rho{}^\sigma=\tfrac{1}{2}\lambda_\rho{}^\sigma\sigma_z\Gamma_\rho{}^\sigma[1-(-1)^{\sigma+s_0+s_3}],\tag{4.2}$$

where $\mathbf{L}$ is the orbital angular momentum operator. Hence the quantities Λ, Γ, λ_0 satisfy

$$(J^2-L^2)S=0,\quad (M-L_z)S=0,\tag{4.3}$$

and the quantities $\mathbf{a}$, $\mathbf{E}$, $\boldsymbol{\lambda}$, $\mathbf{H}$ satisfy

$$\begin{aligned}&(J^2-L^2-2)\mathbf{V}=2i\mathbf{L}\times\mathbf{V},\\ &(M-L_z)V_x=-iV_y,\\ &(M-L_z)V_y=iV_x,\\ &(M-L_z)V_z=0.\end{aligned}\tag{4.4}$$

The latter are the equations for the vector spherical harmonics[13] $\mathfrak{X}$, $\mathfrak{Y}$, $\mathfrak{Z}$.

To decide upon the correct combination of these functions we make use of the generalized parity operator

$$\Pi=P\beta_1\beta_2\tag{4.5}$$

(which reduces to the ordinary parity operator P in the nonrelativistic limit). Since

$$\Pi\phi=\sum(-1)^{\sigma-s_0+1}(P\lambda_\rho{}^\sigma)\Gamma_\rho{}^\sigma C,\tag{4.6}$$

and since the triplet and singlet wave functions are separately eigenfunctions of Π (with eigenvalues ±1), one finds that the most general form for the functions is

$$\begin{aligned}&\Lambda=u_1(r)Y_J{}^M,\\ &\mathbf{a}=u_2(r)\mathfrak{X}_{J-1}{}^M+u_3(r)\mathfrak{Z}_{J+1}{}^M,\\ &\mathbf{E}=u_4(r)\mathfrak{X}_{J-1}{}^M+u_5(r)\mathfrak{Z}_{J+1}{}^M,\\ &\boldsymbol{\lambda}=u_6(r)\mathfrak{Y}_J{}^M,\\ &\Gamma=v_1(r)Y_J{}^M,\\ &\lambda_0=v_2(r)Y_J{}^M,\\ &\mathbf{H}=v_3(r)\mathfrak{X}_{J-1}{}^M+v_4\mathfrak{Z}_{J+1}{}^M,\end{aligned}\tag{4.7}$$

where $u_1\cdots u_6$, $v_1\cdots v_4$ are radial functions.

After substitution of these functions into (3.8a, b) the angular parts may be divided out and general radial equations obtained. We state the results only for the $J=0$ (triplet charge state) and $J=1$ (singlet charge state) cases:

$J=0$

$$\begin{aligned}&(P_0-2m)f_{++}+i(d/dr+2/r)v_4\\ &\quad=g^2\tau_1\cdot\tau_2\{(V_1-V_7-2V_2)f_{--}\\ &\quad+(i/m)(d/dr+2/r)[v_4(V_5+V_6-V_3-V_4)]\},\end{aligned}\tag{4.8a}$$

$$\begin{aligned}&(P_0+2m)f_{--}-i(d/dr+2/r)v_4\\ &\quad=g^2\tau_1\cdot\tau_2\{(V_1-V_7+2V_2)f_{++}\\ &\quad+(i/m)(d/dr+2/r)[v_4(V_3+V_6-V_4-V_5)]\},\end{aligned}\tag{4.8b}$$

$$\begin{aligned}&[P_0+g^2\tau_1\cdot\tau_2(V_1+V_7)]v_4\\ &\quad=-2i(d/dr)\{f_{++}[1+(g^2\tau_1\cdot\tau_2/m)(V_3+V_4+V_5+V_6)]\\ &\quad-f_{--}[1+(g^2\tau_1\cdot\tau_2/m)(V_3+V_5-V_4-V_6)]\},\end{aligned}\tag{4.8c}$$

where $f_{++}=\frac{1}{2}(v_2-v_1)$ and $f_{--}=\frac{1}{2}(v_2+v_1)$. These linear combinations, as may be seen from Eqs. (3.14) and (4.7), are the radial parts of ϕ_{++} and ϕ_{--}, respectively.

For the $J=1$ case, we similarly define the quantities $f_{++}{}^S=\frac{1}{2}(u_2+u_4)$, $f_{--}{}^S=\frac{1}{2}(u_2-u_4)$, $f_{++}{}^D=\frac{1}{2}(u_3+u_5)$, $f_{--}{}^D=\frac{1}{2}(u_3-u_5)$, which are the appropriate radial functions for the $l=0$ and $l=2$ states. Writing $u_1'=-i\sqrt{3}u_1$, $u_6'=\sqrt{3}u_6$ we obtain

$$\begin{aligned}&(P_0-2m)f_{++}{}^S+\tfrac{1}{3}(d/dr+2/r)(2u_6'+u_1')\\ &\quad=g^2\tau_1\cdot\tau_2\{f_{--}{}^S(V_1-V_7-2V_2)-(1/3m)(d/dr+2/r)\\ &\qquad\times[(V_5+V_6-V_3-V_4)(2u_6'-u_1')]\},\end{aligned}\tag{4.9a}$$

$$\begin{aligned}&(P_0+2m)f_{--}{}^S+\tfrac{1}{3}(d/dr+2/r)(2u_6'-u_1')\\ &\quad=g^2\tau_1\cdot\tau_2\{f_{++}{}^S(V_1-V_7+2V_2)+(1/3m)(d/dr+2/r)\\ &\qquad\times[(V_3+V_6-V_4-V_5)(2u_6'+u_1')]\},\end{aligned}\tag{4.9b}$$

$$\begin{aligned}&(P_0-2m)f_{++}{}^D+\tfrac{1}{3}(d/dr-1/r)(u_6'-u_1')\\ &\quad=g^2\tau_1\cdot\tau_2\{f_{--}{}^D(V_1-V_7-2V_2)-(1/3m)(d/dr-1/r)\\ &\qquad\times[(V_5+V_6-V_3-V_4)(u_6'+u_1')]\},\end{aligned}\tag{4.9c}$$

$$\begin{aligned}&(P_0+2m)f_{--}{}^D+\tfrac{1}{3}(d/dr-1/r)(u_6'+u_1')\\ &\quad=g^2\tau_1\cdot\tau_2\{f_{++}{}^D(V_1-V_7-2V_2)-(1/3m)(d/dr-1/r)\\ &\qquad\times[(V_5+V_6-V_3-V_4)(u_6'-u_1')]\},\end{aligned}\tag{4.9d}$$

[13] See N. Kemmer, Helv. Phys. Acta **10**, 47 (1937); H. Corben and J. Schwinger, Phys. Rev. **58**, 953 (1940). The notation used is that of Kemmer. Note that the three components of the $\mathfrak{X}_l{}^m$, etc., listed by him correspond to $\mathfrak{X}_-$, $\mathfrak{X}_z$, and $-\mathfrak{X}_+$, etc.

$$[P_0+g^2\tau_1\cdot\tau_2(V_1+V_7)]u_1'$$
$$=2(d/dr)(f_{++}{}^S-f_{--}{}^S)-4(d/dr+3/r)$$
$$\times(f_{++}{}^D-f_{--}{}^D)+2g^2(\tau_1\cdot\tau_2/m)$$
$$\times\{d/dr[(V_3+V_5)(f_{++}{}^S-f_{--}{}^S)$$
$$+(V_4+V_6)(f_{++}{}^S+f_{--}{}^S)]-2(d/dr+3/r)$$
$$\times[(V_3+V_5)(f_{++}{}^D-f_{--}{}^D)$$
$$+(V_4+V_6)(f_{++}{}^D+f_{--}{}^D)]\}, \quad (4.9e)$$

$$[P_0-g^2\tau_1\cdot\tau_2(V_1+V_7)]u_6'$$
$$=2(d/dr)(f_{++}{}^S+f_{--}{}^S)+2(d/dr+3/r)$$
$$\times(f_{++}{}^D+f_{--}{}^D)-2g^2(\tau_1\cdot\tau_2/m)$$
$$\times\{d/dr[(V_3+V_5)(f_{++}{}^S+f_{--}{}^S)$$
$$+(V_4+V_6)(f_{++}{}^S-f_{--}{}^S)]$$
$$+(d/dr+3/r)[(V_3+V_5)(f_{++}{}^D+f_{--}{}^D)$$
$$+(V_4+V_6)(f_{++}{}^D-f_{--}{}^D)]\}. \quad (4.9f)$$

V. DISCUSSION OF THE $J=0$ AND $J=1$ STATES

The quantity v_4, which is related to the ϕ_{+-} and ϕ_{-+} components in the $J=0$ case, may easily be eliminated from Eqs. (4.8a, b) with the aid of (4.8c). One thus obtains a pair of coupled differential equations for f_{++} and f_{--}. Separating out in the first equation the quantity $-1/m(d^2/dr^2+(2/r)d/dr)f_{++}$, which is the kinetic energy structure with reduced mass, one obtains

$$(P_0-2m)f_{++}+(1/m)[d^2/dr^2+(2/r)d/dr]f_{++}$$
$$=\frac{2f_{++}}{P_0+g^2\tau_1\cdot\tau_2(V_1+V_7)}\left(-\frac{d^2}{dr^2}-\frac{2}{r}\frac{d}{dr}\right)$$
$$\times\left(1+\frac{g^2\tau_1\cdot\tau_2}{m}(V_3+V_4+V_5+V_6)\right)$$
$$+\frac{2f_{++}}{[P_0+g^2\tau_1\cdot\tau_2(V_1+V_7)]^2}$$
$$\times\frac{d}{dr}[P_0+g^2\tau_1\cdot\tau_2(V_1+V_7)]$$
$$\times\frac{d}{dr}\left[1+\frac{g^2\tau_1\cdot\tau_2}{m}(V_3+V_4+V_5+V_6)\right]$$
$$+g^2\tau_1\cdot\tau_2(V_1-V_7-2V_2)f_{--}$$
$$+\text{other terms,}^{14} \quad (5.1a)$$

$$(P_0+2m)f_{--}=g^2\tau_1\cdot\tau_2(V_1-V_7+2V_2)f_{++}$$
$$+\text{other terms.}^{14} \quad (5.1b)$$

By setting $P_0=2m$ and neglecting μ/m corrections to the leading potentials, the first two potentials on the right-hand side of (5.1a) become (see 2.12):

$$-\mu(g^2/4\pi)(\mu/2m)\tau_1\cdot\tau_2\frac{e^{-\mu r}/r}{2m+\frac{1}{2}(g^2/4\pi)\tau_1\cdot\tau_2 e^{-\mu r}/r}, \quad (5.2a)$$

and

$$(\mu/2)(g^2/4\pi)^2(\mu/2m)(\tau_1\cdot\tau_2)^2$$
$$\times\left(\frac{\mu(1+1/\mu r)e^{-\mu r}/\mu r}{2m+\frac{1}{2}(g^2/4\pi)\tau_1\cdot\tau_2 e^{-\mu r}/r}\right)^2. \quad (5.2b)$$

[In obtaining (5.2a) the contact term has been dropped.] The first potential clearly corresponds to the usual Yukawa potential modified by the factor in the denominator. Upon expanding this denominator, one obtains

$$-\mu(g^2/4\pi)\tau_1\cdot\tau_2(\mu/2m)^2e^{-\mu r}/r$$
$$\times[1-\tfrac{1}{2}(g^2/4\pi)\tau_1\cdot\tau_2(\mu/2m)e^{-\mu r}/\mu r+\cdots]. \quad (5.3)$$

While the second term in (5.3) is of order $\mu/2m$ of the leading fourth-order potential obtained by Levy and Klein, it appears from (5.2a) that an expansion of the denominator is poor in the region $r\lesssim 1/\mu$ (for $g^2/4\pi \simeq 2m/\mu$). The second potential, (5.2b), corresponds to part of the one-pair terms obtained by Klein, modified by a similar denominator factor. If one eliminates f_{--} by perturbation theory, which to first order would correspond to neglecting the "other terms" of (5.1b), one obtains a two-pair term which is however of order $\mu/2m$ of the dominant two-pair potential of Klein. This potential corresponds to the two-pair structure when both pairs are in the field at a given time. The latter case arises in the second nonadiabatic approximation to the Δ_+ interaction (and in the crossed meson diagram (see L2, Fig. 1, a_1, a_2)), the first nonadiabatic approximation apparently not allowing "sufficient" retardation for such a situation to occur.[15] The rest of the one pair terms come from a similar source.

Turning to the $J=1$ case, it is clear that the elimination of u_1' and u_6' in (4.9a–d) via (4.9e, f) will yield denominators of the structure $P_0\pm g^2\tau_1\cdot\tau_2(V_1+V_7)$. Since $\tau_1\cdot\tau_2=-3$, the upper sign produces a singularity which occurs approximately at the zero of $2m-\frac{3}{2}(g^2/4\pi)e^{-\mu r}/r$ i.e., at $r\simeq 0.7\hbar/\mu c$ for[16] $g^2/4\pi=2m/\mu$. Although it is not necessarily true that the above singular behavior persists in the more rigorous equations containing integral operator potentials (because there the explicit elimination of the ϕ_{+-} and ϕ_{-+} components is not possible), it is certainly clear that the perturbation expansion is invalid for $g^2/4\pi\gtrsim 2m/\mu$. If one now

[14] The remaining terms were not explicitly written down as their structure is not germane to the subsequent discussion. They consists of velocity dependent potentials generated by the elimination of the ϕ_{+-} and ϕ_{-+} components, and of μ/m corrections to the leading potentials.

[15] We may remark parenthetically that the $\mu/2m$ two-pair terms mentioned above will cancel with the $\mu/2m$ correction to the dominant two-pair structure in a perturbation scheme, as shown by Klein. To see whether this will happen in the present approach, would require detailed calculation.

[16] A similar calculation using the lowest-order kernel recently derived by F. J. Dyson, Phys. Rev. **91**, 1543 (1953) in the new Tamm-Dancoff formalism does not alter this conclusion.

proceeds to eliminate all negative energy components in a perturbation fashion, one obtains the following equations, to lowest order:

$$(P_0-2m)u=-(1/m)(d^2/dr^2)u+V_c u+2^{\frac{1}{2}}V_c w, \quad (5.4a)$$

$$(P_0-2m)w=-(1/m)(d^2/dr^2-6/r^2)w+V_t w+2^{\frac{1}{2}}V_t w, \quad (5.4b)$$

where

$$u=f_{++}{}^S/r, \quad w=\sqrt{2}f_{++}{}^D/r,$$

$$V_c=-(g^2/4\pi)(\mu/2m)^2e^{-\mu r}/r,$$

$$V_t=-(g^2/4\pi)(\mu/2m)^2(1+3/\mu r+3/(\mu r)^2)e^{-\mu r}/r.$$

It is interesting to observe that the tensor and central forces do not appear as in the usual structure [e.g., L2 Eq. (71)]. The reason for this may be seen by returning to Eq. (2.9). Two of the terms appearing in the integrand of the potential are

$$(1/\omega_k{}^2)C_+{}^{(1)}(\mathbf{p})C_+{}^{(2)}(\mathbf{p})\beta_1\gamma_5{}^{(1)}\beta_2\gamma_5{}^{(2)}C_+{}^{(1)}(0)C_+{}^{(2)}(0),$$

and

$$(1/\omega_k{}^2)C_-{}^{(1)}(\mathbf{p})C_+{}^{(2)}(\mathbf{p})\beta_1\gamma_5{}^{(1)}\beta_2\gamma_5{}^{(2)}C_+{}^{(1)}(0)C_+{}^{(2)}(0). \quad (5.5)$$

Taking the nonrelativistic form of these two structures one obtains

$$(1/4m)^2(\boldsymbol{\sigma}^{(1)}\cdot\mathbf{p})(1+\beta_1)(\boldsymbol{\sigma}^{(2)}\cdot\mathbf{p})(1+\beta_2),$$

and

$$-\tfrac{1}{2}(1/4m)\gamma_5{}^{(1)}(1+\beta_1)\boldsymbol{\sigma}^{(2)}\cdot\mathbf{p}(1+\beta_2)$$
$$-(1/4m)^2(\boldsymbol{\sigma}^{(1)}\cdot\mathbf{p})(1+\beta_1)(\boldsymbol{\sigma}^{(2)}\cdot\mathbf{p})(1+\beta_2), \quad (5.6)$$

respectively. The first term is the one considered by Levy and clearly yields the usual tensor force in the ϕ_{++} state. However, adding the two expressions, the tensor part disappears, leaving only

$$-\tfrac{1}{2}(1/4m)\gamma_5{}^{(1)}(1+\beta_1)\boldsymbol{\sigma}^{(2)}\cdot\mathbf{p}(1+\beta_2). \quad (5.7)$$

Had one made a perturbation expansion on the second of these terms, its effect would appear as a fourth- and higher-order potential. On the other hand, from the cancellation observed here and elsewhere in (2.9) one sees that these higher-order potentials sum so as to replace $V_t w$ by $V_c w$ in (5.4a) and $(V_c-2V_t)w$ by $V_t w$ in (5.4b).

VI. CONCLUSIONS

The procedure utilized in the preceding sections allows one to examine the validity of the perturbation treatment of the negative energy components. It was hoped at the outset that the avoidance of one of the perturbation approximations inherent in the Levy-Klein program might lead to a convergent series of potentials. This now appears to be doubtful. The pole that appears in the potential for the deuteron seems to invalidate the μ/m expansions which are necessary to replace the integral operators by multiplicative potentials. Aside from this, the large number of μ/m corrections to the leading potentials tends to cast doubt on this method.

Perhaps a more disturbing feature is the change in the structure of the usual tensor interaction. Here one has an example of a series of supposedly "small" potentials, adding up so as to modify the lowest order potential. This phenomenon is independent of the size of the coupling constant, and hence is characteristic of the pseudoscalar nature of the interaction only. The possibility is thus raised that other "leading" potentials may similarly be modified by series of terms not even considered in a perturbation scheme to a given order.

To see whether these difficulties occur in higher-order approximations would of course require detailed calculations.

The Unitarity of the U Operator

H. EKSTEIN
Armour Research Foundation of Illinois, Institute of Technology, Chicago, Illinois
(Received January 28, 1954)

The U operator, which connects state vectors in interaction representation for different times, can be applied meaningfully to asymptotic values of state vectors $\Phi(\pm\infty)$ if these limits exist. The conditions for this occurrence are stated for the simplest case. If the restriction resulting from the definition of the asymptotic values is respected, all U operators are unambiguously unitary. A more general operator W which can act on all state vectors, can be defined, but it is not unitary.

THE operator $U(t,\tau)$, defined in interaction representation by

$$\Phi(t)=U(t,\tau)\Phi(\tau), \tag{1}$$

is known to be unitary for finite times t, τ, but some doubt and disagreement exists concerning the limits $U(t,-\infty)$ and $U(\infty,\tau)$.[1,2] It will be shown that these operators have, by their definition, a severely restricted domain, but that they are unambiguously unitary if this restriction is respected.

$U(t,-\infty)$ is defined by

$$\Phi(t)=U(t,-\infty)\lim_{\tau\to-\infty}\Phi(\tau) \tag{2}$$

and $U(\infty,t)$ by

$$\lim_{\tau\to\infty}\Phi(\tau)=U(\infty,t)\Phi(t). \tag{3}$$

$U(t,-\infty)$ has meaning only if its domain is restricted to those state vectors which tend to a limit at $-\infty$, and $U(\infty,t)$ only if its range is restricted to such Φ's which tend to a limit for $+\infty$.

Let the Hamiltonian be $H=K+V$, where V is the interaction term. If $\Phi(\pm\infty)$ are to have limits, the corresponding Schrödinger wave functions must behave asymptotically like

$$\Psi\xrightarrow[\tau\to\pm\infty]{}e^{-iK_t}\psi_\pm(x), \tag{4}$$

where $\psi_\pm(x)$ is time-independent. This will happen only if Ψ is entirely outside the range of interaction for the distant future (past), for then

$$\lim_{t\to\pm\infty}V\Psi(t)=0,$$

and the Schrödinger equation leads to the form (4). The explicit conditions for this behavior will now be indicated.

If Ψ is represented as a wave packet,

$$\Psi(x,t)=\int C(E)\psi_E(x)e^{-iEt}dE, \tag{5}$$

where $\psi_E(x)$ are eigenfunctions of $K+V$, then in virtue of well-known properties of the Fourier integral, $\Psi(x,t)$ tends to zero in any finite region of x as t becomes $\pm\infty$ if $C(E)\Psi_E$ is absolutely integrable, and in particular contains no delta function belonging to bound states. Hence, in the distant past and distant future this wave function will be entirely outside the range of the potential. The essential limitation for the domains and ranges $U(t,-\infty)$ and $U(\infty,t)$ is, therefore, the absence of an admixture of bound states.

Since the ranges and domains of the two operators $U(t,-\infty)$ and $U(\infty,t)$ are identical, it is legitimate to extend the well-known relation

$$U(t,t_0)=U(t,t')U(t',t_0) \tag{6}$$

to

$$S=U(\infty,-\infty)=U(\infty,0)U(0,-\infty). \tag{7}$$

Since the operators for infinite times differ in their action only infinitesimally from operators for large times, the unitarity of the U and S operators can be now inferred from the known property of these operators for finite times, as long as the restriction on domain is respected. To express the U operators in terms of time-independent solutions of the Schrödinger equation, one can follow the same procedure as Ma,[1] keeping in mind that with respect to the domain considered, the positive-energy solutions ψ_λ form a complete system. Hence,

$$\int\psi_\lambda\psi_\lambda^*d\lambda=1, \tag{8}$$

and the unitarity of the U operators is thus confirmed. An entirely different operator is defined by

$$\begin{aligned}W(\infty,t)&=\lim_{\tau\to\infty}U(\tau,t),\\ W(t,-\infty)&=\lim_{\tau\to-\infty}U(t,\tau),\end{aligned} \tag{9}$$

with a range (domain) containing all squared-integrable functions. One will require that W should be identical with U within the restricted domain, but otherwise the manner in which limits for indefinitely oscillating matrix elements are defined, is arbitrary. There seems to be no real necessity for defining such an operator, but we can see two motivations for doing so.

[1] S. T. Ma, Phys. Rev. **87**, 652 (1952).
[2] M. Gell-Mann and M. L. Goldberger, Phys. Rev. **91**, 398 (1953).

(a) The replacement of oscillatory functions by their asymptotic mean value is a procedure often used in physics and very successfully applied by Gell-Mann and Goldberger for explicit evaluations.[2] This can be done in the present case either by formal handling of "conditional equalities"[1] or by an explicit prescription which is equivalent to a "dc filtering" of the asymptotic values.[2]

(b) One can think of situations where the initial state is a linear combination of bound and positive-energy states, i.e., an atom the nucleus of which undergoes instantaneous conversion: immediately afterward, the state of the electrons is a mixture of bound and free states of the Hamiltonian describing the nucleus with altered charge. In this case, one would decompose the Schrödinger wave function $\Psi(0)$ into $\Psi_{\text{bound}}+\Psi_{\text{free}}$ and the asymptotic form is

$$\Psi \underset{t\to\infty}{\longrightarrow} e^{-iKt}U(\infty,0)\Psi_{\text{free}}(0)+e^{-i(K+V)t}\Psi_{\text{bound}}(0). \quad (10)$$

It is advantageous now to define an operator $W(\infty,0)$ so that it annuls the bound state part of $\Psi(0)$, i.e.,

$$W(\infty,0)\Psi_{\text{bound}}=0, \quad (11)$$

because it is then unnecessary to decompose $\Psi(0)$ and one obtains immediately the scattered part of the wave function

$$\Psi_{sc} \underset{t\to\infty}{\longrightarrow} e^{-iKt}W(\infty,0)\Psi(0). \quad (12)$$

It is remarkable that the additional requirement (11) leads precisely to the same operator as the one obtained by the limiting procedures discussed under (a), although the motivation for its introduction is entirely different.

It should be noted that these remarks, as well as most of the previous work on the time-dependent scattering, applies only to the simplest case where the incident system is identical with the scattered one. Different considerations are required for multichannel processes.

Letters to the Editor

PUBLICATION of brief reports of important discoveries in physics may be secured by addressing them to this department. The closing date for this department is five weeks prior to the date of issue. No proof will be sent to the authors. The Board of Editors does not hold itself responsible for the opinions expressed by the correspondents. Communications should not exceed 600 words in length and should be submitted in duplicate.

Effect of Hydrostatic Pressure on the Superconducting Transition of Tin*

M. GARBER AND D. E. MAPOTHER
Physics Department, University of Illinois, Urbana, Illinois
(Received March 18, 1954)

THE pressure-induced displacement of the critical field curve for superconductivity has been measured for tin using liquid helium as the pressure fluid. The procedure followed has been to observe the critical field curve over a small temperature range near T_c for several constant pressures. The critical field measurements were made using a sensitive ballistic induction technique. The use of liquid helium as the pressure fluid makes it possible to apply and remove the pressure while the specimen remains at helium temperatures, and also assures that the pressure experienced by the specimen is really hydrostatic. The specimen used was a single crystal cast in the shape of an ellipsoid of revolution.

The data obtained so far are presented in Fig. 1 which shows the displacement of the critical field values as a function of the applied pressure. Results for two runs are plotted, and each point on the curves represents an average of about 10 separate determinations. The vertical lines through the points indicate the spread in the experimental values of ΔH_c over the range of temperature studied (which was from about 3.45°K to 3.70°K). This spread is too great to permit experimental observation of the temperature variation of $\partial H_c/\partial p$ in such a small temperature interval. The value of dT_c/dp given below includes a small calculated adjustment to correct the experimental $\Delta H_c/\Delta p$ to its value at T_c.

The significance of the intercepts in Fig. 1 is that they represent displacements of the critical field curve which result from the application of pressure at helium temperatures. The displacement is permanent in the sense that the specimen must be warmed above helium temperatures in order to restore the zero-pressure critical field curve to its initial position. (Warming the specimen to liquid nitrogen temperature appeared to be sufficient.) A systematic study of the factors affecting the magnitude of the permanent shift has not yet been made but it appears that most of the displacement is present after the initial application of pressure. Presumably this effect results from cold-working the specimen but it is surprising that a hydrostatic pressure of such relatively small magnitude can do this. In the present measurements the specimen was cycled several times to the maximum pressure (about 100 atmospheres) in order to produce a stable zero-pressure transition curve. This procedure resulted in fairly good reproducibility in the pressure coefficient $\Delta H_c/\Delta p$ as can be seen in Fig. 1. The difference in permanent displacement between the two runs is unexplained at present.

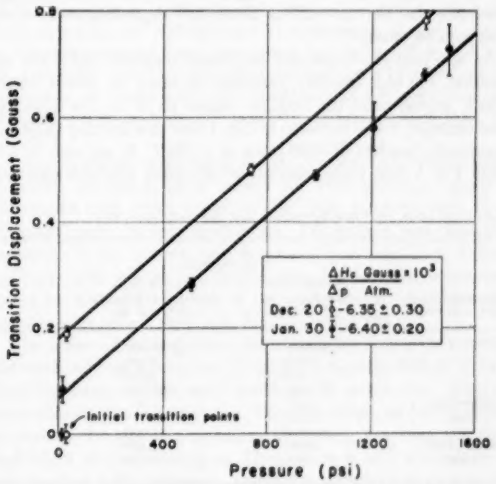

FIG. 1. The displacement of the superconducting transition curve for tin produced by hydrostatic pressure.

The measuring methods used in this work make it possible to determine the critical temperature and the slope of the critical field curve. The values obtained are $T_c=3.728\pm0.0015$°K and $(\partial H_c/\partial T)T_c=149\pm1$ gauss deg^{-1} which are in very close agreement with the values reported by Lock, Pippard, and Schoenberg.[1] The displacement of the critical temperature with respect to pressure calculated from our values of $(\partial H_c/\partial T)T_c$ and an average of the slopes of Fig. 1 yields the value

$$(dT_c/dp)=4.40\pm0.20\times10^{-5}\text{ deg atmos}^{-1}.$$

This value is lower than most previously reported values for dT_c/dp in tin.[2] We believe that this may be due to the fact that earlier workers have not taken into account the possibility of the permanent pressure displacement observed in the present experiments. The data of Kan, Lasarev, and Sudovstov[3] for tin have been reported in sufficient detail to permit an approximate check on this point. Unfortunately only two pressures were used, but their data plotted as in Fig. 1 indicate a substantial intercept on the ΔH_c axis as we have found. The magnitude of their "permanent" displacement if their data are interpreted in this way is in reasonable agreement with our results if one assumes that the magnitude of the permanent displacement is proportional to the maximum pressure applied to the specimen. This interpretation of their data also yields a value of dT_c/dp which is in agreement with our value to within the accuracy of the extrapolations involved.

We gratefully acknowledge the assistance of Dr. B. S. Chandrasekhar and of J. F. Cochran, R. E. Mould, and R. R. Hake in making these measurements. This work is being continued.

* This work has received partial support from the Office of Ordnance Research.

[1] Lock, Pippard, and Schoenberg, Proc. Cambridge Phil. Soc. **47**, 811 (1951).

[2] The values reported earlier have been tabulated in a letter by M. D. Fiske, Phys. Rev. **94**, 495 (1954), together with his own recent data.

[3] Kan, Lasarev, and Sudovstov, J. Exptl. Theoret. Phys. (U.S.S.R.) **18**, 825 (1948).

Hall Coefficient in Germanium*

T. C. HARMAN, R. K. WILLARDSON, AND A. C. BEER
Battelle Memorial Institute, Columbus, Ohio
(Received February 11, 1954)

A NUMBER of recent measurements by various investigators on germanium indicate that the use of simplified Hall-effect equations give values for carrier concentrations which, although generally satisfactory for n-type specimens, fail on p-type specimens to give results consistent with those obtained from other electrical data. A major discrepancy is that between the room-temperature value for hole mobility of 2600 to 2900 cm^2/volt-sec,[1] as determined from Hall and resistivity measurements ($\mu=0.85R\sigma$), and the value of 1700 to 1900 cm^2/volt-sec[2] as determined from drift-mobility experiments. Also, the value of electron-

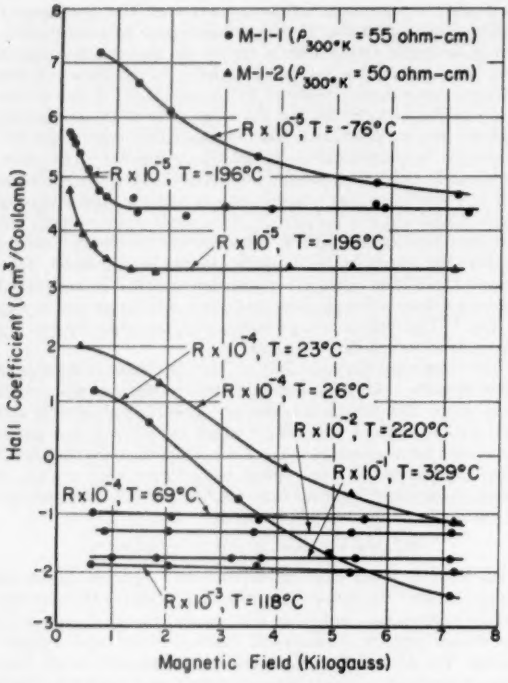
• M-1-1 ($\rho_{300°K}$ = 55 ohm-cm)
▲ M-1-2 ($\rho_{300°K}$ = 50 ohm-cm)
R x 10⁻⁵, T = -76°C
R x 10⁻⁵, T = -196°C
R x 10⁻⁵, T = -196°C
R x 10⁻⁴, T = 23°C
R x 10⁻⁴, T = 26°C
R x 10⁻², T = 220°C
R x 10⁻¹, T = 329°C
R x 10⁻⁴, T = 69°C
R x 10⁻³, T = 118°C
Hall Coefficient (Cm³/Coulomb)
Magnetic Field (Kilogauss)

FIG. 1. The Hall coefficient of p-type Ge as a function of magnetic field.

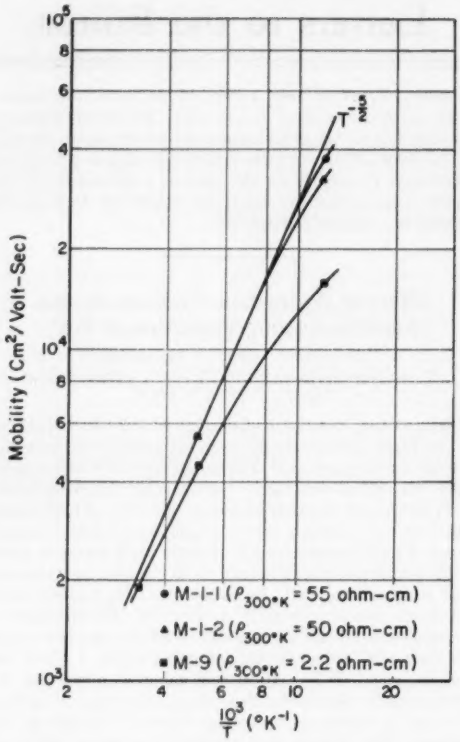

FIG. 2. Hole mobility in p-type Ge as a function of temperature.

hole mobility ratio is 1.4[3] or 1.5[1] as determined from Hall data by means of the usual equations. On the other hand, a careful analysis of resistivity data suggests a value of 2.0,[4] which is also confirmed by the drift-mobility determinations. Further indications that the simplified theory is not adequate in the case of p-type germanium can be found in the magnetic-field dependence of the Hall coefficient. For example, the temperature at which the Hall voltage changes sign decreases with increasing magnetic field. This effect was noted by Dunlap,[1] and it is illustrated in Fig. 1 by the data at room temperature where R is seen to vary from positive to negative with increasing field. This dependence is opposite to what might be expected from calculations we have made, based on an extension of the work of Harding[5] and of Johnson and Whitesell.[6] Also, in the extrinsic region, the quantity $\Delta R/R_{H\to 0}$ is larger than predicted.

The data at −196°C indicate that even in weak magnetic fields the Hall coefficient can be strongly field dependent. Hence, the usual calculations based on weak-field data cannot be expected to yield satisfactory results. Obviously, a better theory is needed.

In the absence of such a theory, the possibility of utilizing the very large magnetic field approximations was examined. A desirable simplification results from such a treatment since it can be shown that, in the single carrier case,

$$R_{H\to\infty}=1/ne, \ (R, e \text{ in practical units}),$$

a relationship which is unchanged for classical or degenerate statistics and for the various power-law dependencies of mean free path on energy.[7]

In applying this equation, exorbitant magnetic fields are not required for high-mobility materials in order to obtain results which approximate the limiting values given by the equation. For example, it will be noted in Fig. 1 that this limiting value was apparently reached at 1000 gauss at −196°C. It will also be seen from Fig. 1 that these calculations of carrier densities eliminate

TABLE I. Comparison of hole mobilities in germanium as determined from Hall measurements and drift-mobility data.

Specimen designation	Resistivity, ohm-cm	Temperature, degrees centigrade	Drift mobility,[a] cm²/volt-sec	Hall mobility: Strong field ($\mu=R_{H\to\infty}/\rho$) cm²/volt-sec	Hall mobility: Weak field $\mu=(8/3\pi)R_{H\to 0}/\rho$, cm²/volt-sec
M-1-1	12	−196	...	38 000	>43 000
	80	−76	...	5500	7800
	55	27	...	2100[b]	3000[b]
M-1-2	10	−196	...	32 000	>39 000
	62	−76	4000–5000	5400	...
	50	27	1900	2100[b]	...
M-9	0.27	−196	...	16 000	17 000
	0.95	−76	4000–5000	4500	5300
	2.2	27	1800	1900	2600

[a] See reference 2.
[b] Extrapolated from lower temperatures.

the weak-field anomaly of an apparent increase in carrier concentration with decreasing temperature in the extrinsic region.

Extrinsic-carrier concentrations were determined for p-type specimens of germanium (55, 50, and 2.2 ohm-cm at 300°K) using the strong-field approximation at −196°C. Mobilities were then calculated from resistivity data. Results are plotted in Fig. 2.

The values obtained from the strong-field calculations are compared with those resulting from the usual weak-field determinations and with drift-mobility data[2] in Table I.

By carrying out measurements in strong magnetic fields and using the equations valid in the limiting cases of such fields, we have found that the calculated mobilities did show good agreement with the results of drift measurements. Also, the ratio of electron to hole mobility at 27°C was approximately 2, the value obtained by Hunter from careful studies on resistivity data. These experiments suggest that differences between mobility values as computed from Hall coefficient and conductivity, and those computed from drift experiments may, for the most part, result from the inadequacies of the weak-field Hall equations in giving the correct values for carrier concentrations in extrinsic p-type germanium. In addition, the extrinsic Hall coefficients determined from strong-field asymptotic behavior were seen to remain relatively constant with decreasing temperature. Hence, there is no anomalous apparent increase in carrier concentrations at the lower temperatures.

The authors wish to thank E. B. Dale and W. L. Mefferd for supplying the germanium single crystals.

* Work supported in part by Air Force Cambridge Research Center.

[1] W. C. Dunlap, Phys. Rev. **71**, 471 (1947); **79**, 286 (1950); **82**, 329 (1951).
[2] M. B. Prince, Phys. Rev. **92**, 681 (1953).
[3] L. P. Hunter *et al.*, Phys. Rev. **91**, 1315 (1953).
[4] L. P. Hunter, Phys. Rev. **91**, 579 (1953).
[5] J. W. Harding, Proc. Roy. Soc. (London) **A140**, 205 (1933).
[6] V. A. Johnson and W. J. Whitesell, Phys. Rev. **89**, 941 (1953).
[7] See A. H. Wilson, *The Theory of Metals* (Cambridge University Press, Cambridge, 1953), Chap. VIII.

Electron Spin Resonance in Metals at Low Fields*

H. S. Gutowsky and P. J. Frank
Noyes Chemical Laboratory, University of Illinois, Urbana, Illinois
(Received March 25, 1954)

KIP, Kittel, and co-workers have observed electron spin resonance in sodium[1] and in lithium[2] metal at microwave frequencies and at 300 Mc/sec.[3] Measurements on these metals at lower frequencies have been made by Carver, Holcomb, and Slichter.[4] We wish to report the results of some independent observations, at frequencies near 25 Mc/sec, of the absorption line shapes for lithium from 77° to 300°K and for sodium from 77° to 385°K.

The apparatus was identical to that employed for broad nuclear magnetic resonance lines[5] except for two concentric pairs of Helmholtz coils which provided the main magnetic field (0 to 25 gauss) and the field modulation. The system was calibrated by means of the electron spin resonance in α,α-diphenyl β-picryl hydrazyl. The lithium and sodium samples were dispersions prepared by high-speed stirring of the molten metal in mineral oil; particle sizes ranged from 1 to 50μ, averaging 15μ.

The observed derivatives of the absorption lines were recorded automatically as a function of applied magnetic field at a fixed radio-frequency. They are Lorentzian in shape but distorted somewhat on the low-field side. This distortion can be attributed in part to the use of a resonance frequency less than the total half-width of the absorption. Thus, there is still absorption at zero applied field; moreover, absorption occurs from each of the opposing circularly polarized components of the oscillating rf field. Becker and Eisner[6] have reported similar detailed results for the narrower hydrazyl resonance at frequencies less than 3 Mc/sec. Feher and Griswold[3] have pointed out the possible importance of skin effects in distorting the line shape.

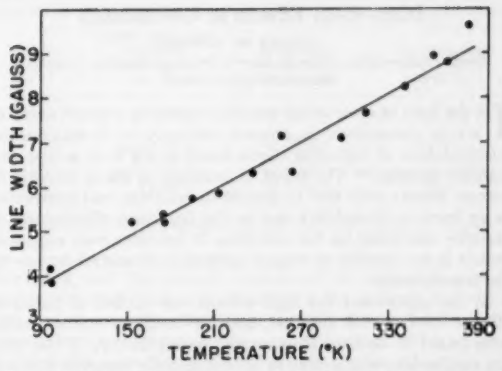

FIG. 1. The temperature dependence of the electron spin resonance absorption in sodium metal dispersed in mineral oil. The line width is defined as the separation between points of maximum slope.

In lithium, the resonance at room temperature has a width of 4.4 gauss between the maximum and minimum of the derivative. Widths of 5 gauss have been reported by Feher and Griswold[3] and by Slichter.[4] The Lorentzian line shape suggests that spin-lattice relaxation processes determine the width, which corresponds to a T_1 of 7.5×10^{-5} sec. This relaxation time is shorter by a factor of 10^2 than Overhauser's theoretical prediction.[7] Feher and Griswold[3] have mentioned that the line width increases at lower temperatures; in our sample at 77°K the width was 4.5 gauss, only slightly greater, if at all, than at room temperature.

On the other hand, the width of the resonance in sodium exhibits a pronounced, reasonably linear dependence upon temperature, as shown in Fig. 1. The width decreases from 9.7 gauss at 385°K to 3.6 gauss at 77°K. The slope of 0.018 gauss deg^{-1} gives a width of about 2 gauss when extrapolated to 0°K. The results were independent of the resonance frequency between 20 and 30 Mc/sec. Feher and Griswold[3] reported a width of 10 gauss at room temperature and noted a temperature dependence as well. The different temperature effects for lithium and sodium present an unresolved problem. Overhauser's analysis[7] predicts an increase in T_1 and therefore a decreasing line width with decreasing temperature. The experimental results suggest that T_1 includes a temperature-dependent and a temperature-independent term, the former increasing with nuclear charge. Holcomb and Norberg[8] have found that nuclear relaxation in the metals is sensitive to impurities and imperfections, which could contribute to the electron relaxation.

Electron spin resonance was observed at 77°K in a sample of high-surface sodium prepared by mixing molten sodium with surface-active alumina (Alcoa F-20; 160 meter^2 g^{-1}). The proportions of sodium and alumina were such that if the sodium film was uniform it was 10A thick. The line shape observed is identical with that for the dispersion in mineral oil, confirming that the resonance is from the sodium and not the supporting medium. Unsuccessful attempts were made to detect the electron resonance in K, Rb, Cs, Cu, Be, Mg, Al, Ta, Nb, and V at 30 Mc/sec at room temperature and in K, Rb, Cs, and Mg at 77°K.

* Supported in part by the U. S. Office of Naval Research and by a Grant-in-Aid from E. I. du Pont de Nemours and Company, Inc.
[1] Griswold, Kip, and Kittel, Phys. Rev. **88**, 951 (1952).
[2] Kip, Griswold, and Portis, Phys. Rev. **92**, 544 (1953).
[3] G. Feher and T. W. Griswold, Phys. Rev. **93**, 952 (1954).
[4] The results are given in part by T. R. Carver and C. P. Slichter, Phys. Rev. **92**, 212 (1953), and by A. W. Overhauser, Phys. Rev. **92**, 411 (1953).
[5] Gutowsky, Meyer, and McClure, Rev. Sci. Instr. **24**, 644 (1953).
[6] S. Becker and M. Eisner, Bull. Am. Phys. Soc. **29**, No. 2, 15 (1954).
[7] A. W. Overhauser, Phys. Rev. **89**, 689 (1953).
[8] D. F. Holcomb and R. E. Norberg, Phys. Rev. **93**, 919 (1954).

High-Field Effects in Germanium

ESTHER M. CONWELL
Physics Laboratories, Sylvania Electric Products, Bayside, New York
(Received April 1, 1954)

IN the light of some of the results obtained in a recent study of n-type germanium,[1] it appears necessary to re-examine the interpretation of high-field effects found at 20°K in n-type germanium samples.[2,3] The effect in question, a sharp increase in current density with field at around 10 volts/cm, was interpreted as an increase in mobility due to the decreased effectiveness of impurity scattering for hot electrons. It has since been suggested that it is due instead to impact ionization of neutral donors by the hot electrons.[4]

In the experiment the high voltage was applied in pulses of 10^{-6} or 10^{-7} second duration, and the resulting current pulses were found to be flat. Thus, carrier multiplication, if this were the mechanism, would have to be substantially complete in about 10^{-6} second. A crude estimate of the time required for this process can be obtained by use of the hydrogen-like model. The cross section for ionization of hydrogen by slow electrons is of the order of the geometrical cross section. The ionization cross section for a neutral donor should be $\kappa^2 (m/m^*)^2$ times this. It has been shown that the hydrogen-like model predicts reasonably well the ionization energy and scattering of electrons by neutral donors if m/m^* is taken to be 4. This value leads to a sufficiently large ionization cross section to make it not implausible that ionization could have been complete in 10^{-6} second in the sample considered.

There is also reason to believe that a given impurity concentration is less effective in scattering at these temperatures than theoretically expected.[1] To maintain the ratio of lattice mobility to impurity mobility at the value required to explain the data as a mobility change would then require a higher value of minority impurity concentration than previously considered, and one that begins to look implausibly high.

It has been argued that the heating of the electrons required to produce substantial impact ionization would first (i.e., at lower fields) have to be manifest as a change in mobility. It is worth pointing out, however, that this change might well be small enough to be easily missed experimentally. If only lattice and impurity scattering were operative, and these in amounts such that the respective low-field mobilities were equal, theory[3] predicts that in the course of a change in electron "temperature" by a factor 4 the mobility would first increase by about 20 percent, then decrease by 10 percent. It is possible that the sample in question had a low enough minority impurity concentration so that lattice and impurity scattering were balanced in this way.

The type of experiment performed by Ryder may make it possible to decide between these alternatives if data from different samples at the same temperature, or the same sample at different temperatures, are available. For the particular sample investigated it was found that at fields beyond the region of the steep increase the current density varied as $\sqrt{E}$. This dependence on E is characteristic of the high field variation of drift velocity under lattice scattering, and indicates that carrier concentration is constant in this range. For two different samples, 1 and 2, at the same temperature, theory[3] predicts that at any E for which both are in $\sqrt{E}$ range: $j_1/j_2 = n_1/n_2$. Thus the high-field value of the ratio n_1/n_2 can be obtained from the experimental j_1/j_2, and compared with the low-field value, obtainable from Hall data for the individual samples. If the two samples have somewhat different impurity concentrations, say 10^{13}/cm³ and 10^{15}/cm³, this should be conclusive. Similarly, in the case where data at different temperatures are available for the same sample, and the fields used are high enough to attain the $\sqrt{E}$ range at both temperatures, theory[3] predicts $j(T_1)/j(T_2) = [\mu_{Lo}(T_1)/\mu_{Lo}(T_2)]^{\frac{1}{2}} n(T_1)/n(T_2)$. The quantity μ_{Lo} is the low-field lattice mobility, and[1] $[\mu_{Lo}(T_1)/\mu_{Lo}(T_2)]^{\frac{1}{2}} \cong (T_2/T_1)^{0.5}$. Again, this enables comparison of the high-field ratio of carrier concentrations to the low-field ratio, obtainable from the usual Hall measurements as a function of temperature. If feasible, experiments of this type in which suitable infrared radiation is used to ionize the donors would also be conclusive.

[1] P. P. Debye and E. M. Conwell, Phys. Rev. **93**, 693 (1954)
[2] E. J. Ryder, Phys. Rev. **90**, 766 (1953).
[3] E. M. Conwell, Phys. Rev. **90**, 769 (1953).
[4] Sclar, Burstein, and Davisson, Phys. Rev. **92**, 858 (1953).

Properties of Plutonium Metal

CYRIL STANLEY SMITH
Institute for the Study of Metals, University of Chicago, Chicago, Illinois
(Received March 5, 1954)

SOME early information on the structure and physical properties of plutonium metal has recently been declassified by the Atomic Energy Commission. The data, as they were known to the Los Alamos metallurgists in 1945, are given in Table I. Figure 1 shows the dilatation and Fig. 2 the electrical resistivity of a slightly impure sample as a function of temperature.

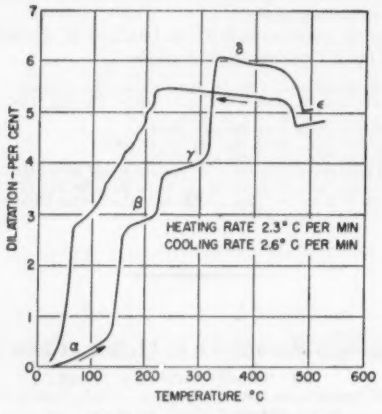

FIG. 1. Dilatation of plutonium metal (slightly impure) on heating and cooling.

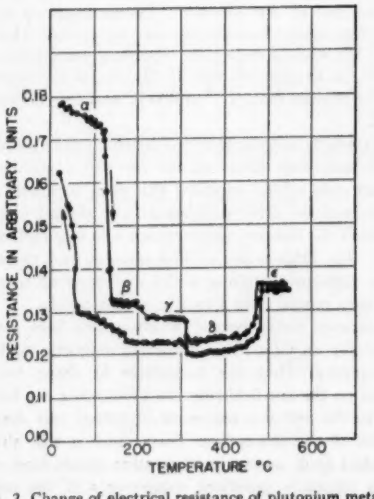

FIG. 2. Change of electrical resistance of plutonium metal on heating and cooling.

TABLE I. Properties of plutonium metal (1945 values, approximate).

Phase	Temperature range of stability	Crystal structure	Density g/cc at 25°C	Linear expansion coefficient (average), per °C	Electrical resistivity, microhm-cm	Temperature coefficient of resistivity
α	below 117°C	Orthorhombic, like uranium (doubtful)	19.8	55×10^{-6}	150 (25°)	-29.7×10^{-4}
β	117 to 200°C	Unknown (complex)	17.8	35×10^{-6}	110 (200°)	*ca* 0
γ	200 to 300°C	Unknown (complex)	...	36×10^{-6}	110 (300°)	*ca* 0
δ	300 to 475°C	Face-centered-cubic	16.0	-21×10^{-6}	102 (400°)	$+ 1.5\times10^{-4}$
ϵ	475 to 637°C	Body-centered-cubic	16.4	4×10^{-6}	120 (500°)	*ca* 0
liquid	above 637 ±5°C	...	...	...	...	...

The properties are astounding. Plutonium is unique among the elements in that there exist at least five solid allotropic modifications at atmospheric pressure. There is a 23 percent difference in atomic volume between the α and δ phases. The electrical resistivity of all phases is high—that of the α phase exceeding all other "metallic" elements at room temperature. The temperature coefficient of resistance of α is negative and the thermal expansivity extremely high. The *negative* expansion coefficient of the δ phase, which is face-centered-cubic in structure, is without parallel among the elements.

Some further details are given in another paper.[1] These data were obtained, under the general supervision of the writer, by members of Eric R. Jette's group in the Chemistry-Metallurgy division of the Los Alamos Laboratory, operated by the University of California for the U. S. War Department. The properties quoted are preliminary values obtained under the extreme pressure of wartime conditions, and it is hoped that more recent and reliable data can soon be released.

[1] C. S. Smith, paper to appear in *Metal Progress*, May, 1954. For British work on the same subject, see Nature **173**, 534 (1954).

Superconducting Alloys

B. T. MATTHIAS AND E. CORENZWIT
Bell Telephone Laboratories, Murray Hill, New Jersey
(Received March 24, 1954)

THE superconducting elements occur in groups throughout the periodic system. One of the early attempts to prepare a superconducting compound of nonsuperconducting elements was by de Haas,[1] who tried to combine two normal elements on either side of a group into a superconducting phase, and he thus discovered Au_2Bi. Later on, however, it became evident that the superconductivity in Au_2Bi had nothing to do with averaging over a superconducting group of elements in the periodic system. Au_2Bi crystallizes in a rather special crystal structure, in which no unalloyed elements can be found.

Only very recently it became apparent that such a possibility of averaging over the periodic system exists. Let us consider the following section of the periodic system:

V	VI	VII	VIII			
Nb	Mo	Tc	**Ru**	Rh	Pd	Superconducting elements are printed in boldface type.
Ta	W	Re	**Os**	Ir	Pt	
b.c.c.		h.c.p.		f.c.c.		

Mo and W are at the right-hand fringe of the body-centered cubic superconductors and are not superconducting any more by themselves. On the other side of the hexagonal close-packed group of superconductors are the face-centered cubic noble metals, which again are no longer superconducting. Raub[2] investigated the alloys between Mo on the one side, and the noble metals on the other side. As he found intermediate phases with Rh, Ir, and Pt which are hexagonal close-packed, it becomes immediately obvious that from a crystallographic viewpoint at least we have here an averaging over the periodic system and in particular over the superconducting hexagonal elements of the seventh and eighth columns. It suggests immediately that Mo alloys with Rh and Ir should become superconducting, an expectation which we have verified. Ru, according to Raub,[2] dissolves up to 35 atomic percent Mo, which is reasonable considering the tendency towards a hexagonal phase in this region. Mo-Ru alloys should therefore show superconducting properties similar to those of technetium, whose superconductivity was recently reported by Daunt and Cobble.[3] We have now found that the superconducting transition point of a 50–50 Mo-Ru alloy is at 10.6°K, which is 0.4° below Daunt's value for Tc. Most of this quantitative agreement is probably accidental. The superconducting transition of pure Ru is near 0.46°K.

In an earlier paper the importance of the average valence electron per atom ratio for the magnitude of the superconducting transition temperature was pointed out.[4] A 50–50 Ru-Mo alloy (if it existed, though the limit according to Raub is 35 atomic percent) should thus have a ratio similar to that of pure Tc, as well as the same crystal structure. This argument is now reflected in the closely corresponding transition temperatures. In a 50–50 Mo-Rh alloy, the valence electron/atom ratio will differ much more from that of Tc, and in this alloy we therefore found a transition temperature of 1.75°K.

In the iridium case we are more fortunate. Raub finds here an additional cubic phase, having the fixed composition Mo_3Ir. This composition will shift the ratio again closer to the favorable value of Tc, and we did find in fact the transition temperature for Mo_3Ir at 8.8°K.

The optimum value for the valence electron/atom ratio had been found to be slightly below 5.[4] It is, however, difficult to evaluate this factor for the transition elements with more than 6 valence electrons. Experiments show that it seems to be symmetric with respect to the middle of a long period of the periodic system, Nb and Tc having similar ratios.

We would like to thank Mrs. A. Feri for a valuable discussion.

[1] de Haas, van Aubel, and Voogel, Leiden Comm. No. 197a,c (1929).
[2] E. Raub, Z. Metallkunde, **45**, 23 (1954).
[3] J. G. Daunt and J. W. Cobble, Phys. Rev. **92**, 507 (1953).
[4] B. T. Matthias, Phys. Rev. **92**, 874 (1953).

Compression to 10,000 Atmos of Solid Hydrogen and Deuterium at 4.2°K*

J. W. STEWART
Physics Department, Harvard University, Cambridge, Massachusetts
AND
C. A. SWENSON
Cryogenic Engineering Laboratory, Massachusetts Institute of Technology, Cambridge, Massachusetts
(Received March 29, 1954)

WE have completed measurements on the hydrostatic compression of solid hydrogen and deuterium at liquid helium temperatures, and present here a brief discussion of the results. The gases were condensed into a $\frac{1}{4}$-in. diameter piston and cylinder combination at low temperatures, and were solidified by im-

TABLE I. The relative volume change and compressibility of solid H_2 and D_2 at 4.2°K.

Pressure (atmos)	Hydrogen $\frac{\Delta V}{V_0}$	Hydrogen $-\frac{1}{V_0}\left(\frac{\partial V}{\partial P}\right)_T \times 10^5$ (atmos^{-1})	Deuterium $\frac{\Delta V}{V_0}$	Deuterium $-\frac{1}{V_0}\left(\frac{\partial V}{\partial P}\right)_T \times 10^5$ (atmos^{-1})
0	0	50	0	31
200	0.076	29	0.056	21
400	0.123	20	0.093	16
600	0.159	15.8	0.121	13.4
1000	0.209	10.7	0.165	10.0
1500	0.252	7.8	0.205	7.4
2000	0.292	5.8	0.242	5.5
3000	0.341	4.0	0.288	4.0
4000	0.374	3.0	0.323	3.0
6000	0.423	2.0	0.373	2.0
8000	0.457	1.5	0.406	1.5
10 000	0.481	1.2	0.430	1.2

mersing the apparatus in liquid helium. A compressive force was applied to the sample holder piston by means of stainless steel compression and tension members which were connected to a low-friction hydraulic press at room temperature. Measurements of the relative motion of the press piston in its cylinder, when compared with a blank run, gave both the length of the sample and its change of volume with pressure. Data were taken for each run with increasing and decreasing pressure to provide a correction for the not inconsiderable friction encountered.

Preliminary extrusion experiments had shown that solid hydrogen is highly plastic at 4.2°K, so our one-sided compression is effectively translated into a purely hydrostatic pressure. The plasticity was so great that, until a seal of the Bridgman type (using metallic potassium as the gasket material) was placed on the piston, an unstable extrusion, which usually resulted in complete loss of the sample, was observed at about 2000 atmospheres for both hydrogen and deuterium. The clearance between piston and cylinder when this occurred was less than 5 microns.

Most of the work on these substances has been done at pressures up to 4000 atmos at Harvard. Single runs were made on each substance with a similar but larger setup at M.I.T. which confirmed the other results and extended them to 10 000-atmos pressure.

The $\Delta V/V_0$ data for both hydrogen and deuterium are given as a function of pressure in Table I. These results can be conveniently represented within the estimated experimental accuracy (better than 5 percent in $\Delta V/V_0$) in terms of equations developed by Birch[1] from Murnaghan's theory of finite strain. The general expression is of the form

$$P=\frac{3}{2}K_0\left[\left(\frac{V_0}{V}\right)^{7/3}-\left(\frac{V_0}{V}\right)^{5/3}\right]\left[1-\xi\left\{\left(\frac{V_0}{V}\right)^{2/3}-1\right\}\right], \quad (1)$$

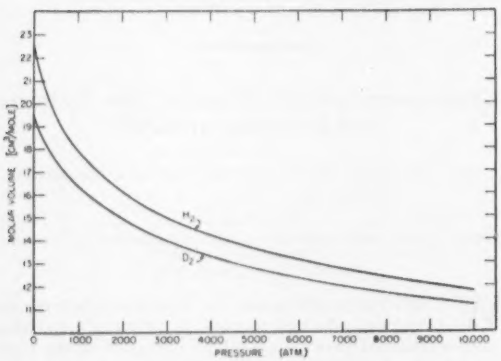

FIG. 1. The molar volumes of solid hydrogen and deuterium as a function of pressure at 4.2°K.

where K_0 is the reciprocal of the initial compressibility and ξ is a constant which is adjusted for best fit to the experimental data. We find for hydrogen $K_0=1990$ atmos and $\xi=-1.9$, and for deuterium, $K_0=3180$ atmos and $\xi=-1.6$.

The compressibilities, $-(1/V_0)(\partial V/\partial P)_T$, for hydrogen and deuterium were obtained by differentiation of Eq. (1). The agreement at low pressures with the work of Megaw[2] is satisfactory. It is interesting to note that the volume of hydrogen is reduced by roughly 50 percent in the first 10 000 atmos, but that an extrapolation of Eq. (1) beyond the experimental range indicates that 180 000 atmos would be required to obtain reduction by another factor of two.

The equality of the compressibilities of hydrogen and deuterium at the higher pressures is fortuitous, since one should actually compare values of $(\partial V/\partial P)_T$ for the same molar volumes of the two, and not $(1/V_0)(\partial V/\partial P)_T$. Such a comparison can be made from Fig. 1 where the molar volumes of solid hydrogen and deuterium are plotted as a function of pressure. We have used Megaw's[2] values at zero pressure, namely 22.65 cc/mole for hydrogen and 19.56 cc/mole for deuterium. Classically these two curves should be the same, but the quantum-mechanical zero-point energy produces a repulsive energy which is larger for hydrogen than for the heavier isotope deuterium under comparable conditions. Since the two curves approach each other as the pressure increases, the relative importance of the zero-point energy must decrease with increasing pressure. However, an extrapolation of Eq. (1) indicates that the two molar volumes never actually become equal, so that the effect of the zero-point energy does not disappear completely.

A more complete account of these experiments and results will be published later. We are indebted to Professor Bridgman for suggesting this work initially, and to both him and Professor H. Brooks for many helpful discussions.

* The part of this work done at Massachusetts Institute of Technology was sponsored by the U. S. Army Office of Ordnance Research.

[1] F. Birch, J. Geophys. Research **56**, 227 (1952).
[2] H. D. Megaw, Phil. Mag. **28**, 129 (1939).

Molecular Field Treatment of Magnetic Ordering Transitions

E. W. ELCOCK
Department of Natural Philosophy, Marischal College, Aberdeen, Scotland
(Received March 15, 1954)

IN a recent paper, Smart[1] has given an interesting treatment of magnetic ordering transitions on the basis of an assumed temperature dependence of the parameters specifying the interactions. The expression for the free energy, upon which his considerations are based, is, however, in error. A less arbitrary evaluation of the free energy (by methods similar to those used by the author[2] in a collective electron treatment of antiferromagnetism) leads to a substantially different and much simpler condition for the occurrence of a transition.

For simplicity and definiteness the case of a body-centered lattice containing $8N$ atoms having spin $S_0=\frac{1}{2}$ will be considered. In the usual way, the lattice is subdivided into four sublattices A_1, A_2, B_1, B_2, such that a given atom has neither nearest or next-nearest neighbors on its own sublattice and only one kind of neighbors on any other sublattice. The nearest-neighbor interaction will be taken as ferromagnetic and the next-nearest-neighbor interaction as antiferromagnetic (Smart,[1] mode IV). The zero-order interaction energy (J), apart from terms independent of the ordering which will have no effect on the results to be obtained, may be written as

$$J=N\{k\varphi'[\zeta_{A1}\cdot\zeta_{A2}+\zeta_{B1}\cdot\zeta_{B2}]-\frac{k\theta'}{2}[\zeta_{A1}+\zeta_{A2}]\cdot[\zeta_{B1}+\zeta_{B2}]\}, \quad (1)$$

where the ζ's are the relative magnetizations of the various sublattices and θ' and φ' are (positive) parameters specifying the

nearest- and next-nearest-neighbor interactions, respectively. The partition function in zero applied field is consequently

$$Z=\Sigma\left\{\frac{8N!}{N_{A1}{}^{+}!N_{A1}{}^{-}!N_{A2}{}^{+}!N_{A2}{}^{-}!N_{B1}{}^{+}!N_{B1}{}^{-}!N_{B2}{}^{+}!N_{B2}{}^{-}!}\right\}\times\exp\left\{-\frac{J}{kT}\right\}, \quad (2)$$

where the + and − refer to the two directions of spin and the sum is to be taken over all arrangements consistent with the condition $N_{A1}{}^{+}+N_{A1}{}^{-}=2N$, $N_{A2}{}^{+}+N_{A2}{}^{-}=2N$, etc. By writing $N_{A1}{}^{+}=N(1+\zeta_{A1})$, $N_{A1}{}^{-}=N(1-\zeta_{A1})$, $N_{A2}{}^{+}=N(1+\zeta_{A2})$, etc., the sum in (2) may be converted into a sum over ζ_{A1}, ζ_{A2}, ζ_{B1}, ζ_{B2}; then, by using Stirling's approximation, the free energy may be obtained as

$$F=-kT\left[N\{\tfrac{1}{4}\beta[\zeta_{A1}+\zeta_{A2}]\cdot[\zeta_{B1}+\zeta_{B2}]-\alpha[\zeta_{A1}\cdot\zeta_{A2}+\zeta_{B1}\cdot\zeta_{B2}]\}+8N\ln 8-\sum_{i=A1}^{B2}\{N\ln(1-\zeta_i{}^2)+2N\zeta_i\tanh^{-1}\zeta_i\}\right], \quad (3)$$

where it is convenient to use reduced parameters $\beta=k\theta'/kT$, $\alpha=k\varphi'/kT$.

The equations determining the equilibrium magnetization may be obtained by minimizing the free energy with respect to ζ_{A1}, ζ_{A2}, ζ_{B1}, ζ_{B2}, and four independent angle variables. By performing the differentiations, it may readily be shown that solutions of the equations determining the equilibrium magnetizations which are of interest here, may be coupled together and written as

$$\zeta_{A1}=\zeta_{A2}=\zeta_{B1}=\zeta_{B2}=\zeta=\tanh[\rho\zeta], \quad (4)$$

where either $\rho=\frac{1}{2}(\beta-\alpha)$ or $\rho=\frac{1}{2}\alpha$ according to whether the solution (4) corresponds to ferromagnetic ordering or to antiferromagnetic ordering of the second kind. Equations (4) are the usual equations of the equivalent field treatment and lead to the result that the ordering will be ferromagnetic or antiferromagnetic of the second kind according as $\beta\gtrless 2\alpha$. By substituting from (4) in (3), the equation for the free energy may now be written as

$$\frac{F}{8Nk}=-T\ln 8+\frac{\rho T}{2}\left[\frac{\zeta\ln(1-\zeta^2)}{\tanh^{-1}\zeta}+\zeta^2\right]. \quad (5)$$

For temperature-independent interaction parameters, $\rho T=T_c$ and (5) reduces to the corresponding expression (17) of Smart's paper. Consider now, however, the case when the interaction parameter ρT is supposed temperature-dependent. By taking (with Smart) the temperature dependence as arising from thermal expansion of the lattice, then, so long as the thermal expansion is supposed independent of the state of magnetization (a necessary assumption in any simple treatment), Eqs. (4) and (5) for the magnetization and free energy are still valid. If the temperature dependence of ρ' is of the simple form

$$\rho'=\rho_0'(1+aT)=(1+b\tau)/\tau, \quad (6)$$

where $\tau=1/\rho_0=T/T_c{}^{\circ}$ and $b=aT_c{}^{\circ}$, $T_c{}^{\circ}$ being the Curie temperature for $a=0$, then from (4) and (6),

$$T=T_c{}^{\circ}\zeta[\tanh^{-1}\zeta-b\zeta]^{-1}. \quad (7)$$

From (4), (5), (6), and (7), we then obtain

$$\frac{F}{8Nk}=-T\ln 8+\frac{T_c{}^{\circ}}{2}\left[\frac{\zeta^2\tanh^{-1}\zeta+\zeta\ln(1-\zeta^2)}{\tanh^{-1}\zeta-b\zeta}\right]. \quad (8)$$

This last expression differs from that given by Smart by the term $\lambda\int\zeta^4 d\zeta$ which plays an important part in Smart's condition for the occurrence of a transition.

In the limit of low temperatures $T\to 0$, $\zeta\to 1$ and, from (8), $F/8Nk\to -T_c{}^{\circ}/2$. With decrease of temperature there will therefore be a transition from an ordered state 1 to an ordered state 2 if and only if

$$T_{c1}>T_{c2} \quad [\text{i.e., } F_1(T_{c1})<F_2(T_{c1})]$$
and
$$T_{c1}{}^{\circ}<T_{c2}{}^{\circ} \quad [\text{i.e., } F_1(0)>F_2(0)]. \quad (9)$$

But from (6), $T_c{}^{\circ}=T_c(1-b)=T_c/(1+aT_c)$, and the necessary and sufficient condition for a transition may be written as

$$1<T_{c1}/T_{c2}<(1+a_1T_{c1})/(1+a_2T_{c2}). \quad (10)$$

Thus, if it is supposed that the value of θ/T_c is known (θ the asymptotic Curie temperature) from the high-temperature susceptibility, then an approximate value of T_{c1}/T_{c2} may be obtained from the known θ/T_c, α/β relation (see Smart, Fig. 2), and (10) will give the order of magnitude of a required to produce a transition. For example, for MnAs, $\theta/T_c=0.75$ and consequently the required value of a is of order $10^{-3}/°\text{K}$, higher than that quoted by Smart, but still in fair agreement with estimates made by Néel[3] based on other considerations.

[1] J. S. Smart, Revs. Modern Phys. **25**, 327 (1953).
[2] E. W. Elcock, Proc. Phys. Soc. (London) (to be published).
[3] L. Néel, Ann. Physik **5**, 337 (1937).

Pauli Principle Scattering and the Resistivity Minimum

J. S. KOEHLER
Department of Physics, University of Illinois, Urbana, Illinois
(Received March 29, 1954)

BLEWITT, Coltman, and Redman[1] have recently performed beautiful experiments which demonstrate that the resistivity minimum found in copper is a grain boundary effect. In these experiments 99.999 percent pure annealed copper single crystals showed no minimum in the range from 1.6°K to 4.2°K. The crystals were then extended by tensile plastic deformation at room temperature, the tensile strain being about 50 percent. No minimum was found after the plastic extension. The crystals were then recrystallized by vacuum annealing at 1000°C. All crystals examined showed a minimum after recrystallization. The very small residual resistivity of these crystals before deformation indicates that the effect does not depend on impurities.

Grain boundaries can give rise to a scattering which becomes more effective as the temperature is lowered. Qualitatively this effect can arise as follows: Suppose that the Fermi surface in the metal under consideration is not a sphere in **k** space (see Fig. 1). Consider an electron having a short **k** vector at the Fermi surface, such as $\mathbf{k}_1$ in the figure. If such an electron crosses a grain boundary and finds that it is traveling along direction 2 in the new grain it will be reflected, since if the electron retains its momentum its energy must be smaller when traveling along 2. But if the energy of the electron along 2 is smaller, then at low temperatures the state appropriate for this electron in motion along 2 is filled, and hence reflection occurs. If, conversely, one assumes that energy

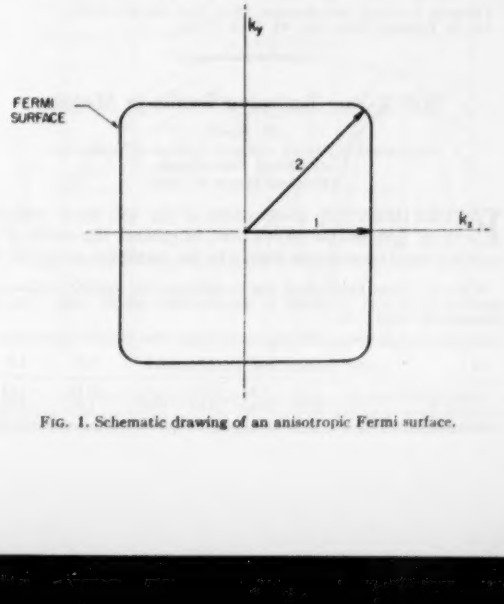

FIG. 1. Schematic drawing of an anisotropic Fermi surface.

is conserved on entering the new grain, then, since the momenta differ, scattering occurs.

Let us consider the influence of temperature. Suppose that the reflection probability is proportional to the fraction of states which are filled for an electron traveling in the 2 direction with an energy such that momentum is conserved [i.e., $E_2=(m_1/m_2)E_1$, where m_1 and m_2 are the effective masses associated with the 1 and 2 directions, respectively, and $m_2>m_1$]. If we suppose that the Fermi surface is cylindrically symmetrical around the 1 direction, then the total probability of the electrons being scattered from 1 to any other state is

$$2\int_0^{\pi/2}\frac{2\pi\sin\theta d\theta}{\exp\left\{\left(\frac{m_1}{m_2}-1\right)\frac{E_1}{kT}\right\}+1} \tag{1}$$

where θ is the angle through which the crystallographic axes in grain 2 are rotated relative to those in grain 1. The assumption has been made that all values of θ are equally likely. The ratio m_1/m_2 of course depends upon θ, i.e., upon the detailed shape of the surfaces of equal energy in $\mathbf{k}$ space. Suppose that

$$(m_1/m_2)E_1=(1-\alpha\sin\theta)E_1. \tag{2}$$

In this case the equi-energy surfaces resemble an oblate spheroid. Upon substitution and integration of Eq. (1) one obtains

$$2\frac{kT}{\alpha E_1}\log(1+e^{-\alpha E_1/kT})+1-\frac{kT}{\alpha E_1}\log 2\cong 1-\frac{kT}{\alpha E_1}\log 2. \tag{3}$$

We shall assume that the resistance introduced is proportional to the total probability of scattering of the electron most likely to be scattered. Thus the grain boundary resistance for the special case considered is given by Eq. (3) and *decreases* as the temperature increases. The particular dependence is in qualitative agreement with the observations of Yntema[3] for copper. It should be noted that the exact shape of the resistance *versus* temperature curve will depend not only on the shape of the Fermi surface, but also on the distribution of orientation changes at grain boundaries.

If the resistivity at absolute zero is determined by a mean free path which is of the order of the grain size, then

$$\rho=2mv/ne^2l, \tag{4}$$

where l is the mean free path, n is the number of electrons per unit volume, and v is the velocity of the electrons at the top of the Fermi distribution. Blewitt states that his grain size is of the order of a millimeter after recrystallization. Inserting values appropriate for copper into (4), one obtains $\rho=1.4\times10^{-10}$ ohm cm which compares reasonably well with results obtained by extrapolating Blewitt's data linearly to absolute zero (i.e., $\rho_{obs}=4.0\times10^{-10}$, 2.7×10^{-10}, and 2.3×10^{-10} ohm cm).

The author would like to thank T. H. Blewitt for stimulating discussions which led to the idea during a visit to Oak Ridge.

[1] Blewitt, Coltman, and Redman, Phys. Rev. **93**, 891 (1954).
[2] G. B. Yntema, Phys. Rev. **91**, 1388 (1953).

Soft X-Ray Emission Bands in Metals

H. JONES
Department of Physics, Carnegie Institute of Technology, Pittsburgh, Pennsylvania
(Received March 26, 1954)

EXPERIMENTAL observations of the soft x-ray emission from light metals[1] shows that, in general, the width of an emission band corresponds closely to the maximum energy of the Fermi distribution of the conduction electrons as calculated by the Sommerfeld free electron formula. According to Koopman's theorem, however, the width of an emission band should be given by the difference between the eigenvalues of the Fock equation for the lowest and the highest occupied states of the conduction band. These eigenvalues contain a term arising from exchange effects and are given by

$$\epsilon_k=\frac{\hbar^2k_0^2}{2m}\alpha^2-\frac{e^2k_0^2}{\pi}y(\alpha),$$

where

$$y(\alpha)=1+\frac{1}{4}\left(\frac{1}{\alpha}-\alpha\right)\log\left(\frac{1+\alpha}{1-\alpha}\right)^2,$$

$\alpha=k/k_0$ and $\hbar k_0$ is the radius of the occupied sphere in momentum space. Hence the width of an emission band is equal to $\zeta_0+e^2k_0/\pi$, when ζ_0 is the Fermi width for free electrons. The additional term due to exchange amounts to 5.1, 4.1, and 8.0 electron volts for Li, Na, and Al, respectively, and thus completely destroys the good general agreement with the value of ζ_0. This effect shows very directly the need for some modification of the Hartree-Fock theory as applied to the conduction electrons of metals. According to the theory of Bohm and Pines[2] the exchange effects should be calculated, not with the Coulomb, but with a screened potential. When this is done the additional term in the band width due to exchange is $(e^2k_0/\pi)(1-\beta-\beta^2/4)$, where $\beta=(\alpha n'/n)^{\frac{1}{2}}$; n is the number of electrons per unit volume and n' is the number of plasma waves per unit volume.

TABLE I. Excess band width due to exchange, for metallic sodium as a function of β, and the ratio of the electronic specific heat C_v to the Sommerfeld value $C_v^{(0)}$.

β	0.5	0.6	0.7	0.8	0.9	1.0
Excess width in ev	1.83	1.30	0.74	0.17	−0.43	−1.04
$C_v/C_v^{(0)}$	0.77	0.83	0.90	0.95	1.0	1.05

Table I shows the excess band width, due to exchange, for metallic sodium as a function of β. The last line shows the ratio of the electronic specific heat C_v to the Sommerfeld value $C_v^{(0)}$ which neglects exchange altogether. An expression for this ratio is given by Pines[3] [Eq. (38)]. The observed band width for Na is rather less than the free electron ζ_0, and the observed electronic specific heat is greater than $C_v^{(0)}$. However it is perhaps open to doubt whether the theory of Bohm and Pines is strictly applicable when β is as large as 0.9 or 1.0.

It may be of some significance that the observed band width for metallic Al is nearly equal to the free electron ζ_0, thus implying that here also a screened potential is operative for the whole conduction band of three electrons per atom, and hence that plasma oscillations occur even in a conduction band where the electrons move in a strong periodic potential.

Finally it may be noticed that if one uses a purely empirical screened potential of the form $e^{-\lambda r}/r$, the excess band width is given by

$$\frac{e^2k_0}{\pi}\left\{1-\frac{\gamma^2}{4}\log\left(1+\frac{4}{\gamma^2}\right)+\gamma\tan^{-1}\frac{2}{\gamma(\gamma^2+3)}\right\},$$

where $\gamma=\lambda/k_0$. In this case the excess band width decreases monotonically to zero as γ increases and could not, therefore, lead to a band width less than ζ_0.

[1] H. W. B. Skinner, Trans. Roy. Soc. (London) **239**, 95 (1940).
[2] D. Bohm and D. Pines, Phys. Rev. **92**, 609 (1953).
[3] D. Pines, Phys. Rev. **92**, 626 (1953).

Interpretation of Ionic Mobilities in Nitrogen

S. GELTMAN
Westinghouse Research Laboratories, East Pittsburgh, Pennsylvania
(Received February 19, 1954)

JOHNSON[1] has interpreted the measured[2] ionic mobilities in nitrogen as being primarily determined by the quadrupole interaction between ion and gas molecule. The purpose of this note is to point out that the agreement between Johnson's roughly calculated mobility and the experimental value is fortuitous, the main defects in Johnson's calculation being the neglect of the polarization interaction and the overestimate of the quadrupole interaction. The interaction between the ion and induced dipole of the molecule (polarization interaction) is $V_p=-\frac{1}{2}e^2\alpha r^{-4}$,

where α is the molecular polarizability. The quadrupole energy is $V_q=-\frac{1}{2}eQ_{\text{mole}}r^{-3}(1-3\cos^2\theta)$, where Q_{mole} is the quadrupole moment of the molecule relative to the molecular axis and θ is the angle between the molecular axis and the line joining the center of the molecule with the ion. When the measured[3,4] values of α and Q_{mole} for N_2 are inserted into the above expressions, it is seen that $|V_p|>|V_q|$ for the whole range of separations at which $|V_p|$ is of the order of kT. For pure polarization scattering the momentum transfer cross section averaged over all thermal energies is approximately equal to the cross section at the kinetic energy $(64/9\pi)kT$. Comparing the two interactions at the separation $r=3.8$A, $|V_p|=(64/9\pi)kT=0.059$ ev ($T=300°$K) while $|V_q(\theta=\pi/2)|=0.018$ ev and $|V_q(\theta=0)|=0.035$ ev.

An exact calculation of the momentum transfer cross section resulting from the interaction V_p+V_q is intractable because the potential is not spherically symmetric and translational kinetic energy is not conserved. However, in the case of a pure polarization interaction the Langevin formula[5] gives the mobility of ions (single positive charge, atomic mass M) in nitrogen as $2.11(1+28/M)^{\frac{1}{2}}$ cm²/volt sec. The inclusion in the Langevin potential model of a repulsive force at small separations would cause an increase in this calculated mobility by at most 15 percent, depending on the effective radius of the repulsion. This agrees reasonably well with the empirical result[3] of 2.04 $(1+28/M)^{\frac{1}{2}}$ cm²/volt sec and indicates that the quadrupole interaction is not of primary importance in determining the ionic mobility at room temperature.

[1] M. H. Johnson, Phys. Rev. **80**, 101 (1950).
[2] C. F. Powell and L. Brata, Proc. Roy. Soc. (London) **A138**, 117 (1932); J. H. Mitchell and K. E. W. Ridler, Proc. Roy. Soc. (London) **A146**, 911 (1934).
[3] From value of dielectric constant or index of refraction, *Handbook of Chemistry and Physics* (Chemical Rubber Publishing Company, Cleveland, 1952–1953), pp. 2161, 2499.
[4] W. V. Smith and R. R. Howard, Phys. Rev. **79**, 132 (1950).
[5] P. Langevin, Ann. Chem. Phys. Series 8, **5**, 245 (1905); H. R. Hasse, Phil. Mag. **1**, 139 (1926). For other applications of Langevin formula see A. M. Tyndall, *The Mobility of Positive Ions in Gases* (Cambridge University Press, Cambridge, 1938), p. 49.

Electrical Conduction in Halide-Contaminated Ice

E. J. Workman, Frank K. Truby, and W. Drost-Hansen
New Mexico Institute of Mining and Technology, Socorro, New Mexico
(Received March 19, 1954)

THE anomalous electrical properties of halide-contaminated ice have been the subject of several papers by the authors.[1-4] Such ice, frozen according to the methods prescribed, exhibits unusual features: (1) it acts as a rectifier; (2) it possesses an extremely high dielectric constant for fields applied in the nonconductivity direction; and (3) the conductive and dielectric properties depend in a complicated way upon temperature, bias, and frequency. The general behavior with respect to the properties enumerated is such as to suggest electronic conduction. This interpretation was given further support by the fact that the passage of an electric current for long time intervals produced no marked change in the conductive behavior of the crystal. It appeared reasonable, therefore, to formulate an explanation based on the premise that the partially shielded proton is displaced under the stress of an applied electric field in such a manner as to increase considerably the ionic contribution to the hydrogen bonding between neighboring molecules. In spite of the relative ease of proton displacement considered essential, the proton appeared to be bound because of the high-energy barrier postulated for proton transfer (26 kcal/mole or even more[5]). Moreover, there is persistence of a sense of direction to the c axis under all conditions of applied field—a condition considered incompatible with the process of molecular rotation inherent in the transfer mechanism.

An experimental re-examination of the conduction process has revealed that the conduction of electricity in the forward direction through the contaminated ice results in the liberation of oxygen and hydrogen at the positive and negative electrodes respectively. The amount of gas liberated is in quantitative agreement with that associated with the total charge transfer. Contrary to our earlier interpretations it now appears certain that the conduction process is ionic—by a proton transfer mechanism.

[1] Frank K. Truby, Phys. Rev. **92**, 543 (1953).
[2] E. J. Workman, Phys. Rev. **92**, 544 (1953).
[3] E. J. Workman and W. Drost-Hansen, Phys. Rev. **94**, 770 (1954).
[4] W. Drost-Hansen and E. J. Workman, Phys. Rev. **94**, 770 (1954).
[5] Edwin S. Campbell, J. Chem. Phys. **20**, 1411 (1952).

Polarization of Nucleons Elastically Scattered from Nuclei*

G. A. Snow, R. M. Sternheimer, and C. N. Yang†
Brookhaven National Laboratory, Upton, New York
(Received March 30, 1954)

SEVERAL recent experiments[1-3] have shown that protons of energy 200–350 Mev scattered from nuclei are polarized. The elastically scattered protons have a polarization (~60 percent) that is somewhat larger than the inelastically scattered ones. Fermi[4] has proposed an explanation of the polarization for *elastic* scattering in terms of a nuclear spin-orbit interaction potential similar to that assumed in the nuclear shell model. He used the Born approximation in his estimates. The purpose of this note is to investigate the polarization effects of a nuclear spin-orbit potential using the transparent nuclear model of Serber.[5] That is, we add to the nuclear complex potential which is constant over a sphere of radius R, a term

$$-\hbar^{-1}U(r)\mathbf{L}\cdot\boldsymbol{\sigma}, \tag{1}$$

where $\mathbf{L}$ and $\hbar\boldsymbol{\sigma}/2$ are the orbital and spin angular momenta of the proton. U is taken to be real since the absorption cross section of protons in nuclear matter is independent of its spin. The radial and energy dependence of U are unknown, as well as its variation with atomic number. We have assumed two specific forms for U:

$$U_1(r)=u_1R\delta(r-R), \quad U_2(r)\cong u_2(R/r)^2. \tag{2}$$

$U_1(r)$ is the one considered by Fermi and is suggested by the Thomas precession of a particle with spin under acceleration, which, in the transparent nuclear model, is concentrated at the boundary of the potential hole. By contrast, $U_2(r)$ is concentrated near the origin. [The exact form of U_2, which was chosen for convenience in numerical computation, is implied in Eq. (8).]

The calculations are performed by a partial-wave analysis. The degree of polarization (as defined by Oxley *et al.*[1]) is

$$P(\theta)=(|f-ig|^2-|f+ig|^2)/(|f-ig|^2+|f+ig|^2), \tag{3}$$

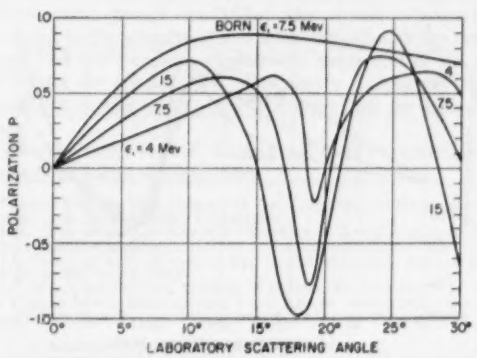

FIG. 1. Polarization P as a function of scattering angle θ for various ϵ_1 calculated from potential U_1 [Eq. (7)] for 316-Mev protons scattered by Be. The top curve gives the Born approximation values for $\epsilon_1=7.5$ Mev.

where

$$f(\theta)=\sum_{l=0}^{L}[(l+1)A_l^{+}+lA_l^{-}]P_l^0(\cos\theta), \tag{4}$$

$$g(\theta)=-\sum_{l=0}^{L}[A_l^{+}-A_l^{-}]P_l^1(\cos\theta), \tag{5}$$

with

$$A_l^{\pm}=[\exp(2i\delta_l^{\pm})-1]/2i. \tag{6}$$

$\delta_l^{\pm}$ are the phase shifts for the partial waves with $J=l\pm\frac{1}{2}$, P_l^m = associated Legendre polynomial, and L = largest integer $<kR$. Using the WKB approximation to evaluate $\delta_l^{\pm}$, we obtain

$$(\delta_l^{\pm})_1=[(iK/2)+k_1][R^2-(l+\tfrac{1}{2})^2/k^2]^{\frac{1}{2}} \pm\tfrac{1}{2}\epsilon_1 lT^{-1}[1-(l+\tfrac{1}{2})^2/(L+\tfrac{1}{2})^2]^{-\frac{1}{2}}, \tag{7}$$

and

$$(\delta_l^{\pm})_2=[(iK/2)+k_1\pm(k\epsilon_2/2T)][R^2-(l+\tfrac{1}{2})^2/k^2]^{\frac{1}{2}}, \tag{8}$$

for the two forms of spin-orbit interaction respectively. Here T = kinetic energy, k_1 and K are the usual optical parameters. $\epsilon_{1,2}$ are energies that characterize the depth of the spin-orbit coupling. $\epsilon_1=Lu_1$ and $\epsilon_2=Lu_2$. The two potential differ in that U_1 emphasizes the high, U_2 the low angular momenta phase shifts.

For definiteness, we have calculated P, using Eqs. (3)–(8), for 316-Mev nucleons scattered by Be. This energy corresponds to the experiments of Marshall *et al.*[2] We take the optical parameters from a recent paper by Taylor,[6] i.e., $R=3.2\times10^{-13}$ cm, $k_1=0.86\times10^{13}$ cm^{-1}, and $K=1.7\times10^{12}$ cm^{-1}, corresponding to a complex nuclear potential $V=(-13+25.6i)$ Mev, and $L=13$. Figure 1 shows $P(\theta)$ for the spin-orbit potential $U_1(r)$ with $\epsilon_1=4$, 7.5, and 15 Mev. For comparison, the top curve in this figure shows the Born approximation result with $\epsilon_1=7.5$ Mev and the same nuclear parameters. Figure 2 shows $P(\theta)$ for $U_2(r)$ with $\epsilon_2=4$, 7.5, and 15 Mev and Fig. 3 shows the differential cross section averaged over spin directions,

$$\langle d\sigma/d\Omega\rangle=\tfrac{1}{2}k^{-2}[|f-ig|^2+|f+ig|^2], \tag{9}$$

for $\epsilon_2=0$–15 Mev.

It is clear from the curves that one can fit the result of Marshall *et al.*[2] that $P(14°)\cong0.6$ with $\epsilon_1=7.5$ Mev (i.e., $u_1=0.58$ Mev) or $\epsilon_2=12$ Mev (i.e., $u_2=0.92$ Mev). These represent spin-orbit interactions that agree roughly in order of magnitude with that in the shell model theory provided one assumes a linear dependence of the spin-orbit interaction with the momentum of the nucleon.

The curves show that for small θ, P is proportional to ϵ. For a given ϵ, P is larger for interaction U_1 than U_2. This results from the fact already mentioned that U_1 emphasizes the larger and more heavily weighted l values more than U_2.

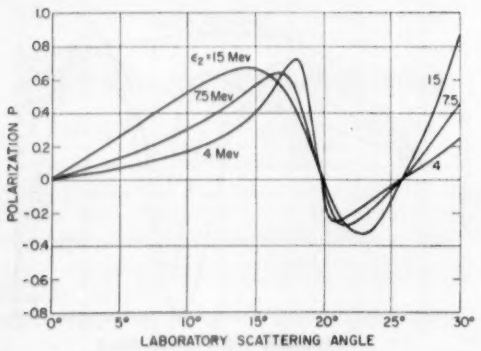

FIG. 2. Polarization P as a function of scattering angle θ for various ϵ_2 calculated from potential U_2 [Eq. (8)] for 316-Mev protons scattered by Be.

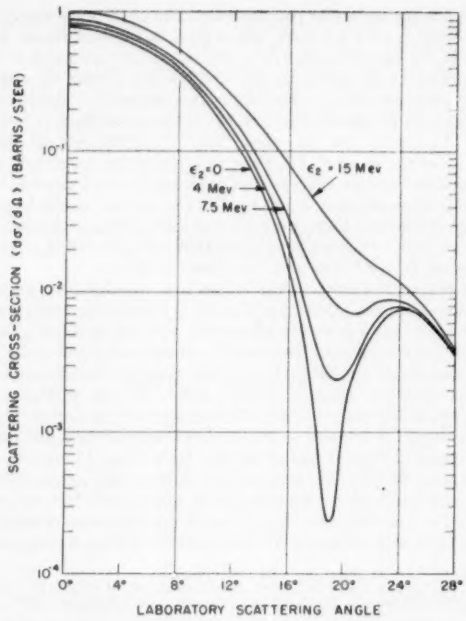

FIG. 3. Differential scattering cross section $\langle d\sigma/d\Omega\rangle$ averaged over spin directions for 316-Mev protons scattered by Be. The curves were calculated from potential U_2 for various ϵ_2.

Perhaps the most interesting result of these calculations is the oscillatory nature of $P(\theta)$. $P(\theta)$ first becomes negative in the region of the first diffraction minimum ($\sim20°$) due to a change of sign of $f(\theta)$. It becomes positive again when $g(\theta)$ also changes sign. The fact that the Born approximation applied to U_1 does not show this, is fortuitously due to f and g having identical angular dependences. The search for negative $P(\theta)$ may be hampered of course by the low intensity of the diffracted beam beyond the first minimum.

Finally it is interesting to note in Fig. 3 how the spin-orbit potential has the effect of washing out the deep minima in $\langle d\sigma(\theta)/d\Omega\rangle$. There are some experimental indications of such an effect.[7] It is also seen that the total diffraction cross section σ_d increases with ϵ. The values of σ_d as obtained from integration of $\langle d\sigma(\theta)/d\Omega\rangle$ are 61, 67, 75, and 105 mb for $\epsilon_2=0$, 4, 7.5, and 15 Mev, respectively.

Perhaps detailed investigations of $P(\theta)$ for various elements and at lower energies will be able to determine the radial and velocity dependence of $U(r)$, although it must be borne in mind that $P(\theta)$ is a sensitive function of all the optical parameters R, k_1, and K as well as $U(r)$. One can also conjecture that the polarization of elastically scattered nucleons will still be present in the Bev range. For example, a calculation was carried out for 1.4-Bev neutrons on Be with $\epsilon_2=15$ Mev, and one obtains $P(\theta=5°)=0.46$ and $P(\theta=7°)=0.81$.

We wish to thank Professor Fermi and Professor Marshall for sending us copies of their papers in advance of publication.

* Work performed under the auspices of the U. S. Atomic Energy Commission.

† On leave of absence from the Institute for Advanced Study, Princeton, New Jersey.

[1] Oxley, Cartwright, and Rouvina, Phys. Rev. **93**, 806 (1954).
[2] Marshall, Marshall, and de Carvalho, Phys. Rev. **93**, 1431 (1954).
[3] Chamberlain, Segrè, Tripp, Wiegand, and Ypsilantis, Phys. Rev. **93**, 1430 (1954).
[4] E. Fermi, Nuovo cimento **11**, 407 (1954).
[5] Fernbach, Serber, and Taylor, Phys. Rev. **75**, 1352 (1949).
[6] T. B. Taylor, Phys. Rev. **92**, 831 (1953).
[7] Richardson, Ball, Leith, and Moyer, Phys. Rev. **83**, 859 (1951).

Low Excited States of F^{19}. I. Proton Inelastic Scattering*

R. W. PETERSON, C. A. BARNES,† W. A. FOWLER, AND C. C. LAURITSEN
Kellogg Radiation Laboratory, California Institute of Technology, Pasadena, California
(Received March 18, 1954)

THE spins, parities, and other properties of the low states of F^{19} are of considerable interest in connection with the shell model and collective aspects[1] of nuclear structure. Of particular interest in this connection are the first and second excited states of F^{19} discovered in this laboratory by Mileikowsky and Whaling.[2] In this and the following notes,[3] studies of the excitation of these states in the inelastic scattering of protons and alpha particles by F^{19} are reported. This note is primarily concerned with the inelastic proton groups and the de-excitation gamma radiation accompanying the inelastic scattering.

In Fig. 1 are shown the magnetically analyzed proton groups observed at 1.431 Mev and at an angle of observation of 159° in the bombardment of a thin layer of AlF_3 on an evaporated Li surface. From this and similar curves the excitation energies of the first two excited states of F^{19} were found to be 113.9±0.8 kev and 199.6±0.7 kev. The corresponding values determined from scintillation counter pulse-height studies of the gamma radiation from these states were 114±1.5 kev and 198±1.5 kev.

To assign spin and parity to the compound states of Ne^{20} involved, preliminary observations have been made on the angular distributions of the protons scattered elastically by fluorine. The following tentative spin and parity assignments for resonances in $F^{19}+p$ are made: 1355 kev, 2^-; 1381 kev,[4] 2^-; 1431 kev,[5] 1^+. In addition we have confirmed[6] the following assignments: 669 kev, 1^+; 872 kev, 2^-; 935 kev, 1^+.

The inelastically scattered protons resulting from the excitation of the first excited state are isotropically distributed at the 1431-kev resonance. The elastically scattered proton groups from thin contamination layers of carbon and oxygen indicated in Fig. 1 become stronger at lower bombarding energies and smaller scattering angles. Overlapping by these groups has made it impossible, to date, to determine angular distributions at lower resonances for the first inelastic group from F^{19}. The second group is found to be isotropic at the 873-kev resonance and the 1355-kev resonance and to follow the expression $(1-0.45\cos^2\theta)$ at the 1381-kev resonance. The probable error in the measurement of the angular distribution coefficients is of the order of 10 percent.

The excitation curves of the first two excited states of F^{19} were observed by detecting the de-excitation gamma radiation in a NaI(Tl) scintillation counter and are shown in Fig. 2 as a function of incident proton energy from 650 to 1500 kev. Many of the resonances in the well-known $F^{19}+p$ reactions appear also as resonances for formation of either or both of these excited states of fluorine. The s-wave (1^+) resonances in Ne^{20} at 669-, 935-, and 1431-kev proton energy lead almost exclusively to the 114-kev states, while the p-wave (2^-) resonance at 873 kev leads almost entirely to the 200-kev state. The p-wave (2^-) resonances at 1355 and 1381 kev and the narrow resonance at 1092 kev lead in comparable quantities to the two states. Between 330 and 650 kev the yield of 114- and 200-kev gamma radiation is very small and has been omitted from Fig. 2.

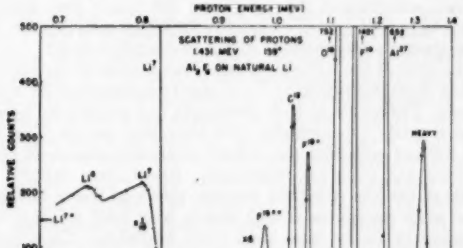

FIG. 1. Proton groups scattered at 1.431-Mev bombarding energy at a laboratory angle of 159° by a thin target of AlF_3 deposited on a backing layer of natural Li. Note two inelastically scattered groups from F^{19} and elastically scattered groups from contaminations of C, O, Na, and heavy elements.

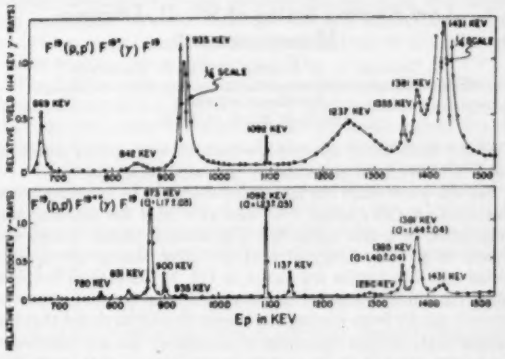

FIG. 2. Excitation of the 114- and 200-kev states of F^{19} by inelastic scattering of protons. The a appearing on the lower curve is (yield at 0°)/(yield at 90°). The cross section for the 114-kev radiation at 1431 kev is $\sim 1.3\times10^{-25}$ cm², and for the 200-kev radiation is $\sim 0.8\times10^{-25}$ cm² at 1381 kev.

The angular distribution of the 114-kev radiation is isotropic within the experimental error (½ percent to 4 percent) at all resonances investigated, and within 10 percent in the weak nonresonant yield between resonances at 750 and 1050 kev. The consistent isotropy suggests an assignment of $J=\frac{1}{2}$ for the 114-kev state. In Letter III by R. Sherr *et al.*[3] it is shown that the parity of this state is odd. The ratio of intensities of the 200-kev radiation at 0° and 90° with respect to the incident proton beam varies between 1.17 at 873 kev and 1.44 at 1381 kev. There is no evidence from 45° and 135° readings of an appreciable deviation from a $(1+A\cos^2\theta)$ distribution. The ratios obtained are consistent with an assignment of $J=5/2$, even parity for the 200-kev state, and $E2$ assignment to the gamma ray. The ratio at 873 kev suggests some attenuation (coefficient of $\cos^2\theta$ reduced to $\sim 2/3$) of the anisotropy by nuclear precession in atomic electric or magnetic fields during the comparatively long lifetime of the state.

Finally, we have observed that the cascade de-excitation of the 200-kev state, through the 114-kev state, occurs with less than 1 percent of the intensity of the direct transition to the ground state. This would seem to eliminate the assignment of 3/2, 5/2, or 7/2 for the 114-kev state, since electric or magnetic dipole transitions to such states would be allowed from the upper $5/2^+$ state.

We are grateful to R. F. Christy and R. P. Feynman for numerous discussions of the problem.

* Assisted by the joint program of the U. S. Office of Naval Research and the U. S. Atomic Energy Commission.
† On leave of absence from the University of British Columbia, Vancouver, British Columbia.
[1] A. Bohr and B. R. Mottelson, Kgl. Danske Videnskab. Selskab. Mat.-fys. Medd. **27**, No. 16 (1953).
[2] C. Mileikowsky and W. Whaling, Phys. Rev. **88**, 1254 (1952).
[3] Thirion, Barnes, and Lauritsen, Phys. Rev. **94**, 1076 (1954); Sherr, Li, and Christy, Phys. Rev. **94**, 1076 (1954); R. F. Christy, Phys. Rev. **94**, 1077 (1954).
[4] J. E. Sanders, Phil. Mag. **44**, 1302 (1953).
[5] We assume that this is the resonance for proton capture radiation reported by R. M. Sinclair at The Rice Institute.
[6] J. Seed and A. P. French, Phys. Rev. **88**, 1007 (1952); C. Y. Chao, Phys. Rev. **80**, 1035 (1950).

Low Excited States of F^{19}. II. Lifetime Measurements*

J. THIRION, C. A. BARNES, AND C. C. LAURITSEN
Kellogg Radiation Laboratory, California Institute of Technology, Pasadena, California
(Received March 18, 1954)

THE lifetimes of the 114-kev and 200-kev excited states[1] of F^{19} have been measured by the recoil technique.[2]

For the lower state the apparatus described in reference 2 was employed. A CaF_2 target (~3 kev at 1 Mev for protons) was evaporated on a thin nickel foil. The incident proton energy was chosen to give an energy of 1431 kev after passing through the nickel foil. The results are shown in Fig. 1. Curve *A* is obtained when an additional nickel foil is placed over the CaF_2 layer to prevent recoils from leaving the target. It will be noted that the gamma-ray counting rate drops off completely for a movement of the target, relative to the gamma-ray collimator, of 0.1 mm. The experimental points on curve *B* are obtained when the recoils are free to leave the target. Because of the thinness of the CaF_2 layer employed, at least 75 percent of the recoils leave the target. The theoretical curves *B*, *C*, *D*, were computed, taking account of the isotropic distribution[1] of the inelastically scattered protons in the center-of-mass system, and the slowing down of the recoils in leaving the CaF_2 layer. (The layer is about 1/7 of the maximum range of the F^{19} recoils.) We conclude that the mean lifetime is $(1.0\pm0.25)\times10^{-9}$ sec. This value is in good agreement with that derived from the absolute cross section for excitation of this level of F^{19} by inelastic scattering of alpha particles, if the latter process is assumed to be electric dipole Coulomb excitation.[3] The transition probability is of the order of 100 times smaller than predicted by the single-particle formula.[4]

In the case of the 200-kev state, the F^{19} recoils (at the 1092-kev resonance) were collimated in a forward cone of half-angle 30°. The recoils were stopped on a plate 8 cm in diameter which could be observed through a collimated channel by a NaI(Tl) scintillation counter. The target was a layer ~8 kev thick of aluminum fluoride formed by exposing the back of a 0.2-mg/cm² Al foil to HF vapor. The distance between the target and recoil stopper was varied from 2 to 12 cm. The resultant curve, Fig. 2, indicates a mean lifetime of 0.8×10^{-7} sec with an uncertainty of about a factor 2. The large uncertainty indicated is due to the low yield and the background produced by high-energy radiation. The lifetime for this state is in satisfactory agreement with that predicted by the Coulomb excitation work[3] on the basis of an electric quadrupole assignment to the gamma ray. The observed transition probability is of the order of magnitude of that predicted by the single-particle model for an electric quadrupole transition.[4]

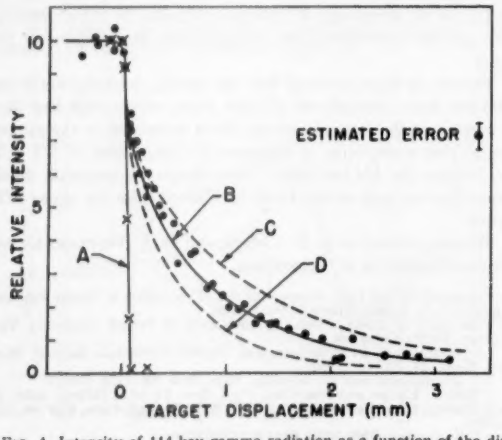

FIG. 1. Intensity of 114-kev gamma radiation as a function of the distance travelled by the fluorine recoils before radiating. Curve *A* is obtained by stopping all recoils at the target in an additional nickel foil. Curves *B*, *C*, and *D* are computed for mean lifetimes of 10^{-9} sec, 1.5×10^{-9} sec, and 0.66×10^{-9} sec, respectively.

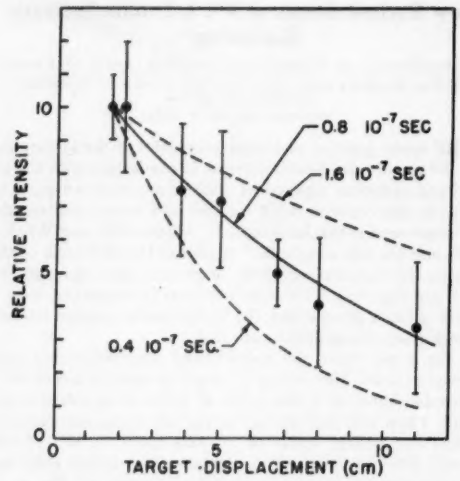

FIG. 2. Intensity of 200-kev gamma radiation as a function of the distance travelled by the fluorine recoils before radiating.

* Assisted by the joint program of the U. S. Office of Naval Research and the U. S. Atomic Energy Commission.
[1] Peterson, Barnes, Fowler, and Lauritsen, preceding Letter [Phys. Rev. **94**, 1075 (1954)].
[2] J. Thirion and V. L. Telegdi, Phys. Rev. **92**, 1253 (1953).
[3] Sherr, Li, and Christy, following Letter [Phys. Rev. **94**, 1076 (1954)].
[4] V. F. Weisskopf, Phys. Rev. **83**, 1073 (1951); S. A. Moszkowski, Phys. Rev. **89**, 474 (1952); B. Stech, Z. Naturforsch. **7a**, 401 (1952).

Low Excited States of F^{19}. III. Coulomb Excitation by α Particles*

R. SHERR,† C. W. LI,‡ AND R. F. CHRISTY
Kellogg Radiation Laboratory, California Institute of Technology, Pasadena, California
(Received March 18, 1954)

WE have investigated the yield of gamma rays resulting from the bombardment of F^{19} by α particles.[1] Up to an α-particle energy of 2.8 Mev we observed only the 1.28-Mev γ ray of the reaction $F^{19}(\alpha,p)Ne^{22*}$, and the 114-kev and 200-kev radiations from the first and second excited states of F^{19} produced by inelastic scattering of the α particles. The γ rays were detected with a $1\frac{1}{2}$ in.×$1\frac{1}{2}$ in. sodium iodide scintillation spectrometer. The pulse spectrum was recorded with a 10-channel analyzer.

The yield of the 1.28-Mev γ ray shows a series of narrow resonances (first observable at ~1.3 Mev) superimposed on a continuum. The yields of both resonances and continuum increase approximately exponentially with increasing energy. The 114- and 200-kev radiations also exhibit observable resonances above 2.0-Mev and 2.3-Mev, respectively. Below these energies the yields of the soft radiations decrease slowly as shown in Fig. 1. (The weak resonances at high energy have been omitted, their contribution to the total yield being negligible.) The absolute values of the cross sections have an estimated uncertainty of 20 percent arising chiefly from uncertainty in target thickness and stopping power. The 114-kev curve may have an additional uncertainty due to the difficulty of separating the 114-kev photopeak from the 200-kev spectrum; we may have underestimated the 114-kev yield by as much as 30 percent. On the other hand, the relative shape of each curve was reproducible to better than 10 percent for different targets and geometries.

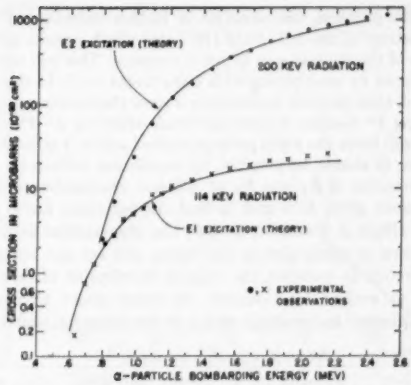

FIG. 1. Excitation of the first (114-kev) and second (200-kev) excited states of F^{19} by α particles.

The excitation curves in Fig. 1 have the general character to be expected of Coulomb excitation.[2] The curves were calculated from the theories for this process developed by Mullin and Guth,[3] Ter-Martyrosian,[4] and Alder and Winther.[5] These curves were chosen to fit the data at low energy. It is not clear whether the divergence at higher energy signifies inadequacy in the theory, or whether it is the result of an increasing contribution of compound nucleus effects. From the yield of the (α,p) reaction we infer that the cross section for formation of a compound nucleus is comparable with the excitation cross section of the 114-kev state in the neighborhood of 1.35 Mev.

The calculations for the 200-kev state assume $E2$ excitation of a $5/2^+$ state from the ground state of $F^{19}(J=1/2^+)$. To improve the calculation near the threshold, we have replaced the parameter ξ of reference 4 by

$$\xi=\frac{Z_1Z_2e}{\hbar}\left(\frac{1}{v_2}-\frac{1}{v_1}\right),$$

where v_1 and v_2 are the relative velocities of the bombarding and scattered particle. At high energy this quantity becomes identical with the expression of Alder and Winther. The absolute cross section for the excitation process is directly connected with the lifetime of the excited state. The calculated curve of Fig. 1 corresponds to a mean life $\tau=2.2\times10^{-7}$ sec, in fair agreement with the direct measurements of the lifetime by Thirion *et al.*,[6] who find $\tau\sim1\times10^{-7}$ sec. Our results support the assignment by Peterson, *et al.*[7] of $J=5/2^+$ to the second excited state of F^{19}.

The calculations for the 114-kev state assumes electric dipole excitation[8] of a $\frac{1}{2}^-$ state. The curve of Fig. 1 corresponds to a lifetime of 1.4×10^{-9} sec for electric dipole decay of this state. The agreement with the directly observed lifetime ($\tau=1.0\pm0.2\times10^{-9}$ sec)[6] is satisfactory. It should be noted, however, that in addition to the experimental uncertainties, there is an estimated uncertainty of a factor 2 in the theoretical Coulomb excitation cross sections (and consequently in the predicted lifetimes).

Measurements of the angular distributions of the 114- and 200-kev radiations were made for a thick target at a bombarding energy of 1.84 Mev. The 114-kev radiation was isotropic within 10 percent, while for the 200-kev radiation we obtained $W(0°)/W(90°)=1.22\pm0.02$. The theory for the reaction[5] predicts 1.26 for the 200-kev radiation; however, finite lifetime effects may reduce this value.[9] The isotropy of the 114-kev radiation supports the $J=\frac{1}{2}$ assignment of Peterson *et al.*[7]

The possibility that the 114-kev state is $\frac{1}{2}^+$ can be eliminated since magnetic dipole Coulomb excitation[8] would have a cross section smaller than that observed by a factor of $v^2/c^2\approx10^{-3}$ when the magnetic dipole moment is chosen to fit the observed lifetime. In addition, the possibility that the state is $\frac{3}{2}^\pm$ is eliminated by the absence of the cascade transition[7] and by the isotropy of the angular distribution in both the α-particle excitation and the proton excitation.[7] We conclude that the first excited state of F^{19} at 114 kev is $\frac{1}{2}^-$ (assuming the ground state to be $\frac{1}{2}^+$), while the second excited state at 200 kev is $5/2^+$.

The $5/2^+$ state is probably that predicted by the shell model for an odd proton in a $d_{5/2}$ state. The $\frac{1}{2}^-$ state is entirely unexpected since the shell model predicts even parities in this region from the filling of the $s_{1/2}$ and $d_{5/2}$ states. It may be related to the $\frac{1}{2}^-$ state at 3.10 Mev[10] in F^{17}, in fact the three lowest states of F^{17} are apparently $5/2^+$, $1/2^+$, and $1/2^-$. The most obvious interpretation of the $\frac{1}{2}^-$ state is in terms of a proton hole in the $p_{1/2}$ shell. The fact that it is almost accidental that this state is not the ground state is certainly in contradiction with the usual interpretations of the shell model.

* Assisted by the joint program of the U. S. Office of Naval Research and the U. S. Atomic Energy Commission.
† On leave of absence from Princeton University, Princeton, New Jersey.
‡ Present address: Department of Radiology, City of Hope, Duarte, California.
[1] Investigations of the present reactions have also been carried out by N. P. Heydenburg and G. M. Temmer, and by G. A. Jones and D. H. Wilkinson (pre-publication reports).
[2] T. Huus and Č. Zupančić, Kgl. Danske Videnskab. Selskab, Mat-fys. Medd. **28**, No. 1 (1953); C. McClelland and C. Goodman, Phys. Rev. **91**, 760 (1953); G. M. Temmer and N. P. Heydenburg, Phys. Rev. **93**, 351 (1954).
[3] C. J. Mullin and E. Guth, Phys. Rev. **82**, 141 (1951).
[4] K. A. Ter-Martyrosian, J. Exptl. Theor. Phys. (U.S.S.R.) **22**, 284 (1952).
[5] K. Alder and A. Winther, Phys. Rev. **71**, 1578 (1953).
[6] Thirion, Barnes and Lauritsen, preceding Letter [Phys. Rev. **94**, 1076 (1954)].
[7] Peterson, Barnes, Fowler, and Lauritsen, this issue [Phys. Rev. **94**, 1075 (1954)].
[8] R. F. Christy, following Letter [Phys. Rev. **94**, 1077 (1954)].
[9] We are indebted to Dr. A. Kerman for these calculations.
[10] F. J. Eppling *et al.*, Phys. Rev. **91**, 438 (1953); F. Ajzenberg and T. Lauritsen, Revs. Modern Phys. **24**, 321 (1952).

Low Excited States of F^{19}. IV. Angular Distributions*

R. F. CHRISTY
Kellogg Radiation Laboratory, California Institute of Technology, Pasadena, California
(Received March 18, 1954)

THE angular distributions[1] of inelastically scattered protons and the subsequent γ rays at resonances in Ne^{20} afford one means of establishing properties of the low excited states of F^{19}. For this purpose the 2^- resonances in Ne^{20} made by p-wave

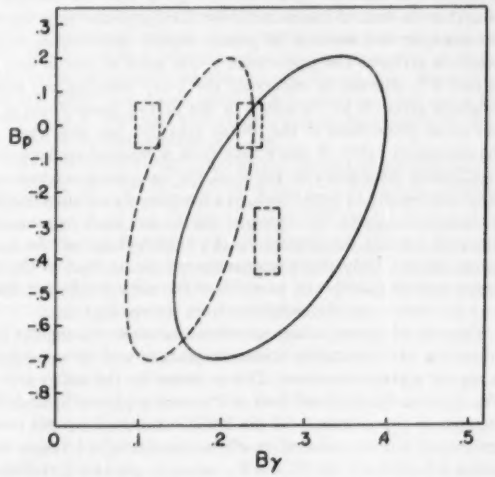

FIG. 1. The asymmetry coefficient B_p of inelastically scattered protons leading to the 200-kev state of F^{19} as related to the coefficient B_γ for the angular asymmetry of the resulting ray at 2^- resonances in Ne^{20} from $F^{19}+p$. The experimental points are plotted as dotted rectangles.

protons on F^{19} in channel spin 1 are most suitable and are discussed below. Since it was not possible to measure the inelastically scattered protons leading to the 114-kev state at these resonances, we discuss only the angular distribution of protons leading to the 200-kev state and of the two γ rays.

The protons to the $5/2^+$ state are distributed as $1+A_p\cos^2\theta = 1+B_pP_2(\cos\theta)$, where, because of the two channel spins 2 and 3 in the outgoing state, $-7/9 \leq A_p \leq 1/3$ or $-0.7 \leq B_p \leq 0.2$. The observations (tabulated below) lie within this range. A $3/2^+$ state would also be consistent with the proton distributions.

With an assignment of $1/2^-$ for the 114-kev state, the corresponding γ ray is spherical, in agreement with observation. For the 200-kev γ ray, we expect an angular distribution $f(\theta)=1+A_\gamma\cos^2\theta=1+B_\gamma P_2(\cos\theta)$. If the state were $3/2^+$, decaying by magnetic dipole, A_γ would be less than or equal to zero; the fact that A_γ is positive eliminates this possibility. For a $5/2^+$ state decaying by electric quadrupole radiation, we get $0.23 \leq A_\gamma \leq 0.75$ or $0.143 \leq B_\gamma \leq 0.4$. Before comparing with experiment, we will discuss some novel features of this problem.

The treatment of the proton spin needs some explanation. In calculating the angular distribution of the inelastically scattered protons, the proton spin is combined with that of the excited F^{19} nucleus to form two channel spins: from each of these, an angular distribution is calculated and the results are the two extreme distributions, the general result being an arbitrary linear combination of the two. In calculating the distributions of the subsequent γ rays, however, the amplitudes from the two channel spins are coherent and the general result contains a term corresponding to the interference of the two channel spins. The extreme distributions can of course be found by diagonalizing the quadratic form. It is interesting to inquire, however, if a different way of combining angular momenta will lead directly to the two extreme distributions which can be combined incoherently. It is readily seen that the appropriate combination for this purpose is the $\mathbf{l}+\mathbf{s}=\mathbf{j}$ of the outgoing proton. The γ-ray distributions for different j values (here 1/2 and 3/2) of the outgoing proton are incoherent and, in fact, for $j=3/2$ we get $A_\gamma=0.23$, whereas for $j=1/2$ we get $A_\gamma=0.75$.

This result leads immediately to the formulation of a general statement as to when we may combine two angular momenta, at a certain stage of a reaction, to form a resultant which may be treated incoherently: Whenever an experiment gives equal weight to all projections of two angular momenta j_1 and j_2 which are to be combined, then we may form $\mathbf{j}_1+\mathbf{j}_2=\mathbf{J}$ and the various J values can be treated incoherently for that particular experiment. For example, in observing the proton angular distribution, equal weight is given to the projections of the spins of proton and of excited F^{19}, whereas in observing the γ-ray distribution, equal weight is given to all directions of the proton (projections of $\mathbf{l}$) and to all projections of the proton spin. We see also when, in the excitation curve of the γ rays from a residual nucleus, two overlapping resonances or states of the compound nucleus can show interference (a term which, as a function of excitation energy, is asymmetric about the resonance center and leads to a rapidly changing angular distribution in the neighborhood of the resonance center). Only those resonances which can lead to the residual state in question by particles of the same j and l can show such interference in the radiations from the residual state.

There is, of course, a correspondence between the angular distributions of inelastically scattered protons and of subsequent γ rays at a given resonance. This is shown by the solid curve in Fig. 1, where B_p, the coefficient of $P_2(\cos\theta)$, is plotted against B_γ. Because of the coherence of the usual channel spins, this correspondence is in the form of an ellipse, instead of a straight line, which is bounded in the B_p and B_γ values by the numbers already computed. Taking the channel spin amplitudes as real numbers, the corresponding experimental points for B_p and B_γ should lie on the perimeter of the ellipse.

In this problem, the situation is further complicated by the long lifetime[2] of the $5/2^+$ state (10^{-7} sec) which permits some precession of the nuclear spin before γ emission. This will result in a B_γ reduced by multiplying with some factor $\alpha<1$. In this case it does not seem possible to calculate α since the environment of the radiating F^{19} nucleus is quite uncertain after the $p-F^{19}$ collision which will leave the atom perhaps excited and in a strange lattice position. It should be possible, by correlating sufficiently precise measurements of B_p and B_γ at different resonances, to test the conclusions given here and to find the reduction factor α. The dotted ellipse is drawn for $\alpha=0.6$. The observations listed below are shown as rectangles in the figure and are not inconsistent with $\alpha\approx0.6$. In addition, the angular distribution of the 200-kev γ ray as excited by Coulomb excitation under alpha-particle bombardment[3] is consistent with α in the range 0.6 to 0.8.

Resonance	A_p	B_p	A_γ	B_γ
873 kev	0 ±0.1	0 ±0.07	0.17 ±0.02	0.11 ±0.015
1355 kev	0 ±0.1	0 ±0.07	0.40 ±0.03	0.235 ±0.015
1381 kev	−0.45 ±0.1	−0.35 ±0.1	0.44 ±0.03	0.255 ±0.015

* Assisted by the U. S. Office of Naval Research and the U. S. Atomic Energy Commission.

[1] Peterson, Barnes, Fowler, and Lauritsen, this issue [Phys. Rev. **94**, 1075 (1954)].

[2] Thirion, Barnes, and Lauritsen, this issue [Phys. Rev. **94**, 1076 (1954)].

[3] Sherr, Li, and Christy, preceding Letter [Phys. Rev. **94**, 1076 (1945)].

Short-Lived Isomeric States of Ag^{110} and In^{116}†

F. I. Boley
Scott Laboratory, Wesleyan University, Middletown, Connecticut
(Received March 1, 1954)

BETA and gamma radiations from the short-lived isomeric states of Ag^{110} and In^{116} have been investigated using a scintillation spectrometer. The detector arrangements were conventional, using RCA 5819 photomultipliers in conjunction with sodium iodide (thallium activated) or anthracene crystals for the detection of gamma or beta rays, respectively. Data were recorded photographically as dots on 35-mm film. This recording technique provides information concerning both the energy spectrum and decay rate of the sample. Details concerning the photographic dot recording method have been described elsewhere.[1]

Ag^{110} was obtained by irradiating 0.001-inch silver foil in the

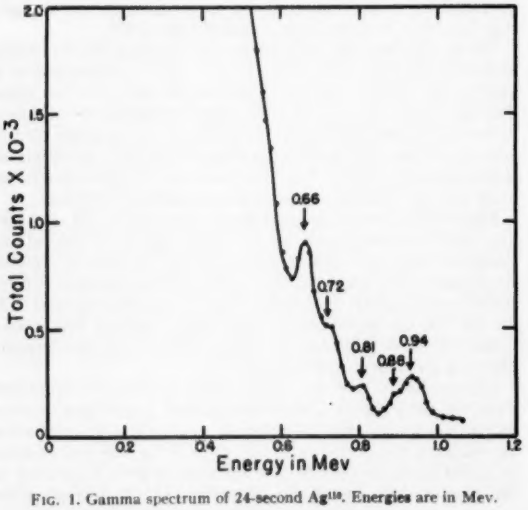

FIG. 1. Gamma spectrum of 24-second Ag^{110}. Energies are in Mev.

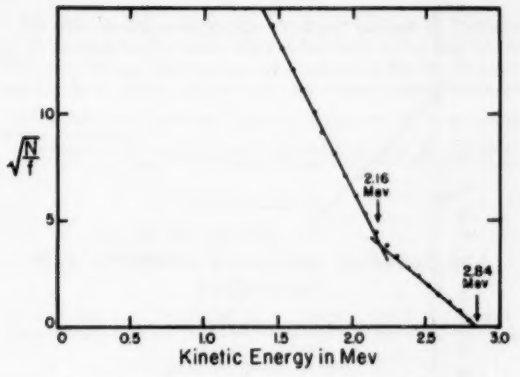

FIG. 2. Fermi plot of beta spectrum of 24-second Ag^{110}.

Brookhaven reactor for a period of approximately two seconds. The transit time from the pile to the spectrometer was approximately ten seconds. The decay rate of the activity indicated a half-life of 24±2 seconds thus insuring proper identification as Ag^{110}.

The Ag^{110} gamma spectrum is shown in Fig. 1 and a Fermi plot of the beta spectrum appears in Fig. 2. Energy calibrations were obtained from the 0.661-Mev gamma ray of Cs^{137} and its conversion line. Gamma rays of 0.66±0.02 Mev and 0.94±0.02 Mev are observed as well as weak, poorly resolved peaks at 0.72±0.02 Mev, 0.81±0.02 Mev, and 0.88±0.02 Mev. The beta spectrum consists of two groups with end points at 2.84±0.05 Mev and 2.16±0.05 Mev. These emissions may be arranged in the decay scheme shown in Fig. 3. The 0.37-Mev beta group was not observed. If present this group undoubtedly would have been masked by the higher-energy groups. This decay scheme meshes with the one given by Cork *et al.*[2] for the decay of the 270-day isomeric state of Ag^{110}.

The present experiment is similar to one performed by Goodrich[3] who found indications supporting the suggestion of Siegbahn[4] that a lower-energy beta transition may occur between the 24-second state and one of the higher Cd^{110} levels. The present experiment yields a beta-to-gamma intensity ratio of 200. Considering the two-second irradiation time and the 40-to-1 ratio of cross sections in favor of the excitation of the 24-second over the 270-day isomer, the 200-to-1 intensity ratio strongly supports the existence of a low-energy beta transition. The above data indicate an end point energy of approximately 0.37 Mev for the group.

The 13-second isomeric state of In^{116} was excited by irradiating finely powdered indium in the Brookhaven reactor for approximately two seconds. Identification was made on the basis of half-life as in the case described above. No gamma rays were detected. The end point of the single beta-ray group was determined to be 3.29±0.06 Mev. There appears to be no transition between the isomeric states of In^{116}. These results support the findings of Slätis *et al.*[5]

Grateful acknowledgment is made to Mr. C. M. Gordon who assisted with the equipment used in taking the data, to Dr. Marvin Fox and other members of the Brookhaven reactor group for irradiation assistance, and to Dr. D. J. Zaffarano at Iowa State College for the use of an automatic "dot counter."

† This work was supported in part by the U. S. Office of Ordnance Research.

[1] F. I. Boley and D. J. Zaffarano, U. S. Atomic Energy Commission Document ISC-154 (unpublished); Hunt, Rhinehart, Weber, and Zaffarano (to be published).
[2] Cork, Rutledge, Branyan, Stoddard, Childs, and LeBlanc, Phys. Rev. **80**, 286 (1950).
[3] Max Goodrich, Phys. Rev. **82**, 759 (1951).
[4] K. Siegbahn, Phys. Rev. **77**, 233 (1950).
[5] Slätis, duToit, and Siegbahn, Phys. Rev. **78**, 498 (1950).

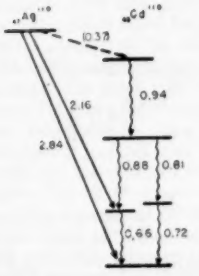

FIG. 3. Proposed decay scheme of 24-second isomeric state of Ag^{110}. Energies are in Mev.

Half-Life and Beta Decay of the Long-Lived Niobium-94

MARIO A. ROLLIER AND EINAR SAELAND
Joint Establishment for Nuclear Energy Research, Kjeller, Norway and Institute of General Chemistry, Polytechnical Institute, Milan, Italy
(Received March 23, 1954)

THE properties of the nuclide Nb^{94} have so far not been observed directly but have only been inferred from other experimental data owing to the difficulty of freeing even the purest niobium, element or compound, from impurities which become activated in the pile. From yield considerations, the most recent tentative assignment of the half-life to this beta-decaying nuclide[1] only indicates a lower limit of 5×10^4 years. Lately an efficient means of separating tantalum from niobium by solvent extraction was indicated,[2] based on the fact that tantalum and niobium have been found to extract into certain polar organic solvents. This enabled us to obtain the residual activity, due to Nb^{94}, of a niobium sample irradiated in the pile.

Spectroscopically pure metallic niobium as well as some niobium salts have been irradiated for 23 days with thermal neutrons in the nuclear reactor "JEEP." The short-lived 6.6-minute Nb^{94m} beta activity was confirmed. The bulk of the slow-decay activity is due to Ta^{182} beta and gamma radiations. Many ways have been tried to free efficiently the niobium metal from the tantalum impurity: anion exchange column, coprecipitation of Ta as potassium fluotantalate, and Ta/Nb solvent extraction using di-isopropyl ketone. Only the last one proved successful. In a Nb_2O_5 sample to which inactive tantalum was first added and then extracted successively four times, the residual activity was brought down to a stable value of 9.5 counts/min per mg Nb_2O_5 counted in a standard end-window Geiger tube assembly for a window-to-sample distance of 9 mm.

Absolute beta counting was carried out on this purified niobium pentoxide, resulting in a specific activity of 4.757×10^{-8} curies/g of irradiated niobium metal. From this value a half-life of 2.7×10^4 years was computed for the nuclide, the average value of the neutron flux during the 23-day irradiation being 1.5×10^{11} neutrons per cm^2 per sec. Considering the necessary approximations used, we estimate that the half-life of Nb^{94} is determined with an accuracy of ±15 percent of the indicated value.

From an aluminum absorption curve the energy of the residual Nb^{94} beta radiation was found to be 0.61 Mev.

The neutron irradiation and the measurement of the short-lived Nb^{94m} were carried out at the Joint Establishment for Nuclear Energy Research (JENER), Kjeller, Norway, the further research at the Institute of General Chemistry of the Polytechnic in Milan (Italy).

[1] Hein, Fowler, and McFarland, Phys. Rev. **85**, 138 (1952).
[2] P. C. Stevenson and H. G. Hicks, University of California Radiation Laboratory Unclassified Report No. 2009, November, 1952 (unpublished) and Analyt. Chem. **25**, 1517 (1953).

Nuclear Properties of Some Isotopes of Californium, Elements 99 and 100†

G. R. Choppin, S. G. Thompson, A. Ghiorso, and B. G. Harvey
Radiation Laboratory and Department of Chemistry, University of California Berkeley, California
(Received March 19, 1954)

In recent publications[1,2] we reported the formation of the nuclides 99^{253}, 99^{254}, and 100^{254} by intense neutron bombardment of plutonium and higher-mass nuclides. Further observations of the nuclear properties of these nuclides have now been made, using, in some cases, samples of higher activity prepared in new neutron bombardments. In addition, a 15-hour alpha-emitting isotope of element 100 has been observed in the products of the neutron bombardment of plutonium.

Cf^{253} and 99^{253}.—The nuclide Cf^{253} decays by β^- emission to 99^{253}. From the rate of growth of the 99^{253} alpha activity in a purified Cf^{253} sample and the rate of decay of separated 99^{253}, the half-life of both these nuclides was found to be approximately 20 days.

Because of the high spontaneous fission rate in californium (due mainly to Cf^{252}), the β^- emitting fission fragments prevented any simple measurement of the β-particle energy of Cf^{253}.

By comparison with Bi^{211} and Po^{214} alpha-energy standards, the energy of the 99^{253} alpha particles was found to be 6.63 ± 0.02 Mev.

99^{254}, 100^{254}, and 100^{255}.—Pure samples of element 100 were

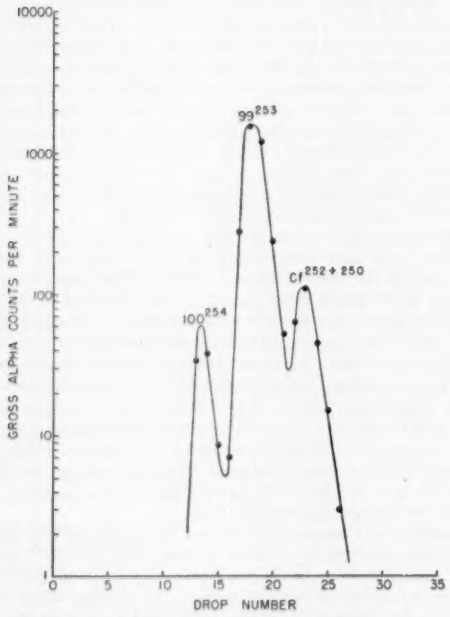

Fig. 1. Elution of elements 98, 99, and 100 from Dowex-50 column with 0.04 *M* ammonium lactate, *p*H 4.50.

separated from 99 and californium by elution through columns of Dowex-50 ion-exchange resin. A typical elution curve is shown in Fig. 1. For this run the bulk of the californium had been removed in a previous ion-exchange column.

Two alpha activities assigned to element 100 have been observed. The more abundant, probably due to 100^{254}, decays with a half-life of 3.2 hours (Fig. 2) by emission of 7.22 ± 0.03-Mev alpha-particles, as previously reported.[2] The other, probably due to 100^{255}, decays with a half-life of about 15 hours by emission of 7.1-Mev alpha particles.

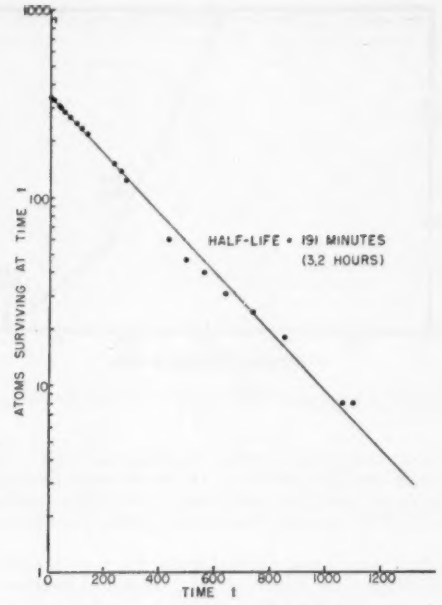

Fig. 2. Decay curve of 100^{254}.

The 7.22-Mev alpha activity of 100^{254} was observed to grow into a separated 99 fraction, and then to decay with a 36-hour half-life, that of its 99^{254} β^- emitting parent (Fig. 3). (These curves are from the first experiments performed early in January and have since been repeated with substantially the same results using orders of magnitude more activity.) The β particles of 99^{254} were found to have a maximum energy of 1.1 ± 0.1 Mev as determined by an anthracene scintillation spectrometer.

The 7.1-Mev alpha activity was also observed in purified element-99 fractions, and thus it was deduced that it also has a β^- emitting parent. Rough decay measurements of this activity in the element-99 fraction indicate that the half-life of this parent, presumably 99^{255}, is approximately one month.

Spontaneous fissions, decaying with a half-life of about 3 hours, were observed in pure element-100 fractions. These are presumably due to 100^{254}. From the ratio of fission to alpha-emitting events ($\sim$0.001), the partial half-life of 100^{254} for spontaneous fission was found to be approximately 200 days. Spontaneous fissions were not observed in purified element-99 samples, but appeared as the 100^{254} grew from the 99^{254} β^- decay.

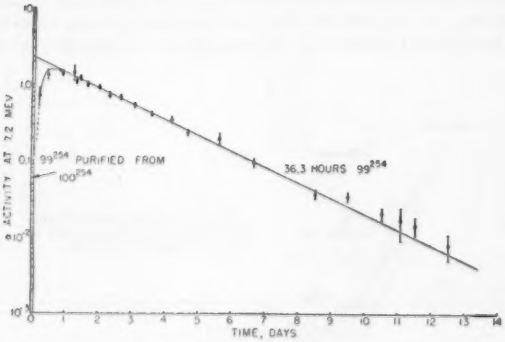

Fig. 3. Decay curve of 99^{254}.

We wish to acknowledge the continued interest of Professor G. T. Seaborg in this work. We are indebted to the staff of the Materials Testing Reactor, and particularly to Dr. W. B. Lewis and Dr. R. R. Smith, for arranging the neutron bombardments.†

† This work was performed under the auspices of the U. S. Atomic Energy Commission.

[1] Thompson, Ghiorso, Harvey, and Choppin, Phys. Rev. **93**, 908 (1954)
[2] Harvey, Thompson, Ghiorso, and Choppin, Phys. Rev. **93**, 1129 (1954)

New Isotopes of Americium, Berkelium and Californium*

A. Ghiorso, S. G. Thompson, G. R. Choppin, and B. G. Harvey
Radiation Laboratory and Department of Chemistry, University of California, Berkeley, California
(Received March 19, 1954)

In a recent publication,[1] the preparation of new heavy isotopes of berkelium (mass number probably 249) and californium (mass numbers greater than 248) by prolonged neutron irradiation of Pu^{239} with thermal neutrons was described. As the result of neutron irradiation of Am^{243} and Bk^{249}, it has been possible to make new observations on the radioactive decay of Am^{244}, and to prepare new berkelium and californium activities.

Am^{244}.—This nuclide was produced by short neutron bombardments of americium, whose principal constituent was Am^{243}. After bombardment the americium was rapidly purified by a combination of precipitation and ion-exchange procedures.[2] The Am^{244} was found to decay by emission of β^- particles; its half-life was 26 minutes, in good agreement with a previously published value.[2]

The beta and gamma radiations of Am^{244} were studied with anthracene and sodium iodide crystal spectrometers. Only one β^- end point, at 1.5 Mev, could be resolved. There were no prominent gamma rays.

Bk^{249}.—A sample of Bk^{249} was subjected to a short neutron bombardment, followed by chemical purification, and a new activity, presumably Bk^{249}, was produced. It decayed by β^- emission with a half-life of 3.13 hours.

The β spectrum showed the existence of two groups, with end points at 900 and 1900 kev. The lower-energy β group was in coincidence with a gamma ray of about 900 kev.

Cf^{250}.—Part of the neutron-irradiated berkelium, after chemical purification, was allowed to decay for five hours to produce the Cf^{250} daughter of the Bk^{250}. The californium was then separated. The Cf^{250} was found to emit 6.05-Mev alpha particles. From the alpha disintegration rate and the beta disintegration rate of the Bk^{250} parent, the alpha half-life of Cf^{250} was found to be about 12 years.

Spontaneous fissions were observed in the samples containing Cf^{250}. The ratio of alpha disintegrations to fissions was 400. The spontaneous fission half-life of Cf^{250} is therefore about 5000 years.

Cf^{249}.—Direct alpha-decay measurements performed over a period of several months on a sample consisting largely of Cf^{249} indicate a half-life for this nuclide of roughly two years. It was found that 26 percent of the alpha particles in the original californium fraction produced from the highly irradiated plutonium were due to Cf^{250}. Thus from the previously mentioned alpha-to-fission ratio of 400 found for pure Cf^{250}, its contribution (approximately 3 percent) to the observed high spontaneous fission rate in the californium fraction (alpha-to-fission ratio=42) can be calculated. The great bulk of the fission rate must therefore be due to Cf^{249}, and a calculation on this basis shows its spontaneous fission half-life to be about 100 years. For the purpose of this calculation it was assumed that in this case the correction for spontaneous fission from Cf^{254} would be small.

Cf^{249}.—The Bk^{249} grows a californium daughter Cf^{249} which decays by emission of 6.0-Mev (10 percent) and 5.82-Mev (90 percent) alpha particles. From the amount of Cf^{249} alpha activity which grew from a known amount of Bk^{249}, the alpha half-life of the Cf^{249} was found to be about 400 years.

It is a pleasure to acknowledge the continued interest of Professor G. T. Seaborg in this work. We are indebted to the entire staff of the Materials Testing Reactor, and particularly to Dr. W. B. Lewis and Dr. R. R. Smith. We wish to thank Almon E. Larsh for assistance with some of the experiments.

* This work was performed under the auspices of the U. S. Atomic Energy Commission.

[1] Thompson, Ghiorso, Harvey, and Choppin, Phys. Rev. **93**, 908 (1954).
[2] See, e.g., G. T. Seaborg in *The Actinide Elements* (McGraw-Hill Book Company, Inc., New York, 1954), National Nuclear Energy Series, Plutonium Project Record, Vol. 14A, Div. IV, Chap. 17.
[3] Street, Ghiorso, and Seaborg, Phys. Rev. **79**, 530 (1950).

Interaction of High-Energy Pions with Nuclei*

E. D. Courant
Brookhaven National Laboratory, Upton, New York
(Received March 30, 1954)

Recent experiments[1-3] have shown that the interaction cross sections of negative π mesons in the energy range of 0.6 to 1.0 Bev on protons are more than twice those of positive π mesons of the same energy range; the (π^-,n) cross section appears to be about equal to the (π^+,p) cross section, as expected from charge symmetry considerations.

This makes it attractive to employ π mesons as tools for the investigation of nuclear structure, in particular of the proton and neutron distributions in nuclei.[4] Johnson and Teller[5] have suggested that the neutrons in a heavy nucleus extend out to a larger radius than the protons. If this is the case, the apparent nuclear radius as measured with two different probe particles will be greater for that probe particle which interacts more strongly with neutrons.

The interaction cross sections of lead for positive and negative π mesons of 700 Mev have been computed using the "optical model"[6] and assuming (a) that the protons and neutrons are uniformly distributed in a sphere of radius R (uniform nucleus model), and (b) that the nucleus is composed of an inner zone of radius R_1 containing Z protons and Z neutrons, and an outer zone of radius R containing $N-Z$ neutrons (Johnson-Teller model). In model (b) the radii R_1 and R are chosen so that the neutron density is the same in both zones, i.e., $R_1/R=(Z/N)^{\frac{1}{3}}$.

In the optical model the nucleus is treated as a region with a complex refractive index. The total cross section may be divided into the diffraction (elastic scattering) portion σ_d and the interaction (absorption) portion σ_a, where

$$\sigma_d=2\pi\int_0^R|1-e^{i\delta(\rho)}|^2\rho d\rho, \tag{1}$$

$$\sigma_a=2\pi\int_0^R(1-|e^{i\delta(\rho)}|^2)\rho d\rho. \tag{2}$$

Here $\delta(\rho)$ is the (complex) phase shift of that part of an incident plane wave which passes through the nucleus along a line which is at a distance ρ from the center. Let $k=p/\hbar$ be the wave propagation number of the incident particle outside the nucleus, and let its propagation number inside the nucleus at a distance r from the center be $k+k_1(r)+\frac{1}{2}iK(r)$. Then

$$\delta(\rho)=2\int_0^{s(\rho)}[k_1(r)+\tfrac{1}{2}iK(r)]dx, \tag{3}$$

where $s(\rho)=(R^2-\rho^2)^{\frac{1}{2}}$, and $r=(\rho^2+x^2)^{\frac{1}{2}}$.

Table I. Interaction cross sections of 700-Mev pions on Pb.

Model	R (10^{-13} cm)	R_1 (10^{-13} cm)	σ_+ (mb)	$\sigma_--\sigma_+$ (mb)
a	8.295		1862	41
b	8.295	7.188	1827	−114
a	7.110		1430	74
b	7.110	6.161	1405	−51

The interaction cross section depends only on K, which is the absorption coefficient in nuclear matter, and not on k_1. This absorption coefficient is related to the cross sections for elementary particle interactions; it equals

$$K=D_p\sigma_p+D_n\sigma_n, \tag{4}$$

where D_p and D_n are the proton and neutron densities, and σ_p and σ_n the cross sections for interaction of the incident particle with protons and neutrons, respectively. Equation (4) is based on the assumption that the elementary cross sections are the same for nucleons bound in the nucleus as for free nucleons, and are not inhibited by the Pauli principle. This should be valid for pions of the order of 1 Bev.

The diffraction portion of the total cross section is mainly confined to angles less than $\theta_1=3/(kR)$. For 1-Bev mesons on lead, $kR\approx 50$, so that $\theta_1\approx 3$ degrees. Therefore the interaction cross section should be relatively easy to determine experimentally by measuring the "total" cross sect on in geometry such that scattering through angles of less than about 3 degrees is not detected. Such an experiment has been proposed by Clark, Cool, and Piccioni.

The interaction cross sections (2) have to be corrected for the Coulomb interaction. At the energies involved this correction can be made on the basis of classical orbit dynamics, resulting in a correction factor

$$\sigma_\pm/\sigma_0=1\mp 2Ze^2/RE, \tag{5}$$

where $\sigma_+(\sigma_-)$ is the cross section for positive (negative) particles of energy E (assumed relativistic and large compared to the height of the Coulomb barrier), and σ_0 is the cross section calculated from Eq. (2); R is the over-all nuclear radius. This condition is obtained by noting that a particle of impact parameter $b=R(1\mp Ze^2/RE)$ just grazes the surface of the nucleus.

The calculations have been performed for π mesons of 700-Mev kinetic energy, for which the cross sections were assumed to be $\sigma(\pi^-,n)=\sigma(\pi^+,p)=14$ mb, and $\sigma(\pi^+,n)=\sigma(\pi^-,p)=38$ mb, as inferred from a graph of the results of references 1 to 3, and the hypothesis of charge symmetry. The radius of lead was taken as $1.2A^{\frac{1}{3}}\times 10^{-13}$ cm and $1.4A^{\frac{1}{3}}\times 10^{-13}$ cm. The results are summarized in Table I.

It appears that there is a difference of about 8 percent of the total cross section between the (π^+,π^-) differences to be expected on the basis of the two models. Therefore experimental determinations of the interaction cross sections of lead for positive and negative pions around 700 Mev should make it possible to decide whether the uniform distribution or the Johnson-Teller distribution is more nearly correct.

It is reasonable to expect that the angular distribution of the elastically scattered mesons will depend just as sensitively on the nucleon density distributions; calculations on this point are being planned.

It is a pleasure to acknowledge stimulating discussions with O. Piccioni, G. Snow, and C. N. Yang.

* Research performed under the auspices of the U. S. Atomic Energy Commission.

[1] Cool, Madansky, and Piccioni, Phys. Rev. **93**, 249, 637 (1954) and private communication.
[2] Shapiro, Leavitt, and Chen, Phys. Rev. **92**, 1073 (1953) and private communication.
[3] S. J. Lindenbaum and L. C. L. Yuan (private communication).
[4] This idea was suggested to the author by O. Piccioni.
[5] M. H. Johnson and E. Teller, Phys. Rev. **93**, 357 (1954).
[6] Fernbach, Serber, and Taylor, Phys. Rev. **75**, 1352 (1949).

Magnetic Storm Effect on Cosmic Radiation

HANNES ALFVÉN
University of Maryland, College Park, Maryland and Tekniska Högskolan, Stockholm, Sweden
(Received March 24, 1954)

IN a recent letter Swann[1] objects to my theory of the cosmic-ray storm effect.[2] He has not observed, however, that the beam I consider expands the whole time when travelling out from the sun, so that the magnetic field in it is proportional to r^{-1} (r=distance to the sun). This means that an observer travelling with the beam observes a decrease in the magnetic field in the beam, and by betatron (or "cygnotron") action this causes a decrease in the energy of the particles in the beam. Hence Swann's starting point that "an observer moving with the beam observes no change of energy" is not correct.

Swann further points out that in an example I have given, a cosmic-ray particle would have "a radius of curvature 15 times smaller than the beam width and so could never cross it." As the magnetic field in the beam is inhomogeneous, the particle, which moves in a trochoid, will drift perpendicular to the beam and could very well cross it.

The conclusion is that the relative decrease in energy could have any value and is not limited to $<2v/c$.

[1] W. F. G. Swann, Phys. Rev. **93**, 905 (1954).
[2] H. Alfvén, Phys. Rev. **75**, 1732 (1949); E. A. Brunberg and A. Dattner, Tellus (to be published); H. Alfvén, Tellus (to be published).

Energy Levels in W^{182}†

C. M. FOWLER, H. W. KRUSE, V. KESHISHIAN, R. J. KLOTZ, AND G. P. MELLOR*
Kansas State College, Manhattan, Kansas
(Received March 19, 1954)

EXCITED W^{182}, following beta-minus emission of Ta^{182} is one of several complex-gamma-emitting nuclei of even-even species. Figure 1, we feel, presents the main features of the energy level scheme. The portion of the diagram from 1222 kev and up, with the exception of the level E, is one of several proposed by Muller[1] and co-workers. Of sixteen gamma rays cited, most of which were measured with high precision by the Dumond curved crystal spectrometer, ten were incorporated by these workers in this portion of the decay scheme. The remaining six gamma rays listed, we place at AB, BC, EH, AD, BD, and BF. These assignments are based upon measurements taken from high-field, high-resolution beta-ray spectrographs. Gamma rays AD and BD were found to differ by 99.9 ± 0.5 kev, BF and BD by 68.0 ± 0.5 kev, and the pair AF, BF by 100.1 ± 0.5 kev. The triad of lines to level C were also sufficiently intense for accurate measurement of energy differences and help support the diagram. Finally, high-energy transitions from nearly all of the levels D through K to A, B, and C have been observed and agree with the proposed scheme. We also have some evidence for the level L, although according to the various possibilities proposed by Muller either level G or L may be present, but not both. Our data actually favor a level at G perhaps one kev lower than that given.

Including a few additional weak low-energy radiations between some of the levels D through L, not previously mentioned, it is seen that this decay scheme accommodates about forty gamma rays. However, at least this many more have been observed and roughly classified by this group. For the most part, these radiations are very weak, and lead, no doubt, to additional levels between C and D. Also there is little doubt that some arise from levels higher than K (or L). The measurement of a single half-life of 115.5 days over a period of five and a half cycles is indication that these weak gamma rays do not arise from contaminants.

Analysis of the beta spectra has proved somewhat disappointing. A group of low-intensity conversion lines so obscures the end point (at 540 kev) that good measurements of the end points and relative intensities of the several other beta spectra present have so far not been realized.

The electron spectrum gives relative K conversion of 10:8.0:8.0 for the three strong lines AD, BF, and BD. Borrowing the gamma-ray intensity data of Muller, the ratios of K conversion coefficients for these gamma rays are 1:1.8:0.85. Taking 0+ and 2+ for the levels A and B, the first and third conversion coefficients are compatible with a 1− assignment for D. This assignment also fixes the conversion coefficient for BF, which fits an $E2$ transition. A choice of 4+ for the level F is consistent with the trend of the levels from D

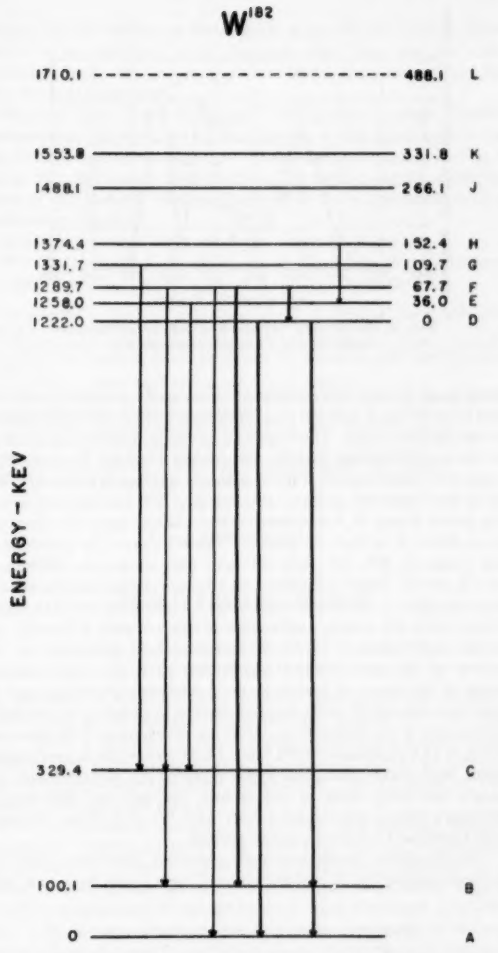

FIG. 1. Proposed energy levels in W^{182}. Transitions shown are discussed in text.

upwards to follow an approximate algebraic relation. Allowing for two additional levels, not shown on the figure for lack of accuracy, at approximately 5 and 205 kev above D, the level energies above D become asymptotic to the expression $E_L = 3.70L(L+1)$. The correct energy values are shown on the right of the figure. The values of L are to be numbered consecutively from D, upward, starting with $L=1$ for the D level.

The levels A, B, and C agree well with the Bohr-Mottelson[2] formulation, with level C taken as $4+$. A further level at 680 ± 5 kev which can be justified from conversion line data would fit the third-excited state predicted by this formulation. It is interesting to note that the level D also fits, in energy, the fourth-excited state predicted by this theory, but the predicted spin value of 8 is manifestly at variance with the $1-$ assignment suggested above.

In addition to the papers previously mentioned, those of Beach *et al.*,[3] Cork *et al.*,[4] and Scharff-Goldhaber[5] were of considerable assistance.

† This work was sponsored by the U. S. Atomic Energy Commission.

* Now with the National Bureau of Standards, Washington, D. C.

[1] Muller, Hoyt, Klein, and Dumond, Phys. Rev. **88**, 775 (1952).

[2] A. Bohr and B. R. Mottelson, Phys. Rev. **90**, 717 (1953).

[3] Beach, Peacock, and Wilkenson, Phys. Rev. **76**, 1585 (1949).

[4] Cork, Keller, Rutledge, and Stoddard, Phys. Rev. **78**, 95 (1950).

[5] G. Scharff-Goldhaber, Phys. Rev. **90**, 587 (1953).

Identification of Californium Isotopes 249, 250, 251, and 252 from Pile-Irradiated Plutonium*

H. DIAMOND, L. B. MAGNUSSON, J. F. MECH, C. M. STEVENS, A. M. FRIEDMAN, M. H. STUDIER, P. R. FIELDS, AND J. R. HUIZENGA
Argonne National Laboratory, Lemont, Illinois

(Received March 24, 1954)

IN a recent communication[1] we reported a large spontaneous fission activity associated with the californium produced from plutonium irradiated with neutrons in the Materials Testing Reactor (MTR) at Arco, Idaho. The important implications of gross amounts of spontaneous fission activity prompts us to give additional information on the mass assignments and nuclear properties of several californium and berkelium isotopes. The heavy elements were chemically separated from two plutonium samples, I and II, which received integrated fluxes of 4×10^{21} and 8×10^{21} neutrons, respectively.

Californium from sample II was analyzed in a 12-inch, 60° mass spectrometer with a multiple filament source. Californium isotopes of mass numbers 249, 250, 251, and 252 were detected in mole percentages given in column 1 of Table I. A small quantity of californium (corresponding to about four percent of the gross californium activity of sample II) was left with the berkelium activity for five weeks, after which time the californium was again chemically separated from the berkelium (this will be referred to as californium sample II′). The mass spectrometric analysis of this californium sample is given in column 2 of Table I. The Cf^{250}/Cf^{251}, Cf^{250}/Cf^{249}, and Cf^{251}/Cf^{252} mole ratios of the two samples are constant within statistical error. The Cf^{249} in sample II′ has, however, been enhanced. This is evidence for assigning to Cf^{249} the 5.81-Mev alpha particles observed to grow into a purified berkelium fraction and to chemically elute in the californium position. The alpha half-life of Cf^{249} is calculated to be 550 ± 150 years from the 5.81-Mev alpha-particle growth rate into a Bk^{249} sample of a measured disintegration rate.

TABLE I. Mass spectrometric analyses of two californium samples, giving isotopic abundances in mole percent.

Cf isotope	Sample II	Sample II′
Cf^{249}	4.3 ± 0.5	28 ± 7
Cf^{250}	$49\ \pm6$	34 ± 8
Cf^{251}	$11\ \pm3$	8 ± 1
Cf^{252}	$36\ \pm5$	30 ± 3

Alpha-pulse analysis of californium sample II by a wire-screen collimator technique[2] showed two prominent alpha groups of 6.12 and 6.03 Mev. The gross 6.12-Mev/6.03-Mev alpha activity ratios in samples I and II were 0.62 ± 0.12 and 3.3 ± 0.3, respectively. Gamma-alpha coincidence measurements on sample II showed a fine-structure peak associated with each of the two prominent californium ground-state alphas. The intensity ratio of the fine-structure peaks was also about 3.3. This behavior is characteristic of the alpha spectra of even-even nuclides.

Alpha-pulse analysis of the californium II′ sample showed 0.4 ± 0.1 percent 5.81-Mev alphas. The spontaneous fission activity on a plate from sample II californium, containing ini-

TABLE II. Nuclear properties of some isotopes of elements 97 and 98.

Isotope	Radiation	Half-life	Alpha energy (Mev)	β^- energy (kev)	Spontaneous fission half-life
$_{97}Bk^{249}$	β^-, α (?) branching ratio $\beta^-/\alpha\approx10^5$	~1 year	$5.4\ \pm0.1$	100 ± 20	$>10^7$ years
$_{98}Cf^{249}$	α	550 ± 150 yr	5.81 ± 0.03		$>10^6$ years
$_{98}Cf^{250}$	α	9.4 ± 2.3 yr	6.03 ± 0.01		$\geq10^4$ years
$_{98}Cf^{251}$	(α)				
$_{98}Cf^{252}$	α	2.1 ± 0.4 yr	6.12 ± 0.01		60 ± 12 years
$_{98}Cf^{252}$	β^-	18 ± 3 days			

[1] Muller, Hoyt, Klein, and Dumond, Phys. Rev. **88**, 775 (1952).

[2] A. Bohr and B. R. Mottelson, Phys. Rev. **90**, 717 (1953).

tially 1375 fission disintegrations/minute, is decaying with a 2.1±0.4 year half-life. A summary of the nuclear properties of some isotopes of berkelium and californium are given in Table II. The decrease in spontaneous fission half-life of the heavy even-A californium isotopes agrees with recent predictions.[8]

We again wish to thank W. B. Lewis and the MTR staff for handling these irradiations. The experimental assistance given by W. C. Bentley, D. W. Engelkemeir, and M. M. Petheram is gratefully acknowledged. It is a pleasure to thank W. M. Manning for his helpful suggestions.

* Nuclear properties of some of these isotopes were measured in other work at Argonne National Laboratory, University of California Radiation Laboratory, and at Los Alamos Scientific Laboratory, not yet published [see also Thompson, Ghiorso, Harvey, and Chopping, Phys. Rev. **93**, 908 (1954)].

[8] Studier, Fields, Diamond, Mech, Friedman, Sellers, Pyle, Stevens, Magnusson, and Huizenga, Phys. Rev. **93**, 1428 (1954).

[9] D. W. Engelkemeir and L. B. Magnusson, Rev. Sci. Instr. (to be published).

[10] J. R. Huizenga, Phys. Rev. **94**, 158 (1954).

Inelastic Scattering of 190-Mev Electrons in Beryllium*†‡

J. A. McIntyre, B. Hahn,§ and R. Hofstadter
Department of Physics and W. W. Hansen Laboratories, Stanford University, Stanford, California

(Received March 19, 1954)

In investigating the elastic scattering of high-energy electrons from various nuclei[1] we reported preliminary evidence of structure in the "elastic" profiles observed at 70° and 90° in beryllium at 125 Mev. We have re-examined this problem with a newly rewound analyzing magnet which permits studies up to 200 Mev. With incident electrons of 190 Mev in a band 1.0-Mev wide we have confirmed this structure and the details have now been more clearly revealed. Figure 1 shows the elastically scattered peak A and two additional inelastically scattered peaks B and C at 70° for a 100-mil beryllium target set at 45° with respect to the incident beam. The abscissa is given in terms of the settings of the potentiometer reading the current through the analyzing magnetic spectrometer. Figure 2 shows similar data at 90°. We have also observed inelastic scattering at 60° and have observed the peaks A and B, but unfortunately did not carry the observations below B to look for peak C. Table I shows the positions of the peaks at 90°, 70°, and 60° and also shows the differences $A-B$, $A-C$. These differences may be converted into the excitation energies of the levels excited in beryllium by 190-Mev electrons when the energy calibration of the abscissa is known. An initial calibration in terms of magnetic field measured at the center of the spectrometer trajectories gave the instantaneous slope of the curve of energy *versus* potentiometer setting as 0.20 Mev per division of potentiometer reading. Averaging the intervals $A-B$ and $A-C$ provides $A-B=12.7$ divisions or 2.54 Mev and $A-C=34.8$ divisions or 6.96 Mev. These values are in good agreement with those excitation levels reported by Britten,[2] and the single low-lying level of Davis and Hafner[3] and Rhoderick.[4] Britten's values are 2.5±0.2 Mev and 6.8±0.3 Mev. Britten's third level at 11.6 Mev was not sought.

The beryllium levels previously observed have been found by inelastic scattering of protons whereas these levels have now been

TABLE I. Summary of data on elastic and inelastic peaks.

Angle \ Peak	A	B	C	$A-B$	$A-C$
60°	418.0	404.0	—	14.0	—
70°	413.6	400.0	378.4	13.6	35.2
90°	404.5	394.0	370.0	10.5	34.5
			Average	12.7±1.5	34.8±1.5

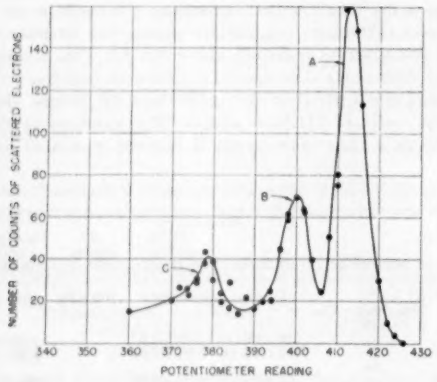

FIG. 1. Elastic peak (A) and first and second inelastic peaks (B and C) in beryllium at 70°.

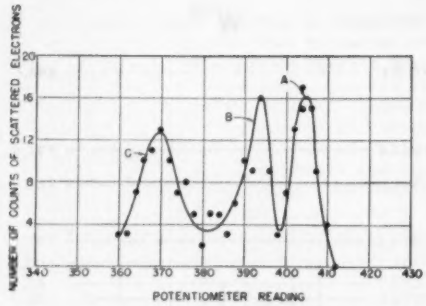

FIG. 2. Elastic peak (A) and first and second inelastic peaks (B and C) in beryllium at 90°.

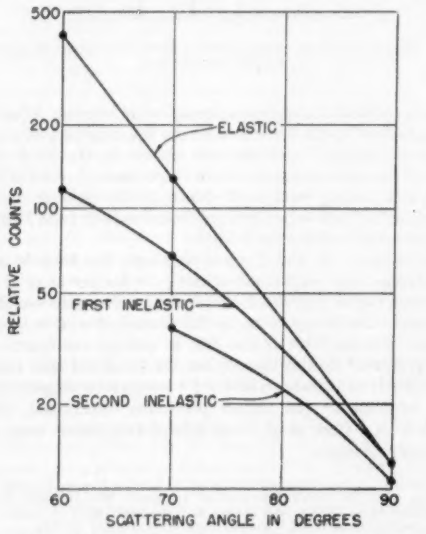

FIG. 3. Elastic and inelastic cross sections on a relative scale as a function of scattering angle.

excited by fast electrons. Presumably a specifically nuclear interaction is not involved, which suggests that there may be similarities between electron excitation of levels and Coulomb excitation by heavy particles.

Figures 1 and 2 and the data at 60° permit a rough, limited measurement of the angular distribution of the cross section for the inelastic scattered electrons. These data are plotted in Fig. 3 along with the elastic cross section. The flatter angular distributions of the inelastic electrons appear to be in agreement with a preliminary theory.[5]

Inelastic processes have also been observed in copper.

We wish to thank A. W. Knudsen, B. Chambers, and V. Prosper for help in setting up the apparatus for these experiments.

* Supported by the joint program of the U. S. Office of Naval Research and the U. S. Atomic Energy Commission.
† This research was supported by the United States Air Force, through the Office of Scientific Research of the Air Research and Development Command.
‡ Aided by a grant from the Research Corporation.
§ Visiting Research Fellow of the *Schweizerische Arbeitsgemeinschaft in Mathematik und Physik*, Switzerland.

[1] Hofstadter, Fechter, and McIntyre, Phys. Rev. **92**, 978 (1953).
[2] R. Britten, Phys. Rev. **88**, 283 (1952).
[3] K. E. Davis and E. M. Hafner, Phys. Rev. **73**, 1473 (1948).
[4] E. H. Rhoderick, Proc. Roy. Soc. (London) **A201**, 348 (1950).
[5] L. I. Schiff (private communication).

Pion Production Ratios*

D. C. PEASLEE
Columbia University, New York, New York
(Received March 18, 1954)

MEASUREMENTS have recently been made[1] on the production of charged pions in the reaction Be^9+p. The π^+/π^- ratio ρ shows a striking energy dependence,[2] decreasing from $\rho\approx 6$ at $E_p=1$ Bev to $\rho=1.8$ at $E_p=2.3$ Bev. The present note interprets this behavior in terms of an "excited state" of the nucleon with isotopic spin $\frac{3}{2}$.

Pion production is envisioned as follows: two nucleons collide, forming a "compound state"; on emerging, one or both of the nucleons are in an excited state, which subsequently decays by π emission. This separation of the process into two distinct stages linked by a quasi-stable excited nucleon state is without justification; it should not, however, vitiate conclusions based on charge independence arguments and forms a convenient physical picture. For the sake of simplicity the nucleon is assumed to have only one excited state, which can decay to the ground state by emission of a single π meson. The excited state must therefore have $T'=\frac{1}{2}$ or $\frac{3}{2}$; meson production can be characterized by the indices 1 or 2, according as one or both nucleons emerge from the collision in an excited state. Because of the threshold for excitation, the production cross section satisfies $\sigma_1>\sigma_2$ for low E_p, while $\sigma_2\gtrsim\sigma_1$ for high E_p. The variation of ρ with E_p can be related to that of σ_1/σ_2, provided that $\rho_1\neq\rho_2$. This immediately excludes the case $T'=\frac{1}{2}$, for then the charge symmetries of the system are identical whether 0, 1, or 2 nucleons are excited, so that $\rho=\rho_1=\rho_2=$const.

The case $T'=\frac{3}{2}$ remains to be examined. For this purpose let $\sigma^{xy}(T^z)$ be the cross section for production of a compound state of isotopic spin T^z by the collision of incident nucleons x, y. Charge independence requires that $\sigma^{np}(1)=\frac{1}{2}\sigma^{pp}(1)=\sigma^s$, but does not relate $\sigma^a=\sigma^{np}(0)$ to σ^s; of course $\sigma^{pp}(0)=0$. Consider a p-p collision with excitation of both nucleons: the compound state has $T^z=1$, $T_s{}^z=1$, and the Clebsch-Gordon coefficients for decomposition into two $T'=\frac{3}{2}$ nucleons yield respective fractional weights of $\frac{2}{3}$ and $\frac{1}{3}$ for the combinations $T_s'=(\frac{1}{2},\frac{1}{2})$ and $T_s'=(\frac{3}{2},-\frac{1}{2})$. The fractional weights for decay of the excited state by π^+, π^0, π^- emission are (100), $(\frac{1}{3}\ \frac{2}{3}\ 0)$, $(0\ \frac{2}{3}\ \frac{1}{3})$ according as $T_s'=\frac{3}{2}, \frac{1}{2}, -\frac{1}{2}$. Combining these factors leads to over-all fractional weights for π production of (13/15, 14/15, 3/15). These last are normalized to give a total production of two π mesons.

For a p-p collision with excitation of one nucleon, the compound state decomposes into $T'=\frac{3}{2}$, $T=\frac{1}{2}$ with fractional weights $\frac{1}{3}$ and $\frac{2}{3}$ for T_s', $T_s=(\frac{1}{2},-\frac{1}{2})$ and $(\frac{1}{2},\frac{1}{2})$, respectively. The resultant over-all fractional weights for π production are $(\frac{1}{2},\frac{1}{2},0)$, normalized to a total of one meson. The total cross sections for π production in a p-p collision are then

$$\begin{aligned}(\pi^+):&\quad (1/15)[26\sigma_2{}^s+15\sigma_1{}^s],\\ (\pi^0):&\quad (1/15)(28\sigma_2{}^s+15\sigma_1{}^s],\\ (\pi^-);&\quad (1/15)[6\sigma_2{}^s].\end{aligned}\tag{1}$$

In a similar way the cross sections for meson production in an n-p collision are

$$\begin{aligned}(\pi^+\text{ or }\pi^-):&\quad (1/15)[14\sigma_2{}^s+(5/2)\sigma_1{}^s+10\sigma_2{}^a],\\ (\pi^0):&\quad (1/15)[2\sigma_2{}^s+10\sigma_1{}^s+10\sigma_2{}^a].\end{aligned}\tag{2}$$

Combining Eqs. (1) and (2) in the ratio 4 to 5 for a Be^9 nucleus leads to

$$\begin{aligned}(\pi^+):&\quad [1.28\sigma_2{}^s+0.54\sigma_1{}^s+0.37\sigma_2{}^a],\\ (\pi^0):&\quad [0.90\sigma_2{}^s+0.82\sigma_1{}^s+0.37\sigma_2{}^a],\\ (\pi^-):&\quad [0.70\sigma_2{}^s+0.09\sigma_1{}^s+0.37\sigma_2{}^a].\end{aligned}\tag{3}$$

When $\sigma_1\gg\sigma_2$, $\rho\approx 6$; when $\sigma_2\gg\sigma_1$, $1\lesssim\rho\lesssim 1.8$, depending on the relative magnitudes of $\sigma_2{}^a$ and $\sigma_2{}^s$.

Of course these considerations are subject to many qualifications, but in terms of the model employed they indicate that (i) wide variation in ρ implies $T'=\frac{3}{2}$ for the excited nucleon state; (ii) the observed variation of ρ suggests $\sigma_1\gg\sigma_2$ for $E_p=1$ Bev, $\sigma_2\gg\sigma_1$ for $E_p=2.3$ Bev. The variation (ii) is plausible if the $T'=\frac{3}{2}$ state is identified with the "resonance" appearing at about 0.2 Bev in π-nucleon scattering, as has been suggested from energy analysis of the produced mesons.[1] According to (ii) and Eq. (3), the relative π^0 production should also show a marked variation with energy: for low E_p, π^0 production exceeds the total charged π production; for high E_p, π^0 production is intermediate between π^+ and π^-.

The same model can be applied to calculation of various other production ratios. For example, in n-p collisions the ratio of (π^-,π^0) plus (π^-,π^+) production to single π^- production is $(5.6\sigma_2{}^s+4\sigma_2{}^a)/\sigma_1{}^s$. For neutrons in the 1–2 Bev range, this ratio is observed[3] to be of order 5, suggesting that $\sigma_2\sim\sigma_1$ for an average $\bar{E}_n\sim 1.5$ Bev. This is compatible with the conclusions from Be^9+p.

It is tempting to speculate on the existence of a further "excited state" of the nucleon with $T''=5/2$, which would decay to the ground state by emission of two mesons. It could not appear in π-nucleon scattering but would be associated with three- and four-meson production in a nucleon-nucleon collision. If the T'' state has a well-defined energy, the threshold for these processes may be high. We could, for example, compute ρ for a p-p collision involving $T''=5/2$ states. The cross sections concerned are $\sigma_3{}^s$ (excitation of one nucleon to $T'=\frac{3}{2}$, the other to $T''=5/2$) and $\sigma_4{}^s$ (excitation of both to $T''=5/2$). The meson production cross sections are

$$\begin{aligned}(\pi^+):&\quad (1/50)(78\sigma_3{}^s+76\sigma_4{}^s),\\ (\pi^0):&\quad (1/50)(39\sigma_3{}^s+88\sigma_4{}^s),\\ (\pi^-):&\quad (1/50)(33\sigma_3{}^s+36\sigma_4{}^s).\end{aligned}\tag{4}$$

Excitation of the $T''=5/2$ state gives a characteristic value $\rho\approx 2$, more or less independent of the ratio σ_3/σ_4. To (4) must of course be added to cross sections (1), which give $\rho>4$. Thus observation of $\rho<4$ would be indication of a $T''=5/2$ state.

The author wishes to thank Dr. Luke C. L. Yuan for stimulating discussions.

* Work supported by the research program of the U. S. Atomic Energy Commission.

[1] L. C. L. Yuan and S. J. Lindenbaum, Phys. Rev. **93**, 1431 (1954).
[2] L. C. L. Yuan (private communication).
[3] Fowler, Shutt, Thorndike, and Whittemore, Phys. Rev. (to be published).

Correction to Deuteron Stripping Cross Sections

LARRY SCHECTER* AND WARREN HECKROTTE
Radiation Laboratory, Department of Physics, University of California, Berkeley, California
(Received March 29, 1954)

THE cross section for stripping 190-Mev deuterons[1] in uranium has been redetermined by fitting the data of Schecter *et al.*[2] to new theoretical determinations of the differential cross sections. These theoretical curves were derived by including the Coulomb scattering of the emergent proton by the uranium nucleus, an effect previously neglected. The results show a significant broadening of the differential cross sections, which serve to depress the total cross section to a value only about half as great as that previously estimated. From thirteen measured proton yields at various angles and energies, as described above,[2] a new weighted mean cross section of 1.4 ± 0.2 barn was calculated. Since Coulomb scattering is negligible at these energies in the light elements, the stripping cross section of 0.35 ± 0.03 barn in beryllium or carbon is unaffected.

A further effect which has been neglected in these calculations is the diffraction of the emergent proton by the nucleus, which would tend to raise the cross section somewhat. The discrepancies between the measured values and those predicted by Serber have been previously discussed.[2]

This research was performed under the auspices of the U. S. Atomic Energy Commission.

* California Research and Development Company, Livermore, California.
[1] R. Serber, Phys. Rev. **72**, 1008 (1947).
[2] Schecter, Crandall, Millburn, Hicks, and Shelton, Phys. Rev. **90**, 633 (1953).

Some (d,ϕ) Reactions in Ni and the Statistical Theory of Nuclear Reactions*

WILLIAM W. PRATT
Department of Physics, State University of Iowa, Iowa City, Iowa
(Received March 22, 1954)

THE angular distributions of protons from (d,ϕ) reactions in Ni^{58} and Ni^{60} have been measured from 15° to 160° using a 3-Mev deuteron beam from the State University of Iowa electrostatic generator. The target was a 0.5-mg/cm² Ni foil. The protons were detected in 100 micron Eastman NTA nuclear track plates, and the proton energy was determined by range measurements in the emulsion.

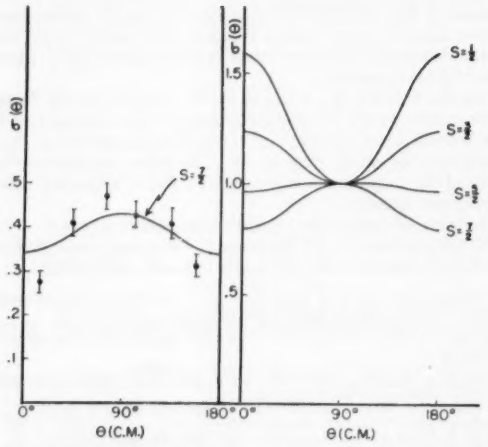

FIG. 2. Angular distribution of protons in the transition to the first excited state of Ni^{61}. The points are experimental points with statistical standard deviation. The solid curves are calculated from the statistical theory assuming the indicated values for the spin S of the final state.

Angular distributions were obtained for the proton groups corresponding to transitions to the ground state in Ni^{59}, to the first excited state in Ni^{61}, and to a third state which has not as yet been identified.[1] None of the angular distributions show any evidence of the forward peak characteristic of a stripping reaction,[2] and it has been found possible to interpret the data in terms of the statistical theory of Wolfenstein.[3]

The results, plotted on the same (arbitrary) scale, are shown in Figs. 1 to 3, together with curves calculated from the statistical theory. It has been assumed that the isotopes Ni^{58} and Ni^{60} with abundances of 68 percent and 26 percent respectively were responsible for these reactions, which were all of approximately equal intensity. Theoretical curves were calculated in each case assuming spin 0^+ for the (even-even) target nucleus and assuming spins $1/2^-$, $3/2^-$, $5/2^-$, $7/2^-$ for the final nucleus. The assumptions of spin 0^+ for the target nucleus and of odd parity for the first few levels of the final nucleus are all dictated by the shell model.[4] The deuteron and proton penetrabilities were calculated using

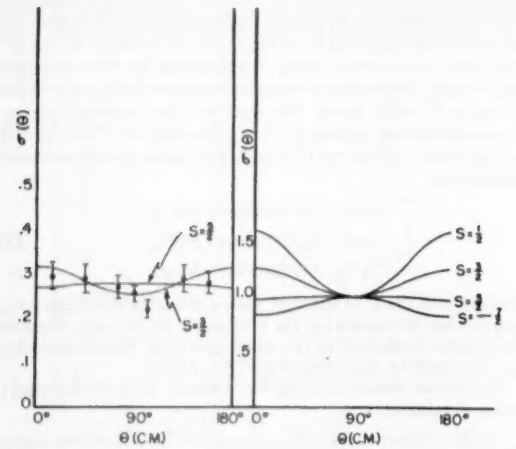

FIG. 1. Angular distribution of protons in the transition to the ground state of Ni^{59}. The points are experimental points with statistical standard deviation. The solid curves are calculated from the statistical theory assuming the indicated values for the spin S of the final state.

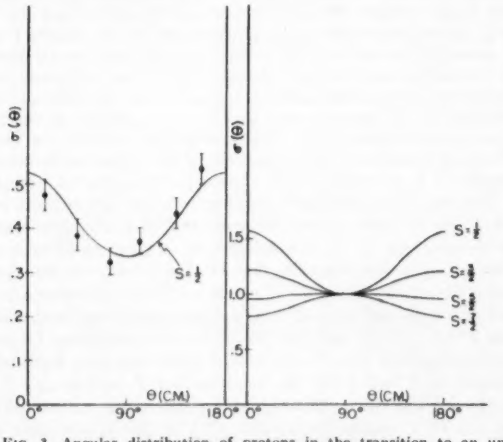

FIG. 3. Angular distribution of protons in the transition to an unidentified state in Ni^{59} or Ni^{61}. The points are experimental points with statistical standard deviation. The solid curves are calculated from the statistical theory assuming the indicated values for the spin S of the final state.

TABLE I. Experimental and theoretical values of the ratio $\sigma(0°)/\sigma(90°)$.

Final spin	$\left[\frac{\sigma(0°)}{\sigma(90°)}\right]_{\text{obs}}$	$\left[\frac{\sigma(0°)}{\sigma(90°)}\right]_{\text{s.p.e.}}$	$\left[\frac{\sigma(0°)}{\sigma(90°)}\right]_{\text{m.p.e.}}$
1/2	1.6	1.57	1.31
3/2	1.2	1.25	1.15
7/2	0.7	0.79	0.84

the W.K.B. approximation, and l values ≥ 3 for the deuterons and ≥ 6 for the protons were neglected. It is estimated that 90 percent of each reaction is due to l values within these limits.

In the case of the reaction $Ni^{58}(d,p)Ni^{59}$ (Fig. 1), the shell model predicts a state $3/2^-$ for the final nucleus. The results are seen to be in good agreement with this prediction, although they are not inconsistent with a final state of spin $5/2^-$. In the case of the reaction $Ni^{60}(d,p)Ni^{61}$* (Fig. 2), the shell model does not predict the spin, although since the lowest available levels are $P^{3/2}$, $f^{5/2}$, and $P^{1/2}$, an odd parity is strongly implied. The observed results are in reasonable agreement with a final state $7/2^-$, and are totally inconsistent with any of the other assumptions (an estimate of the theoretical curve for a $9/2^-$ final state indicates an approximately isotropic angular distribution). The third proton group (Fig. 3) corresponds to a transition to a level at 1.7 Mev in Ni^{59}, or at 1.3 Mev in Ni^{61}. The results are seen to be in excellent agreement with the theoretical results for a $1/2^-$ final state.

The theoretical curves in Figs. 1 to 3 have been calculated for single-particle excitation in the compound nucleus $[F(J)=1$ except for $F(0)=\frac{1}{2}$, in Wolfenstein's[3] Eq. (9)]. If the alternative assumption of multiple particle excitation $[F(J)=2J+1]$ is employed, the resulting angular distributions are somewhat more isotropic. Table I gives the ratio of the differential cross section at 0° to that at 90° as observed and as calculated from the alternative assumptions of single-particle excitation (s.p.e.) and multiple-particle excitation (m.p.e.). The assumption of single-particle excitation is seen to agree somewhat better with the observed results, but the difference is not completely definitive.

The results presented here appear to corroborate the statistical theory of Wolfenstein. We should like to point out that for reactions in which the theory is applicable and in which individual proton groups may be resolved, an analysis of angular distribution data in terms of the statistical theory may be expected to give significant information concerning the spins of the states involved.

* This work was supported in part by the U. S. Atomic Energy Commission.

[1] Additional work using separated isotopes is planned to settle this point among others.

[2] S. T. Butler, Proc. Roy. Soc. (London) **A208**, 559 (1951).
[3] L. Wolfenstein, Phys. Rev. **82**, 690 (1951).
[4] P. F. A. Klinkenberg, Revs. Modern Phys. **24**, 63 (1952).

Polarization of High-Energy Protons Scattered by Complex Nuclei*

S. TAMOR
Radiation Laboratory, University of California, Berkeley, California
(Received March 22, 1954)

WHEN a nucleon of several hundred Mev collides with a nucleus, there is no *a priori* reason to believe that the force it feels is the force exerted on low-energy particles as described, for example, by the shell model. However, it is interesting to attempt to describe the process in terms of elementary interactions with the individual nucleons. With the impulse approximation[1] one can indeed formulate such a scattering problem, provided the nucleon wave function is known. The lack of knowledge of detailed nuclear wave functions is what limits the applicability of such calculations to processes involving deuterons.

TABLE I. Percentage polarization for scattering of protons at various angles. θ is the scattering angle in the center of mass of the nucleon-nucleon system. Except for small relativistic effects this is twice the laboratory angle.

θ	Percent polarization p-d	p-α
30°	18%	43%
45°	35	79
60°	40	92

If one observes, however, that the entire dependence of the matrix element upon the nucleon wave function is contained in the "sticking factor" (overlap integral between the initial and final states), and that the polarization is essentially the ratio of two cross sections, then one is led to suspect that for nuclei possessing a sufficient degree of symmetry, the sticking factors cancel out and the polarization may be calculated without any knowledge of the nuclear wave function. It can be shown that the deuteron and all alpha-particle nuclei have this property. Furthermore on this model all alpha-particle nuclei should give the same polarization.

A method of constructing an S matrix for the scattering from a complex nuclei in terms of the n-p and p-p phase shifts has already been described.[2] Using the tensor force p-p phase shifts of Goldfarb and Feldman,[3] and the n-p phase shifts of Swanson,[4] polarizations have been calculated for incident protons of 240 Mev. The polarizations at various angles are given in Table I.

Note that the phase shifts used give qualitative agreement with the polarization effects found in nucleon-nucleon scattering. It is significant, then, that interference and spin-correlation effects work in such a way as to markedly increase the polarization, in agreement with recent experiments.[5]

It is tempting to generalize the above results, arguing that most light nuclei consist of an alpha-particle-like core plus a few excess nucleons, so that most of the scattering is from the alpha-particle core. On the basis of this picture one may argue that all nuclei of $4 \leq Z \leq 20$ should give about the same polarizations.

A more detailed paper will appear shortly.

* This work was performed under the auspices of the U. S. Atomic Energy Commission.

[1] G. F. Chew, Phys. Rev. **74**, 809 (1948).
[2] S. Tamor, Phys. Rev. **93**, 227 (1954).
[3] L. J. B. Goldfarb and D. Feldman, Phys. Rev. **88**, 1099 (1952).
[4] D. R. Swanson, Phys. Rev. **89**, 749 (1953).
[5] Oxley, Cartwright, Rouvina, Baskir, Klein, Ring, and Skillman, Phys. Rev. **91**, 419 (1953); Chamberlain, Segrè, Tripp, Wiegand, and Ypsilantis, Phys. Rev. **93**, 1430 (1954).

Polarization of Fast Protons Scattered by Nuclei*

G. TAKEDA AND K. M. WATSON
Department of Physics, University of Wisconsin, Madison, Wisconsin
(Received March 19, 1954)

THE polarization of high-energy protons scattered by nuclei has recently been reported.[1] According to the work of Marshall, Marshall, and de Carvalho,[1] the greater part of the polarized component of the scattered beam appears to be elastically scattered by the nucleus. The elastic scattering of fast particles by nuclei is often described using the "optical model";[2] however, it is clear that the simple optical model must be modified by spin-interactions if it is to lead to polarization. For instance, Fermi[3] has recently proposed adding to the optical model potential a spin-orbit interaction which is 15 times the "Thomas correction." This choice was motivated by the strength of the spin-orbit splitting supposed in the Mayer-Jensen shell model of nuclear structure.

In the present note, we wish to remark that a term similar to that suggested by Fermi can arise naturally in the Serber model of high-energy nuclear reactions. In the Serber model, one pictures a fast neutron or proton in a nucleus as scattering against individual nucleons as if they were essentially free. This permits one to describe the scattering by the nucleus in terms of the scattering by free nucleons. In contrast to this are the theories which suppose collective properties of the bound nucleons to

determine the characteristics of the interaction with an incoming particle.

To find the implications of the Serber model, let us first consider the scattering amplitude for proton-proton scattering, $(\mathbf{q}'|t|\mathbf{q})$, where $\mathbf{q}$ and $\mathbf{q}'$ are the respective initial and final relative moments. It will prove convenient to use the parametric representation of Wolfenstein and Ashkin[4] for $(\mathbf{q}'|t|\mathbf{q})$. This will permit us to express the polarization for nucleon-nucleon and nucleon-nucleus collisions in terms of the same set of parameters. Since the polarization appears to be large at small scattering angles[1] θ, we shall simplify the discussion by expanding t in powers of θ, keeping no more than the linear term. (The general expressions may be easily written down, but are too lengthy to give here.) Then

$$(\mathbf{q}'|t|\mathbf{q})=A_0+\boldsymbol{\sigma}_1\cdot\boldsymbol{\sigma}_2A_0'+(\boldsymbol{\sigma}_1+\boldsymbol{\sigma}_2)\cdot(\mathbf{q}'\times\mathbf{q}/q'q)A_1+\cdots, \quad (1)$$

where the A's are complex constants. The $\boldsymbol{\sigma}$'s are the proton spin operators. For n-p scattering a similar expression will obtain, the constants A being replaced by a new set of constants B, characteristic of the n-p interaction.

The optical model potential[5] is expressed in terms of t by

$$v_e=\frac{A}{V_A}\langle t\rangle\int_{V_A}\exp[-i(\mathbf{p}'-\mathbf{p})\cdot\mathbf{x}]d^3x, \quad (2)$$

where A is the mass number and V_A the volume of the nucleus. The integral is taken over the nuclear volume. Also $\mathbf{p}$ and $\mathbf{p}'$ are the initial and final momenta, respectively, of the scattered proton. By $\langle t\rangle$, we mean the average of t for the neutrons and protons in the nucleus, these being considered as "target particles." This average includes an average over their spins. To the extent that these spins are randomly oriented, terms linear in their spin operators tend to average to zero. If, for the sake of argument, we consider $\boldsymbol{\sigma}_2$ in Eq. (1) to refer to a nucleon in the nucleus, then we approximate $\langle t\rangle$ by setting equal to zero in Eq. (1) the terms linear in $\boldsymbol{\sigma}_2$. This gives

$$v_e=\frac{A}{V_A}\left[\bar{A}_0+\boldsymbol{\sigma}\cdot\left(\frac{\mathbf{q}'}{q'}\times\frac{\mathbf{q}}{q}\right)\bar{A}_1\right]\int_{V_A}\exp[-i(\mathbf{p}'-\mathbf{p})\cdot\mathbf{x}]d^3x, \quad (3)$$

where $\boldsymbol{\sigma}$ now is the spin operator of the bombarding proton. Here $\bar{A}_0$ and $\bar{A}_1$ represent the average of the amplitude of Eq. (1) for p-p and n-p collisions; i.e., $\bar{A}_0=A^{-1}[ZA_0+(A-Z)B_0]$, etc., where Z is the atomic number of the nucleus.

The polarization for p-p scattering is

$$P_{p\text{-}p}=\langle t^+\boldsymbol{\sigma}_1 t\rangle_{\text{spin}}/\langle t^+t\rangle_{\text{spin}} \quad (4)$$

$$\simeq 4\,\mathrm{Re}[(A_0+A_0')A_1^*]\sin\theta_{\text{lab}}/(|A_0|^2+3|A_0'|^2), \quad (5)$$

to first order in the laboratory scattering angle, θ_{lab}. By σ_1 we mean the component of $\boldsymbol{\sigma}_1$ in the direction $\mathbf{q}'\times\mathbf{q}$. The n-p polarization is obtained by replacing the A's by B's in Eq. (5).

We shall calculate the polarization for the scattering of a proton by the nucleus in the Born approximation, as did Fermi,[3] which does not seem unreasonable for the lighter nuclei. This is obtained by replacing t by v_e in Eq. (4):

$$P_{p\text{-nuc}}\simeq 4\,\mathrm{Re}[\bar{A}_0^*\bar{A}_1]\sin\theta_{\text{lab}}/|\bar{A}_0|^2. \quad (6)$$

The difference between Eqs. (5) and (6) has a simple origin. For the nucleon-nucleon scattering the *current densities* are averaged over spins. For scattering by a nucleus the *scattering amplitude* is averaged over the spins of the target nucleons.

There seem to be no very simple relations between Eqs. (5) and (6). Indeed, there are 12 real parameters at our disposal. To determine these, we have:

(1) $\mathrm{Im}(A_0)=-v\sigma_{p\text{-}p}/2(2\pi)^2$, where v is the relative velocity of the colliding protons and $\sigma_{p\text{-}p}$ is their total cross section[6] [there is a similar expression for $\mathrm{Im}(B_0)$];

(2) the scattering cross sections in the forward direction;

(3) the $\mathrm{Re}[v_e]$;[6,7]

(4) $P_{p\text{-}p}$, $P_{p\text{-}n}$, and $P_{p\text{-nuc}}$.

We have verified by direct computation that it is possible to fit these eight data (to the extent that they are known) by a considerable range of choices of the twelve available parameters.

On the other hand, more elaborate observations of nucleon-nucleon polarization may eventually provide sufficient information concerning the scattering amplitudes to permit a test of Eq. (6). This equation may also be used as a test of specific models of nucleon-nucleon scattering if the Serber model is accepted.

We finally conclude that the observed[1] polarization does not at present seem in disagreement with the Serber model.

We should like to thank Professor M. Gell-Mann for a stimulating conversation concerning this problem.

* Supported in part by the U. S. Atomic Energy Commission.

[1] Oxley, Cartwright, Rouvina, Baskir, Klein, Ring, and Skillman, Phys. Rev. **91**, 419 (1953); Marshall, Marshall, and de Carvalho, Phys. Rev. **93**, 1431 (1954); Chamberlain, Segrè, Tripp, Wiegand, and Ypsilantis, Phys. Rev. **93**, 1430 (1954).

[2] Fernbach, Serber, and Taylor, Phys. Rev. **75**, 1352 (1949).

[3] E. Fermi, Nuovo cimento **11**, 407 (1954).

[4] L. Wolfenstein and J. Ashkin, Phys. Rev. **85**, 947 (1952).

[5] K. M. Watson, Phys. Rev. **89**, 575 (1953) and N. C. Francis and K. M. Watson, Phys. Rev. **92**, 291 (1953). The application of the optical model in this case is quite straightforward, it being necessary of course to use properly antisymmetrized (in charge and ordinary space) wave functions in evaluating the nucleon-nucleon scattering amplitudes t. In this connection we might clarify a statement made in the second reference above in the paragraph following Eq. (20). It was stated that the discussion of the optical model applied for nucleons when "exchange scattering" is negligible. This did not mean exchange effects for the two-nucleon scattering amplitudes, but rather some additional exchange corrections (which are expected to be small at high energies) due to the nuclear binding. We plan to publish a quantitative analysis of this point in the near future.

[6] T. B. Taylor, Phys. Rev. **92**, 831 (1953).

[7] R. Jastrow, Phys. Rev. **82**, 261 (1951).

Neutron Absorption Cross Section of U^{235} at 2200 m/sec*

H. Palevsky, R. S. Carter, R. M. Eisberg, and D. J. Hughes
Brookhaven National Laboratory, Upton, New York

(Received March 25, 1954)

THE total cross section of U^{235} for neutrons in the thermal energy region has been measured by means of a transmission experiment. The neutron velocity was determined by a time-of-flight method utilizing the Brookhaven slow chopper. The absorption cross section at a neutron velocity of 2200 m/sec was found to be 691 ± 5 barns.

The slow chopper is an instrument that allows a burst of pile neutrons to pass periodically to a detector several meters distant.[1] The velocity of the neutron is determined by measuring the time of flight of the neutron to the detector (an enriched BF_3 counter). The flight time is measured electronically, the standard being a one-megacycle quartz crystal. The major uncertainty in the time-of-flight measurement is the determination of the zero time, i.e., the time the neutrons pass through the shutter. This time is determined by a calibration procedure using the c-axis lattice spacing in graphite (6.70A) measured by x-ray spectrometer techniques. The calibration is accurate to 0.25 percent of the wavelength setting.[2] The transmission of the U^{235} sample for the timed neutrons is obtained by measuring the detector counting rate with the sample in and out of the beam. Background counting rates on these two measurements are obtained by inserting a 0.010-in. Cd foil in the beam. The U^{235} sample in the beam is placed in good geometry with respect to the detector; consequently the transmission is related to the total cross section by the expression

$$T(\lambda)=\exp[-x\ \Sigma_i N_i\sigma_i(\lambda)],$$

where $T(\lambda)$ = transmission of sample at neutron wavelength λ, x = sample thickness, N_i = No. atoms/unit volume of isotope i, and $\sigma_i(\lambda)$ = total neutron cross section at wavelength λ of isotope i.

Measurements were made on five samples of uranium metal, principally U^{235} and U^{238} having various isotopic abundances and thicknesses. In the thermal region the samples of high enrichment of U^{235} are best suited for an accurate determination of the absorp-

tion cross section, in order to reduce the importance of the correction due to the scattering cross section of U^{238}. The partially enriched samples were measured as a check on the possibility of a systematic error due to the analysis of the sample. A comparison of the U^{235} cross section obtained from the partially enriched samples to that obtained from the highly enriched samples was made in the neutron wavelength region beyond the Bragg cutoff of uranium ($\lambda > 4.8$A), where the coherent scattering disappears. Thick and thin samples of high enrichment were measured to see if there was any possibility of a systematic error due to sample thickness. A comparison of these samples was made at neutron wavelengths greater than 4A because the high transmission of the thin sample at thermal energy would result in large statistical errors in the cross section. The results obtained from the five samples were internally consistent to within the statistical uncertainties of the various measurements.

The measured total cross section was corrected, as is indicated above, for the absorption cross section due to the U^{234} and U^{236} in the foil. The average scattering cross section for U^{235} can be estimated from the known scattering cross section of U^{238}. This cross section is taken to be $\sigma_{sc}(U^{235}) = 9$ barns. Upon subtracting the scattering cross section from the measured total cross section of U^{235} at 2200 m/sec, we obtain for the absorption cross section of U^{235} at 2200 m/sec the value 691 ± 5 barns. This is considerably larger than the earlier value of 650 barns.[5]

* Work carried out under contract with the U. S. Atomic Energy Commission.

[1] Seidl, Palevsky, Randall, and Thorne, Phys. Rev. **82**, 345 (1951).
[2] Carter, Palevsky, Myers, and Hughes, Phys. Rev. **92**, 716 (1953).
[3] *Neutron Cross Sections*, Atomic Energy Commission Report AECU 2040 (Technical Information Service, Department of Commerce, Washington, D. C., 1952).

Covariant Formulation of the Tamm-Dancoff Method

S. S. Schweber*
Laboratory of Nuclear Studies, Cornell University, Ithaca, New York
(Received April 1, 1954)

WE have succeeded in formulating the three-dimensional Tamm-Dancoff[1] method in field theory in a covariant form, which permits renormalization in the same way as in the Bethe-Salpeter[2] formalism. We here briefly indicate the treatment of the two-nucleon problem in scalar meson theory, reserving for a future publication a detailed presentation of the method, including a discussion of higher approximations.

The amplitudes which describe the two-nucleon system are defined as follows:

$$f_\tau(x,y) = (\Psi_0(\tau), N(\psi(x)\psi(y))\Psi(\tau)),$$
$$f_\tau(x,y;z_1) = (\Psi_0(\tau), N(\psi(x)\psi(y)\phi(z_1))\Psi(\tau)),$$
$$f_\tau(x,y;z_1z_2) = (\Psi_0(\tau), N(\psi(x)\psi(y)\phi(z_1)\phi(z_2))\Psi(\tau)), \text{ etc.}, \quad (1)$$

where all the quantities on the right-hand side of the above equations are defined in the interaction representation (I.R.). $\Psi_0(\tau)$ is the interacting vacuum state vector of the two-particle system. The symbol N denotes the fact that the normal product of the operators, as defined by Wick,[3] has to be taken. These amplitudes are related to the new Tamm-Dancoff amplitudes recently defined by Dyson.[4] In particular, the two-nucleon amplitude, $f_\tau(x,y)$, satisfies a free Dirac equation in each of its variables, if the space-time points, x and y, are not fixed on the space-like surface τ, since $\psi(x)$ and $\psi(y)$ are I.R. operators. However, if x and y are fixed on the surface τ (denoted by $x/\tau, y/\tau$), then $f(x/\tau, y/\tau)$ is identically equal to the equal-time Bethe-Salpeter two-nucleon amplitude as defined by Gell-Mann and Low,[5] and has the following dependence on the particle coordinates:

$$f(x/\tau, y/\tau) = \chi(\mathbf{x}-\mathbf{y})e^{i\mathbf{P}\cdot(\mathbf{x}+\mathbf{y})}e^{-iEt}, \quad (2)$$

where E and $\mathbf{P}$ are, respectively, the energy and momentum of the state $\Psi(\tau)$, and t is the "time" of τ. (We have taken the energy and momentum of the vacuum state, E_0 and $\mathbf{P}_0$, to be zero.)

In order to derive the equation of motion of the amplitudes in the lowest approximation, which only retains $f_\tau(x,y)$ and $f_\tau(x,y;z)$ in the description of the state, we use the Schrödinger equation

$$\{H_0(\tau)+H_I(\tau)\}\begin{Bmatrix}\Psi_0(\tau)\\ \Psi(\tau)\end{Bmatrix} = \begin{Bmatrix}E_0\Psi_0(\tau)\\ E\Psi(\tau)\end{Bmatrix},$$
$$H_I(\tau) = G\int_\tau d\sigma(x) N(\bar{\psi}(x)\gamma(x)\psi(x)\phi(x)), \quad (3)$$

to derive the following equation for $f(x/\tau, y/\tau)$:

$$\{(E-E_0)-(\alpha\cdot p+\beta M)_a-(\alpha\cdot p+\beta M)_b\}f(x/\tau;y/\tau)$$
$$= (\Psi_0(\tau), [N(\psi(x)\psi(y)), H_I(\tau)]\Psi(\tau))_{x/\tau,\, y/\tau}$$
$$= G(\gamma_0\gamma(x))_a f(x/\tau, y/\tau; x/\tau) + G(\gamma_0\gamma(y))_b f(x/\tau, y/\tau; y/\tau). \quad (4)$$

The three-particle amplitudes occurring on the right-hand side of (4) are evaluated using time-dependent methods. As we are concerned only with the bound state problem, we require for consistency that the integration from $-\infty$ to τ of the three-particle amplitude, i.e.,

$$f_\tau(x,y;z) = -\frac{i}{\hbar c}\int_{-\infty}^{\tau} d\tau' \times (\Psi_0(\tau'), [N(\psi(x)\psi(y)\phi(z), H_I(\tau')]\Psi(\tau')) \quad (5a)$$

yield the same result as if integrated from $+\infty$ to τ; that is, we also have

$$f_\tau(x,y;z) = \frac{i}{\hbar c}\int_{\tau}^{\infty} d\tau' \times (\Psi_0(\tau'), [N(\psi(x)\psi(y)\phi(z), H_I(\tau')]\Psi(\tau')). \quad (5b)$$

In practice, we actually integrate the positive frequency components of $f(x/\tau, y/\tau; z/\tau)$ from $-\infty$ to τ, and the negative frequencies from $+\infty$ to τ. The commutator on the right-hand side of (5) can easily be evaluated and rewritten in terms of normal products of operators using a general theorem due to Dyson.[6] If all the couplings to states other than to the two-nucleon one are neglected, one obtains the following expression for $f_\tau(x,y;z)$, for x/τ, y/τ, z/τ:

$$f(x/\tau, y/\tau; z/\tau) = G\int_{-\infty}^{+\infty} d^4x' \{(S_F(x-x')\gamma(x'))_a \times \Delta_F(z-x') f_{\tau'}(x'/\tau, y/\tau) + (S_F(y-x')\gamma(x'))_b \times \Delta_F(z-x') f_{\tau'}(y/\tau, x'/\tau')\}. \quad (6)$$

In this last equation the point y/τ and x/τ can be propagated to τ' according to the laws of free particle propagation. This expression can now be substituted in the right-hand side of (4) and yields an equation quite analogous to the Bethe-Salpeter equation in the ladder approximation, when the latter is written in a Breit-sum form [i.e., $\Sigma_{j=a,b}(-i\gamma^\mu\partial_\mu + M)_j$], rather than in a product form [$\Pi_{j=a,b}(-i\gamma^\mu\partial_\mu + M)_j$]. As the kernels which appear in the self-energy terms are of the standard S-matrix form, they can be renormalized as in the Bethe-Salpeter equation. The three-dimensional momentum space form of the equation is identical with the two-nucleon equation recently derived by Dyson.[7] The spurious divergences that appear in it can be eliminated using his new, as yet unpublished, method of incorporating the boundary condition that the vacuum is the state of lowest energy.

We should like to acknowledge a stimulating discussion with Dr. A. Klein.

* National Science Foundation postdoctoral fellow.
[1] I. Tamm, J. Phys. U.S.S.R. **9**, 449 (1945); S. M. Dancoff, Phys. Rev. **78**, 382 (1950).
[2] E. E. Salpeter and H. A. Bethe, Phys. Rev. **84**, 1232 (1951).
[3] G. C. Wick, Phys. Rev. **80**, 268 (1950).
[4] F. J. Dyson, Phys. Rev. **90**, 994 (1953).
[5] M. Gell-Mann and F. Low, Phys. Rev. **84**, 350 (1951).
[6] F. J. Dyson, Phys. Rev. **82**, 428 (1951).
[7] F. J. Dyson, Phys. Rev. **91**, 1543 (1953).